Physics of Atomic Nuclei, Vol. 64, No. 5, 2001, pp. 787–801. From Yadernaya Fizika, Vol. 64, No. 5, 2001, pp. 851–865.

Floquet Theory of Neutrino Oscillations in the Earth*

E. Kh. Akhmedov[1), **]

Centro de Física das Interacções Fundamentais (CFIF), Departamento de Física, Instituto Superior Técnico, Av. Rovisco Pais, 1, P-1049 Lisboa, Portugal

Received August 16, 2000

Abstract—We review the Floquet theory of linear differential equations with periodic coefficients and discuss its applications to neutrino oscillations in matter of periodically varying density. In particular, we consider a parametric resonance in neutrino oscillations that is possible in such media and discuss its implications for the oscillations of neutrinos traversing the Earth and passing through the Earth's core.

1. INTRODUCTION

All oscillating systems are very much alike, and there are many similarities between oscillating neutrinos and, for example, pendulums or electromagnetic circuits. In particular, neutrino oscillations in a vacuum or in matter of constant density are analogous to oscillations of a simple pendulum; resonantly enhanced neutrino oscillations in a medium of monotonically varying density, Mikheev–Smirnov–Wolfenstein (MSW) effect [1, 2], are similar to oscillations of two weakly coupled pendulums of slowly changing lengths [3, 4]. It is therefore natural to address the question of whether there are any other resonance phenomena in mechanics or electromagnetism that might have an analog in neutrino physics.

One such phenomenon is a parametric resonance. A parametric resonance can occur in dynamical systems with time-varying parameters if there is a certain correlation between these variations and the values of the parameters themselves. A parametric resonance in systems with periodically varying parameters has been best understood. Periodicity makes it easier to satisfy resonance conditions and also simplifies the relevant analysis, but it is not really necessary: parametric resonance can occur even in stochastic systems (see, for example, [5]). In the present paper, we will concentrate on systems with periodically varying parameters.

A textbook example of a system in which a parametric resonance can occur is a pendulum with a vertically oscillating point of support [6, 7]. Under certain conditions, the topmost, normally unstable, equilibrium point becomes stable. The pendulum can oscillate about this point in the upside-down position. Another example, familiar to everybody, is a swing, which is just a pendulum with periodically changing effective length. It is the parametric resonance that makes it possible to rock a swing.

What would be an analog of the parametric resonance for neutrino systems? Since matter affects neutrino oscillations, periodically varying conditions can be achieved if a beam of oscillating neutrinos propagates through a medium with a periodically modulated density. If certain relations between the period and amplitude of the density modulation and the neutrino oscillation length and mixing angle hold, a parametric resonance occurs, with the result that the oscillations can be strongly enhanced. The probability of a neutrino transition from one flavor state to another may become equal to unity. This phenomenon is very different from the MSW effect. Indeed, at the MSW resonance, the neutrino mixing in matter becomes maximal ($\theta_m = \pi/4$) even if the vacuum mixing angle θ_0 is small. As a result, there arise large-amplitude neutrino oscillations in a medium of constant density equal (or almost equal) to the resonance density or a strong flavor conversion in the case of the medium density slowly varying along the neutrino path and passing through the resonance value.

The situation is quite different in the case of a parametric resonance. In general, the mixing angle in matter does not become large (there is no level crossing). What really happens is an amplification of the transition probability because of specific phase relationships. Thus, in the case of a parametric resonance, it is the phase of oscillations (rather than their amplitude) that undergoes an important modification.

*This article was submitted by the author in English.

[1)]On leave of absence from Russian Research Centre Kurchatov Institute, pl. Kurchatova 1, Moscow, 123182 Russia.

[**]e-mail: akhmedov@cfif.ist.utl.pt

The total flavor conversion can occur even if the mixing angles are small both in a vacuum and in matter.

The possibility of a parametric resonance in neutrino oscillations was suggested independently in [8] and in [9]. Approximate solutions for a sinusoidal matter-density profile were found in those studies. An exact analytic solution for a periodic step-function ("castle wall") density profile was also obtained in [9]. Parametric effects in neutrino oscillations were further studied by Krastev and Smirnov [10], who considered the concerted effect of parametric and MSW resonances and their possible implications for solar and supernova neutrinos. A stochastic parametric resonance in neutrino oscillations was also briefly discussed in that study.

Although a parametric resonance in neutrino oscillations is certainly an interesting physics phenomenon, it requires that very special conditions be satisfied. Unfortunately, these conditions cannot be created in laboratory experiments, because this would require either an overly long baseline or neutrino propagation in a medium of overly high density. Until recently, it was also unclear whether there exists a natural object where these conditions can be satisfied for any known source of neutrinos. This situation changed upon the very important observation by Liu and Smirnov [11] (see also [12]), who showed that the parametric-resonance conditions can be approximately satisfied for the oscillations of atmospheric ν_μ into sterile neutrinos ν_s within the Earth. The density profile along the trajectories of neutrinos traversing the Earth and passing through its core (mantle–core–mantle) is, to a good approximation, a piece of a periodic step-function profile, and their oscillations can be parametrically enhanced. Even though the neutrino travels only 1.5 periods of density modulations (this would be exactly one period and a half if the distances that the neutrinos traverse in the mantle and in the core were equal), the parametric effects on neutrino oscillations in the Earth can be quite strong. Subsequently, it was pointed out in [13] that, in the case of ν_e–$\nu_{\mu(\tau)}$ mixing, the parametric-resonance conditions can also be satisfied (and even to a better accuracy) for $\nu_2 \leftrightarrow \nu_e$ oscillations in the Earth. This, in particular, may have important implications for the solar-neutrino problem. The parametric resonance in the oscillations of solar and atmospheric neutrinos in the Earth was further explored in a number of papers [14–20].

In the present paper, we review the Floquet theory of linear differential equations with periodic coefficients and consider its applications to neutrino oscillations and, in particular, to oscillations of neutrinos within the Earth. The paper is organized as follows. In Section 2, we briefly review Floquet theory and its applications to the analyses of the stability of solutions. In Section 3, we discuss the special features of Floquet theory in the case of time-dependent Schrödinger equations with periodic Hamiltonians. In Section 4, we consider applications of Floquet theory to neutrino oscillations in a medium of periodic step-function (castle wall) density profile. In Section 5, we review the implications of the parametric resonance in neutrino oscillations for neutrinos traversing the Earth and passing through its core. In the last section, the results are discussed and conclusions are drawn.

2. DIFFERENTIAL EQUATIONS WITH PERIODIC COEFFICIENTS

Now, we will briefly review the Floquet theory of sets of linear differential equations with periodic coefficients. A more detailed discussion can be found, for example, in [7, 21].

2.1. Preliminaries

Let us start with a few well-known facts from the general theory of linear differential equations. We consider a set of n homogeneous linear differential equations

$$\dot{\psi} = \mathcal{A}(t)\psi, \tag{1}$$

where ψ is an n-component column vector, $\psi = (\psi_1, ..., \psi_n)^T$; $\mathcal{A}(t)$ is an $n \times n$ matrix with piecewise continuous elements; and an overdot denotes differentiation with respect to t. Equation (1) has n linearly independent continuous nontrivial solutions $\psi^{(j)}(t)$, $j = 1, ..., n$. From the linearity of (1), it follows that any linear combination of solutions is also a solution. Any set of n linearly independent solutions $\psi^{(j)}(t)$ to Eq. (1) forms a so-called fundamental set, and a matrix whose columns are $\psi^{(j)}$ is referred to as a fundamental matrix. Given an initial condition $\psi(t_0) = \psi_0$, Eq. (1) has a unique solution $\psi(t)$. Any solution to Eq. (1) can be represented as a linear combination (with constant coefficients) of solutions that form a fundamental set, or equivalently as a product of a fundamental matrix and a constant vector.

Let $\psi(t)$ be the solution of (1) with the initial condition $\psi(t_0) = \psi_0$. Let us introduce the evolution matrix $U(t, t_0)$ through the relation

$$\psi(t) = U(t, t_0)\psi_0\,. \tag{2}$$

From the definition of the evolution matrix, it immediately follows that

$$U(t, t_0) = U(t, t_1)U(t_1, t_0), \qquad U(t_0, t_0) = I, \tag{3}$$

where I is the $n \times n$ identity matrix. It is easy to check that the columns of $U(t, t_0)$ are solutions to Eq. (1)

with initial conditions $\psi_i^{(j)}(0) = \delta_{ij}$. Thus, $U(t, t_0)$ is a fundamental matrix, and any solution to Eq. (1) can be written in the form (2). The determinant of $U(t, t_0)$ is given by

$$\det[U(t, t_0)] = \exp\left\{\int_{t_0}^{t} \mathrm{tr}[\mathcal{A}(t')]\, dt'\right\}. \quad (4)$$

Equation (4) follows from two facts. (i) The derivative of the determinant is the sum of n determinants obtained by replacing the elements of one row of the original matrix by their derivatives. (ii) The columns of $U(t, t_0)$ are solutions to Eq. (1). Since the elements of $\mathcal{A}$ are nonsingular, $\det[U]$ does not vanish; that is, the matrix $U(t, t_0)$ is nonsingular. From (3), one finds

$$U(t_2, t_1)^{-1} = U(t_1, t_2). \quad (5)$$

Without loss of generality, one can always choose the matrix $\mathcal{A}(t)$ to be traceless. Indeed, the substitution

$$\psi(t) = e^{\alpha(t)}\psi'(t), \quad \alpha(t) = \frac{1}{n}\int^{t} \mathrm{tr}[\mathcal{A}(t')]\, dt' \quad (6)$$

yields

$$\dot{\psi}' = \mathcal{A}'(t)\psi', \qquad \mathcal{A}'(t) = \mathcal{A}(t) - \frac{1}{n}\mathrm{tr}[\mathcal{A}(t)], \quad (7)$$

whence it follows that $\mathcal{A}'$ is traceless. Hereafter, we will always assume that the transformation in (6) has been performed; that is, we will consider only traceless matrices $\mathcal{A}$. Equation (4) then reduces to

$$\det[U(t, t_0)] = 1. \quad (8)$$

Notice that, in general, $U(t, t_0)$ is not unitary.

2.2. Floquet Theory

Let us now address the case of the differential Eqs. (1) with periodic coefficients,

$$\mathcal{A}(t + T) = \mathcal{A}(t), \quad (9)$$

where T is the period. Hereafter, we will always assume that the condition in (9) is satisfied, without specifying this each time explicitly. From the periodicity of $\mathcal{A}(t)$, it follows that, if $\psi(t)$ is a solution to Eq. (1), so is $\psi(t + T)$. Let us consider the solution $\psi(t)$ with initial condition $\psi(s) = \psi_0$. We have $\psi(t + T) = U(t + T, s)\psi_0$. On the other hand, we have $\psi(t + T) = U(t, t_0)\psi(t_0 + T) = U(t, t_0)U(t_0 + T, s)\psi_0$, since $\psi(t + T)$ is also a solution at t. Equating these two expressions for $\psi(t + T)$, one obtains

$$U(t + T, s) = U(t, t_0)U(t_0 + T, s). \quad (10)$$

This is a very important property of the evolution matrix for the differential Eq. (1) with periodic coefficients. Setting $s = t_0 + T$ and $s = t_0 = 0$, one finds from (10) that

$$U(t + T, t_0 + T) = U(t, t_0), \quad (11)$$

$$U(t + T, 0) = U(t, 0)\, U(T, 0). \quad (12)$$

The first of these equations means that the evolution matrix does not change if both its arguments are shifted by the period T (and, by induction, by any integer number k of the periods). From the second equality, it follows, in particular, that the matrix of evolution over k periods satisfies the equation

$$U(kT, 0) = U(T, 0)^k. \quad (13)$$

The matrix of evolution over one period, $U(T, 0) \equiv U_T$, plays a very important role in the theory of differential equations with periodic coefficients; it is referred to as a monodromy matrix.

It was indicated above that, if $\psi(t)$ is a solution to Eq. (1), so is $\psi(t + T)$. In general, this does not mean that $\psi(t + T) = \psi(t)$; that is, solutions to equations with periodic coefficients are not in general periodic. There are, however, solutions that satisfy the condition

$$\psi(t + T) = \sigma\psi(t); \quad (14)$$

that is, they are multiplied by a number when t is shifted by the period. Such solutions are referred to as normal; they play an important role in the analysis of stability of solutions to Eq. (1).

To analyze the properties of normal solutions, let us show that the evolution matrix for the system of linear differential Eqs. (1) with periodic coefficients can be written as the product of a periodic matrix and an exponential matrix. Since the monodromy matrix U_T is nonsingular, it can be represented as an exponential of another matrix:

$$U_T \equiv U(T, 0) = e^{\mathcal{B}T}. \quad (15)$$

Let us now show that the matrix $P(t) = U(t, 0)e^{-\mathcal{B}t}$ is periodic. We have $P(t + T) = U(t + T, 0) \times e^{-\mathcal{B}(t+T)} = U(t, 0)U(T, 0)e^{-\mathcal{B}T}e^{-\mathcal{B}t} = U(t, 0)e^{-\mathcal{B}t} = P(t)$, where we have used (12) and (15). Thus, the evolution matrix can be written as

$$U(t, 0) = P(t)e^{\mathcal{B}t}, \qquad P(t + T) = P(t). \quad (16)$$

From this expression, it follows, in particular, that the vector χ introduced through the relation $\psi = P(t)\chi$ satisfies a differential equation with constant coefficients,

$$\dot{\chi} = \mathcal{B}\chi. \quad (17)$$

Let $\phi_0^{(j)}$ be a (constant) eigenvector of the matrix $\mathcal{B}$ with the eigenvalue $\alpha_j T^{-1}$. It is then also an eigenvector of U_T with the eigenvalue $\sigma_j = e^{\alpha_j}$:

$$\mathcal{B}\phi_0^{(j)} = \frac{\alpha_j}{T}\phi_0^{(j)}; \quad U_T\phi_0^{(j)} = \sigma_j\phi_0^{(j)} = e^{\alpha_j}\phi_0^{(j)}. \quad (18)$$

It is common practice to refer to the numbers σ_j as characteristic numbers and to α_j as characteristic exponents. From (12), (16), and (18), it follows that

any normal solution $\phi^{(j)}(t)$ to Eq. (1) can be written as

$$\phi^{(j)}(t) = U(t,0)\phi_0^{(j)} = P(t)e^{\alpha_j(t/T)}\phi_0^{(j)} \qquad (19)$$
$$= P(t)\sigma_j^{t/T}\phi_0^{(j)}.$$

Thus, the eigenvectors of U_T give rise to normal solutions. The monodromy matrix U_T has n eigenvalues. As follows from (8), they satisfy

$$\prod_{j=1}^{n}\sigma_j = 1. \qquad (20)$$

If all the eigenvalues σ_j are different, U_T has n linearly independent eigenvectors; therefore, there are n linearly independent normal solutions $\phi^{(j)}(t)$ to the set of Eqs. (1). Hence, they form a fundamental set, and any solution to (1) can be written as a linear combination of the normal solutions $\phi^{(j)}(t)$ with constant coefficients. If U_T has repeated eigenvalues, there arises a more complicated situation, which will be discussed below.

It follows from Eq. (19) that the characteristic exponents (or characteristic numbers) determine the boundedness of normal solutions and, therefore, of a general solution to Eq. (1). By way of example, we now consider the case of $n = 2$. We first assume that the characteristic exponents are real. The characteristic numbers σ_1 and σ_2 are then real too. Equation (20) gives $\sigma_1\sigma_2 = 1$; if $\sigma_1 \neq \sigma_2$ (that is, they are simple eigenvalues of U_T), the absolute value of one of them is greater than one. It then follows from Eq. (19) that the corresponding normal solution is unbounded. If the characteristic exponents are pure imaginary, the characteristic numbers are of modulus one—that is, $\sigma_1 = \sigma_2^*$ and $|\sigma_1| = 1$. In this case, both normal solutions are bounded [the matrix $P(t)$ in (19), being continuous and periodic, is obviously bounded]. If the characteristic exponents are complex, normal solutions are bounded when the real parts of all characteristic exponents are nonpositive, while there are unbounded normal solutions if at least one of the characteristic exponents has a positive real part. This property holds in general—that is, for arbitrary n.

Let us now discuss the case of repeated eigenvalues of U_T. We again consider the case of $n = 2$ and assume that the eigenvalues of U_T coincide, $\sigma_1 = \sigma_2 \equiv \sigma$. In this case, the matrix U_T has the general form [2)]

$$U_T = \begin{pmatrix} \sigma & 0 \\ a & \sigma \end{pmatrix}. \qquad (21)$$

[2)]Another possibility would be to have zero element $(U_T)_{21}$ instead of $(U_T)_{12}$, but the corresponding matrix can be reduced to that in (21) by renumbering basis states.

It can readily be seen that, at $a = 0$, the monodromy matrix U_T has two linearly independent and orthogonal eigenvectors corresponding to the same eigenvalue σ; they can be taken, for example, to be $\phi_0^{(1)} = (0,1)^T$ and $\phi_0^{(2)} = (1,0)^T$. For $a \neq 0$, however, there is only one eigenvector, $\phi_0^{(1)}$. It gives rise to a normal solution $\phi^{(1)}(t)$ through Eq. (19). This normal solution can be used as one of the basis solutions $\psi^{(j)}(t)$ constituting a fundamental set, $\psi^{(1)}(t) = \phi^{(1)}(t)$. Let $\psi^{(2)}(t)$ be another solution to Eq. (1), linearly independent of $\psi^{(1)}(t)$; $\psi^{(1)}(t)$ and $\psi^{(2)}(t)$ then form a fundamental set. Since $\psi^{(j)}(t+T)$ are also solutions, they can be written as linear combinations of $\psi^{(1)}(t)$ and $\psi^{(2)}(t)$:

$$\psi^{(1)}(t+T) = \sigma\psi^{(1)}(t),$$
$$\psi^{(2)}(t+T) = a'\psi^{(1)}(t) + b'\psi^{(2)}(t). \qquad (22)$$

Using arbitrariness in the normalization of the vectors $\phi_0^{(j)}$, one can always set $a' = a$. Since σ is a double root of the characteristic equation of the monodromy matrix U_T, $b' = \sigma$. [3)] Equations (22) can therefore be rewritten as

$$\psi^{(1)}(t+T) = \sigma\psi^{(1)}(t), \qquad (23)$$
$$\psi^{(2)}(t+T) = a\psi^{(1)}(t) + \sigma\psi^{(2)}(t). \qquad (24)$$

Let us introduce a matrix M that relates $\psi_0^{(2)}$ and $\psi_0^{(1)} \equiv \phi_0^{(1)}$: $\psi_0^{(2)} = M\psi_0^{(1)}$.[4)] One can now find the relation between $\psi^{(2)}(t)$ and $\psi^{(1)}(t)$:

$$\psi^{(2)}(t) = W(t)\psi^{(1)}(t), \qquad (25)$$
$$W(t) = U(t,0)MU(t,0)^{-1}.$$

Therefore, we have $\psi^{(2)}(t+T) = W(t+T)\psi^{(1)}(t+T) = W(t+T)\sigma\psi^{(1)}(t)$. On the other hand, it follows from (24) and (25) that $\psi^{(2)}(t+T) = a\psi^{(1)}(t) + \sigma\psi^{(2)}(t) = [a + \sigma W(t)]\psi^{(1)}(t)$. Equating these two expressions for $\psi^{(2)}(t+T)$, one finds

$$W(t+T) = W(t) + a/\sigma. \qquad (26)$$

Therefore, the matrix $F(t)$ defined through

$$F(t) = W(t) - \frac{a}{\sigma}\frac{t}{T} \qquad (27)$$

is periodic with the period T. From Eqs. (25) and (27), we then find

$$\psi^{(2)}(t) = \left[\frac{a}{\sigma}\frac{t}{T} + F(t)\right]\psi^{(1)}(t), \qquad (28)$$

[3)]An easy way to see this is to consider Eqs. (22) at $t = 0$ and use the explicit form (21) of the matrix U_T.

[4)]The matrix M is not uniquely defined, but this is immaterial for our purposes.

$$F(t+T) = F(t).$$

This is the result we sought. Together with Eq. (23), it states that, in the case of double roots of the characteristic equation of U_T (that is, in the case of coinciding characteristic exponents), a fundamental set can be chosen to consist of a normal solution and a solution that is a linear combination of linearly growing and periodic functions multiplied by a normal solution. Thus, we conclude that, if $a \neq 0$, there are unbounded solutions. It follows from (28) that, if $a = 0$, then $\psi^{(2)}(t)$, being the product of a periodic matrix and a normal solution, is also a normal solution. It follows that, in this case, both solutions forming a fundamental set can be chosen to be normal. This is in accord with the fact that, for $a = 0$, the matrix U_T in Eq. (21) has two linearly independent eigenvectors.

It is instructive to see how the linear growth of $\psi^{(2)}(t)$ arises from the general expression $\psi^{(2)}(t) = P(t)e^{\mathcal{B}t}\psi_0^{(2)}$. From (15) and (21), one finds

$$\mathcal{B}T = \ln U_T = \ln[\sigma(I+\Delta)] \tag{29}$$
$$= \ln\sigma + \ln(I+\Delta) = \ln\sigma + \Delta - \frac{\Delta^2}{2} + \frac{\Delta^3}{3} - ...,$$

where

$$\Delta = \begin{pmatrix} 0 & 0 \\ a/\sigma & 0 \end{pmatrix}.$$

Since $\Delta^2 = 0$, Eq. (29) gives $\mathcal{B}T = \ln\sigma + \Delta$; hence,

$$e^{\mathcal{B}t} = \sigma^{t/T}e^{\Delta(t/T)} = \sigma^{t/T}\left(I + \frac{t}{T}\Delta\right). \tag{30}$$

Notice that the matrix Δ annihilates $\phi_0^{(1)}$; therefore, (30) does not contradict $\psi^{(1)}(t)$ being a normal solution. Using Eq. (30), one can find that the matrix $F(t)$ entering into Eq. (28) has the simple representation

$$F(t) = P(t)MP(t)^{-1}, \tag{31}$$

from which the periodicity of $F(t)$ is obvious.

The above result can be generalized to the case of $n > 2$. If the characteristic equation of the monodromy matrix U_T has repeated roots (that is, some of the characteristic numbers coincide), a fundamental set can be chosen to consist of normal solutions and solutions that are linear combinations of polynomials in t and periodic matrices multiplied by normal solutions.

We have seen that, in the case where some of the characteristic exponents have positive real parts, there are exponentially growing solutions, while, if some of the characteristic exponents coincide, there are in general polynomially growing solutions. The existence of such unbounded solutions signifies instabilities due to a parametric resonance.

It should be noted that, instead of considering the set of n first-order linear equations (1) with periodic coefficients, one could equivalently consider one equation of order n. By way of example, we indicate that, in the case of $n = 2$, a general second-order equation with periodic coefficients is obtained, which is referred to as the Hill equation. A pendulum with a vertically oscillating point of support mentioned in the Introduction is described by this equation. If the oscillations of the point of support are harmonic, the pendulum is described by the well-known Mathieu equation. In the limit of small-amplitude oscillations of the point of support, the instability condition (the condition of an exponential growth of the deviation from equilibrium) is [6, 7]

$$\Omega \equiv \frac{2\pi}{T} = \frac{2\omega}{k}, \tag{32}$$

where ω is the frequency of the oscillations of the pendulum in the absence of motion of its point of support and k is an integer. Equation (32) relates the frequency Ω of the oscillations of the point of support at which the parametric resonance occurs to the oscillator eigenfrequency. When the amplitude of the oscillations of the point of support is not small, the parametric-resonance condition generally depends not only on the frequency of these oscillations but also on their amplitude. In this case, there are resonance regions of parameters rather than resonance values [7, 21].

In real physical systems, all parameters are of course finite; unboundedness of certain solutions to Eq. (1) with periodic coefficients just reflects the fact that, in general, the dynamics of real systems is only approximately described by linear equations. For large deviations from equilibrium, nonlinear effects become important, so that Eq. (1) must be modified. There are, however, cases where solutions are always bounded even in the linear regime, in which case a description in terms of linear equations can be exact. Nevertheless, a parametric resonance is possible in such systems as well. One example of such a situation is given by Schrödinger equations with periodic Hamiltonians (we will discuss this example in the next section).

3. SCHRÖDINGER EQUATIONS WITH PERIODIC HAMILTONIANS

If the matrix $\mathcal{A}(t)$ in Eq. (1) is anti-Hermitian, the set of Eqs. (1) and (9) can be written as a Schrödinger equation with a periodic Hermitian Hamiltonian,

$$i\dot{\psi} = \mathcal{H}(t)\psi, \qquad \mathcal{H}(t)^\dagger = \mathcal{H}(t), \tag{33}$$
$$\mathcal{H}(t+T) = \mathcal{H}(t),$$

where $\mathcal{H}(t) = i\mathcal{A}(t)$. In the case of constant $\mathcal{H}$, Eq. (33) describes oscillations between the components of ψ characterized by $n-1$ (in general, different) frequencies (of n eigenvalues of $\mathcal{H}$, only $n-1$ are independent since $\mathrm{tr}\mathcal{H} = 0$). In particular, spin precession in a constant magnetic field or neutrino oscillations in a vacuum or in matter of constant density are described by such an equation. Equation (33), with time-dependent periodic Hamiltonians, describes many physical systems—for example, atoms in a laser field or electron paramagnetic resonance. It also describes neutrino oscillations in a medium of periodically modulated density.

Because of the Hermiticity of $\mathcal{H}(t)$, the evolution matrix $U(t, t_0)$ of Eq. (33) is unitary; that is, the norm of the vector ψ is conserved. Therefore, all solutions to Eq. (33) are bounded. In view of this, the parametric resonance in the systems described by Eq. (33) has some special features, which we will discuss below.

One consequence of the unitarity of the evolution matrix $U(t, t_0)$ is that all characteristic exponents are pure imaginary. In addition, we note that, since a polynomial growth of solutions is not allowed in this case, there are, even in the case of repeated roots of the characteristic equations of the monodromy matrix U_T, n linearly independent normal solutions that form a fundamental set. Actually, this is a direct corollary of the fact that a unitary $n \times n$ matrix has exactly n linearly independent eigenvectors, irrespective of whether (or not) all roots of its characteristic equations are simple.

We will now discuss the general properties of solutions to Eq. (33), again considering the case of $n = 2$ as an example. The results will be applied, in particular, to the problem of two-flavor neutrino oscillations in a medium of periodically modulated density.

Let us start with a few general remarks about solutions of the Schrödinger equation with a time-dependent (but not necessarily periodic) Hamiltonian in the case of $n = 2$. First, we notice that, without loss of generality, the Hamiltonian $\mathcal{H}(t)$ can be considered to be real. Indeed, in the case of a complex Hamiltonian, the rephasing of the components $\psi_{1,2}$ of ψ by the factors $\exp(\pm i\beta(t)/2)$, where $\beta(t) = \arg[\mathcal{H}_{12}(t)]$, reduces the Hamiltonian to the form

$$\mathcal{H}(t) = \begin{pmatrix} -A(t) & B(t) \\ B(t) & A(t) \end{pmatrix} \tag{34}$$

with real $A(t)$ and $B(t)$. Notice that this rephasing transformation preserves the trace of the Hamiltonian.

Next, we notice that the Hamiltonian $\mathcal{H}(t)$ in (34) can be written as

$$\mathcal{H}(t) = B(t)\sigma_1 - A(t)\sigma_3, \tag{35}$$

where σ_i are the Pauli matrices. Thus, $\mathcal{H}(t)$ anticommutes with σ_2. From this fact, it immediately follows that, if $\psi(t) = (\psi_1(t), \psi_2(t))^T$ is a solution to the Schrödinger equation, so is $\tilde{\psi}(t) = -i\sigma_2\psi(t)^* = (-\psi_2(t)^*, \psi_1(t)^*)^T$. It is easy to see that $\psi(t)$ and $\tilde{\psi}(t)$ are orthogonal and are therefore linearly independent. Thus, we see that, if one nontrivial solution to the Schrödinger equation for the case of $n = 2$ is known, it automatically gives another nontrivial solution, linearly independent of the original one. The solutions ψ and $\tilde{\psi}$ form a fundamental set; therefore, knowledge of a single nontrivial solution to the Schrödinger equation allows one to obtain a general solution.

We now proceed to the study the Schrödinger equation with periodic coefficients in the case of $n = 2$. Since the monodromy matrix $U_T = \exp(\mathcal{B}T)$ is a unitary 2×2 matrix, it can be written as

$$U_T = Y - i\boldsymbol{\sigma}\cdot\mathbf{X} = \exp[-i(\boldsymbol{\sigma}\cdot\hat{\mathbf{X}})\Phi] \tag{36}$$

with real parameters $\mathbf{X}$ and Y (or $\hat{\mathbf{X}}$ and Φ),[5] which satisfy the relations

$$Y^2 + \mathbf{X}^2 = 1, \qquad \cos\Phi = Y, \qquad \sin\Phi = |\mathbf{X}|; \qquad \hat{\mathbf{X}} \equiv \mathbf{X}/|\mathbf{X}|. \tag{37}$$

It should be noted that the form of the monodromy matrix in Eq. (36) is quite general; that is, it does not depend on the particular form of the functional dependence of $A(t)$ and $B(t)$, whereas the values of the parameters Y and $\mathbf{X} = \{X_1, X_2, X_3\}$ (or Φ and $\hat{\mathbf{X}} = \{\hat{X}_1, \hat{X}_2, \hat{X}_3\}$) are of course determined by this functional dependence. Using (16), one can represent the evolution matrix as

$$U(t, 0) = P(t)e^{-i(\boldsymbol{\sigma}\cdot\hat{\mathbf{X}})\Phi\,(t/T)}, \qquad P(t+T) = P(t). \tag{38}$$

The matrix of evolution over an integer number of periods is

$$U(kT, 0) = (U_T)^k = \exp[-i(\boldsymbol{\sigma}\cdot\hat{\mathbf{X}})k\Phi]. \tag{39}$$

From Eqs. (15) and (36), we obtain

$$\mathcal{B}T = -i(\boldsymbol{\sigma}\cdot\hat{\mathbf{X}})\Phi. \tag{40}$$

Since $\hat{\mathbf{X}}$ is a unit vector, the eigenvalues of the matrix $\boldsymbol{\sigma}\cdot\hat{\mathbf{X}}$ are ± 1; hence, the characteristic exponents $\alpha_{1,2}$ are pure imaginary, and the characteristic numbers $\sigma_{1,2}$ are of modulus one:

$$\alpha_{1,2} = \pm i\Phi, \qquad \sigma_{1,2} = e^{\pm i\Phi}. \tag{41}$$

[5] That these parameters are real can be proven on the basis of the relation $\sigma_2 U(t, t_0)^* \sigma_2 = U(t, t_0)$, which in turn is obtained from the following properties of the Hamiltonian: $\mathcal{H}(t)^* = \mathcal{H}(t)$ and $\{\mathcal{H}(t), \sigma_2\} = 0$.

Let us find normal solutions. The eigenvectors $\phi_0^{(1,2)}$ of the monodromy matrix coincide with the eigenvectors of the matrix $\boldsymbol{\sigma}\cdot\hat{\mathbf{X}}$; they can be written as

$$\phi_0^{(1)} = \frac{1}{\sqrt{2}}\begin{pmatrix} \sqrt{1+\hat{X}_3} \\ \sqrt{1-\hat{X}_3}\, e^{i\delta} \end{pmatrix}, \qquad (42)$$

$$\phi_0^{(2)} = \frac{1}{\sqrt{2}}\begin{pmatrix} -\sqrt{1-\hat{X}_3}\, e^{-i\delta} \\ \sqrt{1+\hat{X}_3} \end{pmatrix},$$

where

$$\delta = \arg(\hat{X}_1 + i\hat{X}_2). \qquad (43)$$

Notice that $\phi_0^{(2)} = \tilde{\phi}_0^{(1)} \equiv -i\sigma_2(\phi_0^{(1)})^*$. Normal solutions are now found as $\phi^{(1,2)}(t) = U(t,0)\phi_0^{(1,2)}$, which yields

$$\phi^{(1)}(t) = P(t)e^{-i\Phi(t/T)}\phi_0^{(1)}, \qquad (44)$$
$$\phi^{(2)}(t) = P(t)e^{i\Phi(t/T)}\phi_0^{(2)}.$$

They form a fundamental set. This means that an arbitrary solution $\psi(t)$ can be represented as a linear combination of $\phi^{(2)}(t)$ and $\phi^{(1)}(t)$ with constant coefficients:

$$\psi(t) = P(t)[C_1\, e^{-i\Phi(t/T)}\phi_0^{(1)} + C_2\, e^{i\Phi(t/T)}\phi_0^{(2)}]. \qquad (45)$$

The normal solutions (44) are the products of periodic functions with periods T and $\tau = (2\pi/\Phi)T$. Thus, the general solution (45) describes modulated oscillations between the components of $\psi(t)$—the parametric oscillations [20].

Let us now discuss the parametric resonance in the system under consideration. In the general case of Eq. (1), the parametric resonance typically corresponds to situations where a solution becomes unbounded; that is, there are some values of t for which the modulus of a component of ψ can exceed any preset number, however large. A characteristic feature of the parametric resonance is that this can happen even for an arbitrarily small amplitude of variations of the coefficients in Eq. (1).

In the case of systems described by Eq. (33), the parametric resonance corresponds to a situation where there exist values of t such that the modulus of a component of a solution can reach a maximum value that is allowed by unitarity, but which is unattainable in the case of the corresponding equation with constant coefficients. This can happen even for an arbitrarily small amplitude of variations of the coefficients in Eq. (33). Notice that the parametric resonance is undefined in the cases where Eq. (33) with constant coefficients itself leads to maximal amplitude oscillations.

To be more specific, we will consider the case of $n = 2$. If the Hamiltonian of the system were constant, the Schrödinger equation (33) would describe oscillations between the components of ψ with frequency $\omega_0 = \sqrt{A^2+B^2}$ and amplitude $\sin^2 2\theta_0 = B^2/(A^2+B^2)$. If $A \neq 0$, this amplitude is always less than unity. We will now consider the case of time-dependent A and B, but we will assume that $A(t)$ never vanishes over the period of evolution of interest.[6)] The transition probability in the quasi-time-independent (adiabatic) regime then never exceeds $\max\{B(t)^2/(A(t)^2+B(t)^2)\} < 1$. The parametric resonance occurs when there are values of t such that the modulus of a component of ψ that was initially equal to zero can reach a maximum value that is allowed by unitarity and which corresponds to the transition probability equal to one. This can happen even if $\max\{B(t)^2/(A(t)^2+B(t)^2)\} \ll 1$ and for arbitrarily small amplitudes of time variations of $A(t)$ and $B(t)$.

Let us find the parametric-resonance condition. We assume that the initial state at $t = 0$ is $\psi_0 = (1,0)^T$. At $t = kT$, we then have

$$\psi(kT) = U(kT,0)\psi_0 \qquad (46)$$
$$= \begin{pmatrix} \cos k\Phi - i\hat{X}_3 \sin k\Phi \\ -ie^{-i\delta}\sqrt{1-\hat{X}_3^2}\sin k\Phi \end{pmatrix}.$$

We will now show that the parametric-resonance condition is [14]

$$\hat{X}_3 = 0. \qquad (47)$$

Indeed, the transition probability reaches the maximum possible value, equal to one, when the survival probability $|\psi_1(t)|^2$ vanishes. From (46), one has $\psi_1(t = kT) = \cos k\Phi$ for $\hat{X}_3 = 0$. The component $\psi_1(t)$ at $t = (k+1)T$ is $\cos(k+1)\Phi$. It is easy to see that, for an arbitrary nonzero value of Φ, there is a value of k for which $\cos k\Phi \leq 0$ and $\cos(k+1)\Phi > 0$, or vice versa. Since all solutions to Eq. (33) with regular coefficients are continuous, this means that there is a value t_1, $kT \leq t_1 < (k+1)T$, for which $\psi_1(t_1) = 0$ and the survival probability vanishes; that is, the component ψ_2 saturates the unitarity limit. Thus, Eq. (47) is the parametric-resonance condition.

[6)] In the case of neutrino oscillations in a vacuum, the condition $A = 0$ corresponds to maximum mixing, while, for neutrino oscillations in a medium of varying density, $A(t) = 0$ corresponds to the MSW resonance.

4. NEUTRINO OSCILLATIONS IN MATTER WITH A CASTLE-WALL DENSITY PROFILE

We will now consider applications of Floquet theory, reviewed in the preceding sections, to neutrino oscillations in a medium of periodically modulated density. In particular, we will address the problem of a parametric resonance in neutrino oscillations.

Let us examine oscillations in a two-flavor neutrino system. The evolution of the system in the flavor-eigenstate basis is described by the Schrödinger equation with Hamiltonian (34), in which the parameters A and B are given by

$$A(t) = \frac{\Delta m^2}{4E}\cos 2\theta_0 - \frac{G_\mathrm{F}}{\sqrt{2}}N(t),$$
$$B = \frac{\Delta m^2}{4E}\sin 2\theta_0, \tag{48}$$

where G_F is the Fermi constant, E is the neutrino energy, $\Delta m^2 = m_2^2 - m_1^2$ ($m_{1,2}$ are the neutrino-mass eigenvalues), and θ_0 is the mixing angle in a vacuum. The effective density $N(t)$ depends on the type of the neutrinos involved in the oscillations:

$$N = \begin{cases} N_e & \text{for } \nu_e \leftrightarrow \nu_{\mu,\tau} \\ 0 & \text{for } \nu_\mu \leftrightarrow \nu_\tau \\ N_e - N_n/2 & \text{for } \nu_e \leftrightarrow \nu_s \\ -N_n/2 & \text{for } \nu_{\mu,\tau} \leftrightarrow \nu_s. \end{cases} \tag{49}$$

Here, N_e and N_n are the electron- and neutron-number density, respectively. For transitions between antineutrinos, one should substitute $-N$ for N in Eq. (4). If the overall matter density or the chemical composition varies along the neutrino path, the effective density N depends on the neutrino coordinate t. The instantaneous oscillation length $l_m(t)$ and the mixing angle $\theta_m(t)$ in matter are given by

$$l_m(t) = \pi/\omega(t), \qquad \sin 2\theta_m(t) = B/\omega(t), \tag{50}$$
$$\omega(t) \equiv \sqrt{B^2 + A(t)^2}.$$

The MSW resonance corresponds to $A(t_\mathrm{res}) = 0$ and $\sin 2\theta_m(t_\mathrm{res}) = 1$.

For a parametric resonance to occur, the specific shape of the matter-density profile is not very important, but it is necessary that the change in the density be synchronized in a certain way with the change in the oscillation phase. In particular, a sinusoidal density profile was considered in [8, 9], in which case the equation describing the evolution of neutrinos reduces to a modified Mathieu equation. In [9], the parametric resonance was also considered for neutrino oscillations in a medium with a periodic step-function density profile, which allows a very simple exact analytic solution. This solution was studied in detail in [14, 20]. Here, we will review this solution and its main features.

Let us consider the case where the effective density $N(t)$ [and, therefore, $A(t)$] is a periodic step function,

$$N(t) = \begin{cases} N_1 \text{ for } 0 \le t < T_1 \\ N_2 \text{ for } T_1 \le t < T_1 + T_2, \end{cases} \tag{51}$$
$$N(t+T) = N(t), \quad T = T_1 + T_2.$$

Here, N_1 and N_2 are constants. It will be referred to as the castle-wall density profile. The function $A(t)$ is given by a similar formula with constants A_1 and A_2. Thus, the Hamiltonian $\mathcal{H}(t)$ is also a periodic function of time with period T. We denote

$$\delta = \frac{\Delta m^2}{4E}, \qquad V_i = \frac{G_\mathrm{F}}{\sqrt{2}}N_i \qquad (i = 1,\ 2). \tag{52}$$

In this notation,

$$A_i = \cos 2\theta_0\,\delta - V_i, \qquad B = \sin 2\theta_0\,\delta, \tag{53}$$
$$\omega_i = \sqrt{(\cos 2\theta_0\,\delta - V_i)^2 + (\sin 2\theta_0\,\delta)^2}.$$

Any instant of time in the evolution of the neutrino system belongs to one of the two kinds of time intervals:

$$0 + nT \le t < T_1 + nT; \tag{54}$$
$$T_1 + nT \le t < T_1 + T_2 + nT, \quad n = 0,\ 1,\ 2, \ldots .$$

In either case, the Hamiltonian $\mathcal{H}$ is a constant matrix ($\mathcal{H}_1$ and $\mathcal{H}_2$, respectively). We define the evolution matrices for the time intervals $(0, T_1)$ and $(T_1, T_1 + T_2)$ as

$$U_1 = \exp(-i\mathcal{H}_1 T_1), \qquad U_2 = \exp(-i\mathcal{H}_2 T_2). \tag{55}$$

The monodromy matrix is then given by

$$U_T = U_2 U_1. \tag{56}$$

Let us introduce the unit vectors

$$\mathbf{n}_1 = \frac{1}{\omega_1}(B,\ 0,\ -A_1) = (\sin 2\theta_1,\ 0,\ -\cos 2\theta_1),$$
$$\mathbf{n}_2 = \frac{1}{\omega_2}(B,\ 0,\ -A_2) = (\sin 2\theta_2,\ 0,\ -\cos 2\theta_2), \tag{57}$$

where $\theta_{1,2}$ are the mixing angles in matter at densities N_1 and N_2: $\theta_1 = \theta_m(N_1)$ and $\theta_2 = \theta_m(N_2)$. One can then write

$$\mathcal{H}_i = \omega_i(\boldsymbol{\sigma}\cdot\mathbf{n}_i). \tag{58}$$

Using Eqs. (55)–(58), one can obtain the monodromy matrix in the form (36) with the parameters Y and $\mathbf{X}$ given by

$$Y = c_1 c_2 - (\mathbf{n_1}\cdot\mathbf{n_2})s_1 s_2, \tag{59}$$

$$\mathbf{X} = s_1 c_2\,\mathbf{n}_1 + s_2 c_1\,\mathbf{n}_2 - s_1 s_2\,(\mathbf{n}_1 \times \mathbf{n}_2), \tag{60}$$

where

$$s_i = \sin\phi_i, \quad c_i = \cos\phi_i, \quad \phi_i = \omega_i T_i \quad (i = 1,\ 2). \tag{61}$$

Notice that the difference of the neutrino eigenenergies in a medium of density N_i is $2\omega_i$, so that $2\phi_1$ and $2\phi_2$ are the oscillation phases acquired over the intervals T_1 and T_2. The evolution matrix for k periods ($k = 0, 1, 2, ...$) is given by Eq. (39).

In terms of the components, the vector $\mathbf{X}$ can be written as

$$\begin{aligned}\mathbf{X} = \{&s_1 c_2 \sin 2\theta_1 + s_2 c_1 \sin 2\theta_2 \\ &- s_1 s_2 \sin(2\theta_1 - 2\theta_2) \\ &- (s_1 c_2 \cos 2\theta_1 + s_2 c_1 \cos 2\theta_2)\}\,.\end{aligned} \tag{62}$$

Equations (36)–(39) and (59)–(4) provide an exact solution to the evolution equation for any instant of time that is an integral multiple of the period T. In order to obtain the corresponding solution for $kT < t < (k+1)T$, one has to evolve the solution at $t = kT$ by applying the evolution matrix

$$U_1(t,\ kT) = \exp[-i\mathcal{H}_1(t - kT)] \tag{63}$$

for $kT < t < kT + T_1$ or

$$\begin{aligned}&U_2(t,\ kT + T_1)U_1 \\ &= \exp[-i\mathcal{H}_2(t - kT - T_1)]\exp[-i\mathcal{H}_1 T_1]\end{aligned} \tag{64}$$

for $kT + T_1 \le t < (k+1)T$, with $\mathcal{H}_{1,2}$ given by Eq. (58).

4.1. Parametric Resonance

Let us assume that the initial neutrino state at $t = 0$ is a flavor eigenstate ν_a. The probability of finding another flavor eigenstate ν_b at an instant $t > 0$ (transition probability) is then $P(\nu_a \to \nu_b,\ t) = |U_{21}(t, 0)|^2$. As was pointed out in Section 3, the evolution of a neutrino system in a medium of periodically varying density has the character of parametric oscillations—modulated oscillations characterized by two periods, T and $\tau = (2\pi/\Phi)T$. As can be seen from Eq. (46), the transition probability after k periods of the density modulation is [14]

$$\begin{aligned}P(\nu_a \to \nu_b,\ t = kT) &= (1 - \hat{X}_3^2)\sin^2\Phi_p, \\ \Phi_p &= k\Phi,\end{aligned} \tag{65}$$

where Φ was defined in (37). This expression is valid for any periodic matter-density profile, irrespective of its shape. Obviously, $\hat{X}_3$ and Φ depend on this shape. For neutrino oscillations in the castle-wall density profile, Eq. (65) corresponds to the evolution over an even number of layers of constant density. After passing an odd number of alternating layers, which can be considered as k periods plus one additional layer of density N_1 (the corresponding evolution time $t = kT + T_1$), the transition probability is also given by Eq. (65), the only difference being that the phase is now [20]

$$\Phi_p = k\Phi + \varphi, \tag{66}$$

where

$$\begin{aligned}\sin\varphi &= s_1 \sin 2\theta_1 / \sqrt{1 - \hat{X}_3^2}, \\ \cos\varphi &= (s_1 \sin 2\theta_1 Y + s_2 \sin 2\theta_2)/\sqrt{\mathbf{X}^2 - X_3^2}.\end{aligned} \tag{67}$$

Equations (65)–(67) give the transition probability at the borders of the layers.

The parametric resonance occurs when the depth of the parametric oscillations described by Eq. (65) becomes equal to unity—that is, when $\hat{X}_3 = 0$. This coincides with condition (47), which was found in Section 3. In the case of the castle-wall density profile under consideration, it takes the form [14] [see Eq. (4)]

$$X_3 \equiv -(s_1 c_2 \cos 2\theta_1 + s_2 c_1 \cos 2\theta_2) = 0. \tag{68}$$

As follows from (65), the maximum transition probability of $P = 1$ can be achieved at the borders of the layers, provided that

$$\Phi_p = \frac{\pi}{2} + n\pi, \qquad n = 0, 1, 2, ... \tag{69}$$

The parametric-resonance condition (68) can be realized in two different ways. One possibility is that both terms on the right-hand side of Eq. (68) vanish. This requires $c_1 = c_2 = 0$ [8–14] or[7)]

$$\begin{aligned}\phi_1 = \frac{\pi}{2} + k'\pi, \qquad \phi_2 = \frac{\pi}{2} + k''\pi, \\ k', k'' = 0, 1, 2, ...\end{aligned} \tag{70}$$

In this case, the other option, $s_1 = s_2 = 0$, leads to the trivial case of $\mathbf{X} = 0$ and $Y = \pm 1$, in which the monodromy matrix coincides (apart from the sign) with the identity matrix, with the result that the transition probability at the borders of the layers vanishes.[8)] The other possible realization of the parametric-resonance condition is that where neither of the terms on the right-hand side of Eq. (68) vanishes, but where they exactly cancel each other.

We will now consider the realization (70) of the parametric-resonance condition (68). The second realization will be illustrated below by a numerical example. At the resonance, the transition probability for

[7)] In [8–10], these conditions were derived for the particular case of $k' = k''$, which includes the most important principal resonance with $k' = k'' = 0$.

[8)] We do not consider the trivial cases of the MSW resonance, for which $X_3 = 0$ because $\cos 2\theta_i = 0$ and $s_i = \pm 1$, $i = 1$ or 2, or $\cos 2\theta_1 = \cos 2\theta_2 = 0$. These cases correspond to $A(t_{\rm res}) = 0$.

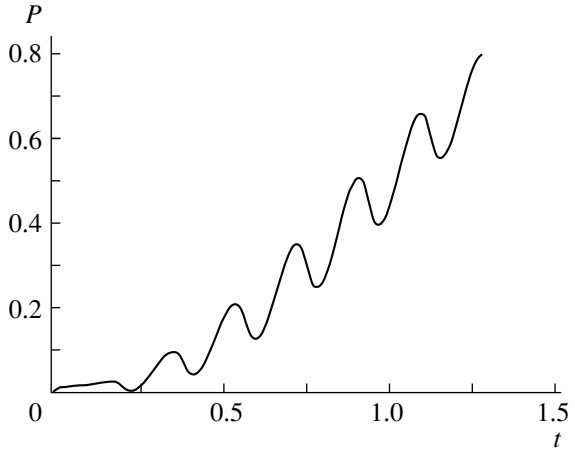

Fig. 1. Coordinate dependence of the neutrino-flavor-transition probability P in a medium with the castle-wall density profile [$\sin^2 2\theta_0 = 0.01$, $\delta = 10^{-12}$ eV, $V_1 = 10^{-13}$ eV, $V_2 = 6.33 \times 10^{-13}$ eV, $T_1 = 5.4 \times 10^{-2}$, and $T_2 = 0.1296$ (all distances are in units of $R = 3.23 \times 10^{13}$ eV^{-1})].

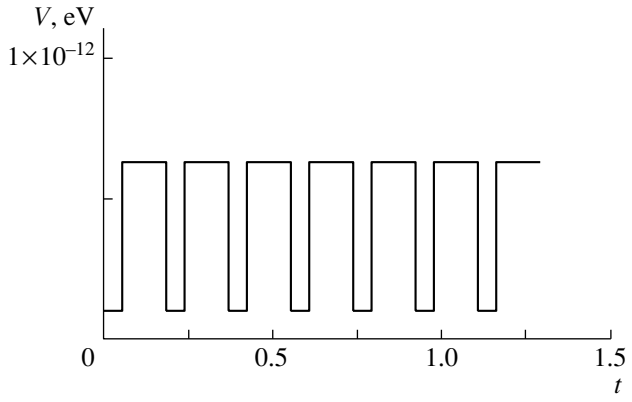

Fig. 2. Coordinate dependence of the matter-induced neutrino potential [$G_F/\sqrt{2} \times$ (density profile)] for the case shown in Fig. 1.

the evolution over k periods of the density modulation takes the simple form

$$P(\nu_a \to \nu_b,\ t = kT) = \sin^2[k(2\theta_2 - 2\theta_1)]. \quad (71)$$

Let us first assume that the densities N_1 and N_2 are either both below the MSW resonance density $N_{\rm MSW}$, which is determined by the relation $G_F N_{\rm MSW}/\sqrt{2} = \cos 2\theta_0\, \delta$, or both above it. This means that the mixing angles in matter, $\theta_{1,2}$, satisfy the inequalities $\theta_{1,2} < \pi/4$ or $\theta_{1,2} > \pi/4$. It is easy to see that, in this case, the difference $2\theta_2 - 2\theta_1$ is always farther away from $\pi/2$ than either $2\theta_1$ or $2\theta_2$. In this case, the transition probability for evolution over one period cannot therefore exceed the maximal transition probabilities in matter of constant density equal to either N_1 or N_2 ($\sin^2 2\theta_1$ or $\sin^2 2\theta_2$). However, the parametric resonance leads to an important gain. In a medium of constant density N_i, the transition probability can never exceed $\sin^2 2\theta_i$, irrespective of the distance that neutrinos travel. In a medium with the castle-wall density profile, the situation is different: if the parametric-resonance conditions (70) are satisfied, the transition probability can become large, provided that neutrinos travel a sufficiently large distance. It can be seen from (71) that the transition probability can become quite sizeable even for small $\sin^2 2\theta_1$ and $\sin^2 2\theta_2$—that is, for small $\max\{B^2/(A(t)^2 + B^2)\}$ in terms of the parameters of the Hamiltonian in (34). This is illustrated in Figs. 1 and 3 for the case of $N_1, N_2 < N_{\rm MSW}$ (the corresponding matter-induced neutrino potentials are shown in Figs. 2 and 4). In the case of $N_1, N_2 > N_{\rm MSW}$, the transition probability behaves similarly. The number of periods that neutrinos have to pass in order to experience a complete (or almost complete) conversion is

$$k \simeq \frac{\pi}{4(\theta_1 - \theta_2)}. \quad (72)$$

It is instructive to consider the limit of small density variations, $|N_1 - N_2| \ll N_1$. In terms of a pendulum with a vertically oscillating point of support, it corresponds to the limit of the small amplitude of these vertical oscillations. In this limit, $\theta_1 \simeq \theta_2$ and Eq. (68) reduces to $\sin(\phi_1 + \phi_2) = 0$ ($\phi_1 + \phi_2 = k\pi$). Since $\phi_i = \omega_i T_i$, this condition can be written as

$$\Omega \equiv \frac{2\pi}{T} = \frac{2\omega}{k}, \quad \text{where} \quad \omega \equiv \omega_1 \frac{T_1}{T} + \omega_2 \frac{T_2}{T}. \quad (73)$$

This coincides with the familiar parametric-resonance condition in the case of small-amplitude variations of the parameter of the system [see Eq. (32)]. It is important to note that the condition in (73) does not depend on the amplitude $N_1 - N_2$ of the density modulation. This illustrates the point that we emphasized in Section 3—a parametric resonance can occur even for an arbitrarily small amplitude of variations of the parameters of the system. Of course, the smaller this amplitude, the longer the evolution time for the total conversion.

Let us now consider the case of $N_1 < N_{\rm MSW} < N_2$ ($\theta_1 < \pi/4 < \theta_2$). The transition probability over n periods at the parametric resonance is again given by Eq. (71). In this case, however, one has $\sin^2(2\theta_2 - 2\theta_1) > \sin^2 2\theta_1, \sin^2 2\theta_2$ for $\theta_2 > \pi/4 + \theta_1/2$ (which is always satisfied for small mixing in matter). This means that, even for the time interval equal to one period of the matter-density modulation, the transition probability exceeds the maximal probabilities of oscillations in matter of constant densities N_1 and

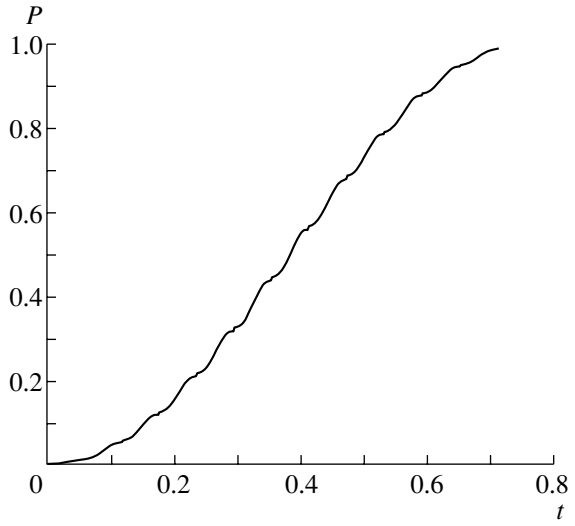

Fig. 3. As in Fig. 1, but for $\delta = 10^{-12}$ eV, $V_2 = 10^{-11}$ eV, $T_1 = 5.4 \times 10^{-2}$, and $T_2 = 5.4 \times 10^{-3}$.

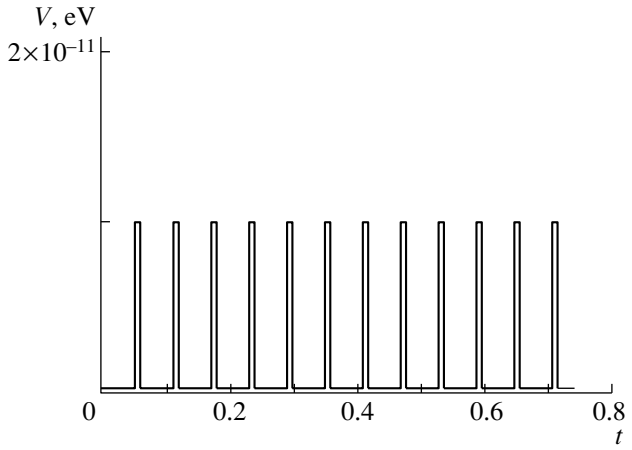

Fig. 4. Coordinate dependence of the matter-induced neutrino potential for the case shown in Fig. 3.

N_2. The case of $N_1 < N_{\rm MSW} < N_2$ is illustrated in Figs. 5–7.

Figures 3 and 4 illustrate the importance of the phase relationships in the case of a parametric resonance. In these figures, the coordinate dependence of the transition probability and the matter-density profile are shown for a specific case in which conditions (70) are satisfied. It can be seen from these figures that the increase in the probability over the time intervals T_2, which correspond to the effective matter density N_2, is very small; in addition, we have $T_2 \ll T_1$ in this case. One could therefore conclude that the evolution within these very narrow intervals is unimportant. However, this conclusion is wrong: if one removes the "spikes" in the matter density profile of Fig. 4—that is, if one replaces it by the profile $N(t) = N_1 = \text{const}$—the resulting transition probability will be very small at all times (Fig. 5).

Further examples of parametrically enhanced neutrino oscillations can be found in Figs. 6 and 7. Figures 1, 3, and 6 correspond to the realization (70) ($c_1 = c_2 = 0$) of the parametric-resonance condition (68); Fig. 7 illustrates the realization in which the two terms in X_3 cancel each other.

5. PARAMETRIC RESONANCE IN NEUTRINO OSCILLATIONS IN THE EARTH

5.1. Evolution of Oscillating Neutrinos in the Earth

The Earth consists of two main structures, the mantle and the core, which, to a very good approximation, can be considered as layers of constant density. We will treat neutrino oscillations in the Earth in this two-layer approximation. Neutrinos arriving at the detector from the lower hemisphere of the Earth at zenith angles Θ in the range of $\cos\Theta$ from -1 to -0.837 (the nadir angle lies in the region $\Theta_n \equiv 180^\circ - \Theta \leq 33.17^\circ$) traverse the Earth's mantle, the core, and then again the mantle—that is, three layers of constant density, with the third layer being identical to the first one. Therefore, such neutrinos experience a periodic castle-wall potential, and their oscillations can be parametrically enhanced. Although these neutrinos traverse, in this case, only three layers (one period and half of the density modulation), the parametric enhancement of the transition probability can be very strong.

In this case, the evolution matrix is $U = U_1 U_2 U_1$. It can be parametrized in a form similar to that in Eq. (36):

$$U = Z - i\boldsymbol{\sigma}\cdot\mathbf{W}, \qquad Z^2 + \mathbf{W}^2 = 1. \tag{74}$$

The matrix U describes the evolution of an arbitrary initial state; therefore, it contains the entire body of information about neutrino oscillations. In particular, the probabilities of neutrino-flavor oscillations, P, and of $\nu_2 \leftrightarrow \nu_e$ oscillations (relevant to the oscillations of solar and supernova neutrinos within the Earth), P_{2e}, are given by [14] [9)]

$$P = W_1^2 + W_2^2, \tag{75}$$

$$P_{2e} = \sin^2\theta_0 + W_1(W_1\cos 2\theta_0 + W_3 \sin 2\theta_0).$$

Equivalently, the probability P can be described by Eqs. (65)–(67) at $k = 1$.

We must now identify the effective densities N_1 and N_2 with the average matter densities N_m and N_c in the Earth's mantle and core, respectively; similarly,

[9)] Different but equivalent expressions can also be found in [13, 22, 23].

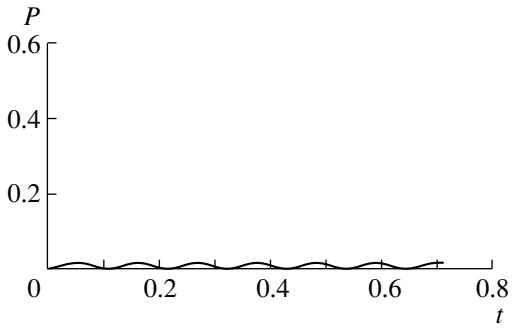

Fig. 5. As in Fig. 3, but for $V_2 = V_1$ [$V(t) = V_1 = \text{const}$].

we change the notation as $V_{1,2} \to V_{m,c}$, $\phi_{1,2} \to \phi_{m,c}$, and $\theta_{1,2} \to \theta_{m,c}$.

In the two-layer approximation, the parameters Z and $\mathbf{W}$ are given by the very simple expressions [14]

$$Z = 2Y\cos\phi_m - \cos\phi_c, \tag{76}$$

$$\mathbf{W} = (2Y\sin\phi_m\sin 2\theta_m + \sin\phi_c\sin 2\theta_c, 0, \\ -(2Y\sin\phi_m\cos 2\theta_m + \sin\phi_c\cos 2\theta_c)), \tag{77}$$

where the vector $\mathbf{W}$ is written in the component form and the parameter Y was defined in (59). If the parametric-resonance condition (68) is satisfied through the realization in (70), the neutrino-flavor-transition probability reduces to [11, 12]

$$P = \sin^2(2\theta_c - 4\theta_m), \tag{78}$$

whereas the probability of $\nu_2 \leftrightarrow \nu_e$ transitions is [13]

$$P_{2e} = \sin^2(2\theta_c - 4\theta_m + \theta_0). \tag{79}$$

These probabilities can be close to unity (the arguments of the sines are close to $\pi/2$) even if the amplitudes of neutrino oscillations in the mantle, $\sin^2 2\theta_m$, and in the core, $\sin^2 2\theta_c$, are rather small. This can happen if the neutrino energy lies in the range $E_c < E < E_m$, where E_m and E_c are the energy values that correspond to the MSW resonance in the mantle and in the core of the Earth. This condition is equivalent to $N_m < N_{\text{MSW}} < N_c$. In the case of the small-mixing-angle MSW solution to the solar-neutrino problem, $\sin^2 2\theta_0 < 10^{-2}$ and P_{2e} virtually coincides with P unless both probabilities are very small.

The trajectories of neutrinos traversing the Earth are determined by their nadir angle of $\Theta_n = 180^\circ - \Theta$. The distances R_m and R_c that neutrinos travel in the mantle (each layer) and in the core are given by

$$R_m = R\left(\cos\Theta_n - \sqrt{r^2/R^2 - \sin^2\Theta_n}\right), \tag{80}$$

$$R_c = 2R\sqrt{r^2/R^2 - \sin^2\Theta_n},$$

where $R = 6371$ km is the Earth's radius and $r = 3486$ km is the core radius. The matter density in the mantle of the Earth ranges from 2.7 g/cm^3 at the surface to 5.5 g/cm^3 at the bottom, and that in the core ranges from 9.9 to 12.5 g/cm^3 (see, for example, [24]). The electron-number fraction Y_e is close to 1/2 both in the mantle and in the core. Taking the average matter densities in the mantle and in the core to be 4.5 and 11.5 g/cm^2, respectively, one finds for $\nu_e \leftrightarrow \nu_{\mu,\tau}$ oscillations involving only active neutrinos that $V_m = 8.58 \times 10^{-14}$ eV and $V_c = 2.19 \times 10^{-13}$ eV. For $\nu_e \leftrightarrow \nu_s$ and $\nu_{\mu,\tau} \leftrightarrow \nu_s$ transitions involving sterile neutrinos, these parameters are smaller by a factor of two.

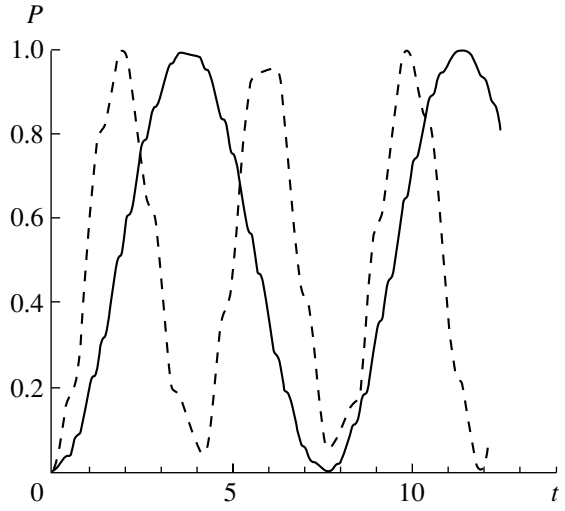

Fig. 6. Coordinate dependence of the transition probability P for the case of total conversion over five periods of the density modulation: (solid curve) ten layers and (dashed curve) three layers. The kinks correspond to the borders of the layers of different densities. The curves were plotted for the realization (70) ($c_1 = c_2 = 0$) of the parametric-resonance condition.

5.2. Parametric-Resonance Conditions for Neutrino Oscillations in the Earth

If the parametric-resonance conditions (70) are satisfied, the oscillations of neutrinos traversing the core of the Earth can be strongly enhanced [11–16] (see Fig. 8). In some cases, condition (69) can also be fulfilled, and the parametric resonance leads to a complete flavor conversion for neutrinos traversing the Earth.

We will now discuss the resonance conditions (70). The phases ϕ_m and ϕ_c depend on the neutrino parameters Δm^2, θ_0, and E and also on the distances R_m and R_c that the neutrinos travel in the mantle and in the core. The path lengths R_m and R_c vary with the nadir angle; however, it can be seen from

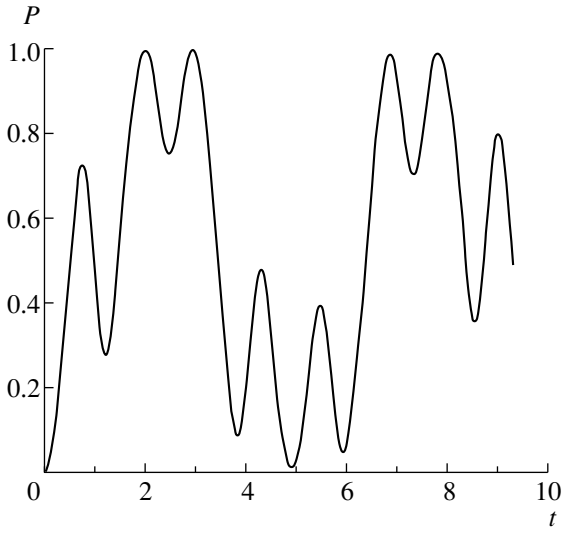

Fig. 7. As in Fig. 6, but for the case where the parametric-resonance condition is realized through the cancellation of the two terms in Eq. (32) (the total conversion is achieved over three layers).

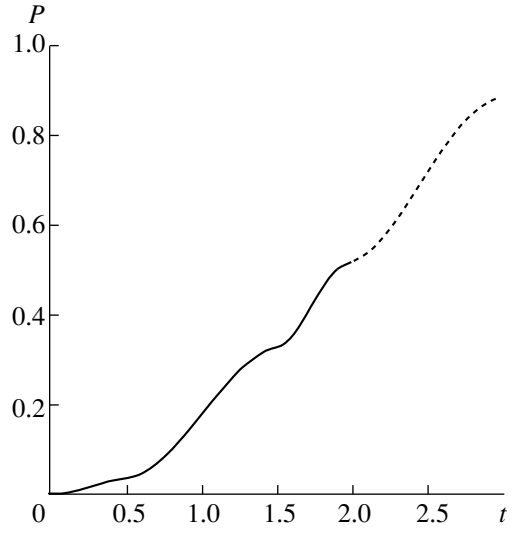

Fig. 8. Transition probability P for $\nu_e \leftrightarrow \nu_{\mu,\tau}$ oscillations in the Earth as a function of the distance t (measured in units of the Earth's radius) along the neutrino trajectory (solid curve) at $\delta \equiv \Delta m^2/4E = 1.8 \times 10^{-13}$ eV, $\sin^2 2\theta_0 = 0.01$, and $\Theta_n = 11.5^\circ$. The hypothetical case of neutrino propagation over full two periods of the density modulation [$t_{\max} = 2(R_m + R_c)$] is represented by the dashed curve.

(80) that their changes are correlated and that they cannot take arbitrary values. It follows that, if, for some values of the neutrino parameters, there exists a value of the nadir angle Θ_n such that, for example, the first condition in Eq. (70) is satisfied, it is not obvious whether the second condition is also satisfied at the same value of Θ_n. In other words, it is not clear whether the realization (70) of the parametric-resonance condition (68) is possible for neutrino oscillations in the Earth for at least one set of the neutrino parameters Δm^2, θ_0, and E. It was shown in [13, 14], however, that not only are the parametric-resonance conditions (70) satisfied (or approximately satisfied) for a rather wide range of nadir angles covering the Earth's core, but they are fulfilled for the ranges of the neutrino parameters that are of interest for the neutrino-oscillation solutions to the solar- and atmospheric-neutrino problems. In particular, the conditions for the principal resonance ($k' = k'' = 0$) are satisfied to a good accuracy for $\sin^2 2\theta_0 \lesssim 0.1$ and $\delta \simeq (1.1{-}1.9) \times 10^{-13}$ eV^2, which includes the ranges relevant to the small-mixing-angle MSW solution of the solar neutrino problem and to the subdominant $\nu_\mu \leftrightarrow \nu_e$ and $\nu_e \leftrightarrow \nu_\tau$ oscillations of atmospheric neutrinos.

The fact that the parametric-resonance conditions (70) can be satisfied so well for neutrino oscillations in the Earth is rather surprising. It is a consequence of a number of remarkable numerical coincidences. It has been known for some time that the potentials V_m and V_c corresponding to the matter densities in the mantle and in the core, the inverse radius of the Earth (R^{-1}), and typical values of $\delta \equiv \Delta m^2/4E$ of interest for solar and atmospheric neutrinos are all on the same order of magnitude—$(3 \times 10^{-14}{-}3 \times 10^{-13})$ eV (see, for example, [11, 25, 26]). It is owing to this surprising coincidence that Earth's medium effects on the oscillations of solar and atmospheric neutrinos may become sizable. For the parametric resonance to occur, a coincidence by an order of magnitude is not sufficient, however: the conditions in (70) must be satisfied at least to within 50% [14]. This is exactly what takes place. In addition, we note that, in a wide range of the nadir angles Θ_n, the δ value at which the resonance conditions (70) are satisfied changes slightly with Θ_n, but fulfillment of these conditions is not destroyed.

That the second realization of the parametric-resonance condition (68)—that in which the two terms in X_3 cancel each other—is also possible for neutrino oscillations in the Earth [19] is even a more surprising fact. This requires that the effective matter densities N_m and N_c and the neutrino path lengths R_m and R_c in the mantle and in the core be tuned, in a very subtle way, to the values of the neutrino parameters θ_0 and $\delta = \Delta m^2/4E$. Albeit looking very contrived, this turns out to be possible. Moreover, the condition in (69) can also be met for some values of the neutrino parameters, and a complete flavor conversion for neutrinos traversing the Earth is possible [19].

6. DISCUSSION AND CONCLUSION

We have reviewed the Floquet theory of linear differential equations with periodic coefficients and discussed its applications to neutrino oscillations in matter of periodically modulated density. In particular, we have shown for the case of two-flavor oscillations that the evolution of the system takes the form of parametric oscillations—modulated oscillations characterized by two periods, the period T of density modulations and $\tau = (2\pi/\Phi)T$, where $\pm i\Phi$ are the characteristic exponents. We have also discussed a parametric resonance in neutrino oscillations and shown that, irrespective of the shape of periodic density modulations, the parametric-resonance condition is $X_3 = 0$, where X_3 is one of the parameters that determine the monodromy matrix given by Eq. (36). We have also reviewed an exact solution in the case of two-flavor neutrino oscillations in a medium having a periodic step-function density profile and discussed its connections with Floquet theory. This solution, which was obtained in [9, 14], allows one to find explicit expressions for the parameters entering into the monodromy matrix, including the characteristic exponents and X_3. We have discussed implications of this exact solution for the oscillations of neutrinos within the Earth, whose density profile can be approximated, to a very good accuracy, by a piece of a periodic step-function profile. We have concentrated on possible parametric-resonance effects in neutrino oscillations within the Earth.

Apart from being an interesting physical phenomenon, a parametric resonance in neutrino oscillations can furnish important additional information about the properties of the neutrino. Therefore, an experimental observation of this effect would be of considerable interest. Prospects for the experimental observation of a parametric resonance in oscillations of solar and atmospheric neutrinos traversing the Earth were discussed in [17, 18]. To a large extent, these prospects depend on the values of some neutrino parameters that have not yet been determined conclusively. The bottom line is that such an experimental observation is difficult, but it may be possible.

A parametric enhancement may lead to noticeable effects in oscillations of supernova neutrinos in the Earth, resulting in characteristic distortions of the spectra of neutrinos traversing the Earth's core [27]. However, a sufficiently accurate measurement of the supernova-neutrino spectrum would require a relatively close supernova ($L \leq 10$ kpc).

An interesting possibility of studying parametric effects in neutrino oscillations would be a very long baseline experiment with intense neutrino beams produced at neutrino factories (for a discussion of neutrino-oscillation experiments at neutrino factories, see, for example, [28]). For baselines larger than approximately 10 700 km, neutrinos would traverse the Earth's core, so that it would be possible to probe parametric-resonance effects in $\nu_e \leftrightarrow \nu_{\mu(\tau)}$ oscillations. Notice, however, that the present feasibility studies concentrate on relatively short baselines, a few thousand kilometers [28]. In addition, the expected average energies of neutrino beams ($E \geq 20$ GeV) in the currently discussed experiments are somewhat higher than what would be desirable in order to study parametric effects.

As we have seen, it is not easy to observe a parametric resonance in oscillations of solar, atmospheric, or supernova neutrinos within the Earth or in experiments at neutrino factories. Can one create the required matter-density profile and observe a parametric resonance in neutrino oscillations in laboratory (that is, short-baseline) experiments? Unfortunately, the answer to this question seems to be negative: this would require either an overly long baseline or neutrino propagation in a medium of overly high density (see [17, 18] for details). One can conclude that the only presently known object where a parametric resonance in neutrino oscillations can occur is our planet, as was first indicated in [11, 12].

ACKNOWLEDGMENT

This work was supported by Fundação para a Ciência e a Tecnologia (grant no. PRAXIS XXI/BCC/16414/98).

REFERENCES

1. S. P. Mikheev and A. Yu. Smirnov, Yad. Fiz. **42**, 1441 (1985) [Sov. J. Nucl. Phys. **42**, 913 (1985)].
2. L. Wolfenstein, Phys. Rev. D **17**, 2369 (1978).
3. S. P. Mikheyev and A. Yu. Smirnov, in *Proceedings of the XII International Conference on Neutrino Physics and Astrophysics,* Ed. by T. Kitagaki and H. Yuta (World Sci., Singapore, 1986), p. 177.
4. S. Weinberg, Int. J. Mod. Phys. A **2**, 301 (1987).
5. *Proceedings of the NATO Advanced Study Research Workshop "Statistical Process in Physics and Biology"*; J. Stat. Phys. **70** (1/2), 1993.
6. L. D. Landau and E. M. Lifshitz, *Mechanics* (Nauka, Moscow, 1973; Pergamon, Oxford, 1976).
7. V. I. Arnold, *Mathematical Methods of Classical Mechanics* (Nauka, Moscow, 1978; Springer-Verlag, New York, 1989).
8. V. K. Ermilova, V. A. Tsarev, and V. A. Chechin, Kratk. Soobshch. Fiz. **5**, 26 (1986).
9. E. Kh. Akhmedov, Preprint No. IAE-4470/1 (1987); Yad. Fiz. **47**, 475 (1988) [Sov. J. Nucl. Phys. **47**, 301 (1988)].
10. P. I. Krastev and A. Yu. Smirnov, Phys. Lett. B **226**, 341 (1989).

11. Q. Y. Liu and A. Yu. Smirnov, Nucl. Phys. B **524**, 505 (1998).
12. Q. Y. Liu, S. P. Mikheyev, and A. Yu. Smirnov, Phys. Lett. B **440**, 319 (1998).
13. S. T. Petcov, Phys. Lett. B **434**, 321 (1998); hep-ph/9805262.
14. E. Kh. Akhmedov, Nucl. Phys. B **538**, 25 (1999); hep-ph/9805272.
15. E. Kh. Akhmedov, A. Dighe, P. Lipari, and A. Yu. Smirnov, Nucl. Phys. B **542**, 3 (1999); hep-ph/9808270.
16. M. Chizhov, M. Maris, and S. T. Petcov, hep-ph/9810501.
17. E. Kh. Akhmedov, hep-ph/9903302.
18. E. Kh. Akhmedov, Pramana **54**, 47 (2000); hep-ph/9907435.
19. M. V. Chizhov, and S. T. Petcov, Phys. Rev. Lett. **83**, 1096 (1999); hep-ph/9903424.
20. E. Kh. Akhmedov and A. Yu. Smirnov, hep-ph/9910433; Phys. Rev. Lett. **85**, 3978 (2000).
21. J. J. Stoker, in *Nonlinear Vibrations in Mechanical and Electrical Systems* (Interscience, New York, 1950), Chap. VI.
22. H. Minakata, H. Nunokawa, K. Shiraishi, and H. Suzuki, Mod. Phys. Lett. A **2**, 827 (1987).
23. A. Nicolaidis, Phys. Lett. B **200**, 553 (1988).
24. F. D. Stacey, *Physics of the Earth* (Wiley, New York, 1969).
25. J. M. Gelb, W.-K. Kwong, and S. P. Rosen, Phys. Rev. Lett. **78**, 2296 (1997).
26. P. Lipari and M. Lusignoli, Phys. Rev. D **58**, 073005 (1998).
27. A. S. Dighe and A. Yu. Smirnov, Phys. Rev. D **62**, 033007 (2000); hep-ph/9907423.
28. S. Geer, Phys. Rev. D **57**, 6989 (1998); Erratum: **59**, 039903 (1999); A. de Rújula, M. B. Gavela, and P. Hernández, Nucl. Phys. B **547**, 21 (1999); M. Campanelli, A. Bueno and A. Rubbia, hep-ph/9905240; V. Barger, S. Geer, and K. Whisnant, Phys. Rev. D **61**, 053004 (2000); O. Yasuda, hep-ph/9910428; I. Mocioiu and R. Shrock, hep-ph/9910554; hep-ph/0002149; V. Barger, S. Geer, R. Raja, and K. Whisnant, Phys. Rev. D **62**, 013004 (2000); M. Freund *et al.,* Nucl. Phys. B **578**, 27 (2000); C. Albright *et al.,* Preprint FERMILAB-FN-692 (2000); A. Cervera *et al.,* Nucl. Phys. B **579**, 17 (2000); M. Freund, P. Huber, and M. Lindner, hep-ph/0004085.

Physics of Atomic Nuclei, Vol. 64, No. 5, 2001, pp. 802–811. From Yadernaya Fizika, Vol. 64, No. 5, 2001, pp. 866–876.

90th ANNIVERSARY OF A.B. MIGDAL'S BIRTHDAY

Strange-Quark Matter within the Nambu–Jona-Lasinio Model*

I. N. Mishustin[1),2),3)], L. M. Satarov[1),2)], H. Stöcker[2)], and W. Greiner[2)]

Received September 8, 2000

Abstract—The equation of state of baryon-rich quark matter is studied within the $SU(3)$ Nambu–Jona-Lasinio model with flavor-mixing interaction. Possible bound states (strangelets) and chiral phase transitions in this matter are investigated at various values of the strangeness fraction r_s. Model predictions are very sensitive to the ratio of the vector and scalar coupling constants, $\xi = G_V/G_S$. At $\xi = 0.5$ and zero temperature, the binding energy takes a maximum value of about 15 MeV per baryon at $r_s \simeq 0.4$. Such strangelets are negatively charged and have typical lifetimes of about 10^{-7} s. Calculations are performed at finite temperatures as well. According to these calculations, bound states exist up to temperatures of about 15 MeV. The model predicts a first-order chiral phase transition at finite baryon densities. The parameters of this phase transition are calculated as functions of r_s. © *2001 MAIK "Nauka/Interperiodica".*

1. INTRODUCTION

Almost 30 years ago, A.B. Migdal put forth the brilliant idea of pion condensation in nuclear matter [1]. Soon, it was realized that this phenomenon may lead to the existence of density isomers [2]. At about this time, Lee and Wick proposed another mechanism leading to the appearance of an abnormal nuclear state [3]. It is related to the restoration of chiral symmetry at high baryon densities. These ideas served as a motivation for initiating new experimental programs aimed at producing hot and dense nuclear matter in energetic collisions of heavy nuclei. These experiments started in Dubna and Berkeley and then continued in Brookhaven and CERN. Nowadays, exciting expectations are associated with new ultrarelativistic heavy-ion colliders (RHIC and LHC).

The general goal of present and future experiments with ultrarelativistic heavy ions is to study the equation of state and the dynamical properties of strongly interacting matter. Presently, the main interest lies in investigating chiral and deconfinement phase transitions predicted by QCD. The ultimate goal is to produce and study, under laboratory conditions, a new state of matter, quark–gluon plasma (QGP). This state of matter can be reached only at high temperatures or particle densities, when elementary constituents, quarks and gluons, are liberated from hadrons.

Since a direct application of QCD at moderate temperatures and nonzero chemical potentials is not possible at present, simpler effective models respecting some basic symmetry properties of QCD are commonly used. The Nambu–Jona-Lasinio (NJL) model [4, 5], which deals with constituent quarks and which respects chiral symmetry, is one of the most popular models of this kind. In recent years, this model has been widely used to describe hadron properties (see the reviews articles [6, 7]), phase transitions in dense matter [8–13], and multiparticle bound states [14–17].

In [18, 19], we used the NJL model to study the properties of quark–antiquark plasma out of chemical equilibrium. In fact, we considered a system with independent densities of quarks and antiquarks. We found not only first-order transitions but also deep bound states even in baryon-free matter with equal densities of quarks and antiquarks. Here, emphasis is put on investigating the possibility of bound states and phase transitions in equilibrated matter at various flavor compositions. In particular, we consider the possibility of bound states in quark matter with a significant admixture of strange quarks, strangelets. Thermal properties of strange-quark matter are also studied.

This paper is organized as follows. In Section 2, a generalized NJL model including flavor-mixing terms is formulated in the mean-field approximation. The predictions of the model for strange matter and the characteristics of its bound states at zero temperature are discussed in Section 3. Finite-temperature effects are considered in Section 4. For new bound states,

*This article was submitted by the authors in English.

[1)]Russian Research Centre Kurchatov Institute, pl. Kurchatova 1, Moscow, 123182 Russia.

[2)]Institut für Theoretische Physik, Universität Frankfurt, Postfach 111932, Robert-Mayer-Strasse 8-10, D-60054 Frankfurt am Main, Germany.

[3)]Niels Bohr Institute, Blegdamsvej 17, DK-2100 Copenhagen, Denmark.

the possible decay modes are discussed in Section 5. The basic results of the present study are summarized in Section 6.

2. FORMULATION OF THE MODEL

Below, we use the $SU(3)$-flavor version of the NJL model suggested in [20]. The corresponding Lagrangian is written as ($\hbar = c = 1$)

$$\mathcal{L} = \overline{\psi}\,(i\,\partial\!\!\!/ - \hat{m}_0)\,\psi \tag{1}$$
$$+G_S \sum_{j=0}^{8} \left[\left(\overline{\psi}\,\frac{\lambda_j}{2}\,\psi \right)^2 + \left(\overline{\psi}\,\frac{i\gamma_5\lambda_j}{2}\,\psi \right)^2 \right]$$
$$-G_V \sum_{j=0}^{8} \left[\left(\overline{\psi}\,\gamma_\mu\frac{\lambda_j}{2}\,\psi \right)^2 + \left(\overline{\psi}\,\gamma_\mu\frac{\gamma_5\lambda_j}{2}\,\psi \right)^2 \right]$$
$$-K\left[\det{}_f\left(\overline{\psi}\,(1-\gamma_5)\,\psi\right) + \det{}_f\left(\overline{\psi}\,(1+\gamma_5)\,\psi\right) \right],$$

where ψ is the column vector consisting of three single-flavor spinors ψ_f; $f = u, d, s$; $\lambda_1, \ldots, \lambda_8$ are the $SU(3)$ Gell-Mann matrices in flavor space; $\lambda_0 \equiv \sqrt{2/3}\,\mathbf{I}$; and $\hat{m}_0 = \mathrm{diag}(m_{0u}, m_{0d}, m_{0s})$ is the matrix of bare (current) quark masses. At $\hat{m}_0 = 0$, this Lagrangian is invariant under $SU_L(3) \otimes SU_R(3)$ chiral transformations. The second and the third term in Eq. (1) correspond, respectively, to the scalar–pseudoscalar and the vector–axial-vector 4-fermion interaction. The last 6-fermion-interaction term breaks $U_A(1)$ symmetry and gives rise to flavor-mixing effects.

In the mean-field approximation, Lagrangian (1) reduces to

$$\mathcal{L}_{\mathrm{MFA}} = \sum_f \overline{\psi}_f\,(i\not{D} - m_f)\,\psi_f \tag{2}$$
$$-\frac{G_S}{2}\sum_f \rho_{Sf}^2 + \frac{G_V}{2}\sum_f \rho_{Vf}^2 + 4K\prod_f \rho_{Sf},$$

where $\not{D} = \partial\!\!\!/ + i\,\gamma_0 G_V \rho_{Vf}$ and

$$\rho_{Sf} = \langle \overline{\psi}_f \psi_f \rangle, \tag{3}$$
$$\rho_{Vf} = \langle \overline{\psi}_f \gamma_0 \psi_f \rangle \tag{4}$$

are the scalar and vector densities of quarks with flavor f. Angular brackets correspond to quantum-statistical averaging. The constituent quark masses m_f are determined by the coupled set of gap equations

$$m_f = m_{0f} - G_S\,\rho_{Sf} + 2K \prod_{f' \neq f} \rho_{Sf'}. \tag{5}$$

The NJL model is an effective nonrenormalizable model. To regularize the divergent contribution of negative-energy states of the Dirac sea, one must introduce an ultraviolet cutoff. Following common practice, we use the 3-momentum cutoff $\theta(\Lambda - p)$ in divergent integrals.[4)] The model parameters m_{0f}, G_S, K, and Λ can be fixed by fitting the observed masses of π, K, and η' mesons and the pion decay constant f_π. According to [20], a reasonable fit is achieved with the following values:

$$m_{0u} = m_{0d} = 5.5\ \mathrm{MeV}, \quad m_{0s} = 140.7\ \mathrm{MeV}, \tag{6}$$
$$G_S = 20.23\ \mathrm{GeV}^{-2}, K = 155.9\ \mathrm{GeV}^{-5}, \tag{7}$$
$$\Lambda = 0.6023\ \mathrm{GeV}.$$

Motivated by the discussions in [6, 21], we choose the following value of the vector coupling constant:[5)]

$$G_V = 0.5\,G_S = 10.12\ \ \mathrm{GeV}^{-2}. \tag{8}$$

Let us consider homogeneous, thermally (but not, in general, chemically) equilibrated quark–antiquark matter at temperature T. Let $a_{\mathbf{p},\lambda}$ ($b_{\mathbf{p},\lambda}$) and $a^+_{\mathbf{p},\lambda}$ ($b^+_{\mathbf{p},\lambda}$) be the destruction and creation operators for a quark (an antiquark) in the $\mathbf{p}, \lambda$ state, where $\mathbf{p}$ is the 3-momentum and λ is a discrete quantum number that denotes spin and flavor (color indices are suppressed). It can be shown [18] that the quark and antiquark phase-space occupation numbers coincide with the Fermi–Dirac distribution functions; that is,

$$\langle a^+_{\mathbf{p},\lambda}\,a_{\mathbf{p},\lambda}\rangle \equiv n_{\mathbf{p}f} \tag{9}$$
$$= \left[\exp\left(\frac{E_{\mathbf{p}f} - \mu_{Rf}}{T}\right) + 1\right]^{-1},$$
$$\langle b^+_{\mathbf{p},\lambda}\,b_{\mathbf{p},\lambda}\rangle \equiv \overline{n}_{\mathbf{p}f} \tag{10}$$
$$= \left[\exp\left(\frac{E_{\mathbf{p}f} - \overline{\mu}_{Rf}}{T}\right) + 1\right]^{-1},$$

where $E_{\mathbf{p}f} = \sqrt{m_f^2 + \mathbf{p}^2}$ and μ_{Rf} and $\overline{\mu}_{Rf}$ stand for the reduced chemical potentials of quarks and antiquarks:

$$\mu_{Rf} = \mu_f - G_V\rho_{Vf}, \tag{11}$$
$$\overline{\mu}_{Rf} = \overline{\mu}_f + G_V\rho_{Vf}. \tag{12}$$

The explicit expression for the vector density can be written as

$$\rho_{Vf} = \rho_f - \overline{\rho}_f, \tag{13}$$

where

$$\rho_f = \nu\int \frac{d^3p}{(2\pi)^3}\,n_{\mathbf{p}f}, \quad \overline{\rho}_f = \nu\int \frac{d^3p}{(2\pi)^3}\,\overline{n}_{\mathbf{p}f} \tag{14}$$

are the number densities of, respectively, quarks and antiquarks of flavor f and $\nu = 2N_c = 6$ is the spin–color degeneracy factor. The net baryon density is obviously defined as

$$\rho_B = \frac{1}{3}\sum_f \rho_{Vf}. \tag{15}$$

[4)] Here, $\theta(x) \equiv (1 + \mathrm{sgn}\,x)/2$.

[5)] See the discussion of this question in [19].

The physical vacuum ($\rho_f = \overline{\rho}_f = 0$) corresponds to the limit $n_{\mathbf{p}f} = \overline{n}_{\mathbf{p}f} = 0$.

In general, the chemical potentials μ_f and $\overline{\mu}_f$ are independent variables. The assumption of chemical equilibrium with respect to creation and annihilation of $q\overline{q}$ pairs leads to the conditions

$$\overline{\mu}_f = -\mu_f, \quad f = u, d, s. \tag{16}$$

These conditions automatically follow from the relations

$$\mu_i = B_i\,\mu_B + S_i\,\mu_S + Q_i\,\mu_Q \quad (i = u, d, s, \bar{u}, \bar{d}, \bar{s}), \tag{17}$$

which are valid for any $q\overline{q}$ system chemically equilibrated with respect to strong interactions. Here, three independent chemical potentials, μ_B, μ_S, and μ_Q, are fixed by the net baryon number B, the strangeness S, and the electric charge Q of the system.

In heavy-ion collisions at high bombarding energies, partonic matter created is characterized by $B \simeq 0$ and $S \simeq 0$; therefore, we have $\overline{\mu}_f \simeq \mu_f \simeq 0$. On the other hand, strangelets are finite droplets with nonzero B and S. Using Eq. (17), one can see that, in this case, $\mu_B,\ \mu_S \neq 0$; therefore, the inequality $\mu_s > \mu_{u,d}$ must hold. This conclusion shows that strong fluctuations are needed for strangelet formation in high-energy nuclear collisions.

If the strangelet lifetimes are sufficiently long, equilibrium with respect to the weak processes

$$s \to u + e^- + \overline{\nu}_e, \quad u + e^- \to s + \nu_e, \quad s + u \leftrightarrow u + d \tag{18}$$

may also be achieved. Assuming that $\mu_e = \mu_{\overline{\nu}} = 0$, one arrives at the conditions

$$\mu_u = \mu_d = \mu_s. \tag{19}$$

As will be shown below, the constituent masses m_s of strange quarks in (mechanically) stable strangelets exceed the chemical potentials of u and d quarks. For $\mu_s > m_s$ and $T \to 0$, the β equilibrium conditions (19) can be realized only after all s quarks have decayed.

Using conditions (16) in the zero-temperature limit, one can see that the density of antiquarks vanishes in baryon-rich chemically equilibrated matter, $\overline{\rho} \to 0$. In the mean-field approximation, the reduced chemical potential of quarks with flavor f coincides with their Fermi energy; that is,

$$\mu_{Rf} = \sqrt{m_f^2 + p_{\mathrm{F}f}^2}, \tag{20}$$

where

$$p_{\mathrm{F}f} = \left(\frac{6\pi^2\rho_f}{\nu}\right)^{1/3} \tag{21}$$

is the corresponding Fermi momentum.

Within the NJL model, the energy density and pressure of matter, as well as the quark condensates ρ_{Sf}, contain divergent terms originating from the negative-energy levels of the Dirac sea. As was noted above, these terms are regularized by introducing the 3-momentum cutoff $\theta(\Lambda - |\mathbf{p}|)$. The scalar density can then be represented as

$$\rho_{Sf} = \nu \int \frac{d^3p}{(2\pi)^3}\frac{m_f}{E_{\mathbf{p}f}}\left[\,n_{\mathbf{p}f} + \overline{n}_{\mathbf{p}f} - \theta(\Lambda - p)\,\right]. \tag{22}$$

The energy density corresponding to Lagrangian (2) can be written [19] as

$$e = e_K + e_{\mathrm{D}} + e_S + e_V + e_{\mathrm{FM}} + e_0. \tag{23}$$

This expression includes the "kinetic" term

$$e_K = \nu \sum_f \int \frac{d^3p}{(2\pi)^3}\,E_{\mathbf{p}f}\,(n_{\mathbf{p}f} + \overline{n}_{\mathbf{p}f}), \tag{24}$$

the "Dirac sea" term

$$e_{\mathrm{D}} = -\nu \sum_f \int \frac{d^3p}{(2\pi)^3}\,E_{\mathbf{p}f}\,\theta(\Lambda - p), \tag{25}$$

the scalar-interaction term

$$e_S = \frac{G_S}{2}\sum_f \rho_{Sf}^2, \tag{26}$$

the vector-interaction term

$$e_V = \frac{G_V}{2}\sum_f \rho_{Vf}^2, \tag{27}$$

and the flavor-mixing term

$$e_{\mathrm{FM}} = -4K\prod_f \rho_{Sf}. \tag{28}$$

The constant e_0 has been introduced in Eq. (23) in order to annihilate the energy density of the physical vacuum. This constant can be expressed in terms of the vacuum values of the constituent masses, m_f^{vac}, and the quark condensates, ρ_{Sf}^{vac}. These values are obtained self-consistently by solving the gap equations (5) in a vacuum—that is, at $n_{\mathbf{p}f} = \overline{n}_{\mathbf{p}f} = 0$.

Explicit analytic formulas for the energy density and the gap equations can be obtained in the case of zero temperature. For $T \to 0$, one has [18]

$$e_K + e_{\mathrm{D}} = \frac{\nu}{8\,\pi^2}\sum_f\left[p_{\mathrm{F}f}^4\,\Psi\left(\frac{m_f}{p_{\mathrm{F}f}}\right) - \Lambda^4\Psi\left(\frac{m_f}{\Lambda}\right)\right], \tag{29}$$

$$\rho_{Sf} = \frac{\nu}{8\pi^2}\left[p_{\mathrm{F}f}^3\,\Psi'\left(\frac{m_f}{p_{\mathrm{F}f}}\right) - \Lambda^3\Psi'\left(\frac{m_f}{\Lambda}\right)\right], \tag{30}$$

where

$$\Psi(x) \equiv 4\int_0^1 dt\, t^2\sqrt{t^2+x^2} \qquad (31)$$

$$= \left(1+\frac{x^2}{2}\right)\sqrt{1+x^2} - \frac{x^4}{2}\ln\frac{1+\sqrt{1+x^2}}{x}.$$

For a system with independent chemical potentials for quarks (μ_f) and antiquarks ($\overline{\mu}_f$), one can use the thermodynamic identity for the pressure of $q\overline{q}$ matter,

$$P = \sum_f(\mu_f\rho_f + \overline{\mu}_f\overline{\rho}_f) - e + sT, \qquad (32)$$

where s is the entropy density,

$$s = -\nu\sum_f\int\frac{d^3p}{(2\pi)^3} \qquad (33)$$

$$\times\left[n_{\mathbf{p}f}\ln n_{\mathbf{p}f}\right.$$

$$\left.+(1-n_{\mathbf{p}f})\ln(1-n_{\mathbf{p}f}) + n_{\mathbf{p}f}\to\overline{n}_{\mathbf{p}f}\right].$$

As was discussed in [18], bound states of $q\overline{q}$ matter or first-order phase transitions in $q\overline{q}$ matter are possible if its equation of state $P = P(\mu_f, \overline{\mu}_f, T)$ contains regions of negative pressure or isothermal compressibility, respectively. At $T = 0$, the state of mechanical equilibrium with a vacuum ($P = 0$) corresponds to the minimum of the energy per particle, $\epsilon = E/\sum_f(N_f + N_{\bar{f}}) = e/\sum_f(\rho_f + \bar{\rho}_f)$, where E is the total energy and $N_{f(\bar{f})}$ is the number of quarks (antiquarks) of flavor f. In the case of pure quark matter, $N_{\bar{f}} = 0$, its baryon number and its energy per baryon are $B = \sum_f N_f/3$ and $E/B = 3\epsilon$, respectively.

To characterize the flavor composition, we introduce the strangeness-fraction parameter

$$r_s \equiv \frac{|S|}{3B} = \frac{|\overline{\rho}_s - \rho_s|}{3\rho_B}. \qquad (34)$$

Below, we consider only the isospin-symmetric mixtures, where $N_u = N_d$ and $N_{\bar{u}} = N_{\bar{d}}$. It can be shown [19] that, in the dilute limit, where all single-flavor densities ρ_f and $\overline{\rho}_f$ are small, ϵ tends to the sum of the constituent quark and antiquark masses in a vacuum that is weighted according to r_s:

$$m_q^{\rm vac}(r_s) = (1-r_s)\,m_u^{\rm vac} + r_s\,m_s^{\rm vac}. \qquad (35)$$

In the case of chemically equilibrated matter at $T = 0$ and fixed r_s, one has

$$\epsilon(\rho_B\to 0, r_s) = m_q^{\rm vac}(r_s). \qquad (36)$$

A bound multiparticle state exists if there is a nontrivial minimum of ϵ as a function of ρ_B and if the binding energy (BE) per baryon is positive:

$$\mathrm{BE} = 3\left[m_q^{\rm vac}(r_s) - \epsilon_{\min}(r_s)\right] > 0. \qquad (37)$$

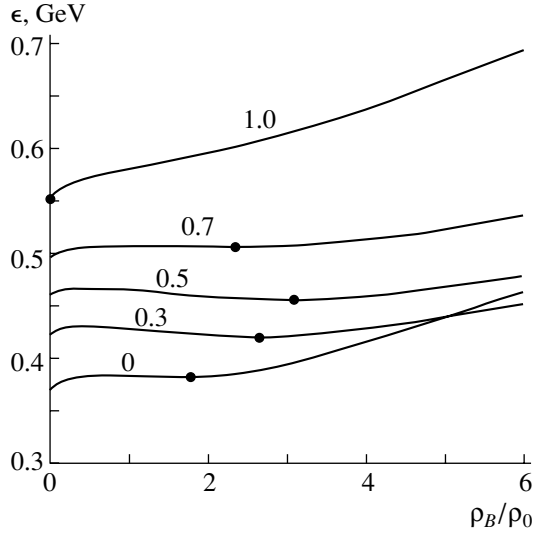

Fig. 1. Energy per particle, ϵ, in pure quark matter at zero temperature as a function of the baryon density at various values of the strangeness fraction r_s (the value of $\rho_0 = 0.17$ fm^{-3} is taken for the normal nuclear density). Points indicate local minima of ϵ.

3. STRANGE-QUARK MATTER AT ZERO TEMPERATURE

Let us first consider quark matter with nonzero net baryon density at $T = 0$. In the chemically equilibrated system, the density of valence antiquarks will be zero for each flavor ($\overline{\rho}_f = 0$). Figure 1 shows the energy per quark as a function of the baryon density $\rho_B = \frac{1}{3}\sum_f\rho_f$. Different curves correspond to different r_s, which, in this case, is the relative concentration of strange quarks. From Eq. (36), it can be seen that, for $\rho_B\to 0$, the energy per quark tends to the corresponding vacuum mass. With growing density, both the attractive scalar and repulsive vector interactions contribute to ϵ (see the discussion of this question in [19]).

It is interesting that, at $r_s \le 0.7$, the attractive interaction is sufficiently strong to produce a nontrivial local minimum at finite ρ_B. In pure u, d matter ($r_s = 0$), this minimum is unbound by about 20 MeV in relation to the vacuum masses of the u and d quarks. On the other hand, it is located at a baryon density of about $1.8\,\rho_0$, which is surprisingly close to the saturation density of normal nuclear matter. Of course, the location of this minimum depends on the model parameters. Nevertheless, one can speculate that, as soon as nucleon-like three-quark correlations, which are not considered in the mean-field approach, are taken into account, this state transforms into a correct nuclear ground state.

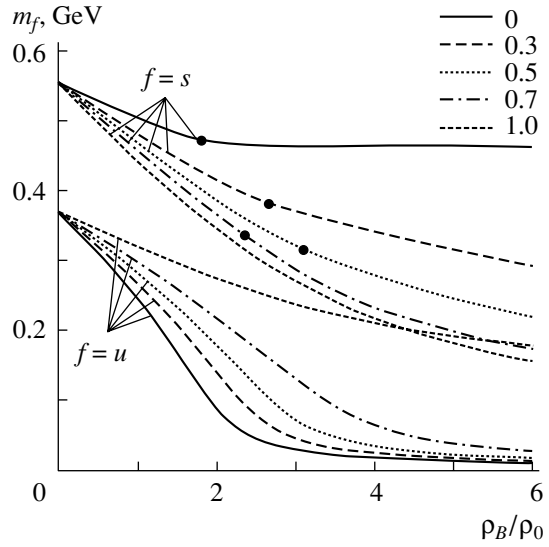

Fig. 2. Constituent masses of u and s quarks as functions of the baryon density at zero temperature. Shown in the right upper corner are the values of the strangeness fraction r_s. Points correspond to minima of the energy per particle at a given value of r_s.

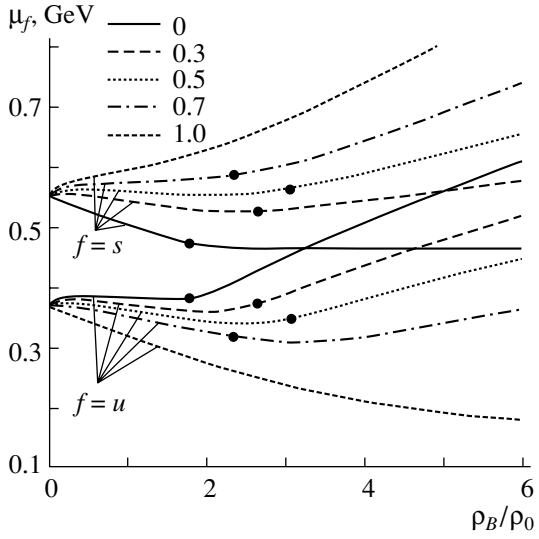

Fig. 3. As in Fig. 2, but for the chemical potentials of u and s quarks.

When r_s grows from 0 to about 0.4, the local minimum deepens and the corresponding baryon density increases to about $3.2\,\rho_0$. At larger r_s, the minimum again becomes shallower and disappears completely at $r_s \simeq 0.7$. At $0.2 < r_s < 0.6$, the minima correspond to true bound states; that is, the energy per quark is lower than the corresponding vacuum mass. But in all cases, these bound states are rather shallow: even the most strongly bound state at $r_s \simeq 0.4$ is bound only by about 15 MeV per baryon. Nevertheless, the appearance of local minima means that finite droplets can be in mechanical equilibrium with the vacuum at $P = 0$. It is natural to identify such droplets with strangelets, hypothetical objects formed by light and strange quarks [22–27].

It should be emphasized here that β equilibrium is not required in the present approach (see the discussion below). For this reason, our most bound strangelets are predicted to be richer in strange quarks ($r_s > 1/3$) than in approaches that assume β equilibrium [22, 23, 25] and which yield $r_s < 1/3$. As a result, these strangelets will be negatively charged.[6)] Indeed, the ratio of the charge Q to the baryon number B is expressed in terms of r_s as

$$\frac{Q}{B} = \frac{2}{3}\frac{\rho_u}{\rho_B} - \frac{1}{3}\frac{\rho_d}{\rho_B} - \frac{1}{3}\frac{\rho_s}{\rho_B} = \frac{1}{2}(1 - 3r_s). \qquad (38)$$

For $r_s \simeq 0.4$, this gives $Q/B \simeq -0.1$. In light of recent discussions (see, for example, [27]) concerning possible dangerous scenarios of the production of negatively charged strangelets at RHIC, we emphasize that the strangelets predicted here are not absolutely bound;[7)] that is, their energy per baryon is higher than that for normal nuclear matter. Hence, the spontaneous conversion of normal nuclear matter to strange-quark matter is energetically impossible.

Figure 2 shows the constituent masses of u and s quarks as functions of the baryon density. The dropping masses manifest a clear tendency to the restoration of chiral symmetry at high densities. The points indicate the masses at the local minima in the corresponding energies per baryon shown in Fig. 1. Note that the stronger the reduction of constituent masses, the deeper the corresponding bound states. For the metastable state at $r_s = 0$, a candidate for the nuclear ground state, the masses of the u and s quarks are equal to, respectively, 0.3 and 0.9 of their vacuum values. For the most bound states at $r_s \simeq 0.4$, the corresponding mass ratios are reduced to 0.15 and 0.6.

The behavior of the chemical potentials of the u and s quarks is shown in Fig. 3. At $r_s \neq 0, 1$, the contribution of the vector interaction [see Eqs. (11), (20)] results in that μ_u and μ_s show a nearly linear growth at large baryon densities. In accordance with the above discussion, one can see that the conditions $\mu_s > \mu_{u,d}$ hold at baryon-density values corresponding to bound states of strange matter.

The properties of multiparticle bound states are summarized in Figs. 4 and 5. Figure 4 shows the

[6)]Negatively charged strangelets were also considered in [24, 26].

[7)]A similar conclusion was drawn in [17].

binding energy per baryon [see Eq. (37)]. The maximum binding, about 15 MeV, is realized at $r_s \simeq 0.4$. One should bear in mind that, in the case of baryon-rich matter, local minima of ϵ result from a strong cancellation between the attractive scalar and repulsive vector interactions. Therefore, they are very sensitive to their relative strengths. The results presented above were obtained for $G_V = 0.5\,G_S$. For the sake of comparison, Figs. 4 and 5 also present model predictions for $G_V = 0$. In this case, the maximum binding energy increases to about 90 MeV per baryon and the corresponding r_s value is shifted to about 0.6. It is interesting to note that, for $G_V = 0$, the bound state appears even in pure u, d matter. The corresponding binding energy is about 20 MeV per baryon.

The points in Fig. 5 indicate the positions of some conventional baryons. By inspecting the figure, one can make a few interesting observations. First, conventional baryons are more bound than strangelets even at $G_V = 0$. This indicates that baryon-like three-quark correlations might indeed be very important in baryon-rich quark matter. Second, the bound-state energies grow monotonically with r_s.

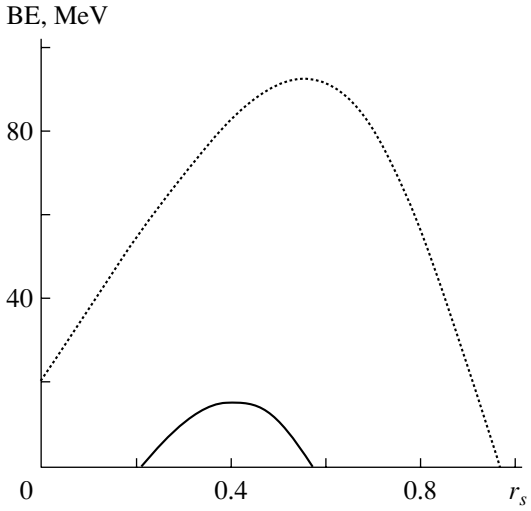

Fig. 4. Binding energies per baryon in pure quark matter as functions of the strangeness fraction r_s at zero temperature: (dotted curve) results of the calculations disregarding vector interaction ($G_V = 0$) and (solid curve) results for $G_V = 0.5 G_S$.

4. QUARK MATTER AT FINITE TEMPERATURES

In this section, we study the properties of deconfined matter at finite temperatures. For this case, calculations can be performed by using the general formulas of Section 2 with the quark and antiquark occupation numbers given by Eqs. (9) and (10). Unless otherwise stated, the results given below correspond to $G_V/G_S = 0.5$.

Figure 6*a* presents the pressure isotherms for the case of zero net strangeness ($r_s = 0$), which is appropriate for fast processes where net strangeness is conserved—for example, in relativistic nuclear collisions. One can see a spinodal-instability region, $\partial_\rho P < 0$, which is characteristic of a first-order phase transition. The corresponding critical temperature is about 35 MeV. The dashed curve (binodal) shows the boundary of mixed-phase states. Bound (zero-pressure) states exist only at temperatures below 15 MeV.

Generally, the equation of state of chemically equilibrated quark matter is characterized by two quantities: the net baryon charge B and the net strangeness S. Therefore, it is interesting to study the thermal properties of this matter at $S \neq 0$. Such states can occur in neutron stars. They can also be realized via the distillation mechanism accompanying a QCD phase transition in heavy-ion collisions [28]. Figure 6*b* shows the pressure isotherms for $r_s = 0.4$. As was discussed above, this case corresponds to the most bound strange matter at $T = 0$. At this value of r_s, bound states exist at $T < 30$ MeV. The dashed curve in Fig. 6*b* again shows the boundary of the two-phase region. It is obtained by solving the Gibbs conditions $P^{(1)} = P^{(2)}$, $\mu_u^{(1)} = \mu_u^{(2)}$, and $\mu_s^{(1)} = \mu_s^{(2)}$, where the indices 1 and 2 label two coexisting phases. In relation to the case of $r_s = 0$, the chiral phase transition occurs in a wider region of T and ρ_B. Applying the Gibbs conditions, one can see that, for $r_s = 0$, the equilibrium pressure isotherms are constant in the mixed-phase region (Maxwell construction). But this is not so for $r_s = 0.4$. From the general conclusions of [29], it follows that, in the case of two conserved charges (baryon number and strangeness), the Maxwell construction is modified in such a way that the equilibrium pressure at fixed T increases with ρ_B in the mixed-phase domain. However, this increase is small (a few percent) and is hardly visible in Fig. 6*b*. By way of example, we indicate that, for $T = 30$ MeV, the equilibrium pressure changes from 5.36 to 5.44 MeV/fm^3. It is interesting that, in the coexisting phases, local values of r_s are slightly different ($r_s^{(1)} < 0.4 < r_s^{(2)}$)—only the global strangeness ratio is fixed ($S/3B = 0.4$).

Figure 7 shows the critical temperatures for the existence of phase transitions and bound states in equilibrated strange matter as functions of r_s. One can see that both temperatures first grow with r_s and then drop to zero at $r_s \simeq 0.8$. The maximal values of T, respectively, 50 and 30 MeV are realized at some intermediate value of $r_s \simeq 0.4$. As was demonstrated earlier in Fig. 4, this value of r_s corresponds to the

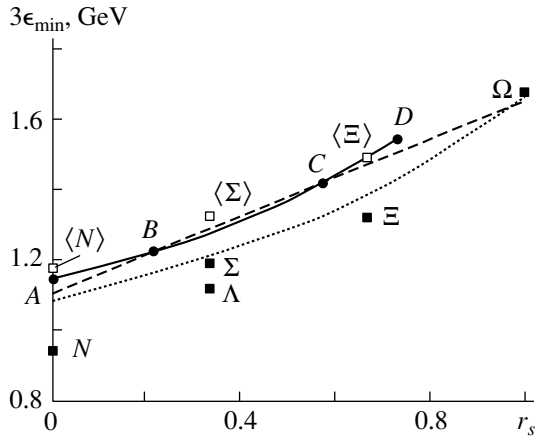

Fig. 5. Minimal energies per baryon in pure quark matter as functions of the strangeness fraction r_s at zero temperature. The dashed curve represents the same energy in the limit of zero particle densities [see Eq. (36)]. The segments of the solid curve correspond to metastable (AB and CD) or bound (BC) states ($G_V = 0.5G_S$). Closed squares show the masses of the lightest baryons. Open squares represent the spin–isospin-averaged masses of these baryons—for example, $\langle N\rangle = [m_N + 4\,m_{\Delta(1232)}]/5$ (for details, see [19]). The dotted curve shows the results in the limit $G_V \to 0$.

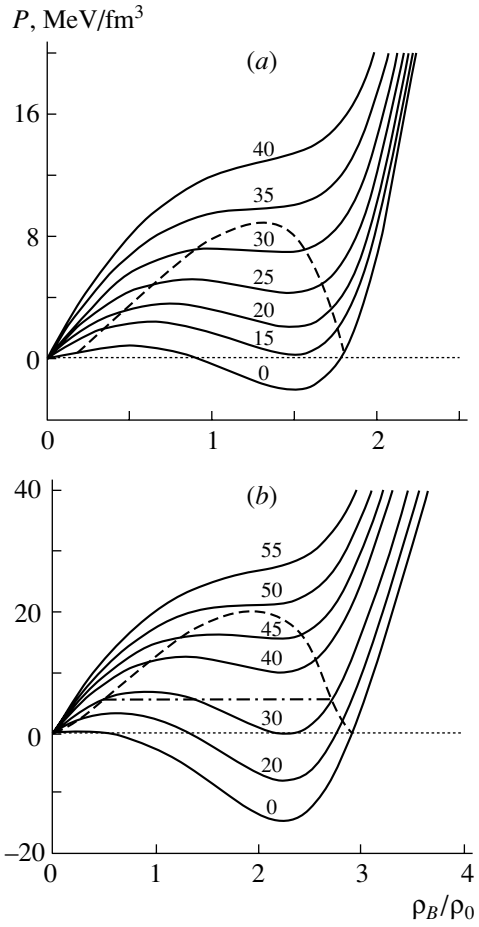

Fig. 6. Pressure isotherms for chemically equilibrated quark matter at $r_s = (a)$ 0 and (b) 0.4. Temperatures are given in MeV on the corresponding solid curves. The boundaries of spinodal regions are shown by the dashed curves. The dash-dotted lines show the equilibrium pressure in the mixed-phase domain at $T = 30$ MeV.

most bound state of strange-quark matter at $T = 0$. Thus, we see an obvious correlation: the deeper the bound state at $T = 0$, the stronger the phase transition at finite temperatures.

It should be emphasized here again that the thermal properties of asymmetric baryon-rich quark matter are very sensitive to the relative strength of scalar and vector interactions [19]. If we set $G_V = 0$, as in the majority of the calculations in the literature, the corresponding critical temperature at $r_s = 0$ increases to about 70 MeV. On the other hand, zero-pressure states disappear completely if one takes $G_V = 0.65\,G_S$. The calculation shows that there is no phase transition for $G_V > 0.71G_S$. It is interesting to note that, in all cases, this first-order phase transition occurs in the region of densities around the normal nuclear density ρ_0.

More detailed information about the first-order (chiral) phase transition predicted by our model is given in Fig. 8, where the critical temperature T_c and the baryon chemical potential $\mu_B = \mu_u + 2\mu_d = 3\mu_u$ are shown for various values of r_s. Again, one can see that maximal $T_c \simeq 50$ MeV corresponds to $r_s \simeq 0.4$.

Two phases coexisting in the mixed-phase domain of the chiral phase transition are characterized by different values of the constituent quark masses. If $q\overline{q}$ matter evolves from a high- to a low-density state, crossing the two-phase domain, there occurs a transition from chirally restored states (with low quark masses $m_f \sim m_{0f}$) to the chirally broken phase (where $m_f \sim m_f^{\rm vac}$). Therefore, a part of the internal energy must be converted into the rest mass. If the total entropy [8)] S and the effective number of degrees of freedom are conserved, the temperature will decrease during this transition. This is clearly seen in Fig. 9, where isentropes with entropy per baryon $S/B = 2$ and $S/B = 5$ are shown for the case of $r_s = 0$. A similar effect was predicted in [30] within the linear σ model. The drop of temperature as the result of this cooling mechanism may serve as an observable signature of the chiral phase transition in nuclear collisions. The above behavior is qualitatively different from that which is expected in the deconfinement transition, where the number of degrees of freedom is smaller in the dilute (hadronic)

[8)] This quantity should not be confused with the net strangeness introduced in Section 2.

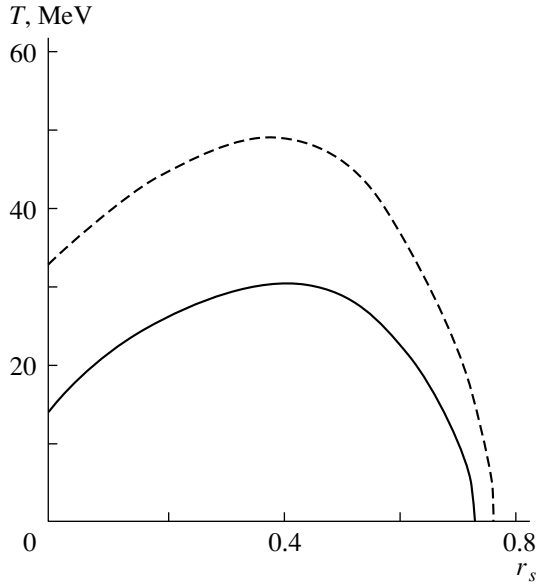

Fig. 7. Critical temperatures for the existence of bound states ($P < 0$, solid curve) and phase transitions ($\partial_\rho P < 0$, dashed curve) in equilibrium quark matter as functions of the strangeness fraction.

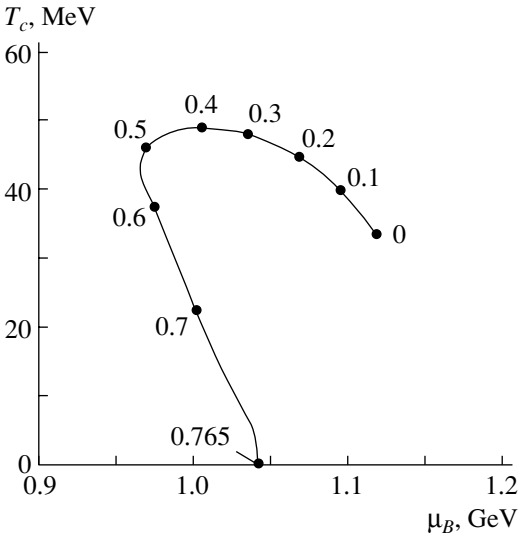

Fig. 8. Critical temperatures and baryon chemical potentials in equilibrated quark matter at fixed values of the strangeness fraction r_s that are indicated by figures on corresponding points.

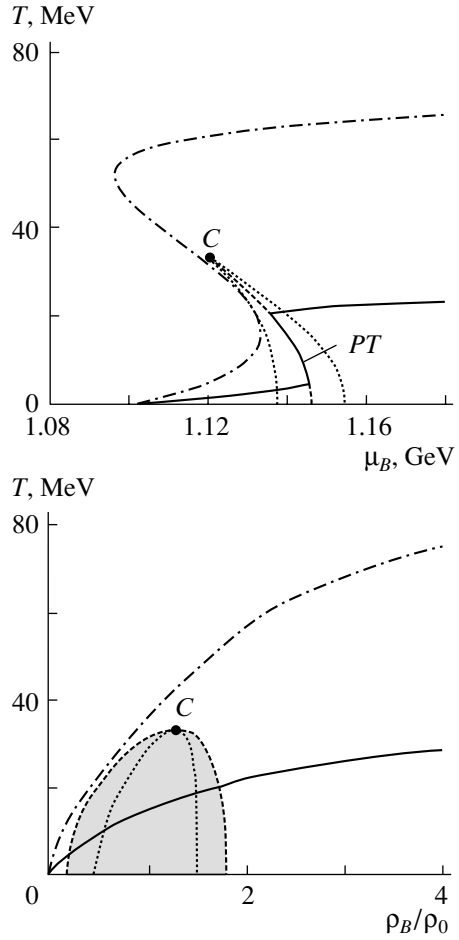

Fig. 9. Isentropes $S/B =$ (solid curve) 2 and (dashed-dotted curve) 5 of quark matter with zero net strangeness ($r_s = 0$). The lower (upper) panel corresponds to the μ_B–T (ρ_B–T) plane. The dotted and dashed curves represent, respectively, the spinodal and binodal boundaries of the two-phase region (shaded in the lower panel). The point C labels the critical point.

phase and where the temperature may increase during hadronization [31].

These results demonstrate that the chiral phase transition is rather similar to a liquid–gas phase transition in normal nuclear matter. In the present case ($T_c \simeq 30$ MeV, $\rho_{Bc} \sim \rho_0$), the critical temperature and the baryon density are not very far from the values predicted by conventional nuclear models [32] ($T_c \simeq 20$ MeV, $\rho_{Bc} \sim 0.5\,\rho_0$). One may expect that, in a more realistic approach that takes into account nucleonic correlations, the chiral transition may become an ordinary "liquid–gas" phase transition. Should this be the case, any other QCD phase transition of the liquid–gas type at a higher baryon density would be doubtful. At least, only one phase transition of this type is predicted within the NJL model.

5. DISCUSSION OF DECAY MODES

Let us briefly discuss the possible decay channels for bound states of quark matter described above. In strange-quark matter (without antiquarks), flavor conversion is only possible through weak decays. As follows from Fig. 3, the condition $\mu_s > \mu_u$ holds at densities corresponding to zero pressure. This means

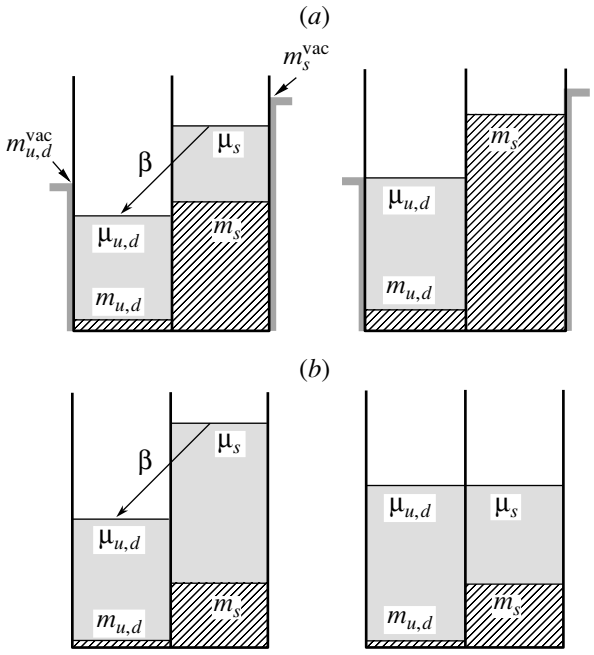

Fig. 10. Schematic pictures of energy levels (shown by shading) occupied by light and strange quarks in cold quark matter at various values of the strangeness fraction r_s. The left and right diagrams in the upper panel (a) show the results obtained within the NJL model for strange ($r_s = 0.4$) and nonstrange ($r_s = 0$) matter. The lower panel (b) shows the same results within the MIT bag model [19]. The hatched boxes in the upper and lower panels correspond, respectively, to the constituent and to the bare quark mass. The arrows indicate the weak decay processes $s \to u + e_- + \overline{\nu}_e$ and $s + u \to u + d$.

that weak processes of the types $s \to u + e^- + \overline{\nu}_e$ and $s + u \to u + d$ are allowed. Since there is no local barrier at any r_s (see Fig. 5), all strange quarks will eventually be converted into light u and d quarks in a system produced initially at some $r_s \neq 0$. Schematically, this conversion process is shown in Fig. 10a, where the initial ($r_s \neq 0$) and the final ($r_s = 0$) state correspond to the left and the right diagram, respectively.

This picture differs markedly from that based on the MIT bag model. Because the quark masses are kept constant ($m_f = m_{0f}$), the condition $\mu_s > m_s$ will be first satisfied at a relatively low baryon density proportional to m_{0s}^3. At higher densities, a certain fraction of s quarks will always be present in β-equilibrated matter (see Fig. 10b).

In the NJL model, however, the s-quark mass is a function of both the baryon density and the strangeness content. It can be seen from Fig. 10a that, at any given r_s, the condition $\mu_{u,d} = \mu_s$ can be satisfied only at sufficiently high baryon densities that correspond to a positive pressure. On the other hand, we always have $\mu_{u,d} < \mu_s$ at the points of zero pressure. Therefore, weak decays will proceed until a system reaches $r_s = 0$ [see right panel in Fig. 10a].

The lifetimes of strangelets at $T = 0$ can be roughly estimated by analogy with neutron decay. The matrix element for s-quark β decay is proportional to $(\Delta E)^{5/2} \sin\theta_{\mathrm{C}}$, where ΔE is the energy gain in the reaction and θ_{C} is the Cabibbo angle ($\sin\theta_{\mathrm{C}} \simeq 0.22$ [33]). As follows from our calculations (see Fig. 3), the energy gain $\Delta E = \mu_s - \mu_u$ depends on r_s, ranging from about 200 MeV at $r_s = 0.4$ to 100 MeV at $r_s = 0$. By scaling with corresponding quantities for neutron decay, one can express the lifetime of a strangelet as

$$\tau \sim \tau_n \left(\frac{\Delta m}{\Delta E}\right)^5 \sin^{-2}\theta_{\mathrm{C}}, \qquad (39)$$

where $\Delta m = m_n - m_p \simeq 1.2$ MeV and $\tau_n \simeq 880$ s is the neutron lifetime [33]. This estimate gives $\tau \sim 10^{-7}$–10^{-6} s, depending on r_s. It is not surprising that this is close to the lifetimes of charged pions and conventional hyperons.

6. CONCLUSION

On the basis of the NJL model, we have investigated the equation of state of chemically equilibrated deconfined quark matter at various temperatures, baryon densities, and strangeness contents. The model predicts the existence of loosely bound, negatively charged strangelets with maximal binding energies of about 15 MeV per baryon at $r_s \simeq 0.4$. In just the same way as in [17], no absolutely stable strange-quark matter has been found. The estimated lifetimes of these states may be as long as 10^{-7} s. It has been shown that the properties of baryon-rich quark matter are very sensitive to the relative magnitude of the vector and the scalar interaction. At the standard values of the vector and scalar couplings, $G_V/G_S = 0.5$, metastable bound states of chemically equilibrated matter exist at $T < 15$ MeV, while, at $G_V = 0$, this temperature increases to 40 MeV.

Our calculation has revealed a first-order chiral phase transition at finite baryon densities and moderate temperatures. In the case of zero net strangeness ($r_s = 0$), the critical temperature is in the region around 30 MeV and the critical baryon density is around ρ_0. We believe that this phase transition is reminiscent of the ordinary liquid–gas phase transition in nuclear matter. We have found that the maximal critical temperature $T_c \simeq 50$ MeV is reached when the ratio of the net strangeness to the baryon charge is $S/B \simeq 1.2$. The model predicts a strong cooling of matter during the phase transition owing to generation of the constituent mass.

We hope that these results will generate a certain optimism in searches for unusual states of matter in relativistic heavy-ion collisions.

ACKNOWLEDGMENTS

This work was supported by the Russian Foundation for Basic Research (project no. 00-15-96590), the Alexander von Humboldt Foundation, the Graduiertenkolleg "Experimentelle und Theoretische Schwerionenphysik," GSI, BMBF, and DFG.

REFERENCES

1. A. B. Migdal, Zh. Éksp. Teor. Fiz. **61**, 2209 (1971) [Sov. Phys. JETP **34**, 2209 (1971)].
2. A. B. Migdal, G. A. Sorokin, O. A. Markin, and I. N. Mishustin, Zh. Éksp. Teor. Fiz. **72**, 1247 (1977) [Sov. Phys. JETP **45**, 654 (1977)].
3. T. D. Lee and G. C. Wick, Phys. Rev. D **9**, 2291 (1974).
4. Y. Nambu and G. Jona-Lasinio, Phys. Rev. **122**, 345 (1961); **124**, 246 (1961).
5. V. G. Vaks and A. I. Larkin, Zh. Éksp. Teor. Fiz. **40**, 282 (1961) [Sov. Phys. JETP **13**, 192 (1961)].
6. U. Vogl and W. Weise, Prog. Part. Nucl. Phys. **27**, 195 (1991).
7. S. P. Klevansky, Rev. Mod. Phys. **64**, 649 (1992).
8. M. Asakawa and Y. Yazaki, Nucl. Phys. A **504**, 668 (1989).
9. S. Klimt, M. Lutz, and W. Weise, Phys. Lett. B **249**, 386 (1990).
10. J. Cugnon, M. Jaminon, and B. van den Bossche, Nucl. Phys. A **598**, 515 (1996).
11. K. G. Klimenko and A. S. Vshivtsev, Zh. Éksp. Teor. Fiz. **111**, 1921 (1997) [JETP **84**, 1047 (1997)].
12. J. Berges and K. Rajagopal, Nucl. Phys. B **538**, 215 (1999).
13. T. M. Schwarz, S. P. Klevansky, and G. Rapp, Phys. Rev. C **60**, 055205 (1999).
14. V. Koch, T. S. Biro, J. Kunz, and U. Mosel, Phys. Lett. B **185**, 1 (1987); V. Koch, B. Blättel, and U. Mosel, Phys. Lett. B **194**, 331 (1987).
15. M. Buballa, Nucl. Phys. A **611**, 393 (1996); M. Buballa and M. Oertel, Nucl. Phys. A **642**, 39 (1998).
16. I. N. Mishustin, in *Proceedings of the International Conference Nuclear Physics at the Turn of the Millenium, Wilderness, 1996,* Ed. by H. Stöcker, A. Gallman, and J. H. Hamilton (World Sci., Singapore, 1997), p. 522.
17. M. Buballa and M. Oertel, Phys. Lett. B **457**, 261 (1999).
18. I. N. Mishustin, L. M. Satarov, H. Stöcker, and W. Greiner, Phys. Rev. C **59**, 3343 (1999).
19. I. N. Mishustin, L. M. Satarov, H. Stöcker, and W. Greiner, Phys. Rev. C **62**, 034901 (2000).
20. P. Rehberg, S. P. Klevansky, and J. Hüfner, Phys. Rev. C **53**, 410 (1996).
21. W. Ehehalt and W. Cassing, Nucl. Phys. A **602**, 449 (1996).
22. E. Witten, Phys. Rev. D **30**, 272 (1984).
23. E. Farhi and R. L. Jaffe, Phys. Rev. D **30**, 2379 (1984).
24. C. Greiner, P. Koch, and H. Stöcker, Phys. Rev. Lett. **58**, 1825 (1987).
25. E. P. Gilson and R. L. Jaffe, Phys. Rev. Lett. **71**, 332 (1993).
26. J. Schaffner-Bielich, Nucl. Phys. A **639**, 443 (1998).
27. W. Busza, R. L. Jaffe, J. Sandweiss, and F. Wilczek, hep-ph/9910333.
28. C. Greiner and H. Stöcker, Phys. Rev. D **44**, 3517 (1991).
29. N. K. Glendenning, Phys. Rev. D **46**, 1274 (1992).
30. O. Scavenius, A. Mocsy, I. N. Mishustin, and D. H. Rischke, nucl-th/0007030.
31. M. A. Halasz, A. D. Jackson, R. E. Shrock, *et al.,* Phys. Rev. D **58**, 096007 (1998).
32. A. I. Goodman, J. I. Kapusta, and A. Z. Mekjian, Phys. Rev. C **30**, 851 (1984).
33. Particle Data Group (C. Caso *et al.*), Eur. Phys. J. C **3**, 1 (1998).

Physics of Atomic Nuclei, Vol. 64, No. 5, 2001, pp. 812–833. From Yadernaya Fizika, Vol. 64, No. 5, 2001, pp. 877–898.

90th ANNIVERSARY OF A.B. MIGDAL'S BIRTHDAY

Quark Combinatorics and Meson-Production Ratios in Hadronic Z^0 Decays*

V. V. Anisovich, V. A. Nikonov, and J. Nyiri[1)]

Petersburg Nuclear Physics Institute, Russian Academy of Sciences, Gatchina, 188350 Russia

Received August 24, 2000

Abstract—A vast body of experimental data accumulated in the past few years in hadronic Z^0 decays allows one to check quark-combinatorics relations for a new type of processes—namely, quark jets in the decays $Z^0 \to q\bar{q} \to$ hadrons. In this paper, we review quark-combinatorics rules for the yields of vector and pseudoscalar mesons, V/P, in the central and fragmentation regions of hadronic Z^0 decays. It is emphasized that, in the central region, a direct verification of quark-combinatorics rules is rather problematic because of a considerable background associated with the decay of highly excited resonances; however, such a verification is possible in the fragmentation region, at $x_{\rm hadron} \sim 0.5$–1, where the contribution of resonance decays is suppressed owing to a fast decrease of the spectra with increasing $x_{\rm hadron}$. It is shown that, in the fragmentation region, experimental data on ρ^0/π^0 and p/π^+ are in reasonable agreement with the predictions of quark combinatorics. The ratios of the heavy-meson yields, B^*/B and D^*/D, are also discussed: the data demonstrate good agreement with the quark combinatorial results. We analyze the structure of the suppression parameters for strange- and heavy-quark production in soft processes and estimate their orders of magnitude in multiperipheral processes; the ratio $K^\pm/\pi^\pm$ at $x_{\rm hadron} \sim 0.5$–0.8 and the production probabilities for $c\bar{c}$ and $b\bar{b}$ mesons are in good agreement with the estimates. © *2001 MAIK "Nauka/Interperiodica".*

1. INTRODUCTION

The relations of quark combinatorics for hadron yields were originally based on a qualitative treatment of a multiparticle production process as a process in which the production of a cloud of noncorrelated quarks and antiquarks is followed by their occasional fusion into mesons and baryons [1, 2]. In this picture, the quark-combinatorics approach echoes a statistical treatment of nuclear decays [3]; as a matter of fact, it was initiated by the success of statistical methods in describing multinucleon processes. There is yet another common point in treating multinucleon and multiquark processes: the stage of final-state interactions. In multinucleon reactions, the Watson–Migdal factor [4] leads to an increase in the low-energy contributions to nucleon–nucleon final-state interactions. In multiquark reactions, the analogous effect of $q\bar{q}$ and qqq final-state interactions, as one can guess, should enhance the production of the comparatively low-mass mesons and baryons: the hypothesis that a few low-mass $q\bar{q}$ and qqq multiplets make a dominant contribution to the spectra of product hadrons was put forth in [5].

This particular story reflects a general trend of how methods and approaches used in nuclear physics affected the physics of strong interactions. But as time goes on, our understanding of QCD, the theory of strong interactions, becomes deeper, so that a new level of understanding of quark–gluon physics in the soft-interaction region furnishes a sufficient motivation for reviewing the relations of quark combinatorics.

1.1. Quark Combinatorics for Hadron Production

As was indicated above, the rules of quark combinatorics were initially suggested for finding probabilities of hadron yields in multiparticle production processes [1, 2]. Later, they were extended to meson-decay processes (see [6]). In [1, 2] (see also [5]), hadronic production processes were treated on the basis of the following qualitative picture. In a multiparticle production process, there is a stage of a cloud of constituent quarks. When joining, they form mesons ($q\bar{q}$), baryons (qqq), and antibaryons ($\bar{q}\bar{q}\bar{q}$). The probabilities of forming hadrons of different sorts

*This article was submitted by the authors in English.

[1)]KFKI Research Institute for Particle and Nuclear Physics, Hungarian Academy of Sciences, PO Box 49, H-1525 Budapest, Hungary.

are determined by combinatorial rules that were obtained under the assumption that quarks and antiquarks of the sea are produced uncorrelated and that there is neither spin nor isospin alignment.

Our knowledge of the multiparticle production mechanism—that is of the structure of amplitudes responsible for inclusive production—is now, however, more complete, thus allowing us to investigate the basis of quark combinatorics at a new level. In the present paper, we investigate (i) the ratio of vector/pseudoscalar meson yields both for the central and for the fragmentation region of quark jets in hadronic Z^0 decays (Sections 2 and 3, respectively) and (ii) the structure of the suppression parameters for the production of strange and heavy quarks in multiperipheral processes (Section 4).

The time is ripe for this review, for, in the meantime, quark combinatorics has become widely used to consider meson resonances of masses 1.0–2.5 GeV, with the aim of determining the quark–gluon content of these states by investigating *resonance* → *meson* transitions [7–9]. In the investigation of exclusive decay processes [7–9], the qualitative picture of the cloud structure of sea quarks is not used (which renders the conclusions more model-independent). However, the notion of a "suppression parameter" for the production of strange quarks plays an important role, and it is identical to that which is used in multiparticle production processes. Thus, we have to rethink quark combinatorics on a new basis, both theoretically and experimentally.

1.2. Hadronic Z^0 Decays

Here, we discuss the yields of vector $(\rho^0, \omega, \bar{K}^*)$ and pseudoscalar (π, K) mesons in hadronic Z^0 decays. Currently, there exists rich experimental information about these processes, which are determined by $Z^0 \to q\bar{q} \to hadrons$ transitions. First, we consider the production of light-flavor mesons created in quark jets, $Z^0 \to u\bar{u}$, $Z^0 \to d\bar{d}$, and $Z^0 \to s\bar{s}$, with probabilities in the proportion [10]

$$u\bar{u} : d\bar{d} : s\bar{s} \simeq 0.26 : 0.37 : 0.37. \qquad (1)$$

The large mass of the Z^0 boson makes it possible to observe, in $Z^0 \to q\bar{q} \to hadrons$ hadronic decays, the characteristic features of both multiparticle production (central region of quark jets) and meson-decay processes (fragmentation production).

The data accumulated by the ALEPH [11], L3 [12], DELPHI [13], and OPAL [14] collaborations provide the spectra of vector and pseudoscalar mesons, $d\sigma/dx(Z^0 \to V + X)$ and $d\sigma/dx(Z^0 \to P + X)$, in a broad interval of x, so that it becomes possible to compare them with the predictions of quark combinatorics.

1.3. Hadron Production in the Central Region and Vector-to-Pseudoscalar Ratio

In Section 2, we consider the hadron production in the central region in the quark jet. We discuss the prompt-vector-meson (V) and prompt-pseudoscalar-meson (P) yields. For particles belonging to the same $q\bar{q}$ multiplet, we obtain

$$\frac{V_{\rm prompt}}{P_{\rm prompt}} = 3. \qquad (2)$$

This is a well-known result of quark combinatorics [1, 2, 5] for hadron–hadron collisions. Hence, our analysis shows that the ratio $V_{\rm prompt}/P_{\rm prompt}$ takes the same value for the Pomeron ladder in hadron–hadron collisions and for quark jets, despite the different structures of color exchanges in these processes.

As we have already said, the rules of quark combinatorics for hadron–hadron collisions were introduced in [1, 2, 5]. Investigations of the QCD Pomeron [15, 16] shed light on the quark–gluon structure of the multiperipheral ladder in hadron collisions and allowed us to deal with meson yields in the central region on a new level. In Appendix A, we therefore give a new analysis of the results of quark combinatorics for $V_{\rm prompt}/P_{\rm prompt}$ at $x \sim 0$ using Lipatov's Pomeron [16] as a guide.

1.4. Suppression of Strange-Quark Production

An important feature in hadron production is the suppression of the production probability for a strange quark in the multiperipheral ladder:

$$u\bar{u} : d\bar{d} : s\bar{s} = 1 : 1 : \lambda \qquad (3)$$

with $0 \le \lambda \le 1$. This topic is discussed in Section 4: it is shown that $\lambda \simeq m^2/m_s^2$, where m and m_s are the masses of nonstrange and strange constituent quarks, respectively.

This suppression results in a suppression of the production of mesons containing strange quarks that is observed in hadronic Z^0 decays.

1.5. Soft Color Neutralization of Quarks in Hadronic Z^0 Decays

In considering processes of central production in $Z^0 \to q\bar{q} \to hadrons$ decays, we start with the standard mechanism of soft color neutralization of outgoing quarks: newly born quark–antiquark pairs are produced in the multiperipheral ladder (see Fig. 1*a*), which provides the transfer of color from a quark to an antiquark. The discontinuity of the self-energy diagram in Fig. 1*b* (determined by cutting through hadronic states, dashed line) determines the cross section for $Z^0 \to hadrons$ transitions, while

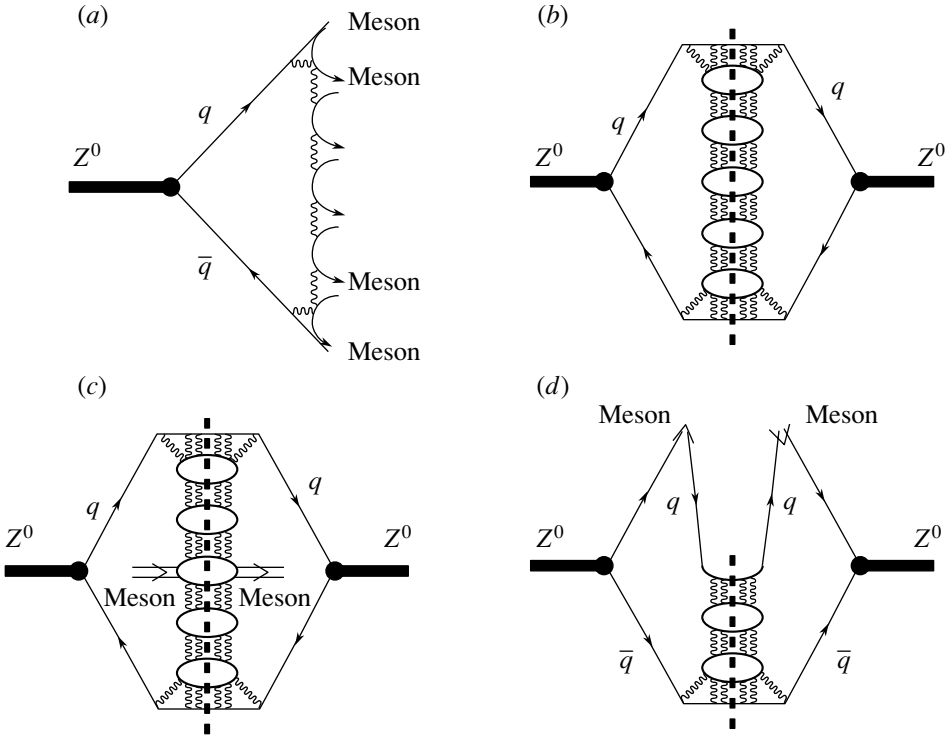

Fig. 1. Hadronic decay of the Z^0 meson: (a) multiperipheral ladder providing the transfer of color from the quark to the antiquark; (b) self-energy diagram [cutting through hadronic states (dashed line) determines the hadronic cross section]; (c) diagram for the inclusive-meson-production cross section in the central region, $d\sigma(Z^0 \to \text{meson} + X)/dx$, at $x \sim 0$; and (d) diagram for the inclusive-meson-production cross section in the fragmentation region at $x \sim 0.2$–1.

the quark–gluon block inside the big quark loop determines confinement forces.

Likewise, the cross section for inclusive meson production in the central region is provided by the discontinuity of the diagram in Fig. 1c. The *meson* $\to q\bar{q} \to$ *meson* quark loop shown in Fig. 1c with the production of vector or pseudovector mesons determines the relative probabilities of these particles. The chain of quark loops shown in Figs. 1b, 1c, and 1d (below, we denote this chain as A) contains both color-singlet ($c = 1$) and color-octet ($c = 8$) components: $A = A_1 + A_8$. According to the rules of $1/N$ expansion [17], the main contribution is due to the octet component. The idea that the quark leaves the confinement trap by producing new quark–antiquark pairs is rather old; it was discussed long ago (see, for example, [5], Sections 7 and 9, and [18]). A new step in understanding the confinement mechanism was made by Gribov [19]. Following his ideas and assuming that the t-channel exchange of a quark is a constructive element of the jet, we use the jet structure shown in Fig. 1a.

Spectroscopic calculations (see, for example, [20]) support the hypothesis that confinement forces are of the scalar type; accordingly, we assume that the chain A realizes $J^P = 0^+$ t-channel exchange.

The calculation of the block for central meson production in Section 2 proves that Eq. (2) holds if the wave functions of mesons (V and P) belonging to the same multiplet are equal.

1.6. Prompt Hadron Production and Production due to the Decay of Highly Excited Resonances

The equality in (2) is valid for prompt meson production, while the decays of highly excited states violate this ratio, as is observed experimentally, leading to an increase in the rate of light-meson production due to resonance decay. As to ρ/π and K^*/K, the decays increase the contribution of the pseudoscalar component. According to [11], $\rho^0/\pi^0 = 0.15 \pm 0.03$ and $K^*/K = 0.40 \pm 0.06$, which indicates a large contribution to the spectra from the decays of highly excited states.

The production and decay of highly excited states in hadron–hadron collisions was discussed in [21]. The conclusion was similar: the mean multiplicities of product light mesons and baryons result mainly from the cascade decays of highly excited resonances.

The multiperipheral structure of the ladder allows us to estimate the resonance masses that are important for meson production; they are on the order of or less than 2 GeV (Section 5).

That there are decays of highly excited resonances must be taken into account in verifying quark combinatorial rules. We discuss several ways of solving this problem.

1.7. Heavy-Meson Production in $Z^0 \to b\bar{b}$ and $Z^0 \to c\bar{c}$ Decays

One way is to check quark combinatorics for heavy-particle yields, where cascade multiplication is suppressed. An ideal example could be the production of mesons containing a b quark. In fact, the ratio B^*/B for beauty mesons that was observed experimentally agrees with (2). When the lowest S-wave multiplet dominates in the production of heavy mesons, one has [provided that Eq. (2) is satisfied] $B \simeq B_{\rm prompt} + B^*_{\rm prompt} = 4B_{\rm prompt}$, and the ratio of vector-to-pseudoscalar mesons is $B^*/B \simeq 0.75$.

Experiments that studied Z^0 decays yield $B^*/B = 0.771 \pm 0.075$ [22], 0.72 ± 0.06 [23], 0.76 ± 0.10 [24], and 0.76 ± 0.09 [25], the mean value being 0.75 ± 0.04.

For charmed mesons, $D^*/D = 0.60 \pm 0.05$ [26], 0.62 ± 0.03 [27], and 0.57 ± 0.05 [28]. The mean value is 0.61 ± 0.03, which suggests an increase in the contribution from the decay of non-S-wave multiplets.

It should be emphasized that the V/P ratios for beauty and charmed mesons are saturated in the fragmentation region owing to the transitions $Z^0 \to b\bar{b}$ and $Z^0 \to c\bar{c}$. In Section 3, we therefore reanalyze quark combinatorics for the fragmentation region of hadronic Z^0 decays.

The cross section for meson production in the fragmentation region is determined by the discontinuity of the diagram in Fig. 1*c* (the cut of the ladder diagram is shown by the dashed line). Direct calculations demonstrate that Eq. (2) is satisfied to a rather high accuracy for the fragmentation region as well, provided that the wave functions of the vector and pseudoscalar mesons are equal.

1.8. Production of Light-Flavor Mesons in the Fragmentation Region of Hadronic Z^0 Decays

Investigation of meson production in the fragmentation region opens the way to test the rules of quark combinatorics for light-flavor hadrons and to verify Eq. (2) in particular. As was said above, the spectra of light-flavor hadrons are dominated by the contribution of the component associated with the decay of highly excited states. In the case of jet processes, this component is still dominant in the central region (at $x \sim 0$), but not in the fragmentation one. The hadronic spectra for jets are maximal at $x \sim 0$, fast decreasing with the growth of x. As a result, the component that is due to resonance decay decreases fast because decay products share the value of $x_{\rm resonance}$, thus entering the region of smaller x. In due course, this leads to a fast growth of the relative contribution from prompt particle production. Therefore, measurements of particle yields at $x \sim 0.5$–1.0 provide the opportunity of testing quark combinatorics in a model-independent way.

In Section 3, we compare the ρ^0/π^0 and K^*/K ratios measured in [11] at large x with quark-combinatorics predictions; in Section 5, we discuss the baryon-to-meson ratio p/π^+. This comparison demonstrates reasonable agreement of experimental data with the predictions of quark combinatorics.

1.9. Suppression of Heavy-Quark Production

The multiperipheral dynamics of the quark–gluon ladder in the processes of Fig. 1 results in a strong suppression of the production of new heavy-quark pairs, $Q\bar{Q}$. The suppression parameter (relative probability) is of order $\lambda_Q \simeq m^2/(m_Q^2 \ln^2(\Lambda^2/m_Q^2))$, where m_Q is the heavy-quark mass and Λ is the QCD scale parameter, $\Lambda \sim 200$ MeV. One has $\lambda_c \simeq 2.8 \times 10^{-3}$ and $\lambda_b \simeq 1.1 \times 10^{-4}$.

The inclusive production of $c\bar{c}$ and $b\bar{b}$ mesons in Z^0 decays agrees with this estimate (Section 4).

1.10. ω/ρ^0 Ratio and Interference of Flavor Amplitudes at $x \sim 1$

The rules of quark combinatorics yield $\omega_{\rm prompt}/\rho^0_{\rm prompt} = 1$. It can be proven that the decays of highly excited states have only a slight effect on this equality. Indeed, the masses of ρ and ω are almost equal, so that the phase spaces of the decay processes affect identically the probabilities of their yields. Experiments confirm this statement: at $x \sim 0.1$–0.2, the value of $\omega/\rho^0 = 1$ is observed. However, the experimental value is $\omega/\rho^0 < 1$ at larger x. This reveals the interference of flavor amplitudes. The fact is that the decay vertices for $Z^0 \to u\bar{u}$ and $Z^0 \to d\bar{d}$ have opposite signs, thus enhancing the coherent production of ρ^0 mesons and suppressing the production of ω (Section 6).

2. PROMPT PRODUCTION IN THE CENTRAL REGION OF THE QUARK JET: THE RATIO $V/P = 3$

In this section, we discuss the prompt production of vector and pseudoscalar mesons (for the sake of definiteness, ρ and π mesons) in the central region of a

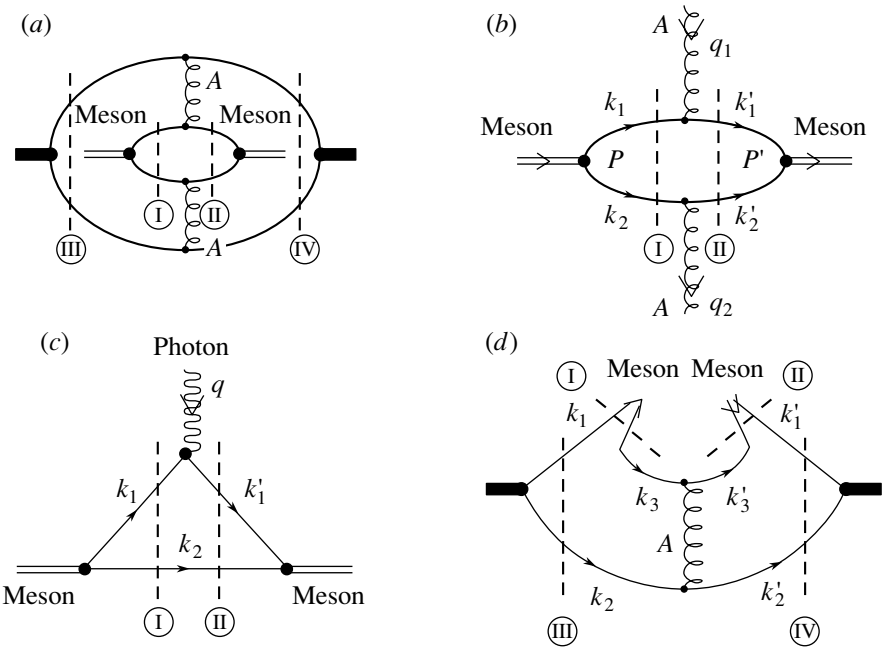

Fig. 2. (*a, b*) Production blocks for a meson in the central region (dashed lines show the cuts of diagrams in the spectral integral); (*c*) form-factor diagram determining the meson wave function; and (*d*) cuts of the diagram for the inclusive-meson-production cross section in the fragmentation region.

quark jet. The production cross section is determined by the discontinuity of the diagram in Fig. 1*c*; it is redrawn in Fig. 2*a*. A feature peculiar to ρ and π production is the presence of a loop diagram, which is shown separately in Fig. 2*b*. Below, we calculate these loop diagrams for ρ and π using the spectral-integration technique, which is discussed in detail in [29, 30]. Within this technique, the loop diagrams are expressed in terms of the ρ and π light-cone wave functions.

First, we present the result of our calculations.

From the direct calculations, it follows that the inclusive cross section for ρ and π mesons at $x \sim 0$ is given by

$$\frac{d\sigma}{dx}(Z^0 \to \rho + X) = \frac{1}{16\pi^2}$$
$$\times \int_0^1 \frac{d\xi}{\xi(1-\xi)} \int d^2\mathbf{k}_\perp \psi_\rho^2(\xi, \mathbf{k}_\perp) \times 3\Pi_Z(W_1^2, W_2^2),$$
$$\frac{d\sigma}{dx}(Z^0 \to \pi + X) = \frac{1}{16\pi^2} \qquad (4)$$
$$\times \int_0^1 \frac{d\xi}{\xi(1-\xi)} \int d^2\mathbf{k}_\perp \psi_\pi^2(\xi, \mathbf{k}_\perp) \times \Pi_Z(W_1^2, W_2^2).$$

Here, ψ_ρ and ψ_π are the quark wave functions for the ρ and π mesons, while ξ and $\mathbf{k}_\perp$ are quark light-cone variables [the momentum fraction carried by a quark along the z axis and its momentum in the (x, y) plane, respectively]. In (4), one can see explicit expressions associated with the production of ρ and π mesons. The remaining part (contribution from the large quark loop and from ladder diagrams) is denoted in (4) by $\Pi_Z(W_1^2, W_2^2)$, which depends on the invariant energies squared for the quark chains, W_1^2 and W_2^2. Multiperipheral kinematics yields

$$W_1^2 W_2^2 \simeq \xi(1-\xi)(m^2 + k_\perp^2)M_Z^2, \qquad (5)$$

where M_Z is the mass of the Z^0 boson.

The factor of 3 in the ρ-production cross section results from a summation over polarizations of the vector particle.

Equation (4) directly demonstrates that, if the quark wave functions of ρ and π are identical, which is assumed by the quark multiplet classification of these mesons, we have $d\sigma(Z^0 \to \rho + X)/dx : d\sigma(Z^0 \to \pi + X)/dx = 3:1$ at $x \sim 0$. We emphasize once again that Eq. (4) and the diagrams in Figs. 1*c*, 2*a*, and 2*b* stand for promptly produced mesons.

2.1. Spectral Representation for the Loop Diagram in Fig. 2a

The calculation of the diagram in Fig. 2*a* in terms of spectral integration involves the following steps (see also [29, 30]):

(i) The quark loops in Fig. 2*a* are taken to be off the energy shell.

(ii) The discontinuities are calculated for the off-energy-shell quark loops (the relevant cuts are shown by the dashed lines I, II, III, and IV).

(iii) The spectral integrals are determined by the discontinuities of the integrands.

Let us first consider the double spectral integral corresponding to cuts III and IV. These are the spectral integrals with respect to the effective masses squared, M^2 and M'^2, in the transitions $Z^0 \to q\bar{q}$ and $q\bar{q} \to Z^0$:

$$\int\limits_{4m^2}^{\infty} \frac{dM^2 dM'^2}{\pi^2} \frac{g_Z(M^2) g_Z(M'^2)}{(M^2 - M_Z^2)(M'^2 - M_Z^2)} \times \int d\Phi(P_Z; p_1, p_2) d\Phi(P'_Z; p_3, p_4) \times S_Z\, T(p; q_1, q_2) A(W_1^2, q_1^2) A(W_2^2, q_2^2). \quad (6)$$

Here, $g_Z(M^2)$ is the vertex function for the transition $Z^0 \to q\bar{q}$ and M_Z is the Z^0-boson mass. The factors $d\Phi(P_Z; p_1, p_2)$ and $d\Phi(P'_Z; p_3, p_4)$ are the phase spaces associated with the cuts III and IV, while S_Z is the spin factor for the big quark loop in Fig. 2*a*. The amplitudes $A(W_i^2, q_i^2)$ $(i = 1, 2)$ refer to the quark–gluon chains with the t-channel scalar quantum numbers (see discussion in Section 1.5), and $T(p; q_1, q_2)$ is the block corresponding to the small quark loop (the $q\bar{q}$ loop for the production of ρ and π mesons).

The characteristic feature of the spectral integral (6) is the large value of M_Z. For this reason, one can replace, to a rather high precision, the poles of the spectral integrand by half-residues:

$$\frac{1}{M^2 - M_Z^2} \to -i\pi\delta(M^2 - M_Z^2),$$
$$\frac{1}{M'^2 - M_Z^2} \to i\pi\delta(M'^2 - M_Z^2). \quad (7)$$

Equation (6) stands for the discontinuity of the amplitude that results in opposite signs for the half-residues in (7). Equation (7) means that the block inside the big quark loop can be considered, to a high precision, as a block of the real process. This is a well-known feature of high-energy jets; below, we use it to estimate meson-production amplitudes.

We are not especially interested in the spectral integral (6), which is determined by the big quark loop, since it is quite common to π and to ρ production. Our objective is the spectral integral corresponding to the amplitude $T(p; q_1, q_2)$, which is the ρ- or π-meson-production block. This block is shown separately in Fig. 2*b*.

2.2. Calculation of the Loop Diagram in Fig. 2b

The amplitude of the loop diagram in Fig. 2*b* represented as a double dispersion integral is

$$M = T(p; q_1, q_2) 2p_0 (2\pi)^3 \delta^{(3)}(\mathbf{p} + \mathbf{q}_1 - \mathbf{q}_2 - \mathbf{p}'), \quad (8)$$

where

$$T(p; q_1, q_2) = \int\limits_{4m^2}^{\infty} \frac{ds ds'}{\pi^2} \int d\phi\, \frac{G_{\mathrm{meson}}(s)}{s - \mu^2} \frac{G_{\mathrm{meson}}(s')}{s' - \mu^2}\, S_{\mathrm{meson}}.$$

Here, μ is the product-meson mass, s and s' are the squares of the invariant masses in the intermediate $q\bar{q}$ states, and G_{meson} is the vertex for the *meson* $\to q\bar{q}$ transition. The ratio $G_{\mathrm{meson}}(s)/(s - \mu^2)$ determines the product-meson wave function apart from a spin factor, and S_{meson} is the spin factor of the loop diagram in Fig. 2*b*.

Let us explain the structure of the spectral integral (8) in more detail.

The cut quark loop must be integrated over the phase space of intermediate $q\bar{q}$ states, $\Phi(P; k_1, k_2)$ and $\Phi(P'; k'_1, k'_2)$, with the invariant phase space being determined as

$$d\Phi(P; k_1, k_2) = \frac{1}{2} \frac{d^3 k_1}{(2\pi)^3 2k_{10}} \frac{d^3 k_2}{(2\pi)^3 2k_{20}} (2\pi)^4 \delta^{(4)}(P - k_1 - k_2). \quad (9)$$

This integration is carried out with allowance for the conservation law for momenta flowing through the ladder (wavy lines in Fig. 2*b*); the momenta are denoted by q_1 and q_2. Thus, the phase-space integration of the cut diagram is given by

$$d\Phi(P; k_1, k_2) d\Phi(P'; k'_1, k'_2) (2\pi)^3 2k'_{10} \times \delta^{(3)}(\mathbf{k}'_1 - \mathbf{k}_1 - \mathbf{q}_1)(2\pi)^3 2k'_{20} \delta^{(3)}(\mathbf{k}'_2 - \mathbf{k}_2 + \mathbf{q}_2), \quad (10)$$

where $k_i^2 = k_j'^2 = m^2$, $P^2 = s$, and $P'^2 = s'$. We use light-cone variables for the product-meson wave functions; the simplest way to introduce them is to go over to the infinite-momentum frame. The 4-momenta $P = (P_0, \mathbf{P}_\perp, P_z)$ and $k_i = (k_{i0}, \mathbf{k}_{i\perp} k_{iz})$ are then written in the limits $P_z \to \infty, k_{iz} \to \infty$, and $k'_{iz} \to \infty$. After introducing the light-cone variables ($\xi_i = k_{iz}/P_z$, $\xi'_i = k'_{iz}/P_z$, $m_{i\perp}^2 = m^2 + k_{i\perp}^2$, $m_{i\perp}'^2 = m^2 + k_{i\perp}'^2$) and taking q_{iz} to be small ($q'_{iz}/P_z \to 0$, the constraint of multiperipheral kinematics), we rewrite (10) as follows:

$$\frac{1}{16\pi}\times\frac{d\xi_1 d\xi_2}{\xi_1\xi_2}\delta(1-\xi_1-\xi_2)d^2k_{1\perp}d^2k_{2\perp}\delta^{(2)}(\mathbf{k}_{1\perp}+\mathbf{k}_{2\perp})\delta\left(s-\frac{m_{1\perp}^2}{\xi_1}-\frac{m_{2\perp}^2}{\xi_2}\right)$$
$$\times\delta\left(s'+(\mathbf{q}_{1\perp}-\mathbf{q}_{2\perp})^2-\frac{m_{1\perp}'^2}{\xi_1}-\frac{m_{2\perp}'^2}{\xi_2}\right)\times(2\pi)^3 2P_0\delta^{(3)}(\mathbf{P}+\mathbf{q}_1-\mathbf{q}_2-\mathbf{P}') \quad (11)$$
$$\equiv d\phi(\xi_1,\xi_2;\mathbf{k}_{1\perp},\mathbf{k}_{2\perp};\mathbf{q}_{1\perp},\mathbf{q}_{2\perp})\times(2\pi)^3 2P_0\delta^{(3)}(\mathbf{P}+\mathbf{q}_1-\mathbf{q}_2-\mathbf{P}').$$

The factor $d\phi$ stands for phase-space integration in the spectral integral (8): $d\phi\equiv d\phi(\xi_1,\xi_2;\mathbf{k}_{1\perp},\mathbf{k}_{2\perp};\mathbf{q}_{1\perp},\mathbf{q}_{2\perp})$.

In the approximation given by (2.2.1), where the jet block inside the big quark loop is considered as a real process, one may fix $q_1=q_2=0$, in which case the inclusive cross section is proportional to $T(p;0,0)$. After taking δ functions in (2.2.2) into account, the formula for $T(p;0,0)$ takes the rather simple form

$$T(p;0,0) \quad (12)$$
$$=\frac{1}{16\pi^3}\int_0^1\frac{d\xi}{\xi(1-\xi)}\int d^2k_\perp\left(\frac{G_{\rm meson}(s)}{s-\mu^2}\right)^2 S_{\rm meson},$$

where $s=m_\perp^2/(\xi(1-\xi))$.

The amplitude $T(p;0,0)$ alone does not determine the inclusive cross section $d\sigma/dx(Z^0\to{\rm meson}+X)$ because the amplitudes $A(W_1^2,0)$ and $A(W_2^2,0)$ depend on ξ and $k_\perp^2$ [see (5)]. Taking into account this dependence, we find at $x\sim 0$ that

$$\frac{d\sigma}{dx}(Z^0\to{\rm meson}+X) \quad (13)$$
$$\sim\frac{1}{16\pi^3}\int_0^1\frac{d\xi}{\xi(1-\xi)}\int d^2k_\perp\left(\frac{G_{\rm meson}(s)}{s-\mu^2}\right)^2$$
$$\times S_{\rm meson}\,\Pi(W_1^2,W_2^2).$$

The spin factor $S_{\rm meson}$ is closely related to the normalization of the product-meson wave function.

2.3. Spin Factors S_ρ and S_π

Below, we calculate the spin factors S_ρ and S_π at $q_1=q_2=0$. They are given by

$$S_\pi=-{\rm tr}\Big(i\gamma_5(\hat k_1+m)(\hat k_1'+m)i\gamma_5$$
$$\times(-\hat k_2'+m)(-\hat k_2+m)\Big), \quad (14)$$
$$S_\rho=-{\rm tr}\Big(\gamma_\alpha^\perp(\hat k_1+m)(\hat k_1'+m)\gamma_\alpha^\perp$$
$$\times(-\hat k_2'+m)(-\hat k_2+m)\Big).$$

Here, we considered that the quark–gluon ladder carries the quantum numbers of the scalar state, $J^P=0^+$; hence, the quark-ladder vertex is equal to unity.

The ρ-meson vertex has the form

$$\gamma_\alpha^\perp=g_{\alpha\alpha'}^\perp\gamma_{\alpha'}\quad g_{\alpha\alpha'}^\perp=g_{\alpha\alpha'}-\frac{P_\alpha P_{\alpha'}}{P^2}. \quad (15)$$

In the spin factor S_ρ, summation is performed over the polarizations of the meson. For the spin factors, we have

$$S_\pi=8m^2 s\quad S_\rho=32\,m^2(s+2m^2). \quad (16)$$

Let us now demonstrate that similar spin factors determine the normalization of the ρ-meson and the pion wave functions.

2.4. ρ-Meson and Pion Wave Functions

Within the light-cone technique, it is reasonable to introduce the wave function for a particle and its normalization by using the form factor for this particle. The procedure for defining the wave function was discussed in detail elsewhere [29, 30]. For the $q\bar q$ state, this procedure schematically appears to be as follows.

The form factor for a composite system (for the sake of definiteness, we consider the pion form factor) is determined by the triangle diagram in Fig. 2*c*, where the photon interacts with the composite system. The form factor is represented as a double spectral integral with respect to the masses of the incoming and the outgoing pion; the relevant cuts are shown by the dashed lines I and II in Fig. 2*c*.

The amplitude of the triangle diagram for the pion has the form

$$A_\nu^{\rm (tr)}=(p_\nu+p_\nu')\,F_\pi(q^2), \quad (17)$$

where p and p' are the momenta of, respectively, the incoming and the outgoing pion; the index ν refers to photon polarization; and $F_\pi(q^2)$ is the pion form factor, whose double spectral representation is given by

$$F_\pi(q^2)=\int_{4m^2}^\infty\frac{ds ds'}{\pi^2}\int d\Phi^{\rm (tr)}(k_1,k_1',k_2)$$
$$\times\frac{G_\pi(s)}{s-\mu^2}\,T_\pi(s,s',q^2). \quad (18)$$

Here, $d\Phi^{\rm (tr)}(k_1,k_1',k_2)$ is the phase space of the triangle diagram,

$$d\Phi^{\rm (tr)}(k_1,k_1',k_2)=d\Phi(P;k_1,k_2)d\Phi(P';k_1',k_2') \quad (19)$$

$$\times(2\pi)^3 2k'_{20}\delta^{(3)}(\mathbf{k}'_2-\mathbf{k}_2),$$

and P and P' are the total momenta of the $q\bar{q}$ system, respectively, before and after the event of interaction with the photon—that is, $P=k_1+k_2$ and $P'=k'_1+k'_2$ ($P^2=s$ and $P'^2=s'$). The spin factor of the triangle diagram, T_π, is determined by the trace

$$(-)\mathrm{tr}\left[i\gamma_5(\hat{k}'_1+m)\gamma_\nu^\perp(\hat{k}_1+m)i\gamma_5(-\hat{k}_2+m)\right] \tag{20}$$

$$=\left(P_\nu^\perp+P_\nu'^\perp\right)T_\pi(s,s',q^2).$$

The index $\perp$ stands for vectors orthogonal to the photon momentum:

$$\gamma_\nu^\perp=g_{\nu\nu'}^\perp\gamma_{\nu'},\ \ P_\nu^\perp=g_{\nu\nu'}^\perp P_{\nu'},\ \ g_{\nu\nu'}^\perp=g_{\nu\nu'}-\frac{q_\nu q_{\nu'}}{q^2}. \tag{21}$$

At $q^2=0$, one has $F_\pi(0)=1$. A direct calculation on the basis of Eq. (2.2.4) in the limit $q^2\to 0$ yields

$$1=\int\limits_{4m^2}^{\infty}\frac{ds}{\pi}\left(\frac{G_\pi(s)}{s-\mu^2}\right)^2\rho(s)\,S_\pi^{(\mathrm{wf})}(s), \tag{22}$$

where $\rho(s)$ is the phase space of the $q\bar{q}$ system,

$$\rho(s)=\frac{1}{2}\int d\Phi(P;k_1,k_2)=\frac{1}{16\pi}\sqrt{\frac{s-4m^2}{s}}, \tag{23}$$

and $S_\pi^{(\mathrm{wf})}(s)$ is the trace of the quark loop diagram for the pion,

$$S_\pi^{(wf)}(s) \tag{24}$$

$$=(-)\mathrm{tr}\left[i\gamma_5(\hat{k}_1+m)i\gamma_5(-\hat{k}_2+m)\right]=2s.$$

Using the light-cone variables, we can recast Eq. (22) into the form

$$1=\frac{1}{16\pi^2}\int\limits_0^1\frac{d\xi}{\xi(1-\xi)}\int d^2\mathbf{k}_\perp\left(\frac{G_\pi(s)}{s-\mu^2}\right)^2 2s, \tag{25}$$

where $s=(m^2+k_\perp^2)/(\xi(1-\xi))$. This equation enables us to introduce the pion wave function as

$$\psi_\pi(\xi,\mathbf{k}_\perp)=\frac{G_\pi(s)}{s-\mu^2}\sqrt{2s}, \tag{26}$$

where the normalization is fixed by the standard requirement.

Likewise, we introduce the ρ-meson wave function: it is defined by the form factor that is the spin matrix $F_{\alpha\alpha'}(q^2)$. In problems that do not deal with the polarization properties of a vector particle, it is convenient to use the trace of the form-factor matrix, $\sum_\alpha F_{\alpha\alpha}(q^2)$, which is normalized by the condition

$$\sum_{\alpha=1,\,2,\,3}F_{\alpha\alpha}(0)=3. \tag{27}$$

The trace $\sum_\alpha F_{\alpha\alpha}(q^2)$ is determined by an expression similar to (2.2.4), with the obvious substitutions $G_\pi\to G_\rho$ and $T_\pi\to T_\rho$. As a result, we find that the normalization for the averaged form factor is

$$1=\frac{1}{3}\sum_{\alpha=1,\,2,\,3}F_{\alpha\alpha}(0)$$

$$=\int\limits_{4m^2}^{\infty}\frac{ds}{\pi}\left(\frac{g_\rho(s)}{s-\mu^2}\right)^2\rho(s)S_\rho^{(\mathrm{wf})}(s), \tag{28}$$

where

$$S_\rho^{(\mathrm{wf})}(s)=-\frac{1}{3}\,\mathrm{Sp}\left[\left(\gamma_\alpha-P_\alpha\frac{\hat{P}}{P^2}\right)(\hat{k}_1+m)\right. \tag{29}$$

$$\left.\times\left(\gamma_\alpha-P_\alpha\frac{\hat{P}}{P^2}\right)(-\hat{k}_2+m)\right].$$

The $\rho\to q\bar{q}$ vertex $\gamma_\alpha-P_\alpha\hat{P}/P^2$ selects three degrees of freedom of the ρ meson. We have

$$S_\rho^{(\mathrm{wf})}(s)=\frac{8}{3}(s+2m^2). \tag{30}$$

In the infinite-momentum frame, Eq. (2.2.4) can be rewritten as

$$1=\frac{1}{16\pi^3}\int\limits_0^1\frac{d\xi}{\xi(1-\xi)}\int d^2\mathbf{k}_\perp\psi_\rho^2(\xi,\mathbf{k}_\perp), \tag{31}$$

where

$$\psi_\rho(\xi,\mathbf{k}_\perp)=\frac{G_\rho(s)}{s-\mu^2}\sqrt{\frac{8}{3}(s+2m^2)}. \tag{32}$$

2.5. V/P Ratio for the Central Region and Color Degrees of Freedom

The normalization conditions for the ρ-meson and pion wave functions define unambiguously the ratio of the yields for prompt production, $\rho/\pi=3$, provided that the wave functions of these mesons are similar. Indeed, expression (13) expressed in terms of the wave functions ψ_ρ and ψ_π immediately yield (4).

In the above derivation, we have not taken into account explicitly color degrees of freedom. This, however, can easily be done. For the *meson* $\to q\bar{q}$ vertex, the color operator is equal to $I/\sqrt{N_c}$, where I is an identity matrix in color space. For the chain of the quark loop diagrams, we have two color amplitudes, a singlet and an octet one (A_1 and A_8, respectively). The couplings of the amplitudes A_1 and A_8 to quarks [$g(A_1)$ and $g(A_8)$] are proportional to I and $\boldsymbol{\lambda}$ (Gell-Mann matrices). All color operators take the same form for pion and for ρ-meson production. Because of that, the color factors are immaterial for the ρ/π

ratio—since these operators are identical, they cancel in the production ratio.

As was stated above, the main contribution to inclusive meson production comes from the ladder diagram A_8. This is because the coupling constant for the $c=8$ amplitude is greater than that for the $c=1$ amplitude. In terms of $1/N_c$ expansion, we have $g(A_1)/g(A_8) \sim 1/\sqrt{N_c}$.

3. INCLUSIVE PRODUCTION OF MESONS IN THE FRAGMENTATION REGION

The cross section for inclusive meson production in the fragmentation region is determined by the discontinuity of the diagram in Fig. 2*d*. The spectral representation for this diagram is written as an integral with respect to the masses of the initial and final $q\bar{q}$ states in the transitions $Z^0 \to q\bar{q}$ and $q\bar{q} \to Z^0$ and with respect to the $q\bar{q}$ masses in the $q\bar{q} \to$ *meson* and *meson* $\to q\bar{q}$ transitions. The amplitude of the diagram in Fig. 2*d* has the form

$$\int\limits_{4m^2}^{\infty} \frac{dM^2 dM'^2}{\pi^2} \frac{g_Z(M^2) g_Z(M'^2)}{(M^2 - M_Z^2)(M'^2 - M_Z^2)} \times \int\limits_{4m^2}^{\infty} \frac{ds ds'}{\pi^2} \psi_{\rm meson}(s) \psi_{\rm meson}(s') \qquad (33)$$
$$\times\, d\phi_3(k_1, k_2, k_3) d\phi_3(k_1', k_2', k_3') A(W^2, (k_2 - k_2')^2) \times \frac{S^{\rm (fr)}_{\rm meson}}{\sqrt{S^{\rm (wf)}_{\rm meson}(s) S^{\rm (wf)}_{\rm meson}(s')}}.$$

The vertices $g_Z(M^2)$ and $g_Z(M'^2)$ are written for the transitions $Z^0 \to q\bar{q}$ and $q\bar{q} \to Z^0$. The spectral integrals with respect to s and s' stand for $q\bar{q} \to$ *meson* and *meson* $\to q\bar{q}$ (where the mesons stand for π and ρ). The product-meson wave function $\psi_{\rm meson}$ was introduced explicitly in Section 2 for the pion and for the ρ meson, and the factors $d\phi_3(k_1, k_2, k_3)$ and $d\phi_3(k_1', k_2', k_3')$ define integration over the phase spaces in the left- and right-hand parts of the diagram in Fig. 2*d*:

$$d\phi_3(k_1, k_2, k_3) = \frac{1}{2} \frac{d^3 k_1}{(2\pi)^3 2k_{10}} \frac{d^3 k_2}{(2\pi)^3 2k_{20}} \times (2\pi)^4 \delta^{(4)}\left(\tilde{P} - k_1 - k_2\right) \qquad (34)$$
$$\times \frac{1}{2} \frac{d^3 k_3}{(2\pi)^3 2k_{30}} (2\pi)^4 \delta^{(4)}(P - k_1 - k_3).$$

Here, $\tilde{P}^2 = M^2$ and $P^2 = s$.

The block $A\left(W^2, (k_2 - k_2')^2\right)$ defines the multiperipheral ladder (wavy line in Fig. 2*d*). This block depends on the momentum transfer squared $(k_2 - k_2')^2$ and the total energy squared W^2:

$$W^2 \simeq M_Z^2 (1 - x). \qquad (35)$$

Here, x is the momentum fraction carried by the product meson, $x = 2p/M_z$, where p is the longitudinal component of the meson momentum, $p_{\rm meson} = (p + \mu_\perp^2/2p, 0, p)$.

The spectra $d\sigma(Z^0 \to {\rm meson} + X)/dx$ fall fast with increasing x: this decrease is governed by $A\left(W^2, (k_2 - k_2')^2\right)$.

All the characteristic features of (3) listed above are the same for pion and for ρ-meson production, the wave functions ψ_π and ψ_ρ also being assumed to be identical. The difference may be contained in the spin factors $S_\pi^{\rm (fr)}$ and $S_\rho^{\rm (fr)}$, which are

$$S_\pi^{\rm (fr)} = (-){\rm tr}\Big[\gamma_\nu'^\perp (1 + R\gamma_5)(\hat{k}_1' + m) i\gamma_5 (\hat{k}_3' + m)(\hat{k}_3 + m) \times i\gamma_5 (\hat{k}_1 + m)\gamma_\nu^\perp (1 + R\gamma_5)(-\hat{k}_2 + m)(-\hat{k}_2' + m)\Big], \qquad (36)$$

$$S_\rho^{\rm (fr)} = (-){\rm tr}\Big[\gamma_\nu'^\perp (1 + R\gamma_5)(\hat{k}_1' + m)\gamma_\alpha'^\perp (\hat{k}_3' + m)(\hat{k}_3 + m) \times \gamma_\alpha^\perp (\hat{k}_1 + m)\gamma_\nu^\perp (1 + R\gamma_5)(-\hat{k}_2 + m)(-\hat{k}_2' + m)\Big],$$

where R is determined by the ratio g_A/g_V (see also Section 6). The factor $\gamma_\nu^\perp(1 + R\gamma_5)$ is related to the $Z^0 \to q\bar{q}$ vertex, which is determined by the vector and axial-vector interactions (the ratio of the coupling constants is about 2.63 for the u quark and 1.43 for the d quark). For $S_\pi^{\rm (fr)}$, summation is performed over the polarizations of the Z^0 boson (index ν); $\gamma_\nu^\perp$ is orthogonal to $k_1 + k_2$, while $\gamma'^\perp_\nu$ is orthogonal to $k_1' + k_2'$. For the ρ-meson spin factor $S_\rho^{\rm (fr)}$, summation

is performed over the polarizations of the Z^0 boson (index ν) and of the ρ meson (index α), with $\gamma_\alpha^\perp$ and $\gamma_\alpha'^\perp$ being orthogonal, respectively, to (k_1+k_3) and to $(k_1'+k_3')$ [see also (15)].

The normalization factors $S_{\rm meson}^{\rm (wf)}(s)$ and $S_{\rm meson}^{\rm (wf)}(s')$ in (3) are related to the definition of the meson wave functions [see (26) and (32)]. The explicit expressions for spin factors (36) are presented in Appendix B. With the aid of these expressions, we can evaluate numerically the ratios of prompt-meson yields in the decay reactions with a smaller energy release. In the case of Z^0 decay, where $M_Z \gg m$ and $M_Z \gg \mu$, a reasonably good approximation for (3) is to replace the integrals with respect to M^2 and M'^2 by half-residues at the poles $M^2 = M_z^2$ and $M'^2 = M_z^2$. We then have the following kinematics for real jets:

$$k_1 = k_1' \quad k_2 = k_2'. \tag{37}$$

In this approximation, we can set $k_3 = k_3'$ and $s = s'$. For light mesons, we then have

$$\frac{S_\pi^{\rm (fr)}}{S_\pi^{\rm (wf)}} \simeq 2M_Z^2(1+R^2), \quad \frac{S_\rho^{\rm (fr)}}{S_\rho^{\rm (wf)}} \simeq 6M_Z^2(1+R^2). \tag{38}$$

For the ratio of the prompt yields, this leads to $\rho : \pi = 3:1$ in the fragmentation region $x \sim 0.5$–1 (more generally, $V : P = 3:1$ for hadronic decays $Z^0 \to q\bar{q}$ with $q = u, d, s$).

The same ratio appears for the production of heavy quarks, $Z^0 = Q\bar{Q}$, where $Q = c, b$. By way of example, we indicate that, in the case of the b quark, the spin factors are

$$\frac{S_B^{\rm (fr)}}{S_B^{\rm (wf)}} \simeq 2\left[M_Z^2 + 2m_b^2 + R^2(M_Z^2 - 4m_b^2)\right]$$
$$\frac{S_{B^*}^{\rm (fr)}}{S_{B^*}^{\rm (wf)}} = 6\left[M_Z^2 + 2m_b^2 + R^2(M_Z^2 - 4m_b^2)\right]. \tag{39}$$

Thus, the ratio $B^*_{\rm prompt} : B_{\rm prompt}$ is also equal to 3.

3.1. V/P Ratio in the Fragmentation Region: Comparison with Experimental Data

We have seen that $V/P = 3$ both in the fragmentation region and in the central region. In the central region, however, a comparison of quark-combinatorics predictions with experimental data is hampered by the presence of a number of decay products of highly excited resonances, while, in the fragmentation region, this contribution is suppressed by fast decreasing spectra. This means that the fragmentation region allows us to perform a model-independent verification of quark combinatorics. Here, we carry out such a comparison on the basis of ALEPH data [11].

To deal with meson spectra at $x \sim 0.2$–0.8, we have fitted the spectra $(1/\sigma_{\rm tot})d\sigma/dx$ to the sum of exponentials, $\sum C_i e^{-b_i x}$; the results of the calculations are presented in Fig. 3 for $\pi^\pm, \pi^0, \rho^0$, and $(p, \bar{p})$. The ratio of the fitted curves drawn with the calculation errors (shaded area) is shown in Fig. 4*a* for ρ^0/π^0. We see that, for $0.6 < x < 0.8$, the data are in reasonable agreement with the predicted value of $\rho/\pi = 3$.

Figures 4*b* and 4*c* demonstrate the K^{*0}/K^0 and $K^{*\pm}/K^\pm$ ratios: the data do not contradict the prediction, but the errors are overly large to draw a definitive conclusion.

4. SUPPRESSION OF STRANGE- AND HEAVY-QUARK PRODUCTION

In hadronic multiparticle production processes (in jet processes of the $Z^0 \to$ *hadrons* type or in high-energy hadron–hadron collisions), the production of strange quarks is suppressed. A strong suppression is observed for the production of heavy quarks $Q = c, b$. One can guess that this suppression, being of the same nature for different reactions, is associated with the mechanism of the production of new quarks at large separations of color objects. This mechanism is seen in its pure form in two-body decays (the corresponding diagram is shown in Fig. 5*a*). The block of the production of a new $q\bar{q}$ pair in a two-body decay is identical to that of meson production in jet processes (Fig. 5*b*); therefore, it is reasonable to assume that the mechanism suppressing the production of new quarks is similar for these processes.

4.1. Two-Meson Decay of $q\bar{q}$ States and Soft Hadronization

The decay of a $q\bar{q}$ state proceeds as follows: the quarks of the excited state leave the region where they were kept by the confinement barrier; at a sufficiently large separation, a new quark–antiquark pair will inevitably be produced: together with the incident quarks, these new quarks then form mesons (free particles). Schematically, this process (which is the leading one in terms of $1/N$ expansion) is represented by the diagram in Fig. 5*a*: two quarks fly away (with momenta p_1 and p_2), with the result that, at large quark separations, the gluon field produces a new $q\bar{q}$ pair (quarks with momenta k_2 and k_3); the primary quark (now with momentum k_1) then joins the newly born one (k_2), creating a meson. Likewise, another newly born quark (k_3) joins the other primary quark

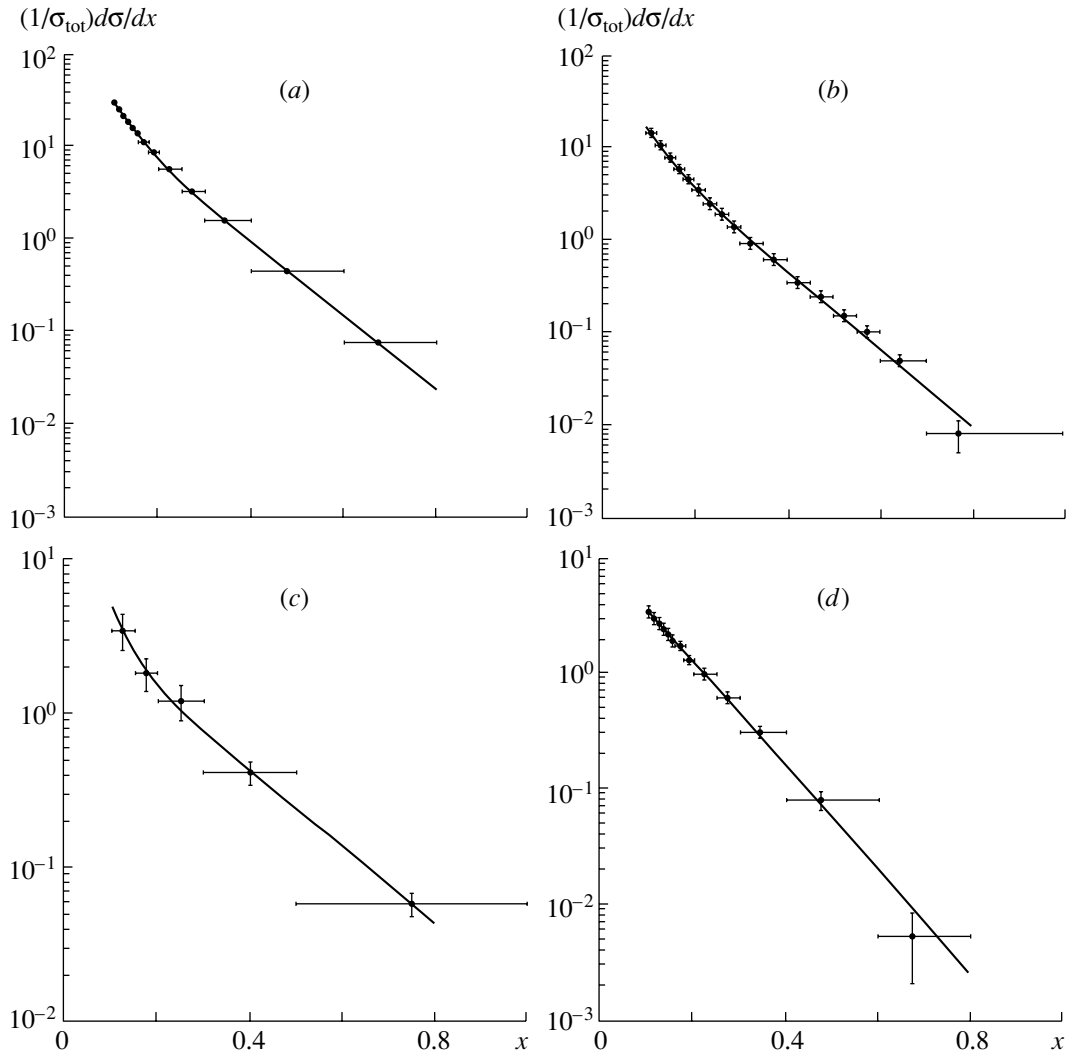

Fig. 3. Spectra $(1/\sigma_{\text{hadron}})\, d\sigma_{Z^0\to\text{meson}+X}/dx$ [11] for (*a*) $\pi^{\pm}$, (*b*) π^0, (*c*) ρ^0, and (*d*) $(p,\bar{p})$ and their fits in terms of the exponential functions $\Sigma C_i \exp(-b_i x)$ [11].

(now with momentum k_4), producing the second meson.

The block of quark–antiquark production for the transition

$$q(p_1) + \bar{q}(p_2) \to q(k_1) + \bar{q}(k_2) + q(k_3) + \bar{q}(k_4)\ , \tag{40}$$

a key process that determines decay physics, is shown separately in Fig. 5*c*. The process in (40) is responsible for the escape of the quarks from the confinement trap. In simulating the hadronization-transition amplitude (40), quark combinatorics uses the hypothesis of soft hadronization. The idea was formulated in the 1970s; even now, the soft-hadronization hypothesis looks rather reliable and productive. It suggests that, in the ladder of product quarks (Figs. 1*a*, 5*c*), a leading contribution comes from low momentum transfers (of order $R^{-2}_{\text{confinement}}$). Within the spacetime picture, this means that new $q\bar{q}$ pairs are produced at large separations, where color objects leave the confinement well.

The soft-hadronization hypothesis applied to decay processes treats the ladder diagram in Fig. 5*c* for the decay amplitude in Fig. 5*a* in the same way as for jet production (Fig. 5*b*): the process in (40) is an elementary subprocess both for the high-energy ladder and for the two-body-decay amplitude, and the momentum transfers that enter into the amplitude in (40) appear to be small on the hadronic scale, $R^{-2}_{\text{confinement}}$.

4.2. Spectral Representation of the Decay Diagram

Below, we consider in detail the decay amplitude described by the diagram in Fig. 5*a*, performing calculations, as before, within the spectral representa-

tion by using the light-cone wave functions for $q\bar{q}$ states. In terms of the variables

$$P = p_1 + p_2, \quad k_{12} = k_1 + k_2, \quad k_{34} = k_3 + k_4,$$
$$M^2 = (k_1 + k_2)^2, \quad s_{12} = (k_1 + k_2)^2, \quad (41)$$
$$s_{34} = (k_3 + k_4)^2,$$

this amplitude can be expressed as

$$A(q\bar{q}\text{state} \to \text{two mesons})$$
$$= \int_{4m^2}^{\infty} \frac{dM^2}{\pi} \Psi_{\text{in}}(M^2) d\Phi(P; p_1, p_2) \quad (42)$$
$$\times \int_{(m+m_s)^2}^{\infty} \frac{ds_{12} ds_{34}}{\pi^2}$$
$$\times t(p_1, p_2; k_1, k_2, k_3, k_4)$$
$$\times d\Phi(k_{12}; k_1, k_2)\, d\Phi(k_{34}; k_3, k_4) \Psi_1(s_{12}) \Psi_2(s_{34}).$$

That the masses of newly born quarks $i = 2, 3$ are denoted here by m_s opens the way to consider decays leading to strange-quark production. The transition amplitude (40), shown schematically in Fig. 5*c*, is denoted by $t(p_1, p_2; k_1, k_2, k_3, k_4)$. The decay amplitude (42) is written in terms of the meson wave functions: for the initial state, it is $\Psi_{\text{in}}(M^2)$, while, for the outgoing mesons, they are $\Psi_1(s_{12})$ and $\Psi_2(s_{34})$. We do not specify here the meson spin structure of the quark propagator: we consider it below in a more detailed analysis of the transition amplitude (40).

Thus, the decay amplitude A is the convolution of the transition amplitude (40) with the wave functions of the initial and outgoing mesons:

$$A(q\bar{q}\,\text{state} \to \text{two mesons}) = \Psi_{\text{in}} \otimes t \otimes \Psi_1 \Psi_2. \quad (43)$$

Further, we use light-cone variables; for $p_{iz} \to \infty$ and $k_{iz} \to \infty$, we have

$$k_i = (k_{iz} + \frac{m^2 + k_{i\perp}^2}{2k_{iz}}, \mathbf{k}_{i\perp}, k_{iz}), \quad i = 1, 4;$$
$$k_i = (k_{iz} + \frac{m_s^2 + k_{i\perp}^2}{2k_{iz}}, \mathbf{k}_{i\perp}, k_{iz}), \quad i = 2, 3; \quad (44)$$
$$p_1 = (p_{iz} + \frac{m^2 + p_{i\perp}^2}{2p_{iz}}, \mathbf{p}_{i\perp}, p_{iz}), \quad i = 1, 2.$$

Let us make use of the reference frame where the outgoing particles move along the z axis. We set

$$P = (P_z + \frac{M^2}{2P_z}, 0, P_z),$$
$$k_{12} = (k_{12z} + \frac{s_{12}}{2k_{12z}}, 0, k_{12z}), \quad (45)$$
$$k_{34} = (k_{34z} + \frac{s_{34}}{2k_{34z}}, 0, k_{34z}).$$

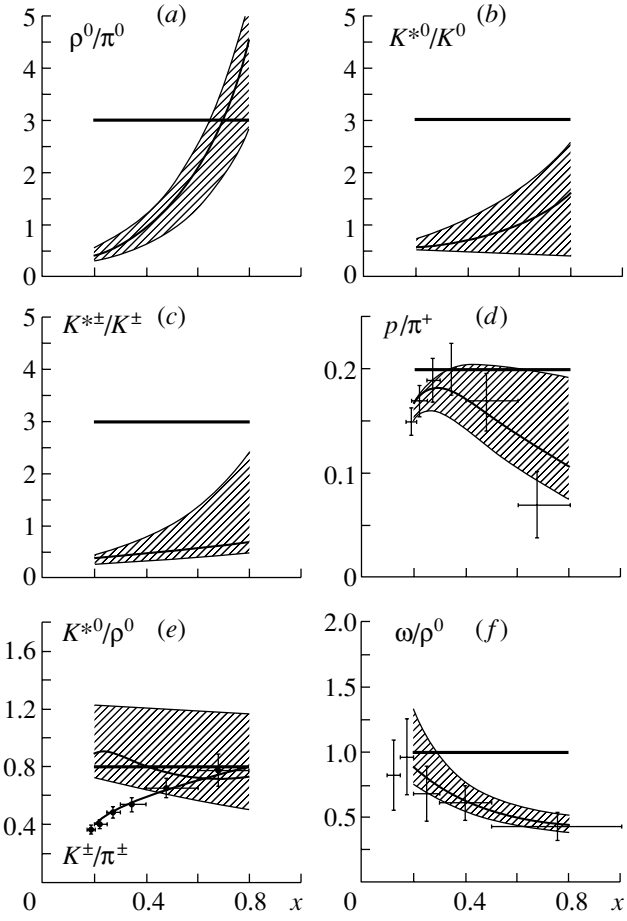

Fig. 4. (*a*) ρ^0/π^0, (*b*) K^{*0}/K^0, (*c*) $K^{*\pm}/K^{\pm}$, (*d*) p/π^+, (*e*) K^{*0}/ρ^0 and $K^{\pm}/\pi^{\pm}$, and (*f*) ω/ρ^0 ratios obtained from an exponential fit to ALEPH data [11] (thin lines and shaded areas). Thick lines represent the predictions of quark-combinatorics rules. Figures 4*d*, 4*e*, and 4*f* also show the p/π^+, $K^{\pm}/\pi^{\pm}$, and ω/ρ^0 ratios, which were obtained from a histogram description of the spectra from [11].

The phase spaces $d\Phi(k_{12}; k_1, k_2)$ and $d\Phi(k_{34}; k_3, k_4)$ contain delta functions that ensure energy–momentum conservation and which yield

$$M^2 = \frac{m^2 + p_{1\perp}^2}{x_1} + \frac{m^2 + p_{2\perp}^2}{x_2},$$
$$s_{12} = \frac{m^2 + k_{1\perp}^2}{y_1} + \frac{m_s^2 + k_{2\perp}^2}{y_2}, \quad (46)$$
$$s_{34} = \frac{m_s^2 + k_{3\perp}^2}{y_3} + \frac{m^2 + k_{4\perp}^2}{y_4},$$

where $x_i = p_{iz}/(p_{1z} + p_{2z})$ and $y_i = k_{iz}/(k_{1z} + k_{2z})$ for $i = 1, 2$ and $y_i = k_{iz}/(k_{3z} + k_{4z})$ for $i = 3, 4$.

4.3. Region Dominated by the Transition Amplitude $t_{q\bar{q}\to q\bar{q}q\bar{q}}$

Let us address the main point that consists in evaluating the momentum-space region selected by the transition amplitude in Fig. 5*c* within the soft-hadronization hypothesis, which means that the ladder diagram in Fig. 5*c* has a peripheral structure: it requires the square of the momentum transfer to the $q\bar{q}$ block to be small, of order $1/R^2_{\text{confinement}}$. Thus, we have

$$-(p_1-k_1)^2 \simeq (\mathbf{p}_{1\perp}-\mathbf{k}_{1\perp})^2 \sim R^{-2}_{\text{confinement}}, \quad (47)$$
$$-(p_2-k_4)^2 \simeq (\mathbf{p}_{2\perp}-\mathbf{k}_{4\perp})^2 \sim R^{-2}_{\text{confinement}}.$$

Likewise, the momentum transfer squared in the quark propagator (see Fig. 5*c*) is of order

$$(p_1-k_1-k_2)^2 \simeq -(\mathbf{p}_{1\perp}-\mathbf{k}_{1\perp}-\mathbf{k}_{2\perp})^2. \quad (48)$$

Let us now discuss the peripheral constraint (47) in more detail. By way of example, we consider $(p_1-k_1)^2$. We have

$$(p_1-k_1)^2 = (p_{1z}-k_{1z}+\frac{m^2+p_{1\perp}^2}{2p_{1z}}-\frac{m^2+k_{1\perp}^2}{2k_{1z}})^2$$
$$-(\mathbf{p}_{1\perp}-\mathbf{k}_{1\perp})^2-(p_{1z}-k_{1z})^2. \quad (49)$$

The gluon carries a small fraction of the longitudinal momentum of the primary quark; therefore, we have

$$p_{1z} \gg p_{1z}-k_{1z} \equiv \Delta, \quad (50)$$

whence it follows that

$$(k_1-p_1)^2 \simeq \frac{\Delta}{p_{1z}}(k_{1\perp}^2-p_{1\perp}^2)-(\mathbf{k}_{1\perp}-\mathbf{p}_{1\perp})^2 \quad (51)$$
$$\simeq -(\mathbf{k}_{1\perp}-\mathbf{p}_{1\perp})^2.$$

The peripheral constraint means that $y_1 \gg y_2$. In numerical calculations, however, this does not require very large invariant energies squared, s_{12} and s_{34}, which determine the blocks of quark fusion. By way of example, we indicate that, at $y_2/y_1 \sim 1/10$, one has $s_{12} \sim 10m^2 \sim 1$ GeV^2 for $m \simeq 350$ MeV, which gives, for the quark relative momentum, a value of about 300–400 MeV.

4.4. The Decay Amplitude $A(q\bar{q}$ *state* $\to$ *two mesons)*

We now write the formula for $t(p_1,p_2;k_1,k_2,k_3,k_4)$ in the simplest approximation, taking into account only the t-channel propagators. We have

$$t(p_1,p_2;k_1,k_2,k_3,k_4) = \frac{g}{m_g^2+(\mathbf{p}_{1\perp}-\mathbf{k}_{1\perp})^2}$$
$$\times\frac{g^2\,(m_s-\boldsymbol{\gamma}(\mathbf{p}_{1\perp}-\mathbf{k}_{1\perp}-\mathbf{k}_{2\perp}))}{m_s^2+(\mathbf{p}_{1\perp}-\mathbf{k}_{1\perp}-\mathbf{k}_{2\perp})^2} \quad (52)$$
$$\times\frac{g}{m_g^2+(\mathbf{p}_{2\perp}-\mathbf{k}_{4\perp})^2},$$

where $\boldsymbol{\gamma}$ is a Dirac matrix. To avoid ultrared divergences, the effective mass m_g of the soft gluon is introduced in the gluon propagator (see, for example, [31]).

Equation (4.4.4) does not state that the transition amplitude $t(p_1,p_2;k_1,k_2,k_3,k_4)$ selects large distances. At this point, the amplitude in (4.4.4) can be improved by incorporating form factors into the gluon-emission vertex:

$$g \to g((\mathbf{p}_{1\perp}-\mathbf{k}_{1\perp})^2), \quad g \to g((\mathbf{p}_{2\perp}-\mathbf{k}_{4\perp})^2). \quad (53)$$

With the aid of Eqs. (4.4.4) and (53), the amplitude A can be represented as

$$A(q\bar{q}\,\text{state}\to\text{two mesons}) = \int_0^1 \frac{dx_1dx_2\delta(1-x_1-x_2)}{16\pi^2x_1x_2}\int d\mathbf{p}_{1\perp}d\mathbf{p}_{2\perp}\delta(\mathbf{p}_{1\perp}+\mathbf{p}_{2\perp})$$
$$\times\int_{y_1\gg y_2}\frac{dy_1dy_2\delta(1-y_1-y_2)}{16\pi^2y_1y_2}\int d\mathbf{k}_{1\perp}d\mathbf{k}_{2\perp}\delta(\mathbf{k}_{1\perp}+\mathbf{k}_{2\perp})$$
$$\times\int_{y_4\gg y_3}\frac{dy_3dy_4\delta(1-y_3-y_4)}{16\pi^2y_3y_4}\int d\mathbf{k}_{3\perp}d\mathbf{k}_{4\perp}\delta(\mathbf{k}_{3\perp}+\mathbf{k}_{4\perp})\Psi_{in}(x_1,x_2;\mathbf{p}_{1\perp},\mathbf{p}_{2\perp}) \quad (54)$$
$$\times\frac{g((\mathbf{p}_{1\perp}-\mathbf{k}_{1\perp})^2)}{m_g^2-(\mathbf{p}_{1\perp}-\mathbf{k}_{1\perp})^2}\frac{g^2(m_s+\boldsymbol{\gamma}(\mathbf{p}_{1\perp}-\mathbf{k}_{1\perp}-\mathbf{k}_{2\perp}))}{m_s^2+(\mathbf{p}_{1\perp}-\mathbf{k}_{1\perp}-\mathbf{k}_{2\perp})^2}\frac{g((\mathbf{p}_{2\perp}-\mathbf{k}_{4\perp})^2)}{m_g^2+(\mathbf{p}_{2\perp}-\mathbf{k}_{4\perp})^2}$$
$$\times\Psi_1(y_1,y_2;\mathbf{k}_{1\perp},\mathbf{k}_{2\perp})\Psi_2(y_3,y_4;\mathbf{k}_{3\perp},\mathbf{k}_{4\perp}).$$

In terms of this expression for the decay amplitude, we can discuss the rules of quark combinatorics.

In the approximation

$$\frac{g^2\,(m_s-\boldsymbol{\gamma}(\mathbf{p}_{1\perp}-\mathbf{k}_{1\perp}-\mathbf{k}_{2\perp}))}{m_s^2+(\mathbf{p}_{1\perp}-\mathbf{k}_{1\perp}-\mathbf{k}_{2\perp})^2} \to \frac{g^2}{m_s} \quad (55)$$

(we have neglected here the momenta in the propagator for newly born quarks), which is quite rough, but which nevertheless yields a qualitatively correct result, we have

$$A(q\bar{q}\,\text{state} \to \text{two mesons}) = \frac{\alpha_s}{m_s} \cdot (\Psi_{in} \otimes t \otimes \Psi_1\Psi_2)\,. \quad (56)$$

This equation tells us that the probability of producing nonstrange and strange quarks, $u\bar{u} : d\bar{d} : s\bar{s} = 1 : 1 : \lambda$, is determined by the ratio of the squares of the masses of nonstrange (u, d) and strange (s) quarks. Introducing the constituent quark masses in the soft region, $m_u \simeq m_d \equiv m = 350$ MeV and $m_s \simeq 500$ MeV, we obtain

$$\lambda \simeq \frac{m^2}{m_s^2} \simeq 0.5. \quad (57)$$

Equations (55) and (56) validate the statements of quark combinatorics as applied to the decay processes [7–9, 32]. Of course, we suppose here the identity of the wave functions for mesons that belong to the same multiplet.

Equation (57) gives us a rough estimate of λ, for, in (55), we have neglected momentum transfers squared that are commensurate with light-quark masses. In more sophisticated evaluations of λ, one may take into account the momentum dependence of the quark propagator:

$$\frac{1}{m_s^2 + (\mathbf{p}_{1\perp} - \mathbf{k}_{1\perp} - \mathbf{k}_{2\perp})^2} \to \frac{1}{m_s^2 + \langle k^2\rangle}. \quad (58)$$

Here, $\langle k^2\rangle$ is a typical momentum squared inherent in the decay process being considered. Therefore, we have

$$\lambda = \frac{m^2 + \langle k^2\rangle}{m_s^2 + \langle k^2\rangle}. \quad (59)$$

For standard decays of light resonances, $\langle k^2\rangle \sim 0.1$–$0.3\ (\text{GeV}/c)^2$, and this leads to an increase in λ in relation to the estimate in (57). Indeed, $\lambda \sim 0.7$ was found in the analysis peformed in [32]. Actually, Eq. (59) demonstrates that λ can vary, depending on the reaction type.

4.5. Suppression Parameter λ in Hadronic Z^0 Decays

Let us now consider $q\bar{q}$-pair production in $Z^0 \to q\bar{q} \to hadrons$ jet processes (see Fig. 5*b*). All the above considerations, which have been applied to the decay of a resonance into two mesons, are valid here as well. As a result, we obtain the formula

$$A(Z^0 \to \text{two mesons} + X) = \frac{\alpha_s}{m_s}\,(q\bar{q}\ \text{from jet ladder} \otimes t \otimes \Psi_1\Psi_2)\,, \quad (60)$$

which is a counterpart of (56). This formula differs from (56) only by the initial state, which is the wave function of the $q\bar{q}$ pair for the jet ladder, but not for the state defined by the wave function Ψ_{in}. This means that the ratio of the probabilities for the production of a strange and a nonstrange quark is given by the factor m^2/m_s^2. As in the decay process, one therefore has

$$\lambda \simeq \frac{m^2}{m_s^2} \simeq 0.5. \quad (61)$$

Experimental data on the $K^\pm/\pi^\pm$ yield ratio do not contradict this evaluation. The $K^\pm/\pi^\pm$ ratio as a function of x is shown in Fig. 4*e*. It can be seen that, at $x = 0.2$, $K^\pm/\pi^\pm \simeq 0.35$. With increasing x, the $K^\pm/\pi^\pm$ ratio grows, reaching the value of about 0.8 at $x = 0.7$. Such an increase is rather legible: the point is that K mesons are produced both owing to the formation of a new $s\bar{s}$ pair in the ladder (with probability λ) and owing to the fragmentation production of an $s\bar{s}$ pair in the transition $Z^0 \to s\bar{s}$. The relative probabilities of the prompt production processes $Z^0 \to u\bar{u}, d\bar{d}, s\bar{s}$ are in the ratio $u\bar{u} : d\bar{d} : s\bar{s} \simeq 0.26 : 0.37 : 0.37$. Because of that, the production of K mesons at large x is

$$K^+ \sim (0.37 \times 1 + 0.26 \times \lambda). \quad (62)$$

Let us discuss this formula in more detail. A K^+ meson can be produced in two processes: (i) the fragmentation production of an $\bar{s}$ quark (the relative probability is 0.37) and a subsequent pickup of a u quark from the $q\bar{q}$ sea in a jet (the relative probability is 1), and (ii) the fragmentation production of a u quark (the relative probability is 0.26) and the pickup of an $\bar{s}$ quark from the sea (the relative probability λ).

The same quantity for pions is

$$\pi^+ \sim (0.37 \times 1 + 0.26 \times 1). \quad (63)$$

Therefore, the K^+/π^+ ratio at large x is

$$\frac{K^+}{\pi^+} = \frac{0.37 + 0.26\lambda}{0.37 + 0.26} \simeq 0.8 \quad (64)$$

at $\lambda = 0.5$. As can be seen from Fig. 4*e*, which shows $\lambda(x)$ determined as the $K^\pm/\pi^\pm(x)$ ratio, this value agrees with experimental data from [22].

The small value of the K^+/π^+ ratio at $x = 0$ is a direct consequence of a large probability of the production of highly excited resonances: resonance decays produce more pions than kaons. For the problem of breeding strange and nonstrange states in the decay process in question, it is rather interesting to consider the K^*/ρ ratio—experimental data for K^{*0}/ρ^0 are also shown in Fig. 4*e* (shaded area). Remarkably, the K^{*0}/ρ^0 ratio has no tendency to decrease with decreasing x: this means that the rate of K^{*0} breeding

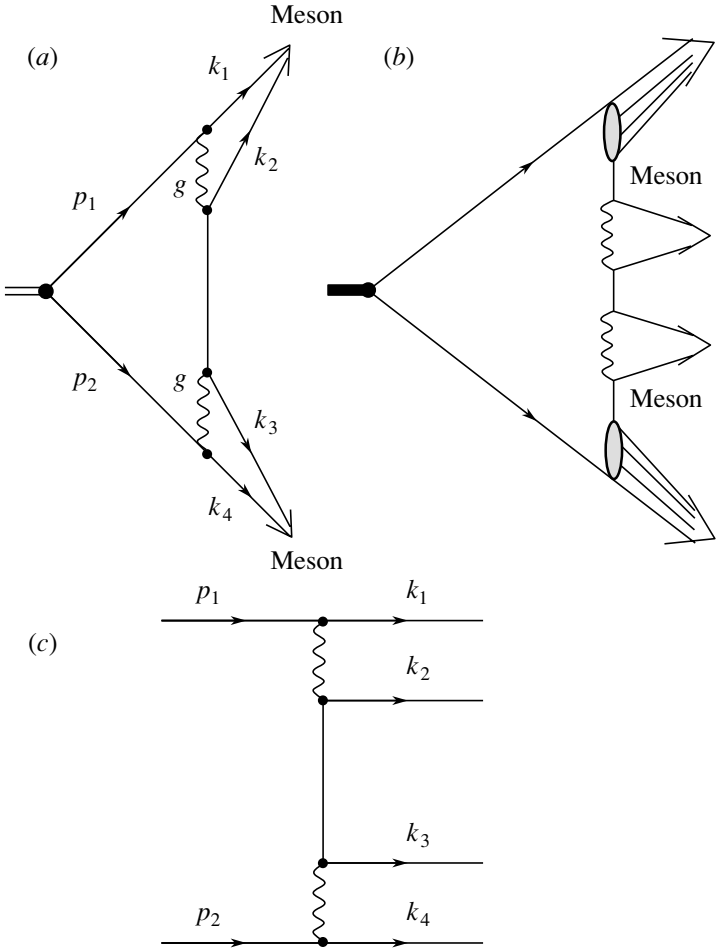

Fig. 5. (*a*) Meson decay diagram; (*b*) transition $q\bar{q} \to meson + meson$ as a constructive element of the multiperipheral chain in hadronic Z^0 decay; and (*c*) diagram for the peripheral production of a new $q\bar{q}$ pair.

in the decays is approximately identical to the rate of ρ^0 breeding. Unfortunately, experimental errors are overly large to draw more definitive conclusions about the behavior of $\lambda(x)$.

4.6. Production of Heavy Quarks

The supression parameter for the production of a strange quark cannot be reliably determined. This is because the masses of strange and nonstrange quarks are small in relation to the mean transverse momenta of quarks in the production process [see Eq. (59)]. We can draw a more definitive conclusion about the suppression parameter λ_Q for the production of heavy quarks $Q = c, b$. This parameter is defined by the same formula (4.4.4) for multiperipheral production, so that we have

$$\lambda_Q \simeq \frac{m^2}{m_Q^2 \ln^2 \frac{\Lambda^2}{m_Q^2}}. \qquad (65)$$

Here, we have considered that the gluon–quark coupling constant decreases with increasing quark mass, $\lambda_Q \sim \alpha^2(m_Q^2)$. The QCD scale constant Λ is on the order of 200 MeV.

To estimate λ_c and λ_b, we use the values of $m = 0.35$ GeV, $m_c = M_{J/\psi}/2 = 1.55$ GeV, $m_b = M_\Upsilon/2 = 4.73$ GeV, and $\Lambda = 0.2$ GeV. As a result, we arrive at

$$\lambda_c \simeq 2.8 \times 10^{-3}, \qquad \lambda_b \simeq 1.1 \times 10^{-4}. \qquad (66)$$

The value of λ_c should reveal itself in the inclusive production of J/ψ and χ mesons, while λ_b is to be seen in reactions featuring Υ: $Z^0 \to (\sum J/\psi + \sum \chi) + X$ and $Z^0 \to \sum \Upsilon + X$. These reactions are determined by the processes $Z^0 \to c\bar{c} \to c + (\bar{c}c + \bar{q}q\text{-sea}) + \bar{c}$ and $Z^0 \to b\bar{b} \to b + (\bar{b}b + \bar{q}q\text{-sea}) + \bar{b}$: for the production of a $c\bar{c}$ or a $b\bar{b}$ meson, a new pair of heavy quarks must be produced, since the quarks formed at the first stage of the decay, $Z^0 \to c\bar{c}$ or $Z^0 \to b\bar{b}$, have a rather large gap on the rapidity scale. Within the definition

$$\lambda_c \simeq \Gamma\Big(c\bar{c} \to c + (\bar{c}c + \bar{q}q\text{-sea}) + \bar{c}\Big)/\Gamma(c\bar{c}), \quad (67)$$

$$\lambda_b \simeq \Gamma\Big(b\bar{b} \to b + (\bar{b}b + \bar{q}q\text{-sea}) + \bar{b}\Big)/\Gamma(b\bar{b}),$$

we estimate $\Gamma(c\bar{c} \to c + (\bar{c}c + \bar{q}q\text{-sea}) + \bar{c})$ and $\Gamma(b\bar{b} \to b + (\bar{b}b + \bar{q}q\text{-sea}) + \bar{b})$ on the basis of available data from [10]:

$$\Gamma\Big(c\bar{c} \to c + (\bar{c}c + \bar{q}q\text{-sea}) + \bar{c}\Big)$$
$$\sim \Gamma\Big(J/\psi(1S)X + J/\psi(2S)X + \chi(1P)X\Big), \quad (68)$$

$$\Gamma\Big(b\bar{b} \to b + (\bar{b}b + \bar{q}q\text{-sea}) + \bar{b}\Big)$$
$$\sim \Gamma\Big(\Upsilon(1S)X + \Upsilon(2S)X + \Upsilon(3S)X\Big).$$

Experimental data yield [10]

$$\Gamma(c\bar{c})/\Gamma(\text{hadrons}) = 0.177 \pm 0.008,$$
$$\Gamma(b\bar{b})/\Gamma(\text{hadrons}) = 0.217 \pm 0.001,$$

$$\Gamma\Big(J/\psi(1S)X + J/\psi(2S)X + \chi(1P)X\Big)/\Gamma(\text{hadrons}) = (1.17 \pm 0.13) \times 10^{-2},$$
$$\Gamma\Big(\Upsilon(1S)X + \Upsilon(2S)X + \Upsilon(3S)X\Big)/\Gamma(\text{hadrons}) = (1.4 \pm 0.9) \times 10^{-4}. \quad (69)$$

Thus, we have

$$\Gamma\Big(J/\psi(1S)X + J/\psi(2S)X + \chi(1P)X\Big)/\Gamma(c\bar{c})$$
$$= (2.07 \pm 0.23) \times 10^{-3}, \quad (70)$$
$$\Gamma\Big(\Upsilon(1S)X + \Upsilon(2S)X + \Upsilon(3S)X\Big)/\Gamma(b\bar{b})$$
$$= (0.31 \pm 0.19) \times 10^{-4},$$

in reasonable agreement with (66).

5. THE PROBLEM OF SATURATION OF PRODUCT $q\bar{q}$ AND qqq STATES BY MESONS AND BARYONS; BARYON-TO-MESON RATIO AND WATSON–MIGDAL FACTOR

In quark combinatorics formulated in [1, 2], the baryon quark number reveals itself as the probability of the production of a baryon containing this quark. For the hadronization of the quark q_i in $(q, \bar{q})_{\text{sea}}$, the production rule has the form

$$q_i + (q, \bar{q})_{\text{sea}} \to \frac{1}{3}B_i + \frac{2}{3}M_i + \frac{1}{3}M + (M, B, \bar{B})_{\text{sea}}, \quad (71)$$

where B_i and M_i are baryons and mesons containing the quark q_i and M, B, and $\bar{B}$ stand, respectively, for mesons, for baryons, and for antibaryons of the sea.

Generally, one can write

$$M = \sum_L \mu_L M_L\,, \qquad B = \sum_L \beta_L M_L, \quad (72)$$
$$M_i = \sum_L \mu_L^{(i)} M_L^{(i)}\,, \qquad B_i = \sum_L \beta_L^{(i)} M_L^{(i)},$$

where the subscripts $L = 0, 1, 2, \ldots$ define the multiplet, while μ_L, $\mu_L^{(i)}$ and β_L, $\beta_L^{(i)}$ are the probabilities of the production of, respectively, mesons and baryons of a given multiplet in the quark-hadronization process. These probabilities are determined by characteristic relative momenta of the fused quarks.

5.1. Baryon-to-Meson Ratio

Our present understanding of the multiperipheral ladder is not sufficient to reanalyze (71) on the level adopted in Sections 2 and 3 for V/P. Nevertheless, data on $Z^0 \to p + X$ and $Z^0 \to \pi^+ + X$ decays definitively confirm Eq. (71). For p/π^+ at large x, quark combinatorics [5] predicts

$$p/\pi^+ \simeq 0.20. \quad (73)$$

Figure 4*d* shows the p/π^+ ratio given by a fit to the data from [11] (shaded area) and the prediction of quark combinatorics (73): the agreement at $x > 0.2$ is quite good.

Let us comment on the result of our calculation, $p/\pi^+ \simeq 0.20$, for leading particles in jets. In the jet created by a quark, the leading hadrons are produced in the proportion given by (71): $B_i : 2M_i : M$. We consider only the production of hadrons belonging to the lowest (baryon and meson) multiplets; hence, we retain in (72) only the $L = 0$ terms (hadrons from the quark S-wave multiplets). In our estimations, we assume that $\beta_0 \simeq \mu_0$; therefore, we substitute $B_i \to B_i(0)$, $M_i \to M_i(0)$, and $M \to M(0)$. The precise content of $B_i(0)$, $M_i(0)$, and $M(0)$ depends on the proportions in which the sea quarks are produced. We assume flavor symmetry breaking for sea quarks, $u\bar{u}\colon d\bar{d}\colon s\bar{s} = 1\colon 1\colon \lambda$, with $0 \le \lambda \le 1$. For the sake of simplicity, we first set $\lambda = 0$ (actually the ratio p/π depends weakly on λ). For the u-quark initiated jet, we then have

$$B_u(0) \to \frac{2}{15}p + \frac{1}{15}n + (\Delta \text{ resonances}), \quad (74)$$

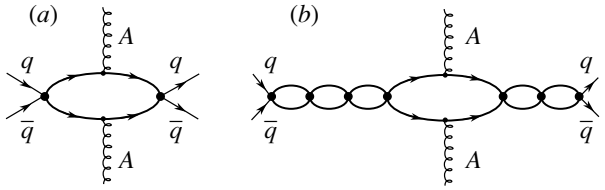

Fig. 6. Diagrams for the central production of a $q\bar{q}$ pair: the set of loop diagrams responsible for the Watson–Migdal factor.

$$M_u(0) \to \frac{1}{8}\pi^+ + \frac{1}{16}\pi^0 + \frac{1}{16}(\eta + \eta') + (\text{vector mesons}),$$

$$M(0) \to \frac{1}{16}\pi^+ + \frac{1}{16}\pi^0 + \frac{1}{16}\pi^- + \frac{1}{16}(\eta + \eta') + (\text{vector mesons}).$$

The hadron content of the d-quark initiated jet is determined by the isotopic conjugation $p \to n$, $n \to p$, and $\pi^+ \to \pi^-$, and the content of antiquark jets is governed by charge conjugation; in jets of strange quarks, only sea mesons (M) contribute to the p/π^+ ratio.

Taking into account the ratio $B_i : 2M_i : M = 1 : 2 : 1$ and the probabilities of the production of quarks of different flavors q_i, given by (1), we obtain $p/\pi^+ \simeq 0.21$ for $\lambda = 0$. We can easily deduce the p/π^+ ratio for arbitrary λ: the decomposition of the ensembles $B_i(0)$, $M_i(0)$, and $M(0)$ with respect to hadron states was performed in [5] (see Appendix D, Tables D.1 and D.2, in that study). As was emphasized above, however, this ratio is a slowly varying function of λ: at $\lambda = 1$, we have $p/\pi^+ \simeq 0.20$.

5.2. Production of Highly Excited Resonances and Watson–Migdal Factor

For quark combinatorics, the saturation of $q\bar{q}$ and qqq states by real hadrons is of paramount importance. The probability of saturation is defined by the coefficients $(\mu_L, \mu_L^{(i)})$ and $(\beta_L, \beta_L^{(i)})$ in (72). A basic question is what contribution from high multiplets is sufficiently sizable not to be negligible in the spectra.

Let us consider in more detail the production of mesons in the central region: $q\bar{q} \to M$. The central production of $q\bar{q}$ states is described by the diagrams in Fig. 6 (loop diagram, Fig. 6*a*, and interactions of product quarks, Fig. 6*b*). Diagrams of the type in Fig. 6*b* for final-state interactions lead to the relativistic Watson–Migdal factor. To estimate the number of highly excited states produced, we must find out which states are determined by the $q\bar{q}$ system in the multiperipheral ladder.

The constructive element of the ladder is a process shown in Fig. 5*b*. It was emphasized in Section 4 that, in this process, new $q\bar{q}$ pairs are created at relatively large separations (on the hadronic scale), at $r \sim 1$ fm: these separations are equal to those in $q\bar{q} \to M$ transitions. The orbital angular momenta of the $q\bar{q}$ system for this transition can be written as $L \sim kr$. For relative quark momenta of $k \lesssim 0.6$ GeV/c, we have

$$L \lesssim 3. \tag{75}$$

Relying on the behavior of the Regge trajectory, one can assess meson masses μ to which this relation corresponds. The trajectories for $q\bar{q}$ states are linear up to $\mu \sim 2.5$ GeV [33],

$$\alpha(\mu^2) \simeq \alpha(0) + \alpha'(0)\mu^2; \tag{76}$$

the slope $\alpha'(0)$ is approximately equal to $\alpha'(0) \simeq 0.8$ GeV^{-2}; and the intercept falls within the interval $0.25 \lesssim \alpha(0) \lesssim 0.5$. For large μ, the estimation therefore yields $\mu^2 \sim \alpha(\mu^2)/\alpha'(0)$; with $\alpha(\mu^2) \sim 3$, we have $\mu^2 \sim 4$ GeV^2. Thus, we conclude that, in the multiperipheral ladder, it would be natural to expect the production of $q\bar{q}$ mesons with masses

$$\mu \lesssim 2 \text{ GeV}. \tag{77}$$

It is instructive to write down $q\bar{q}$ states that belong to this interval and which saturate the expansions in (72). The $q\bar{q}$ states are characterized by the orbital angular momentum L; the quark spin $S = 0, 1$; and the total angular momentum J. Yet another characteristic of the $q\bar{q}$ state is the radial quantum number n. The region $\mu \lesssim 2$ GeV is populated by the following $n^{2S+1}L_J$ $q\bar{q}$ multiplets with $n = 1$ [10, 33]:

$$\begin{gathered} 1^1S_0, \quad 1^3S_1 \\ 1^1P_1 \quad 1^3P_J \quad (J = 0, 1, 2) \\ 1^1D_2 \quad 1^3D_J \quad (J = 1, 2, 3) \\ 1^1F_3 \quad 1^3F_J \quad (J = 2, 3, 4). \end{gathered} \tag{78}$$

As Eq. (75) tells us, all these states contribute significantly to meson production.

The contribution of $n > 1$ states is determined by the structure of quark final-state interaction (see Fig. 5*b*). For each partial wave, the sum of the diagrams featuring final-state interaction is

$$\frac{1}{1 - B(s_{q\bar{q}})}\Pi(s_{q\bar{q}}, s'_{q\bar{q}})\frac{1}{1 - B^*(s'_{q\bar{q}})}, \tag{79}$$

where $\Pi(s_{q\bar{q}}, s'_{q\bar{q}})$ is final-state-interaction block and $1/[1 - B(s_{q\bar{q}})]$ is the relativistic Watson–Migdal factor,

$$B(s_{q\bar{q}}) = \int\limits_{4m^2}^{\infty} \frac{ds}{\pi}\frac{N(s)\rho(s)}{s - s_{q\bar{q}}} \tag{80}$$

$$= \mathrm{Re}\, B(s_{q\bar{q}}) + iN(s_{q\bar{q}})\rho(s_{q\bar{q}}).$$

Here, the function $N(s)$ characterizes the interaction of quarks for a given partial wave.

The cross section for the production of a $q\bar{q}$ pair with invariant mass squared $s_{q\bar{q}}$ is determined by Eq. (79) at $s'_{q\bar{q}} = s_{q\bar{q}}$:

$$d\sigma\Big(q\bar{q}(s_{q\bar{q}}) + X\Big) \tag{81}$$
$$\sim \Pi(s_{q\bar{q}}, s_{q\bar{q}})\,\frac{1}{(1 - B(s_{q\bar{q}}))\,(1 - B^*(s_{q\bar{q}}))}.$$

It follows from quark–hadron duality that $d\sigma\Big(q\bar{q}(s_{q\bar{q}}) + X\Big)$ describes, on average, the spectrum of product resonances:

$$d\sigma\Big(q\bar{q}(s_{q\bar{q}}) + X\Big) \tag{82}$$
$$\simeq d\sigma\Big(\sum(\text{resonances near } s_{q\bar{q}}) + X\Big).$$

The averaging of the resonance-production cross section is performed over a certain vicinity of $s_{q\bar{q}}$. In this way, we see that the structure of the Watson–Migdal factor determines not only the rate of decrease in $d\sigma\Big(q\bar{q}(s_{q\bar{q}}) + X\Big)$ with increasing invariant mass but also the quantitative contribution of $n > 1$ resonances.

There are the following $q\bar{q}$ multiplets of the radial excitations in the region $\mu \lesssim 2$ GeV [33]:

$$n^1S_0 \quad n^3S_1 \quad (n = 2, 3) \tag{83}$$
$$n^1P_1 \quad n^3P_{0,1,2} \quad (n = 2).$$

The probability of the production of these states is determined by the decrease in $d\sigma\Big(q\bar{q}(s_{q\bar{q}}) + X\Big)$—in particular, by the Watson–Migdal factor.

In summary, we definitely expect a copious production of resonances belonging to $n = 1$ $q\bar{q}$ multiplets [see (78)]. With a smaller degree of definiteness, we can judge the production of $n > 1$ resonances presented in (83): if the Watson–Migdal factor suppresses strongly the contribution of large $s_{q\bar{q}}$, the production of multiplets is suppressed as well; however, a different situation is also possible.

Only a small part of resonances belonging to the multiplets in (78) and located in the region 1500–2000 MeV are included in the tables presented in [10]; a considerable number of resonances were discovered and identified only recently (see [33–36] and references therein). Moreover, numerous decay channels related to multiparticle states have not yet been identified. This casts some doubt on the procedure for reconstructing prompt probabilities on the basis of the exclusion of known resonances [37–39].

There is yet another effect because of which the realization of the program from [37–39] is questionable at present: the effect of the accumulation of widths of overlapping resonances by one of them [40]. An identification of broad states of width about $\Gamma/2 \sim 400 - 600$ MeV in the mass region 1500–2000 MeV looks rather ambiguous at the present level of the experimental data, although the existence of such states seems probable if we expect the existence of exotic mesons (glueballs and hybrids) in this mass region (see [40] for details).

6. COHERENT PRODUCTION OF ω AND ρ^0 MESONS AT LARGE x

Indications of coherent phenomena in hadronic Z^0 decays follow from the ω/ρ^0 ratio at $x \sim 1$ (see Fig. 4*f*). In multiparticle processes, where ρ and ω are produced without any interference of flavor components, this ratio is

$$\omega/\rho^0 = 1. \tag{84}$$

Because of the approximate equality of the ρ and ω masses, Eq. (84) is not violated by the decays of highly excited resonances. Figure 4*f* demonstrates the validity of (84) at $x \sim 0.1$–0.2. At $x \sim 0.5$–1.0, however, the ω/ρ^0 ratio is definitively less than unity, thus unambigously suggesting the interference of flavor components of the $Z^0 \to u\bar{u}$ and $Z^0 \to d\bar{d}$ amplitudes.

Let us consider ω and ρ production in a quark jet. If the hadronization of quarks in jets, $Z^0 \to u + X$ and $Z^0 \to d + X$, occurs in a noncoherent way, the leading quark in the u jet picks up an antiquark $\bar{u}$ from the sea, giving rise to the transition $u\bar{u} \to (u\bar{u} + d\bar{d})/2 + (u\bar{u} - d\bar{d})/2 = \omega/\sqrt{2} + \rho^0/\sqrt{2}$. Likewise, the transition $d\bar{d} \to (u\bar{u} + d\bar{d})/2 - (u\bar{u} - d\bar{d})/2 = \omega/\sqrt{2} - \rho^0/\sqrt{2}$ occurs in the d jet. If there is no interference of u and d jets, Eq. (84) is valid for each of them. But if the amplitudes of ω and ρ production do interfere, Eq. (84) is violated. Let us consider the ω/ρ^0 ratio for such a case.

The amplitude of the fragmentation production of u and d quarks is determined by the $Z^0 \to q_i\bar{q}_i$ vertex, which has the structure $\left[\bar{\psi}_i\gamma^\mu(g_V^i - g_A^i\gamma_5)\psi_i\right] Z_\mu$; we have $g_A^{(u)} = 1/2$ and $g_V^{(u)} = 1/2 - 4/3\sin^2\theta_W$ for the u quark and $g_A^{(d)} = -1/2$ and $g_V^{(d)} = -1/2 + 2/3\sin^2\theta_W$ for the d quark. For the axial-vector interaction, we therefore have

$$A \to 0.5\left[u + (q\bar{q}\text{-sea} + \bar{u})\right] \tag{85}$$
$$-0.5\left[d + (q\bar{q}\text{-sea} + \bar{d})\right]$$

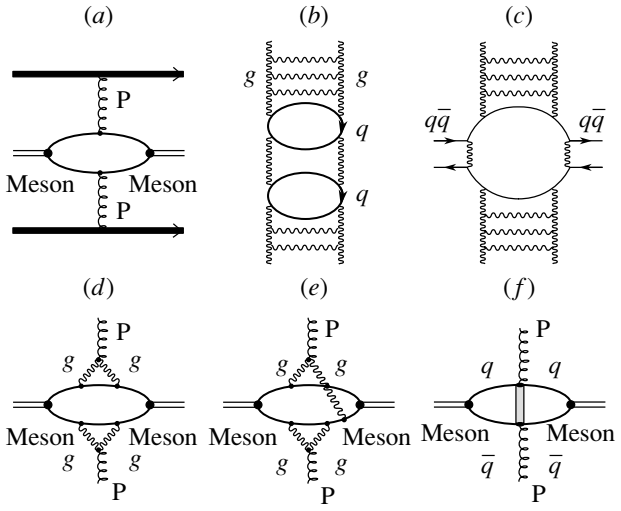

Fig. 7. Diagrams for meson production in the central region in high-energy hadron–hadron collisions.

$$\to 0.5\left[u\bar{u}+X_{u\bar{u}}\right]-0.5\left[d\bar{d}+X_{d\bar{d}}\right].$$

If $X_{u\bar{u}}$ and $X_{d\bar{d}}$ stand for the same state, $X_{u\bar{u}}=X_{d\bar{d}}\equiv X$, then

$$A\to\frac{1}{2}(u\bar{u}-d\bar{d})+X=\sqrt{2}\omega+X. \qquad (86)$$

The amplitude that is due to the vector interaction is

$$V\to 0.19\left[u+(q\bar{q}\text{-sea}+\bar{u})\right]$$
$$-0.35\left[d+(q\bar{q}\text{-sea}+\bar{d})\right] \qquad (87)$$
$$\to 0.19\left[u\bar{u}+X_{u\bar{u}}\right]-0.35\left[d\bar{d}+X_{d\bar{d}}\right].$$

At $X_{u\bar{u}}=X_{d\bar{d}}$, we have

$$V\to\sqrt{2}(-0.16\omega+0.54\rho^0)+X. \qquad (88)$$

For axial-vector and vector interaction, the ratios are therefore given by

$$\left(\frac{\omega}{\rho^0}\right)_{\text{axial}}=0, \qquad \left(\frac{\omega}{\rho^0}\right)_{\text{vector}}=8.8\times10^{-2}. \qquad (89)$$

Hence, coherent processes strongly suppress the production of ω mesons in relation to ρ^0 mesons. The experimental value at $x\sim0.5$–1 is $\omega/\rho^0\simeq0.4$, which enables us to evaluate the contribution of coherent processes at about 50%.

7. CONCLUSION

The rules of quark combinatorics follow from the quark structure of hadrons, which directly reveals itself in the ratio $\rho_{\text{prompt}}/\pi_{\text{prompt}}=3$. This equality is valid for multiparticle production processes such as hadronic Z^0 decays and high-energy hadron collisions; these relations are satisfied if the ρ-meson wave function is identical to the pion wave function.

The spectra observed in multiparticle production processes are formed owing primarily to the decay of highly excited resonances. In the meson sector, states of mass up to 1500–2000 MeV contribute significantly; we can suppose that, in the baryon sector, this would be the contribution of states up to 2000–3000 MeV. The reconstruction of the spectra of highly excited resonances does not seem possible at the present level of knowledge. Therefore, one should investigate the prompt particle yields using large-x jets, where the contribution of resonance-decay products is considerably suppressed.

The ratio $\rho^0/\pi^0=3$, which is observed in hadronic Z^0 decay at $x\sim0.5$–0.8, agrees with the predictions of quark combinatorics reasonably well.

The p/π^+ value is also in agreement with the quark combinatorial predictions at large x, thus revealing a small (about 25%) probability of meeting a diquark loop in the chain of quark loops.

The peripheral production of new $q\bar{q}$ pairs in multiparticle production processes allows us to introduce the suppression parameter for the production of strange and heavy-flavor quarks. The suppression parameters are determined by the ratio of the quark masses, their values being in agreement with experimental data.

In the central region for $x\lesssim0.2$, experiments yield $\omega/\rho^0\simeq1$, which also agrees with the quark combinatorial rules. For $x>0.5$, however, experimental data definitively tell us that $\omega/\rho^0<1$, which is an indication of the interference of flavor amplitudes with the fragmentation production of u and d quarks: the signs of flavor amplitudes favor $\omega/\rho^0<1$.

To conclude, we can state that the predictions of quark combinatorics for the hadronic decays of the Z^0 boson agree reasonably well with experimental data.

ACKNOWLEDGMENTS

We are deeply indebted to L.G. Dakhno for many stimulating discussions.

This work was supported in part by the Russian Foundation for Basic Research (project no. 98-02-17236).

APPENDIX A

V/P Ratio in High-Energy Hadron–Hadron Collisions

We demonstrate here that the ratio $V_{\text{prompt}}/P_{\text{prompt}}=3$ is not peculiar to decay processes—it is inherent in hadronic multiparticle production processes as well.

We consider the cross section for the central production of mesons, which is governed by the two-Pomeron diagram in Fig. 7*a*. The probability of meson production is determined by the structure of

the Pomeron ladder; here, we use a QCD-motivated Pomeron based on the pQCD Pomeron from [16]. In [16], the Pomeron was constructed by inserting the running coupling constant and the soft-interaction boundary condition. The Pomeron found under these constraints, Lipatov's Pomeron [16], has an infinite set of poles in the j plane; it is a suitable object for using it as a guide in analyzing the soft-interaction region. Previously, such an extension of Lipatov's Pomeron to the soft region was used in [41]; below we follow the results from [41].

The gluon ladder that corresponds to Lipatov's Pomeron is shown in Fig. 7*b*. In order to describe soft interactions, quark loops can be incorporated into the gluon ladder, since, according to the rules of $1/N$ expansion [17], quark loops do not introduce an additional smallness. Cutting quark loops (see Fig. 7*c*) yields the diagram that corresponds to the cross section for the inclusive production of a $q\bar{q}$ pair—that is, the production of meson states. In this sense, the diagram in Fig. 7*c* is redrawn as that in Fig. 7*d*: the quark–Pomeron vertex is defined by the interaction of two Reggeized gluons with a quark. The spin structure of such a vertex can easily be calculated (see [41], Appendix C) by using the analysis of the leading-s terms in Reggeon kinematics (large s and small t) for the *vector particle + fermion* vertex [42].

In the leading terms of the $1/N$ expansion, there exist diagrams of the type in Fig. 7*e*, where the gluons of the upper (or lower) Pomeron interact with two quarks simultaneously (generally, these diagrams can be represented as that in Fig. 7*f*). As was shown in [41], the sum of all these contributions (Figs. 7*d*, 7*e*, etc.) results in the color-screening effect: the quark-loop amplitude is nearly zero for the above quark configurations at $r_{q\bar{q}} \lesssim 0.2$ fm (the existence of color-screening effects in hadron-production processes has long since been known [43, 44]).

The color-screening effect for the quark-loop diagram in the Pomeron ladder [41] allows us to restrict the calculations of $V_{\rm prompt}/P_{\rm prompt}$ to the process in Fig. 7*a*, because this diagram is responsible for the leading effect at large $q\bar{q}$ separations, $r_{q\bar{q}} \gtrsim 0.2$ fm.

The loop diagram in Fig. 7*a* is defined by a formula that is quite similar to (8)—only the spin factors are replaced as $S_\pi \to S_\pi^{(\rm P)}$ and $S_\rho \to S_\rho^{(\rm P)}$, which is due to taking into account the vertices P_{qq}. The spin factors $S_\pi^{(\rm P)}$ and $S_\rho^{(\rm P)}$ are given by

$$S_\pi^{(\rm P)} = -\mathrm{tr}\left(i\gamma_5(\hat{k}_1+m)\hat{n}_+(\hat{k}_1+m)i\gamma_5(-\hat{k}_2+m)(-\hat{n}_-)(-\hat{k}_2+m)\right), \quad (A.1)$$

$$S_\rho^{(\rm P)} = -\mathrm{tr}\left(\gamma_\alpha^\perp(\hat{k}_1+m)\hat{n}_+(\hat{k}_1+m)\gamma_\alpha^\perp(-\hat{k}_2+m)(-\hat{n}_-)(-\hat{k}_2+m)\right),$$

where $\hat{n}_+$ is the quark–Pomeron vertex (coupling to the upper Pomeron in Fig. 7*a*) and $(-\hat{n}_-)$ is the antiquark–Pomeron vertex (coupling to the lower Pomeron); we have also considered that the Pomerons in the diagram in Fig. 7*a* for the inclusive cross section carry zero momenta.

If the upper Pomeron in the graph in Fig. 7*a* moves along the z axis with momentum $p_A = (p_0, 0, p_z) \simeq (p_z, 0, p_z)$ and if the lower one moves in the opposite direction, we have

$$n_- = (1, 0, -1), \qquad n_+ = (1, 0, 1). \quad (A.2)$$

As in Section 2, the loop diagram has been calculated in terms of the spectral integration; because of that, we have $k_1^2 = k_2^2 = m^2$. Once the operators $\hat{n}_+$ and $\hat{n}_-$ have been commuted with $\hat{k}_1$ and $\hat{k}_2$, we arrive at

$$S_\pi^{(\rm P)} = -\mathrm{tr}\left(i\gamma_5(\hat{k}_1+m)i\gamma_5(-\hat{k}_2+m)\right) \times 4(n_+k_1)(n_-k_2), \quad (A.3)$$

$$S_\rho^{(\rm P)} = -\mathrm{tr}\left(\gamma_\alpha^\perp(\hat{k}_1+m)\gamma_\alpha^\perp(-\hat{k}_2+m)\right) \times 4(n_+k_1)(n_-k_2).$$

Apart from a common factor, $S_\pi^{(\rm P)}$ and $S_\rho^{(\rm P)}$ coincide with the normalization spin factors of the pion and ρ-meson wave functions given by (24) and (29):

$$S_\pi^{(\rm P)} = 4(n_+k_1)(n_-k_2)S_\pi^{(\rm wf)},$$
$$S_\rho^{(\rm P)} = 4(n_+k_1)(n_-k_2)3S_\rho^{(\rm wf)}. \quad (A.4)$$

This equation demonstrates that the two-Pomeron diagram in Fig. 7*a*, which defines the cross section for the inclusive production of ρ and π in the central region of hadron–hadron collisions, yields $\rho_{\rm prompt}/\pi_{\rm prompt} = 3$.

APPENDIX B

Spin Factors for Fragmentation Production

Below, the explicit expressions for $S_P^{(\rm fr)}/S_P^{(\rm wf)}$ and $S_V^{(\rm fr)}/S_V^{(\rm wf)}$ are given for $Z^0 \to b\bar{b} \to \to B + X$ and $Z^0 \to b\bar{b} \to B^* + X$ processes.

For the pseudoscalar particle, we have

$$\frac{S_P^{(\rm fr)}}{S_P^{(\rm wf)}} = A_1 + R^2\, A_2, \quad (B.1)$$

where

$$A_1 = \left((m_b-m)^2 - s'\right)\left(M^2+2m_b^2\right) + \left((m_b-m)^2 - s\right)\left(M'^2+2m_b^2\right), \tag{B.2}$$

$$A_2 = M^2\left(1-\frac{m_b^2}{M'^2}\right)\left((m_b-m)^2-s'\right) + M'^2\left(1-\frac{m_b^2}{M^2}\right)\left((m_b-m)^2-s\right)$$
$$-3m_b^2\left((m_b-m)^2-s'\right) - 3m_b^2\left((m_b-m)^2-s\right). \tag{B.3}$$

For the fragmentation production of the vector particle, the result is

$$\frac{S_V^{(\mathrm{fr})}}{S_V^{(\mathrm{wf})}} = \frac{M^2}{ss'}A_3 + \frac{M'^2}{ss'}A_4 + \frac{2m^2}{ss'}(A_3+A_4)$$
$$+\frac{R^2}{M'^2M^2s's}\left(M^4(M'^2-m_b^2)A_3\right. \tag{B.4}$$
$$\left.+M'^4(M^2-m_b^2)A_4 - 3M'^2M^2m_b^2(A_3+A_4)\right),$$

where

$$A_3 = (s+s')(m_b^2-m^2)^2$$
$$+ss'(3m^2-m_b^2-10m_bm-4s')$$
$$+s'^2(3m_b^2-2m_bm-m^2), \tag{B.5}$$
$$A_4 = (s+s')(m_b^2-m^2)^2$$
$$+ss'(3m^2-m_b^2-10m_bm-4s)$$
$$+s^2(3m_b^2-2m_bm-m^2).$$

REFERENCES

1. V. V. Anisovich and V. M. Shekhter, Nucl. Phys. B **55**, 455 (1973).
2. J. D. Bjorken and G. E. Farrar, Phys. Rev. D **9**, 1449 (1974).
3. S. T. Butler and C. A. Pearson, Phys. Rev. Lett. **7**, 69 (1961); A. Schwarzschild and C. Zupancic, Phys. Rev. **129**, 854 (1963); J. Randrup and S. E. Koonin, Nucl. Phys. A **356**, 223 (1981); D. H. E. Gross *et al.,* Z. Phys. A **309**, 41 (1982).
4. K. M. Watson, Phys. Rev. **88**, 1163 (1952); A. B. Migdal, Zh. Éksp. Teor. Fiz. **28**, 10 (1955) [Sov. Phys. JETP **1**, 7 (1955)].
5. V. V. Anisovich, M. N. Kobrinsky, J. Nyiri, and Yu. M. Shabelski, *Quark Model and High Energy Collisions* (World Sci., Singapore, 1985).
6. M. A. Voloshin, Yu. P. Nikitin, and P. I. Porfirov, Yad. Fiz. **35**, 1006 (1982) [Sov. J. Nucl. Phys. **35**, 586 (1982)].
7. S. S. Gershtein, A. K. Likhoded, and Yu. D. Prokoshkin, Z. Phys. C **24**, 305 (1984).
8. C. Amsler and F. E. Close, Phys. Lett. B **353**, 385 (1995); Phys. Rev. D **53**, 295 (1996).
9. V. V. Anisovich, Phys. Lett. B **364**, 195 (1995); V. V. Anisovich, Yu. D. Prokoshkin, and A. V. Sarantsev, Phys. Lett. B **382**, 429 (1996); A. V. Anisovich and A. V. Sarantsev, Phys. Lett. B **413**, 137 (1997); V. V. Anisovich, V. A. Nikonov, and L. Montanet, Phys. Lett. B **480**, 19 (2000).
10. Particle Data Group (C. Caso *et al.*), Eur. Phys. J. C **3**, 1 (1998).
11. ALEPH Collab. (R. Barate *et al.*), Phys. Rep. **294**, 1 (1998).
12. L3 Collab. (M. Pacciari *et al.*), Phys. Lett. B **393**, 465 (1997); **407**, 389 (1997).
13. DELPHI Collab. (P. Abreu *et al.*), Phys. Lett. B **475**, 429 (2000); **449**, 364 (1999).
14. OPAL Collab. (K. Ackerstaff *et al.*), Eur. Phys. J. C **4**, 19 (1998); **5**, 411 (1998).
15. E. A. Kuraev, L. N. Lipatov, and V. S. Fadin, Zh. Éksp. Teor. Fiz. **71**, 840 (1976) [Sov. Phys. JETP **44**, 443 (1976)]; Ya. Ya. Balitskiĭ and L. N. Lipatov, Yad. Fiz. **28**, 1597 (1978) [Sov. J. Nucl. Phys. **28**, 822 (1978)].
16. L. N. Lipatov, Zh. Éksp. Teor. Fiz. **90**, 1536 (1986) [Sov. Phys. JETP **63**, 904 (1986)].
17. G.'t Hooft, Nucl. Phys. B **72**, 461 (1974); G. Veneziano, Nucl. Phys. B **117**, 519 (1976).
18. V. V. Anisovich, in *Proceedings of the 9th LNPI Winter School, 1974,* Vol. 3, p. 1.
19. V. N. Gribov, Eur. Phys. J. C **10**, 71 (1999); hep-ph/9807224; Eur. Phys. J. C **10**, 91 (1999); hep-ph/9902279.
20. T. Barnes, AIP Conf. Proc. **432**, 3 (1998); *Proc. Hadron'97,* Ed. by S.-U. Chung and H. J. Willutzki (AIP, Woodbury, 1998).
21. V. V. Anisovich, M. G. Huber, M. N. Kobrinsky, and B. Ch. Metsch, Phys. Rev. D **42**, 3045 (1990); V. V. Anisovich and B. Ch. Metsch, Phys. Rev. D **46**, 3195 (1992).
22. ALEPH Collab. (D. Busculic *et al.*), Z. Phys. C **69**, 393 (1996).
23. DELPHI Collab. (P. Abreu *et al.*), Z. Phys. C **68**, 353 (1995).
24. L3 Collab. (M. Pacciari *et al.*), Phys. Lett. B **345**, 353 (1995).
25. OPAL Collab. (K. Ackerstaff *et al.*), Z. Phys. C **74**, 413 (1997).
26. ALEPH Collab. (R. Barate *et al.*), Preprint CERN/EP/99-94.
27. DELPHI Collab. (P. Abreu *et al.*), Preprint CERN/EP/99-66.
28. OPAL Collab. (K. Ackerstaff *et al.*), Eur. Phys. J. C **5**, 1 (1998).
29. V. V. Anisovich, D. I. Melikhov, and V. A. Nikonov, Phys. Rev. D **52**, 5295 (1995); **55**, 2918 (1997).
30. V. V. Anisovich, D. I. Melikhov, B. Ch. Metsch, and H. R. Petry, Nucl. Phys. A **563**, 549 (1993).
31. D. B. Leinweber *et al.,* Phys. Rev. D **58**, 031501 (1998).

32. K. Peters and E. Klempt, Phys. Lett. B **352**, 467 (1995).
33. A. V. Anisovich, V. V. Anisovich, and A. V. Sarantsev, hep-ph/0003113; Phys. Rev. D **62**, 051502 (2000).
34. C. A. Baker, C. J. Batty, P. Blüm, *et al.,* Phys. Lett. B **449**, 114 (1999).
35. WA 102 Collab. (D. Barberis, F. G. Binon, F. E. Close, *et al.*), hep-ex/0001017.
36. A. V. Anisovich, C. A. Baker, C. J. Batty, *et al.,* Phys. Lett. B **452**, 187 (1999); **452**, 173 (1999); **452**, 180 (1999); Nucl. Phys. A **651**, 253 (1999).
37. Yi-Jin Pei, Z. Phys. C **72**, 39 (1996).
38. P. V. Chliapnikov, Phys. Lett. B **462**, 341 (1999).
39. V. Uvarov, Nucl. Phys. A **663**, 663 (2000).
40. V. V. Anisovich, D. V. Bugg, and A. V. Sarantsev, Phys. Rev. D **58**, 111503 (1998); A. V. Anisovich, V. V. Anisovich, and A. V. Sarantsev, Z. Phys. A **357**, 173 (1997).
41. L. G. Dakhno and V. A. Nikonov, Eur. Phys. J. A **5**, 209 (1999).
42. V. N. Gribov, L. N. Lipatov, and G. V. Frolov, Yad. Fiz. **12**, 994 (1970) [Sov. J. Nucl. Phys. **12**, 543 (1971)].
43. A. H. Mueller, in *Proceedings of the 17th Recontre de Moriond: Elementary Hadronic Processes and New Spectroscopy, Les Arcs, Savoie, 1982,* Ed. by J. Tran Thanh Van (Frontières, Gif sur Yvette, 1982).
44. S. J. Brodsky, in *Proceedings of the 13th International Symposium on Multiparticle Dynamics, Volendam, 1982,* Ed. by W. Metzger, E. W. Kittel, and A. Stergiou (World Sci., Singapore, 1983).

Physics of Atomic Nuclei, Vol. 64, No. 5, 2001, pp. 834–842. From Yadernaya Fizika, Vol. 64, No. 5, 2001, pp. 899–907.

QCD at a Finite Isospin Density: From the Pion to Quark–Antiquark Condensation*

D. T. Son[1),3)] and M. A. Stephanov[2),3)]

Received September 20, 2000

Abstract—QCD at a finite isospin chemical potential μ_I is studied. This theory has no fermion-sign problem and can be simulated on a lattice by using present-day techniques. We solve this theory analytically in two limits: low μ_I, where chiral perturbation theory is applicable, and asymptotically high μ_I, where perturbative QCD is at work. At a low isospin density, the ground state is a superfluid pion condensate. At a very high density, it is a Fermi liquid with Cooper pairing. The pairs carry the same quantum numbers as the pions. Motivated by this observation, we put forward a conjecture that the transition from hadron to quark matter is smooth. The conjecture passes several nontrivial tests. Our results imply a nontrivial phase diagram in the space of the temperature and chemical potentials of isospin and baryon number. At asymptotically large values of μ_I and small values of the baryon chemical potential, the ground state is in a phase similar to the Fulde–Ferrell–Larkin–Ovchinnikov phase. It is characterized by a spatially modulated superfluid order parameter $\langle \bar{u}\gamma_5 d\rangle$ and may be the asymptotic limit of the inhomogeneous pion-condensation phase advocated by Migdal and others. © *2001 MAIK "Nauka/Interperiodica"*.

1. INTRODUCTION

Good knowledge of QCD in the regime of finite temperatures and a finite baryon density is crucial for understanding a wide range of physical phenomena. In cosmology, one faces the problem of understanding how the Universe evolved through the QCD phase transition at temperature $T \sim 150$ MeV. Due to the smallness of baryon asymmetry, finite-temperature QCD should be sufficient to deal with this problem. For the physics of heavy-ion collisions, however, one needs to know how QCD behaves when both the temperature and the baryon chemical potential are finite. Lastly, neutron stars require knowledge of matter in the "dense" regime—that is, at large baryon densities and very low temperatures. Much less is known about the last two regimes in relation to that of high-temperature baryon–antibaryon-symmetric QCD.

Let us use neutron stars as an example to illustrate the range of questions one would like to have answers to. The equation of state (EOS) of nuclear matter at high densities determines the mass–radius relationship and the maximum mass of neutron stars. The Walečka model of nuclear matter predicts that the EOS becomes stiffer at higher densities and approaches the Zeldovich limit, $\epsilon = p$ (where the velocity of sound approaches the speed of light), at very high densities. At asymptotically high densities, however, one expects nuclear matter to become a weakly interacting quark liquid, with a much softer EOS, $\epsilon = 3p$. At what density does the transition occur, and is it a phase transition or a crossover?

Migdal [1] and others [2] suggested that, at very high densities, pion condensation might happen. It is also argued that, at still higher densities, kaons are condensed [3]. One would like to know whether pion and kaon condensations do indeed occur in nuclear matter before the transition to quark matter.

Finally, there is strong recent interest in the phenomenon of color superconductivity [4, 5]. One very interesting prediction is that, at a sufficiently high chemical potential, the ground state of QCD is a "color-flavor-locking" state [6], which breaks chiral symmetry. However, while reliable results can be obtained at asymptotically high densities, where strong coupling is small [7–9], it is not known how one can extend these results to the region of smaller, more realistic, densities, without relying on uncontrollable approximations.

Lacking reliable analytic means for approaching QCD in the strong-coupling regime, one naturally invokes numerical methods. First-principle lattice numerical Monte Carlo calculations provide a solid basis for our knowledge of the finite-temperature

*This article was submitted by the authors in English.

[1)]Physics Department, Columbia University, 538 W. 120th St. New York, NY 10027, USA.

[2)]Department of Physics, University of Illinois, M/C 237, 845 W. Taylor St. no. 2236, Chicago, IL 60607-7059, USA.

[3)]RIKEN–BNL Research Center, Brookhaven National Laboratory, Upton, NY 11973, USA.

regime. However, the regime of a finite baryon chemical potential μ_B is still inaccessible by Monte Carlo, because present methods for evaluating the QCD partition function require taking a path integral with a measure that includes a complex fermion determinant. At zero chemical potential, one can simply ignore the determinant (as in the popular quenched approximation) and still find reasonable results for physical quantities. At finite μ_B, however, this procedure leads to qualitatively unacceptable answers, as was realized long ago [10]. It was understood more recently that the quenched approximation fails at finite μ_B because it describes an unphysical theory containing, in addition to normal quarks, so-called conjugate quarks having the opposite baryon charge [11].

As a side remark, one notes that, although conjugate quarks are absent in real QCD, there are many theories where they are naturally present. One class of such theories is QCD with two colors, where quarks are self-conjugate [12]. Another class contains theories with quarks in the adjoint color representation [13]. In all these theories, the positivity of the fermion determinant ensures the applicability of lattice Monte Carlo methods. However, the particle content of all these theories is very different from that in the real world.

The failure of the quenched approximation in real QCD at finite μ_B and our inability to include a complex fermion determinant in a Monte Carlo simulation is one of the main reasons that our understanding of QCD at a finite baryon density is still rudimentary.

One aspect in which QCD at a finite baryon density is different from finite-temperature QCD is that the transition from hadronic to quark degrees of freedom occurs owing to a large density of a conserved charge (such as the baryon number), while temperature plays no role. This is the motivation for us to address QCD at a finite chemical potential μ_I of isospin (more precisely, of the third component of isospin, I_3), which is conserved by strong interaction.

Before going into details, we would like to comment on the relevance of this regime to the real world. Nature does provide us with nonzero-μ_I systems in the form of isospin-asymmetric matter (for example, within neutron stars); however, the latter contains both isospin density and baryon number density. In contrast, the idealized system considered in this study does not carry baryon number: the chemical potentials of the two light quarks, u and d, are equal in magnitude, $|\mu_I|/2$, and opposite in sign. Strictly speaking, such a system is unstable with respect to weak decays; does not conserve isospin; and, as we will see, is not electrically neutral. Therefore, that it does not exist in the thermodynamic limit. Since we are interested in the dynamics of strong interaction alone, one can imagine, however, that all relatively unimportant electromagnetic and weak effects are switched off. Once this has been done, we obtain a nontrivial regime that, as we will see below, is accessible to present lattice Monte Carlo methods, while being analytically tractable in various interesting limits. As a result, the system that we consider has a potential to improve substantially our understanding of cold dense QCD. This regime carries many attractive traits of two-color QCD [12, 13], but it is realized in a physically relevant theory—QCD with three colors.

2. POSITIVITY AND QCD INEQUALITIES

Since the fermion determinant of our theory is real and positive in Euclidean space, some rigorous results on the low-energy behavior can be obtained from QCD inequalities [13, 14]. Let us recall how the inequalities are derived in vacuum QCD. The starting point is the following property of the Euclidean Dirac operator $\mathcal{D} = \gamma(\partial + iA) + m$:

$$\gamma_5 \mathcal{D} \gamma_5 = \mathcal{D}^\dagger. \tag{1}$$

Among other things, this implies positivity of the determinant, $\det \mathcal{D} \geq 0$. For the correlation function for a generic meson $M = \bar{\psi}\Gamma\psi$, we can find, by using (1) and the Buniakowski–Schwartz inequality, that

$$\begin{aligned} \langle M(x) M^\dagger(0) \rangle_{\psi,A} &= -\langle \mathrm{tr} \mathcal{S}(x,0) \Gamma \mathcal{S}(0,x) \overline{\Gamma} \rangle_A \\ &= \langle \mathrm{tr} \mathcal{S}(x,0) \Gamma i\gamma_5 \mathcal{S}^\dagger(x,0) i\gamma_5 \overline{\Gamma} \rangle_A \\ &\leq \langle \mathrm{tr} \mathcal{S}(x,0) \mathcal{S}^\dagger(x,0) \rangle_A, \end{aligned} \tag{2}$$

where $\mathcal{S} \equiv \mathcal{D}^{-1}$ and $\overline{\Gamma} \equiv \gamma_0 \Gamma^\dagger \gamma_0$. The inequality is saturated for mesons with $\Gamma = i\gamma_5\tau_i$, since $\mathcal{D}$ commutes with the isospin τ_i, which means that the pseudoscalar correlation functions majorate all other $I = 1$ meson correlation functions.[4)] As a consequence, one obtains an important restriction on the pattern of spontaneous symmetry breaking. For example, symmetry breaking cannot be driven by a condensate of $\langle \bar{\psi}\gamma_5\psi \rangle$. Indeed, the generators of broken axial $SU(2)$ symmetry that act on such a presudoscalar condensate would have produced 0^+ Goldstone bosons $\bar{\psi}\tau_i\psi$.

At a finite isospin density, $\mu_I \neq 0$, positivity still holds [15], and certain inequalities can be derived (in contrast to the case of $\mu_B \neq 0$ when there is no positivity; hence, no inequality can be derived). Now, $\mathcal{D} = \gamma(\partial + iA) + \frac{1}{2}\mu_I \gamma_0 \tau_3 + m$, and Eq. (1) is not true anymore, since the operation on the right-hand side of (1) changes the relative sign of μ_I. If, however,

[4)] It is important, as is the case for $I = 1$, that there is no disconnected piece after ψ integration in (2). The proof does not apply to the σ-meson correlation function, $\Gamma = 1$.

$m_u = m_d$, interchanging up and down quarks compensates for this sign change (the u and d quarks play the role of mutually conjugate quarks [11]); that is,

$$\tau_1\gamma_5\mathcal{D}\gamma_5\tau_1 = \mathcal{D}^\dagger. \quad (3)$$

Instead of the isospin τ_1 in (3), one can also use τ_2 (but not τ_3). Equation (3) replaces Eq. (1), which is now invalid, and ensures that $\det\mathcal{D} \geq 1$. Repeating the derivation of the QCD inequalities by using Eq. (3), we find that the lightest meson, or the condensate, must be in channels featuring $\bar\psi i\gamma_5\tau_{1,2}\psi$—that is, a linear combination of $\pi^- \sim \bar u\gamma_5 d$ and $\pi^+ \sim \bar d\gamma_5 u$ states. Indeed, it is shown below that, in both two analytically tractable regimes of small and large μ_I, the lightest mode is a massless Goldstone mode, which is a linear combination of $\bar u\gamma_5 d$ and $\bar d\gamma_5 u$.

3. SMALL ISOSPIN DENSITIES: PION CONDENSATE

When μ_I is small, chiral perturbation theory can be used to treat the problem. To have a rough estimate of how small μ_I should be, we require that no particles other than pions be excited owing to the chemical potential. This gives $\mu_I \simeq m_\rho$ as an upper limit on the applicability of chiral perturbation theory.

For zero quark mass and zero μ_I, the pion is a massless Goldstone boson of spontaneously broken $SU(2)_L \times SU(2)_R$ chiral symmetry. Actually, the quarks have small masses, which break this symmetry explicitly. Under the assumption of equal quark masses, the symmetry of the Lagrangian is $SU(2)_{L+R}$. The low-energy dynamics of the system is governed by the familiar chiral Lagrangian; in terms of the matrix pion field $\Sigma \in SU(2)$, it is given by

$$\mathcal{L} = \frac{1}{4}f_\pi^2\mathrm{tr}(\partial_\mu\Sigma\partial_\mu\Sigma^\dagger - 2m_\pi^2\mathrm{Re}\Sigma).$$

This Lagrangian contains only two phenomenological parameters: the pion decay constant, f_π, and the pion mass in a vacuum, m_π. We will see that interesting physics occurs at $\mu_I > m_\pi$; since $m_\pi \ll m_\rho$, there is a nontrivial range of μ_I where the chiral Lagrangian is a reliable and useful treatment.

The isospin chemical potential further breaks $SU(2)_{L+R}$ down to $U(1)_{L+R}$. Its effect can be included in the effective Lagrangian to leading order in μ_I, without introducing additional phenomenological parameters. Indeed, μ_I enters into the QCD Lagrangian in the same way as the zeroth component of a gauge potential [13]. Thus, the finite-μ_I chiral Lagrangian is obtained by promoting global $SU(2)_L \times SU(2)_R$ symmetry to a local gauge symmetry: gauge invariance completely fixes the way in which μ_I enters into the chiral Lagrangian [13]; that is,

$$\mathcal{L}_{\mathrm{eff}} = \frac{f_\pi^2}{4}\mathrm{tr}\nabla_\nu\Sigma\nabla_\nu\Sigma^\dagger - \frac{m_\pi^2 f_\pi^2}{2}\mathrm{Retr}\Sigma. \quad (4)$$

The covariant derivative is defined as

$$\nabla_0\Sigma = \partial_0\Sigma - \frac{\mu_I}{2}(\tau_3\Sigma - \Sigma\tau_3), \qquad \nabla_i\Sigma = \partial_i\Sigma, \quad (5)$$

which follows from the transformation property of Σ under rotations by the isospin generator $I_3 = \tau_3/2$.

With the aid of (4), it is straightforward to determine the vacuum alignment of Σ as a function of μ_I and the spectrum of excitations around the vacuum. We will be interested in negative μ_I, which favors neutrons over protons, as in neutron stars. The results are very similar to those in two-color QCD at a finite baryon density [13]. From (4), one finds that the potential energy for Σ is

$$V_{\mathrm{eff}}(\Sigma) = \frac{f_\pi^2\mu_I^2}{8}\mathrm{tr}(\tau_3\Sigma\tau_3\Sigma^\dagger - 1) - \frac{f_\pi^2 m_\pi^2}{2}\mathrm{Retr}\Sigma. \quad (6)$$

The first term in (6) favors the directions of Σ that anticommute with τ_3 (that is, τ_1 and τ_2), while the second term prefers the vacuum direction $\Sigma = 1$. It turns out that the minima of (6) at all μ_I are captured by the ansatz

$$\overline{\Sigma} = \cos\alpha + i(\tau_1\cos\phi + \tau_2\sin\phi)\sin\alpha. \quad (7)$$

Substituting (7) into (6), one can see that the potential energy depends only on α, but not on ϕ:

$$V_{\mathrm{eff}}(\alpha) = \frac{f_\pi^2\mu_I^2}{4}(\cos 2\alpha - 1) - f_\pi^2 m_\pi^2\cos\alpha. \quad (8)$$

Minimizing $V_{\mathrm{eff}}(\alpha)$ with respect to α, one finds that the system behaves differently in two distinct regimes:

(i) For $|\mu_I| < m_\pi$, the system is in the same ground state as at $\mu_I = 0$: $\alpha = 0$ or $\overline{\Sigma} = 1$.

This result is easily understandable. The positive energy $m_\pi - |\mu_I|$ is required to excite the lowest pion state; therefore, no pion is excited at zero temperature. The ground state of the Hamiltonian at such μ_I values coincides with the normal vacuum of QCD. The isospin density is zero in this case.

(ii) When $|\mu_I|$ exceeds m_π, the minimum of (8) occurs at

$$\cos\alpha = m_\pi^2/mu_I^2. \quad (9)$$

In this regime, the energy required to excite a π^- quantum, $m_\pi - |\mu_I|$, is negative; thus, it is energetically favorable to excite a large number of these quanta. Since pions are bosons, the result is a Bose condensate of π^-. If the pions did not interact, the density of the condensate would be infinite. However, the repulsion between the pions stabilizes the system at a finite value of the isospin density. This value can

be found by differentiating the ground-state energy with respect to μ_I:

$$n_I = -\frac{\partial \mathcal{L}_{\text{eff}}}{\partial \mu_I} = f_\pi^2 \mu_I \sin^2\alpha = f_\pi^2 \mu_I \left(1 - \frac{m_\pi^4}{\mu_I^4}\right). \tag{10}$$

For $|\mu_I|$ just above the condensation threshold, $|\mu_I| - m_\pi \ll m_\pi$, Eq. (10) reproduces the equation of state of a dilute nonrelativistic pion gas [13],

$$n_I = 4f_\pi^2(|\mu_I| - m_\pi).$$

At larger μ_I, $|\mu_I| \gg m_\pi$, the isospin density is linear in μ_I,

$$n_I = f_\pi^2 \mu_I, \qquad |\mu_I| \gg m_\pi.$$

From Eq. (10), one can find the pressure and the energy density as functions of μ_I. The quantity of interest is the ratio of the two,

$$\frac{p}{\epsilon} = \frac{\mu_I^2 - m_\pi^2}{\mu_I^2 + 3m_\pi^2}. \tag{11}$$

This ratio starts from 0 at the threshold and fast approaches unity with increasing $|\mu_I|$. Thus, we see that, as far as the chiral Lagrangian is still applicable, the EOS approaches the Zeldovich limit of maximal stiffness at high densities, in just the same way as for nuclear matter in the Walečka model.

The fact that the minimum of the potential (6) is degenerate with respect to the angle ϕ corresponds to the spontaneous breakdown of $U(1)_{L+R}$ symmetry generated by I_3 in Lagrangian (4). This is not unexpected since the ground state is essentially a pion superfluid, with one massless Goldstone mode. Since we start from a theory with three pions in a vacuum, there are, in addition to the massless mode, two massive modes in the superfluid. One can be identified with π^0, while the other is a linear combination of π^+ and π^-, which is denoted here by $\tilde{\pi}^+$ since it coincides with π^+ at the condensation threshold. The mass (defined as the rest energy) of these modes can be obtained by expanding Lagrangian (4) around the minimum. The result reads (cf. [13])

$$m_{\pi^0} = |\mu_I|,$$
$$m_{\tilde{\pi}^+} = |\mu_I|\sqrt{1 + 3(m_\pi/\mu_I)^4}. \tag{12}$$

At the condensation threshold, $m_{\pi^0} = m_\pi$ and $m_{\tilde{\pi}^+} = 2m_\pi$, while, for $|\mu_I| \gg m_\pi$, both masses approach $|\mu_I|$ (see Fig. 1).

The values of the chiral condensate, $\langle \bar{u}u + \bar{d}d\rangle$, and of the pion condensate, $\langle \bar{u}\gamma_5 d\rangle$, follow from (9):

$$\langle \bar{u}u + \bar{d}d\rangle = 2\langle \bar{\psi}\psi\rangle_{\text{vac}} \cos\alpha, \tag{13}$$
$$\langle \bar{u}\gamma_5 d\rangle + \text{h.c.} = 2\langle \bar{\psi}\psi\rangle_{\text{vac}} \sin\alpha;$$

that is, the chiral condensate "rotates" into the pion condensate as a function of $|\mu_I|$.

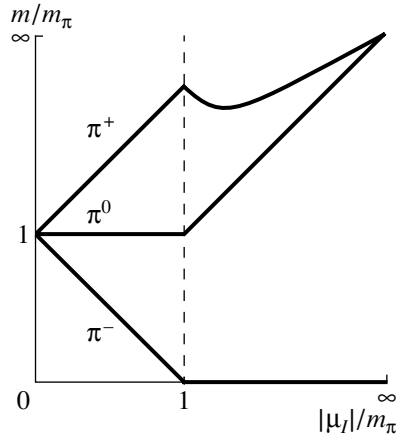

Fig. 1. Schematic plot of masses (rest energies) of the lowest excitations in QCD at finite (negative) μ_I in the regime of applicability of chiral perturbation theory ($m_\pi, \mu_I \ll m_\rho$).

It is also possible to find baryon masses—that is, the energy required for generating a single baryon in the system. The most interesting baryons are those that have the lowest energy and the highest isospin—that is, the neutron n and the Δ^- isobar. There are two effects of μ_I on the baryon masses. The first comes from the baryon isospin, which effectively reduces the neutron mass by $\frac{1}{2}|\mu_I|$ and the Δ^- mass by $\frac{3}{2}|\mu_I|$. If these were the only effect, the effective Δ^- mass would vanish at $|\mu_I| = \frac{2}{3}m_\Delta$. For larger $|\mu_I|$, there would arise the baryon or the antibaryon Fermi surface, which would lead to a nonzero baryon susceptibility $\chi_B \equiv \partial n_B/\partial\mu_B$. However, the other effect comes into play much earlier than this occurs: the negative pions in the condensate tend to repel the baryons, increasing their masses.

These effects can be treated within baryon chiral perturbation theory [16]. For example, the (Euclidean) Lagrangian describing nucleons and their interactions with pions at finite μ_I can be written as

$$\mathcal{L}_N = \bar{N}\gamma_\mu \nabla_\mu N + m_N\left(\bar{N}_L \Sigma N_R + \text{h.c.}\right), \tag{14}$$

where

$$\nabla_0 N = \left(\partial_0 - \frac{\mu_I}{2}\tau_3\right) N, \qquad \nabla_i N = \partial_i N.$$

Diagonalizing this bilinear Lagrangian in the pion background given by $\Sigma = \bar{\Sigma}$ from (7), one obtains the nucleon masses. In the approximation of nonrelativistic baryons, the results for the neutron and for the Δ^- isobar are given by

$$m_n = m_N - \frac{|\mu_I|}{2}\cos\alpha, \tag{15}$$
$$m_{\Delta^-} = m_\Delta - \frac{3|\mu_I|}{2}\cos\alpha.$$

Equation (3) can be interpreted as follows: as the result of the rotation (7) of the chiral condensate, the nucleon mass eigenstate becomes a superposition of vacuum n and p states. The expectation value of the isospin in this state is proportional to $\cos\alpha$ appearing in (3). With $\cos\alpha$ given in Eq. (9), we see that the two effects mentioned above cancel each other when $m_\pi \ll |\mu_I| \ll m_\rho$. Thus, the baryon mass never vanishes, and $\chi_B = 0$ at zero temperature in the region of applicability of the chiral Lagrangian.

As one forces more pions into the condensate, the pions are packed closer and their interaction becomes stronger. When $|\mu_I| \sim m_\rho$, the chiral perturbation theory fails. To find the equation of state in this regime, full QCD must be employed. As we have seen, this can be done by using present lattice techniques since the fermion-sign problem is nonexistent at finite μ_I, in just the same way as in two-color QCD [12].

4. ASYMPTOTICALLY HIGH ISOSPIN DENSITIES: QUARK–ANTIQUARK CONDENSATE

In the opposite limit of very large isospin densities, or $|\mu_I| \gg m_\rho$, the description in terms of quark degrees of freedom applies since the latter interact weakly because of asymptotic freedom. In our case of large negative μ_I, or n_I, the ground state contains an equal number of d quarks and $\bar{u}$ antiquarks per unit volume. If one neglects the interaction, the quarks fill two Fermi spheres with the equal radii $|\mu_I|/2$. Switching on the interaction between the fermions leads to instability that is associated with the formation and condensation of Cooper pairs and which is similar to Bardeen–Cooper–Schrieffer (BCS) instability in metals or to diquark pairing at a high baryon density [4]. To the leading order of perturbation theory, quarks interact via one-gluon exchange. It can easily be seen that the strongest attraction is observed in the color-singlet channel; therefore, a Cooper pair consists of a $\bar{u}$ antiquark and a d quark. The ground state is therefore a fermionic superfluid.

However, perturbative one-gluon exchange does not discriminate between the scalar $(\bar{u}d)$ channel and the pseudoscalar $(\bar{u}\gamma_5 d)$ channel: the attraction is the same in both cases. But one can expect that the instanton-induced interaction, however small, will favor the $\bar{u}\gamma_5 d$ channel rather than the $\bar{u}d$ one. Thus, the condensate is pseudoscalar and breaks parity,

$$\langle \bar{u}\gamma_5 d\rangle \neq 0. \qquad (16)$$

This is consistent with our earlier observation that QCD inequalities constrain the $I = 1$ condensate to be a pseudoscalar at any μ_I. We note that the order parameter in (16) has the same quantum numbers as the pion condensate at lower densities. We will discuss this coincidence later.

Because of Cooper pairing, the fermion spectrum acquires a gap Δ at the Fermi surface,

$$\Delta = b|\mu_I| g^{-5} e^{-c/g}, \qquad c = 3\pi^2/2, \qquad (17)$$

where g should be evaluated at the scale $|\mu_I|$. The singular $e^{-c/g}$ behavior is associated with the long-range magnetic interaction, as in the superconducting gap at large μ_B [7]. The constant c is smaller by a factor of $\sqrt{2}$ in relation to the latter case because of the stronger one-gluon attraction in the singlet $q\bar{q}$ channel than in the $\bar{\mathbf{3}}$ diquark channel. Consequently, the gap in (17) is exponentially larger than the diquark gap at comparable values of the baryon chemical potential. Using the methods proposed in [8], one can estimate $b \approx 10^4$. As in BCS theory, the critical temperature at which the superfluid state disappears is of order Δ.

Asymptotically, Δ is much less than $|\mu_I|$, and superfluidity affects slightly the equation of state. The ratio p/ϵ approaches $1/3$ from below in the limit $|\mu_I| \to \infty$.

5. QUARK–HADRON CONTINUITY AND CONFINEMENT

Since the order parameter (16) has the same quantum numbers and breaks the same symmetry as the pion condensate in the low-density regime, it is plausible that there is no phase transition along the μ_I axis. In this case, an increase in the density leads to a smooth transformation of the Bose condensate of weakly interacting pions into the superfluid state of $\bar{u}d$ Cooper pairs. The situation is very similar to that in strongly coupled superconductors with a "pseudogap" [17] and, possibly, to that in high-temperature superconductors [18]. This also parallels the continuity between nuclear and quark matter in three-flavor QCD as conjectured by Schäfer and Wilczek [19]. We therefore conjecture that, in two-flavor QCD, one can move continuously from the hadron phase to the quark phase without encountering a phase transition. We emphasize here that this conjecture must be verified by lattice calculations.

At first glance, this conjecture seems to contradict common wisdom that there is a "deconfinement" phase transition from the hadron phase to the quark phase. It is logically possible that there exists a first-order phase transition at an intermediate value of μ_I. However, there are several nontrivial arguments that make the continuity hypothesis highly plausible.

The first argument arises from a consideration of baryons. One notices that all fermions have a gap

at large $|\mu_I|$; this means that all excitations carrying baryon number are massive. In particular, the baryon-number susceptibility χ_B vanishes at zero temperature. This is also true at small $|\mu_I|$. It is thus natural to expect that all excitations with a nonzero baryon number are massive at any value of μ_I and that χ_B remains zero at $T = 0$ for all μ_I. This also suggests one way to verify the continuity on a lattice.

Another argument comes from a consideration of the limit of a large number of colors, N_c. Let us recall that, in finite-temperature QCD, there is a mismatch at large N_c between the number of gluon degrees of freedom, which is $\mathcal{O}(N_c^2)$, and the number of hadron degrees of freedom, which is $\mathcal{O}(N_c^0)$. This fact is a strong hint of a first-order confinement–deconfinement phase transition such that the effective number of degrees of freedom jumps from $\mathcal{O}(N_c^0)$ to $\mathcal{O}(N_c^2)$. It is easy to see, however, that the behavior of thermodynamic quantities as functions of N_c is the same in the "hadronic" phase (low μ_I) and the "quark" phase (large μ_I). Indeed, it can easily be shown that, at very large μ_I, the isospin density n_I is proportional to the number of quarks, which is $\mathcal{O}(N_c)$:

$$n_I = \frac{N_c}{3}\frac{\mu_I^3}{8\pi^2}. \qquad (18)$$

In the small-μ_I region, the isospin density is given by Eq. (10). In the large-N_c limit, the pion decay constant scales as $f_\pi^2 = \mathcal{O}(N_c)$; thus, the isospin density in the pion gas is also proportional to N_c.[5)] What occurs is that the repulsion between pions becomes weaker as one goes to larger N_c; thus, more pions can be stacked at a given chemical potential. As a result, the N_c dependence of thermodynamic quantities is the same in the quark and in the hadronic regime, although for seemingly very different reasons.

Let us now return to the question of confinement. Naively, one would think that, at asymptotically large μ_I, $\bar{u}$ and d quarks are packed at a very high density, and that the system should become deconfined. At finite temperatures, there is no rigorous way to distinguish between the confined and the deconfined phase in QCD with quarks in the fundamental representation. However, a sharp distinction can be made between the two phases at zero temperature (and finite μ_I). In the confined phase, all particle excitations carry integer baryon number; the deconfined phase can be defined as a phase where there exist finite-energy excitations carrying fractional baryon charge. The pion superfluid at small μ_I is clearly in the confined phase. There is, however, the question of whether quark matter at large μ_I is confined or deconfined.

It might seem that, at very large μ_I, there exist excitations with fractional baryon number. These are fermionic quasiparticles near the Fermi surface, which are related to the original quarks and antiquarks by a Bogolyubov–Valatin transformation. The opening of a BCS gap makes the energy of these excitations larger than Δ, but it is still finite.

To see that the logic above has a fault and that there are no such excitations, one needs to consider the dynamics of very soft gluons. A crucial observation is that, at large μ_I, gluons softer than Δ are not screened either by the Meissner or by the Debye effect.[6)] The Meissner effect is absent because the condensate does not break gauge symmetry (in contrast to the color superconducting condensate [4]). Debye screening is also absent because, on scales softer than Δ, there are no charge excitations in the medium: Cooper pairs are neutral, while fermions are too heavy to be excited. Thus, the gluon sector below the scale Δ is described by pure $SU(3)$ gluodynamics, which is a confining theory. This means that there are no quark excitations above the ground state: all particles and holes must be confined in color-singlet objects, mesons and baryons, just as in vacuum QCD.

If there is no transition along the μ_I axis, we expect confinement at all values of μ_I. At large μ_I, the confinement scale $\Lambda'_{\rm QCD}$ is much less than Δ since the running strong coupling α_s at the scale Δ is small. In more detail, let us trace the running of the strong coupling from the UV to the IR limit. First, α_s increases until the scale $g\mu_I$ is reached when it "freezes" owing to Debye screening and Landau damping. The freezing regime continues until we reach the scale Δ, after which the coupling runs again as in pure gluodynamics. Since the coupling is still small at the scale Δ, it can become large only at some scale $\Lambda'_{\rm QCD}$ much lower than Δ. Thus, at large $|\mu_I|$, there are three different scales separated by large exponential factors, $\mu_I \gg \Delta \gg \Lambda'_{\rm QCD}$.

That the scale of confinement is much smaller than the gap at large μ_I has an important consequence for finite temperature. One can actually predict a temperature-driven deconfinement phase transition at a temperature T'_c of order $\Lambda'_{\rm QCD}$. Indeed, quarks are unimportant at such low temperatures, so that the

[5)] At physical values of N_c, f_π, and m_π, the values of n_I given by Eqs. (10) and (18) and naively continued into the regime of intermediate μ_I intersect at $\mu_I \approx 800$ MeV. This agrees with the value of $\mu_I \sim m_\rho$, where one would expect the crossover between the quark and hadron regimes to occur. This is a quantitative indication that a phase transition is not necessary.

[6)] This is similar to the behavior of the unbroken $SU(2)_c$ sector of two-flavor color superconductors [20].

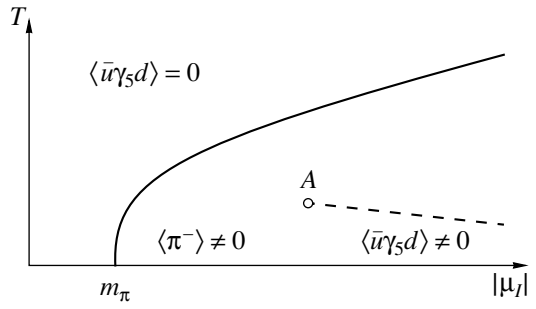

Fig. 2. Phase diagram of QCD at a finite isospin density.

transition must be of the first order as in pure gluodynamics. In particular, one expects the temperature dependence of the baryon-number susceptibility to change from $e^{-3\Delta/T}$ to $e^{-\Delta/T}$ around T_c' because of deconfinement.

The smallness of the confinement scale $\Lambda'_{\rm QCD}$ in relation to the BCS gap Δ allows one to conclude that the binding energy of quarks and antiquarks is small and that the hadronic spectrum follows the pattern of the constituent quark model, with Δ playing the role of the constituent quark mass. This means that mesons weigh 2Δ and baryons weigh 3Δ, approximately. A good analog of the large-μ_I regime is vacuum QCD with only heavy quarks. As in the latter case, the string tension and string breaking are determined by parametrically different energy scales ($\Lambda'_{\rm QCD}$ and Δ, respectively). Hence, the area law should work up to some distance much larger than $\Lambda_{\rm QCD}^{-1}$, even when fundamental quarks are present. For the same reason, one also expects high-spin excited states of hadrons to be narrow at large μ_I.

The energy hierarchy also leads to a curious dispersion relation for hadrons in the isospin-dense regime. By way of example, we consider the ρ^- meson, which is a bound state of a $\bar{u}$ antiquark and a d quark. At zero total momentum, these $\bar{u}$ and d are on opposite sides of the Fermi surface. With increasing total momentum, the two constituents move along the Fermi surface, remaining close to the latter until the total momentum becomes larger than μ_I—that is, twice the Fermi momentum. Thus, the dispersion curve for the ρ^- meson must remain essentially flat in the momentum interval $(0, |\mu_I|)$. For baryons, the energy is almost independent of momentum in the interval $(0, 1.5|\mu_I|)$. Therefore, the group velocity of hadrons virtually vanishes in these intervals. Above these intervals, it should be equal to the speed of light. It would be interesting to follow, on a lattice, the evolution of the dispersion curves for ρ^- from small to large μ_I.

6. PHASE DIAGRAMS ON THE (T, μ_I) AND (μ_I, μ_B) PLANES

By considering nonzero μ_I, we make the phase diagram of QCD three-dimensional: (T, μ_B, μ_I). Two planes in this three-dimensional space are of special interest: the $\mu_B = 0$ (T, μ_I) plane, which is completely accessible to present lattice techniques, and the $T = 0$ (μ_I, μ_B) plane, which contains neutron-star matter.

Let us first consider the simpler case of the phase diagram on the (T, μ_I) plane. Two phenomena determine the phase diagram on this plane (Fig. 2): pion condensation and confinement. At sufficiently high temperatures, the condensate given by (16) melts (solid line in Fig. 2). For large $|\mu_I|$, this critical temperature is proportional to the BCS gap (17). There are two phases that differ by symmetry: the high-temperature phase, where the explicit flavor $U(1)_{L+R}$ symmetry is restored, and the low-temperature phase, where this symmetry is spontaneously broken. The phase transition is in the $O(2)$ universality class.[7)] The critical temperature T_c vanishes at $|\mu_I| = m_\pi$ and is an increasing function of μ_I in both regimes that we studied: $|\mu_I| \ll m_\rho$ and $|\mu_I| \gg \Lambda_{\rm QCD}$. Thus, it is likely that $T_c(\mu_I)$ is a monotonic function of μ_I. Moreover, it was explained above that, at large $|\mu_I|$, there is a first-order deconfinement phase transition at some temperature T_c' much lower than $T_c(\mu_I)$. Since there is no phase transition at $\mu_I = 0$ (for small $m_{u,d}$) or at $T = 0$ (under the assumption of quark–hadron continuity), this first-order line must end at some point A on the (T, μ_I) plane (dashed line in Fig. 2).

The phase diagram in the $(\mu_I, \mu_{\rm B})$ plane at zero temperature proves to be quite complicated. We defer a more detailed study of this plane for future work. Here, we will only consider the regime where $|\mu_I| \gg \mu_B$, both being much larger than $\Lambda_{\rm QCD}$, so that perturbative QCD can be used. For $\mu_B = 0$ and $|\mu_I| \gg \Lambda_{\rm QCD}$, we have seen that the system is a superfluid with a gap Δ. Finite μ_B provides a mismatch between the $\bar{u}$ and the d Fermi sphere. The superconducting state becomes unfavorable at some value of μ_B of order Δ. It is known [22] that the destruction of this state occurs through two separate phase transitions. As one increases μ_B, a first-order phase transition occurring at μ_B slightly below $\Delta/\sqrt{2}$

[7)] The width of the Ginzburg region is suppressed by $(\Delta/\mu_I)^4$ at large $|\mu_I|$, as in usual BCS superconductors, and also by $1/N_c^2$, at large N_c, as in the case of the QCD chiral transition [21].

drives the system into the Fulde–Ferrell–Larkin–Ovchinnikov (FFLO) state [22], which is characterized by a spatially modulated superfluid order parameter $\langle \bar{u}\gamma_5 d\rangle$ with a wave number of order $2\mu_B$. This spatial dependence is still unknown, mostly because the FFLO state has not been observed in metals. The FFLO state persists only until $\mu_B = 0.754\Delta$, when it goes over, through a second-order phase transition, to a $\langle \bar{u}\gamma_5 d\rangle = 0$ state. The latter must be a color superconductor with one-flavor diquark condensates $\langle uu\rangle$ and $\langle dd\rangle$, owing to the attraction between quarks of the same flavor. In that region of the (μ_I, μ_B) phase diagram, which is directly relevant to neutron stars, $\mu_B > |\mu_I|$, the color superconducting FFLO phase was studied by Alford, Bowers, and Rajagopal [23].

The most interesting feature of the FFLO state is that it has the same symmetries as the inhomogeneous pion-condensation state, which might be formed in electrically neutral nuclear matter at high densities, as argued by Migdal [1] and others [2]. Thus, the FFLO phase can be thought of as a realization of Migdal's pion condensate in the regime of asymptotically high densities. It is also conceivable that the two phases are actually one, continuously connected on the (μ_I, μ_B) phase diagram.

Note added. Further research [24] reveals that the physics below the scale Δ is described by "gluodynamics of continuous media" with a large dielectric constant. As a result, the scale of confinement, $\Lambda'_{\rm QCD}$, is small and decreases exponentially with the chemical potential $|\mu_I|$. This means that the line of the first order deconfinement transition goes down as indicated in Fig. 2.

7. CONCLUSION

Our original and primary motivation for considering QCD at finite isospin densities has been to have a dense regime of realistic, three-color QCD that can be studied on a lattice. Based on analytic calculations in the asymptotic regimes of low and high densities, we have found that there is likely no phase transition along the μ_I axis at zero temperature. This conjecture should be verified on the lattice. An obvious way is to study the thermodynamics of the system. If our continuity conjecture is correct, all thermodynamic quantities should be smooth functions of μ_I. In this case, we also suggest that the ratio p/ϵ is a nonmonotonic function of μ_I: it grows from zero at the threshold $|\mu_I| = m_\pi$ to some value close to unity, then decreases to some minimal value, and then approaches 1/3 from below at large $|\mu_I|$. At zero temperature, the baryon susceptibility must vanish at any μ_I. We also predict that, on the (T, μ_I) plane, there is a line of first-order phase transitions, which terminates at a second-order point.

The phase diagram on the (μ_I, μ_B) plane, which is the most relevant to neutron-star physics, remains inaccessible to lattice calculations. Based on our preliminary investigations, we have concluded that the phase diagram on this plane should have a rather complicated topology. The most interesting feature of this diagram appears to be the existence of the FFLO phase, which is reliably predicted at $|\mu_I| \gg \mu_B$, both being large. This phase has the same symmetry as the pion-condensation state conjectured by Migdal; both might be different regions of a single connected region on the phase diagram.

ACKNOWLEDGMENTS

We are grateful to J. Kogut, L. McLerran, R. Pisarski, and E. Shuryak for discussions; K. Rajagopal for drawing our attention to [22]; and the DOE Institute for Nuclear Theory at the University of Washington for its hospitality.

The work of D.T. Son was supported in part by DOE (grant no. DE/FG02-92ER40699).

REFERENCES

1. A. B. Migdal, Zh. Éksp. Teor. Fiz. **61**, 2210 (1971) [Sov. Phys. JETP **36**, 1052 (1971)].
2. R. F. Sawyer, Phys. Rev. Lett. **29**, 382 (1972); D. J. Scalapino, Phys. Rev. Lett. **29**, 386 (1972); see also G. Baym and D. K. Campbell, *Mesons and Nuclei,* Ed. by M. Rho and D. Wilkinson (North-Holland, Amsterdam, 1979), Vol. 3.
3. D. B. Kaplan and A. E. Nelson, Phys. Lett. B **175**, 57 (1986).
4. B. C. Barrois, *Non-perturbative Effects in Dense Quark Matter*, PhD Thesis (Caltech, 1979); D. Bailin and A. Love, Phys. Rep. **107**, 325 (1984).
5. M. Alford, K. Rajagopal, and F. Wilczek, Phys. Lett. B **422**, 247 (1998); R. Rapp, T. Schäfer, E. V. Shuryak, and M. Velkovsky, Phys. Rev. Lett. **81**, 53 (1998); Ann. Phys. (N.Y.) **280**, 35 (2000).
6. M. Alford, K. Rajagopal, and F. Wilczek, Nucl. Phys. B **537**, 443 (1999).
7. D. T. Son, Phys. Rev. D **59**, 094019 (1999); hep-ph/9812287.
8. W. E. Brown, J. T. Liu, and H.-C. Ren, Phys. Rev. D **61**, 114012 (2000); **62**, 054013; **62**, 054016 (2000).
9. D. T. Son and M. A. Stephanov, Phys. Rev. D **61**, 074012 (2000); Erratum: **62**, 059902 (2000).
10. I. Barbour, N.-E. Behilil, E. Dagotto, *et al.,* Nucl. Phys. B **275** (FS17), 296 (1986); J. B. Kogut, M.- P. Lombardo, and D. K. Sinclair, Phys. Rev. D **51**, 1282 (1995); Nucl. Phys. B (Proc. Suppl.) **42**, 514 (1995).
11. M. A. Stephanov, Phys. Rev. Lett. **76**, 4472 (1996).

12. E. Dagotto, F. Karsch, and A. Moreo, Phys. Lett. B **169B**, 421 (1986); E. Dagotto, A. Moreo, and U. Wolff, Phys. Rev. Lett. **57**, 1292 (1986); Phys. Lett. B **186**, 395 (1987); S. Hands, J. B. Kogut, M.-P. Lombardo, and S. E. Morrison, Nucl. Phys. B **558**, 327 (1999); S. Hands and S. E. Morrison, hep-lat/9902012; hep-lat/9905021.
13. J. B. Kogut, M. A. Stephanov, and D. Toublan, Phys. Lett. B **464**, 183 (1999); J. B. Kogut, M. A. Stephanov, D. Toublan, *et al.,* Nucl. Phys. B **582**, 477 (2000).
14. D. Weingarten, Phys. Rev. Lett. **51**, 1830 (1983); E. Witten, Phys. Rev. Lett. **51**, 2351 (1983); S. Nussinov, Phys. Rev. Lett. **52**, 966 (1984); D. Espriu, M. Gross, and J. F. Wheater, Phys. Lett. B **146B**, 67 (1984).
15. M. Alford, A. Kapustin, and F. Wilczek, Phys. Rev. D **59**, 054502 (1999).
16. See, for example, H. Georgi, *Weak Interaction and Modern Particle Theory* (Benjamin-Cummings, Menlo Park, 1984).
17. A. J. Leggett, J. Phys. (Paris) **41**, C7-19 (1980); P. Nozières and S. Schmitt-Rink, J. Low Temp. Phys. **59**, 195 (1985).
18. M. Randeria, cond-mat/9710223 and references therein.
19. T. Schäfer and F. Wilczek, Phys. Rev. Lett. **82**, 3956 (1999).
20. D. H. Rischke, Phys. Rev. D **62**, 034007 (2000).
21. J. B. Kogut, M. A. Stephanov, and C. G. Strouthos, Phys. Rev. D **58**, 096001 (1998).
22. P. Fulde and A. Ferrell, Phys. Rev. **135**, A550 (1964); A. I. Larkin and Yu. N. Ovchinnikov, Zh. Éksp. Teor. Fiz. **47**, 1136 (1964) [Sov. Phys. JETP **20**, 762 (1964)].
23. M. Alford, J. Bowers, and K. Rajagopal, hep-ph/0008208.
24. D. H. Rischke, D. T. Son, and M. A. Stephanov, hep-ph/0011379.

Physics of Atomic Nuclei, Vol. 64, No. 5, 2001, pp. 843–848. Translated from Yadernaya Fizika, Vol. 64, No. 5, 2001, pp. 908–913.

NUCLEI
Experiment

Anomalies in the Orbital Magnetism of Neutrons in the ^{190,192}Pt Nuclei

I. B. Kovgar, A. I. Levon, R. S. Poznyak, and O. V. Sevastyuk

Institute for Nuclear Research, National Academy of Sciences of Ukraine, pr. Nauki 47, UA-252028 Kiev, Ukraine

Received November 2, 1999; in final form, May 16, 2000

Abstract—For the ^{190,192}Pt nuclei, the g factors of the $\nu 9/2^-[505] \otimes \nu 11/2^+[615]$ 10^- isomeric states populated in the relevant $(\alpha, 2n)$ reactions are measured by the method of an integrated disturbed angular distribution in an external magnetic field. From these measurements, it follows that the g factors are 0.009(8) and 0.010(6) for ^{190}Pt and ^{192}Pt, respectively. From the above g factors, it is found that the anomalous g_l factor of the neutron is $\delta g_l(n) = -0.017(6)$. © *2001 MAIK "Nauka/Interperiodica".*

1. INTRODUCTION

Experimental g factors are of importance for revealing the structure of the corresponding states, since they are quite sensitive to fine details of this structure. Moreover, they sometimes contribute to establishing medium-induced changes in the magnetic properties of intranuclear nucleons. Anomalies in orbital g_l factors (deviation from Dirac values) can be determined from the g factors of states formed by two nucleons belonging to the same species and having oppositely directed spins. In this way, the anomaly of the orbital g_l factor of neutrons was determined from the g factor of a 10^- state in the ^{190}Os nucleus as measured by a modified NMR method implemented for oriented nuclei [1]. The results revealed a significant deviation from data known by that time and from theoretical predictions. We made an attempt at determining an anomaly in the orbital magnetism of neutrons in nuclei neighboring Os by using the method of an integrated disturbed angular distribution (IDAD). Here, we present results obtained by measuring the g factors of 10^- isomeric states in ^{190}Pt and ^{192}Pt. Previously, these nuclei were studied by gamma-spectroscopy methods in a beam by using $(\alpha, 4n\gamma)$ and $(\alpha, 2n\gamma)$ reactions [2, 3], and the results of such investigations were employed in determining the g factors discussed here.

2. DESCRIPTION OF THE EXPERIMENT

The excited states of ^{190}Pt and ^{192}Pt were populated and aligned in the reactions ^{188,190}Os$(\alpha, 2n)^{190,192}$Pt in a 26.8-MeV alpha-particle beam from the U-120 cyclotron installed at the Institute for Nuclear Research (Kiev). An osmium target enriched to 63% in ^{188}Os and to 79% in ^{190}Os was prepared by depositing a metal powder onto a thick bismuth substrate. Colloid graphite was used to glue the powder and to fix it on the substrate. Upon traversing the target ($\sim 60\,\mathrm{mg/cm^2}$), the beam energy was reduced to about 20 MeV, whereby the excitation function for the relevant $(\alpha, 2n)$ reaction was covered from the maximum to its half. The beam stopped in the bismuth substrate, but this did not lead to a significant enhancement of the background [the threshold for the reaction ^{207}Bi$(\alpha,2n)$ is 20.3 MeV]. Channels other than $(\alpha, 2n)$ do make sizable contributions to the gamma spectrum.

The gamma-ray IDAD method in an external magnetic field (see, for example, [4]) was used to measure the g factors in question. The angle through which the angular-distribution function is rotated owing to the interaction of the magnetic moment $\mu = g\mu_N I$ of an isomeric state having a spin I and a lifetime τ with a magnetic field B is given by

$$\Delta\theta = \omega_\mathrm{L}\tau = g\mu_N B/\hbar, \qquad (1)$$

where ω_L is the Larmor precession frequency. Prior to hitting the target, the beam was additionally rotated in the magnetic field through the angle θ_B. This also leads to a rotation of the angular-distribution function. Apart from this, we must take into account the reduction of the angular distribution of gamma rays because of isomer interaction with internal crystal fields in the target. Eventually, the IDAD can generally be represented as [4]

$$W(\theta, \tau) = \sum_k A_k \bar{G}_k P_k \left[\cos(\theta - \bar{G}_k \omega_\mathrm{L}\tau - \theta_B)\right], \qquad (2)$$

where θ is the angle at which the detector is arranged with respect to the beam axis, A_k are coefficients in

Table 1. Coefficients A_2 used to estimate their reduction by quadrupole interaction in the 10^- isomeric state in ^{190,192}Pt

$I_i \to I_f$	E_γ, keV	A_2 [2]	A_2 [3]	E_γ, keV	A_2 [2]	A_2 [3]
$12^- \to 10^-$	524	-	0.34(12)	454	0.17(3)	0.34(5)
$10^- \to 8^-$	605	0.20(6)	-	566	0.37(3)	0.37(6)
$10^- \to 8^{-*}$	219	0.17(4)	0.32(10)	208	0.10(2)	0.06(6)
$9^- \to 7^{-*}$	591	0.25(3)	0.26(12)	585	0.17(2)	0.13(3)
$7^- \to 5^{-*}$	167	0.22(2)	0.28(10)	134	0.22(2)	0.14(3)
	^{190}Pt $\bar{G}_2 = 0.96(9)$			^{192}Pt $\bar{G}_2 = 0.6(2)$		

* Transitions involving delayed components.

the undisturbed angular distribution, $\bar{G}_k$ are coefficients that take into account the reduction of the angular distribution due to the interaction in the target, and P_k are Legendre polynomials.

A magnetic field of 2.92(1) T changing within 0.1% over the beam cross section was generated by an electromagnet. The calculated beam-rotation angle θ_B in the field of a complicated configuration was 8.14°, the magnetic-field configuration being measured by a Hall sensor.

The choice of target requires special attention. In measurements like that being discussed, a disturbing effect is due to the quadrupole interaction of a long-lived isomeric state with the surrounding medium. In order to avoid the reduction of the angular distribution of gamma rays emitted by recoil nuclei when implantation in the target occurs, use is usually made of targets having a cubic crystal lattice (there is no electric-field gradient in this case). We decided on a target that consisted of osmium powder and was similar to that employed in the measurements of the angular distributions in [2, 3] (the only difference was that, here, the gaps between powder grains were filled with colloid graphite). Metal osmium has an A_3 hexagonal lattice. However, the reduction of the angular distribution is not critical for measuring g factors even for transitions that deexcite states whose lifetimes are 69 and 404 ns. Moreover, the reduction in the term $A_k\bar{G}_k$ was taken automatically into account, because the experimental coefficients $A_k^{\text{expt}} = A_k\bar{G}_k$ in the angular distributions were used in the present analysis. However, it is necessary to estimate $\bar{G}_k$ in order to extract $\omega_L\tau$ from $\bar{G}_k\omega_L\tau$. Since data on the quadrupole interaction of Pt in the Os lattice are not available in the literature, the quadrupole interaction of the 5^- state of ^{206}Hg in the Hg lattice at $T = 77$ K was extrapolated to Hg in Os by using data for ^{197}Au and ^{193}Ir in various lattices [4]. The quadrupole-frequency value of $\nu_Q = 0.58(2)$ MHz, which was obtained in this way, is overly small to be taken into consideration for $\tau <$ 20 ns transitions. For $\tau \approx 280$ ns, however, it leads to the reduction factor equal to the hard-core limit [4], s_{20}:

$$\bar{G}_2(\tau) = s_{20} = \sum_n \left[1 + (n\omega_0\tau)^2\right]^{-1} \approx 0.24. \quad (3)$$

The quadrupole interaction is weaker for Pt in Os than for Hg in Os. This follows from a comparison of the A_2 values (see Table 1) for transitions following the decay of 10^- isomers whose lifetimes are 69 and 404 ns (the reduction occurs) and for fast transitions (there is no reduction in this case) characterized by the same or close spin values, like the $12^- \to 10^-$ transition populating the 10^- isomer or the $10^- \to 8^-$ transition from the negative-parity band. Despite the discrepancies between the data from [2] and [3] and large uncertainties, we can conclude that the reduction in ^{190}Pt is indeed small and can be disregarded at the current experimental accuracy. For ^{192}Pt, the value of $\bar{G}_2(\tau) \approx 0.6$ was obtained from the ratio of the coefficients A_2 and was taken into account in eventual results.

The relevant gamma rays were recorded by two Ge(Li) detectors that had a resolution of 2.2 keV and an efficiency of about 10% at an energy of 1.34 MeV and which were arranged at angles of $\pm 135°$ with respect to the beam. The gamma spectra measured for two opposite magnetic-field directions were analyzed by two methods: (a) by fitting a peak and (b) by summing counts in each peak channel, whereupon the background fitted over a wide region around the peak was subtracted from the result of this summation.

In order to estimate the accuracy in determining the peak area, we compared the ratio of the exposure factors q_1 and q_2 with the ratio of the detector efficiencies ε_1 and ε_2, which must be identical for all transitions in the spectrum. They can be obtained from the expressions

$$\left(\frac{q_1}{q_2}\right)^2 = \frac{N(+\theta)\uparrow}{N(+\theta)\downarrow}\frac{N(-\theta)\uparrow}{N(-\theta)\downarrow}, \quad (4)$$

$$\left(\frac{\varepsilon_1}{\varepsilon_2}\right)^2 = \frac{N(+\theta)\uparrow N(+\theta)\downarrow}{N(-\theta)\uparrow N(-\theta)\downarrow}, \quad (5)$$

where the effects of precession and beam rotation cancel and where $N(\pm\theta)(\uparrow\downarrow)$ stands for the number of counts in the detectors at $\pm\theta$ for opposite field directions ($\uparrow$ and $\downarrow$).

For small Larmor precessions, the measured angles of Larmor precession can be determined from the relation

$$R = S\,\Delta\theta_{\mathrm{L}}, \quad (6)$$

where $\Delta\theta_{\mathrm{L}} = \omega_{\mathrm{L}}\tau$ if direct isomeric transitions are observed (the deviations from the exact value are 0.2, 0.7, and 1.5% for $\Delta\theta_{\mathrm{L}} = 100$, 200, and 300 mrad, respectively), R is the asymmetry of counts that was measured for up–down field directions, and S is the logarithmic derivative of the angular distribution at the angle of the detector arrangement. The quantity R is determined as

$$R = \frac{1-\sqrt{\rho}}{1+\sqrt{\rho}}, \quad (7)$$

where

$$\rho = \frac{N(+\theta)\uparrow N(-\theta)\downarrow}{N(+\theta)\downarrow N(-\theta)\uparrow}. \quad (8)$$

Expression (6) must be modified to take into account the concerted effect of Larmore precession and beam rotation in the field of the electromagnet. In those cases where the transition deexciting the isomer cannot be recorded, but where the next transition is observed, it is necessary to take into account the fast population of the level that is deexcited by this transition. Therefore, we have

$$R = S\left\{\theta_B + \sum_i \frac{I_d^{(i)}}{I_{fd}}\Delta\theta_{\mathrm{L}}^{(i)}\right\}, \quad (9)$$

where $I_d^{(i)}$ is the intensity of the ith delayed component and I_{fd} is the total (delayed plus fast) intensity (see Fig. 1). In the case of $\omega\tau \geqslant 200$ mrad, the reduction of the angular distribution is taken into account in the expression

$$R = S\left\{\frac{I_{fd}-I_d}{I_{fd}}\theta_B + \frac{I_d}{I_{fd}}\frac{\sin 2(\omega_{\mathrm{L}}\tau+\theta_B)}{\sqrt{1+(2\omega_{\mathrm{L}}\tau)^2}}\right\}. \quad (10)$$

Those parts of the energy-level diagrams that are necessary in the present context are displayed in Fig. 2. The intensities of gamma rays from [2] were corrected for internal conversion, and the transition intensities obtained in this way are also shown in Fig. 2. The coefficients A_2 were borrowed from [2] as the most precise ones. For ^{190}Pt and ^{192}Pt, the coefficients A_2 and A_4 were used in the calculations invoking the logarithmic derivative

$$S = \frac{1}{W}\frac{dW}{d\theta} = \frac{12A_2+5A_4}{8+2A_2}. \quad (11)$$

The averaged lifetime values obtained in [5–7] are also quoted in Fig. 2. In all calculations, we first determined the precession angles $\omega_{\mathrm{L}}\tau$ for each transition being discussed. The precession angles were averaged, whereupon the g factors were computed by using the experimental lifetime values. The experimental data and the results of the calculations are presented in Table 2.

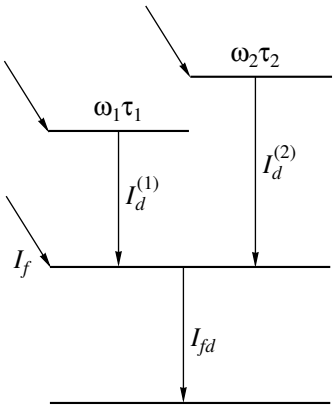

Fig. 1. Definitions of the symbols in expressions (9) and (10).

In analyzing data on the 219.1-, 447.3-, and 591.4-keV transitions in the ^{190}Pt nucleus, we made use of expression (9). The g factor of the 10^- state in ^{192}Pt was determined on the basis of data on the 207.9-, 446.1-, and 584.7-keV transitions by varying $\omega_{\mathrm{L}}\tau$ in expression (10) to obtain a numerical fit to the experimental value of R. A lower limit on the error in $\omega_{\mathrm{L}}\tau$ and g was obtained by calculating $\omega_{\mathrm{L}}\tau$ at $R' = R - \Delta R$. An upper limit cannot be derived by a similar method, since Eq. (10) does not have solutions at $R' = R + \Delta R$. Therefore, the above error was taken for a lower and for an upper limit.

3. DISCUSSION

In the decays of the 10^- isomers in the ^{190}Pt and ^{192}Pt nuclei, the reduced probabilities are $B(E2, 10^- \to 8^-) \approx (2-5)\times 10^{-2}$ W.u. and $B(M1, 10^- \to 9^-) \approx (0.5-2)\times 10^{-4}$ W.u. Large delay factors indicate that the structure of these isomers differs from the structure of the members of the band built on the 5^- state. At the same time, the transition proceeding between the 10^- isomer in ^{192}Pt and the 10^+ state at 2583.5 keV (see [2, 3]) suggests the $i_{13/2}$ neutron configuration

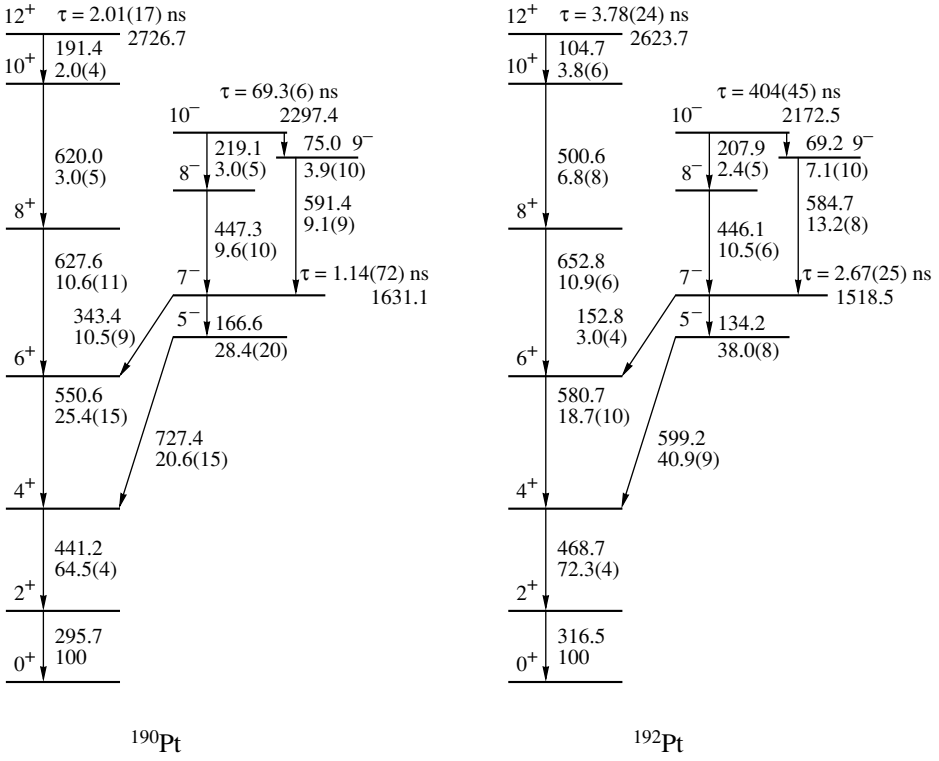

Fig. 2. Decay-diagram sections for ^{190,192}Pt [2, 3] that illustrate the analysis of experimental data. The transition energies and the total transition intensities are displayed in the figure.

in its structure. On this basis, it was concluded in [2, 3] that the 10^- isomer in ^{190,192}Pt is similar to the well-known 10^- isomer in ^{190}Os with a lifetime of 10 min, its structure $\nu 9/2^-[505] \otimes \nu 11/2^+$ [615] being formed by two neutrons [8]. Calculations on the basis of the nonaxial rotor plus two quasiparticles also lend support to the $(i_{13/2}h_{9/2})$ configuration of this isomer [9].

This interpretation is confirmed by the measurements of the g factors. In the strong-coupling limit, the g factor of a two-particle state is given by

$$g = \frac{1}{I+1}\left(g_R + g_{K_1}K_1 + g_{K_2}K_2\right), \qquad (12)$$

where g_R and g_K are, respectively, the collective and the single-particle g factor. The value of $g_K = 0.186(3)$ for the $9/2^-[505]$ orbital can be obtained from the experimental value $g = +0.214(2)$ [10] of the g factor of the $9/2^-$ state in ^{191}Os by using the value of $g_R = g(2^+) = +0.340(12)$ for ^{190}Os [11]. In a similar way, the value of $g_K = -0.180(5)$ for the $13/2^+[606]$ orbital can be deduced from the experimental value $g = -0.116(3)$ [1] of the g factor of the $13/2^+$ state in ^{193}Pt with the aid of the value of $g_R = g(2^+) = +0.302(18)$ for ^{192}Pt [12, 13]. In order to obtain $g_{K=11/2}$, the value of $g_{K=13/2}$ must be corrected for the distinctions between K and $\langle s_z\rangle$ by using the expression

$$g_K = g_l + \frac{\langle s_z\rangle}{K}(g_s - g_l). \qquad (13)$$

In this way, we found $g_{K=11/2} = -0.202(10)$. The g-factor value of $g(10^-) = +0.003(2)$ calculated for ^{192}Pt by using expression (12) and the above values of g_K is in excellent agreement with the experimental result.

The measured g factor of the 10^- state can be used to determine the anomalous orbital g factor, $\delta g_l = g_l - g_l^{\text{free}}$, arising because of meson-exchange currents. The most reliable way to determine it is based on the use of the experimental g factors of states in which two particles off the even–even core that have oppositely directed spins are bound in such a way that the total angular momentum is maximal [14]. The single-particle g factor of neutrons can be represented as

$$g_K = \delta g_l + \frac{\langle s_z\rangle}{K}\left(g_s^{\text{eff}} - \delta g_l\right). \qquad (14)$$

For the $K = K_1 + K_2 = I$ state, we obtain

$$g(I) = \frac{I}{I+1} \qquad (15)$$

Table 2. Results obtained by measuring precession and by analyzing the isomeric states of the ^{190,192}Pt nuclei

E_γ, keV	$I_i \to I_f$	R	S	$\Delta\theta_{\rm L}$	$\omega_{\rm L}\tau$	g
			^{190}Pt			
219.1	$10^- \to 8^-$	0.048(40)	0.25(6)	0.050(165)	0.050(165)	0.006(17)
447.3	$8^- \to 7^-$	0.103(16)	0.60(10)	0.028(40)	0.090(125)	0.010(14)
591.4	$9^- \to 7^-$	0.068(16)	0.37(4)	0.041(48)	0.096(112)	0.010(12)
			^{192}Pt			
207.9	$10^- \to 8^-$	0.049(30)	0.15(3)		0.30(23)*	0.009(7)**
446.1	$8^- \to 7^-$	0.096(15)	0.51(3)		0.40(32)*	0.013(10)**
584.7	$9^- \to 7^-$	0.056(13)	0.23(3)		0.29(20)*	0.009(7)**

* The values are presented as $\bar{G}_2\omega_{\rm L}\tau$.

** The presumed reduction is $\bar{G}_2 = 0.6(2)$.

$$\times \left\{ \frac{g_R}{I} + \delta g_l + \frac{\langle s_z\rangle^1 + \langle s_z\rangle^2}{I}\left(g_s^{\rm eff} - \delta g_l\right)\right\}.$$

The main contribution to $g(l)$ comes from the second term in (15). The contribution associated with the collective g factor is small because g_R is divided by I, where I is large. Since the spin contributions compensate each other almost completely (third term in the bracketed expression), the remaining modest correction due to spin magnetism can be taken into account quite reliably. The quantity $\langle s_z\rangle$ was calculated within the Nilsson model. The ^{190}Os nucleus is prolate; in Pt isomers, there is a prolate-to-oblate transition. The ^{190}Pt nucleus has a triaxial shape, while ^{192}Pt is oblate ($\gamma = 60^\circ$) [15]. A description of the 10^- isomers in ^{190}Pt and ^{192}Pt, as well as in ^{190}Os, on the basis of Nilsson's concepts is acceptable only for axisymmetric prolate shapes. The quantity $\langle s_z\rangle$ was calculated at the value of $\beta_2 = 0.15$, which is known from experiments for ^{192}Pt [16] (-0.434 and $+0.442$ for the $9/2^-[505]$ and $11/2^+[615]$ orbitals, respectively). The anomalous neutron orbital g factor calculated by using expression (15) and the value of $g_R = 0.302(18)$ is

$$\delta g_l(n) = -0.017(6). \qquad (16)$$

In this calculation, we set $g_s^{\rm eff} = 0.65{\rm g}_s^{\rm s.p}$ for both orbitals (the distinction between $g_s^{\rm eff}$ and ${\rm g}_s^{\rm s.p.}$ in a nucleus is due to the core spin polarization, which takes different values for different states [4]); the resulting error, which does not exceed 0.0005, was taken into account in the total uncertainty. The use of the $\langle s_z\rangle$ values calculated at $\beta_2 = -0.15$ yields a similar result—namely, $\delta g_l(n) = -0.014(6)$. The inclusion of the value of $\beta_4 = -0.04$ from [17] in the calculation does not change this result.

Our value of $\delta g_l(n)$ is at odds with the value of $\delta g_l(n) = -0.095(15)$, which was deduced from the g factor of the 10^- isomer in ^{190}Os [1]. The last value is also inconsistent with the systematics of $\delta g_l(n)$ values obtained by various methods [4]: about (0.10–0.15) for protons and about $-$(0.02–0.06) for neutrons; nor does it lend support to Yamazaki's assumption [18] on the increase of $(8 \pm 3)\%$ in the effective nuclear magneton within the nucleus in the relation to the magneton of a free nucleon. The assumption of Yamazaki was put forth in order to explain the deviation of the ratio $\delta g_l(p)/\delta g_l(n)$ from $-N/Z$; specifically, the values of $\delta g_l(p) = +0.15(2)$ and $\delta g_l(n) = -0.05(3)$ follow from an analysis of the g factors in the region around ^{208}Pb. The above ratio is expected under the assumption of the isovector character of δg_l because of meson-exchange currents. The increase in the nuclear magneton implies a decrease in the nucleon mass within the nucleus, the latter being behind one of the explanations of the EMC effect [19]. In accord with Yamazaki's assumption, our results confirm the deviation of the ratio $\delta g_l(p)/\delta g_l(n)$ [which was found to be close to -60 even at the smallest value of $\delta g_l(p)$] from $-N/Z$ (which is close to the value of -1.5 for Pt isotopes).

4. CONCLUSION

The g factors of the 10^- isomers in ^{190,192}Pt have been measured. The results have confirmed that the internal structure of these isomers is $\nu 9/2^-[505] \otimes \nu 11/2^+[615]$. On this basis, we have also been able to find that the anomalous orbital g factor of neutrons is $\delta g_l(n) = -0.017(6)$. It is difficult to explain so dramatic a deviation from the value of $\delta g_l(n) = -0.095(6)$, which was determined from the $g(10^-)$

factor in ^{190}Os [1]. If we assume that the 10^- state is spherical (not deformed) and use the corresponding procedure for determining δg_l, it is possible to obtain a positive value of +0.04(2), which contradicts all data accumulated so far and theoretical conjectures on the nature of δg_l.

ACKNOWLEDGMENTS

This work was financially supported by the Ministry for Science of Ukraine (grant no. 2.5.1/065).

REFERENCES

1. G. Schutz *et al.,* Phys. Rev. Lett. **56**, 1051 (1986).
2. S. A. Hjorth *et al.,* Nucl. Phys. A **262**, 328 (1976).
3. J. C. Cunnane *et al.,* Phys. Rev. C **13**, 2197 (1976).
4. A. B. Levon and O. F. Nemets, *Electromagnetic Moments of Excited and Radioative Nuclei* (Naukova Dumka, Kiev, 1989), pp. 471–472.
5. E. Browne and B. Singh, Nucl. Data Sheets **79**, 277 (1996).
6. V. S. Shirley, Nucl. Data Sheets **64**, 205 (1991).
7. B. Singh, Nucl. Data Sheets **61**, 243 (1990).
8. B. Harmatz and T. H. Handley, Nucl. Phys. **56**, 1 (1964).
9. H. Toki *et al.,* Nucl. Phys. A **279**, 1 (1977).
10. S. Ohya *et al.,* Phys. Rev. C **54**, 1129 (1996).
11. A. E. Stuchbery *et al.,* Z. Phys. A **342**, 373 (1992).
12. E. Bodenstedt *et al.,* Z. Phys. A **342**, 249 (1992).
13. A. E. Stuchbery, G. J. Lampard, and H. H. Bolotin, Nucl. Phys. A **528**, 447 (1991).
14. T. Yamazaki, *Mesons in Nuclei,* Ed by M. Rho and D. Wilkinson (North-Holland, Amsterdam, 1979), Vol. 2, p. 651.
15. R. Bengtsson *et al.,* Phys. Lett. B **183**, 1 (1987).
16. S. Raman *et al.,* At. Data Nucl. Data Tables **42**, 1 (1989).
17. A. K. Jain and R. K. Sood, Rev. Mod. Phys. **62**, 393 (1990).
18. T. Yamazaki, Phys. Lett. B **160B**, 227 (1985).
19. The European Muon Collab., Phys. Lett. B **123B**, 275 (1983).

Translated by A. Isaakyan

Physics of Atomic Nuclei, Vol. 64, No. 5, 2001, pp. 849–854. Translated from Yadernaya Fizika, Vol. 64, No. 5, 2001, pp. 914–919.

NUCLEI
Experiment

Inverse Beta Decay in a Nonequilibrium Antineutrino Flux from a Nuclear Reactor

V. I. Kopeikin, L. A. Mikaelyan, and V. V. Sinev

Russian Research Centre Kurchatov Institute, pl. Kurchatova 1, Moscow, 123182 Russia

Received January 27, 2000; in final form, March 13, 2000

Abstract—The evolution of the reactor-antineutrino spectrum toward equilibrium above the inverse-beta-decay threshold during the reactor operating period and the decay of residual $\bar{\nu}_e$ radiation after reactor shutdown are considered. It is found that, under certain conditions, these processes can play a significant role in experiments seeking neutrino oscillations. © *2001 MAIK "Nauka/Interperiodica".*

1. INTRODUCTION

The flux and the spectrum of reactor antineutrinos depend not only on the current reactor state, which is specified by the power level and the isotope composition of the nuclear fuel used, but also on the preceding evolution of the fuel. The spectrum of antineutrinos produced in the beta decay of fission products and other radioactive nuclei accumulated in the reactor core begin to evolve toward equilibrium after the start-up of a reactor. After reactor shutdown, the antineutrino radiation diminishes for a long time.

In [1, 2], equilibration of the spectrum and the reduction of the soft section of the $\bar{\nu}_e$ spectrum, where the effects of preceding evolution are pronounced, were analyzed in connection with the problem of searches for the neutrino magnetic moment in experiments studying $\bar{\nu}_e e^-$ scattering.

In this study, we consider the inverse-beta-decay process

$$\bar{\nu}_e + p \to e^+ + n \qquad (1)$$

and antineutrino spectrum above the threshold for this reaction (1.804 MeV). Presently, reaction (1) is of interest mainly as a tool for seeking neutrino oscillations in reactor experiments.

In this case, the oscillations in question are manifested in the disappearance of some fraction of the $\bar{\nu}_e$ flux and in a characteristic modulation of the $\bar{\nu}_e$ spectrum, the latter being specified by the factor

$$P = 1 - \sin^2(2\theta)\sin^2(1.27\Delta m^2 R/E), \qquad (2)$$

where $\sin^2 2\theta$ is the mixing parameter, Δm^2 is the mass parameter measured in electronvolts squared, R is the distance (in meters) between the source and detector, and E is the detected neutrino energy measured in megaelectronvolts.

In experiments seeking the above oscillations, the $\bar{\nu}_e$ spectrum and flux measured with the aid of reaction (1) are compared with their values expected in the absence of the oscillations. In this case, use is made of the reactor $\bar{\nu}_e$ spectrum obtained independently ($\bar{\nu}_e$ spectrum at the production instant). Uncertainties in determining this spectrum restrict the sensitivity of the method, and systematic error in the spectrum shape may generally mimic or mask the oscillation effect. Procedures that are applied to analyze data from experiments seeking oscillations were described in more detail elsewhere (see, for example, [3]). As a rule, equilibration of the spectrum and the reduction of the $\bar{\nu}_e$ spectrum do not lead to considerable effects in the region $E > 1.8$ MeV. However, their role can be greatly enhanced in some cases that will be discussed in Section 4.

This article is organized as follows. In Section 2, we give a brief account of available data on the spectrum of reactor $\bar{\nu}_e$ in the region $E > 1.8$ MeV and on the cross section for reaction (1). In Section 3, we consider the evolution of the spectrum in the reactor operating period and residual antineutrino radiation in the reactor shutdown period and determine the relevant cross sections. Section 4 is devoted to discussing the results.

2. SPECTRA AND CROSS SECTIONS (STANDARD APPROACH)

Let us briefly review the basic properties of the reactor-antineutrino spectrum in the energy region above 1.8 MeV and the spectrum-averaged cross section for reaction (1) (see, for example, [1, 2, 4–8] and references therein).

The standard approach is based on the following assumptions:

Yields of some fission fragments (in %)

Fission fragment	Fissile nucleus			
	^{235}U	^{239}Pu	^{241}Pu	^{238}U
^{97}Zr	5.95	5.30	4.89	5.50
^{132}I	4.30	5.40	4.14	5.16
^{93}Y	6.40	3.89	3.15	4.97
^{106}Ru	0.40	4.31	6.18	2.55
^{144}Ce	5.48	3.74	4.39	4.50
^{90}Sr	5.82	2.10	1.57	3.12

(i) The $\bar{\nu}_e$ spectrum is formed exclusively by the beta decays of the fragments produced in a reactor upon the fission of ^{235}U, ^{239}Pu, ^{238}U, and ^{241}Pu isotopes.

(ii) For each isotope, the equilibrium spectrum is established within a small time interval that can be neglected. At the instant under consideration, the reactor-antineutrino spectrum $\rho(E)$ measured in $(\mathrm{MeV})^{-1}$ units per fission event can then be expressed in terms of the spectra $\rho(E)$ for four fissile isotopes. Specifically, we have

$$\rho(E) = \sum \alpha_i \rho_i(E), \tag{3}$$

where α_i is the contribution of a given isotope to the number of fission events occurring in a reactor at this instant, the subscript values of $i = 5$, 9, 8, and 1 labeling the quantities associated with the fissile isotopes ^{235}U, ^{239}Pu, ^{238}U, and ^{241}Pu, respectively.

Because of ^{235}U depletion and the accumulation of fissile plutonium isotopes, the contributions α_i entering into Eq. (3) change, which leads to a change in the total spectrum $\rho(E)$ over the reactor operating period. As was mentioned above, the spectra $\rho_i(E)$ are assumed to be time-independent. Information about current α_i values is presented by the reactor personnel, the relative error in these values being set to 5%.

The spectra $\rho_i(E)$ for ^{235}U, ^{239}Pu, and ^{241}Pu were obtained in [5] by the conversion method, which enables one to reconstruct the relevant antineutrino spectrum on the basis of the total spectrum of beta-decay electrons from the set of the fragments of a given fissile isotope. For a few tens of hours, thin layers of the aforementioned isotopes were exposed to a thermal-neutron flux from the reactor installed at ILL (Grenoble), and the current spectra of electrons from the beta decay of fragments were simultaneously measured in the energy region above 2.0 MeV for ^{235}U and in the energy region above 1.8 MeV for ^{239}Pu and ^{241}Pu. After approximately 12 hours of irradiation, the beta spectra reached saturation and changed no longer. Therefore, the antineutrino spectra $\rho_i(E)$ reconstructed on the basis of these β spectra are actually those that are established after about one day of fuel irradiation. For ^{238}U, use was made of the spectrum calculated in [6] because the beta spectrum was not measured for the fragments of this isotope.

The expected number of events of the interaction between antineutrinos and target protons was calculated in terms of the cross section σ_{V-A} for reaction (1),

$$\sigma_{V-A} = \sum \alpha_i \sigma_i, \tag{4}$$

where $\sigma_i = \int \rho_i(E)\sigma(E)dE$, $\sigma(E)$ being the reaction cross section for monoenergetic antineutrinos [7].

In terms of 10^{-43} cm^2 units per fission event, the σ_i values calculated in this way are

$$\sigma_5 = 6.39 \pm 1.9\%, \sigma_9 = 4.18 \pm 2.4\%, \qquad \sigma_1 = 5.76 \pm 2.1\%, \sigma_8 = 8.88 \pm 10\%. \tag{5}$$

These calculations were performed with the β constants corresponding to the free-neutron lifetime of $\tau = 887.4$ s $\pm$ 0.2%. The resulting error in the cross section (4) is 2.7% (68% C.L.).

To a higher precision, the cross section for reaction (1) is known from an experiment performed by the Kurchatov Institute–Collège de France–LAPP collaboration at a distance of 15 m from the Bugey PWR reactor [8]:

$$\sigma_{\mathrm{meas}} = 5.750 \times 10^{-43}\ \mathrm{cm}^2/(\text{fission event}) \pm 1.4\%(68\%\mathrm{C.L.}). \tag{6}$$

This result corresponds to the following contributions α_i from fissile isotopes:

$$\alpha_5 = 0.538, \alpha_9 = 0.328, \alpha_8 = 0.078, \alpha_1 = 0.056. \tag{7}$$

The proportion in (7) for the number of isotope-fission events is typical for PWR reactors, which were used in the majority of experiments seeking the oscillations in question. Within the errors, the cross section in (6) agrees with the reaction cross section σ_{V-A} found for the given composition of nuclear fuel:

$$\sigma_{\mathrm{meas}}/\sigma_{V-A} = 0.987 \pm 1.4\%(\text{experiment}) \pm 2.7\%(V-A). \tag{8}$$

The experimental value in (6) is treated as a metrological reference for the cross section in the absence of oscillations. A feature peculiar to this reference is that, in each specific case of its application, it must be rescaled to the relevant composition of nuclear fuel. As a result, the error in the cross section increases to about 1.6%.

For reactors of the type being considered, the duration of the operating period is approximately one

year. After that, the reactor is shut down for 30–40 days, and one-third of the fuel is replaced by a new load of fuel. Therefore, the fuel is irradiated for three years.

The detector background is measured during reactor shutdown periods. It is assumed that antineutrino emission in the region $E > 1.8$ MeV ceases completely within one day after reaction shutdown.

The above information forms a basis for analyzing and interpreting the results of experiments seeking neutrino oscillations in reactor experiments.

3. SPECTRA AND CROSS SECTIONS (INCLUSION OF NONEQUILIBRIUM EFFECTS)

1. Let us determine more precisely sources that contribute to the formation of the reactor-antineutrino spectrum $\rho(E)$,

$$\rho(E) = {}^{F}\rho(E) + {}^{C}\rho(E). \quad (9)$$

The first term in (9) describes radiation from the set of fragments produced in ^{235}U, ^{239}Pu, ^{238}U, and ^{241}Pu fission, their interactions with neutrons being disregarded here; the second term takes into account additional radiation arising in radiative neutron capture by accumulated fragments.

For an irradiation time of $t_{\text{on}} > 1$ day, each of the spectra $\rho(E, t_{\text{on}})$ for the four isotopes ^{235}U, ^{239}Pu, ^{238}U, and ^{241}Pu were calculated as functions of the duration of fuel irradiation. In this calculation, the fission rate was assumed to be constant for each isotope. The residual-radiation spectra $\rho(E, t_{\text{off}})$ were also calculated as functions of the time t_{off} from the end of fission.

The calculations were performed by summing, at each instant, the contributions from individual fission fragments with allowance for their yields from the fission process, decay diagrams, and lifetimes. The database that we used contains information about 571 fission fragments whose cumulative yields are not less than $10^{-4}\%$ each. As a matter of fact, the activity of the majority of the fragments that can contribute in the energy region $E > 1.8$ MeV reaches saturation within one day after the onset of the fission process, and a further increase is due to only six fission products whose properties are well known. Three of them—^{97}Zr ($E_{\max} = 1.922$ MeV), ^{132}I ($E_{\max} = 2.140$ MeV), and ^{93}Y ($E_{\max} = 2.890$ MeV)—attain equilibrium within ten days. A further slow increase is determined by the ^{106}Ru and ^{144}Ce half-lives:

$$^{106}\text{Ru} \xrightarrow[E_{\max} = 0.04\ \text{MeV}]{T_{1/2} = 372\ \text{day}} \text{Rh} \xrightarrow[E_{\max} = 3.541\ \text{MeV}]{T_{1/2} = 30\ \text{s}} \text{Pd (stab)},$$

$$^{144}\text{Ce} \xrightarrow[E_{\max} = 0.32\ \text{MeV}]{T_{1/2} = 285\ \text{day}} \text{Pr} \xrightarrow[E_{\max} = 2.996\ \text{MeV}]{T_{1/2} = 17\ \text{min}} \text{Nd}(T_{1/2} = 3 \times 10^{15})\ \text{yr}. \quad (10)$$

Finally, some contribution comes from ^{90}Y ($T_{1/2} = 64$ h, $E_{\max} = 2.279$ MeV) as well, which is in equilibrium with its very long-lived predecessor ^{90}Sr ($T_{1/2} = 28.6$ yr). The yields of these fission fragments are quoted in the table.

2. The antineutrino spectra calculated for ^{235}U and ^{239}Pu are displayed in Figs. 1*a* and 1*b* (equilibration) and in Figs. 2*a* and 2*b* (decrease). For four fissile isotopes, Figs. 3 and 4 show, respectively, the cross sections $\sigma_i(t_{\text{on}})$ for reaction (1) in the fission process and the decrease in $\sigma_i(t_{\text{off}})$ in the residual-radiation spectra. In Figs. 1–4, the spectra and cross sections are presented in dimensionless units and are normalized to the corresponding values after a lapse of $t_{\text{on}} = 1$ day from the onset of the fission process.

3. The correction ${}^{C}\rho(E)$ was calculated with allowance for fragments accumulated in a reactor, the cross sections for radiative neutron capture, and the spatial and energy distributions of the neutron flux over the reactor core. The results presented in Fig. 5 refer to a standard operating period of a PWR reactor.

The relevant contribution ${}^{C}\rho(E)$ to the cross section for reaction (1) is about 0.2% at the end of the operating period. After reactor shutdown, the spectrum ${}^{C}\rho(E)$ decreases fast, not making a significant contribution to residual radiation.

4. DISCUSSION OF RESULTS

(i) In the approximation specified in Section 2, the flux and the spectrum of reactor antineutrinos are unambiguously determined by the current reactor state. After sharp changes in this state, the characteristics of the $\bar{\nu}_e$ flux take the corresponding equilibrium values within a time as short as one day. In particular, the antineutrino flux falls down to zero within one day after reactor shutdown.

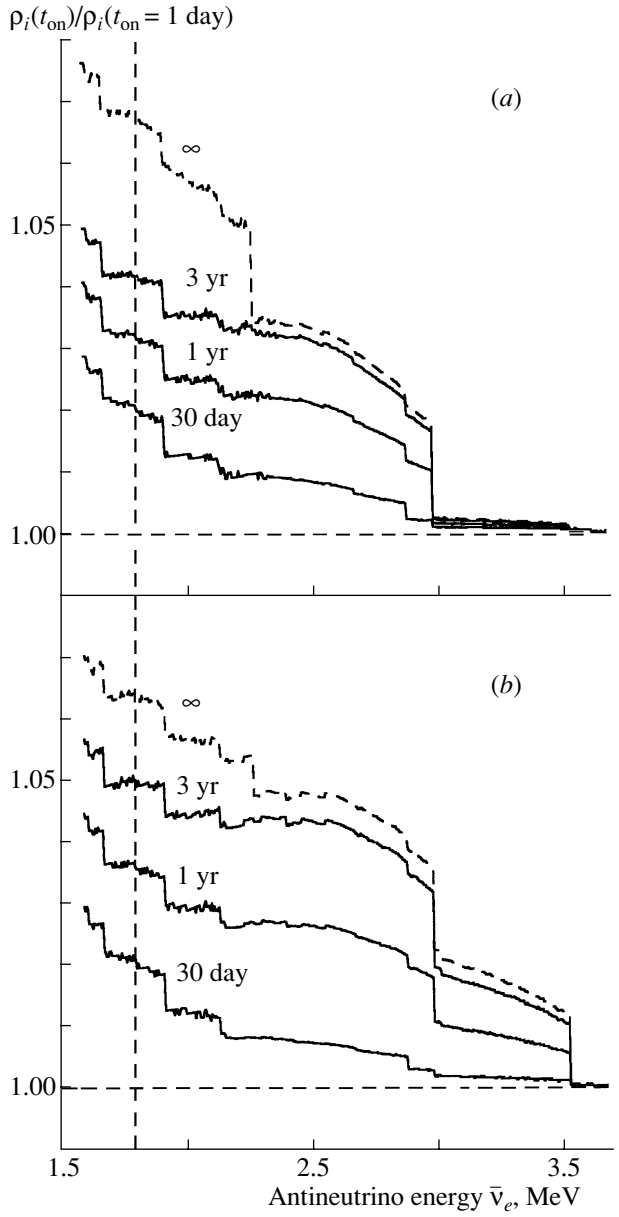

Fig. 1. Ratio of the antineutrino spectra for (*a*) ^{235}U and (*b*) ^{239}Pu fission to the spectrum after one day of irradiation. The numbers on the curves indicate the irradiation time.

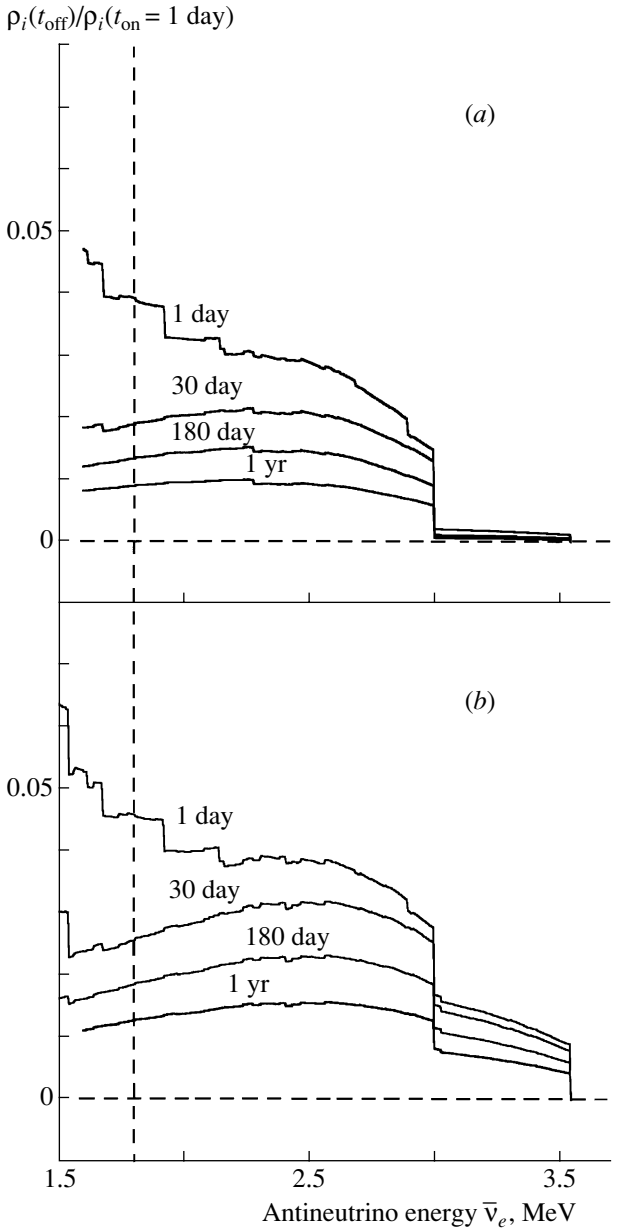

Fig. 2. Ratio of the antineutrino spectra of the residual radiation from (*a*) ^{235}U and (*b*) ^{239}Pu irradiated for two years to the spectrum after one day of irradiation. The numbers on the curves indicate the time that have elapsed after the termination of irradiation.

As a matter of fact, the antineutrino flux in the region $E > 1.8$ MeV has been found to have a nonequilibrium component, whose relaxation time exceeds the duration of the reactor operating period. In view of this, a determination of the $\bar{\nu}_e$ spectrum and of the corresponding values of the cross section for reaction (1) requires tracing the preceding evolution of reactor operation over a long time and taking into account power levels, shutdown periods, and the discharge of spent reactor fuel. In each specific case, this can be done, if needed to a sufficient precision.

The sample of the results in Section 3, which were obtained under the assumption that the fission of uranium and plutonium isotopes proceeds at a constant rate, has enabled us to reveal qualitative features of effects induced by the nonequilibrium component.

(ii) First of all, we note that the resulting corrections to the spectrum and cross sections are relatively small, but they are not negligible. In the antineutrino-energy range 1.8–3.5 MeV, the relative contribution of the additional radiation during the reactor

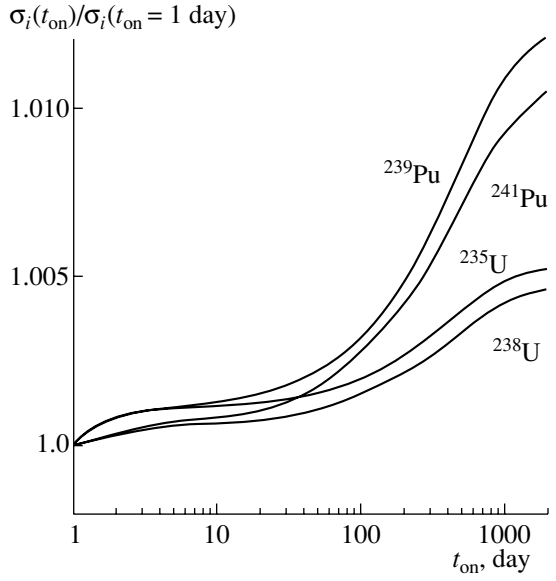

Fig. 3. Ratio of the inverse-beta-decay cross sections for fissile uranium and plutonium isotopes irradiated for the time t_{on} to that after one day of irradiation.

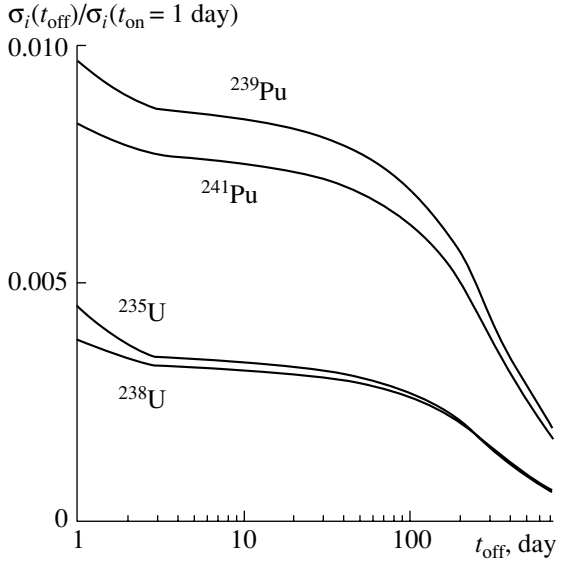

Fig. 4. Ratio of the cross sections for inverse beta decay induced by the residual-radiation antineutrinos for uranium and plutonium isotopes irradiated for two years to the cross section after one day of irradiation as a function of the time t_{off} after the termination of irradiation.

operating period (Figs. 1, 5) is about 4%, which is somewhat greater than the error of the ILL spectra [5].

The corrections to the cross sections σ_i in Fig. 3 and the correction associated with radiative neutron capture may change the cross sections σ_{V-A} by 0.4–0.6%. As a result, relation (8) will change accordingly. Corrections on the same order of magnitude may arise if the cross section (6) is used as a reference value for the cross section in the absence of the oscillations.

(iii) Here, we consider a situation where residual radiation from a stopped reactor can play a significant role and provide numerical examples illustrating the scale of the effects under discussion.

Let us consider an experiment where antineutrinos from reactors are recorded by one detector positioned in such a way that the reactors are at markedly different distances from the detector. Such an experimental setting was implemented, for example, in Rovno (distances of 18 and 98 m) and in the Bugey-3 experiment (15 and 95 m) [9]; three reactors in Krasnoyarsk were located at distances of 57, 57, and 234 m from the detector [10]. The idea of these experiments consists in using the shutdown and operating periods to determine the background level and the signals from each individual reactor. By comparing these signals, one can reveal the oscillation effect or set limits on the oscillation parameters.

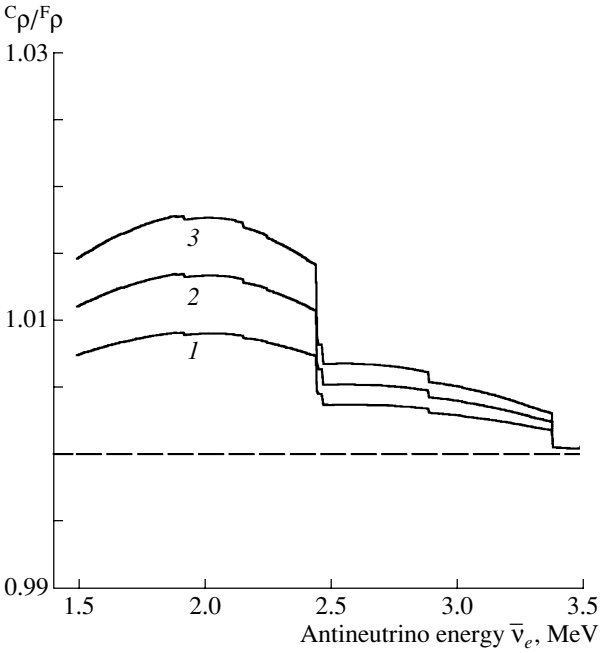

Fig. 5. Ratio of the spectrum component $^{C}\rho(E)$ associated with neutron capture by fission products in a PWR reactor to the fission spectrum $^{F}\rho(E)$. Curves *1*, *2*, and *3* correspond to the beginning, middle, and end of the reactor operating period.

By way of example, we consider two identical PWR reactors of thermal power 2.8 GW each and a detector positioned at distances of 15 and 100 m from the near and the far reactor, respectively, so that the signal from the near reactor is approximately 45 times as great as that from the far one. In this case, the numbers of events of reaction (1) that are induced by the near and the far reactor per 1 t of a

$CH_{1.8}$ target per day are $N_{near}^{op} \approx 12\,000$ day^{-1} t^{-1} and $N_{far}^{op} \approx 260$ day^{-1} t^{-1}, respectively.

When both reactors are shut down, the detector records, however, the residual interaction in addition to the background. Within one to two days after the shutdown of the near reactor, the number of interaction events induced by the residual radiation from it in the detector per unit time decreases by a factor of about 200, falling down to a value of $N_{near}^{off} \approx 70$ day^{-1} t^{-1}, which is approximately 25% of the signal from the far reactor. After that, the signal from the residual radiation decreases smoothly (see Fig. 4) until the discharge of the spent fuel begins, which significantly affects detector readings.

Obviously, these cases require a new approach to processing and analyzing experimental data.

5. CONCLUSION

The effect of the equilibration of the reactor-antineutrino spectrum on the cross section for the inverse-beta-decay process (1) with the threshold of 1.8 MeV has been considered.

The increase in the antineutrino flux due to an increase in the cross section (this effect was previously ignored) is about 0.6% over the reactor operating period. This value is commensurate with the accuracy (the standard error is 1.4%) in the measurement of the cross section itself. A correction at this level must also be introduced in the ratio of the measured cross section to the cross section calculated on the basis of the antineutrino spectrum that was determined independently and which corresponds to one day of reactor operation.

We have calculated the additional contribution to the antineutrino spectrum from neutron capture by fission products and determined the corresponding increase (0.2%) in the cross section for reaction (1).

It has been found that corrections previously ignored in the standard experimental scheme aimed at searches for neutrino oscillations (one detector and near and far reactors) may be as large as 25%.

ACKNOWLEDGMENTS

We are grateful to Prof. K. Schreckenbach for placing valuable information at our disposal and to our colleagues participating in the CHOOZ collaboration for stimulating discussions.

This work was supported by the Russian Foundation for Basic Research (project nos. 00-15-06708 and 00-02-16035).

REFERENCES

1. V. I. Kopeikin, L. A. Mikaelyan, and V. V. Sinev, Yad. Fiz. **61**, 2222 (1998) [Phys. At. Nucl. **61**, 2109 (1998)].
2. V. I. Kopeikin, L. A. Mikaelyan, and V. V. Sinev, hep-ph/9904384; Yad. Fiz. **63**, 1087 (2000) [Phys. At. Nucl. **63**, 1012 (2000)].
3. CHOOZ Collab. (M. Appolonio *et al.*), hep-ex/9907037; Phys. Lett. B **466**, 415 (1999).
4. V. I. Kopeikin, L. A. Mikaelyan, and V. V. Sinev, Yad. Fiz. **60**, 230 (1997) [Phys. At. Nucl. **60**, 172 (1997)].
5. K. Schreckenbach *et al.,* Phys. Lett. B **160B**, 325 (1985); A. Hahn *et al.,* Phys. Lett. B **218**, 365 (1989).
6. P. Vogel *et al.,* Phys. Rev. C **24**, 1543 (1981).
7. P. Vogel, Phys. Rev. D **29**, 1918 (1984); C. A. Fayans, Yad. Fiz. **42**, 929 (1985) [Sov. J. Nucl. Phys. **42**, 590 (1985)].
8. V. Vyrodov *et al.,* Pis'ma Zh. Éksp. Teor. Fiz. **61**, 161 (1995) [JETP Lett. **61**, 163 (1995)]; Y. Declais *et al.,* Phys. Lett. B **338**, 383 (1994).
9. B. Achkar *et al.,* Nucl. Phys. B **434**, 503 (1995).
10. V. Vyrodov *et al.,* Pis'ma Zh. Éksp. Teor. Fiz. **59**, 364 (1994) [JETP Lett. **59**, 390 (1994)].

Translated by R. Tyapaev

Physics of Atomic Nuclei, Vol. 64, No. 5, 2001, pp. 855–860. From Yadernaya Fizika, Vol. 64, No. 5, 2001, pp. 920–925.

NUCLEI
Experiment

Astrophysical *S* Factor for *dd* Interaction at Ultralow Energies*

Vit. M. Bystritskiĭ[1)], V. M. Bystritsky[**], S. A. Chaikovsky[2)], M. Filipowicz[3)], V. M. Grebenyuk, E. Guła[4)], V. I. Makhrin[2)], G. A. Mesyats[5)], S. S. Parzhitski, F. M. Pen'kov, N. A. Ratakhin[2)], V. A. Sinebryukhov[2)], S. A. Sorokin[2)], V. A. Stolupin, E. N. Volkov[2)], and J. Woźniak[3)]

Joint Institute for Nuclear Research, Dubna, Moscow oblast, 141980 Russia

Received July 5, 2000

Abstract—Experimental results are presented that were obtained by measuring the astrophysical *S* factor for *dd* interaction at very low deuteron collision energies by using the liner-plasma technique. The experiment was performed at the high-current generator of the High-Current Electronics Institute (Tomsk, Russia). The values found for the *S* factor at the deuteron collision energies of 1.80, 2.06, and 2.27 keV are $S_{dd} = 114 \pm 68$, 64 ± 30, and 53 ± 16 keV b, respectively. The corresponding *dd* cross sections obtained as the product of the barrier factor and the measured astrophysical *S* factor are $\sigma^n_{dd}(E_{\rm col} = 1.80\ keV) = (4.3 \pm 2.6) \times 10^{-33}{\rm cm}^2$, $\sigma^n_{dd}(E_{\rm col} = 2.06\ keV) = (9.8 \pm 4.6) \times 10^{-33}{\rm cm}^2$, and $\sigma^n_{dd}(E_{\rm col} = 2.27\ keV) = (2.1 \pm 0.6) \times 10^{-32}{\rm cm}^2$. © *2001 MAIK "Nauka/Interperiodica".*

1. INTRODUCTION

Investigation of *dd* nuclear fusion at ultralow energies (about 1 keV) is very important for exploring the physics of few-body nucleon systems [1, 2] and for solving some astrophysics problems [3, 4] and the problems of nucleon–nucleon interaction [5–12]. Classical accelerators cannot be used to study nuclear reactions at very low energies because the relevant cross sections at such energies lie in the range 10^{-43}–$10^{-32}{\rm cm}^2$, so that the intensities of accelerated beams are overly low for direct measurements [13, 14].

At present, there is virtually no experimental information about *dd* interaction in the energy region around 1 keV. A new experimental method for investigating strong interactions between light nuclei at very low energies was proposed in [4, 13, 15–17]. This method employs high-intensity radially converging ion beams generated during plasma liner implosion (*Z* pinch). The intensity of the accelerated ion flow can reach 10^{20}–10^{21} particles per pulse [18–23].

The first experimental investigations of *dd* reactions on the basis of a high-current accelerator ($I =$ 750 kA, *I* being the current through the liner) at the High-Current Electronics Institute in Tomsk showed that the new method can be promising for investigation of strong interactions at ultralow energies [14, 15, 24–26].

Here, we present the results obtained by measuring the *S* factor for the *dd* reaction

$$d + d \rightarrow {}^3{\rm He} + n(2.46\ {\rm MeV}) \qquad (1)$$

at collision energies of 1.80, 2.06, and 2.27 keV.

2. METHOD OF MEASUREMENT

The astrophysical *S* factor can be determined by measuring the neutron yield from reaction (1). We used the well-known formula [27]

$$\sigma(E) = \frac{S(E)}{E} e^{-2\pi\eta}, \qquad (2)$$

which represents the cross section as the product of the barrier factor responsible for Coulomb repulsion and the astrophysical *S* factor weakly dependent on the deuteron collision energy *E*. In expression (2), η is the Sommerfeld parameter given by

$$2\pi\eta = 2\pi\frac{Z^2}{\hbar v} = 31.29\left(\frac{\mu}{E}\right)^{1/2}, \qquad (3)$$

where *Z* is the deuteron charge, μ is the reduced mass of colliding deuterons ($\mu = m_d/2$, with m_d being the deuteron mass in amu), and v is the relative velocity of the deuterons.

*This article was submitted by the authors in English.

[1)]University of California (Irvine), Irvine, CA 92717-4575, USA.
[2)]High-Current Electronics Institute, Tomsk, Russia.
[3)]Faculty of Physics and Nuclear Techniques, Academy of Mining and Metallurgy, Cracow, Poland.
[4)]Institute of Nuclear Physics, Cracow, Poland.
[5)]Institute of Electrophysics,Yekaterinburg, Russia.
**e-mail: bystvm@nusun.jinr.ru

Taking into account the energy dispersion of the deuterons and the Coulomb energy losses, we can represent the yield $N_n(x)$ of neutrons from reaction (1) for a target thickness x as

$$N_n(x) = N_d n_t \varepsilon_n \int_0^\infty f(E)dE \int_0^x S(E'(E,x')) \times \frac{e^{-2\pi\eta'}}{E'(E,x')}dx', \quad (4)$$

where $f(E)$ is the energy distribution of deuterons hitting the target, ε_n is the neutron-detection efficiency, N_d is the number of deuterons hitting the target, n_t is the target density, and $2\pi\eta' = 31.29\left(\frac{\mu}{E'(E,x')}\right)^{1/2}$.

According to previous experiments, the function $f(E)$ was considered as a Gaussian distribution, with the FWHM values taken from [24, 28]. The function $E'(E,x')$ describes the energy losses of liner deuterons in the target due to Coulomb scattering. The energy losses can be described by the formula [29]

$$\frac{dE}{dx} = -\frac{\pi}{2E} n_t e^4 L, \quad (5)$$

where e is an elementary charge and L is the so-called Coulomb logarithm for plasma deuterons (under the conditions of the present experiment, $L = 12.8$ [29]). For the initial condition $E'(x' = 0) = E$, where E' (the deuteron collision energy in the c.m. frame) corresponds to the energy E of a deuteron that has traveled a distance x', the solution to this equation can be written as [29]

$$E'(E,x') = (E^2 - \pi n_t e^4 L x')^{1/2}. \quad (6)$$

We have calculated the Coulomb energy losses, taking into account the interaction of liner deuterons with target deuterons, but neglecting the interaction with target electrons (this is valid for a fully ionized target plasma [29]). This assumption was verified on the basis of other theoretical models describing charged-particle energy losses in plasmas [30–32]. The conditions of our experiment allow one to assume that all liner deuterons are stopped in the target and that the total neutron yield $N_n^{\rm tot}$ can be determined as $N_n(x \to \infty)$.

Because the S factor weakly depends on energy, we can simplify Eq. (4). The S factor used in Eq. (4) is averaged with the distribution function $P(E)$ describing the neutron-detection probability as a function of the deuteron collision energy:

$$\overline{S(E)} = \int_E S(E)\, P(E)dE. \quad (7)$$

The distribution function $P(E)$ can be obtained from Eq. (4) by introducing the variable of integration $E'(E,x')$ from Eq. (6) and by changing the order of integration. The distribution $P(E)$ normalized to unity can be written as

$$P(E) = \exp(-2\pi\eta) \times \frac{\int_E^\infty f(E')\,dE'}{\int_0^\infty \exp(-2\pi\eta)dE \int_E^\infty f(E')\,dE'}. \quad (8)$$

To simplify Eq. (4), $\overline{S(E)}$ can be replaced by $S(E_{\rm col})$ with $E_{\rm col} = \int_E EP(E)dE$. This simplification is valid to linear terms in the expansion of $S(E)$ near the maximum of the distribution $P(E)$.

The notation $E_{\rm col}$ was introduced to distinguish the average collision energy of the deuterons contributing to the neutron yield from the average collision energy $\bar{E}$ of hitting deuterons, the latter being defined as $\bar{E} = \int_E E\, f(E)dE$.

Taking into account the above assumptions, we can represent the total neutron yield $N_n^{\rm tot}$ as

$$N_n^{\rm tot} = N_d n_t \varepsilon_n S(E_{\rm col}) \int_0^\infty f(E)dE \int_0^\infty \frac{e^{-2\pi\eta'}}{E'(E,x')}dx'. \quad (9)$$

According to (9), the experimental dd S factor for the average deuteron collision energy $E_{\rm col}$ can be written as

$$S(E_{\rm col}) = \frac{N_n^{\rm exp}}{N_d n_t \varepsilon_n \int_0^\infty f(E)dE \int_0^\infty \frac{e^{-2\pi\eta'}}{E'(E,x')}dx'}, \quad (10)$$

where $N_n^{\rm exp}$ is the number of neutrons from the dd reaction.

To analyze the experimental conditions of target transparency, the effective target thickness $\tilde{l}$ was introduced through the relation [15]

$$N_n(\tilde{l}) = 0.9 N_n^{\rm tot}, \quad (11)$$

where $N_n(\tilde{l})$ is the recorded neutron yield from reaction (1) for the target thickness $\tilde{l}$.

3. DESCRIPTION OF THE EXPERIMENT

Our experiment was performed at the Institute of High-Current Electronics (Tomsk), Russian Academy of Science, by using a high-current generator [33]. The layout of the experimental setup is displayed in Fig. 1.

A hollow-cylinder supersonic gaseous deuterium jet with a Mach number of 4 was formed by an electromagnetic valve and a de Laval nozzle. A target of CD_2 deposited on a Cu rod was placed along the

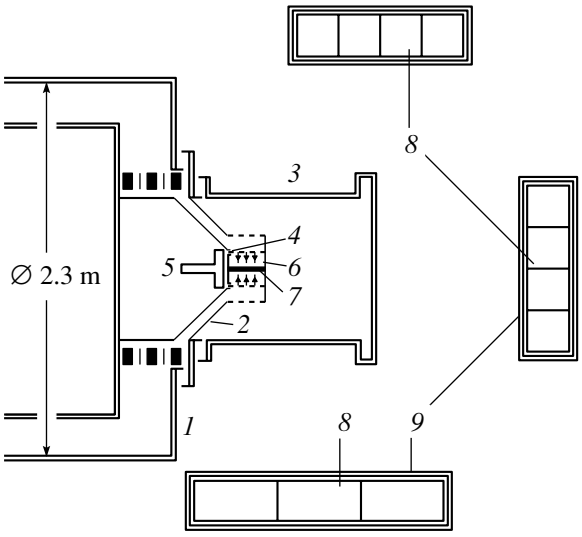

Fig. 1. Layout of the experimental setup: (*1*) high-current generator, (*2*) load unit, (*3*) measuring chamber, (*4*) supersonic nozzle, (*5*) electromagnetic valve, (*6*) gaseous liner, (*7*) CD_2 solid target, (*8*) thermal-neutron detectors, and (*9*) lead shield.

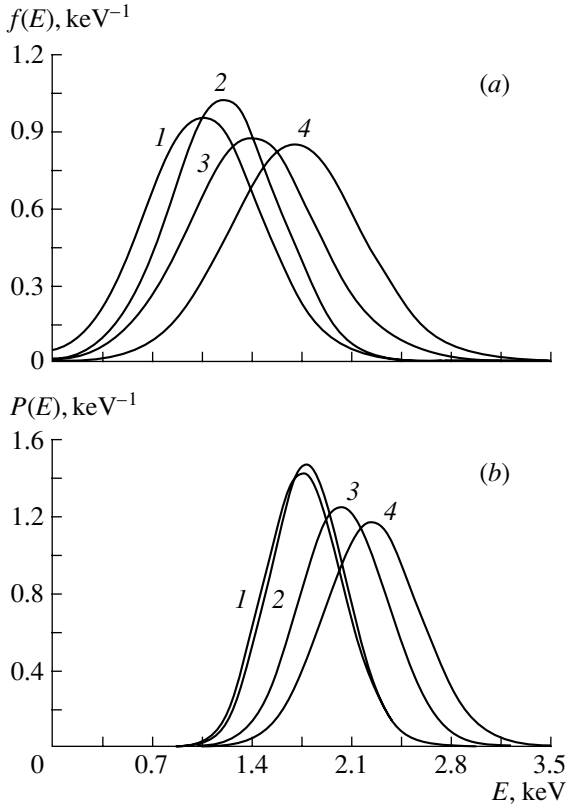

Fig. 2. (*a*) Differential energy distributions of deuterons hitting the target for $\bar{E} =$ (*1*) 1.05, (*2*) 1.2, (*3*) 1.4, and (*4*) 1.7 keV. (*b*) Calculated differential distributions of the detection probabilities for neutrons with average energies $E_{\rm col} =$ (*1*) 1.79, (*2*) 1.80, (*3*) 2.06, and (*4*) 2.27 keV. The distributions are normalized to unity.

liner axis. The liner and target parameters are given in Table 1.

For background measurements, we employed a bare Cu rod or one coated with CH_2. The liner mass and the compression velocity were estimated by measuring the current through the liner and the compression time [15].[6)] The dynamics of liner compression was investigated by using an optical streak camera with varying axial split positions and magnetic probes placed at various distances from the liner axis.

It should also be mentioned that, under constant initial conditions, the deviation of the liner mass from one shot to another can be about 10%.

In this experiment, neutrons from *dd* reactions were recorded by three thermal neutron detectors with proportional BF_3 counters placed in a paraffin moderator. Each of the detectors consisting of 10 BF_3 counters was placed at a distance of 0.9 m from the target center (Fig. 1). The neutron-detection efficiency was measured with the calibrated ^{252}Cf source placed within the measuring chamber *3* (Fig. 1) at the center of Z-pinch formation. The total neutron-detection efficiency of three BF_3 detectors was 5×10^{-3}.

A lead shielding 12 mm thick surrounded the BF_3 detectors to protect them against powerful x-ray bursts generated during the pulse of the high-current generator.

Information about the recorded events included (i) the time of generation and the amplitude of a signal from the BF_3 detectors and (ii) the time of generation of a signal from the magnetic B-dot probe (a fundamental parameter that describes the dynamics of liner implosion).

More details concerning the recording electronics can be found in [15, 17, 25, 35].

Table 1. Experimental conditions (M is the liner mass averaged over all shots; l_d is the liner length; $d_l^{\rm in}$ and $d_l^{\rm out}$ are, respectively, the inner and the outer liner diameter; d_t is the target diameter; and t is the thickness of the CD_2 layer on the Cu rod)

M, μg	l_d, cm	N_d	n_t, cm^{-3}	$d_l^{\rm in}$, mm	$d_l^{\rm out}$, mm	d_t, mm	t, mm
6.88	2.5	2.07×10^{18}	8.0×10^{22}	32	36	5.5	0.25

[6)] The liner mass and its compression time were calculated according to the zero-dimensional model proposed in [34]. In this model, the liner is treated as an infinitely thin superconducting shell, imploded under the pressure of its own magnetic field.

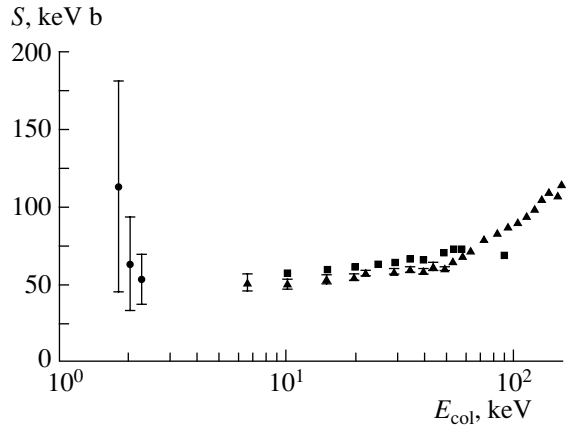

Fig. 3. Astrophysical S factor as a function of the deuteron collision energy: (squares) values from [37], (triangles) values from [38], and (circles) values measured in our experiment.

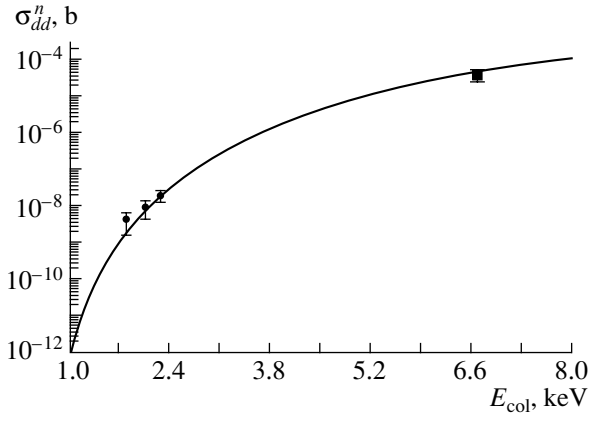

Fig. 4. *dd* cross section as a function of the deuteron collision energy: (curve) dependence calculated according to (2) by using $S = 53.8$ keV b [37], (square) experimental value from [38], and (circles) values found on the basis of (2) by using the measured S factors (for the deuteron collision energies E_{col} of 1.80, 2.06, and 2.27 keV).

4. EXPERIMENTAL RESULTS

For four average deuteron collision energies of $E_{col} = 1.79, 1.80, 2.06,$ and 2.27 keV, experimental data were analyzed under the assumptions described in Section 2. For these collision-energy values, we estimated the astrophysical S factors on the basis of (10), assuming that radially accelerated deuterons interact with a fully ionized plasma. From our estimates and from the results presented in [36], it follows that, under our experimental conditions, the temperature of the target surface reaches 20–30 eV during plasma implosion.

Figure 2*a* shows the collision-energy distribution of deuterons hitting the target, while Fig. 2*b* shows the calculated differential distributions of the detection probabilities for neutrons from *dd* interactions with respect to the deuteron collision energy. The results of our analysis of these experimental data are given in Table 2.

Table 2. Experimental results [$\bar{E}$ is the collision energy of all deuterons that is averaged over all shots; E_{col} is the average collision energy of the deuterons contributing to the experimentally measured neutron yield from reaction (1); $\triangle E_{col}$ is the root-mean-square energy dispersion of the probability-density distribution function for recorded neutrons from *dd* fusion; N_n^{th} is the total number of neutrons recorded by thermal-neutron detectors; and $N_{n,back}^{th}$ is the number of neutrons recorded in the background measurements, $N_n^{exp} = N_n^{th} - N_{n,back}^{th}$]

Experiment	1	2	3	4
FWHM, %	80	65	65	55
$\bar{E}$ [keV]	1.05	1.2	1.4	1.7
E_{col} [keV]	1.79	1.80	2.06	2.27
$\triangle E_{col}$ [keV]	0.28	0.27	0.32	0.34
N_n^{th}	2 ± 2	7 ± 2	22 ± 8	86 ± 25
$N_{n,back}^{th}$	2 ± 2	2 ± 2	3 ± 2	4 ± 3
N_n^{exp}	≤ 4	5 ± 3	19 ± 9	82 ± 24
S, keV b	≤ 170	114 ± 68	64 ± 30	53 ± 16
$\tilde{l}n_t$, 10^{18}cm^{-2}	1.40	1.42	1.96	2.42

The FWHM values depend on the accuracy of the liner-speed estimate (about $\pm 10\%$), which was obtained by comparing the measured and the calculated compression time (in zero-dimensional model), and also on the energy dispersion of deuterons due to the appearance of liner surface instabilities with a characteristic fringe wavelength of 1 to 2 mm. The liner compression velocities in the regions of the respective "hump" or "dip" could differ by 10%, which leads to a deuteron-energy dispersion of 20%.

The experimental values of the astrophysical S factor that were found by formula (10) for the deuteron collision energies of 1.80, 2.06, and 2.27 keV are presented in Fig. 3. Other values of the S factor for *dd* interactions in the collision-energy range 6.9–160 keV [37, 38] are also shown for the sake of comparison. As can be seen from Fig. 3, our measured S factors are in agreement, within the statistical error, with the S values measured for deuteron collision energies in the range 7–45 keV.

The *dd* cross sections were calculated on the basis of (2) by using the measured S factors for deuteron collision energies $E_{col} - \Delta E_{col}$, and E_{col}, $E_{col} + \Delta E_{col}$. The results are presented in Table 3

Table 3. Results of calculations [$N_n^{\rm calc}$ is the number of neutrons from dd reactions that is calculated according to Eq. (9) with the S factor averaged in the energy range 7–45 keV (50 keV b); and $\sigma_{dd}^n(E_{\rm col})$, $\sigma_{dd}^n(E_{\rm col}+\triangle E_{\rm col})$, $\sigma_{dd}^n(E_{\rm col}-\triangle E_{\rm col})$ are the cross sections calculated according to (2)]

$N_n^{\rm calc}$	1.2	2.2	14.9	77.4
$\sigma_{dd}^n(E_{\rm col}),{\rm cm}^2$	$\leq 6.1\times10^{-33}$	4.3×10^{-33}	9.8×10^{-33}	2.1×10^{-32}
$\sigma_{dd}^n(E_{\rm col}+\triangle E_{\rm col}),{\rm cm}^2$	$\leq 2.7\times10^{-32}$	1.8×10^{-32}	3.9×10^{-32}	7.4×10^{-32}
$\sigma_{dd}^n(E_{\rm col}-\triangle E_{\rm col}),{\rm cm}^2$	$\leq 8.9\times10^{-34}$	7.0×10^{-34}	1.7×10^{-33}	4.2×10^{-33}

and in Fig. 4. The calculated and the experimental cross sections agree within the statistical error.

To check how our results depend on the model of interaction between the liner and the target deuterons, the Coulomb energy losses were also calculated by taking into account the interaction between the liner and the target electrons (as well as target deuterons) according to the model proposed in [29]. In this case, the S factor was one order of magnitude larger than the previous one for a given energy range because the deuteron range in the target is shorter. Such an increase in the S factor cannot be explained either by the presence of narrow resonances in the dd cross section, because a large energy dispersion of accelerated liner deuterons is observed, or by plasma instabilities giving rise to an additional neutron yield, because this contradicts the results of background measurements. Our results fully confirm that the new method for studying strong interactions between light nuclei, which uses Z pinch, is very promising for further investigations into the ultralow-energy range.

ACKNOWLEDGMENTS

We are grateful to Prof. R.B. Baksht and Prof. A. Toor for stimulating discussions and to B.F. Boreiko and S.W. Shlahtun for their assistance during the installation of the experiment.

This work was supported by the Russian Foundation for Basic Research (project no. 00-02-17203).

REFERENCES

1. S. P. Merkuriev *et al.,* in *Proceedings of the International Conference on the Theory of Few-Body and Quark–Hadronic Systems, Dubna, 1987,* p. 6.
2. J. L. Friar, in *Proceedings of the International Conference on the Theory of Few-Body and Quark–Hadronic Systems, Dubna, 1987,* Preprint No. D4-87-692, OIYaI (Joint Institute for Nuclear Research, Dubna, 1987), p. 70.
3. C. Rolfs, in *Proceedings of International Enrico Fermi School in Physics, Villa Monastero, 1987,* Ed. by P. Kienle, R. A. Ricci, and A. Rubbino (North-Holland, Amsterdam, 1989), Course C.3, p. 417; J. N. Bahcall and M. H. Pinsonneault, Rev. Mod. Phys. **64**, 885 (1992); M. Arnould and J. Forestini, in *Procedings of the Third International Summer School on Nuclear Astrophysics, La Rabida, Huelve, 1988* (Springer-Verlag, 1988), Research Reports in Physics, p. 48.
4. V. B. Belyaev *et al.,* Nukleonika **40**, 85 (1995).
5. H. J. Assenbaum *et al.,* Z. Phys. A **327**, 461 (1987).
6. C. Angulo *et al.,* Z. Phys. A **345**, 231 (1993).
7. S. E. Koonin and M. Mukerjee, Phys. Rev. C **42**, 1639 (1990).
8. U. Greife *et al.*, Z. Phys. A **351**, 107 (1995).
9. C. Bargholz, Nucl. Phys. A **474**, 1 (1987).
10. J. L. Friar *et al.,* Phys. Lett. B **251**, 11 (1990).
11. B. F. Kharchenko *et al.,* Yad. Fiz. **55**, 86 (1992) [Sov. J. Nucl. Phys. **55**, 49 (1992)].
12. A. C. Phillips, Nucl. Phys. A **184**, 337 (1972).
13. V. B. Belyaev *et al.,* Preprint No. D15-92-324, OIYaI (Joint Institute for Nuclear Research, Dubna, 1992).
14. Vit. M. Bystritskii *et al.,* IEEE **2**, 1215 (1995).
15. V. M. Bystritsky *et al.,* Preprint No. D15-98-239, OIYaI (Joint Institute for Nuclear Research, Dubna, 1998); Laser Part. Beams **18**, 1 (2000).
16. V. B. Belyaev *et al.,* Preprint No. D15-95-375, OIYaI (Joint Institute for Nuclear Research, Dubna, 1995).
17. V. M. Bystritsky *et al.,* Nukleonika **42**, 775 (1997).
18. P. G. Burkhalter *et al.,* J. Appl. Phys. **50**, 1 (1979).
19. N. F. Kovsharov *et al.,* Prib. Tekh. Éksp., No. 6, 84 (1987).
20. F. S. Feller *et al.,* Phys. Fluids **31**, 2053 (1988).
21. M. A. Libberman and A. B. Budko, AIP Conf. Proc. **195**, 174 (1989).
22. U. H. Rahman *et al.,* Phys. Fluids **28**, 1226 (1985).
23. S. A. Sorokin and S. A. Chaĭkovskiĭ, Fiz. Plazmy **19**, 856 (1993) [Plasma Phys. Rep. **19**, 444 (1993)].
24. Vit. M. Bystritskii *et al.,* Preprint No. D15-96-11, OIYaI (Joint Institute for Nuclear Research, Dubna, 1996).
25. T. L. Bulgakov *et al.,* Yad. Fiz. **60**, 1349 (1997) [Phys. At. Nucl. **60**, 1217 (1997)].
26. Vit. M. Bystritskii *et al.,* in *Proceedngs of International Conference on Plasma, Prague, 1996.*
27. K. R. Lang, *The Astrophysical Formulae* (Springer-Verlag, Berlin, 1974).
28. V. I. Oreshkin, Izv. Vyssh. Uchebn. Zaved., Fiz., No. 12, 6 (1995).
29. D. V. Sivukhin, in *Reviews of Plasma Physics,* Ed. by M. A. Leontovich (Atomizdat, Moscow, 1964; Consultants Bureau, New York, 1968), Vol. 4.

30. K. Nui and T. Abe, in *Proceedings of the 3rd International Conference on High-Power Electron and Ion Beam, Novosibirsk, 1979,* Vol. 2, p. 518.
31. L. A. Artsimovich, *Controlled Thermonuclear Reactions,* Ed. by A. Kolb and R. S. Pease (Fizmatgiz, Moscow, 1961; Gordon and Breach, New York, 1964), p. 170.
32. Vit. M. Bystritskii *et al.,* AIP Conf. Proc. **195**, 522 (1989).
33. A. V. Luchinskiĭ, Izv. Vyssh. Uchebn. Zaved., Fiz., No. 12, 52 (1995).
34. W. Clark *et al.,* J. Appl. Phys. **53**, 4099 (1982).
35. T. L. Bulgakov *et al.,* in *Proceedings of the XVII International Symposium on Nuclear Electronics, Varna, 1997,* Preprint No. D13-98-66, OIYaI (Joint Institute for Nuclear Research, Dubna, 1998), p. 126.
36. N. G. Karlyakhanov *et al.,* Fiz. Plazmy **22**, 998 (1996) [Plasma Phys. Rep. **22**, 903 (1996)].
37. R. E. Brown and N. Jarmie, Phys. Rev. C **41**, 1391 (1990).
38. A. Krauss *et al.,* Nucl. Phys. A **465**, 150 (1987).

Physics of Atomic Nuclei, Vol. 64, No. 5, 2001, pp. 861–869. Translated from Yadernaya Fizika, Vol. 64, No. 5, 2001, pp. 926–934.

NUCLEI
Theory

Mass–Energy Distribution of Fragments from the Fission of Excited Nuclei within Three-Dimensional Langevin Dynamics

P. N. Nadtochy, A. V. Karpov, D. V. Vanin, and G. D. Adeev

Omsk State University, pr. Mira 55A, Omsk, 644077 Russia
Received December 28, 1999; in final form, September 13, 2000

Abstract—Two-dimensional mass–energy distributions of fission fragments are calculated for the first time on the basis of three-dimensional stochastic Langevin equations. In these calculations, the emission of light prescission particles is taken into account within the statistical model. The results demonstrate that calculations within three-dimensional Langevin dynamics make it possible to describe most comprehensively the properties of the mass–energy distribution of fission fragments and the mean multiplicity of prescission neutrons. © *2001 MAIK "Nauka/Interperiodica".*

1. INTRODUCTION

Among various theoretical approaches used to describe the observables of the fission process, those that are based on the multidimensional Fokker–Planck equation [1] for the distribution of collective variables or on the set of Langevin equations [1, 2], which is equivalent to it, have proven to be successful over the last twenty years of investigations. In solving the multidimensional Fokker–Planck equation, one inevitably has to invoke approximate methods [2, 3]; at the same time, the corresponding set of Langevin equations for many problems of collective nuclear dynamics can be solved without recourse to any approximations.

This is the reason why the opinion prevalent in the past few years has been [2, 4] that the stochastic approach to fission dynamics on the basis of Langevin equations is the most promising, the more so as it is readily implementable in practical calculations.

In order to describe the maximum possible number of observables characterizing the fission process, it is necessary to solve Langevin equations for as many collective variables as is possible. However, introducing each new collective variable leads to a catastrophically sharp growth of the time and volume of the relevant computations. For this reason, only one-dimensional [5, 6] and two-dimensional calculations have been performed so far within the Langevin approach. The two-dimensional calculations made it possible to obtain either the energy distribution for symmetric fission [7–10] or the mass distribution of fission fragments that corresponds to the most probable kinetic energy [11, 12].

Only within three-dimensional Langevin calculations can we obtain the two-dimensional mass–energy distribution, which includes a full body of information about the mass and the kinetic-energy distribution of fission fragments. In particular, the one-dimensional mass and energy distributions can be obtained on the basis of the two-dimensional mass–energy distribution. Not only does a theoretical analysis of two-dimensional mass–energy distributions make it possible to perform a correct comprehensive comparison with experimental data, but it is also of interest for studying a correlation of distributions. The correlation in mass and kinetic-energy distributions of fragments carries additional valuable information about the scission configuration of a fissile nucleus and, hence, makes it possible to estimate the strength of nuclear viscosity and to clarify its mechanism. Thus far, mass–energy distributions have been investigated on the basis of the Nix–Swiatecki zero-viscosity dynamical model [13] or on the basis of the diffusion model [1, 14].

In this article, we present the first results of calculations that are based on three-dimensional Langevin dynamics and which take into account the evaporation of light prescission particles. We calculate the two-dimensional mass–energy distribution and, on its basis, obtain the one-dimensional mass and energy distributions and correlation dependences—the mean kinetic energy of fission fragments ($\langle E_k \rangle$) as a function of the fragment masses, the variance of the energy distribution ($\sigma^2_{E_k}$) as a function of the fragment masses, and the variance of the mass distribution (σ^2_M) as a function of kinetic energy. For investigation, we chose the reaction $^{12}\mathrm{C} + ^{194}\mathrm{Pt} \rightarrow ^{206}\mathrm{Po}$ ($E_{\mathrm{lab}} = 99\mathrm{MeV}$) [15], which was studied in detail

1063-7788/01/6405-0861$21.00

experimentally and which leads to the formation of a compound nucleus at a temperature T in excess of 1 MeV. The latter makes it possible to neglect shell effects and nucleon-pairing effect in calculating the potential energy and transport coefficients in dynamical equations. By comparing the calculated characteristics and available experimental data, we show that the inclusion of a third collective coordinate in the analysis improves agreement between the theoretical and experimental results in relation to the two-dimensional model.

2. DESCRIPTION OF THE MODEL

For the nuclear-surface shape [the profile function $\rho_s^2(z)$ whose rotation about the symmetry axis determines the nuclear surface], we choose the (c, h, α) parametrization [16], which was widely and successfully used in the majority of the calculations. In particular, statistical calculations within the Strutinsky shell-correction method [16], dynamical calculations of the mass–energy distribution within the diffusion model [1, 3, 14], and a great number of two-dimensional calculations of various characteristics of the fission process within the Langevin approach [9, 10] relied on the (c, h, α) parametrization.

In the shape parametrization that we choose, the equation of the nuclear surface can be represented as

$$\rho_s^2(z) = \begin{cases} c^{-2}\left(c^2 - z^2\right)\left(A_s c^2 + Bz^2 + \alpha z c\right) \\ \qquad \text{for } B \geq 0 \\ c^{-2}\left(c^2 - z^2\right)\left(A_s c^2 + \alpha z c\right)\exp(Bcz^2) \\ \qquad \text{for } B < 0, \end{cases} \tag{1}$$

where ρ_s is the polar radius and z is the coordinate along the nuclear-symmetry axis. The quantities A_s and B are expressed in the terms of the nuclear-shape parameters (c, h, α) [9, 16] as

$$B = 2h + \frac{c-1}{2}, \tag{2}$$

$$A_s = \begin{cases} c^{-3} - \frac{B}{5} \text{ for } B \geq 0 \\ -\frac{4}{3}\dfrac{B}{\exp(Bc^3) + \left(1 + \frac{1}{2Bc^3}\right)\sqrt{-\pi Bc^3}\,\mathrm{erf}\left(\sqrt{-Bc^3}\right)} \text{ for } B < 0, \end{cases}$$

where c is the elongation parameter (the length of a nucleus in units of the initial-sphere radius R_0 is equal to $2c$) and the parameter h describes the change in the neck thickness at a given elongation. The line $h = 0$ approximately corresponds to the bottom of the fission valley in the liquid-drop model [16]. The coordinate α determines the ratio of the masses of the would-be fragments.

The authors of [9] investigated the problem of choosing collective coordinates and showed, on the basis of two-dimensional calculations, that, in describing the fission process, the coordinates (ρ, h) should be preferred to (c, h), where ρ is the distance between the centers of mass of the nascent fragments. For the mass-asymmetry coordinate, Strutinsky [17] proposed employing, instead of α, the coordinate η, the ratio of the difference of the would-be-fragment masses to the mass of the whole compound nucleus. We note that (ρ, η) are the first two collective coordinates in the scheme for introducing collective coordinates that was developed in [18] and which is based on the multipole moments of the nuclear density.

Although the coordinates (ρ, η) have a clear physical meaning, the use of these coordinates in three-dimensional Langevin calculations leads to serious computational difficulties. Solving the dynamical problem in the coordinates (ρ, h, η) (instead of (c, h, α)) leads to a considerable increase in the machine time. The reason for this is that it is impossible to find explicitly the dependences of the shape parameters (c, h, α) on the parameters (ρ, h, η). In view of this, we chose the geometric shape parameters for collective coordinates.

In the stochastic approach [1, 2, 19], the evolution of collective degrees of freedom was treated as the Brownian motion of a particle in a heat bath formed by single-particle nuclear degrees of freedom. The set of relevant Langevin equations has the form

$$\begin{aligned} \dot{q}_i &= \mu_{ij} p_j, \\ \dot{p}_i &= -\frac{1}{2} p_j p_k \frac{\partial \mu_{jk}}{\partial q_i} - \frac{\partial F}{\partial q_i} - \gamma_{ij}\mu_{jk} p_k + \theta_{ij}\xi_j, \\ & i, j, k = 1,\ 2,\ 3, \end{aligned} \tag{3}$$

where $\mathbf{q} = (c, h, \alpha)$ is the set of collective coordinates; $\mathbf{p} = (p_c, p_h, p_\alpha)$ are the momenta conjugate to these coordinates; m_{ij} ($\|\mu_{ij}\| = \|m_{ij}\|^{-1}$) and γ_{ij} are the inertia tensor and the friction tensor, respectively;

$F(\mathbf{q})$ is the free energy of the system under investigation; $\theta_{ij}\xi_j$ is a random force; and θ_{ij} is its amplitude, which is related to the diffusion tensor D_{ij} by the equation

$$D_{ij} = \theta_{ik}\theta_{kj}. \quad (4)$$

The diffusion tensor in turn satisfies the Einstein relation

$$D_{ij} = T\gamma_{ij}. \quad (5)$$

The eigenvalues and eigenvectors of the diffusion matrix D_{ij}, which are used to calculate a random force [4], were found by the Jacobi method [20]. A random value ξ_j has the following statistical properties:

$$\langle \xi_i \rangle = 0,$$
$$\langle \xi_i(t_1)\xi_j(t_2)\rangle = 2\delta_{ij}\delta(t_1 - t_2). \quad (6)$$

The angular brackets in (6) denote averaging over the statistical ensemble.

The set of Eqs. (3) was integrated numerically by using the Heun difference scheme [4].

Until recently, numerous theoretical studies [1, 3, 11] evaluated the conservative force as the gradient of the potential energy. It is well known [21, 22] that, in the case of excited nuclear systems, we must use the free energy instead of the potential energy, which determines the mechanical force. In the Fermi gas model, the free-energy functional has the form

$$F(\mathbf{q}) = V(\mathbf{q}) - a(\mathbf{q})T^2, \quad (7)$$

where $V(\mathbf{q})$ is the potential energy and $a(\mathbf{q})$ is the level-density parameter. The explicit form of the function $a(\mathbf{q})$ is discussed below.

The potential energy was calculated on the basis of the liquid-drop model with a sharp boundary of the nuclear surface and with the Myers–Swiatecki parameters [23]. In contrast to [1, 3], where it was assumed, in calculating the potential energy, that the α dependence of the potential energy has the form $V(c,h,\alpha) = V(c,h,\alpha=0) + C(c,h)\,\alpha^2/2$ [$C(c,h)$ is the local stiffness of the potential along the coordinate α], we evaluate the potential energy without such assumptions. The potential energy, the inertia tensor, and the friction tensor were calculated by using an equidistant mesh with $151 \times 101 \times 51$ nodes and the values of $c \in [0.7, 3.7]$, $h \in [-0.6, 0.4]$, and $\alpha \in [-0.2, 0.2]$. The interpolation between nodes was performed on the basis of the Lagrange formulas.

The inertia tensor was calculated in the Werner–Wheeler approximation for the irrotational flow of an incompressible liquid [24]. For the inertia-tensor components as functions of the nuclear deformation, Fig. 1 shows the results calculated along the mean trajectory. By the mean trajectory, we imply the particle trajectory obtained in dynamical calculations by means of averaging over the ensemble of Brownian particles or, what is the same, in the absence of a random force (the initial conditions were chosen at the saddle point for $\alpha = 0$ and $p_\alpha = 0$). In this case, the mean trajectory lies in the $\alpha = 0$ plane. The intersection of the mean trajectory and the scission surface determines the mean scission point. For its coordinates at a preset value of the coefficient of friction, our calculations with a specified scission surface yielded $c_{\rm sc} = 2.2$ and $h_{\rm sc} = -0.11$. This is in good agreement with the results obtained within the diffusion model [1, 3]. The values of the Coulomb energy and of the prescission kinetic energy at this point determine the mean kinetic energy of fragments. Figure 2 shows the mean trajectory on the potential-energy surface and the scission line obtained as the intersection of the scission surface and the $\alpha = 0$ plane.

In order to describe the dissipation of the collective kinetic energy into the internal energy, we used the one-body mechanism of friction [25–27]. The friction tensor was calculated by the formula

$$\gamma_{ij} = \frac{1}{2}\rho_m\bar{v}\left\{\frac{\partial\rho}{\partial q_i}\frac{\partial\rho}{\partial q_j}\Delta\sigma + \frac{32}{9}\frac{1}{\Delta\sigma}\frac{\partial V_1}{\partial q_i}\frac{\partial V_1}{\partial q_j}\right.$$
$$+ k_s\pi\left[\int_{z_{\min}}^{z_N}\left(\frac{\partial\rho_s^2}{\partial q_i} + \frac{\partial\rho_s^2}{\partial z}\frac{\partial D_1}{\partial q_i}\right)\left(\frac{\partial\rho_s^2}{\partial q_j} + \frac{\partial\rho_s^2}{\partial z}\frac{\partial D_1}{\partial q_j}\right)\left(\rho_s^2 + \left(\frac{1}{2}\frac{\partial\rho_s^2}{\partial z}\right)^2\right)^{-1/2} dz\right. \quad (8)$$
$$\left.\left. + \int_{z_N}^{z_{\max}}\left(\frac{\partial\rho_s^2}{\partial q_i} + \frac{\partial\rho_s^2}{\partial z}\frac{\partial D_2}{\partial q_i}\right)\left(\frac{\partial\rho_s^2}{\partial q_j} + \frac{\partial\rho_s^2}{\partial z}\frac{\partial D_2}{\partial q_j}\right)\left(\rho_s^2 + \left(\frac{1}{2}\frac{\partial\rho_s^2}{\partial z}\right)^2\right)^{-1/2} dz\right]\right\}.$$

Here, ρ_m is the nuclear density; $\bar{v}$ is the mean velocity of an intranuclear nucleon; $\Delta\sigma$ is the area of the window—that is, the neck between the two would-be fragments; D_1 and D_2 are the positions of their centers of mass with respect to the coordinate of the center of mass of the entire system; $z_{\min}$ and $z_{\max}$

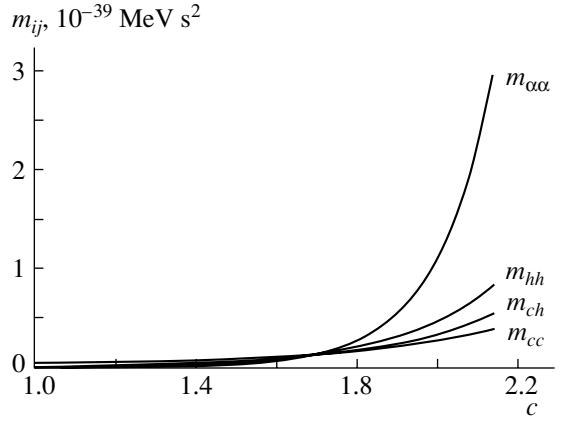

Fig. 1. Nuclear-deformation dependence of the inertia-tensor components that was calculated along the mean trajectory.

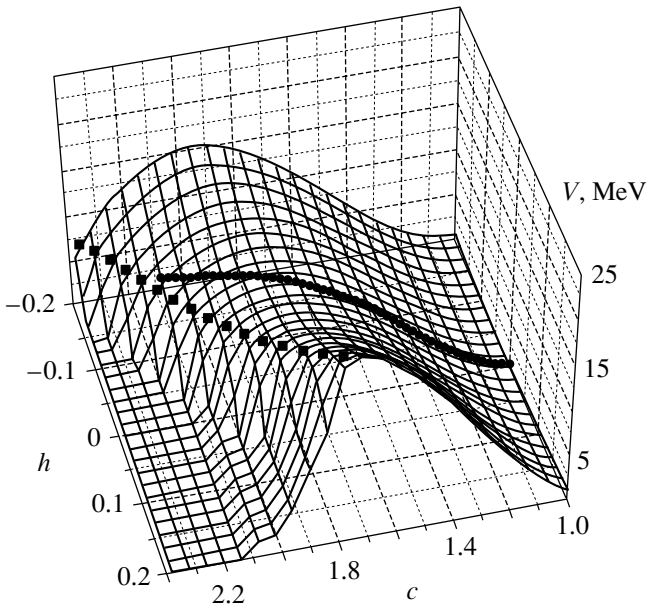

Fig. 2. Potential-energy surface in the coordinates (c, h) in the plane $\alpha = 0$. The thick curve and the curve formed by closed squares represent, respectively, the mean trajectory and the scission line (for details, see main body of the text).

are the left and the right boundary of a nuclear surface; $z_{\rm N}$ is the neck coordinate; and V_1 is the volume of one of the would-be fission fragments. The additional term (the second term in the braced expression) takes into account the nucleon flux through the neck connecting the two parts of the fissile nucleus. This additional term was evaluated by different methods in [26] and in [27]. Griffin and Dworzecka [28] considered a quantum version of one-body dissipation and demonstrated that, in an actual nucleus, the viscosity is only about 10% of that calculated by the wall formula [bracketed expression in (8)]. In view of this, Nix and Sirk proposed a modified version of the one-body mechanism of dissipation [29]. They dubbed it surface-plus-window dissipation. In this mechanism, the contribution to dissipation from the interaction of nucleons with the nuclear surface is reduced nearly by a factor of 4—from an analysis of the experimental values of the isoscalar- and octupole-resonance width, the reduction factor k_s was found to be d$k_s = 0.27$, the value of $k_s = 1$ corresponding to the full one-body viscosity.

In our calculations, we set $k_s = 0.25$. In the future, we will investigate the effect of k_s on the parameters of the mass–energy distribution and on the mean multiplicity of prescission neutrons.

Figure 3 displays the nuclear-deformation dependence of the friction-tensor components that was calculated along the mean trajectory at $k_s = 0.25$. The dashed curve represents the component $\gamma_{\alpha\alpha}$ computed without allowing for the term that was introduced in [26, 27] [second term in Eq. (8)] and which describes the transfer of nuclear matter through the neck connecting the nascent fragments. From the figure, we can see how great the effect of this additional term on the diffusion-tensor component $D_{\alpha\alpha}$ along the mass-asymmetric coordinate is, whereby we can estimate its influence on the mass variance. It should be noted that, until recently, this term was disregarded in calculating the friction tensor [11].

For the dynamical equations (3), the initial conditions were chosen as follows. The orbital angular momentum l of the compound nucleus was set to zero, and the values of the collective coordinates were sampled on the ridge line separating the ground state of the compound nucleus and the fission valley. The momentum distribution was chosen to be equilibrium. In this case, the distribution function has the form

$$P(\mathbf{q}_0, \mathbf{p}_0, t = 0) \sim \exp\left\{-\frac{V(\mathbf{q}_0) + E_{\rm coll}(\mathbf{q}_0, \mathbf{p}_0)}{T}\right\}, \quad (9)$$

where $V(\mathbf{q}_0)$ is the nuclear ridgeline potential energy, which depends on the deformation and which is reckoned from the ground state, and $E_{\rm coll}(\mathbf{q}, \mathbf{p}) = \frac{1}{2}\sum_{i,j}\mu_{ij}(\mathbf{q})\,p_i p_j$ is the kinetic energy of the collective motion of the fissile nucleus being considered. The numerical procedure for choosing the initial values of $\mathbf{q}_0$ and $\mathbf{p}_0$ was implemented by using the Neumann method with the generating function (9).

Along with the choice of the initial conditions on the ridgeline, we also performed dynamical calculations of evolution from the ground state. In this case,

the initial conditions were sampled in accordance with the distribution function

$$P(\mathbf{q}_0, \mathbf{p}_0, l, t=0) \sim \exp\left\{-\frac{V(\mathbf{q}_0)+E_{\rm coll}(\mathbf{q}_0,\mathbf{p}_0)}{T}\right\}\delta(\mathbf{q}-\mathbf{q_0})\,F(l), \quad (10)$$

where $\mathbf{q}_0 = (c=1, h=0, \alpha=0)$. The function $F(l)$ describes the distribution with respect to the orbital angular momenta of the compound nuclei formed in the fusion process [4, 5].

Following the proposal of Strutinsky [16], we assumed that the disintegration of the nucleus into fragments occurs at the neck radius equal to $R_0/3$. In the space of collective coordinates, this condition determines the scission surface. In tracing the motion of the nucleus toward the scission surface, we used, over the entire trajectory in the collective-coordinate space, the energy-conservation law in the form

$$E^* = E_{\rm int} + E_{\rm coll} + V(\mathbf{q}) + E_{\rm evap}(t), \quad (11)$$

where E^* is the total compound-nucleus excitation energy determined in the input reaction channel from the incident-ion energy and the mass difference between the colliding nuclei and the compound system, $E_{\rm int}$ is the excitation energy of the single-particle degrees of freedom of the compound nucleus (internal energy), and $E_{\rm evap}(t)$ is the nuclear excitation energy that light particles have carried away by the instant t.

The probability of light-particle emission was determined on the basis of the decay widths of compound nuclei through the corresponding channels. The decay widths were calculated by the formulas [30, 31]

$$\Gamma_j = \frac{g_j m_j}{(\pi\hbar)^2}\frac{1}{\rho_0(E^{(0)}_{\rm int})} \times \int\limits_{V_j}^{E^{(j)}_{\rm int}-B_j} \sigma^{(j)}_{\rm inv}(E)\rho_j(E^{(j)}_{\rm int}-B_j-E)EdE, \quad (12)$$

where $j = n, p, d, t, {}^3\mathrm{He}, \alpha$, and

$$\Gamma_\gamma = \frac{1}{(\pi\hbar c)^2}\frac{1}{\rho_0(E^{(0)}_{\rm int})}\int\limits_0^{E^{(0)}_{\rm int}} \sigma_\gamma(E)\rho_\gamma(E^{(0)}_{\rm int}-E)E^2dE. \quad (13)$$

Here, g_j, m_j, and B_j, are, respectively, the spin factor, the mass, and the binding energy of the jth particle, while V_j is the Coulomb barrier for it; ρ_0 is the density of excited levels of the compound nucleus; ρ_j and ρ_γ are the densities of excited states of the residual nuclei upon the emission of the jth particle and a photon, respectively; $\sigma^{(j)}_{\rm inv}$ is the cross section for the absorption of the jth particle by the residual nucleus; σ_γ is the cross section for dipole-photon absorption; and $E^{(0)}_{\rm int}$ and $E^{(j)}_{\rm int}$ are the internal energies of, respectively, the original and the residual nucleus with allowance for the nucleon-pairing energy.

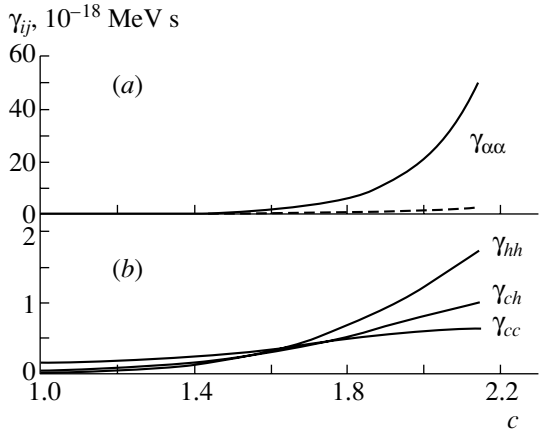

Fig. 3. Nuclear-deformation dependence of the friction-tensor components that are calculated along the mean trajectory at $k_s = 0.25$: (a) component $\gamma_{\alpha\alpha}$ (solid curve) with and (dashed curve) without allowance for the term describing mass transfer between the nascent fragments [second term in Eq. (8)] and (b) components γ_{cc}, γ_{ch}, and γ_{hh}.

In calculating the density of excited levels, we also took into account collective effects with the aid of formulas presented in [31]. In addition, we took into account the nuclear-deformation effect on the level-density parameter in the form

$$a(\mathbf{q}) = \alpha A + \beta A^{2/3} B_s(\mathbf{q}), \quad (14)$$

where the values of $\alpha = 0.073$ and $\beta = 0.095$ were borrowed from [32] and where $B_s(\mathbf{q})$ is the collective-coordinate-dependent functional of the surface energy of a nucleus within the model of a liquid drop with a sharp boundary [16, 33].

The thermal-bath temperature T used in the calculations was determined within the Fermi gas model:

$$T = (E_{\rm int}/a(\mathbf{q}))^{1/2}. \quad (15)$$

The procedure used here to combine the statistical model and the dynamical approach is as follows. At each step τ of integration of the Langevin equations (3) by formulas (12) and (13), we evaluated the partial-decay widths Γ_j. From their sum, we then determined the mean lifetime of the compound nucleus prior to the emission of some light particle as $\tau_{\rm tot} = \hbar/\sum_j \Gamma_j$. After this, we generated, in the interval $[0, 1]$, a uniformly distributed random number ξ and compared it with the ratio $\tau/\tau_{\rm tot}$. If the condition $\xi < \tau/\tau_{\rm tot}$ was satisfied, it was assumed that the emission of some light particle occurs [34].

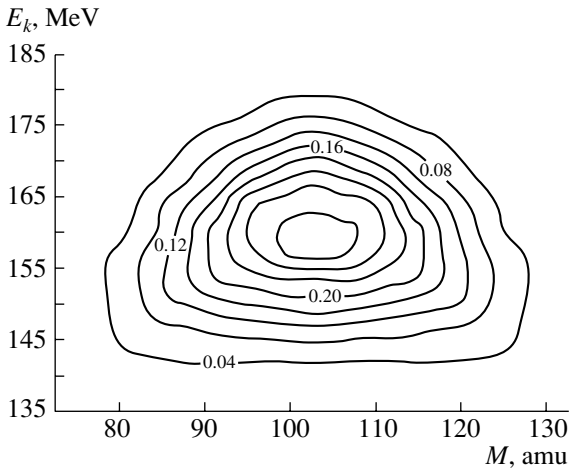

Fig. 4. Contour diagram of the mass–energy distribution according to the calculation from the ridge surface. The distribution is normalized to 200%. The numbers on the isolines indicate the yield of fission fragments (in %).

The choice of a particle species was performed by the Monte Carlo method in accordance with the probability of compound-nucleus decay through a given channel and with the calculated decay widths.

3. RESULTS OF THE CALCULATIONS AND DISCUSSION

As was indicated above, we calculated the properties of the fission process for the reaction

$$^{12}\mathrm{C} + ^{194}\mathrm{Pt} \rightarrow ^{206}\mathrm{Po} \quad (E_{\mathrm{lab}} = 99\ \mathrm{MeV}).$$

The fullest and clearest way to present the calculated mass–energy distributions of fission fragments is to make use of the contour level plots for the distribution $Y(E_k, M)$. Our method for calculating the two-dimensional mass–energy distribution of fission fragments is based on the concept of the scission surface and is set forth in [1]. It is assumed that the total kinetic energy E_k of fragments is the sum of the energy V_c of Coulomb repulsion of the fragments and the kinetic energy of their relative motion (prescission kinetic energy), E_{ps},

$$E_k = V_c + E_{\mathrm{ps}}, \tag{16}$$

these energies being determined at the nuclear-scission instant. The mean kinetic energy is then determined as

$$\langle E_k \rangle = \langle V_c \rangle + \langle E_{\mathrm{ps}} \rangle . \tag{17}$$

The expression for the kinetic-energy variance has the form

$$\sigma^2_{E_k} = \sigma^2_{V_c} + \sigma^2_{E_{\mathrm{ps}}} + 2\sigma_{V_c E_{\mathrm{ps}}}, \tag{18}$$

where

$$\sigma^2_{V_c} = \langle V_c^2 \rangle - \langle V_c \rangle^2 ,$$

$$\sigma^2_{E_{\mathrm{ps}}} = \langle E_{\mathrm{ps}}^2 \rangle - \langle E_{\mathrm{ps}} \rangle^2 , \tag{19}$$

$$\sigma_{V_c E_{\mathrm{ps}}} = \langle V_c E_{\mathrm{ps}} \rangle - \langle V_c \rangle \langle E_{\mathrm{ps}} \rangle .$$

The fragment masses were calculated by the formulas

$$M_R = \frac{\int\limits_{z_N}^{z_{\max}} \rho_s^2(z, \mathbf{q}_{\mathrm{sc}}) dz}{\int\limits_{z_{\min}}^{z_{\max}} \rho_s^2(z, \mathbf{q}_{\mathrm{sc}}) dz}, \tag{20}$$

$$M_L = \frac{\int\limits_{z_{\min}}^{z_N} \rho_s^2(z, \mathbf{q}_{\mathrm{sc}}) dz}{\int\limits_{z_{\min}}^{z_{\max}} \rho_s^2(z, \mathbf{q}_{\mathrm{sc}}) dz},$$

where M_R and M_L are, respectively, the left- and the right-fragment mass, while $\mathbf{q}_{\mathrm{sc}}$ are the nuclear-shape parameters (c, h, α) determined as the points of intersection of Langevin stochastic trajectories and the scission surface.

The results of our calculations for the two-dimensional mass–energy distribution of fission fragments from the area of the ridge of the potential-energy surface are shown in Fig. 4. It can be seen from the figure that the shape of the contour lines near the maximum is close to elliptical and that, as we move away from the maximum, the contour lines assume the shape of a triangle with smoothed angles, a pattern that qualitatively complies with that observed experimentally. It is more convenient to compare quantitatively the calculated characteristics of the two-dimensional mass–energy distribution of fragments with experimental data in terms of the one-dimensional mass and energy distributions and the correlation dependences.

Per fission event, we obtain two mass events (two fission fragments) and one energy event (kinetic energy of fragment divergence), so that the mass and energy distributions are normalized to 200% and 100%, respectively. The one-dimensional distributions can be obtained by integrating the two-dimensional distribution with respect to the corresponding parameter; that is,

$$Y(M) = \int Y(E_k, M) dE_k,$$

$$Y(E_k) = \int Y(E_k, M) dM. \tag{21}$$

The one-dimensional energy and mass distributions shown in Figs. 5*a* and 6*a*, respectively, appear to be curves with one maximum. Both in experimental studies and in theoretical calculations, they are usually approximated by Gaussian curves with the

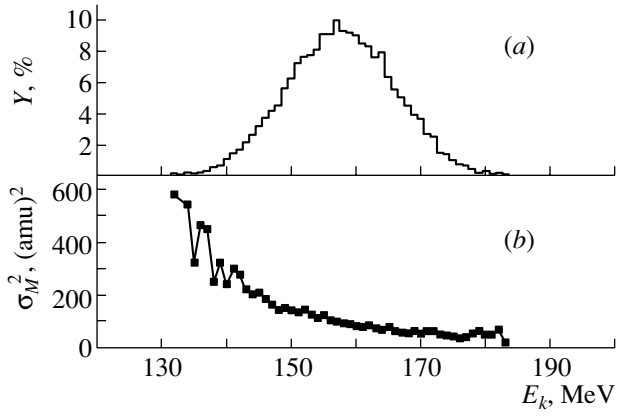

Fig. 5. (*a*) Yield of fragments and (*b*) variance of the mass distribution as functions of the fragment energy.

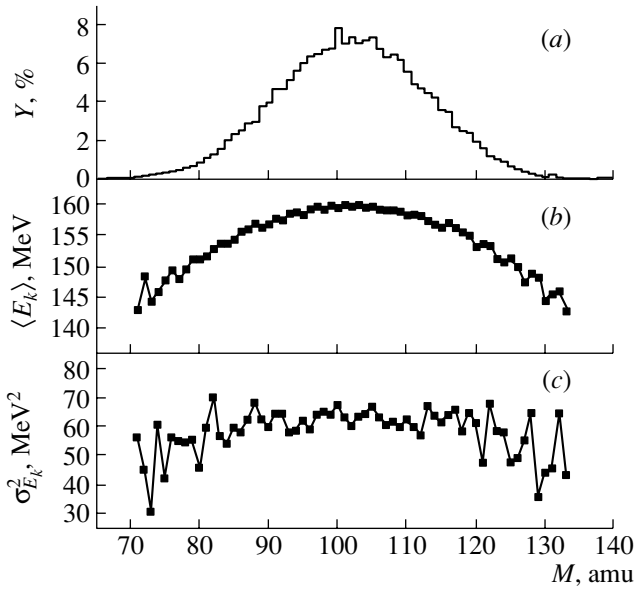

Fig. 6. (*a*) Yield of fragments, (*b*) mean kinetic energy, and (*c*) variance of the energy distribution as functions of the fragment mass.

corresponding mean values and variances. We have obtained the following results:

$$\langle E_k \rangle_{\rm rs} = 160.5\,{\rm MeV},\ \ (\sigma^2_{E_k})_{\rm rs} = 69 \pm 3\,{\rm MeV}^2,$$

$$(\sigma^2_M)_{\rm rs} = 115 \pm 5\,({\rm amu})^2,\ \ \langle \nu_{\rm pre} \rangle_{\rm rs} = 0.53;$$

$$\langle E_k \rangle_{\rm gr} = 158.9\,{\rm MeV},\ \ (\sigma^2_{E_k})_{\rm gr} = 106 \pm 14\,{\rm MeV}^2,$$

$$(\sigma^2_M)_{\rm gr} = 132 \pm 17\,({\rm amu})^2,\ \ \langle \nu_{\rm pre} \rangle_{\rm gr} = 2.3;$$

$$\langle E_k \rangle_{\rm ex} = 146.5 \pm 0.8\,{\rm MeV},$$

$$(\sigma^2_{E_k})_{\rm ex} = 106 \pm 3\,{\rm MeV}^2,$$

$$(\sigma^2_M)_{\rm ex} = 165 \pm 4\,({\rm amu})^2,\ \ \langle \nu_{\rm pre} \rangle_{\rm ex} = 2.8.$$

The subscripts "rs" and "gr" label the results of our dynamical calculations from, respectively, the ridge surface and the ground state, while the subscript "ex" labels the experimental values of the corresponding quantities [15].

In calculating the mass–energy distribution of fission fragments from the ridge surface, we set the orbital angular momentum l of a compound nucleus to zero. As is well known, the orbital angular momentum substantially affects the variance of the mass distribution, but it has virtually no effect on the parameters of the energy distribution. In view of this, the experimental value of the mass variance was rescaled to zero orbital angular momentum by using the method described in [15, 35]. The result is $\sigma^2_M(l=0) = 117 \pm 4\,({\rm amu})^2$.

It can be seen that the mean number of prescission neutrons, $\langle \nu_{\rm pre} \rangle$, that was obtained in our calculations from the ridge surface is markedly different from the experimental value, although, in the calculations from the ground state, it is in fairly good agreement with experimental data. This can be explained by the fact that, for light compound nuclei, a major part of all neutrons evaporate prior to reaching the ridge surface separating the ground state and the valley of nascent fragments. The mean multiplicities of charged prescission particles and of photons are not presented here, since events of their emission are extremely rare, which was indeed observed experimentally.

From our results, it is obvious that, both in the calculation from the ridge and in the calculation from the ground state, the resulting values of $\langle E_k \rangle$, $\sigma^2_{E_k}$, and σ^2_M agree fairly well with experimental data. It is interesting to compare the results of our study and the results obtained on the basis of two-dimensional Langevin dynamics. In the (c, h, α) parametrization, two-dimensional calculations in terms of the coordinates (ρ, h) and (ρ, η) were performed in [36] without taking into account the orbital angular momentum and the evaporation of light prescission particles. The results obtained there are

$$\langle E_k \rangle = 163.9\,MeV,\ \ \sigma^2_{E_k} = 133.3\,MeV^2,$$

$$\sigma^2_M = 226\,({\rm amu})^2.$$

We see that results in three-dimensional Langevin dynamics better agree with experiment data than the results of the above two-dimensional calculations.

The results of the two-dimensional calculations show [11, 12], that the agreement with experimental data, at least for the variance of the mass distribution, must improve upon going over from the model of

a liquid drop with a sharp boundary to the liquid-drop model that takes into account the finite range of nuclear forces and the nuclear-surface diffuseness [37].

Here, we have also obtained the correlation dependences of the mean kinetic energy and the variance of the energy distribution on the fragment masses and the kinetic-energy dependence of the variance of the mass distribution.

These dependences are displayed in Figs. 6*b*, 6*c*, and 5*b*. For the reaction considered here, we are unaware of experimental data on the correlation between the parameters of mass–energy distribution. It should be noted, however, that the behavior of the curves is similar to the behavior observed in the experiments that were reported in [38, 39] and which were performed for reactions characterized by close values of the excitation energy and of the mass numbers of compound nuclei. The growing scatter of the correlation dependences is due to an increase in the statistical error of the calculations as we approach the tails of the distributions.

4. CONCLUSION

Here, we have presented the first results of calculations of the mass–energy distribution $Y(E_k, M)$ within three-dimensional Langevin dynamics. On this basis, we have obtained the one-dimensional mass ($Y(M)$) and energy ($Y(E_k)$) distributions of fission fragments. For the parameters of the mass–energy distribution, we have also calculated the correlation dependences $E_k(M)$, $\sigma^2_{E_k}(M)$, and $\sigma^2_M(E_k)$. The emission of light prescission particles has been taken into account in all these calculations.

In our opinion, a further problem is to perform systematic calculations—that is, calculations for a wide set of compound nuclei over broad intervals of the fissility parameter and excitation energies. We deem that such calculations must employ initial conditions in the ground state and take into account the orbital angular momentum of the compound nucleus.

As was noted above, the potential energy has been calculated here within the model of a liquid drop with a sharp boundary. For future calculations, we plan to employ the potential energy determined on the basis of the liquid-drop model taking into account the finite range of nuclear forces [37].

ACKNOWLEDGMENTS

We are grateful to G.I. Kosenko for cooperation at the first stage of this study, to A.Ya. Rusanov and G.Yu. Krappe for numerous enlightening discussions, and to L.V. Muzýka for assistance in the preparation of the manuscript.

This work was supported in part by INTAS (grant no. 93–1560ext).

REFERENCES

1. G. D. Adeev and V. V. Pashkevich, Nucl. Phys. A **502**, 405c (1989).
2. Y. Abe, S. Ayik, P.-G. Reinhard, and E. Suraud, Phys. Rep. **275**, 49 (1996).
3. G. D. Adeev, I. I. Gonchar, V. V. Pashkevich, *et al.,* Fiz. Élem. Chastits At. Yadra **19**, 1229 (1988) [Sov. J. Part. Nucl. **19**, 529 (1988)].
4. P. Fröbrich and I. I. Gontchar, Phys. Rep. **292**, 131 (1998).
5. I. I. Gonchar, Fiz. Élem. Chastits At. Yadra **26**, 932 (1995) [Phys. Part. Nucl. **26**, 394 (1995)].
6. I. I. Gonchar, L. A. Litnevsky, and P. Fröbrich, Comput. Phys. Commun. **107**, 223 (1997).
7. T. Wada, N. Carjan, and Y. Abe, Nucl. Phys. A **538**, 283c (1992).
8. G.-R. Tillack, R. Reif, A. Schulke, *et al.,* Phys. Lett. B **296**, 296 (1992).
9. J. Bao, Y. Zhuo, and X. Wu, Z. Phys. A **352**, 321 (1995).
10. G. I. Kosenko, D. V. Vanin, and G. D. Adeev, Yad. Fiz. **61**, 2142 (1998) [Phys. At. Nucl. **61**, 2031 (1998)].
11. D. V. Vanin, G. I. Kosenko, and G. D. Adeev, Phys. Rev. C **59**, 2114 (1999).
12. D. V. Vanin, P. N. Nadtochdy, G. I. Kosenko, and G. D. Adeev, Yad. Fiz. **63**, 1957 (2000) [Phys. At. Nucl. **63**, 1865 (2000)].
13. J. R. Nix and W. J. Świątecki, Nucl. Phys. **71**, 1 (1965); J. R. Nix, Nucl. Phys. A **130**, 241 (1969).
14. O. I. Serdyuk, G. D. Adeev, and I. I. Gonchar, Yad. Fiz. **46**, 710 (1987) [Sov. J. Nucl. Phys. **46**, 399 (1987)].
15. G. G. Chubaryan, M. G. Itkis, S. M. Luk'yanov, *et al.,* Yad. Fiz. **56** (3), 3 (1993) [Phys. At. Nucl. **56**, 286 (1993)].
16. M. Brack, J. Damgaard, H. C. Pauli, *et al.,* Rev. Mod. Phys. **44**, 320 (1972).
17. V. M. Strutinskiĭ, Zh. Éksp. Teor. Fiz. **45**, 1900 (1963) [Sov. Phys. JETP **18**, 1305 (1964)].
18. T. Ledergerber, H. C. Pauli, and Y. Yariv, Nucl. Phys. A **280**, 214 (1977).
19. H. A. Kramers, Physica (Utrecht) **7**, 284 (1940).
20. V. V. Voevodin and G. Kim, *Computational Methods and Programming* (Mosk. Gos. Univ., Moscow, 1962), pp. 269–278.
21. A. Bohr and B. R. Mottelson, *Nuclear Structure*, Vol. 2: *Nuclear Deformations* (Benjamin, New York, 1975; Mir, Moscow, 1977).
22. A. V. Ignatyuk, *Statistical Properties of Excited Nuclei* (Énergoatomizdat, Moscow, 1983).
23. W. D. Myers and W. J. Świątecki, Ark. Fys. **36**, 343 (1967).
24. K. T. R. Davies, A. J. Sierk, and J. R. Nix, Phys. Rev. C **13**, 2385 (1976).
25. J. Blocki *et al.,* Ann. Phys. (N.Y.) **113**, 330 (1978).
26. J. Randrup, W. J. Świątecki, Nucl. Phys. A **429**, 105 (1984).
27. H. Feldmeier, Rep. Prog. Phys. **50**, 915 (1987).

28. J. J. Griffin and M. Dworzecka, Nucl. Phys. A **455**, 61 (1986).
29. J. R. Nix and A. J. Sierk, in *Proceedings of International School-Seminar on Heavy Ion Physics, Dubna, 1986,* Ed. by M. I. Zarubina and E. V. Ivashkevich (Ob'ed. Inst. Yad. Issled., Dubna, 1987), p. 453; *Proceedings of 6th Adriatic Conference on Nuclear Physics: Frontiers of Heavy Ion Physics, Dubrovnik, Yugoslavia, 1987,* Ed. by N. Cindro *et al.* (World Sci., Singapore, 1990), p. 333.
30. V. Weisskopf, Phys. Rev. **52**, 295 (1937).
31. A. S. Iljinov, M. V. Mebel, *et al.,* Nucl. Phys. A **543**, 517 (1992).
32. A. V. Ignatyuk, M. G. Itkis, V. N. Okolovich, *et al.,* Yad. Fiz. **21**, 1185 (1975) [Sov. J. Nucl. Phys. **21**, 612 (1975)].
33. S. Cohen, F. Plasil, and W. J. Świątecki, Ann. Phys. (N.Y.) **82**, 557 (1974).
34. N. D. Mavlitov, P. Fröbrich, and I. I. Gontchar, Z. Phys. A **342**, 195 (1992).
35. A. Ya. Rusanov, M. G. Itkis, and V. N. Okolovich, Yad. Fiz. **60**, 773 (1997) [Phys. At. Nucl. **60**, 683 (1997)].
36. D. V. Vanin, A. V. Karpov, P. N. Nadtochiĭ, and G. D. Adeev, Vestn. Omsk. Univ., No. 3, 44 (1999).
37. H. J. Krappe, J. R. Nix, and A. J. Sierk, Phys. Rev. C **20**, 992 (1979).
38. E. M. Gruzintsev, M. G. Itkis, V. N. Okolovich, *et al.,* Yad. Fiz. **39**, 1100 (1984) [Sov. J. Nucl. Phys. **39**, 694 (1984)].
39. E. M. Gruzintsev, M. G. Itkis, V. N. Okolovich, and G. N. Smirenkin, Yad. Fiz. **39**, 1336 (1984) [Sov. J. Nucl. Phys. **39**, 844 (1984)].

Translated by A. Isaakyan

Physics of Atomic Nuclei, Vol. 64, No. 5, 2001, pp. 870–881. Translated from Yadernaya Fizika, Vol. 64, No. 5, 2001, pp. 935–947.

NUCLEI
Theory

Deuteron Photodisintegration in the Bethe–Salpeter Formalism

K. Yu. Kazakov* **and S. E. Sus'kov****

Far East State University, ul. Sukhanova 8, Vladivostok, 690600 Russia

Received November 26, 1999; in final form, February 21, 2000

Abstract—A relativistically invariant analysis of the deuteron-photodisintegration reaction is performed. The reaction $\gamma d \to pn$ is considered in the plane-wave approximation on the basis of the Bethe–Salpeter equation with a separable kernel. The results obtained in this way are compared with the results based on nonrelativistic models and on the quasipotential approximation. It is shown that the most important relativistic contributions to the relevant angular distributions are associated with the dependence of the Bethe–Salpeter amplitude on the relative energy of nucleons and on the boost transformation of this amplitude. © *2001 MAIK "Nauka/Interperiodica".*

1. INTRODUCTION

At present, experiments studying quasielastic lepton scattering on nuclei are considered to be one of the main and the most reliable sources of information about the structure of nuclei. It should be emphasized that deuteron photodisintegration stands out among such reactions. The reaction $\gamma d \to np$ has received a comprehensive study at low and intermediate incident-photon energies (a survey of relevant experiments and theoretical methods for investigating this process can be found in [1]). A theoretical analysis of available data in the above kinematical regions yielded important information about the deuteron wave function and made it possible to determine various contributions to the reaction that are generated by meson-exchange currents (MES) and by the excitation of isobaric configurations.

Experimental investigation of deuteron photodistegration is in the forefront of the research programs of physics centers worldwide. In this connection, we would like to mention experiments that employ 30- to 50-MeV polarized photons at the ADONE storage ring [2] and which were performed to study the assumption that, in reactions involving intermediate energy nuclei, it is necessary to take explicitly into account Δ-isobar degrees of freedom and experiments at Yerevan Physics Institute that measure the asymmetry of deuteron disintegration induced by 0.9- to 1.7-GeV photons and which explore the problem of the applicability of quark-counting sum rules at high energies [3].

Future investigations of deuteron disintegration induced by photons with energies up to 8 GeV according to the RCNP program [4] and investigations at the SLAC–NPAS accelerator with a beam of 2.8-GeV photons [5] will make it possible to analyze the quark structure of the nucleus. The experimental program for the linear accelerator at TJNAL includes studying the reaction $\gamma d \to pn$ with the aim of obtaining precise data over a wide kinematical domain. The first results from a measurement of the differential cross section for deuteron photodisintegration at TJNAL were obtained in 1998 [6] for photons of energy about 4 GeV and are in good agreement with the results of previous measurements at low energies. At the same time, a preliminary analysis of theoretical results deduced from an investigation of deuteron photodisintegration at high energies (about 1 GeV and above) did not unambiguously reveal the role of nonnucleonic degrees of freedom in the nucleus [7].

Nonetheless, results obtained in this energy region lead to the conclusion that relativistic effects are important there. In order to investigate the photodisintegration reaction at high energies of the incident photon, it is necessary to develop a relativistic description of both the deuteron structure and the reaction mechanism. However, there are presently no calculations that would describe the entire body of available information. Moreover, it has not yet been found whether a theory that is based on degrees of freedom traditional for nuclear physics (nucleons, mesons, isobars) is able to describe experimental data self-consistently and comprehensively.

Traditional methods for studying deuteron photodisintegration are based on isolating leading contributions in the expansion of the electromagnetic current in powers of p/m. In the majority of such studies, it is implicitly assumed that the constituents

*e-mail: kazakovk@ifit.phys.dvgu.ru
**e-mail: suskovs@ifit.phys.dvgu.ru

forming the deuteron and the reaction final state behave nonrelativistically and that electromagnetic interaction can be considered independently (there are difficululties here that are associated with ensuring gauge invariance [8, 9]). The relevant calculations employ the Schrödinger equation with various phenomenological potentials like the Paris and the Bonn potential. In our opinion, however, these methods do not possess the required degree of generality, because they are applicable only at low energies.

It is important to emphasize the following. Exotic components in the wave function of a nucleus manifest themselves against the background of nucleon–nucleon (NN) interaction. The problem of taking correctly into account nuclear effects (in particular, developing a relativistic formalism and including binary processes) and effects of background is always crucial when it is necessary to extract information about exoticism from data on some process. Simplified estimates of nuclear effects may lead to erroneous conclusions. In order to take correctly into account these effects, it is desirable to have exactly solvable nuclear models.

A general relativistic approach to strongly coupled systems and processes involving such systems can be developed by invoking the field-theoretical Lorentz-invariant Bethe–Salpeter equation [10, 11]. On the basis of this equation, the dynamics of an NN system is described in terms of Bethe–Salpeter amplitudes (the Bethe–Salpeter formalism is surveyed in [12], and a comprehensive list of references on the subject can be found in [13]).

Since an implementation of this approach in practice involves considerable mathematical and computational difficulties, various approximate methods, including the quasipotential approximation, were evolved on the basis of the Bethe–Salpeter formalism. In this connection, we would like to mention above all the Logunov–Tavkhelidze–Blankenbecler–Sugar [14], Kadyshevsky [15], and Gross [16] equations. In practice, a quasipotential equation usually cannot be solved without recourse to approximations concerning, in particular, the kernel of NN interaction; therefore, it is difficult to assess the accuracy of this approach. The results of the calculations along these lines can be found in [16, 17].

Various approaches to taking into account relativistic effects are used to construct a relativistic description of bound states. For example, relativistic deuteron wave functions were constructed in [18] as elements of a Fock column defined on the light-front surface. A similar procedure was adopted in [19], where deuteron photodisintegration was considered on the basis of a field-theoretical gauge-invariant model on the light front.

The approach that is based on the technique of dispersion integration with respect to the masses of compound masses [20] and which was applied to performing a relativistically covariant calculation of deuteron photodisintegration at photon energies in the range E_γ=0–400 MeV [21, 22] is worthy of special note. Within this formalism, it is possible to investigate in detail final-state interaction (FSI) and the effect of inelasticity in NN scattering channels on the deuteron-photodisintegration cross section. Such a relativistic calculation of the amplitude with allowance for FSI makes it possible to obtain an accurate description of the total cross section at photon energies of $E_\gamma < 50$ MeV. For higher energies, it was concluded that relativistic effects are of importance in this region and that MECs can contribute significantly there.

On the whole, a preliminary conclusion from the analysis of the theoretical situation is that the contribution of relativistic effects is of importance at high momentum transfers. However, a considerable scatter of the results that is observed in this kinematical region indicates that a consistent relativistic approach to the problem has yet to be developed.

At present, a relativistic treatment of the deuteron predominantly relies on the Bethe–Salpeter equation, which is manifestly Lorentz-invariant and which makes it possible to take self-consistently into account relativistic effects; in particular, this implies a symmetric inclusion of nucleon and antinucleon degrees of freedom and of binary processes. So far, the Bethe–Salpeter equation has been applied only to elastic electron–deuteron scattering [23], backward proton–deuteron scattering [24], deep-inelastic scattering on a deuteron [25, 26], and a description of the static properties of the deuteron [27, 28]. In view of this, it would be very interesting to explore the deuteron-photodisintegration reaction on the basis of the Bethe–Salpeter formalism.

Shebeko and Korchin [29] were among the first to apply the Bethe–Salpeter formalism to the deuteron photodisintegration reaction. Within this formalism, they proposed a consistent derivation of the expressions for the reaction amplitudes in terms of the Bethe–Salpeter amplitudes for the initial and for the final state and of the Mandelstam electromagnetic current. In addition, these authors specified a procedure for taking into account binary processes in the current and allowed for FSI. However, they performed no specific calculations.

By considering the deuteron-photodisintegration reaction as a example, we develop here a relativistically covariant description of nucleonic degrees of freedom and of relativistic effects in nuclei. This is implemented on the basis of the Bethe–Salpeter equation for the NN system. We believe that this

approach will make it possible to reveal, in the scattering amplitude, some important features that cannot be established within nonrelativistic approaches. The calculations are performed in the plane-wave impulse approximation with allowance for the ${}^1S_3^{++}$- and ${}^1D_3^{++}$ partial-wave states in the Bethe–Salpeter deuteron amplitude. The problem is solved by using the relativistically covariant separable potential Graz-II [30].

2. BETHE–SALPETER EQUATION AND QUASIPOTENTIAL APPROXIMATION

The problem of describing a relativistic NN system is formulated on the basis of the Bethe–Salpeter equation. The Bethe–Salpeter equation for the amplitude of the scattering of two nucleons with the 4-momenta p and p' or relative motion and the total 4-momentum P has the form

$$T(p,p';P) = \mathcal{V}(p,p';P) + \frac{i}{(2\pi)^4}\int d^4k\mathcal{V}(p,k;P)G(k;P)T(k,p';P), \quad (1)$$

where $\mathcal{V}$ is the kernel of the equation—it is obtained as the sum of all irreducible Feynman diagrams in the field-theoretical model chosen for NN interaction—while $G(k;P)$ is the two-particle Green's function.

The Bethe–Salpeter amplitude for the continuous spectrum at $P^2 = s > 4m^2$ is expressed in terms of the T matrix and the Green's function as

$$\chi(k;pP) = [(2\pi)^4 i\delta^{(4)}(p-k) - G(k;P)T(k,p;P)] \times\chi^{(0)}(p;P), \quad p\cdot P = 0, \quad (2)$$

where $\chi^{(0)}(p;P)$ is the amplitude describing the motion of free particles.

If the T matrix has a pole corresponding to a bound state of mass M_d at $P^2 = M_d^2 < 4m^2$, the vertex function for this state satisfies the homogeneous Bethe–Salpeter equation

$$\Gamma(p;P) = \frac{i}{(2\pi)^4}\int d^4k\mathcal{V}(p,k;P)G(k;P)\Gamma(k;P); \quad (3)$$

accordingly, the Bethe–Salpeter amplitude for the bound state is given by

$$\psi(p;P) = G(p;P)\Gamma(p;P). \quad (4)$$

Equations (1) and (3) possess a manifest relativistic invariance. Yet another feature peculiar to them is that integration is performed there with respect to all four components of the intermediate relative 4-momentum k, both nucleons here being off the mass shell.

A field theoretical analysis of the integral equations (1) and (3) is complicated by the presence of the relative energy in them, the complex analytic properties of the kernel and the Green's function, and the spinor structure of the amplitude. A possible way to simplify such an analysis is to make use of the relativistic quasipotential approximation.

A general procedure for reducing the Bethe–Salpeter equation to the quasipotential equation is well known [17]. A class of approximate three-dimensional relativistic equations can be obtained by approximating the free two-particle Green's function as the product of two free-nucleon propagators, $G = S^{(1)}S^{(2)}$ [for the sake of simplicity, we perform our analysis in the c.m. frame, where $P = (\sqrt{s},\mathbf{0})$]; that is,

$$G(k;\sqrt{s}) = \frac{[\hat{P}/2+\hat{k}+m]^{(1)}}{(\frac{\sqrt{s}}{2}+k_0)^2 - E_{\mathbf{k}}^2 + i\varepsilon}\frac{[\hat{P}/2-\hat{k}+m]^{(2)}}{(\frac{\sqrt{s}}{2}-k_0)^2 - E_{\mathbf{k}}^2 + i\varepsilon}, \quad (5)$$

where $E_{\mathbf{k}} = \sqrt{m^2+\mathbf{k}^2}$.

We single out the Blankenbecler–Sugar set of approximate Green's functions. In the c.m. frame, both nucleons are then equidistant from the mass shell in intermediate states, since their relative energy is chosen to be zero. As a result, the propagator has the form

$$g(k;\sqrt{s}) = -2\pi i\delta(k_0)\frac{\Lambda^{(1)}(\mathbf{k}_1)\Lambda^{(2)}(\mathbf{k}_2)}{E_{\mathbf{k}}(s-4E_{\mathbf{k}}^2+i\varepsilon)}, \quad (6)$$

where Λ stands for projection operators that explicitly single out positive-energy states. Upon the substitution of the propagator given by Eq. (6) into the Bethe–Salpeter equation, we arrive at the quasipotential Bethe–Salpeter equation for describing the NN system. A similar analysis of the application of the covariant quasipotential approximation to describing the electromagnetic properties of two-nucleon systems was performed in [31].

In numerically solving the Bethe–Salpeter equation, use is often made of the ladder approximation, where the kernel $\mathcal{V}$ is represented as the sum of one-boson-exchange diagrams. A solution to Eq. (3) can then be found in Euclidean space (see, for example, [24–28]. This is a serious drawback of this approximation, because the relative energy of the particles is on the imaginary axis in this solution. Moreover, there arise additional difficulties in calculating observables in terms of the Bethe–Salpeter amplitudes, since an analytic continuation from Euclidean space to Minkowski space is ambiguous and very cumbersome. For this reason, it is desirable to have a solution directly in Minkowski space.

A physical solution can be obtained by the method of integral representation of perturbation theory [32]. In [33], a general solution to the Bethe–Salpeter equation was obtained in terms of the generalized spectral representation for the bound-state vertex

function and for the kernel of the equation. However, that analysis was performed only for scalar particles.

An alternative way to analyze the Bethe–Salpeter equation consists in invoking a nonlocal separable kernel of the type [30, 34, 35]

$$\mathcal{V}(p_0,\mathbf{p},k_0,\mathbf{k}) = \sum_{a,b=1}^{N} \lambda_{ab} v_a(p_0,\mathbf{p}) v_b(k_0,\mathbf{k}). \quad (7)$$

In this case, the resulting scattering amplitudes and the Bethe–Salpeter vertex functions are physical quantities and possess analytic properties that are determined by the form factors $v_a(p)$. For a separable kernel whose form factors appear to be a relativistic generalization of the Yamaguchi form factor [36], the authors of [34, 37, 38] investigated the properties of the NN interaction within the Bethe–Salpeter formalism.

For the purposes of the ensuing analysis, we perform a partial-wave expansion of the Bethe–Salpeter deuteron vertex function $\Gamma(k;P)$. In the c.m. frame, we have (here, we explicitly single out its dependence on the spin variable M and omit the isospin part)

$$\Gamma_M(p;P) = \sum_{\alpha} g_\alpha(p_0,|\mathbf{p}|;\sqrt{s})\Gamma^\alpha_M(-\mathbf{p}), \quad (8)$$
$$M = \pm 1, 0,$$

where the summation index α is determined by the quantum numbers S, L, J, and ρ; that is, the ρ spin [39], which singles out nucleon and antinucleon states, appears here in addition to the traditional spin, orbital angular, and total momenta (S, L, and J, respectively); $\Gamma^\alpha_M(-\mathbf{p})$ is the spin–angular component; and g_α is the radial function.

In general, summation in expression (8) must be performed over eight partial-wave amplitudes. In addition to physical channels that involve positive-energy nucleon states ($^3S_1^{++}$-, $^3D_1^{++}$), there arise channels involving negative-energy states:

$$^3P_1^{+-}, {}^3P_1^{-+}, {}^1P_1^{+-}, {}^1P_1^{-+}, {}^3S_1^{--}, {}^3D_1^{--}.$$

The corresponding radial vertex functions are odd in the relative energy, whence it follows that they vanish when the particles occur on the mass shell.

In the following, we will not consider partial-wave channels characterized by a negative nucleon energy. Thus, there remain two coupled channels, $^3S_1$–$^3D_1$, whose vertex functions are given by [28]

$$\sqrt{8\pi}\Gamma^{^3S_1^{++}}_M(p;P) = \mathcal{N}_{\mathbf{p}_1}\mathcal{N}_{\mathbf{p}_2}(m+\hat{p}_1)(1+\gamma_0) \quad (9)$$
$$\times \hat{e}_M(m-\hat{p}_2)g_0(p_0,|\mathbf{p}|;\sqrt{s}),$$
$$\sqrt{16\pi}\Gamma^{^3D_1^{++}}_M(p;P) = -\mathcal{N}_{\mathbf{p}_1}\mathcal{N}_{\mathbf{p}_2}(m+\hat{p}_1)$$
$$\times(1+\gamma_0)(\hat{\varepsilon}_M + \frac{3}{2}(\hat{p}_1-\hat{p}_2)$$
$$\times\frac{(p\cdot e_M)}{\mathbf{p}^2})(m-\hat{p}_2)g_2(p_0,|\mathbf{p}|;\sqrt{s}),$$

where $\sqrt{s}=M_d$, $p_1=(E_\mathbf{p},\mathbf{p})$, and $p_2=(E_\mathbf{p},-\mathbf{p})$ are the on-mass-shell nucleon momenta; $\mathcal{N}_\mathbf{p}^{-1} = \sqrt{2E_\mathbf{p}(m+E_\mathbf{p})}$ is a normalization factor; and $e_M = (0,\mathbf{e}_M)$ is the deuteron polarization 4-vector,

$$\sum_{M=-1}^{+1} e^\mu_M e^{\nu *}_M = -g^{\mu\nu} + \frac{P^\mu P^\nu}{M_d^2}, \qquad e_M\cdot P = 0. \quad (10)$$

Although the Bethe–Salpeter vertex function does not have a nonrelativistic limit in a rigorous mathematical sense, it can be compared with the quasipotential and the nonrelativistic vertex functions. For this purpose, we make use of the normalization condition for the bound-state amplitude. If the kernel $\mathcal{V}$ is independent of the total energy P of the system, we have

$$1 = -\int \frac{d^4k}{(2\pi)^4 i}\bar{\Gamma}(p;P)\left.\frac{\partial G(p;P)}{\partial P^2}\right|_{P^2=M_d^2}\Gamma(p;P). \quad (11)$$

In terms of the radial vertex function (9), this condition assumes the form

$$\frac{1}{2\pi^2 i M_d}\times$$
$$\times\int_0^\infty dk_0\int_0^\infty d|\mathbf{k}|\,\mathbf{k}^2\frac{g_L(k_0,|\mathbf{k}|;\sqrt{s})^2(E_\mathbf{k}-\frac{M_d}{2})}{((\frac{M_d}{2}-E_\mathbf{k}+i\epsilon)^2-k_0^2)^2} = P_L, \quad (12)$$
$$P_0+P_2=1.$$

For the quasipotential vertex function $\tilde{g}_L$, we accordingly obtain

$$\frac{2m^2}{\pi^2 M_d}\int d|\mathbf{k}|\,\mathbf{k}^2\frac{\tilde{g}_L(0,|\mathbf{k}|)^2}{E_\mathbf{k}(M_d^2-4E_\mathbf{k}^2)^2} = P_L. \quad (13)$$

Comparing these two expressions, we can find that the Bethe–Salpeter vertex function and the Blankenbecler–Sugar quasipotential function are related by equation

$$\left.\frac{g_L(k_0,|\mathbf{k}|)}{E_\mathbf{k}-\frac{M_d}{2}}\right|_{k_0=\frac{M_d}{2}-E_\mathbf{k}} \approx \frac{4}{\sqrt{\pi}}\sqrt{\frac{m^2}{E_\mathbf{k}}}\frac{\tilde{g}_L(0,|\mathbf{k}|)}{M_d^2-4E_\mathbf{k}^2}. \quad (14)$$

The Blankenbecler–Sugar vertex function is identical to the nonrelativistic vertex function under the condition [40]

$$g_L(|\mathbf{k}|) \equiv \sqrt{\frac{m}{E_\mathbf{k}}}\tilde{g}_L(0,|\mathbf{k}|).$$

In numerically calculating the deuteron-photodisintegration cross section, we will make use of a

rank-3 separable kernel, $N = 3$ in Eq. (7). The nonrelativistic Graz-II potential, which is employed to describe the properties of the NN system in the ${}^3S_1$–${}^3D_1$ coupled channels (for details, see [40]), served as a prototype of this potential. The radial vertex functions are given by

$$g_0(k_0, |\mathbf{k}|; s) = A(s)\frac{1-\gamma_1 k^2}{(k^2-\beta_{11}^2)^2} + B(s)\frac{k^2}{(k^2-\beta_{12}^2)^2}, \quad (15)$$

$$g_2(k_0, |\mathbf{k}|; s) = C(s)\frac{k^2(1-\gamma_2 k^2)}{(k^2-\beta_{21}^2)^2(k^2-\beta_{22}^2)^2},$$

$$s = M_d^2,$$

where $k^2 = k_0^2 - \mathbf{k}^2$; the coefficients A, B, and C are solutions to a linear set of homogeneous Bethe–Salpeter equations; and the parameters β_{ab} and γ_a are chosen in such a way that the T matrix reproduces the ${}^3S_1$ and ${}^3D_1$ phase shifts in the energy region extending up to 500 MeV, the low-energy parameters of NN scattering, and the static properties of the deuteron like the binding energy and the quadrupole and the magnetic moment. For the nuclear parameters, we choose values at which the probability of the ${}^3D_1$-wave state in the deuteron is $P_2 = 4\%$.

The quasipotential vertex function, which is used in the ensuing calculations, was found as a solution to the homogeneous Bethe–Salpeter equation with the Blankenbecler–Sugar two-particle Green's function (6) and the separable nonrelativistic Graz-II potential. In our calculations, the parameters λ_{ab} were changed in relation to the corresponding parameters of the kernel in the Bethe–Salpeter equation. For the radial part $\tilde{g}_L$, we then obtain a result that is independent of the relative energy of the nucleons.

3. RELATIVISTIC IMPULSE APPROXIMATION

Let us consider the deuteron-photodisintegration reaction where, in the initial state, a real photon with a 4-momentum q^μ interacts with a deuteron whose 4-momentum is K. The reaction final state is determined by a neutron–proton (np) pair that is characterized by a total 4-momentum P and by the 4-momentum p of relative motion.

In the np c.m. frame, where $P_0^\mu = (\sqrt{s}, \mathbf{0})$ and $p^\mu = (0, \mathbf{p})$, with $\sqrt{s}$ being the total energy of the pair, the differential cross section for the scattering process in question can be represented as

$$\frac{d\sigma}{d\Omega_p} = \frac{\alpha}{16\pi s}\frac{|\,\mathbf{p}\,|}{\omega}\overline{|\,\varepsilon_\lambda^\nu \mathcal{M}_{fi,\nu}\,|^2}, \quad (16)$$

where $\alpha = e^2/(4\pi)$ is the fine-structure constant; $\mathcal{M}_{fi,\nu}$ is the invariant amplitude, which is equal to the matrix element $\mathcal{M}_{fi,\nu} = \langle f\,|\,\hat{J}_\nu\,|\,i\rangle$ of the electromagnetic-interaction operator $\hat{J}_\nu$ between the initial (deuteron) and the final (np pair) state of the two-nucleon system; ε_λ^μ is the photon polarization 4-vector; $\lambda = \pm 1$; and ω is the photon energy in the np c.m. frame. Since particle polarizations are not discussed here, it is assumed that the differential cross section is averaged over the spin states of the initial state and is summed over the spin states of the final state. In order to simplify the calculations, we choose a reference frame where the incident-photon momentum is aligned with the z axis; that is, $q^\mu = (\omega, 0, 0, \omega)$.

In analyzing experimental data, the differential cross section (16) is considered as a function of the incident-photon energy E_γ and the angle θ_p between the direction of the photon momentum and the direction of the scattered-proton momentum in the c.m. frame, where the 3-momentum of the relative motion of the nucleons, the photon energy, and the square of the energy of the np pair satisfy the kinematical relations

$$|\mathbf{p}| = \sqrt{\frac{s}{4} - m^2}, \quad \omega = \frac{s - M_d^2}{2\sqrt{s}}, \quad (17)$$

$$s = M_d^2 + 2E_\gamma M_d.$$

The invariant reaction amplitude $\mathcal{M}_{fi,\nu}$ is expressed in terms of the Bethe–Salpeter amplitudes for the initial [Eq. (4)] and the final [Eq. (2)] state as [29]

$$\mathcal{M}_{fi,\nu} = \int d^4k d^4l \bar{\chi}_{Sm_s}(l; pP)\Lambda_\nu(l, k; P, K)\psi_M(k; K), \quad (18)$$

where the np Bethe–Salpeter amplitude $\bar{\chi}_{Sm_s}$ is characterized by the total spin S ($S = 0, 1$) and by its projection m_s onto the z axis, the Bethe–Salpeter deuteron amplitude ψ_M is characterized by the spin projection M, and Λ_ν is the Mandelstam vertex specifying the electromagnetic interaction with the two-nucleon system.

In general, the amplitude in Eq. (18) must be analyzed with allowance for FSI, so that it is necessary to know the off-mass-shell T matrix [see Eq. (2)]. Moreover, the Mandelstam vertex involves the single and the two-particle component determining the contribution of binary processes to the scattering amplitude, $\Lambda_\nu = \Lambda_\nu^{[1]} + \Lambda_\nu^{[2]}$. Within the formalism developed here, the gauge invariance of the reaction amplitude, $q^\nu \mathcal{M}_{fi,\nu} = 0$, is ensured by fulfillment of the Ward–Takahashi identity for the Mandelstam vertex, provided that the Bethe–Salpeter amplitudes for the initial and for the final state satisfy the Bethe–Salpeter equation with the same kernel.

Presently, an analysis of the amplitude in the Bethe–Salpeter formalism with allowance for binary processes involves formidable difficulties of a mathematical and a computational character. For this reason, we restrict our consideration to approximations concerning the description of both the mechanism governing photon interaction with the NN system and the structure of the system in the continuous spectrum. Specifically, we assume that

(i) $\Lambda_\mu^{[2]} = 0$ (impulse approximation);

(ii) $T(p,k;P) = 0$ (plane-wave approximation).

Let us now discuss the quantities that appear in the matrix element (18).

Bethe–Salpeter amplitude for the continuous spectrum. According to the adopted approximations, the Bethe–Salpeter amplitude for the final state [np pair in the c.m. frame; see Eq. (2)], which is characterized by the 3-momentum $\mathbf{p}$ of relative motion, the energy $\sqrt{s}$, and the spin $S = 0, 1$ and its projection m_s, is determined by an antisymmetric combination of Dirac spinors; that is,

$$\chi^{(0)}_{Sm_s}(k_0, \mathbf{k}; \sqrt{s}\mathbf{p}) = \delta(k_0) \times \Big[\chi_{Sm_s}(\mathbf{p})(\eta_0 + \eta_1)\delta^{(3)}(\mathbf{k} - \mathbf{p}) + (-1)^{S+1} \times \chi_{Sm_s}(-\mathbf{p})(\eta_0 - \eta_1)\delta^{(3)}(\mathbf{k} + \mathbf{p})\Big], \quad (19)$$

where

$$\chi_{Sm_s}(\mathbf{p}) = (2\pi)^4 \sum_{\lambda_p, \lambda_n = \pm\frac{1}{2}} C^{Sm_s}_{\frac{1}{2}\lambda_p \frac{1}{2}\lambda_n} u_{\lambda_p}(\mathbf{p}) u_{\lambda_n}(-\mathbf{p})$$

and η_0 and η_1 are the isospin functions that correspond to the total-isospin values of $T = 0$ and $T = 1$, respectively. The Dirac spinors involved are normalized in the covariant way: $u^+u = 2E$.

Bethe–Salpeter amplitude for the discrete spectrum. The Bethe–Salpeter equation for the deuteron is solved numerically in the rest frame of the nucleus. The vertex function in the amplitude given by (18) is defined in a moving reference frame. Therefore, it is necessary to perform the inverse transformation. Let us specify the relevant Lorentz transformation. Under the adopted kinematical conditions, in which case the deuteron 3-momentum is $\mathbf{K} = -\mathbf{q}$ (that is, it is antiparallel to the z axis), the transformation to the moving reference frame is specified by the equations $K^\mu = \mathcal{L}^\mu_\nu K_0^\nu$ and $P^\mu = \mathcal{L}^\mu_\nu P_0^\nu$, where K_0^ν and P_0^ν are the momenta of, respectively, the deuteron and the np pair in their rest frame. The Lorentz transformation matrix $\mathcal{L}^\nu_\mu$ then has the form

$$\mathcal{L}^\nu_\mu = \begin{pmatrix} \sqrt{1+\eta} & 0 & 0 & -\sqrt{\eta} \\ 0 & 1 & 0 & 0 \\ 0 & 0 & 1 & 0 \\ -\sqrt{\eta} & 0 & 0 & \sqrt{1+\eta} \end{pmatrix}, \quad (20)$$

where the parameter η is defined as

$$\sqrt{\eta} = \frac{E_\gamma}{\sqrt{s}}, \quad \sqrt{1+\eta} = \frac{E_\gamma + M_d}{\sqrt{s}}.$$

Upon going over from the moving reference frame to the rest frame, the Bethe–Salpeter vertex function becomes

$$\Gamma_M(k;K) = \Lambda(\mathcal{L})\Gamma_M(\mathcal{L}^{-1}k; K_0), \quad (21)$$

where $\Lambda(\mathcal{L})$ is the operator that is responsible for the transformation of the spin components of the amplitude, $\Lambda(\mathcal{L}) = \Lambda^{(1)}(\mathcal{L})\Lambda^{(2)}(\mathcal{L})$. Here, we have

$$\Lambda^{(l)}(\mathcal{L}) = \left(\frac{1+\sqrt{1+\eta}}{2}\right)^{1/2} \left(1 + \frac{\gamma_0\gamma_3\sqrt{\eta}}{1+\sqrt{1+\eta}}\right)^{(l)}. \quad (22)$$

From the value of the parameter η, we can deduce information about the magnitude of boost effects, which is determined by changes in the dynamical and spin degrees of freedom. From Eq. (21), it can be seen that both the 4-momentum of the relative motion and the nucleon spin degrees of freedom undergo changes under the boost transformation.

For $\eta \to 0$, the matrix given by (20) and the operator given by (22) tend to the identity matrix and the identity operator, respectively, $\mathcal{L} \to I$ and $\Lambda \to I$. This corresponds to the static limit for the Bethe–Salpeter amplitude and occurs at the photodisintegration threshold, because we have $E_\gamma/M_d \ll 1$ in this case [see Eq. (17)].

Electromagnetic-interaction vertex. Let us now consider the Mandelstam vertex. The single-particle contribution to the total vertex has the form

$$\Lambda^{[1]}_\nu(p,k,P,K) = i(2\pi)^4\delta^{(4)}\left(\frac{q}{2} + k - p\right)\Gamma^{(1)}_\nu(q)S^{(2)}\left(\frac{P}{2} - p\right)^{-1} + i(2\pi)^4\delta^{(4)}\left(\frac{q}{2} - k + p\right)\Gamma^{(2)}_\nu(q)S^{(1)}\left(\frac{P}{2} + p\right)^{-1}, \quad (23)$$

where $\Gamma^{(l)}_\nu$ is the off-mass-shell γNN vertex for the lth nucleon and $S^{(l)}(p)$ is the corresponding exact propagator. Calculation of the function Γ_ν off the mass shell, as well as calculation of the propagator $S(p)$, is a problem in itself, since such a calculation requires invoking specific field-theoretical models of

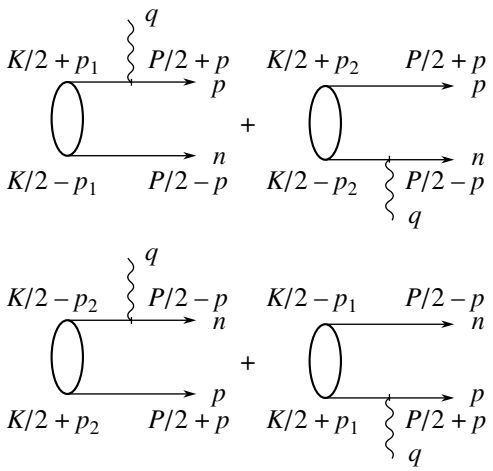

Fig. 1. Deuteron-photodisintegration diagrams corresponding to the plane-wave impulse approximation.

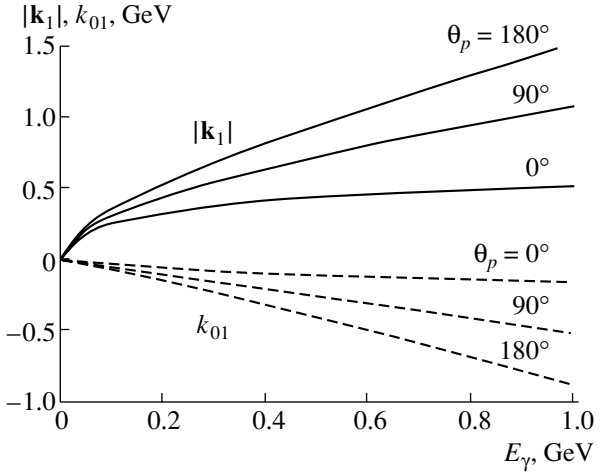

Fig. 2. Absolute value $|\mathbf{k}_1|$ of the relative three momentum (solid curves) and relative energy k_{01} (dashed curves) of the nucleons in the deuteron versus the photon energy E_γ at various proton emission angles θ_p.

the nucleon [41]. In determining the Bethe–Salpeter amplitude for the NN system, we discarded the contribution of self-energy corrections in the Bethe–Salpeter equation. We can then take the electromagnetic vertex for the nucleon on the mass shell [29]:

$$\Gamma_\nu^{(l)}(q) = \gamma_\nu \left(F_1^{(s)}(q) + \tau_3^{(l)} F^{(v)}(q)\right) + \frac{i}{2m}\sigma_{\nu\mu}q^\mu \left(F_2^{(s)}(q) + \tau_3^{(l)} F_2^{(v)}(q)\right). \quad (24)$$

Here, $F_{1(2)}^{(s)}(q)$ and $F_{1(2)}^{(v)}$ are, respectively, the isoscalar and the isovector Pauli–Dirac form factors for the nucleon that are normalized as follows: $F_1^{(s)}(0) = 1/2$, $F_2^{(s)}(0) = (\kappa_p + \kappa_n)/2$, $F_1^{(v)}(0) = 1/2$, and $F_2^{(v)}(0) = (\kappa_p - \kappa_n)/2$, where $\kappa_{p,n}$ are the anomalous parts of the proton and the neutron magnetic moment, respectively.

Substituting (19), (21), and (23) into expression (18) and performing integration, we obtain

$$\mathcal{M}_{fi,\nu} = \frac{i}{16\pi^4}\sum_{l=1,2}\bar{\chi}_{Sm_s}^{(0)}(0,\mathbf{p};\sqrt{s}\mathbf{p})\Gamma_\mu^{(l)}(q^2=0) \times\Lambda(\mathcal{L})S^{(l)}(k;K_0)\Gamma_M(k_{0l},\mathbf{k}_l;K_0), \quad (25)$$

where $k_l = \mathcal{L}^{-1}(p + (-1)^l q/2)$. Summation in (25) is performed over the nucleons in the deuteron. The corresponding contributions are represented by the diagrams in Fig. 1.

We would like to highlight an important circumstance that follows from expression (25). First, the relevant matrix element in the plane-wave impulse approximation is proportional, as might have been expected, to the Bethe–Salpeter vertex function taken at specific values of the relative energy k_{0l} and the nucleon 3-momentum $\mathbf{k}_l$. Second, k_{0l} and $\mathbf{k}_l$ depend on the boost-transformation parameter η. By way of example, we indicate that, for the 4-momentum of the first nucleon (proton), we have

$$k_{01} = \sqrt{\eta}\,|\mathbf{p}_{||}| - (\sqrt{\eta} + \sqrt{1+\eta})\,\frac{\omega}{2}, \quad \mathbf{k}_{\perp 1} = \mathbf{p}_\perp, \quad \omega = M_d\sqrt{\eta}, \quad \mathbf{k}_{||1} = \sqrt{1+\eta}\,\mathbf{p}_{||} - (\sqrt{\eta} + \sqrt{1+\eta})\,\frac{\mathbf{q}}{2}, \quad (26)$$

where the symbols $||$ and $\perp$ in the subscripts label, respectively, the longitudinal and the transvese component of a vector with respect to the direction of the photon momentum $\mathbf{q}$. The relative energy and the modulus of the proton momentum in the deuteron at a fixed scattering angle are displayed in Fig. 2 versus the incident-photon energy. It should be emphasized that, according to (26), the relative energy k_{01} can take negative values at some specific values of the photon energy.

For the ensuing calculations, it is convenient to represent expression (25) in a matrix form. Technical details of the procedure can be found in [42]. The reaction amplitude $\mathcal{M}_{fi,\nu}$ can then be represented as the sum of four traces:

$$\mathcal{M}_{fi,\nu} = -\mathrm{tr}\left(\bar{\chi}_{Sm_s}(\mathbf{p})\Gamma_{p,\nu}S\left(\frac{K_0}{2} + k_1; K_0\right) \times\Gamma_M(k_1;K_0)\Lambda(\mathcal{L}^{-1})\right) -\mathrm{tr}\left(\bar{\chi}_{Sm_s}(\mathbf{p})\Gamma_M(k_2;K_0)\tilde{S}\left(\frac{K_0}{2} - k_2; K_0\right)\Lambda(\mathcal{L}^{-1})\Gamma_{n,\nu}\right) +(-1)^S\mathrm{tr}\left(\bar{\chi}_{Sm_s}(-\mathbf{p})\Gamma_{n,\nu}\Lambda(\mathcal{L})S\left(\frac{K_0}{2}\right.\right. \quad (27)$$

$$+k_1;K_0)\,\Gamma_M(-k_1;K_0)\Lambda(\mathcal{L}^{-1})\big)$$
$$+(-1)^S\mathrm{tr}\left(\bar{\chi}_{Sm_s}(-\mathbf{p})\Gamma_M(-k_2;K_0)\right.$$
$$\left.\times\tilde{S}\left(\frac{K_0}{2}-k_2;K_0\right)\Lambda(\mathcal{L}^{-1})\Gamma_{p,\nu}\right).$$

The quantities appearing in (27) are determined by relevant matrix expressions. For example, the Bethe–Salpeter vertex functions for positive-energy states are given by (9), while the Bethe–Salpeter amplitudes for the final state can be represented as

$$\bar{\chi}_{1m_s}(\mathbf{p})=\frac{1}{2\sqrt{2}(m+E_{\mathbf{p}})}$$
$$\times(m-\hat{p}_2)\hat{\xi}^*_{m_s}(1+\gamma_0)(m+\hat{p}_1),$$
$$\bar{\chi}_{00}(\mathbf{p})=\frac{1}{2\sqrt{2}(m+E_{\mathbf{p}})} \qquad (28)$$
$$\times(m-\hat{p}_2)\gamma_5(1+\gamma_0)(m+\hat{p}_1)$$

(for the spin values of $S=1$, 0, respectively), where ξ_{m_s} is the vector-particle polarization 4-vector, which satisfies the conditions of completeness and orthonormality,

$$\sum_{m_s=-1}^{+1}\xi^{\mu}_{m_s}\xi^{\nu *}_{m_s}=-g^{\mu\nu}+\frac{P^{\mu}P^{\nu}}{s},\qquad \xi_{\nu}P^{\nu}=0, \qquad (29)$$

while the normalization factors $\mathcal{N}_{\mathbf{p}}$ and the vectors $p_{1,2}$ are defined in Eq. (9).

For the real photon, the electromagnetic vertex for the proton, $\Gamma_{p,\nu}$, and the electromagnetic vertex for the neutron, $\Gamma_{n,\nu}$, are given by

$$\Gamma_{p,\nu}=\gamma_{\nu}+\frac{i\kappa_p}{2m}\sigma_{\nu\mu}q^{\mu},\qquad \Gamma_{n,\nu}=\frac{i\kappa_n}{2m}\sigma_{\nu\mu}q^{\mu}. \qquad (30)$$

The nucleon propagator in expression (27) has the form

$$\tilde{S}(k)=\frac{\hat{k}-m}{k^2-m^2+i\epsilon} \qquad (31)$$

and is related to the propagator S by the equation $\tilde{S}=C^{-1}S^TC$, where $C=i\gamma^2\gamma^0$.

By using expression (27), we find that the square of the modulus of $\varepsilon^{\nu}\mathcal{M}_{fi,\nu}$ can be represented as

$$|\,\varepsilon^{\nu}_{\lambda}\mathcal{M}_{fi,\nu}\,|^2=4\left(\frac{1+\sqrt{1+\eta}}{2}\right)^2$$
$$\times\sum_{S=0,1}\left(|\,X^S_0\,|^2+2\alpha\mathrm{Re}(X^S_0X^{S*}_1)\right. \qquad (32)$$
$$+\alpha^2\left(|\,X^S_1\,|^2-2Re(X^S_0X^{S*}_2)\right)$$
$$\left.-2\alpha^3\mathrm{Re}(X^S_1X^{S*}_2)+\alpha^4\,|\,X^S_2\,|^2\right).$$

Here, $\alpha=\sqrt{\eta}/(1+\sqrt{1+\eta})$ and the amplitudes X^S_i $(i=0,1,2)$ are given by

$$X^S_0=\mathrm{tr}\left(\bar{\chi}_{Sm_s}(\mathbf{p})\,\varepsilon^{\nu}_{\lambda}\Gamma_{p,\nu}\,S(s_1;K_0)\Gamma_M(k_1;K_0)\right)$$
$$+\text{ neutron},$$
$$X^S_1$$
$$=\mathrm{tr}\left(\bar{\chi}_{Sm_s}(\mathbf{p})\,\varepsilon^{\nu}_{\lambda}\Gamma_{p,\nu}\,\gamma_0\hat{n}_3S(s_1;K_0)\Gamma_M(k_1;K_0)\right) \qquad (33)$$
$$-\mathrm{tr}\left(\bar{\chi}_{Sm_s}(\mathbf{p})\,\varepsilon^{\nu}_{\lambda}\Gamma_{p,\nu}\,S(s_1;K_0)\Gamma_M(k_1;K_0)\gamma_0\hat{n}_3\right)$$
$$+\text{ neutron},$$
$$X^S_2=\mathrm{tr}\left(\bar{\chi}_{Sm_s}(\mathbf{p})\,\varepsilon^{\nu}_{\lambda}\Gamma_{p,\nu}\,\gamma_0\hat{n}_3S(s_1;K_0)\right.$$
$$\left.\times\Gamma_M(k_1;K_0)\gamma_0\hat{n}_3\right)+\text{ neutron},$$

where $n_3=(0,0,0,1)$ is a unit vector and $s_1=K_0/2-k_1$.

These are the most general expressions used below to analyze various contributions from relativistic effects to the differential cross section (16). In performing summation over the polarizations of the particles involved in the reaction being considered, we have made use of the completeness conditions for the deuteron and nucleon polarization vectors [Eqs. (10) and (29), respectively]. In averaging over the photon polarization states, we have employed the Coulomb gauge ($\varepsilon^0=0$, $\boldsymbol{\varepsilon}\cdot\mathbf{q}=0$), in which the completeness condition has the form

$$\sum_{\lambda=\pm1}(\varepsilon_{\lambda})^*_i(\varepsilon_{\lambda})_j=\delta_{ij}-\frac{q_iq_j}{\mathbf{q}^2},\quad i,j=x,y. \qquad (34)$$

4. RESULTS AND DISCUSSION

In Figs. 3 and 4, the calculated differential cross section for deuteron photodisintegration is presented as a function of the proton emission angle θ_p at various values of the incident-photon energy E_{γ}. In order to draw definitive conclusions on the relative importance of relativistic effects, we have performed calculations (i) within the nonrelativistic model (without MECs and FSI) by using the deuteron wave functions computed for the Bonn and the Paris potential and the operator of electromagnetic-current density for nucleons in the form

$$\hat{\mathbf{J}}(\mathbf{x})=\sum_{l=1,2}\frac{F^{(s)}_1+\tau^{(l)}_zF^{(v)}_1}{2}$$
$$\times[\delta^{(3)}(\mathbf{x}-\mathbf{r}_l)\frac{\hat{\mathbf{p}}_l}{2m}+\frac{\hat{\mathbf{p}}_l}{2m}\delta^{(3)}(\mathbf{x}-\mathbf{r}_l)] \qquad (35)$$
$$+\mathrm{curl}\left[\sum_{l=1,2}\frac{G^{(s)}_M+\tau^{(l)}_zG^{(v)}_M}{2}\delta^{(3)}(\mathbf{x}-\mathbf{r}_l)\frac{\boldsymbol{\sigma}_l}{2m}\right],$$

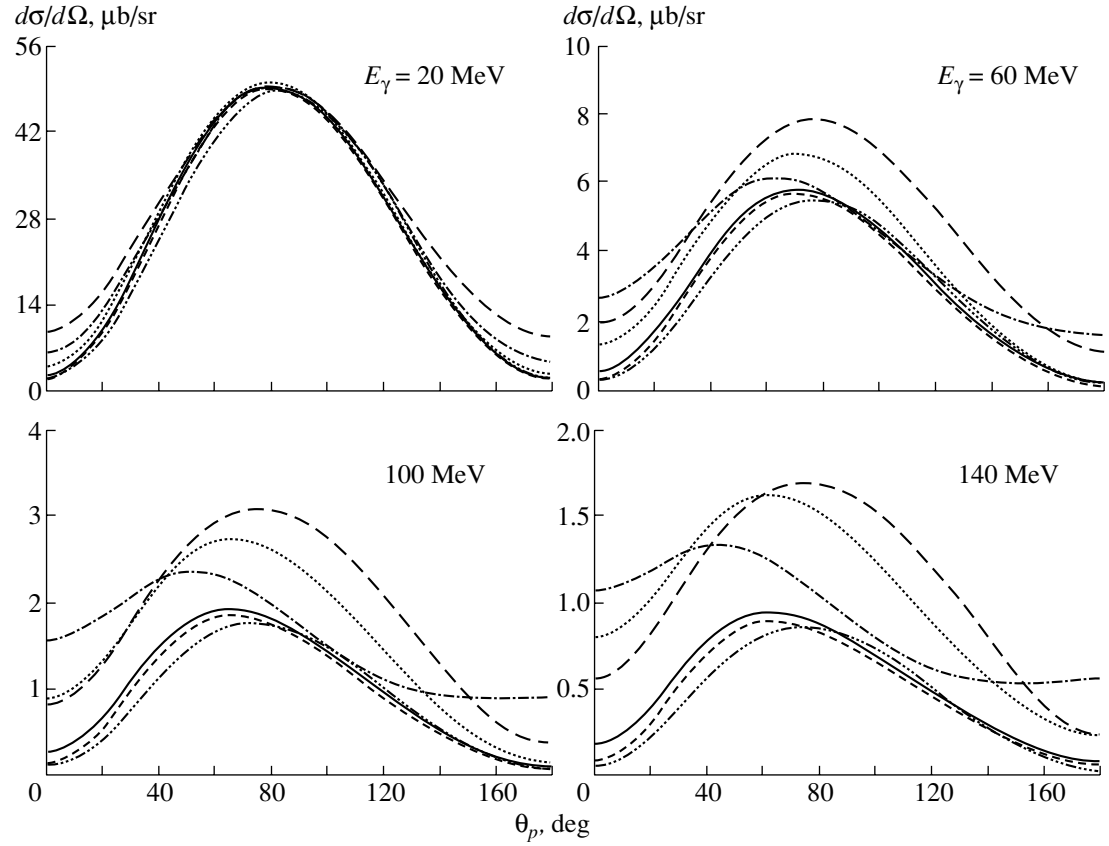

Fig. 3. Differential cross section for deuteron photodisintegration at various values of the photon energy: (dotted and dash-dotted curves) results of the calculations in the nonrelativistic model with the wave functions for the Bonn and the Paris potential, respectively; (solid curve) results of the calculations within the Bethe–Salpeter formalism; (long dashes) results of the calculations in the quasipotential approximation; (dash-and-three-dot curves) results of the calculations in the static approximation of the Bethe–Salpeter formalism; and (short dashes) results of the calculations within the Bethe–Salpeter formalism for scalar nucleons.

where $\hat{\mathbf{p}}_l = -i\partial/\partial\mathbf{r}_i$ and $G_M^{(s)}$ and $G_M^{(v)}$ are, respectively, the isoscalar and the isovector Stokes form factor; (ii) within the quasipotential approximation by using expressions (32) and (33), where the radial Bethe–Salpeter vertex functions for the ++ partial-wave channels were identified, according to the condition in (14), with the corresponding quasipotential vertex functions representing solutions to the Bethe–Salpeter equation with the Blankenbecler–Sugar propagator (6) and with Gratz-II separable nonrelativistic potential [this approximation corresponds to constraining the relative energy of the nucleons by the conditions $k_{01} = 0$ and $k_{02} = 0$ in the radial vertex function g_L for the deuterons and by the conditions $M_d/2 - k_{01} = E_{\mathbf{k}_1}$ and $M_d/2 + k_{02} = E_{\mathbf{k}_2}$ in the nucleon propagator $S(k; K_0)$]; and (iii) within the Bethe–Salpeter formalism, where the computations in terms of the Bethe–Salpeter amplitudes invoke expressions (32) and (33) and the $^3S_1^{++}$ and $^3D_1^{++}$ states.

Moreover, we have performed additional investigations aimed at isolating contributions from relativistic effects. By way of example, we have explored, within the Bethe–Salpeter formalism, the role of the effect associated with the boost transformation of the deuteron vertex function. For this purpose, we have used (i) the static approximation that amounts to completely ignoring the transformations associated with the boost operation in the matrix element (25) [this is achieved by imposing the condition $g_L(k_{0l}, \mathbf{k}_l)|_{\eta=0} = g_L(p_{0l}, \mathbf{p}_l)$, where $p_{0l} = (-1)^l\omega/2$ and $\mathbf{p}_l = \mathbf{p} + (-1)^l\omega/2$ $(l = 1, 2)$] and in the Lorentz transformation operator (22) [this corresponds to setting $\Lambda(\mathcal{L})|_{\eta=0} = I$] and (ii) the approximation of scalar nucleons. The results obtained within the latter, where the effect of the boost transformation is determined exclusively by the change in the dynamical variables $k_l = \mathcal{L}(p + (-1)^l q/2)$, having no connections with the transformation of the spinor structure of the Bethe–Salpeter amplitudes, are compared with the results in the static approximation.

Such a comparison makes it possible to reveal the role of the spin degrees of freedom.

Figure 3 shows the calculated differential cross section for deuteron photodisintegration at low energies. Let us consider this cross section at the photon energy of $E_\gamma = 20$ MeV. From the figure, we can see that, for proton emission angles in the range $\theta_p = 60°–100°$, the curves obtained within the different models considered here behave almost identically. Deviations are observed only at angles close to 0° and 180°. This is due to the variations in the probability of the $^3D_1$-wave state in the deuteron. It should be noted that a nearly perfect $\sin^2\theta_p$ behavior of the cross section is reproduced in this case.

As soon as the photon energy reaches the value of $E_\gamma = 60$ MeV, there appear, however, noticeable distinctions between the curves. First of all, we can see a decrease in the differential-cross-section values over the entire range of the angles θ_p. The maxima are shifted toward the value of $\theta_p = 70°$. In this kinematical region, the values of the differential cross section calculated within the Bethe–Salpeter formalism differ significantly from the results of the nonrelativistic calculations with the Paris and the Bonn potential. Figure 3 shows that the role of the boost effect is still insignificant here. The results in the quasipotential approximation considerably exceed those obtained in the Bethe–Salpeter approach, but the two approaches yield similar dynamical patterns. This distinction is due to the explicit dependence of the Bethe–Salpeter vertex function on the relative energy k_0.

At $E_\gamma = 100$ MeV, the differential cross sections are still smaller. Here, we can see a strong dependence of the results of the calculations on the choice of potential model. The distinctions between the results of the relativistic calculations within the Bethe–Salpeter formalism and the results of the calculations in the nonrelativistic models become more pronounced. At the photon energy of $E_\gamma =$ 140 MeV, these distinctions are still greater. The curves computed in the quasipotential approximation lie much higher than those representing the results in the Bethe–Salpeter approach. As before, boost effects are insignificant.

Figure 4 presents the calculated differential cross section at intermediate and high photon energies. It can be seen that, as the incident-photon energy is increased, the differential cross section as obtained on the basis of the Bethe–Salpeter formalism tends to be nearly isotropic. The curves computed within the nonrelativistic models show a dip in the angular region $\theta_p = 80°–120°$. For this reason, the corresponding cross sections for forward and backward scattering considerably exceed values obtained from

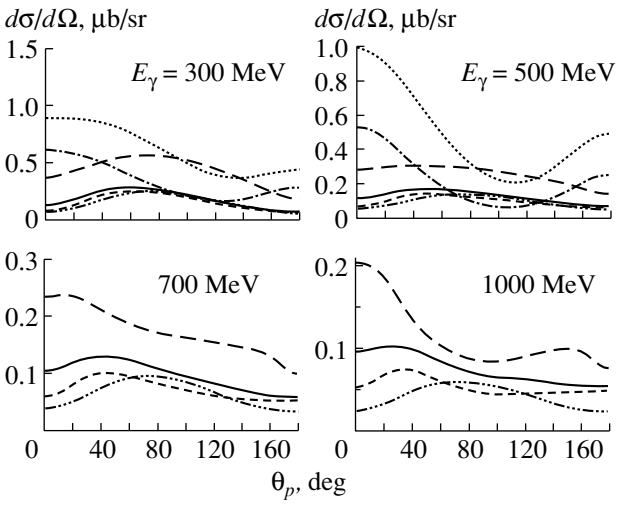

Fig. 4. As in Fig. 3, but for intermediate and high photon energies.

a relativistic analysis. This is because the approach based on nonrelativistic physics is incorrect at high energies, which are beyond its applicability range [1].

Up to energies of $E_\gamma = 500$ MeV, the behavior of the differential cross section in the quasipotential approximation nearly reproduces the behavior of the cross section within the Bethe–Salpeter formalism. However, there appear distinctions above this energy value. The role of boost effects associated with dynamical variables and with spinor structures becomes more pronounced with increasing photon energy, especially for forward scattering.

Let us now discuss the ratio of the differential cross sections at different values of the proton emission angle θ_p (see Fig. 5). Specifically, we consider the ratio $d\sigma(0°)/d\sigma(90°)$. It can be seen that this ratio is rather sensitive to the choice of potential model. For example, the results of the calculations performed with the Bonn and the Paris potential differ significantly in magnitude. Moreover, the behavior of the curves computed in the potential models differs qualitatively from the behavior of the curves obtained within the Bethe–Salpeter formalism and the quasipotential approach. This is because the ratio in question is sensitive to the contribution of relativistic effects, which become sizable here at photon energies as low as 150 MeV. The distinctions between the curves obtained within the relativistic approaches become more pronounced with increasing energy.

Figure 5 also shows the calculated ratio of the cross section for forward ($\theta_p = 0°$) and backward ($\theta_p = 180°$) scattering. We would like to emphasize that the relativistic approaches lead to a maximum in this ratio at $E_\gamma = 120$ MeV. A similar maximum, which is shifted, however, to the region of higher

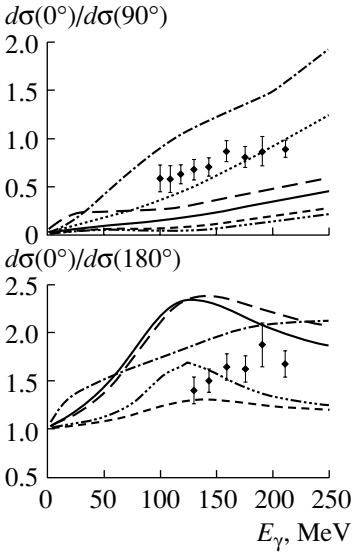

Fig. 5. Ratio of the differential cross section for forward scattering to the differential cross sections for scattering at the angles of 90° and 180°. The experimental data were borrowed from [43]. The notation for the curves is identical to that in Fig. 3.

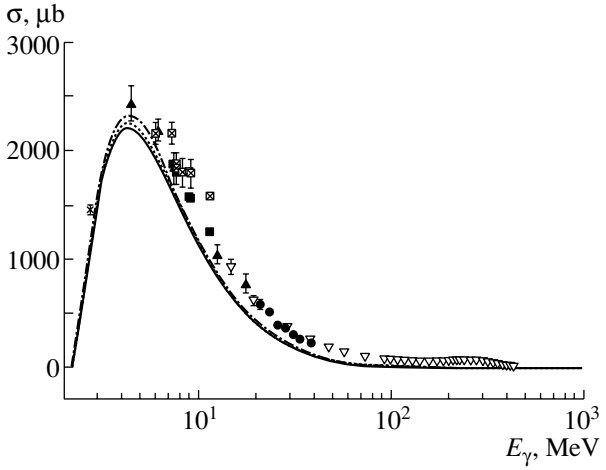

Fig. 6. Experimental data on the total cross section for deuteron photodisintegration from [1, 43] (points), along with the results of various theoretical calculations (curves): (solid curve) results of the calculations within the Bethe–Salpeter formalism and (dotted and dash-dotted curves) results of the calculations within the nonrelativistic model with the wave functions for the Paris and the Bonn potential, respectively.

energies, is observed in experimental data. The boost effect is pronounced almost over the entire kinematical region of photon energies that is considered here.

Figure 6 shows the calculated total differential cross section for deuteron photodisintegration. It can be seen that, with increasing incident-photon energy, this cross section first increases sharply to a maximum in the region around $E_\gamma = 4$ MeV and then decreases fast, approaching a plateau in the region $E_\gamma = 100$–1000 MeV. From the figure, we can see that the theoretical curves are below experimental data almost over the entire kinematical region. This underestimation is due to the disregard of two-body and FSI effects. In addition to including these disregarded effects, it is also necessary, for rendering calculations within the Bethe–Salpeter formalism viable at high energies, to use the Bethe–Salpeter amplitude obtained as a solution to the Bethe–Salpeter equation with the kernel whose parameters are determined from a partial-wave analysis of NN scattering at higher energies.

5. CONCLUSIONS

A relativistically covariant analysis of the deuteron-photodisintegration reaction has been performed on the basis of the Bethe–Salpeter equation. The results obtained within this approach have been compared with those computed within the phenomenological potential model and within the quasipotential approximation. Owing to this, we have been able to reveal the role of various relativistic effects, including relativistic kinematics, the dynamics of NN interaction, and the boost effect on the dynamical and spin degrees of freedom of the Bethe–Salpeter amplitude in the angular distributions versus the photon energy have led to the following conclusions:

The results of our analysis have led to the following conclusions:

(i) Phenomenological potential models are inapplicable at high photon energies E_γ, since they predict an incorrect behavior of the differential cross section. In contrast to these models, the quasipotential approximation yields cross sections that agree with the results of other relativistic approaches and which ensure a correct form of the angular distributions (see, for example [1, 19]).

(ii) The Bethe–Salpeter approach makes it possible to take into account, in the most general way, the Lorentz invariance of the reaction amplitudes and the relativistic dynamical structure of two-nucleon systems. A feature peculiar to this formalism is that the amplitude for the NN system depends on the relative energy k_{0l} of bound nucleons. In the impulse approximation, this dependence is manifest in the reaction amplitude. In our opinion, this makes it possible to study recoil effects associated with energy transfer from the incident photon to one of the deuteron nucleons.

(iii) The role of the boost effects becomes more pronounced with increasing incident-photon energy and is of greatest importance for forward scattering.

(iv) At high energies (in excess of 500 MeV), the results greatly depend on the choice of model. This suggests that calculations in this kinematical region must be performed more carefully—above all, they must employ more realistic Bethe–Salpeter amplitudes and wave functions whose determination is directly associated with constructing a more realistic interaction kernel that is applicable in this energy region.

We deem that it is important to perform further computations within the Bethe–Salpeter formalism with allowance for FSI and binary processes, since this will make it possible to draw a comparison with experimental data. In this respect, our calculations are of a purely methodological character.

ACKNOWLEDGMENTS

We are grateful to V.V. Burov, S.G. Bondarenko, Yu.M. Bystritsky, A.A. Goi, A.V. Molochkov, and A.V. Shebeko for stimulating discussions.

REFERENCES

1. H. Arenhövel and M. Sanzone, Few-Body Syst., Suppl. **3**, 1 (1991).
2. D. Babusci *et al.,* Nucl. Phys. A **633**, 683 (1998).
3. F. Adamain *et al.,* in *Abstracts of XI Particle and Nuclei International Conference, Uppsala, Sweden, 1999,* p. 93.
4. H. Ejiri, private communication (*XIV International Seminar on High Energy Physics Problems, Dubna, 1998*).
5. J. E. Belz *et al.,* Phys. Rev. Lett. **74**, 646 (1995).
6. C. Bocha *et al.,* nucl-ex/9808001.
7. R. Crawford *et al.,* Nucl. Phys. Electronic. npa603-303.
8. E. Kazes, T. E. Feuchtwang, P. H. Cutler, and H. Grotch, Ann. Phys. (N.Y.) **142**, 80 (1982).
9. V. V. Burov, S. M. Dorkin, A. Yu. Korchin, *et al.,* Yad. Fiz. **59**, 822 (1996) [Phys. At. Nucl. **59**, 784 (1996)].
10. E. E. Salpeter and H. A. Bethe, Phys. Rev. **84**, 1232 (1951).
11. S. Mandelstam, Proc. R. Soc. London, Ser. A **233**, 248 (1955).
12. N. Nakanishi, Prog. Theor. Phys. Suppl. **43**, 1 (1969).
13. M-T. Noda, N. Nakanishi, and N. Seto, Prog. Theor. Phys. Suppl. **95**, 78 (1988).
14. A. A. Logunov and A. N. Tavkhelidze, Nuovo Cimento **29**, 370 (1963).
15. V. G. Kadyshevsky, Nucl. Phys. B **6**, 125 (1968).
16. J. Adam, Jr., J. W. van Orden, and F. Gross, Nucl. Phys. A **640**, 391 (1998).
17. G. E. Brown and A. D. Jackson, *The Nucleon-Nucleon Interaction* (North-Holland, Amsterdam, 1976; Atomizdat, Moscow, 1979).
18. J. Carbonell, B. Desplanques, V. A. Karmanov, and J. F. Mathoit, Phys. Rep. **300**, 215 (1998).
19. A. E. L. Dieperink and S. I. Nagorny, Phys. Lett. B **456**, 9 (1999).
20. V. V. Anisovich, M. N. Kobrinsky, D. I. Melikhov, and A. V. Sarantsev, Nucl. Phys. A **544**, 747 (1992).
21. A. V. Anisovich and V. A. Sadovnikova, Yad. Fiz. **59**, 648 (1996) [Phys. At. Nucl. **59**, 616 (1996)].
22. A. V. Anisovich and V. A. Sadovnikova, Eur. Phys. J. A **2**, 199 (1998).
23. M. J. Zuilhof and J. A. Tjon, Phys. Rev. C **22**, 2369 (1980).
24. L. P. Kaptari, B. Kampfer, S. M. Dorkin, and S. S. Semikh, Phys. Rev. C **57**, 1097 (1998).
25. A. Yu. Umnikov, F. C. Khanna, K. Yu. Kazakov, and L. P. Kaptari, Phys. Lett. B **334**, 163 (1994).
26. C. Ciofi degli Atti, L. P. Kaptari, and S. Scopetta, Eur. Phys. J. A **5**, 191 (1999).
27. N. Honzawa and S. Ishida, Phys. Rev. C **45**, 47 (1992).
28. L. P. Kaptari *et al.,* Phys. Rev. C **54**, 986 (1996).
29. A. Yu. Korchin and A. V. Shebeko, Preprint No. 88-56, KhFTI (Institute of Physics and Technology, Kharkov, 1988); Yad. Fiz. **54**, 357 (1991) [Sov. J. Nucl. Phys. **54**, 214 (1991)].
30. G. Rupp and J. A. Tjon, Phys. Rev. C **41**, 472 (1990).
31. W. Jaus and W. S. Woolcock, Helv. Phys. Acta **57**, 644 (1984).
32. N. Nakanishi, *Graph Theory and Feynman Integral* (Gordon and Breach, New York, 1971).
33. K. Kusaka, K. M. Simpson, and A. G. Williams, Phys. Rev. D **56**, 5071 (1997).
34. G. Rupp and J. A. Tjon, Phys. Rev. C **45**, 2133 (1992).
35. K. Schwarz, J. Haidenbauer, and J. Fröhlich, Phys. Rev. C **33**, 456 (1986).
36. K. Schwarz *et al.,* Acta Phys. Austriaca **53**, 191 (1981).
37. G. Rupp and J. A. Tjon, Phys. Rev. C **37**, 1729 (1988).
38. S. G. Bondarenko, V. V. Burov, and S. M. Dorkin, in *Proceedings of XII International Seminar on High Energy Physics Problems,* Ed. by A. M. Baldin and V. V. Burov. (Ob'edin. Inst. Yad. Issled., Dubna, 1994), p. 227.
39. J. J. Kubis, Phys. Rev. D **45**, 47 (1992).
40. G. Rupp, Nucl. Phys. A **508**, 131 (1990).
41. J. W. Bos and J. H. Koch, Nucl. Phys. A **563**, 539 (1993).
42. S. G. Bondarenko, V. V. Burov, M. Beyer, and S. M. Dorkin, Phys. Rev. C **58**, 3143 (1998).
43. H. Levi Sandri *et al.,* Phys. Rev. C **39**, 1247 (1989).

Translated by A. Isaakyan

Physics of Atomic Nuclei, Vol. 64, No. 5, 2001, pp. 882–890. Translated from Yadernaya Fizika, Vol. 64, No. 5, 2001, pp. 948–957.

NUCLEI
Theory

Parity Nonconservation in the Circular Polarization of Primary Photons of the Radiation Accompanying Electron Conversion in the $5/2^- \to 5/2^+$ Nuclear Transition in the $^{229}Pa_{91}$ Nucleus

D. P. Grechukhin[†] **and A. V. Lomonosov**[*]

Russian Research Centre Kurchatov Institute, pl. Kurchatova 1, Moscow, 123182 Russia

Received October 1, 1999; in final form, January 24, 2000

Abstract—The ground state of $^{229}Pa_{91}$ is a $5/2^{\pm}$ doublet, with the splitting energy being 220 ± 50 eV. A direct observation of P-odd effects in this system is of great interest, since this may furnish information about the parity-nonconserving effective one-nucleon potential. Since a transition between two opposite-parity doublet states is accompanied by a strong conversion, it is possible to study P-odd mixing by exploring the conversion-electron helicity and the circular polarization $\mathcal{P}_\gamma$ of the lines of atomic radiation that arises upon the filling of a hole in the $6s_{1/2}$, $6p_{1/2}$, and $6p_{3/2}$ shells of the $^{229}Pa_{91}$ atom. Since $\mathcal{P}_\gamma$ is about 3–5% for individual atomic transitions, experiments aimed at observing parity-nonconservation effects on this basis are feasible. © *2001 MAIK "Nauka/Interperiodica".*

1. INTRODUCTION

The present article completes the series of publications [1–3] reporting on our investigation into the parity-nonconservation effect in the $5/2^- \to 5/2^+$ conversion transition in the $^{229}Pa_{91}$ nucleus, whose ground state appears to be a system of two opposite-parity ($\pm$) $I = 5/2$ states—that is, a doublet split in energy by $\Delta E = 220 \pm 50$ eV owing to the quasi-crossing of proton orbitals in the strongly deformed $^{229}Pa_{91}$ nucleus [4].

Of greatest interest are experiments that reveal effects linear in the Fermi weak-coupling constant G_F—for example, the helicity of conversion electrons in a multipole-order-mixed nuclear transition[1)] or the circular polarization of primary photons from atomic radiation accompanying this transition. Here, we analyze the possibility of implementing an experiment aimed at observing this circular polarization.

The doublet of states in the $^{229}Pa_{91}$ nucleus is interpreted here as the $[523]5/2,-,5/2$ and $[642]5/2,+,5/2$ single-particle proton orbitals (the classification of orbits according to Nilsson [5] is $[Nn_Z\Lambda]\Omega,\Pi,I$). The strongly deformed nucleus $^{229}Pa_{91}$ is described within the generalized model proposed in [6]. The nucleon functions were obtained in a deformed-nucleus potential of the Woods–Saxon form and, as a check upon the results, in the deformed nuclear oscillator potential from [5]. The details of the calculations can be found in [1].

The parity-nonconserving weak-interaction potential $\hat{V}^N_{\rm PNC}$ leads to the mixing of these states:

$$\left|\widetilde{\frac{5}{2}^-}\right\rangle = \left|[523]\frac{5}{2},-,\frac{5}{2}\right\rangle + ib\left|[642]\frac{5}{2},+,\frac{5}{2}\right\rangle,$$
$$\left|\widetilde{\frac{5}{2}^+}\right\rangle = \left|[642]\frac{5}{2},+,\frac{5}{2}\right\rangle + ib\left|[523]\frac{5}{2},-,\frac{5}{2}\right\rangle. \quad (1)$$

Here, b is a coefficient that characterizes the admixture of the opposite-parity state and which is given by

$$ib = \frac{\langle[642]\frac{5}{2},+,\frac{5}{2}|\hat{V}^N_{\rm PNC}|[523]\frac{5}{2},-,\frac{5}{2}\rangle}{\Delta E}. \quad (2)$$

The phases of the wave functions are chosen in such a way that these matrix elements are pure imaginary quantities:

$$\left\langle[523]\frac{5}{2},-,\frac{5}{2}\right|\hat{V}^N_{\rm PNC}\left|[642]\frac{5}{2},+,\frac{5}{2}\right\rangle^*$$
$$= -\left\langle[523]\frac{5}{2},-,\frac{5}{2}\right|\hat{V}^N_{\rm PNC}\left|[642]\frac{5}{2},+,\frac{5}{2}\right\rangle. \quad (3)$$

The Hermitian effective-potential operator that acts on an intranuclear nucleon (proton) and which violates parity has the form [7]

$$\hat{V}^N_{\rm PNC}(\mathbf{R},\hat{\mathbf{p}},\hat{\boldsymbol{\sigma}}) \quad (4)$$
$$= \frac{G_F}{2m_pc}\alpha(N,Z)\{(\hat{\boldsymbol{\sigma}}\cdot\hat{\mathbf{p}})\rho(\mathbf{R}) + \rho(\mathbf{R})(\hat{\boldsymbol{\sigma}}\cdot\hat{\mathbf{p}})\},$$

[†] Deceased.

[*] e-mail: lomon@cerber.mbslab.kiae.ru

[1)] This effect was previously estimated in [3].

where $G_F = 10^{-5}\hbar^3/m_p^2 c$ is weak-coupling constant, m_p is the proton mass, $\hat{\mathbf{p}}$ is the nucleon-momentum operator, $\hat{\boldsymbol{\sigma}}$ is the nucleon-spin operator, $\rho(\mathbf{R})$ is the nucleon-density distribution over the volume of the deformed nucleus, and $\alpha(N,Z)$ is a coefficient that depends on the form of single-particle potentials adopted in averaging over the intranuclear nucleons [$\alpha(N,Z) \sim 1$]. Data on parity-nonconservation effects in resonance-neutron interactions with heavy nuclei suggest that this coefficient is enhanced by one to two orders of magnitude (see, for example, [8]), which in turn enhances observed effects. Nonetheless, we set $\alpha(N,Z) = 1$ in our ensuing calculations.

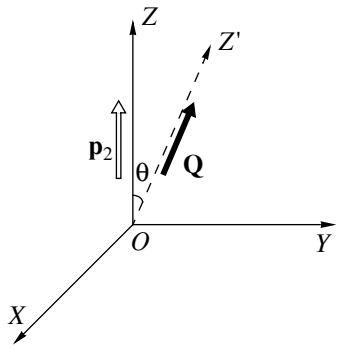

Coordinate frame used.

2. POLARIZATION OF THE ELECTRON SHELL OF THE ATOM IN THE PARITY-MIXED ($E1+M1$) TRANSITION IN THE $5/2^{\pm}$ STATE OF THE $^{229}Pa_{91}$ ISOTOPE

2.1. Basic Definitions

Let us consider the nuclear conversion process in a $(E1+M1)$ multipole transition. Here, the nucleus goes over from the $|E_1 I_1 M_1\rangle$ state to the $|E_2 I_2 M_2\rangle$ ($\hbar\omega = E_1 - E_2$) final state; concurrently, an electron goes over from the $(n_1 l_1 j_1)^{2j_1+1}$ filled shell to the continuum state $|\mathbf{p}_2\nu_2\rangle$ ($\mathbf{p}_2$ is the electron momentum, and ν_2 is the spin projection onto a fixed axis). As a result, the electron has a nonzero helicity, and it can be expected that the hole state $(n_1 l_1 j_1)^{2j_1}$ $(n_1 l_1 j_1)^{-1}$ of the electron group will be polarized, provided that the electron momentum $\mathbf{p}_2$ is fixed. In the subsequent radiative transition of the atomic electron into the hole state, the emitted photon then possesses a circular polarization.

In [1–3], it was established that a maximum effect is to be expected in the conversion event involving the filled subshells of the protoactinium atom for the $(6s_{1/2})^2_{J=0}$, $(6p_{1/2})^2_{J=0}$, and $(6p_{3/2})^4_{J=0}$ configurations (J is the total angular momentum of the atomic subshell).[2)] This is accompanied by the emergence of, respectively, the $(6s_{1/2})^1(6s_{1/2})^{-1}$, $(6p_{1/2})^1(6p_{1/2})^{-1}$, and $(6p_{3/2})^3(6p_{3/2})^{-1}$ hole configurations in the electron shell. The hole spin $\mathbf{j}_1$ is oriented with respect to the conversion-electron momentum $\mathbf{p}_2$; hence, it is necessary to detect, in relevant experiments, the direction of the electron momentum $\mathbf{p}_2$ and the electron energy,[3)] since this energy fixes the shell where the hole has been formed. For the z axis in the laboratory frame, we choose the direction of the electron momentum $\mathbf{p}_2$ (see figure).

2.2. Conversion Process Involving the $(6s_{1/2})^2$ and $(6p_{1/2})^2$ Subshells

The wave function for the initial state of the system has the form

$$\Psi_{I_1M_1}(\mathbf{r}_\mathrm{I}, \mathbf{r}_\mathrm{II}) = \psi_{I_1M_1}\Psi_{J\mathcal{M}}(\mathbf{r}_\mathrm{I}, \mathbf{r}_\mathrm{II}), \qquad (5)$$

where $\psi_{I_1M_1} \equiv |\widetilde{5/2^-}\rangle$ is the nuclear wave function (1); $\mathbf{r}_\mathrm{I}$ and $\mathbf{r}_\mathrm{II}$ are the radius vectors of the electrons in the filled $(n_1 l_1 j_1)^2_{J=0}$ subshell; and $\Psi_{J\mathcal{M}}(\mathbf{r}_\mathrm{I}, \mathbf{r}_\mathrm{II})$ is its wave function given by

$$\Psi_{J\mathcal{M}}(\mathbf{r}_\mathrm{I}, \mathbf{r}_\mathrm{II}) = \sum_{\alpha\beta} C^{J\mathcal{M}}_{j_1\alpha\, j_1\beta}\Psi_{j_1 l_1\alpha}(\mathbf{r}_\mathrm{I})\Psi_{j_1 l_1\beta}(\mathbf{r}_\mathrm{II}), \qquad (6)$$

with $C^{J\mathcal{M}}_{j_1\alpha\, j_1\beta}$ being the relevant Clebsch–Gordan coefficient. For identical fermions, odd values of J are forbidden by the Pauli exclusion principle. The one-electron wave function $\Psi_{j_1 l_1 m_1}(\mathbf{r})$ is a solution to the Dirac equation in a spherically symmetric field and can be represented in the bispinor form [9]

$$\Psi_{j_1 l_1 m_1}(\mathbf{r}) = \begin{cases} g_{l_1 j_1}(r)\Omega_{j_1 l_1 m_1}(\mathbf{r}/r) \\ \imath f_{l_1 j_1}(r)\Omega_{j_1 l_1' m_1}(\mathbf{r}/r), \end{cases} \qquad (7)$$

where $\Omega_{j_1 l_1 m_1}(\mathbf{r}/r)$ is a spherical spinor,

$$\Omega_{j_1 l_1 m_1}(\mathbf{r}/r) = \sum_{\mu_1\nu_1} C^{j_1 m_1}_{l_1\mu_1\, s\nu_1} Y_{l_1\mu_1}(\mathbf{r}/r)v_{\nu_1}, \qquad (8)$$

[2)] Strictly speaking, it is not clear whether the $(5f_{5/2})^2(6d_{3/2})^1(7s_{1/2})^2$ shell of the valence band undergoes any changes—and if so, what changes—upon the formation of chemical compounds used in targets and sources; however, the $(6s_{1/2})^2$, $(6p_{1/2})^2$, and $(6p_{3/2})^4$ configurations of deep orbits seem to remain unchanged.

[3)] However, the nuclear-transition energy is known to a rather poor precision, 220 ± 50 eV; therefore, a further consideration is meaningful if this energy is determined to within 1 eV.

with $Y_{\lambda\mu}(\vartheta,\varphi)$ being normalized spherical harmonics [$Y^*_{\lambda\mu}(\vartheta,\varphi) = (-1)^\mu Y_{\lambda-\mu}(\vartheta,\varphi)$], and $g_{l_1j_1}(r)$ and $f_{l'_1j_1}(r)$ are radial functions normalized by the condition

$$\int_0^\infty dx[g^2_{l_1j_1}(x) + f^2_{l'_1j_1}(x)] = 1. \tag{9}$$

Further, we fix the wave function for the final state of the system as

$$\Psi_{I_2M_2}(\mathbf{r}_\mathrm{I},\mathbf{r}_\mathrm{II}) = \psi_{I_2M_2}\Psi_2(\mathbf{r}_I,\mathbf{r}_{II}), \tag{10}$$

where $\psi_{I_2M_2} \equiv \widetilde{|5/2^+\rangle}$. In the final state, we have an electron in a continuum, $|\varepsilon_2,\nu_2\rangle$, and one electron in the $n_1l_1j_1$ orbit. The wave function for the continuum can be represented as [9]

$$\Psi_{\varepsilon_2\nu_2}(\mathbf{r}) = \frac{4\pi}{p_2}\sqrt{\frac{\varepsilon_2+mc^2}{2\varepsilon_2}} \times \sum_{j_2l_2m_2}(\Omega^+_{j_2l_2m_2}(\mathbf{p}_2/p_2)v_{\nu_2})i^{l_2}\exp(-i\delta_{l_2j_2}) \times \begin{cases} G_{l_2j_2}(r)\Omega_{j_2l_2m_2}(\mathbf{r}/r) \\ iF_{l'_2j_2}(r)\Omega_{j_2l'_2m_2}(\mathbf{r}/r), \end{cases} \tag{11}$$

$$v_{+1/2} = \begin{pmatrix} 1 \\ \\ 0 \end{pmatrix}, \quad v_{-1/2} = \begin{pmatrix} 0 \\ \\ 1 \end{pmatrix},$$

its asymptotic expression at infinity being a superposition of a plane wave and a converging spherical wave. For $r \to \infty$, the wave functions of an electron in a continuum are normalized as

$$G_{l_2j_2}(r) \longrightarrow \sin\left(p_2r - l_2\frac{\pi}{2} + \delta_{l_2j_2}\right), \tag{12}$$

$$F_{l'_2j_2}(r) \longrightarrow i^{l'_2+1-l_2} \times\sqrt{\frac{\varepsilon_2-mc^2}{\varepsilon_2+mc^2}}\sin(p_2r - l'_2\frac{\pi}{2} + \delta_{l_2j_2}). \tag{13}$$

The wave function for the final-state electron is the superposition

$$\Psi_2(\mathbf{r}_\mathrm{I},\mathbf{r}_\mathrm{II}) = \sum_{m_2} b(I_1M_1,(n_1l_1j_1)^2 \to I_2M_2,n_1l_1j_1m_2,\mathbf{p}_2\nu_2) \times\frac{1}{\sqrt{2}}\{\Psi_{j_1l_1m_2}(\mathbf{r}_\mathrm{I})\Psi_{\varepsilon_2\nu_2}(\mathbf{r}_\mathrm{II}) - \Psi_{j_1l_1m_2}(\mathbf{r}_\mathrm{II})\Psi_{\varepsilon_2\nu_2}(\mathbf{r}_\mathrm{I})\}, \tag{14}$$

where the amplitudes $b(I_1M_1,(n_1l_1j_1)^2 \to I_2M_2,n_1l_1j_1m_2,\ \mathbf{p}_2\nu_2)$ are proportional to the matrix element of the interaction operator $\hat{H}_\mathrm{int}$ for the transition from the initial state to the final state.

2.3. Conversion Process Involving the $(6p_{3/2})^4$ Subshell

For the filled $(n_1l_1j_1)^4_{F=0}$ subshell, the wave function has the form

$$\Psi_{00}(\mathbf{r}_\mathrm{I},\mathbf{r}_\mathrm{II},\mathbf{r}_\mathrm{III},\mathbf{r}_\mathrm{IV}) = \sum_{t\delta} C^{00}_{Tt\ j_1\delta}\Psi_{j_1t}(\mathbf{r}_\mathrm{I},\mathbf{r}_\mathrm{II},\mathbf{r}_\mathrm{III})\Psi_{j_1l_1\delta}(\mathbf{r}_\mathrm{IV}), \tag{15}$$

where $\mathbf{r}_\mathrm{I}$, $\mathbf{r}_\mathrm{II}$, $\mathbf{r}_\mathrm{III}$, and $\mathbf{r}_\mathrm{IV}$ are the radius vectors of electrons in this subshell and $\Psi_{j_1t}(\mathbf{r}_\mathrm{I},\mathbf{r}_\mathrm{II},\mathbf{r}_\mathrm{III})$ is the wave function for the $(n_1l_1j_1)^3_{j_1}$ subshell,

$$\Psi_{j_1t}(\mathbf{r}_\mathrm{I},\mathbf{r}_\mathrm{II},\mathbf{r}_\mathrm{III}) = \frac{1}{\sqrt{3!}}\sum_{J=0,2,\ldots}A_J\sum_{\mathcal{M}\gamma}C^{j_1t}_{J\mathcal{M}\ j_1\gamma}\Psi_{J\mathcal{M}}(\mathbf{r}_\mathrm{I},\mathbf{r}_\mathrm{II}) \times\Psi_{j_1l_1\gamma}(\mathbf{r}_\mathrm{III}). \tag{16}$$

The wave function $\Psi_{J\mathcal{M}}(\mathbf{r}_\mathrm{I},\mathbf{r}_\mathrm{II})$ is given by Eq. (6), while the fractional-parentage coefficients are $A_0 = 1$ and $A_2 = -\sqrt{5}$ in our case.

The wave function for the final-state electron is

$$\Psi_2(\mathbf{r}_\mathrm{I},\mathbf{r}_\mathrm{II},\mathbf{r}_\mathrm{III},\mathbf{r}_\mathrm{IV}) = \sum_{m_2} b(I_1M_1,(n_1l_1j_1)^4 \to I_2M_2,n_1l_1j_1m_2,\mathbf{p}_2\nu_2) \times\frac{1}{2}\{-\Psi_{\varepsilon_2\nu_2}(\mathbf{r}_\mathrm{I})\Psi_{j_1m_2}(\mathbf{r}_\mathrm{II},\mathbf{r}_\mathrm{III},\mathbf{r}_\mathrm{IV}) + \Psi_{\varepsilon_2\nu_2}(\mathbf{r}_\mathrm{II})\Psi_{j_1m_2}(\mathbf{r}_\mathrm{I},\mathbf{r}_\mathrm{III},\mathbf{r}_\mathrm{IV}) - \Psi_{\varepsilon_2\nu_2}(\mathbf{r}_\mathrm{III})\Psi_{j_1m_2}(\mathbf{r}_\mathrm{I},\mathbf{r}_\mathrm{II},\mathbf{r}_\mathrm{IV}) + \Psi_{\varepsilon_2\nu_2}(\mathbf{r}_\mathrm{IV})\Psi_{j_1m_2}(\mathbf{r}_\mathrm{I},\mathbf{r}_\mathrm{II},\mathbf{r}_\mathrm{III})\}, \tag{17}$$

where the amplitudes $b(I_1M_1,(n_1l_1j_1)^4 \to I_2M_2,n_1l_1j_1m_2,\mathbf{p}_2\nu_2)$ are proportional to the matrix element of the interaction operator $\hat{H}_\mathrm{int}$ for the transition from the initial to the final state.

2.4. Evaluation of the Matrix Element for the Conversion Transition

Taking into account expressions (6) and (15) for the initial-state wave functions and expressions (14) and (17) for the final-state wave functions, we represent the matrix element as

$$\langle I_1M_1, J(F) = 0\ \mathcal{M}(f) = 0|\hat{H}_\mathrm{int}|I_2M_2,n_1j_1l_1m_2,\mathbf{p}_2\nu_2\rangle = -e^2\sqrt{N[j_1]}C^{00}_{j1m_1\ j-m_1} \times\iint d\mathbf{r}d\mathbf{R}\ \frac{\exp(ik|\mathbf{r}-\mathbf{R}|)}{|\mathbf{r}-\mathbf{R}|} \times\big[(\Psi^+_{\varepsilon_2\nu_2}(\mathbf{r})\Psi_{j_1l_1m_1}(\mathbf{r}))\langle I_2M_2|\hat{\rho}_N(\mathbf{R})|I_1M_1\rangle - \frac{1}{c}(\Psi^+_{\varepsilon_2\nu_2}(\mathbf{r})\boldsymbol{\alpha}\Psi_{j_1l_1m_1}(\mathbf{r}))\langle I_2M_2|\hat{\mathbf{j}}_N(\mathbf{R})|I_1M_1\rangle\big], \tag{18}$$

where $k = \omega/c$ is the wave number, $\boldsymbol{\alpha}$ are Dirac matrices, $\hat{\rho}_N(\mathbf{R})$ is the nuclear-charge-density operaror, $\hat{\mathbf{j}}_N(\mathbf{R})$ is the operator of the intranuclear-nucleon-current density [$\mathrm{div}\hat{\mathbf{j}}_N(\mathbf{R}) = -\partial\hat{\rho}_N(\mathbf{R})/\partial t$], $N[j_1] = 2$ for the $(6s_{1/2})^2$ and $(6p_{1/2})^2$ subshells, and $N[j_1] = 4$ for the $(6p_{3/2})^2$ subshell. In the laboratory frame, the conversion-electron momentum $\mathbf{p}_2$ has the components $(0, 0, p_2)$. By using the decomposition from [3] into multipole contributions (see [9, 10]), we recast the transition matrix element (18) into the form

$$\begin{aligned}\langle I_1 M_1, J(F) = 0\ \mathcal{M}(f)\\ = 0|\hat{H}_{\mathrm{int}}|I_2 M_2, n_1 j_1 l_1 m_2, \mathbf{p}_2\nu_2\rangle\\ = -e^2\sqrt{N[j_1]}C^{00}_{j_1 m_1\ j_1 - m_1}\\ \times\Big(\sum_{E\Lambda}[H^{E\Lambda}]_{21} + \sum_{M\Lambda}[H^{M\Lambda}]_{21}\Big),\end{aligned} \tag{19}$$

where

$$[H^{E\Lambda}]_{21} \tag{20}$$

$$= \sum_{\Lambda\lambda}\frac{4\pi i k^{\Lambda+1}}{(2\Lambda+1)!!}R_N^{\Lambda}\langle I_2||E\Lambda||I_1\rangle C^{I_2 M_2}_{\Lambda\lambda\ I_1 M_1}[\xi_{E\Lambda}]_{21},$$

$$[H^{M\Lambda}]_{21} \tag{21}$$

$$= \sum_{\Lambda\lambda}\frac{-4\pi i k^{\Lambda+1}}{(2\Lambda+1)!!}R_N^{\Lambda}\langle I_2||M\Lambda||I_1\rangle C^{I_2 M_2}_{\Lambda\lambda\ I_1 M_1}[\xi_{M\Lambda}]_{21},$$

R_N being the radius of the nucleus.

The reduced matrix elements for the $E1$ transition in the protoactinium nucleus ($I_1 = I_2 = I$) [1] are given by

$$-eR_N\langle 2||E1||1\rangle C^{IM_2}_{IM_1\ 1\lambda} \tag{22}$$

$$= \left\langle [642]\frac{5}{2}, +, \frac{5}{2}\left|\hat{\mathfrak{M}}_e(1,\lambda)\right|[523]\frac{5}{2}, -, \frac{5}{2}\right\rangle,$$

where the $E1$ transition operator has the form

$$\hat{\mathfrak{M}}_e(1,\lambda) = e\frac{N}{A}RY_{1\lambda}(\mathbf{R}). \tag{23}$$

For the $M1$ nuclear transition, we have

$$-eR_N\langle 2||M1||1\rangle C^{IM_2}_{IM_1\ 1\lambda} \tag{24}$$

$$= -i\sqrt{2}\left\langle\widetilde{\frac{5}{2}^+}\left|\hat{\mathfrak{M}}_m(1,\lambda)\right|\widetilde{\frac{5}{2}^-}\right\rangle,$$

where the $M1$ transition operator is given by

$$\hat{\mathfrak{M}}_m(1,\lambda) = \sqrt{\frac{3}{4\pi}}\Big(\frac{e\hbar}{2m_p c}\Big)\big[g_l\hat{l}_\lambda + g_s\hat{s}_\lambda + g_R\hat{R}_\lambda\big]. \tag{25}$$

Here, $\mu_{\mathrm{B}} = e\hbar/2m_p c$ is the nuclear magneton, $\hat{\mathbf{l}}$ is the operator of the nucleon orbital angular momentum, $\hat{\mathbf{s}}$ is the nucleon-spin operator, and $\hat{\mathbf{R}}$ is the operator of the nuclear-core angular momentum. If the spin polarization of the core is disregarded, we have $g_s = 5.585$, $g_l = 1$, and $g_R = Z/A$ for the proton.

The electron matrix elements $[\xi_{E1}]_{21}$ and $[\xi_{M1}]_{21}$ are given by

$$\begin{aligned}[\xi_{E1}]_{21} = \frac{\sqrt{3a_0}}{p_2}\sqrt{\frac{\varepsilon_2 + mc^2}{2\varepsilon_2}}\\ \times\sum_{j_2 l_2 m_2}C^{j_2 m_2}_{l_2 0\ s\nu_2}\sqrt{2l_2+1}\big[i^{l_2}\exp(-i\delta_{l_2 j_2})\big]^*\\ \times\{l_2 j_2[E1]n_1 l_1 j_1\}[j_2 l_2, 1, j_1, l_1]C^{j_1 m_1}_{j_2 m_2 1\lambda},\end{aligned} \tag{26}$$

$$\begin{aligned}[\xi_{M1}]_{21} = \frac{i\sqrt{3a_0}}{p_2}\sqrt{\frac{\varepsilon_2 + mc^2}{2\varepsilon_2}}\\ \times\sum_{j_2 l_2 m_2}C^{j_2 m_2}_{l_2 0\ s\nu_2}\sqrt{2l_2+1}\big[i^{l_2}\exp(-i\delta_{l_2 j_2})\big]^*\\ \times\{l_2 j_2[M1]n_1 l_1 j_1\}[j_2 l_2, 1, j_1, l_1']C^{j_1 m_1}_{j_2 m_2\ 1\lambda},\end{aligned} \tag{27}$$

where

$$[j_2 l_2, 1, j_1 l_1] = \sqrt{\frac{2j_2+1}{2j_1+1}}\,C^{l_1 0}_{l_2 0\ 10}\,u(j_2 s 1 l_1; l_2 j_1),$$

$u(abcd; ef) = \sqrt{(2e+1)(2f+1)}W(abcd; ef)$ being a normalized Racah function. The relevant radial integrals of the relativistic wave functions for the initial- and final-state electrons can be represented as [11]

$$\begin{aligned}\{l_2 j_2[E1]n_1 l_1 j_1\} = \int_0^\infty dx\ h_1^{(1)}(ka_0 x)[G_{l_2 j_2}(x)g_{l_1 j_1}(x) + F_{l_2' j_2}(x)f_{l_1' j_1}(x)]\\ + \int_0^\infty dx\ h_0^{(1)}(ka_0 x)[G_{l_2 j_2}(x)f_{l_1' j_1}(x) - F_{l_2' j_2}(x)g_{l_1 j_1}(x)]\\ + [j_2(j_2+1) - l_2(l_2+1) - j_1(j_1+1) + l_1(l_1+1)]\\ \times\int_0^\infty dx\ h_0^{(1)}(ka_0 x)[G_{l_2 j_2}(x)f_{l_1' j_1}(x) + F_{l_2' j_2}(x)g_{l_1 j_1}(x)],\end{aligned} \tag{28}$$

$$\{l_2 j_2[M1]n_1 l_1 j_1\} = \frac{j_2(j_2+1) - l_2(l_2+1) - j_1(j_1+1) + l_1'(l_1'+1)}{\sqrt{3}} \tag{29}$$
$$\times \int_0^\infty dx\; h_1^{(1)}(ka_0 x)[G_{l_2 j_2}(x) f_{l_1' j_1}(x) + F_{l_2' j_2}(x) g_{l_1 j_1}(x)],$$

where $x = r/a_0$; a_0 is the Bohr radius; and $h_\lambda^{(1)}(ka_0 x)$ is a spherical Hankel function of the first kind, its asymptotic behavior at large argument values being

$$h_\lambda^{(1)}(z) \overset{z\to\infty}{\to} (-i)^{\lambda+1}\frac{e^{iz}}{z}. \tag{30}$$

Under the condition that the conversion electron has a fixed momentum $\mathbf{p}_2$, we further define, for an electron shell with a hole, the polarization spin-tensor

$$\rho_{Qq}^{\mathrm{lab}}(j_2, \mathbf{p}_2) = \sum_{m_2}\sum_{m_2'} C_{j_2 m_2' Qq}^{j_2 m_2} \tag{31}$$
$$\times b^*(I_1 \to I_2, m_2', \mathbf{p}_2) b(I_1 \to I_2, m_2, \mathbf{p}_2).$$

In this expression, we have omitted some immaterial arguments of the amplitudes b, which were introduced above in Eqs. (14) and (17). Assuming that, in the initial state, the nucleus being considered is not oriented, we perform averaging over the possible projections M_1 of the nuclear spin I_1 in the initial state. We also perform summation over the experimentally unobservable projections M_2 of the nuclear spin I_2 and the emitted-electron polarizations ν_2.

In the coordinate frame chosen here, the orthonormalized spin-tensor of shell orientation (polarization) has the form

$$\tau_{Q0}^{\mathrm{lab}}(j_2, \mathbf{p}_2) = \frac{\overline{\rho_{Q0}^{\mathrm{lab}}(j_2, \mathbf{p}_2)}}{\overline{\rho_{00}^{\mathrm{lab}}(j_2, \mathbf{p}_2)}}. \tag{32}$$

For $Q = 1$, a direct calculation yields

$$\tau_{10}^{\mathrm{lab}}(j_2, \mathbf{p}_2) = -\frac{\langle I_2||M1||I_1\rangle}{\langle I_2||E1||I_1\rangle}\frac{1}{\sum\limits_{l_2 j_2} |\{l_2 j_2[E1]n_1 l_1 j_1\}|^2\,[j_2 l_2, 1, j_1, l_1]^2}$$
$$\times \sum_{j_2 l_2 \tilde{j}_2 \tilde{l}_2} C_{l_2 0\, 10}^{\tilde{l}_2 0} u(j_2 1 1 j_1; j_1 \tilde{j}_2) u(l_2 s 1 \tilde{j}_2; j_2 \tilde{l}_2)[j_2 l_2, 1, j_1, l_1][\tilde{j}_2 \tilde{l}_2, 1, j_1, l_1'] \tag{33}$$
$$\times \Big(-i\{l_2 j_2[E1]n_1 l_1 j_1\}^* \{\tilde{l}_2 \tilde{j}_2[M1]n_1 l_1 j_1\}\big[i^{l_2}\exp(-i\delta_{l_2 j_2})\big]\big[i^{\tilde{l}_2}\exp(-i\delta_{\tilde{l}_2 \tilde{j}_2})\big]^*$$
$$+ i\{l_2 j_2[E1]n_1 l_1 j_1\}\{\tilde{l}_2 \tilde{j}_2[M1]n_1 l_1 j_1\}^*$$
$$\times \big[i^{l_2}\exp(-i\delta_{l_2 j_2})\big]^*\big[i^{\tilde{l}_2}\exp(-i\delta_{\tilde{l}_2 \tilde{j}_2})\big]\Big).$$

For $j_1 \geq 3/2$, the value of $Q = 2$ is possible, in which case we have

$$\tau_{20}^{\mathrm{lab}}(j_2, \mathbf{p}_2)$$
$$= \frac{1}{\sum\limits_{l_2 j_2} |\{l_2 j_2[E1]n_1 l_1 j_1\}|^2\,[j_2 l_2, 1, j_1, l_1]^2}$$
$$\times \sum_{j_2 l_2 \tilde{j}_2 \tilde{l}_2} \sqrt{\frac{2l_2+1}{2\tilde{l}_2+1}}$$
$$\times C_{l_2 0\, 20}^{\tilde{l}_2 0} u(j_2 1 2 j_1; j_1 \tilde{j}_2) u(l_2 s 2 \tilde{j}_2; j_2 \tilde{l}_2) \tag{34}$$
$$\times [j_2 l_2, 2, j_1, l_1][\tilde{j}_2 \tilde{l}_2, 2, j_1, l_1]$$
$$\times (\{l_2 j_2[E1]n_1 l_1 j_1\}^* \{\tilde{l}_2 \tilde{j}_2[E1]n_1 l_1 j_1\}$$
$$\times \big[i^{l_2}\exp(-i\delta_{l_2 j_2})\big]\big[i^{\tilde{l}_2}\exp(-i\delta_{\tilde{l}_2 \tilde{j}_2})\big]^*.$$

In deriving Eqs. (33) and (34), we have made use of the expansion in the small parameter $|\langle I_2||M1||I_1\rangle|^2/|\langle I_2||E1||I_1\rangle|^2$.

The spin-tensor $\tau_{10}^{\mathrm{lab}}(j_2, \mathbf{p}_2)$ is completely determined by the parity-nonconservation effect, whereas $\tau_{20}^{\mathrm{lab}}(j_2, \mathbf{p}_2)$ is formed by the pure multipoles of the $E1$ and $M1$ transitions. Nonetheless, $\tau_{20}^{\mathrm{lab}}(j_2, \mathbf{p}_2)$ for the $6p_{3/2}$ orbit enters into the observed circular-polarization effect.[4)]

[4)] An observation of the effect associated with the $6p_{3/2}$ orbit can be more convenient experimentally, since the $(7s_{1/2})^2 \to (6p_{3/2})^{-1}$ transition energy is $\hbar\omega_\gamma \sim 15$–$20$ eV.

2.5. Effect of an Unfilled Valence Band of the Protoactinium Atom on the Orientation Spin-Tensors for States of a Shell Featuring the $(6s_{1/2})^{-1}$, $(6p_{1/2})^{-1}$, and $(6p_{3/2})^{-1}$ Hole States

In the normal configuration of the protoactinium atom, the $(5f_{5/2})^2(6d_{3/2})^1(7s_{1/2})^2$ subshells of the valence band can have different sets of angular momenta: $j_{(7s_{1/2})^2} = 0$, $j_{(6d_{3/2})^1} = 3/2$, and $j_{(5f_{5/2})^2} = 0, 2, 4$. Thus, the total angular momentum $\mathbf{j}_\Sigma = \mathbf{j}_{(6d_{3/2})^1} + \mathbf{j}_{(5f_{5/2})^2}$ of the electrons of the valence band can take the following values:

$j_{(6d_{3/2})^1}$	$j_{(5f_{5/2})^2}$	j_Σ
3/2	0	3/2
3/2	2	1/2, 3/2, 5/2, 7/2
3/2	4	5/2, 7/2, 9/2, 11/2

The wave function for the initial state of the valence band of the atom has the form of the following superposition:

$$\Psi_{j_\Sigma} = \sum_{m_\Sigma} b_{m_\Sigma}(j_\Sigma)\Psi_{j_\Sigma m_\Sigma}. \qquad (35)$$

The total angular momentum of an ion that has a hole in the $n_1 l_1 j_1$ subshell is $\mathbf{J}_1 = \mathbf{j}_1 + \mathbf{j}_\Sigma$. States that are characterized by the same value of J_1 can be mixed by the residual electrostatic interaction, with the result that the radiative-transition probability changes. The splitting of this energy term is about 1 eV, which is usually much greater than radiative level widths; therefore, it is possible to observe individual radiative transitions to states characterized by different values of the angular momentum J_1.

Prior to photon emission, the wave function of the system being considered has the form

$$\Psi_{J_1} = \sum_{m_2, m_\Sigma} b_{m_1}(j_1) b_{m_\Sigma}(j_\Sigma)\Psi_{n_1 l_1 j_1 m_1}\Psi_{j_\Sigma m_\Sigma} \qquad (36)$$
$$= \sum_{J_1 \mathcal{M}_1} b_{\mathcal{M}_1}\Psi_{J_1 \mathcal{M}_1},$$

where

$$b_{\mathcal{M}_1} = \sum_{m_2, m_\Sigma} C^{J_1 \mathcal{M}_1}_{j_1 m_1\, j_\Sigma m_\Sigma} b_{m_1}(j_1) b_{m_\Sigma}(j_\Sigma). \qquad (37)$$

In a state having a fixed angular momentum J_1, which determines the photon circular polarization in a radiative transition, the orientation spin-tensor is given by

$$\tau^{\mathrm{lab}}_{Qq}(J_1, \mathbf{p}_2) = \sum_{\mathcal{M}_1, \mathcal{M}'_1} C^{J_1 \mathcal{M}'_1}_{J_1 \mathcal{M}_1\, Qq} b^*_{\mathcal{M}'_1} b_{\mathcal{M}_1}. \qquad (38)$$

We further assume that, in the initial state (prior to a conversion event), the valence-band angular momentum $\mathbf{j}_\Sigma$ is not oriented. Accordingly, the valence-band orientation spin-tensor has the form

$$\tau^{\mathrm{lab}}_{Nn}(\mathbf{j}_\Sigma) = \sum_{m_\Sigma, m'_\Sigma} C^{j_\Sigma m'_\Sigma}_{j_\Sigma m_\Sigma\, Nn} b^*_{m'_\Sigma} b_{m_\Sigma}, \qquad (39)$$

in which case we have $\tau^{\mathrm{lab}}_{Nn}(\mathbf{j}_\Sigma) = \delta_{N0}\delta_{n0}$.

Performing summation over angular-momentum projections and using Eqs. (36), (38), and (39), we obtain

$$\tau^{\mathrm{lab}}_{Qq}(J_1, \mathbf{p}_2) = u(J_1 j_\Sigma Q j_1; j_1 J_1)\tau^{\mathrm{lab}}_{Qq}(j_1, \mathbf{p}_2), \qquad (40)$$

where $\tau^{\mathrm{lab}}_{Qq}(j_1, \mathbf{p}_2)$ is the orthonormalized shell-orientation (shell-polarization) spin-tensor that is defined in (32) and which disregards the effect of the electrons of the valence band of the atom.

Let us consider the case where the subshell angular momentum is $j_1 = 1/2$, so that the rank of the possible spin-tensor is not higher than $Q = 1$. At $J_1 = j_\Sigma + 1/2$, we have

$$\tau^{\mathrm{lab}}_{10}(J_1, \mathbf{p}_2) = \sqrt{\frac{J_1 + 1}{3J_1}}\tau^{\mathrm{lab}}_{10}(j_1, \mathbf{p}_2), \qquad (41)$$

while, at $J_1 = j_\Sigma - 1/2$, the corresponding result is

$$\tau^{\mathrm{lab}}_{10}(J_1, \mathbf{p}_2) = -\sqrt{\frac{J_1}{3(J_1 + 1)}}\tau^{\mathrm{lab}}_{10}(j_1, \mathbf{p}_2). \qquad (42)$$

If the subshell angular momentum J_1 is sufficiently high, we have $\sqrt{(J_1+1)/3J_1} \to \sqrt{1/3}$ and $-\sqrt{J_1/3(J_1+1)} \to -\sqrt{1/3}$.

Thus, the inclusion of the interaction between the angular momentum of the hole state of an electron shell in the atom and the angular momentum of the valence-band electron leads to a reduction of the polarization of this hole state.

2.6. Numerical Calculations

In [1], we calculated the reduced nuclear probabilities for the electric dipole transition, $B(E1; 5/2^- \to 5/2^+)$, and for the magnetic dipole transition, $B(M1; \widetilde{5/2^-} \to \widetilde{5/2^+})$. Expressions (33) and (34) for the spin-tensors of orientation of the electron shell with the $(6s_{1/2})^{-1}$, $(6p_{1/2})^{-1}$, and $(6p_{3/2})^{-1}$ holes involve the ratio of the reduced nuclear matrix elements for the $E1$ and $M1$ transitions,

$$\left|\frac{\langle I_2||M1||I_1\rangle}{\langle I_2||E1||I_1\rangle}\right| = \sqrt{\frac{2B(M1; \widetilde{5/2^-} \to \widetilde{5/2^+})}{B(E1; 5/2^- \to 5/2^+)}}. \qquad (43)$$

This ratio (see Table 1) was borrowed from our preceding calculations [1]. In the following, we restrict ourselves to calculating the magnitude of the effect.

Table 1. Ratio of the reduced matrix elements for the magnetic dipole transition ($\langle\widetilde{5/2^+}||M1||\widetilde{5/2^-}\rangle$) and the electric dipole transition $\langle 5/2^+||E1||5/2^-\rangle$

β_{20}	$\left\|\frac{\langle I_2\|M1\|I_1\rangle}{\langle I_2\|E1\|I_1\rangle}\right\|$
0.20	$\frac{2.95}{\Delta E}$
0.23	$\frac{2.52}{\Delta E}$
0.25	$\frac{2.31}{\Delta E}$
Experiment	$\frac{0.84}{\Delta E}$

Note: The first three rows display the results obtained on the basis of the model employing the Woods–Saxon potential and the corresponding value of the quadrupole-deformation parameter β_{20} ($\beta_{40} = 0.08$), while the fourth row gives the value determined from the experimental isomer lifetime $\tau_{\rm expt}$ for $\beta_{20} = 0.23$ (ΔE is measured in eV).

Table 2. Polarization spin-tensor $\tau_{10}^{\rm lab}(j_1, \mathbf{p}_2)$ for the protoactinium-atom electron shell featuring a hole state in the $6s_{1/2}$, $6p_{1/2}$, and $6p_{3/2}$ subshells

ΔE, eV	$\lvert\tau_{10}^{\rm lab}(j_1, \mathbf{p}_2)\rvert$					
	I			II		
	$6s_{1/2}$	$6p_{1/2}$	$6p_{3/2}$	$6s_{1/2}$	$6p_{1/2}$	$6p_{3/2}$
170	0.137	0.105	0.017	0.0460	0.0352	0.0057
180	0.133	0.101	0.016	0.0446	0.0339	0.0055
190	0.129	0.097	0.016	0.0434	0.0327	0.0054
200	0.126	0.094	0.016	0.0423	0.0317	0.0052
210	0.123	0.091	0.015	0.0413	0.0307	0.0051
220	0.120	0.089	0.015	0.0403	0.0299	0.0050
230	0.118	0.087	0.015	0.0395	0.0291	0.0049
240	0.115	0.084	0.014	0.0387	0.0284	0.0049
250	0.113	0.082	0.014	0.0379	0.0277	0.0048
260	0.111	0.081	0.014	0.0372	0.0271	0.0047
270	0.109	0.079	0.014	0.0366	0.0265	0.0047

Note: Here and in Table 3, we quote results obtained with $B(E1; 5/2^- \to 5/2^+)$ determined on the basis of (I) the model employing a deformed Woods–Saxon potential and (II) the experimental isomer lifetime $t_{\rm expt}$.

In order to describe the electron shell of the protoactinium atom, we make use of the relativistic Hartree–Fock–Slater method [12] [the normal configuration of the valence band is $(5f_{5/2})^2(6d_{3/2})^1 \times (7s_{1/2})^2$].

For the electron shell of the protoactinium atom with a hole in the $6s_{1/2}$, $6p_{1/2}$, and $6p_{3/2}$ subshells, Table 2 displays the calculated values of the orientation spin-tensor $\tau_{10}^{\rm lab}(j_1, \mathbf{p}_2)$. The calculations were performed for two values of the reduced nuclear probability $B(E1; 5/2^- \to 5/2^+)$, that obtained within the model employing a deformed Woods–Saxon potential and that determined from the experimental isomer lifetime $t_{\rm expt}$ [1].

As was indicated above, a nonzero value of the polarization spin-tensor $\tau_{10}^{\rm lab}(j_1, \mathbf{p}_2)$ stems from the interference contribution of the $E1$ and $M1$ multipoles. At the same time, the alignment tensor $\tau_{20}^{\rm lab}(j_1, \mathbf{p}_2)$ is completely determined in our approximation by the contribution of the $E1$ multipole and, in accordance with Eq. (34), depends only slightly on the transition energy ΔE. For the electron shell of the atom with a hole in the $6p_{3/2}$ subshell, the alignment spin-tensor $\tau_{20}^{\rm lab}(j_1, \mathbf{p}_2)$ is 0.35 and 0.38 if the reduced nuclear probability $B(E1; 5/2^- \to 5/2^+)$ is set, respectively, to the value obtained with a deformed Woods–Saxon potential and to the value deduced from the experimental isomer lifetime $t_{\rm expt}$ [1].

In [13], we compared the values of the polarization spin-tensor $\tau_{10}^{\rm lab}(j_1, \mathbf{p}_2)$ for different configurations of the valence band of the protoactinium atom, whereby we assessed the sensitivity in calculating the conversion spectrum to various models of atomic potentials; in this way, we were also able to estimate the hybridization of the electron shell of the atom and the magnitude of the predicted effect.

3. CIRCULAR POLARIZATION OF A PHOTON EMITTED FROM A PRELIMINARILY POLARIZED SHELL OF THE $^{229}Pa_{91}$ ION

3.1. Formulation of the Problem and Determination of Observables

That the spin-tensor $\tau_{1q}^{\rm lab}(J_1, \mathbf{p}_2)$ is nonzero leads to the emergence of a circular polarization of an atomic photon emitted in the $j_3 \to [j_1]^{-1}$ transition. On the basis of the degree of this polarization, we can assess the degree of mixing of the $E1$ and $M1$ multipoles in the nuclear transition. The emitted-photon energy is less than 50 eV; hence, the photon wavelength is much greater than the the characteristic dimension of the protoactinium atom, so that the long-wave approximation is valid The ion final state upon photon emission is $|\varepsilon_3 j_3 l_3 m_3\rangle$. It is convenient to perform calculations in a reference frame where

the z' axis is aligned with the photon-momentum vector $\mathbf{Q}$ (see figure). For the electron-shell wave function, a transition from the laboratory frame to this reference frame (Q frame) is implemented according to the equation

$$\Psi^{\rm lab}_{j_1 l_1 m_2}(\mathbf{r}) = \sum_{\varsigma_1} \mathfrak{D}^{j_1}_{m_2\varsigma_1}(\theta_i)\Psi^{Q}_{j_1 l_1 \varsigma_1}(\mathbf{r}), \qquad (44)$$

where $\mathfrak{D}^{j_1}_{m_2\varsigma_1}(\theta_i)$ are rotation-matrix elements [14].

An event of nuclear-multipole conversion involving the $n_1 l_1 j_1$ shell of the atom specifies the set of spin-tensors (32) for the ion in the laboratory frame if the conversion-electron momentum $\mathbf{p}_2$ is recorded.

In the long-wave approximation, the operator of electron interaction with the electromagnetic field of the atom for the $E1$ multipole has the form

$$\hat{H}^{E1}_{\rm lwa} = -\sum_i \big(\hat{\boldsymbol{\mathcal{D}}}(\mathbf{r}_i)\hat{\mathbf{E}}_{\mathbf{Q}}(\mathbf{r},t)\big), \qquad (45)$$

where $\hat{\boldsymbol{\mathcal{D}}}(\mathbf{r}_i) = -|e|\mathbf{r}_i$ is the electron-dipole-momentum operator and $\hat{\mathbf{E}}_{\mathbf{Q}}(\mathbf{r},t)$ is the electromagnetic-field-strength operator [14].

For the emission of a long-wave photon, the matrix element of the interaction operator $\hat{H}^{E1}_{\rm lwa}$ has the form

$$\langle 3|\hat{H}^{E1}_{\rm lwa}|2\rangle = i\sqrt{\frac{2\pi\hbar c Q}{V}}\exp\left\{\frac{i}{\hbar}(\varepsilon_3+\hbar\omega_\gamma-\varepsilon_1)t\right\} \times \sum_{m_2} b(I_1M_1,[n_1l_1j_1]^{2j_1+1} \to I_2M_2, n_1l_1j_1m_2, \mathbf{p}_2\nu_2) \qquad (46)$$
$$\times \sum_{\nu=\pm1}\sum_{\varsigma_1,\varsigma_3}\langle\Psi^{\rm lab}_{j_3l_3\varsigma_3}(\mathbf{r})|\hat{\mathcal{D}}_\nu(\mathbf{r})|\Psi^{\rm lab}_{j_1l_1\varsigma_1}(\mathbf{r})\rangle \times \mathfrak{D}^{j_1}_{m_2\varsigma_1}(\theta_i)\mathfrak{D}^{j_2}_{m_3\varsigma_3}{}^{*}(\theta_i).$$

The probability of photon emission into the solid angle $d\mathcal{O}_{\mathbf{Q}}$ is

$$N_\nu(\mathbf{Q},d\mathcal{O}_{\mathbf{Q}}) = \frac{2\pi}{\hbar}\delta(\varepsilon_3+\hbar\omega_\gamma-\varepsilon_1) \times\Big[\frac{VQ^2dQ}{(2\pi\hbar)^3}\Big]d\mathcal{O}_{\mathbf{Q}}\frac{2p\hbar cQ}{V} \times\frac{2j_3+1}{3(2j_1+1)}\sum_N(-1)^N(2N+1) \qquad (47)$$
$$\times u(1j_3Nj_1;j_11)C^{1\nu}_{1\nu\,N0} \times\tau^{\rm lab}_{N0}(j_1,\mathbf{p}_2)\;P_N(\mathbf{Q})\langle j_3l_3||\hat{\mathcal{D}}(\mathbf{r})||j_1l_1\rangle,$$

where $P_N(\mathbf{Q})$ is a Legendre polynomial. In calculating the matrix element of the $E1$ transition operator, use was made of the Wigner–Eckart theorem

$$\langle\Psi^{\rm lab}_{j_3l_3\varsigma_3}(\mathbf{r})|\hat{\mathcal{D}}_\nu(\mathbf{r})|\Psi^{\rm lab}_{j_1l_1\varsigma_1}(\mathbf{r})\rangle = C^{j_3\varsigma_3}_{j_1\varsigma_1\;1\nu}\langle j_3l_3||\hat{\mathcal{D}}(\mathbf{r})||j_1l_1\rangle. \qquad (48)$$

The photon circular polarization is

$$\mathcal{P}_\gamma = \frac{N_{-1}(\mathbf{Q},d\mathcal{O}_{\mathbf{Q}}) - N_{+1}(\mathbf{Q},d\mathcal{O}_{\mathbf{Q}})}{N_{-1}(\mathbf{Q},d\mathcal{O}_{\mathbf{Q}}) + N_{+1}(\mathbf{Q},d\mathcal{O}_{\mathbf{Q}})}. \qquad (49)$$

In the case considered here, only spin-tensors of rank not higher than two ($N = 0, 1, 2$) are nonzero; taking into account Eq. (47), we obtain

$$\mathcal{P}_\gamma = \frac{\frac{3}{\sqrt{2}}u(j_11j_31;1j_11)\,\tau^{\rm lab}_{10}(j_1,\mathbf{p}_2)\cos\theta_{\mathbf{Q}}}{1+\sqrt{\frac{5}{2}}u(j_12j_31;1j_11)\,\tau^{\rm lab}_{20}(j_1,\mathbf{p}_2)\big(\frac{3}{2}\cos^2\theta_{\mathbf{Q}}-\frac{1}{2}\big)}. \qquad (50)$$

Let us consider the $E1$ radiative transitions of the electrons belonging to the protoactinium-ion valence band to the $(6s_{1/2})^{-1}$, $(6p_{1/2})^{-1}$, and $(6p_{3/2})^{-1}$ hole states. We have

$$\left[(6p_{1/2})^2 j_3 = \frac{1}{2} \to (6s_{1/2})^{-1} j_1 = \frac{1}{2}\right],$$
$$\tau^{\rm lab}_{20}(j_1,\mathbf{p}_2) \equiv 0,$$
$$\mathcal{P}_\gamma = \sqrt{3}\tau^{\rm lab}_{10}(j_1,\mathbf{p}_2)\cos\theta_{\mathbf{Q}};$$
$$\left[(6p_{3/2})^4 j_3 = \frac{3}{2} \to (6s_{1/2})^{-1} j_1 = \frac{1}{2}\right],$$
$$\tau^{\rm lab}_{20}(j_1,\mathbf{p}_2) \equiv 0,$$
$$\mathcal{P}_\gamma = -\frac{\sqrt{3}}{2}\tau^{\rm lab}_{10}(j_1,\mathbf{p}_2)\cos\theta_{\mathbf{Q}};$$
$$\left[(7s_{1/2})^2 j_3 = \frac{1}{2} \to (6p_{1/2})^{-1} j_1 = \frac{1}{2}\right],$$
$$\tau^{\rm lab}_{20}(j_1,\mathbf{p}_2) \equiv 0,$$
$$\mathcal{P}_\gamma = \sqrt{3}\tau^{\rm lab}_{10}(j_1,\mathbf{p}_2)\cos\theta_{\mathbf{Q}};$$
$$\left[(7s_{1/2})^2 j_3 = \frac{1}{2} \to (6p_{3/2})^{-1} j_1 = \frac{3}{2}\right],$$
$$\mathcal{P}_\gamma = \frac{\frac{\sqrt{15}}{2}\tau^{\rm lab}_{10}(j_1,\mathbf{p}_2)\cos\theta_{\mathbf{Q}}}{1+\frac{\sqrt{5}}{2}\tau^{\rm lab}_{20}(j_1,\mathbf{p}_2)\big(\frac{3}{2}\cos^2\theta_{\mathbf{Q}}-\frac{1}{2}\big)}.$$

Table 3. Circular polarization of atomic photons

Atomic transition	$\lvert\mathcal{P}_\gamma\rvert$, %	
	I	II
$(6p_{1/2})^2 j_3 = 1/2 \to (6s_{1/2})^{-1} j_1 = 1/2$	15.0	5.0
$(6p_{3/2})^4 j_3 = 3/2 \to (6s_{1/2})^{-1} j_1 = 1/2$	7.5	2.5
$(7s_{1/2})^2 j_3 = 1/2 \to (6p_{1/2})^{-1} j_1 = 1/2$	11.0	3.7
$(7s_{1/2})^2 j_3 = 1/2 \to (6p_{3/2})^{-1} j_1 = 3/2$	1.8	0.6

By using the results obtained by calculating the polarization spin-tensors for the electron shell of the protoactinium-atom valence band, we have estimated the possible values of photon circular polarization. The estimates were obtained for the photon emission angle of $\theta_{\mathbf{Q}} = \pi/4$ with respect to the direction of the conversion-electron momentum $\mathbf{p}_2$. Since the energy of the conversion transition in the $^{229}\mathrm{Pa}_{91}$ isomer is quite uncertain, we present only the maximum values (in percent) for the degree $\mathcal{P}_\gamma$ of circular photon polarization (see Table 3). For individual lines, $\mathcal{P}_\gamma$ is about 3 to 5 percent, so that experiments aimed at observing the parity-nonconservation effect seem quite promising.

4. CONCLUSION

The possibility of extracting the parameters of the effective weak-interaction potential from an experiment measuring the circular polarization of primary photons of the radiation that accompanies conversion in the parity-mixed ($E1 + M1$) transition between the components of the $5/2^{\pm}$ doublet of states in the $^{229}\mathrm{Pa}_{91}$ nucleus has been demonstrated. If the primary-photon energy and the conversion-electron energy have been determined to a precision such that the nuclear-transition energy is found to within 1 eV, the cascade process in an experiment of the type being discussed is clearly separated by a detection event from other processes. If, however, the accuracy in determining the nuclear-transition energy is insufficient, the experiment in question would yield data integrated in the conversion-electron energy (only the direction of the conversion-electron momentum and the energy of the atomic-radiation photon can be recorded in this case. There then arise two problems:

(i) In order to identify the line that corresponds to the transition to a given hole state, it is necessary to analyze the spectrum of atomic radiation.

(ii) It is necessary to analyze the contribution of Auger processes, since they generate an irremovable background in such an experiment.

In integrated data, the circular polarization of photons belonging to atomic radiation receives contributions from all processes leading to the formation of a hole state in the electron shell of the atom[5)] and reducing the photon circular polarization.

ACKNOWLEDGMENTS

We are grateful to A.L. Barabanov and B.V. Danilin for discussions on some aspects of this study and for enlightening comments and proposals.

This work was supported by the Russian Foundation for Basic Research (project no. 3 00-15-96590).

REFERENCES

1. D. P. Grechukhin and A. V. Lomonosov, Yad. Fiz. **63**, 431 (2000) [Phys. At. Nucl. **63**, 365 (2000)].
2. D. P. Grechukhin and A. V. Lomonosov, Yad. Fiz. **62**, 2288 (1999) [Phys. At. Nucl. **62**, 2106 (1999)].
3. D. P. Grechukhin and A. V. Lomonosov, Yad. Fiz. **63**, 793 (2000) [Phys. At. Nucl. **63**, 724 (2000)].
4. I. Ahmad *et al.,* Phys. Rev. Lett. **49**, 1758 (1982).
5. S. G. Nilsson, K. Dan. Vidensk. Selsk., Mat.-Fys. Medd. **29** (16), 1 (1955).
6. A. Bohr and B. R. Mottelson, *Nuclear Structure* (Benjamin, New York, 1975; Mir, Moscow, 1971, 1977), Vols. 1, 2.
7. R. J. Blin-Stoyle, *Fundamental Interactions and the Nucleus* (North-Holland, Amsterdam, 1973; Mir, Moscow, 1976).
8. J. J. Szhymansky *et al.,* Phys. Rev. C **49**, 3297 (1994).
9. A. I. Akhiezer and V. B. Berestetskii, *Quantum Electrodynamics* (GIFML, Moscow, 1959; Wiley, New York, 1965).
10. V. B. Berestetskiĭ, A. Z. Dolginov, and K. A. Ter-Martirosyan, Zh. Éksp. Teor. Fiz. **20**, 527 (1950).
11. D. P. Grechukhin and A. A. Soldatov, Preprint IAÉ-3174 (Institute of Atomic Energy, Moscow, 1979).
12. J. C. Slater, *Quantum Theory of Molecules and Solids,* Vol. 4: *The Self-Consistent Field for Molecules and Solids* (McGraw-Hill, New York, 1974; Mir, Moscow, 1978).
13. D. P. Grechukhin and A. V. Lomonosov, Preprint IAÉ-6126/2 (Institute of Atomic Energy, Moscow, 1999).
14. A. S. Davydov, *Quantum Mechanics* (Nauka, Moscow, 1973; Pergamon, Oxford, 1976).

Translated by A. Isaakyan

[5)] By way of example, we indicate that the $(6p_{1/2})^{-1}$ hole state in the electron shell arises not only in the conversion process involving the $(6p_{1/2})^2$ subshell but also in the conversion process involving the $(6s_{1/2})^2$ subshell and leading to the formation of the polarized $(6s_{1/2})^{-1}$ hole state with the subsequent $E1$ radiative transition of the electron from the $(6p_{1/2})^2$ subshell, part of the polarization of the $(6s_{1/2})^{-1}$ hole state being transferred to the $(6p_{1/2})^{-1}$ state.

Physics of Atomic Nuclei, Vol. 64, No. 5, 2001, pp. 891–901. Translated from Yadernaya Fizika, Vol. 64, No. 5, 2001, pp. 958–968.

ELEMENTARY PARTICLES AND FIELDS
Experiment

Experimental Estimation of the Charm-Production Cross Section in pp Interactions at 70 GeV/c with the Aid of the SVD Setup

N. S. Amaglobeli[1)], E. N. Ardashev[2)], S. G. Basiladze, G. A. Bogdanova, M. Yu. Bogolyubsky[2)], I. V. Boguslavsky[3)], N. K. Bulgakov[2)], A. M. Vischnevskaya, V. Yu. Volkov, A. P. Vorobiev[2)], N. A. Galyaev[2)], I. M. Gramenitsky[3)], O. V. Grishina, Ya. V. Grishkevich, P. F. Ermolov, O. S. Zaitseva[2)], V. N. Zapolsky[2)], E. G. Zverev, S. A. Zotkin, N. A. Ivanova[2)], G. I. Karlov[2)], V. I. Kireev[3)], A. E. Kiryunin[2)], V. V. Kozlov, V. A. Kramarenko, A. V. Kubarovsky, G. O. Kuratashvili[1)], L. L. Kurchaninov[2)], A. Ya. Kutov[3)], A. N. Larichev, M. S. Levitsky[2)], A. K. Leflat, S. I. Lyutov, K. S. Medved[3)], M. M. Merkin, A. A. Minaenko[2)], A. M. Moiseev[2)], S. Nedev[4)], S. V. Orfanitsky, A. V. Pleskach[2)], A. I. Popov[2)], V. V. Popov, B. V. Prosin[2)], S. M. Ruzin, V. P. Rukovichkin, V. M. Rybnikov, V. N. Ryadovikov[2)], V. A. Samsonov[3)], A. V. Selikov, Yu. V. Tevzadze[1)], L. A. Tikhonova, V. T. Tolmachev[3)], T. P. Topuria[3)], B. A. Utochkin[2)], A. G. Kholodenko[2)], Yu. V. Khrenov[3)], Yu. P. Tsyupa[2)], S. V. Chekulaev[2)], B. G. Chiladze[1)], E. K. Shabalina, M. D. Shafranov[3)], and Sh. M. Esakia[1)]

SVD Collaboration

Institute of Nuclear Physics, Moscow State University, Vorob'evy gory, Moscow, 119899 Russia

Received December 27, 1999; in final form, June 6, 2000

Abstract—Charmed-particle production in pp interactions at 70 GeV/c was studied with the SVD setup at the IHEP accelerator (Protvino). The experimental procedure used and the data-selection methods are described. Data obtained by using a quickly cycling bubble chamber and a magnetic spectrometer are analyzed. The number of inelastic-interaction events recorded in the chamber is 109 000, with the charge multiplicity being $n_{ch} \geqslant 4$. The corresponding statistics are 4.96 event/μb. Part of the events were recorded in the magnetic spectrometer. Three three-prong decays of charged particles near the primary vertex are found on the films, two of these being recorded with the spectrometer. All three are interpreted as D^- decays. Two neutral decays observed simultaneously in the chamber and in the spectrometer are interpreted as $\bar{D}^0$ decays. The total cross section for $c\bar{c}$ production in the Feynman variable region $-1 < x_F < +1$ is estimated at $\sigma(c\bar{c}) = 1.6^{+1.1}_{-0.7}\,(\text{stat.}) \pm 0.3\,(\text{syst.})\,\mu\text{b}$. The cross-section values and the mean values $\langle|x_F|\rangle$ and $\langle p_\perp\rangle$ for D mesons are compared with other experimental results in the energy range 58–800 GeV. The data of this experiment are compatible with the cross-section estimates obtained in the beam-dump experiment at 70 GeV and with those predicted by perturbative QCD. © *2001 MAIK "Nauka/Interperiodica".*

1. INTRODUCTION

Since the discovery of hadrons composed of heavy quarks (1974), their investigation has continued intensively at the largest accelerators worldwide. By and large, data from CERN and FNAL experiments that studied charmed-particle production in hadron interactions at energies above 200 GeV agree satisfactorily with the predictions of perturbative QCD.

However, the situation is different in the near-threshold energy region, where the features of $c\bar{c}$ production can change substantially for some reasons that require correcting perturbative QCD [1–3] and also because of nonperturbative effects associated with the possible intrinsic-charm mechanism [4] and with the properties of fragmentation [5]. These points are of considerable interest for QCD [6]. When the preparation of our experiment at the IHEP accelerator energies (60–70 GeV) began, there had been

[1)]Institute for High Energy Physics, Tbilisi State University, Universitetskaya ul. 9, GE 380086 Tbilisi, Georgia.

[2)]Institute for High Energy Physics, Protvino, Moscow oblast, 142284 Russia.

[3)]Joint Institute for Nuclear Research, Dubna, Moscow oblast, 141980 Russia.

[4)]Chemical-Technological and Metallurgy University, Sofia, Bulgaria.

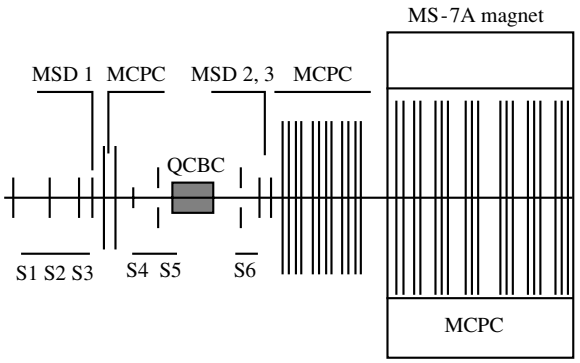

Fig. 1. Layout of the SVD-1 setup: (S1–S6) scintillation counters, (MCPC) multichannel proportional chambers, (MSD) microstrip silicon detectors, and (QCBC) quickly cycling bubble chamber.

only first results on charmed-particle production in experiments of two types. These were an experiment at the BIS spectrometer [7, 8], where particles were recorded by using a Cherenkov counter or by measuring their effective masses, and the so-called beam-dump experiment [9], which employed the neutrino channel and a setup that recorded directly produced charged leptons from the semileptonic modes of charged-hadron decay. It should be noted that, in those experiments, the decay vertex was not recorded for short-lived charmed hadrons and that the measurements of the cross sections for charmed-particle production yielded anomalously large values of 5–50 μb. These were data that furnished a strong motivation for performing a new experiment at a Spectrometer with a Vertex Detector (SVD) [10, 11].

Here, we present the result obtained by studying charmed-particle production in proton–proton interactions at 70 GeV/c.

Preliminary results of this experiment (E-161) were reported in [12, 13].

2. EQUIPMENT AND EXPERIMENTAL PROCEDURE

Figure 1 shows the layout of the SVD-1 setup, which comprises a quickly cycling bubble chamber (QCBC) as a vertex detector, a wide-aperture magnetic spectrometer, and a system for beam monitoring and event triggering.

The QCBC construction was described in detail elsewhere [14]. The QCBC operates with a frequency of 20–30 Hz (up to 10 expansions per beam spill); its diameter and depth are 150 and 50 mm, respectively; pictures were taken on two photographic films by a fast photorecorder [15]. The beam-particle flux was chosen to be relatively high—there were, on average, 30–40 particles per frame. The track density was 100–130 bubbles per centimeter, the bubble diameter being 25–30 μm.

The wide-aperture magnetic spectrometer equipped with wire proportional chambers (PC) and constructed on the basis of an MS-7A electromagnet [16] with 3-m-long poles along the beam direction, its aperture being 1.8 m wide and 1.3 m high, was included in SVD-1 in order to determine the momenta of charged secondaries. The field was sufficiently uniform in the spectrometer operating volume, its strength being about 1.18 T; the strength of the scattered magnetic field outside the operating volume was 0.3 T at a distance of 1.5 m from the magnet yoke.

Functionally, the SVD magnetic spectrometer is a double-arm device. Its first arm is formed by a forward block of 12 PC planes that is positioned in front of the magnet; in particular, it is used to measure low momenta of particles emitted at large angles. The proportional chambers of this block that have an operating area of 1 m^2 and a gap of 2 mm between them are combined into three quadruples in such a way that the wires have the $UYVX$ orientation, where Y and X are the vertical and the horizontal wire, respectively, while the U and V are tilted at an angle of 10.5° to the vertical. The total number of signal anode wires is 5424 in these chambers.

The central block, positioned inside the magnet aperture, consists of 19 PCs with a gap of 2 mm between them and an operating area of 1.0×1.5 m^2 [17]. Four forward chambers are combined into UY and VY doublets, while the remaining 15 chambers are grouped into UYV triplets. These chambers form the second arm of the spectrometer and make it possible to measure the momenta of particles captured by the magnet. Altogether they contain 12608 signal anode wires.

The PC amplifiers, signal-recording electronics operating according to the CAMAC–COMPLEX protocol, and the local network of data transfer were described in [18–21].

In view of a small field depth in photographing, the QCBC was irradiated by a ribbon-shaped beam, which was 40 mm in height and below 2 mm in width within the chamber operating volume. To eliminate the background from particles that come at an instant not coinciding with that of the highest chamber sensitivity, the beam was fed to the chamber in a pulsed mode for 50 μs synchronously with a drop to a minimum in the pressure-release cycle. This mode was provided by a special system of beam-intensity modulation (SBIM) [22].

A trigger system consisting of scintillation counters and microstrip silicon detectors (MSD) [23] controlled SBIM operation and the photographing process. This system was intended for recording beam

particles before they entered the chamber and for producing the trigger for interaction. The use of MSDs with a spacing of 200 μm between them also permitted efficiently controlling the size of the profile of incident-particle beam. The trigger signal appeared in the case where there occurred a beam-particle interaction within the QCBC and where, in addition, two charged particles were simultaneously recorded by scintillation counters located behind the QCBC outside the beam region. Since liquid hydrogen in the operating volume formed only a part of the complete amount of medium on the beam path in the vicinity of the QCBC, including the walls of the vacuum cover and the chamber, about 60% of trigger signals were due to the interactions outside the chamber volume.

3. STRUCTURE OF DATA PROCESSING

Events featuring the possible decays of charmed particles were separated on the basis of two independent scans of QCBC films on the scan tables with a large magnification. All events originating from beam-particle interactions and involving $n_{\mathrm{ch}} > 2$ charged secondaries in the fiducial volume of the bubble chamber were recorded. The region corresponding, in a frame, to a rectangle having side lengths of 10 and 5 mm, the longer side being along the beam direction, and the center at the primary vertex was scanned carefully.

The small size of this region (so-called charm box) permits reducing the contamination from strange-particle decays. In this region, we selected the one-prong ($C1$), three-prong ($C3$), and five-prong ($C5$) decays of charged particles and the two-prong ($V2$), four-prong ($V4$), and six-prong ($V6$) decays of neutral particles; we also recorded secondary interactions featuring an even number of tracks (N_{even}) for the interactions of charged secondaries and those featuring an odd number of tracks (N_{odd}) for the interactions of neutral secondaries.

The smallest distance L_{min} at which the secondary and the primary vertex can be distinguished visually with a probability close to 100% was experimentally determined to be $L_{\mathrm{min}} = 0.2$ mm [24].

The track measurements on QCBC films were performed on the PUOS-4 (IHEP) and PUOS-2 (JINR) tables. The track-point accuracy of these devices was 2.5 μm.

The primary processing of the results of track measurements in individual projections makes it possible to find the decays of heavy short-lived particles directly on QCBC films by using the values of the impact parameter δ and of the transverse decay length L_T. The δ value is the least distance on the frame plane between the line representing a least squares fit to the measured track points and the primary-vertex coordinates. This value is independent of the momentum of the particle that decayed [25]. The L_T value is $L_T = L \sin\theta_c$, where L is the charmed-particle decay length and θ_c is the charmed-particle emission angle with respect to the incident-beam direction. Since the masses of charmed hadrons are large and since their lifetimes are small, the L_T value for charmed-particle decays is short, much shorter on average than that for strange-hadron decays. The procedure for preliminarily processing QCBC film measurements was described in more detail elsewhere [24].

The spatial reconstruction of tracks in the QCBC operating volume was performed on the basis of the GEOSVD code [26, 27].

An original method (variable-momentum method) was developed to analyze SVD data instead of the usual methods employed for track reconstruction in the magnetic spectrometer [28]. In the procedure of track identification and reconstruction, the variable-momentum method relies on *a priori* information about the angular properties of tracks and about the coordinates of the interaction vertex in the vertex detector [29]. The values of the polar (λ) and the azimuthal (φ) angle obtained in the QCBC serve as inputs for a reconstruction of each charged-particle track in the spectrometer. For each specific particle, this makes it possible to identify unambiguously the trajectory curved by the magnetic field and to determine the particle momentum by minimizing the distance between the particle trajectory calculated for the spectrometer magnetic field and the hits in the U, Y, and V planes of the proportional chambers of the magnetic-spectrometer tracking system. Applications of the method are exemplified in Fig. 2, which shows the reconstruction of a multiprong event featuring the production and decay of a K_S^0 meson recorded in the QCBC. It can be seen that all 14 tracks captured by the spectrometer aperture are found and reconstructed. A more detailed analysis of these events was presented in [29].

Table 1 displays the main measuring properties of the SVD setup that were obtained experimentally by processing QCBC films [30] on the basis of the variable-momentum method for the magnetic spectrometer.

To improve the selection criteria used and the interpretation of our data, we simulated the production and decays of charmed hadrons in pp interactions at 70 GeV/c [31] and processes that involve strange particles and which appear to be the main source of background. This simulation was performed by the Monte Carlo method implemented on the basis of the PYTHIA code (version 5.702). According to these calculations, the total production cross section for events featuring a charmed hadron pair was 1.07 μb,

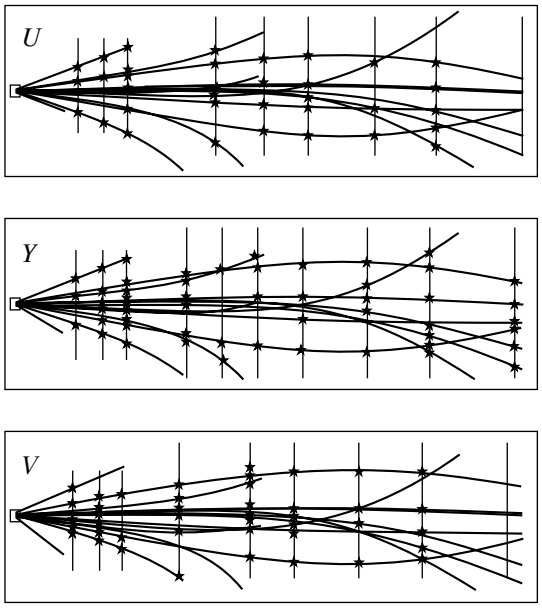

Fig. 2. Multiprong event of inelastic pp interaction as recorded in the QCBC and reconstructed in the U, Y, and V projections. The charge signs and momenta were determined for all particles that traversed the spectrometer aperture.

which was mainly due to $\Lambda_c^+\bar{D}$ and $D\bar{D}$ associated production (0.51 and 0.52 μb, respectively).

The simulation showed that 74% of $D^\pm$ mesons, 70% of $\bar{D}^0$ mesons, and 47% of Λ_c^+ hyperons decay at a distance L from the primary vertex between $L_{\min} = 0.2$ mm and $L_{\max} = 5.0$ mm within a cylinder of radius 2.5 mm, with its axis being directed along the beam momentum. The inclusive cross sections calculated on the basis of PYTHIA for K_S^0-meson and Λ^0- and Σ^0-hyperon production agree with the data obtained with the MIRABELLE bubble chamber at 69 GeV/c [32]. The simulations also showed that, if only information from QCBC scanning was used for $C1$ and $V2$ decays, the background from strange particles was two orders of magnitude higher than the sought effect. This background is substantially reduced (by a factor of about 5) when the transverse-length (L_T) criterion was used for event selection. A further reduction of the background to $V2$ decays can be ensured owing to a sufficiently accurate determination of particle effective masses by the spectrometer (see Table 1). The background to $C1$ decays remains high, and this topology will be eliminated from a further analysis for this reason.

The background to $C3$ decays stems from the overlap of the vee from a $V2$ decay and the track of the charged particle from the corresponding primary vertex. This background source is virtually eliminated by imposing the requirement that each track from a $C3$ decay have an impact parameter in the region $\delta > 5$ μm. The background from $C3$ $K^\pm$-meson decays is about 30% for all recorded $C3$ decays; it is reduced to 6% upon the application of the L_T selection criterion. The use of the L_T criterion nearly removes the background to the $V4$, $V6$, etc., decays. For a further analysis, we selected events with a single secondary vertex, including $V2$, $V4$, $V6$, $C3$, and $C5$ decay topologies, and events with two secondary vertices of any decay topologies, including $C1$. In this case, the decays were selected according to the following criteria:

(i) The decay length L was chosen within the interval 0.2–5 mm.

(ii) The transverse decay length L_T was required to be within 0.2 mm.

(iii) Both tracks from a $V2$ decay were required to traverse the spectrometer aperture.

(iv) Each track from $C3$ decays was required to have an impact-parameter value in the region $\delta > 5$ μm.

4. EXPERIMENTAL RESULTS

Table 2 displays the results obtained from a double scan of QCBC films. The number of simulated events that involved $C3$ decays, $V2$ decays, and two secondary vertices is 2.1, 482, and 5.9, respectively.

In our analysis of experimental data, three events featuring a $C3$ decay and 67 events featuring a $V2$ decay passed the selection criteria described in the preceding section. According to the Monte Carlo calculations, the background from strange-particle decays is 0.09 and 88 events for $C3$ and $V2$ topologies, respectively. Twenty-five events involving $V2$ decays were recorded simultaneously in the QCBC and in the magnetic spectrometer. In analyzing the effective masses, we were able to associate 23 of these with K_S^0 and Λ^0 ($\bar{\Lambda}^0$) decays (with the calculated background being 22 events) and the remaining two events with the $\bar{D}^0$ decays. According to the criterion $L_T \leqslant 0.2$ mm, six events featuring a double secondary activity ($C1V2$) were assigned to the associated production of strange particles. That no event featuring $c\bar{c}$ production with two observed vertices was recorded in this experiment by using the above selection criteria can be explained by a statistical fluctuation. Indeed, $2.7^{+2.3}_{-1.7}$ events involving two secondary vertices in the final state could be found via scanning, as follows from the $c\bar{c}$-production cross section and its errors (see below) and from the PYTHIA simulation; in this case, the probability of observing no event lies in the interval between 0.7 and 37%.

Table 1. Features of the SVD setup

Feature	Value
Accuracy in determining the coordinate x, spectrometer (in mm):	
(a) averaged over all secondary tracks	$\langle\sigma_x\rangle = 0.8$
(b) for beam tracks	$\langle\sigma_x^b\rangle = 0.4$
Root-mean-square error in the polar-angle projection onto the horizontal plane (in mrad):	
(a) measurement error (spectrometer)	$\langle\Delta\phi_{\text{sp}}\rangle = 0.1$
(b) total error including multiple-scattering contribution at $p = 5$ GeV/c	$\langle\Delta\phi_{\text{tot}}\rangle = 0.5$
Root-mean-square error in the dip angle (in mrad):	
(a) QCBC	$\langle\Delta\lambda_{\text{cham}}\rangle = 0.7$
(b) spectrometer	$\langle\Delta\lambda_{\text{sp}}\rangle = 0.8$
Momentum resolution at 70 GeV/c (in %)	$\Delta p/p = 2.5$
Effective-mass resolution (in %):	
(a) K^0 mesons	0.4
(b) Λ^0 hyperons	0.2

Table 2. Results of a double scan of QCBC films

Topology	Primary vertex	$C1$	$C3$	$V2$	$C5, V4, V6$	Secondary interactions		Two secondary vertices
						N_{even}	N_{odd}	
Number of events	108 863	331	6	473	0	482	55	6
Efficiency of a double scan	0.99	0.96	>0.96	0.96	–	0.97	0.95	0.97

The ten-prong event featuring a $C3$ decay in Fig. 3 was found on films obtained in the absence of a magnetic field. This event satisfies all selection criteria; additionally, three tracks of its primary vertex have sizable values of the impact parameter. This allowed us to assign this $C3$ decay to the decay of a charmed hadron ($D^{\pm}$ or Λ_c^+). In this case, the background expected from $K^{\pm}$-meson decays is less than 0.01 event.

Four selected events (two featuring a $C3$ and the other featuring a $V2$ decay), provided with spectrometric information, were analyzed by using the procedures for geometrical reconstruction and kinematic fitting. Tables 3 and 4 display the basic properties of these events.

The tabulated values of the maximum internal transverse momentum of particles, $p_{\perp}^{\text{in}}$, that was calculated with respect to the direction of decaying-hadron emission are well above those expected for K^-, K_S^0, and Λ^0 decays (about 0.25 GeV/c). The invariant charged-particle masses calculated under the assumption of strange-particle decays differ significantly from the tabular values. Tables 3 and 4 also quote the values of $p_{\perp}^{ch}$, x_{F}^{ch}, and p_{lab}^{ch} for the observed charged component of a charmed particle. Here, x_{F}^{ch} is the Feynman variable value averaged over all possible decay modes of charged and neutral D mesons. The errors caused by averaging do not exceed 10%. More specific decay modes can be obtained from the following analysis. If, for charmed-hadron decay, the vertex coordinates are measured to a sufficient accuracy and if the 3-momenta of all charged particles from the decay are reconstructed in the spectrometer, then only the absolute value of the charmed-hadron momentum remains unknown. The absence of undetected neutral particles in the decay mode makes it possible to determine the masses of decay particles and to refine their momenta by means of a kinematical fit subjected to three constraints ($3C$ fit). In the case of an undetected neutral particle in the decay mode ($0C$ fit), one calculates $M^2 = m_c^2 + m_b^2 - 2m_c\left(m_b^2 + p_{\perp}^2\right)^{1/2}$ [33], where m_c is the mass of the charmed hadron that has decayed, m_b is the effective mass of the system of charged particles from its decay, and $p_{\perp}$ is the transverse momentum

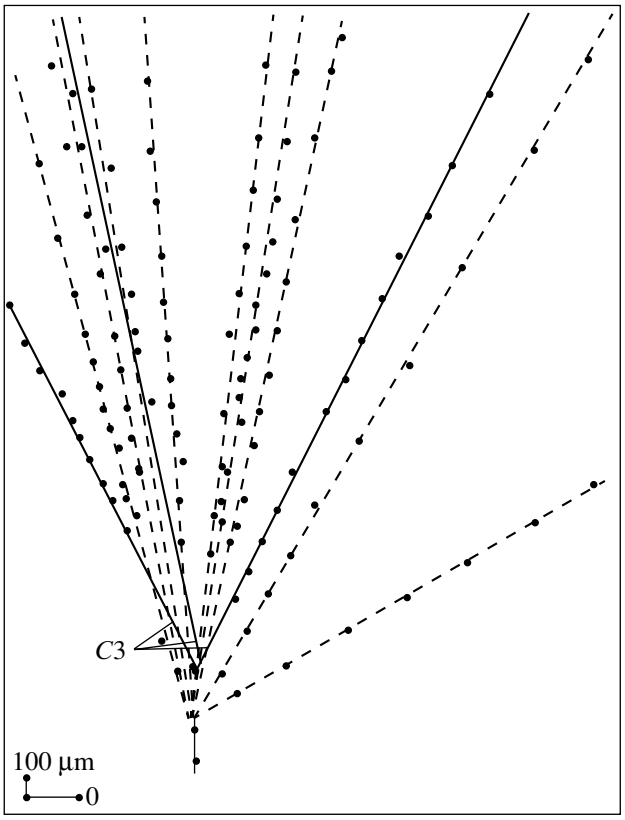

Fig. 3. Ten-prong *pp* interaction that involve a $C3$ decay and which were recorded only on QCBC films and digitized by using the PUOS-4 measuring projector. The properties of the event are described in the main body of the text and in Table 3.

of this system. Further, we assume that one or two π^0 mesons are emitted if $M + \Delta M < 0.4$ GeV or $M - \Delta M > 0.4$ GeV, respectively. Fulfillment of the condition $M + \Delta M < 0.7$ GeV suggests the presence of a K^0 meson in the decay process, while fulfillment of the condition $M - \Delta M > 0.7$ GeV implies the emergence of the $K^0 + \pi^0$ system.

Tables 3 and 4 present the M values, the most probable channels of D^- and $\bar{D}^0$ decays, and the invariant masses of the charged-particle systems associated with these channels. These tables also provide information about the primary vertices of the selected events, which is indicative of the presence of tracks with impact-parameter values $\delta > 3\sigma$ and which is compatible with the assumption that there is a second charmed particle in the events under consideration.

The total cross section $\sigma(c\bar{c})$ for the pair production of charmed hadrons was determined by comparing the observed number of events with that expected from our Monte Carlo simulation (PYTHIA code) under the conditions of the present experiment. In the interval $-1 < x_F < +1$, this cross section was calculated by the formula

$$\sigma(c\bar{c}) = \frac{m_{\rm MC}\sigma_{\rm MC}}{m_{\rm expt}\varepsilon_1\varepsilon_2\varepsilon_3}\left(W_1\frac{N_s^{\rm expt}}{N_s^{\rm MC}\varepsilon_4} + W_2\frac{N_{V2}^{\rm expt}}{N_{V2}^{\rm MC}\varepsilon_{V2}}\right), \quad (1)$$

where $m_{\rm MC}$ and $m_{\rm expt}$ are the millibarn-equivalent values preset in the Monte Carlo calculations and obtained in our experiment, respectively; $\sigma_{\rm MC}$ is the total $c\bar{c}$-production cross section obtained from the PYTHIA simulation; ε_1 and ε_4 are the efficiencies of the scanning of QCBC films for events featuring, respectively, one and two vertices; ε_2 is the efficiency taking into account the losses of $c\bar{c}$ events of small multiplicity in triggering; ε_3 is the efficiency associated with the selection of particles according to the transverse length L_T for one-vertex events; $N_s^{\rm MC}$ and $N_s^{\rm expt}$ are, respectively, the number of simulated events featuring secondary vertices within the QCBC (all topologies, with exception of one-vertex $V2$ and $C1$ decays) and the number of analogous events observed experimentally; $N_{V2}^{\rm MC}$ and $N_{V2}^{\rm expt}$ are, respectively, the number of simulated events involving $V2$ decays and the number of analogous events observed experimentally; ε_{V2} is the total efficiency of the detection of $V2$ events; and W_1 and W_2 are the statistical weights of the $N_s^{\rm expt}$ and $N_{V2}^{\rm expt}$ events.

For these variables, Table 5 gives the values used to determine the cross section $\sigma(c\bar{c})$. Further, we discuss some details of these calculations.

The experimental millibarn-equivalent value was obtained from the total sample of observed inelastic events of multiplicity $n_{\rm ch} > 2$ and from the cross section given in [34, 35] for inelastic *pp* interactions at 70 GeV/c.

The efficiencies ε_1 and ε_4 were taken from the data in Table 2. The efficiency ε_2 was assessed by comparing our experimental multiplicity distributions of charged particles and analogous distributions in *pp* interactions at 69 GeV/c from the experiment at the MIRABELLE chamber [35], only the multiplicity distribution of events that involve charmed-hadron production and which are simulated by PYTHIA [24] being taken into account. The efficiency ε_3 was estimated on the basis of the Monte Carlo simulation.

Three events with $C3$ topology (Table 3) and two events with $V2$ topology (Table 4) were taken for $N_s^{\rm expt}$ and $N_{V2}^{\rm expt}$, respectively.

The total efficiency of the detection of $V2$ events, ε_{V2}, is determined by the probability of obtaining simultaneous information from the QCBC and the spectrometer (0.33) and by the efficiency and the estimate of event losses due to a limited setup acceptance (0.76), as obtained from the Monte Carlo

Table 3. Properties of events involving a $C3$ decay

Properties of $C3$ decay	Number of event		
	1	2	3
Decay vertex			
Total charge	–	−1	−1
Distance between the vertices (μm)	290	512	2820
Distance L_T (μm)	15	17	85
Presence of tracks with impact parameters $\delta > 3\sigma$ with respect to the primary vertex	All three tracks	Single track	Two tracks
Maximum internal transverse momentum $p_\perp^{\text{in}}$ (GeV/c)	–	0.46	0.31
Invariant mass of charged particles for the $K^- \to \pi^+\pi^-\pi^-$ hypothesis (GeV)	–	1.134	1.030
Transverse momentum of the charged system, $p_\perp^{\text{ch}}$ (GeV/c)	–	0.45	0.64
Mean value of the Feynman variable of the charged system, x_{F}^{ch}	–	0.29	0.10
Laboratory momentum of the charged system, $p_{\text{lab}}^{\text{ch}}$ (GeV/c)	–	22.94	13.12
The most probable mode of D^--meson decay	–	$K^*(892)\,\pi^-\pi^0\pi^0$	$\pi^+\pi^-\pi^-K^0$
M (GeV)	–	0.55	0.82
Invariant mass of charged particles for this mode of D^--meson decay (GeV)	–	1.286	1.030
Primary vertex			
Total number of tracks	10	4	6
Number of tracks with impact parameters $\delta > 3\sigma$	2	1	2
Number of secondary particles reconstructed in the spectrometer	–	1	4
Possible mode of Λ_c^+ decay	–	$nK^+\pi^0$ $\Lambda^0\pi^+\pi^0$	$p\pi^+K^-$
Laboratory momentum of Λ_c^+ for this decay mode (GeV/c)	–	–	26.8

simulations. The value obtained experimentally for the pion-detection efficiency with respect to x_{F} is $\varepsilon_\pi^{\text{expt}} = 0.66 \pm 0.04$ [30], which is in accord with the value of $\varepsilon_\pi^{\text{theor}} = 0.72$ calculated by the Monte Carlo method [10]. For the spectrometer, similar values of the pion-detection and the charmed-particle-detection efficiency follow from the similarity of their x_{F} distributions presented in [30, 36].

The statistical weights W_1 and W_2 found with allowance for Poisson fluctuations in the number of the observed events are $W_1 = 0.95$ and $W_2 = 0.05$.

As a result, the total-cross-section value of $\sigma(c\bar{c}) = 1.6^{+1.1}_{-0.7}\,(\text{stat.}) \pm 0.3\,(\text{syst.})$ μb has been obtained according to expression (1).

The systematic error stems mainly from the uncertainty in the number of expected $c\bar{c}$ events because of an unknown contribution of the $D\bar{D}$- and $\Lambda_c^+\bar{D}$-production channels, their ratio changing between 1 and 0.2.

The mean values $\langle|x_{\text{F}}|\rangle$, $\langle p_\perp\rangle$, and $\langle p_{\text{lab}}\rangle$ for the observed D mesons are compiled in Table 6, along with those from the PYTHIA simulation. The mean value $\langle|x_{\text{F}}|\rangle^{\text{ch}}$ for the charged component of the D mesons was obtained from the experimental data presented in Tables 3 and 4. We determined the total value $\langle|x_{\text{F}}|\rangle$, taking into account the neutral-component contribution estimated with the aid of the PYTHIA code ($\langle|x_{\text{F}}|\rangle^{\text{neut}} / \langle|x_{\text{F}}|\rangle = 0.34$ for $D^\pm$ mesons and $\langle|x_{\text{F}}|\rangle^{\text{neut}} / \langle|x_{\text{F}}|\rangle = 0.45$ for $\bar{D}^0$ mesons). The mean values of the transverse and laboratory momenta ($\langle p_\perp\rangle$ and $\langle p_{\text{lab}}\rangle$, respectively) were determined in a similar way.

Table 4. Properties of events involving $V2$ decay

Properties of $V2$ decay	Number of event	
	1	2
Decay vertex		
Total charge	0	0
Distance between the vertices (μm)	570	430
Distance L_T (μm)	11	18
Presence of tracks with impact parameters $\delta > 3\sigma$ with respect to the primary vertex	No	Two tracks
Maximum internal transverse momentum $p_\perp^{\text{in}}$ (GeV/c)	0.70	0.41
Invariant mass of the charged particles for	1.010	0.417
the $K^0 \to \pi^+\pi^-$ and $\Lambda^0 \to p\pi^-$ hypotheses (GeV)	1.472	1.143
Transverse momentum of the charged system, $p_\perp^{\text{ch}}$ (GeV/c)	0.13	0.57
Mean value of the Feynman variable for the charged system, x_{F}^{ch}	0.04	−0.08
Laboratory momentum of the charged system, $p_{\text{lab}}^{\text{ch}}$ (GeV/c)	8.12	4.97
The most probable mode of $\bar{D}^0$-meson decay	$K^+\pi^-\pi^0\pi^0$	$K^+\pi^-\pi^0\pi^0$
M (GeV)	0.52	0.78
Invariant mass of the charged particles for this mode of $\bar{D}^0$-meson decay (GeV)	1.147	1.044
Primary vertex		
Total number of tracks	6	6
Number of tracks with impact parameters $\delta > 3\sigma$	2	3
Number of secondary tracks reconstructed in the spectrometer	1	5
Possible mode of Λ_c^+ decay	$p\bar{K}_0\,(\pi^0)$	–
Laboratory momentum of Λ_c^+ for this decay mode (GeV/c)	>54.1	–

Table 6 also shows the fitted values of the exponent n in the form $d\sigma/dx_{\text{F}} = (1 - |x_{\text{F}}|)^n$. For D mesons, the ratio of the experimental mean decay length $\langle L \rangle$ to the mean value $\langle L_{\text{MC}} \rangle$ calculated on the basis of PYTHIA is given in the penultimate column of Table 6. It can be seen that, by and large, the experimental and the simulated data agree rather well.

Our present data can be compared with some results obtained for the total cross section $\sigma\,(c\bar{c})$ in the 70-GeV beam-dump experiments at the IHEP accelerator [36–38]. For the case of total proton-beam absorption implemented in those experiments, the estimates $\sigma\,(c\bar{c}) < 4.8\ \mu$b (for the SKAT chamber) [37], $\sigma\,(c\bar{c}) = 0.9^{+1.1}_{-0.9}\ \mu$b and $\sigma\,(c\bar{c}) < 2.7\ \mu$b (for a neutrino detector) [36], and $\sigma\,(c\bar{c}) = -0.3 \pm 1.2\ \mu$b and $\sigma\,(c\bar{c}) < 1.6\ \mu$b (for a neutrino detector) [38] were obtained for the interval $-1 < x_{\text{F}} < +1$ by measuring the yields of directly produced leptons and neutrinos. The indicated upper limits on the cross sections corresponded to a 90% confidence level. The value of $\sigma\left(D\bar{D}\right) = 5 \pm 4\ \mu$b was obtained from the data of the experiment reported in [9], where a spark spectrometer was used to separate the electron modes of charmed-meson decay. We see that the $\sigma\,(c\bar{c})$ value obtained in the present study is compatible with the results of the beam-dump experiments.

In the studies with the BIS-2 spectrometer, the cross section for D-meson production was determined in neutron interactions with hydrogen and carbon nuclei at a mean energy of 58 GeV [39, 40] in the region $x_{\text{F}} > 0.5$. The cross section for hydrogen, $\sigma_{\bar{D}^0 X}\,(x_{\text{F}} > 0.5) = 3.2\ \pm\ 1.1\ \mu$b [39], was obtained

Table 5. Values of the parameters needed for calculating the cross section $\sigma(c\bar{c})$

m_{MC}, ev/μb	m_{expt}, ev/μb	σ_{MC}, ev/μb	ε_1	ε_2	ε_3	ε_4	N_s^{expt}	N_{V2}^{expt}	N_s^{MC}	N_{V2}^{MC}	ε_{V2}
10	4.96 ± 0.05	1.07	0.97 ± 0.01	0.91 ± 0.03	0.96	0.97	3	2	6.20	2.58	0.25 ± 0.05

Table 6. Properties of the D meson

	$\langle\lvert x_{\mathrm{F}}\rvert\rangle$	$\langle p_\perp\rangle$, GeV/c	$\langle p_{\mathrm{lab}}\rangle$, GeV/$c$	$\langle L\rangle / \langle L\rangle_{\mathrm{MC}}$	n
E-161 experiment	0.20 ± 0.07	0.53 ± 0.13	17.6 ± 5.3	0.67 ± 0.32	3.0 ± 1.3
Monte Carlo (PYTHIA)	0.18	0.64	18.0	1.0	3.5

for $\bar{D}^0$ mesons, where X is a charmed meson or a Λ_c^+ baryon. The cross section for D^--meson production on hydrogen must be close to the above value because, for $x_{\mathrm{F}} > 0.5$, the relevant inclusive cross sections for production on carbon in [40], $\sigma_{\bar{D}^0} = 28 \pm 14$ μb and $\sigma_{D^-} = 26 \pm 13$ μb, nearly coincide.

Among D-meson events selected in this experiment, only in one can a D meson have $x_{\mathrm{F}} > 0.5$ with a probability of 50% in accordance with two possible directions of emission of the neutral decay system. As a consequence, the estimate of the cross section is $\sigma_{DX}(x_{\mathrm{F}} > 0.5) < 1.2$ μb at a 90% confidence level.

The estimates of the cross section for the pair production of D mesons for $x_{\mathrm{F}} > 0.5$ from experiments with 250-GeV and 400-GeV protons correspond to $\sigma_{D\bar{D}} < 0.14$ μb [41] and $\sigma_{D\bar{D}} = 0.6^{+0.6}_{-0.3}$ μb [42], respectively. These values indicate that the D-meson cross section obtained in the BIS-2 experiment contradicts the data of other experiments at the IHEP accelerator energies and experimental data obtained at higher energies.

Basic experimental data on the cross section for the pair production of D mesons for $-1 < x_{\mathrm{F}} < +1$ in proton–nucleon interactions at energies in the interval 200–800 GeV [41–46] are shown in Fig. 4, along with our result (E-161). A comparison of the experimental data on $\sigma\left(D\bar{D}\right)$ with the QCD predictions for the total cross section $\sigma(c\bar{c})$ and with our results is legitimate, since the extra contribution of the Λ_c^+-hyperon-production channel is below 10% in the range 200–800 GeV.

The theoretical curves presented in Fig. 4 were obtained in [3] within two approximations. The dash-dotted curves represent the results of the calculations performed in the next-to-leading order (NLO) of perturbative QCD. The solid curves are the pioneering results taking into account the effect of resummation of the contribution from soft gluons emitted by colliding partons at the NLO + NLL level, where NLL corresponds to the approximation next to the leading-logarithm approximation. These calculations employed the theoretical parameter values of $m_c =$ 1.5 GeV and $\Lambda_{\mathrm{QCD}} = 120$ MeV and the MRSR2 parameterization for the parton structure functions [47]. The calculations were performed for the scale-parameter values of $\mu = m_c$ and $\mu = 2m_c$. Figure 4 shows that the correction for soft-gluon emission reduces the interval of uncertainties associated with variations in the parameter μ and enhances the estimate of the near-threshold cross section $\sigma(c\bar{c})$ by a factor of about 2. The theoretical predictions were calculated in [3] for energies in excess of 100 GeV; therefore, the curves presented in Fig. 4 were extrapolated down to 70 GeV.

Figure 4 demonstrates that our result is compatible with the general experimental dependence and with the theoretical predictions.

Since the near-threshold production of heavy quarks—in particular, charmed quarks—is of considerable interest for QCD, the SVD collaboration

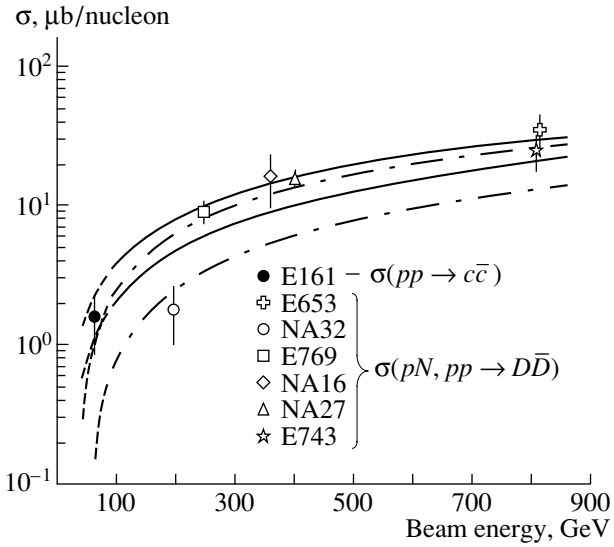

Fig. 4. Cross section for charmed-particles production in proton–nucleon interactions [13, 41–46]. The results of QCD calculations [3] at the NLO + NLL and the NLO level are depicted by solid and dash-dotted curves, respectively. The two upper (lower) curves correspond to $\mu = m_c$ ($\mu = 2m_c$).

plans to continue studying in detail the properties of charmed particles by obtaining a sample of 10^3–10^4 events owing to an upgrade of the SVD setup [11]. The upgrade will consist in replacing the bubble chamber by a vertex detector equipped with microstrip plates and in incorporating a photon recorder and a threshold Cherenkov counter into the setup.

ACKNOWLEDGMENTS

This work was supported by the Russian Foundation for Basic Research (project nos. 95-02-05226 and 96-02-17927).

REFERENCES

1. M. Mangano, P. Nason, and G. Ridolfi, Nucl. Phys. B **405**, 507 (1993).
2. S. Frixione, M. Mangano, P. Nason, and G. Ridolfi, Preprint No. CERN-TH/97-16, CERN (Geneva, 1997).
3. R. Bonciani, S. Catani, M. Mangano, and P. Nason, Nucl. Phys. B **529**, 424 (1998).
4. S. Brodsky, P. Hoyer, C. Peterson, and N. Sakai, Phys. Lett. B **93B**, 451 (1980); S. Brodsky and C. Peterson, Phys. Rev. D **23**, 2745 (1981); R. Vogt and S. Brodsky, Nucl. Phys. B **438**, 261 (1995); V. A. Litvin and A. K. Likhoded, Yad. Fiz. **62**, 728 (1999) [Phys. At. Nucl. **62**, 679 (1999)].
5. A. K. Likhoded and S. R. Slabospitsky, Yad. Fiz. **60**, 1097 (1997) [Phys. At. Nucl. **60**, 981 (1997)].
6. M. Beneke, Preprint No. CERN-TH/98-202, CERN (Geneva, 1998); A. Pineda and J. Soto, Nucl. Phys. B (Proc. Suppl.) **64**, 428 (1998); M. Beneke and V. A. Smirnov, Preprint No. CERN-TH/97-315, CERN (Geneva, 1997).
7. BIS-2 Collab. (A. N. Aleev *et al.*), Yad. Fiz. **35**, 1175 (1982) [Sov. J. Nucl. Phys. **35**, 687 (1982)].
8. BIS-2 Collab. (A. N. Aleev *et al.*), Yad. Fiz. **37**, 1474 (1983) [Sov. J. Nucl. Phys. **37**, 877 (1983)].
9. A. E. Asratyan *et al.,* Phys. Lett. B **79B**, 497 (1978).
10. A. M. Andriishin *et al.,* Preprint No. 84-3, IFVÉ (Institute for High-Energy Physics, Protvino, 1984).
11. E. N. Ardashev *et al.,* Preprint No. 99-28/586, NIIYaF MGU (Institute of Nuclear Physics, Moscow State University, Moscow, 1999).
12. M. Shafranov, in *Proceedings of the XXVII International Conference on High Energy Physics, Glasgow, 1994,* p. 1029.
13. E. N. Ardashev *et al.* (E-161), Preprint No. 97-40/491, NIIYaF MGU (Institute of Nuclear Physics, Moscow State University, Moscow, 1997); Preprint No. 99-27/585, NIIYaF MGU (Institute of Nuclear Physics, Moscow State University, Moscow, 1999).
14. E. N. Ardashev *et al.,* Nucl. Instrum. Methods Phys. Res. A **356**, 210 (1995).
15. V. A. Samsonov, Prib. Tekh. Éksp., No. 5, 48 (1998).
16. I. V. Boguslavsky *et al.,* Soobshch. Ob'edin. Inst. Yad. Issled., Dubna, No. R1-90-247 (1990).
17. G. A. Bogdanova *et al.,* Preprint No. 97-8/459, NIIYaF MGU (Institute of Nuclear Physics, Moscow State University, Moscow, 1997).
18. S. G. Basiladze and O. Z. Éloev, in *Development of Computer Interfaces for Measuring Equipment* (Mosk. Gos. Univ., Moscow, 1985), p. 61.
19. S. G. Basiladze, Prib. Tekh. Éksp., No. 5, 6 (1983); S. G. Basiladze, V. V. Suvorov, and O. Z. Éloev, Prib. Tekh. Éksp., No. 6, 52 (1983).
20. S. G. Basiladze and O. Z. Éloev, in *Development of Computer Interfaces for Measuring Equipment* (Mosk. Gos. Univ., Moscow, 1985), p. 58.
21. S. G. Basiladze, V. I. Korzh, V. A. Kramarenko, and O. Z. Éloev, in *Hardware and Software Support for Systems of Experimental-Investigation Automation* (Mosk. Gos. Univ., Moscow, 1986), p. 120.
22. V. A. Vakhrameev *et al.,* Preprint No. 90-151, IFVÉ (Institute for High-Energy Physics, Protvino, 1990).
23. M. Yu. Bogolyubsky *et al.,* Preprint No. 91-172, IFVÉ (Institute for High-Energy Physics, Protvino, 1991); G. A. Bogdanova *et al.,* Preprint No. 92-32/281, NIIYaF MGU (Institute of Nuclear Physics, Moscow State University, Moscow, 1992).
24. M. Yu. Bogolyubsky *et al.,* Preprint No. 97-50, IFVÉ (Institute for High-Energy Physics, Protvino, 1997).
25. D. Crennel *et al.,* Nucl. Instrum. Methods **158**, 111 (1978).
26. V. D. Kravtsov and V. A. Khmel'nikov, Soobshch. Ob'edin. Inst. Yad. Issled., Dubna, No. R1-93-353 (1993).
27. V. D. Kravtsov and A. Ya. Kutov, Soobshch. Ob'edin. Inst. Yad. Issled., Dubna, No. R10-93-354 (1993).
28. J. C. Lassale *et al.,* Nucl. Instrum. Methods **176**, 371 (1980).
29. P. F. Ermolov, A. V. Kubarovsky, and M. S. Levitsky, Prib. Tekh. Éksp., No. 5, 39 (1998).
30. A. V. Kubarovsky, Preprint No. 98-50/551, NIIYaF MGU (Institute of Nuclear Physics, Moscow State University, Moscow, 1998).
31. M. Yu. Bogolyubsky, M. A. Zaporozhets, and L. A. Tikhonova, Preprint No. 95-34/398, NIIYaF MGU (Institute of Nuclear Physics, Moscow State University, Moscow, 1995); M. Yu. Bogolyubsky, I. V. Boguslavsky, A. V. Kubarovsky, and L. A. Tikhonova, Prib. Tekh. Éksp., No. 3, 35 (1999).
32. V. V. Ammosov *et al.,* Nucl. Phys. B **115**, 269 (1976).
33. M. Aguilar-Benitez *et al.,* Z. Phys. C **31**, 491 (1986).
34. Yu. P. Gorin *et al.,* Yad. Fiz. **14**, 998 (1971) [Sov. J. Nucl. Phys. **14**, 560 (1972)].
35. V. V. Babintsev *et al.,* Preprint No. M-25, IFVÉ (Institute for High-Energy Physics, Protvino, 1976).
36. S. A. Bunyatov and Yu. A. Nefedov, Yad. Fiz. **60**, 1045 (1997) [Phys. At. Nucl. **60**, 935 (1997)].
37. V. V. Ammosov *et al.,* Yad. Fiz. **53**, 999 (1991) [Sov. J. Nucl. Phys. **53**, 617 (1991)].
38. S. V. Belikov *et al.,* Yad. Fiz. **58**, 1993 (1995) [Phys. At. Nucl. **58**, 1886 (1995)].

39. BIS-2 Collab. (A. N. Aleev *et al.*), Yad. Fiz. **56** (9), 147 (1993) [Phys. At. Nucl. **56**, 1235 (1993)].
40. A. N. Aleev *et al.,* Z. Phys. C **37**, 243 (1988).
41. G. A. Alves *et al.* (E769), Phys. Rev. Lett. **77**, 2388 (1996).
42. M. Aguilar-Benitez *et al.* (NA27), Z. Phys. C **40**, 321 (1988).
43. S. Barlag *et al.* (NA32), Z. Phys. C **39**, 451 (1988).
44. M. Aguilar-Benitez *et al.* (NA16), Phys. Lett. B **135B**, 237 (1984).
45. R. Ammar *et al.* (E743), Phys. Rev. Lett. **61**, 2185 (1988).
46. K. Kodama *et al.* (E653), Phys. Lett. B **263**, 573 (1991).
47. A. D. Martin, R. G. Roberts, and W. J. Stirling, Phys. Lett. B **387**, 419 (1996).

Translated by E. Kozlovskiĭ

Physics of Atomic Nuclei, Vol. 64, No. 5, 2001, pp. 902–906. From Yadernaya Fizika, Vol. 64, No. 5, 2001, pp. 969–974.

ELEMENTARY PARTICLES AND FIELDS
Experiment

Mean Free Path of $Z = 2$ Nuclei from ^{3}Hep Interactions in Liquid Hydrogen*

V. V. Glagolev[1),], M. Kravčíková, R. M. Lebedev[†1)], G. Martinská, G. D. Pestova[1)], L. Šándor[2)], T. Siemiarczuk[3)], J. Urbán, and W. Wiślicki[3)]**

University of P.J. Šafárik, Jesenná 5, SK-04154 Košice, Slovak Republic

Received August 8, 2000

Abstract—Results are presented for the total and the apparent cross section measured in ^{3}Hep interactions at an incident momentum of 8.0 GeV/c and for an anomalously short mean free path of $Z = 2$ secondary nuclei from these interactions. About 14000 $Z = 2$ nuclei leading to 2319 secondary interactions are studied. An admixture of 0.5% of anomalons is found with a mean free path of 1.5 cm to be compared with around 250 cm for primary interactions. Our results are compared with other data from the interactions of He nuclei with protons at various energies. © *2001 MAIK "Nauka/Interperiodica".*

1. INTRODUCTION

A short mean free path of relativistic nuclear fragments of high-energy heavy ions has been occasionally observed since 1954 in nuclear emulsion experiments carried out in cosmic rays. The first provocative piece of evidence for anomalous nuclear cascade interactions induced by heavy cosmic-ray nuclei was reported in [1], and the effect was concentrated in the first few centimeters from the primary-interaction vertex. Because of limited statistics in cosmic rays, these results could not gain recognition.

The first experiment to study anomalous nuclei with significant statistics by using the nuclear-emulsion technique was realized when relativistic nuclear beams became available from the Berkeley Bevalac in 1980. Nuclear interactions induced by ^{16}O and ^{56}Fe beams of energy 2 GeV per projectile nucleon showed anomalously short mean free paths for nuclear fragments within a few centimeters after their emission [2]. A statistical analysis introduced the so-called interaction model trying to describe the effect under the assumption that only a small part of projectile fragments have a cross section larger by one order of magnitude. In the following years, several experiments were performed in this field, and their results confirmed a significantly shorter mean free path of about 2–15% of the projectile fragments [3]. Later experiments used, as detectors, not only nuclear emulsions but also bubble chambers, plastic detectors, and Cherenkov counters. Some results support the anomalous effect [4], but, in other cases, the effect was not confirmed [5]. There also exist a series of theoretical attempts at understanding and describing the anomalous behavior. Among other things, they invoke quark–gluon effects, open color states, quasimolecular states, nuclear-density effects, and metastable nuclear states [6]. Despite an extensive amount of published results, the current situation is complicated—no consensus has been reached on the question of whether the effect is real or not; moreover, we do not have either a theory that would explain the anomalous shortening of the mean free paths of fragments or a general idea that would explain the ambiguity of experimental results. Thus, the question of anomalons remains open for further experiments.

2. DESCRIPTION OF THE EXPERIMENT

Our previous efforts aimed at studying the mean free paths of secondary He nuclei with protons [7, 8] preceded the analysis of data from ^{3}Hep interactions induced by a ^{3}He beam of momentum 8.0 GeV/c. This is the fourth in the series of experiments studying ^{3}He and ^{4}He interactions with protons by using the 1-m hydrogen bubble chamber installed at the Joint Institute for Nuclear Research (JINR, Dubna). The experimental setup used was described in detail

*This article was submitted by the authors in English.

†Deceased.

1)Joint Institute for Nuclear Research, Dubna, Moscow oblast, 141980 Russia.

2)Institute of Experimental Physics, Slovak Academy of Sciences, Watsonova 47, SK-04353 Košice, Slovak Republic.

3)Institute for Nuclear Studies, ul. Hoza 69, PL-00-681 Warsaw, Poland.

**e-mail: glagolev@sunhe.jinr.ru

Table 1. Cross sections (total and apparent) for Hep interactions at various He momenta

Interaction	Momentum, GeV/c	σ_{app}, mb	σ_{tot}, mb
^{3}Hep	8.0	112.1 ± 1.7	125.5 ± 1.3
	13.5	106.0 ± 1.6	118.0 ± 1.2
^{4}Hep	8.6	135.4 ± 3.7	149.0 ± 2.1
	13.6	138.2 ± 3.2	152.5 ± 1.7

elsewhere [9]. A hydrogen bubble chamber is simultaneously a pure proton target and a full-solid-angle detector. In experiments where nuclear beams are incident on a fixed proton target, all fragments of incoming nuclei are fast in the laboratory frame; therefore, they can be detected, well measured, and identified nearly without losses (almost all losses due to the chamber threshold momentum are concentrated in the elastic channel). A low hydrogen density and the measured track momentum enabled us to identify secondary charged particles on the basis of the ionization check.

These conditions allowed (i) a suitable selection of primary interactions with even topology (that is, a crosscheck of $Z = 2$ tracks by using electric-charge conservation), (ii) a unique identification of doubly charged tracks on the ionization basis, and (iii) a reliable selection and identification of $Z = 2$ fragments because the momenta of secondary ^{3}He nuclei are close to the beam momentum and because the production angles are in the forward cone of 10°.

All these conditions are of paramount importance for a determination of the mean free path in the interactions of light nuclei with protons and for the ensuing analysis of the anomalon effect.

For data processing, the standard chain was used: the pictures were scanned twice for all topologies, and measurements for three projections were used for a geometric reconstruction and a subsequent kinematical analysis of events. This was carried out by using an appropriate version of the CERN program system based on the HYDRA library. The ionization of secondary charged particles was estimated visually.

The complete data sets for ^{4}Hep and ^{3}Hep interactions at two reaction energies contain [7, 8, 10] (i) 3688 secondary interactions found on the corresponding 20231 $Z = 2$ fragment tracks for ^{4}Hep at 13.6 GeV/c, (ii) results of the analysis of the same interactions at the lower incoming momentum of 8.6 GeV/c that were observed on the basis of even vaster statistics of 4197 secondary interactions found from 23435 $Z = 2$ fragments from primary interactions, (iii) 1069 secondary interactions found for 7211 $Z = 2$ fragments in the case of ^{3}Hep interactions at 13.5 GeV/c, and (iv) 2319 secondary interactions corresponding to 14020 $Z = 2$ He fragments at the lower ^{3}He beam momentum of 8.0 GeV/c.

Table 2. Mean free path versus the distance from the primary vertex

x, cm	λ, cm	$\Delta\lambda$,cm
1	177.6	14.2
3	215.1	19.0
5	238.6	22.3
7	293.0	30.5
9	326.2	36.1
11	244.6	23.8
13	252.0	25.4
15	232.8	22.9
17	278.4	30.5
19	231.8	23.6
21	271.5	30.5
23	231.8	24.5
26	218.4	16.4
30	258.1	21.9
34	254.5	22.4
40	232.3	14.9
48	244.6	18.2
56	235.6	19.9
65	242.3	24.0

It can be seen that the samples used are statistically well based in relation to the other ones [7].

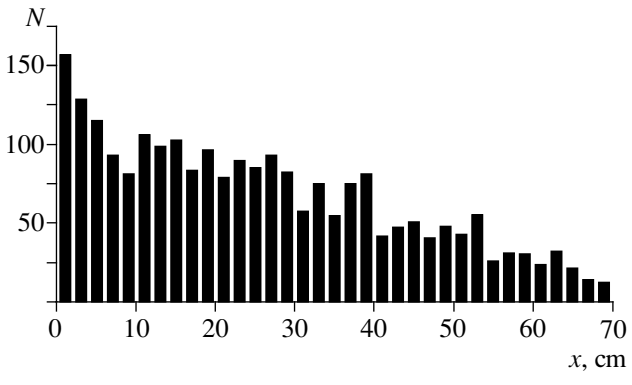

Fig. 1. Distribution of distances between the primary and the secondary vertex.

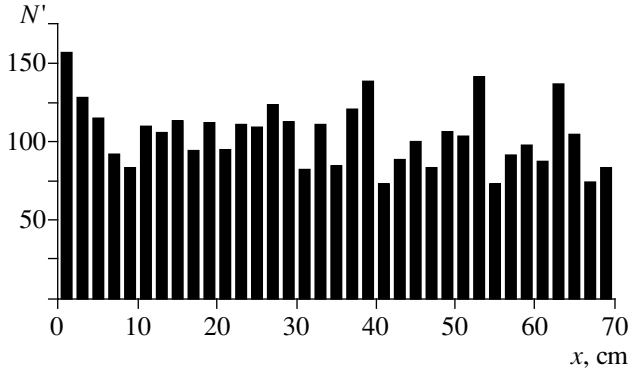

Fig. 2. As in Fig. 1, but after geometric corrections.

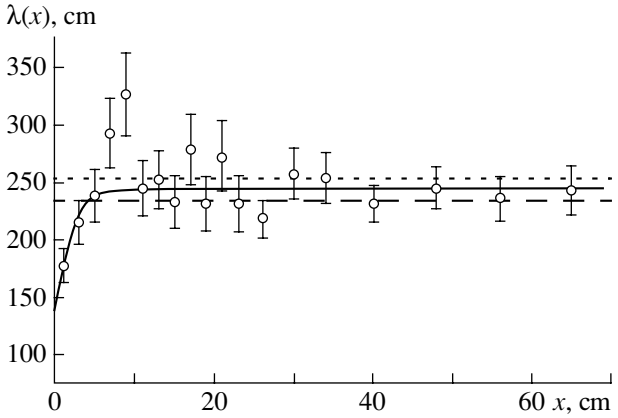

Fig. 3. Mean free path as a function of the distance between the primary and secondary interactions (the notation for the curves is explained in the main body of the text).

3. CROSS SECTIONS FOR ^{3}Hep INTERACTIONS AT 8.0 GeV/c

The total and topological cross sections for ^{4}Hep collisions at momenta of 8.6 and 13.6 GeV/c and for ^{3}Hep collisions at 13.5 GeV/c are published in [11].

In the case of ^{3}Hep interactions at 8.0 GeV/c, the entire sample was doubly scanned, but only a limited part of it was measured and fully processed. Two independent scannings gave 23735 ^{3}Hep interactions of different topologies, which correspond to 187692 primary nuclei. The average scanning efficiency was 99%, and the fiducial volume was $l_e = 34.6 \pm 0.1$ cm for primary interactions.

Because of limited statistics, the losses of events in the elastic channel could not be determined in the way used in [11, 12]. But we made use of these results and arrived at the conclusion that the losses can be estimated at 12%, irrespective of the incoming energy and nuclei. Taking into account comparable statistics at the two values of the ^{3}He momentum, we estimated the losses at $N_{\text{invis}} = 2848 \pm 174$, which corresponds to 26583±232 primary ^{3}Hep interactions at 8.0 GeV/c. The total and apparent interaction cross sections were determined by using the standard formula. The numerical results are

$$\sigma_{\text{tot}} = 125.5 \pm 1.3 \text{ mb}, \qquad \sigma_{\text{app}} = 112.1 \pm 1.7 \text{ mb}.$$

The apparent cross-section value σ_{app} corresponds to the mean free path of $\lambda_{\text{app}} = 253.7 \pm 3.8$ cm, which will be used in the next sections.

The values obtained here for the cross sections are compared in Table 1 with those published in our previous studies [11, 12] for He isotopes at different energies.

4. MEAN FREE PATH FOR SECONDARY ^{3}Hep INTERACTIONS AT A PRIMARY MOMENTUM OF 8.0 GeV/c

Our experimental data were subjected to two independent scanning procedures for revealing secondary interactions. The fragments formed have been followed to the end of the chamber fiducial volume. For secondary tracks with $Z = 2$, 2319 interactions have been found for 14020 events with even topology. The overall scanning efficiency was $\varepsilon = (99.1 \pm 0.5)\%$. Particular attention has been given to the dependence of the scanning efficiency on the distance x between the primary and secondary vertices. Within the statistical errors, we have found constant scanning efficiency, independent of x.

As a matter of fact, all fragments of the incoming nuclei do not have the same volume to give rise to a secondary interaction, but this depends on the place where the primary interaction occurs. In view of this, a geometric correction taking into account this fact has been applied to the data; accordingly, the events have been weighted in the following way:

$$w_i = \begin{cases} 1, & \text{for } x < L_0 \\ \dfrac{1 - e^{-(L-L_0)/\lambda}}{1 - e^{-(L-x)/\lambda}}, & \text{for } x > L_0. \end{cases}$$

Here, $L_0 = 8$ cm is the distance from the physical end of the chamber to the end of the fiducial volume for the primary interactions; $L = 78$ cm is the length of the fiducial volume for secondary interactions; and λ stands for $\lambda_{\text{app}} = 253.7 \pm 3.8$ cm—the mean free path of primary ^{3}He nuclei at 8.0 GeV/c.

The effect of the geometric correction is illustrated in Figs. 1 and 2, which display the corresponding raw and weighted distributions of the distance between the primary and secondary vertices.

Table 3. Results of various fits to $\lambda(x)$ for ^{3}Hep interactions at 8.0 GeV/c

Function	λ_n,cm	λ_a, cm	α, %	χ^2/NDF
$\lambda_n = \text{const}$	234.3 ± 4.9	–	–	2.18
$f(\lambda_n, \lambda_a, \alpha)$	$244.02^{+5.1}_{-5.5}$	$1.47^{+0.88}_{-0.71}$	$0.45^{+0.15}_{-0.13}$	0.93
$f(\lambda_n = \text{fix}, \lambda_a, \alpha)$	$\lambda_n = \lambda_{vis}$	$1.82^{+0.95}_{-0.65}$	$0.57^{+0.16}_{-0.14}$	1.28

Table 4. Fitted values of the parameters λ_n, λ_a, and α and χ^2/NDF

Experiment	λ_n, cm	λ_a, cm	α, %	χ^2/NDF
^{4}Hep, 13.6 GeV/c[7]	$240.7^{+4.7}_{-4.6}$	$1.9^{+2.0}_{-1.7}$	$0.40^{+0.21}_{-0.13}$	1.46
^{4}Hep, 8.6 GeV/c[7]	$230.0^{+6.1}_{-5.3}$	$7.5^{+3.7}_{-2.2}$	$1.06^{+0.45}_{-0.31}$	1.17
^{3}Hep, 13.5 GeV/c[8]	$270.4^{+14.6}_{-12.7}$	$6.0^{+3.7}_{-2.5}$	$1.56^{+0.76}_{-0.54}$	0.38
^{3}Hep, 8.0 GeV/c	$244.02^{+5.1}_{-5.5}$	$1.47^{+0.88}_{-0.71}$	$0.45^{+0.15}_{-0.13}$	0.93

Table 5. Mean free path of secondary $Z = 2$ nuclei

Experiment	$\lambda(x < 10\text{ cm})$	$\lambda(x > 10\text{ cm})$	λ_{app}, cm
^{4}Hep, 13.6 GeV/c[7]	212.9 ± 7.3	246.1 ± 4.7	211.5 ± 5.8
^{4}Hep, 8.6 GeV/c[7]	189.9 ± 5.7	228.5 ± 4.2	207.2 ± 4.8
^{3}Hep, 13.5 GeV/c[8]	195.7 ± 11.5	277.7 ± 9.9	270.2 ± 4.1
^{3}Hep, 8.0 GeV/c	238.1 ± 10.2	241.6 ± 5.6	253.7 ± 3.8

Upon applying the efficiency and geometric corrections, the number of secondary interactions changes to 3629; of these, 574 are produced at a distance less than 10 cm behind the primary vertex. In the resulting sample of events, the x dependence of the mean free path λ was calculated according to the formula

$$\lambda(x) = \sum_{i=1}^{n} S_i/n,$$

where $\sum S_i$ is the total length of the paths of the interacting and noninteracting $Z = 2$ fragments in the interval $\Delta x = x_{i+1} - x_i$ with $\Delta x = 2$ cm and n is the number of secondary interactions found in this interval. This way enables us to make the estimate of $\lambda(x)$ independent of the place of the primary interaction. The resulting values of λ are given in Table 2 versus x, the errors being purely statistical.

Our experimental values were fitted in terms of the function

$$\lambda(x) = [(1-\alpha)\exp(-x/\lambda_n) + \alpha\exp(-x/\lambda_a)] / [(1-\alpha)/\lambda_n \exp(-x/\lambda_n) + \alpha/\lambda_a \exp(-x/\lambda_a)]^{-1},$$

which corresponds to the customary assumption that the set of secondary nuclei contains an abnormal component with an enhanced cross section. This two-component function represents one of the simplest hypotheses describing the decrease in the mean free path at short distances and is a convenient and commonly used parametrization of data. It involves three free parameters: λ_n and λ_a, which are the normal and the anomalous mean free path, respectively, and α, which is the fraction of the anomalous cross section. However, it should not be taken literally in view of the present status of experimental findings.

The experimental distribution of the mean free path $\lambda(x)$ of $Z = 2$ secondary nuclei versus the distance x is shown in Fig. 3, where the solid curve represents a fit obtained under the assumption that there is an anomalous component in addition to the primary one, the dashed line is a fit assuming only a normal component and yielding a constant value of $\lambda = 234.3$ cm, and the dotted line corresponds to a fit with fixed $\lambda_{\text{app}} = 253.7$ cm for the primary ^{3}Hep interactions at 8.0 GeV/c. Table 3 contains the fitted parameter values, together with χ^2/NDF.

To demonstrate more clearly the statistical significance of the results, the χ^2 contour maps are drawn in Fig. 4, where the contours labeled with *1*, *2*, ... correspond to confidence levels of 1, 2, ... standard deviations. As can be seen from Fig. 4, the zero

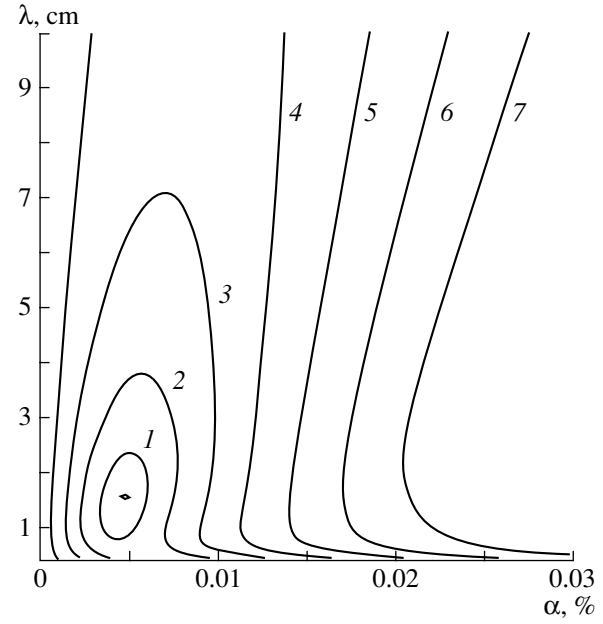

Fig. 4. χ^2 contour maps.

hypothesis ($\alpha = 0$) is excluded by more than four standard deviations. The results of a two-component fit to a experimental data for $Z = 2$ fragments from ^{3}Hep and ^{4}Hep interactions at the above two energy values are shown in Table 4.

The measured mean free paths for $x < 10$ cm and $x > 10$ cm are compared in Table 5 with the apparent value of the mean free path for primary interactions.

From the values obtained here, one can see that the results for ^{3}Hep interactions at 8.0 GeV/c do not contradict the results of previous experiments (Tables 4 and 5). In these data, there is no indication of some regular tendency between the anomalous parameters (λ_a and α) and the number of nucleons or the reaction energy. The largest anomalous fraction of $\alpha = 1.56\%$ [8] has been found in ^{3}Hep collisions at the higher energy value. This experiment gives nearly the same values of the mean free path for $x < 10$ cm and for $x > 10$ cm. The anomalous effect is less pronounced in this experiment, and the fraction of 0.45% corresponds to $\lambda_a = 1.47$ cm. Within two standard deviations, the fitted parameters of the anomalous component—the mean free path and the fraction in question—are consistent for the two nuclear species and for the two energy values (see Table 4).

5. CONCLUSION

We have studied ^{3}Hep interactions at 8.0 GeV/c. In particular, we have determined the total and the apparent cross sections for these interactions and compared these results with those from our previous studies. The mean free path of secondary doubly charged tracks has been examined in terms of the two-component hypothesis as a continuation of our previous work on anomalons. The values obtained for the anomalous fraction and the mean free path do not contradict previous results. The comparison has not shown any systematics associated with the reaction energy or with the number of nucleons. The problem of anomalons remains open, so that further experiments are required to get more conclusive and decisive data.

REFERENCES

1. A. Milone, Nuovo Cimento **12**, 548 (1954).
2. E. M. Friedlander *et al.,* Phys. Rev. Lett. **45**, 1084 (1980).
3. B. Norén, Cosmics and Subatomic Phys. Report No. LUIP8804LUNFD6 / (NFFK-7087)1-101 (1988).
4. D. Ghosh *et al.,* Phys. Rev. Lett. **54**, 396 (1985); H. B. Barber *et al.,* Phys. Rev. Lett. **48**, 856 (1982); M. M. Aggarwal *et al.,* Phys. Lett. B **112B**, 31 (1982); N. Klein *et al.,* J. Phys. G **9**, 1239 (1983); E. M. Friedlander *et al.,* Phys. Rev. C **27**, 1489 (1983); P. L. Jain *et al.,* Phys. Rev. Lett. **52**, 2231 (1984).
5. V. G. Ableev *et al.,* Preprint No. R1-84-476, JINR (Joint Institute for Nuclear Research, Dubna, 1984); J. D. Stevenson *et al.,* Phys. Rev. Lett. **52**, 515 (1984); P. L. Jain *et al.,* Phys. Rev. C **25**, 3216 (1982); H. Drechsel *et al.,* Phys. Rev. Lett. **55**, 1258 (1985); R. L. Clarke *et al.,* Phys. Rev. D **33**, 19 (1986).
6. S. Fredrikson and M. Jändel, Phys. Rev. Lett. **48**, 14 (1982); B. F. Bayman *et al.,* Phys. Rev. Lett. **49**, 532 (1982); P. J. S. Watson *et al.,* Phys. Rev. D **27**, 542 (1983); B. A. Arbuzov *et al.,* Yad. Fiz. **42**, 542 (1985) [Sov. J. Nucl. Phys. **42**, 342 (1985)]; Y. E. Kim, Phys. Rev. Lett. **57**, 2508 (1986).
7. M. Bánó *et al.,* Phys. Lett. B **166B**, 453 (1986).
8. M. Bánó *et al.,* Phys. Lett. B **196**, 255 (1987).
9. B. S. Aladashvili *et al.,* Nucl. Instrum. Methods **129**, 10 (1975); JINR Commun. No. 1-7645 (Dubna, 1973).
10. M. Bánó *et al.,* Report No. SINS-2121/P-VI/PH/A (Otwock-Świerk, 1991).
11. V. V. Glagolev *et al.,* Z. Phys. C **60**, 421 (1993); JINR Commun. No. P1-90-561 (Dubna, 1990).
12. H. Braun *et al.,* Czech. J. Phys. B **39**, 1267 (1989).

Physics of Atomic Nuclei, Vol. 64, No. 5, 2001, pp. 907–909. From Yadernaya Fizika, Vol. 64, No. 5, 2001, pp. 975–977.

ELEMENTARY PARTICLES AND FIELDS
Experiment

Cross Sections for ^{4}He Interaction with Protons at 5 GeV/c*

A. V. Blinov, M. V. Chadeyeva, V. E. Grechko†, and V. F. Turov

Institute of Theoretical and Experimental Physics, Bol'shaya Cheremushkinskaya ul. 25, Moscow, 117259 Russia

Received February 24, 2000

Abstract—The total and topological ^{4}Hep cross sections, as well as the cross sections for individual αp-interaction channels and the differential cross sections $d\sigma/dt$ for elastic αp scattering, were measured by using a 2-m hydrogen bubble chamber exposed to a separated beam of 5-GeV/c α particles from the ITEP synchrotron (the kinetic energy of initial protons in the nuclear rest frame was $T_p = 620$ MeV). The data obtained are compared with the results of previous experiments and with theoretical predictions based on Glauber–Sitenko multiple-scattering theory. © *2001 MAIK "Nauka/Interperiodica"*.

Systematic investigations of nuclear reactions in few-nucleon systems at intermediate energies have been carried out at ITEP for the last few years by making use of extremely light nuclei (^{3}H, ^{3}He, ^{4}He) as a beam and liquid-hydrogen bubble chambers (80 cm and 2 m) as a target (see, for example, [1] for bibliography and background). Data on the cross sections for ^{4}He interaction with protons and αp elastic scattering below the pion-production threshold in the elementary NN process were reported in [1]. The momentum of the ^{4}He nuclei averaged over the bubble-chamber fiducial volume was 2.7 GeV/c (the kinetic energy of initial protons in the nuclear rest frame was $T_p = 220$ MeV). Here, we present some new data on αp-interaction cross sections at 5 GeV/c ($T_p = 620$ MeV), in which case pions are copiously produced. In this energy range, data on the cross sections for individual ^{4}Hep-interaction channels have been obtained for the first time. Data on the total and differential cross sections for αp scattering are compared with the results of previous experiments in the energy range considered and with the predictions of Glauber–Sitenko multiple-scattering theory. The present experiment is the only one based on nonelectron techniques in this energy range. For the first time, a similar experimental scheme (with an α-particle beam incident on a bubble chamber) was implemented with the JINR 100-cm liquid-hydrogen bubble chamber at initial momenta of 8.6 and 13.6 GeV/c (see [1]).

The 2-m liquid-hydrogen bubble chamber was exposed to a separated beam of 5-GeV/c α particles from the ITEP synchrotron. About 120000 pictures have been obtained with an average of about eight initial particles for the chamber extension. About 18000 events have been measured. Special features of our experimental procedure are described in [1].

The total cross section is defined as

$$\sigma_{\text{tot}} = \frac{1}{nl} \ln \frac{1}{1 - N_{\text{int}}/N_0}, \qquad (1)$$

where n is the number of hydrogen nuclei in 1 cm^3, l is the fiducial length, N_0 is the number of initial tracks, and N_{int} is the total number of interactions in the fiducial volume with allowance for a systematic loss of two-prong events.

Two- and three-prong αp events were identified by means of a kinematical analysis and track-ionization measurements. A correction was introduced for the loss of two-prong events with a large dip angle. This correction was determined from the distribution over the angle between the event plane and the plane spanned by the initial track and the vector directed along the magnetic field in the chamber. The loss of inelastic two-prong events was about 14%. The loss of elastic-scattering events with a short recoil-proton track for $|t| < 0.03$ (GeV/c)^2, where the differential cross sections have not been determined, was evaluated by extrapolating the data in the interval $0.035 < |t| < 0.1$ (GeV/c)^2 on the exponential function to the region $|t| < 0.03$ (GeV/c)^2. For $|t| < 0.01$ (GeV/c)^2, the differential cross section for elastic scattering has not been measured because of poor statistics.

The topological cross sections, the number of events in each channel, and the cross sections for αp interactions at 5 GeV/c are presented in Table 1 (only statistical errors are indicated).

The total αp-interaction cross section is 121.5 ± 2.9 mb (the error is purely statistical). The systematic

*This article was submitted by the authors in English.
†Deceased.

Table 1. Topological cross sections and cross sections for individual αp-interaction channels at a momentum of 5 GeV/c ($T_p = 620$ MeV)

Topology of an event	Topological cross section, mb	Channel	Number of events	Cross section, mb
2*	59.9±2.8	$^4\mathrm{He}p \to {}^4\mathrm{He}p$	1695	31.4±2.8
		$^4\mathrm{He}p \to {}^3\mathrm{He}pn$	2507	22.2±0.4
		$^4\mathrm{He}p \to {}^4\mathrm{He}n\pi^+$	233	2.0±0.1
		$^4\mathrm{He}p \to {}^4\mathrm{He}p\pi^0$	295	2.6±0.2
		$^4\mathrm{He}p \to {}^3\mathrm{He}pn\pi^0(\pi^0)$	97	0.80±0.08
3*	60.2±0.7	$^4\mathrm{He}p \to {}^3\mathrm{He}d\pi^0$	59	0.50±0.07
		$^4\mathrm{He}p \to {}^3\mathrm{H}pp$	1952	16.1±0.4
		$^4\mathrm{He}p \to ddp$	335	2.8±0.2
		$^4\mathrm{He}p \to dppn$	2567	21.2±0.4
		$^4\mathrm{He}p \to pppnn(\pi^0)$	1394	11.5±0.3
		$^4\mathrm{He}p \to {}^3\mathrm{H}d\pi^+$	101	0.80±0.08
		$^4\mathrm{He}p \to {}^3\mathrm{H}pn\pi^+$	362	3.0±0.2
		$^4\mathrm{He}p \to ddn\pi^+$	79	0.65±0.07
		$^4\mathrm{He}p \to dpnn\pi^+(\pi^0)$	128	1.10±0.09
		$^4\mathrm{He}p \to ppnnn\pi^+(\pi^0)$	79	0.65±0.07
		$^4\mathrm{He}p \to {}^3\mathrm{H}pp\pi^0$	117	1.00±0.09
		$^4\mathrm{He}p \to ddp\pi^0$	53	0.40±0.06
		$^4\mathrm{He}p \to dppn\pi^0(\pi^0)$	93	0.80±0.08
4*–5*	1.4 ± 0.1			

error in the absolute normalization of the cross section is about 3%.

The differential cross sections for αp elastic scattering at 5 GeV/c are presented in Table 2. These data can be very well parameterized by the exponential function $d\sigma/dt = Ae^{Bt}$ with $A = (9.4 \pm 0.5) \times 10^2$ mb/(GeV/c)^2 and $B = 31 \pm 1$ (GeV/c)$^{-2}$ (χ^2/NDF = 0.4).

Table 2. Differential cross sections for αp elastic scattering at 5 GeV/c ($T_p = 620$ MeV)

$-t$, (GeV/c)^2	$d\sigma/dt$, mb/(GeV/c)^2
0.035	311±19
0.045	246±15
0.055	172±13
0.065	134±12
0.075	97±10
0.085	70±8
0.100	52±5

For the theoretical interpretation of the elastic-scattering data, we have used Glauber–Sitenko multiple-scattering theory that takes into account the spin–isospin structure of the NN-scattering amplitude and which represents a simple generalization of the conventional Glauber theory of nondiffractive NN scattering.

The details of this theoretical approach are given in [1]. In our present calculations, we also parameterize the ground-state density of the ^{4}He nucleus in the Gaussian form $\rho(r) \sim \exp(-r^2/R^2)$ with $R = 1.25$ fm [1].

The figure shows the differential cross sections $d\sigma/dt$ for $^4\mathrm{He}p$ elastic scattering at a momentum of 5 GeV/c ($T_p = 620$ MeV) and the results of the calculations that were performed within Glauber–Sitenko multiple-scattering theory and which take

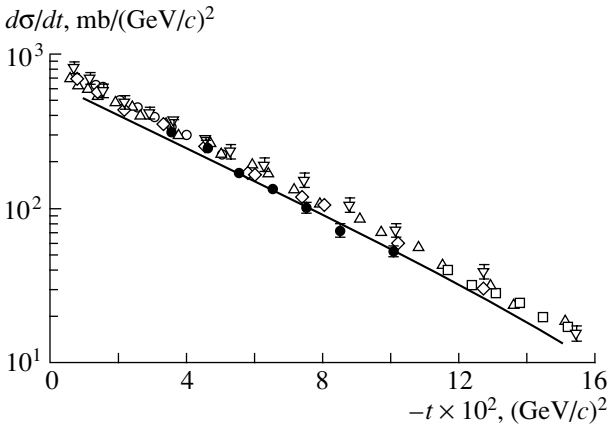

Differential cross section for the reaction ^{4}He$p \to {}^4$Hep. Points represent experimental data from (•) the present study ($T_p = 620$ MeV), (◊) [2] ($T_p = 500$ MeV), (△) [3] ($T_p = 560$ MeV), (▽) [4] ($T_p = 587$ MeV), (□) [5] ($T_p = 600$ MeV), and (○) [6] ($T_p = 695$ MeV). The solid line corresponds to the theoretical predictions (at $T_p = 620$ MeV) based on Glauber–Sitenko multiple-scattering theory taking into account the spin–isospin structure of the NN-scattering amplitude.

into account the spin–isospin structure of the NN-scattering amplitude (curve). For the sake of comparison, the data on ^{4}Hep elastic scattering at $T_p =$ 500 MeV [2], 560 MeV [3], 587 MeV [4], 600 MeV [5], and 695 MeV [6] are also displayed here. As can be seen from the figure, the shapes of the distributions from all these experiments are quite similar. All data are consistent. Note that independent experiments based on different experimental techniques yield very close results. Multiple-scattering theory perfectly describes the shape of the distribution, but the theoretical curve is slightly below the experimental data.

The total αp cross section obtained in this experiment at $T_p = 620$ MeV ($\sigma_{\text{tot}} = 121.5 \pm 2.9$ mb) is in good agreement with the result from [7] at $T_p = 563$ MeV ($\sigma_{\text{tot}} = 123.7 \pm 0.9$ mb). Some deviation from the theoretical value calculated for the total cross section by means of the optical theorem ($\sigma_{\text{tot}}^{\text{th}} = 113.4$ mb at $T_p = 620$ MeV) is caused by the inaccuracy of the theoretical scheme used here (see [1] for details).

The main results of our study are as follows:

(i) Using the 2-m ITEP liquid-hydrogen bubble chamber exposed to a separated beam of α particles with a momentum of 5 GeV/c ($T_p = 620$ MeV), we have measured the total and topological αp cross sections, as well as the cross sections for individual αp-interaction channels. The data on the cross sections for αp-reaction channels in this energy range have been obtained for the first time. The value of the total αp cross section from the present experiment is in good agreement with data from the literature.

(ii) The data on the differential αp cross sections are in good agreement with previous data in the energy range considered here and with the predictions of multiple-scattering theory.

ACKNOWLEDGMENTS

We thank the staff of the 2-m hydrogen bubble chamber, of the laboratory of separated beams, and of the laboratory of cryogenic engineering, who took part in the experiment, as well as the personnel manning the scanning devices and computers. We are very grateful to I.V. Kirpichnikov for his regular assistance throughout this work.

Note added. Our new data on the cross sections for ^{4}Hep inelastic scattering can be of considerable use in cosmology for improving the accuracy of calculations of nonequilibrium cosmological-nucleosynthesis processes [8].

REFERENCES

1. S. K. Abdullin *et al.,* Nucl. Phys. A **569**, 753 (1994); Yad. Fiz. **56** (4), 204 (1993) [Phys. At. Nucl. **56**, 536 (1993)].
2. G. A. Moss *et al.,* Phys. Rev. C **21**, 1932 (1980).
3. H. Courant *et al.,* Phys. Rev. C **19**, 104 (1979).
4. E. T. Boschitz *et al.,* Phys. Rev. C **6**, 457 (1972).
5. J. Fain *et al.,* Nucl. Phys. A **262**, 413 (1976).
6. G. N. Velichko *et al.,* Yad. Fiz. **42**, 1325 (1985) [Sov. J. Nucl. Phys. **42**, 837 (1985)].
7. P. Schwaller *et al.,* Nucl. Phys. A **316**, 317 (1979).
8. E. V. Sedelnikov, Yad. Fiz. **63**, 2000 (2000) [Phys. At. Nucl. **63**, 1907 (2000)].

Physics of Atomic Nuclei, Vol. 64, No. 5, 2001, pp. 910–916. From Yadernaya Fizika, Vol. 64, No. 5, 2001, pp. 978–985.

ELEMENTARY PARTICLES AND FIELDS
Experiment

Structures and Angular Distributions of Slow and Relativistic Charged Particles Produced in ^{7}Li–Emulsion Interactions at 3 GeV/c per Projectile Nucleon*

N. N. Abd-Allah and M. Mohery

Physics Departments, Faculty of Science, Sohag, Egypt
Received November, 29, 1999; in final form, April 4, 2000

Abstract—Experimental results on the multiplicity distributions of various particles produced in the interactions of ^{7}Li with emulsion nuclei at a momentum of 3 GeV/c per projectile nucleon are reported. A comparison with data on collisions induced by other nuclei at a nearly identical momentum per nucleon is presented in order to reveal the dependence on the projectile mass. The internal structure of ^{7}Li is explored by studying the projectile fragment. The mean multiplicity of shower particles, $\langle n_s \rangle$, induced by ^{7}Li is found to be less than that in the case of ^{6}Li projectiles. The angular distributions of target fragments and relativistic charged secondaries are investigated. No shock-wave phenomena are observed. Forward-to-backward ratios are calculated for each case. The probability distributions for relativistic secondaries produced per unit rapidity are studied in detail, along with the rapidity densities and their dependence on the projectile and the target mass. A comparison of the angular spectra of shower particles produced in central and peripheral collisions supports the limiting-fragmentation hypothesis. The collisions in question seem to become more central with increasing shower-particle multiplicity.

1. INTRODUCTION

Interest in nucleus–nucleus collisions quickened considerably when beams of relativistic heavy ions became available. Investigation of these interactions is expected to provide useful information about the multiparticle production mechanism.

It has always been interesting to study the general characteristics of different projectiles at different energies and mass numbers. The present experiment studying the interaction of ^{7}Li projectiles with emulsion at 3 GeV/c per nucleon is of special interest for two reasons: (i) This projectile provides a new point belonging to a wide spectrum of heavy-ion nuclear reactions carried out; therefore, it could lend support to certain theoretical models describing the mechanisms of high-energy nuclear reactions. (ii) It is interesting to see the effect of the neutron difference between ^{6}Li and ^{7}Li projectiles interacting with similar targets.

In high-energy nuclear collisions, it is convenient to introduce Lorentz-invariant kinematical variables to describe the phase-space domain into which particles are emitted. For example, the rapidity η describes the motion of particles along the beam direction.

The angular distributions of shower, gray, and black particles are reported and analyzed in detail. Angular distributions provide valuable data on single-particle distributions of s particles in multiple production in nucleus–nucleus interactions at high energies.

2. EXPERIMENTAL PROCEDURE

Stacks of Br-2 nuclear emulsions were exposed to a ^{7}Li beam accelerated to a momentum of 3 GeV/c per projectile nucleon at the Dubna synchrophasotron. The stacks had dimensions of 20 cm × 10 cm × 600 μm (undeveloped emulsions). The intensity of irradiation was 10^4 particle/cm^2, and the beam diameter was about 1 cm. Away from the surface and bottom by at least 50 μm (undeveloped emulsion), only very thick, dark beam tracks were chosen for double scanning along the track, fast scanning in the forward direction and slow scanning in the backward direction. The pellicles of each stack were doubly scanned by using a method such that each track was followed until it either interacted or left the pellicle. The scanned beam tracks were further examined by measuring the delta-electron density on each of them to exclude tracks having a charge less than the beam-particle charge [1].

*This article was submitted by the authors in English.

1063-7788/01/6405-0910$21.00

Table 1. Mean multiplicities of shower, gray, and black particles ($\langle n_s \rangle$, $\langle n_g \rangle$, and $\langle n_b \rangle$, respectively) produced in the interactions of ^{6}Li, ^{7}Li [8], and ^{7}Li projectiles with emulsion nuclei in various n_h intervals

Interval	Projectile	$\langle n_s \rangle$	$\langle n_g \rangle$	$\langle n_b \rangle$
$n_h < 7$	^{6}Li	2.91 ± 0.12	0.80 ± 0.03	1.44 ± 0.06
	^{7}Li	2.16 ± 0.09	0.82 ± 0.03	1.55 ± 0.06
	^{7}Li*	2.37 ± 0.14	0.85 ± 0.05	1.28 ± 0.06
$7 \leqslant n_h < 13$	^{6}Li	5.33 ± 0.47	2.92 ± 0.25	6.49 ± 0.53
	^{7}Li	3.91 ± 0.32	2.66 ± 0.22	6.76 ± 0.56
	^{7}Li*	4.00 ± 0.22	3.20 ± 0.12	6.34 ± 0.19
$13 \leqslant n_h < 27$	^{6}Li	10.13 ± 0.69	6.64 ± 0.47	12.94 ± 0.93
	^{7}Li	6.16 ± 0.43	5.75 ± 0.40	12.72 ± 0.88
	^{7}Li*	6.59 ± 0.40	7.20 ± 0.28	13.69 ± 0.28
$n_h \geqslant 28$	^{6}Li	12.63 ± 1.93	13.16 ± 2.01	16.88 ± 2.57
	^{7}Li	7.83 ± 1.25	13.05 ± 2.09	18.51 ± 2.96
	^{7}Li*	6.92 ± 0.50	13.48 ± 0.48	18.79 ± 0.54

* Our study.

In the measured events, secondary particles were classified as follows: (i) black particle tracks having a range $L < 3$ mm in emulsion (this range corresponds to a proton kinetic energy of less than 26 MeV); (ii) gray particle tracks having relative ionization $I^* = I/I_0 > 1.4$, where I is the particle-track ionization and I_0 is the ionization of a shower track in the narrow forward cone of angle $\theta \leqslant 3^\circ$, and $L > 3$ mm, which corresponds to a proton kinetic energy of 26–400 MeV; (iii) heavily ionizing particle tracks (h) including black or gray (or both) particle tracks; (iv) shower particles having $I^* \leqslant 1.4$ [tracks of this type with an emission angle of $\theta \leqslant 3^\circ$ were further subjected to rigorous multiple-scattering measurements for determining momenta and, consequently, for separating the product pions and singly charged projectile fragments (protons, deuterons, tritons)]; and (v) multiply charged ($Z \geqslant 2$) projectile fragments subdivided into $Z = 2, 3, \ldots, Z_{\text{beam}}$ tracks according to the measured delta electrons.

The total charge of projectile fragments, $Z^* = \sum n_i Z_i$, where n_i is the number of fragments of charge Z_i in an event, were calculated in each event. For each track, our measurements resulted in a determination of (a) the space angle θ (the angle between the direction of the beam and that of a given track) and (b) the azimuthal angle ϕ (the angle between the projection of a given track onto the plane orthogonal to the beam and the direction orthogonal to the beam in this plane (in the counterclockwise direction).

All relevant details concerning emulsion stacks, methods of measurement, etc., can be found in [1–5].

Over a total length of 113.83 m of scanned tracks, we found 723 inelastic interactions. Therefore, the mean free path of ^{7}Li nuclei in the emulsion was $\lambda_e = 15.74 \pm 0.8$ cm.

3. MULTIPLICITY CHARACTERISTICS

Energy transfer during high-energy nuclear collisions produces relativistic particles (pions). In this section, we study the dependence of secondary particles on the heavily ionizing tracks (n_h). It is known that the impact parameter is difficult to measure experimentally. For this reason, we consider the multiplicity n_h of target fragments as a measure of the impact parameter [1–3, 6, 7]. The higher the multiplicity n_h, the lower the impact parameter, and vice versa. The mean multiplicities of shower, gray, and black particles ($\langle n_s \rangle$, $\langle n_g \rangle$, and $\langle n_b \rangle$, respectively) from the interactions of ^{6}Li and ^{7}Li projectiles with emulsion nuclei at, respectively, 4.5 and 3 GeV/c per nucleon are quoted in Table 1 as functions of n_h intervals (collision impact parameter). This table demonstrates that, with increasing n_h (decreasing impact parameter), $\langle n_s \rangle$, $\langle n_g \rangle$, and $\langle n_b \rangle$ increase, which indicates that the number of nucleons from the incident beam that have interacted with target nuclei increases; the data in the table also indicate that, in each region of n_h, $\langle n_g \rangle$ and $\langle n_b \rangle$ are equal to each other within the statistical error. For all intervals of n_h, the values of

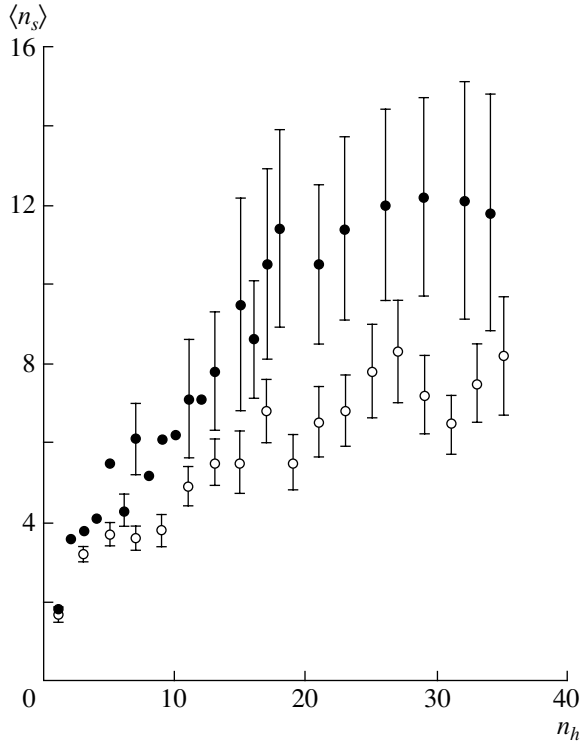

Fig. 1. Mean multiplicity $\langle n_s \rangle$ as a function of n_h for the interactions of (•) ^{6}Li projectile of momentum 4.5 GeV/c and (○) ^{7}Li projectile of momentum 3 GeV/c per projectile nucleon with emulsion nuclei.

$\langle n_s \rangle$ are less for ^{7}Li than for ^{6}Li, which means the projectile-energy dependence of the mean multiplicity of shower particles, dominated by pions.

In order to find out why the mean multiplicity $\langle n_s \rangle$ of shower particles is less for ^{7}Li than for ^{6}Li, we plotted $\langle n_s \rangle$ as a function of n_h in Fig. 1. In this figure, the flat region ($n_h \approx 15$ and greater), often referred to as a plateau, is observed. This region corresponds to a full overlap of the projectile and target nuclei—that is, to a collision characterized by an impact parameter equal the difference between the nuclear radii. Collisions belonging to this type are referred to as central collisions. It exhibits the absence of projectile fragmentation and the emission of a large number of secondary fragments (pions and slow singly charged fragments). Thus, the mean difference of $\langle n_s \rangle$ between ^{6}Li and ^{7}Li in the flat region from Fig. 1 is found to be 3.7. This value corresponds to the kinetic energy according to the confirmed relation $\langle n_s \rangle = aE_t^b$, where $a = 1.55$ and $b = 0.43$ [9–11], which yields $E_t \approx 7.5$ GeV. The value of 7.5 GeV is equivalent to the energy of two nucleons. Thus, we have arrived at the important conclusion that two nucleons, mostly neutrons, are not involved in the collisions of ^{7}Li with emulsion. Therefore, the decrease in $\langle n_s \rangle$ associated with ^{7}Li is due to a decrease in the number of participant nucleons (often two neutrons). The production of a neutron [12] and the emission of gamma rays are possible, and ^{7}Li can break up in such a way that one of its parts interacts strongly with the target, while the other part goes away, suffering virtually no interaction (stripping reaction).

4. MULTIPLICITY OF SECONDARY PARTICLES AND TARGET SPECTATORS

For the inelastic interactions of ^{7}Li with emulsion nuclei, Table 2 presents the mean multiplicities $\langle n_s \rangle$, $\langle n_g \rangle$, $\langle n_b \rangle$, and $\langle n_h \rangle$ for the various charged secondaries. The data were compared with other data [13–16] on the interactions of ^{4}He, ^{6}Li, ^{7}Li, and ^{12}C with emulsion nuclei. For each projectile, the mean number of interacting nucleons, $\langle N_{\text{int}} \rangle$, was calculated on the basis of experimental data by the formula

$$N_{\text{int}} = A_{\text{proj}} - \left(A_{\text{proj}}/Z_{\text{proj}}\right) \sum Z_f,$$

where A_{proj} and Z_{proj} are, respectively, the mass and the charge number of the projectile and $\sum Z_f$ is the net charge of the projectile fragments that did not undergo interactions. Although the energy of ^{6}Li and ^{4}He projectiles (4.5 GeV/c per nucleon) was higher than the energy of ^{7}Li projectiles (3 GeV/c per nucleon), the mass number of ^{7}Li is greater than the mass numbers of ^{6}Li and ^{4}He. From many references [7, 14, 17], we found that the multiplicities of all particles increase with the projectile mass. Table 2 shows that $\langle N_s \rangle$ for ^{7}Li is less than the corresponding values for ^{4}He and ^{6}Li. In order to explain this result, we consider that, owing to the special structure of ^{7}Li, the emission of a $Z = 2$ projectile spectator (stripped He nucleus) proceeds with higher probability (0.38 ± 0.02) per event. In this case, $\langle N_g \rangle$ is less than the corresponding values in ^{4}He and ^{6}Li interactions.

5. STRUCTURES OF ^{7}Li FROM AN ANALYSIS OF PROJECTILE FRAGMENTS

We can reveal various features of the fragmentation process, including the event rate in ^{7}Li–emulsion interactions as a function of $Z_{\max}$, the highest charge of projectile fragments emitted in an interaction event. We analyzed 723 events of the interactions of ^{7}Li with emulsion nuclei at 3 GeV/c per projectile nucleon. At least one charged projectile fragment was observed in 613 events where we studied $Z_{\max}$, of projectile fragments. Projectile-fragmentation events featuring no heavily ionizing particle ($n_h = 0$ events) have been investigated. The sample contains 110 of these

Table 2. Mean multiplicities of secondary particles from the interactions of ^{4}He, ^{6}Li, ^{7}Li, ^{12}C [13–16], and ^{7}Li (our study) projectiles with emulsion nuclei

	^{4}He	^{6}Li	^{7}Li	^{7}Li*	^{12}C
$\langle n_s \rangle$	4.27 ± 0.13	5.70 ± 0.29	3.60 ± 0.19	3.90 ± 0.10	7.6 ± 0.20
$\langle n_g \rangle$	4.60 ± 0.20	4.23 ± 0.21	3.80 ± 0.12	3.50 ± 0.20	5.9 ± 0.30
$\langle n_b \rangle$	4.70 ± 0.20	4.91 ± 0.30	5.37 ± 0.18	5.10 ± 0.20	4.3 ± 0.20
$\langle n_h \rangle$	9.30 ± 0.20	9.14 ± 0.37	9.17 ± 0.29	8.60 ± 0.30	9.2 ± 0.30
$\langle N_{\text{int}} \rangle$	2.60 ± 0.20	3.36 ± 0.13	3.92 ± 0.12	3.94 ± 0.13	5.2 ± 0.16
$\langle n_\alpha \rangle$		0.36 ± 0.01	0.41 ± 0.01	0.38 ± 0.02	1.49 ± 0.13

* Our study.

Table 3. Values of the forward-to-backward ratio F/B for the angular distributions of particles produced in nuclear collisions

Beam	Momentum per nucleon	F/B			
	GeV/c	Shower	Gray	Black	Ref.
p	3	10.15 ± 1.40	3.36 ± 0.20	1.30 ± 0.05	[19]
α	4.5	11.50 ± 0.66	3.00 ± 0.10	1.42 ± 0.004	[18]
^{7}Li	3	32.70 ± 2.6	5.18 ± 0.21	1.60 ± 0.07	Our study
^{12}C	4.5	38.93 ± 3.21	4.69 ± 0.18	1.49 ± 0.04	[5]

events ($n_h = 0$)—that is, about 15% of the total set of inelastic events. Figure 2 shows the probability of events in ^{7}Li–emulsion interactions as a function of $Z_{\max}$.

It should be noted that the probability is maximal for $Z_{\max} = 2$ events—that is, for events with α-particle projectile fragments as maximally charged fragments. This result is interpreted as that which is associated with an even–even nucleus of total spin $I = 0$ as a constituent of the ^{7}Li nucleus. The author of [4] deemed that the structure of ^{6}Li interacting with emulsion is $\alpha + d$ or $\alpha + p + n$, while our results suggest that the structure of ^{7}Li interacting with emulsion is mainly $\alpha + t$ or $\alpha + d + n$.

6. ANGULAR CHARACTERISTICS OF CHARGED SECONDARIES

The angular distributions of target fragments—that is, black and gray particles emitted in ^{7}Li interaction with emulsion nuclei at 3 GeV/c per projectile nucleon—are shown in Figs. 3 and 4. The distributions due to ^{4}He–Em collisions at 4.5 GeV/c per nucleon [18], p–Em interactions at 3 GeV/c per nucleon [19], and ^{12}C–Em interactions at 4.5 GeV/c per nucleon [20] are also given in the same figures. These distributions do not depend on the mass of beam nuclei and do not have any feature or bump structure that might indicate the occurrence of nuclear-shock-wave phenomena. The forward ($\theta < 90°$) to backward ($\theta > 90°$) ratio (F/B) for these distributions was calculated and is presented in Table 3. A weak dependence of this ratio on the projectile mass is observed in target-fragment distributions, which exhibit an increase in the collision impact with increasing projectile mass. This results are in agreement with the results of Tariq *et al.* [5].

The angular distributions of shower particles produced in collisions of p, ^{4}He, ^{7}Li, and ^{12}C with emulsion are shown in Fig. 5. This figure demonstrates that the angular distributions of showers are similar and that prominent peaks are observed at smaller angles. Furthermore, the ratio F/B was calculated for charged relativistic shower particles and is given in Table 3. A strong dependence of the ratio F/B in the case of relativistic charged secondaries implies that they are closely associated with projectile nucleons. These results agree with those from [21].

7. RAPIDITY DISTRIBUTIONS

The pseudorapidity is defined as $\eta = -\ln \tan(\theta/2)$, where θ is the angle of secondary-particle emission with respect to the primary-beam direction. The normalized pseudorapidity distributions (particle-number densities in rapidity space) of relativistic

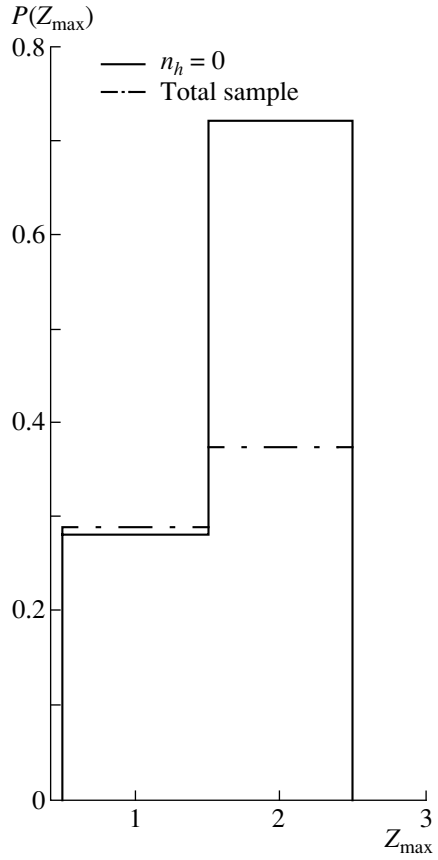

Fig. 2. Probability of $n_h = 0$ events and total sample of events as a function of Z_{max}, the highest charge of a projectile fragment in an event.

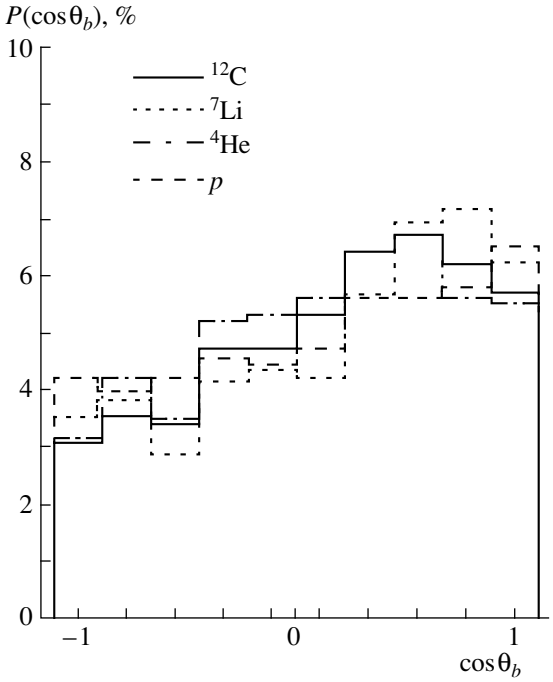

Fig. 3. Angular distributions of black particles produced by various projectiles.

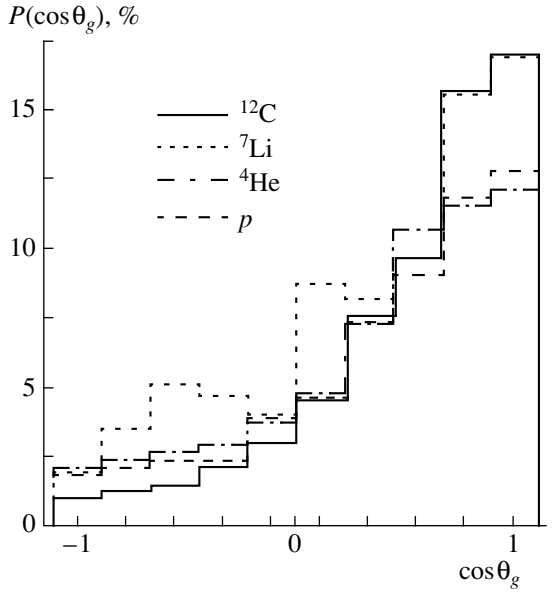

Fig. 4. As in Fig. 3, but for gray particles.

charged secondaries emitted in ^{7}Li–Em collisions at 3 GeV/c per projectile nucleon and in ^{28}Si–Em [5] and p–Em [20] collisions at 4.5 GeV/c per projectile nucleons are displayed in Fig. 6. The distributions are normalized to the total number N_{ev} of interactions in each sample. The η distributions for the cases of p and ^{7}Li (that is, for small mass numbers of projectiles) are observed to be independent of the projectile mass at small η values. The heights and widths of the distribution increase with the projectile mass. The centroid in the case of nucleus–nucleus collisions is much higher than that in the case of proton–nucleus interactions.

Particle-density distributions for various n_h intervals are shown in Fig. 7 in order to reveal a possible target dependence. The total sample of ^{7}Li inelastic interactions with emulsion nuclei was divided into ensembles of collisions with hydrogen (H) and with light (C, N, O) and heavy (Ag, Br) groups of target nuclei [2, 22]. Figure 7 demonstrates that, in the case of nucleus–nucleus collisions, the centroids of the distributions grow and are shifted toward smaller η values with increasing target mass, whereas, in the case of interactions induced by protons [5], the distribution is merely displaced to the region of lower η values with increasing target size. Thus, one can conclude that the distributions corresponding to lower and higher η values are associated with the target and projectile nuclei, respectively. Hence, rapidity space can be divided into three regions: the target-fragmentation,

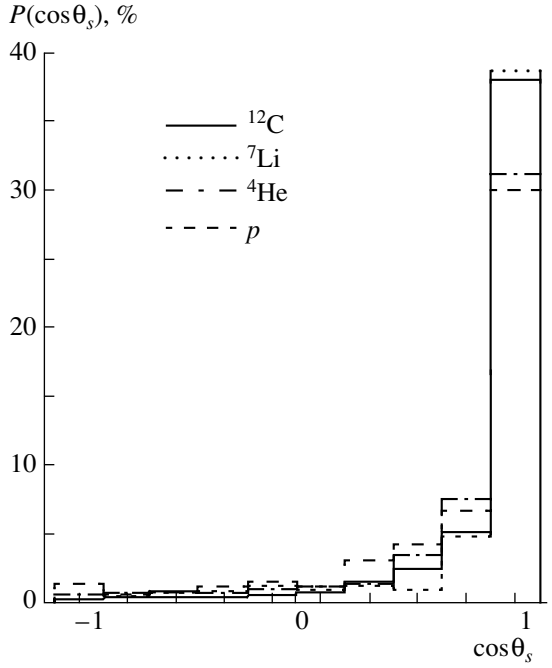

Fig. 5. As in Fig. 3, but for all shower particles.

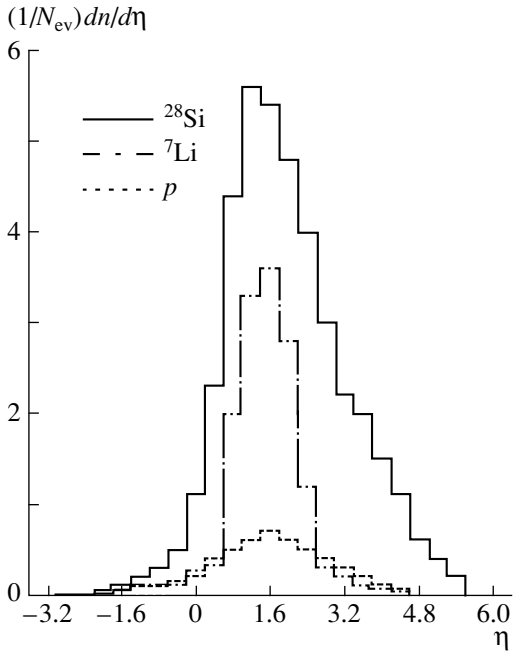

Fig. 6. Pseudorapidity distributions of secondary charged shower particles.

the projectile-fragmentation, and the central/pionic region. The target-fragmentation region corresponds to small η values—that is, to large emission angles associated with target nuclei. The projectile-fragmentation region is assumed to be populated by fragments of the projectile nucleus that correspond to larger values of η—that is, to small emission angles. The central region is believed to be enriched in particles produced in the interactions of colliding nuclei and is independent of either of the two fragmentation regions.

The pseudorapidity distribution for all shower particles originating from $n_h = 0$ events is displayed in Fig. 8, along with the corresponding distribution of shower particles from $Z^* = 0$ central events—that is, from events where the total charge of projectile fragments in the narrow forward cone $\theta \leqslant 3^\circ$ is equal to zero. A pronounced rapidity gap is observed between the two distributions. Owing to the absence of spectators and the complete dominance of participants, the distribution of central events extends from the target-fragmentation to the projectile-fragmentation region. The distribution of $n_h = 0$ events is dominated by the projectile spectators; thus, it is concentrated largely in the projectile-fragmentation region. These features pertain to the limiting-fragmentation hypothesis.

In order to examine the n_s dependence of the pseudorapidity of shower particles produced in ^{7}Li–emulsion interactions, the data are partitioned into three different n_s groups: $n_s \leqslant 8$, $9 < n_s \leqslant 14$, and

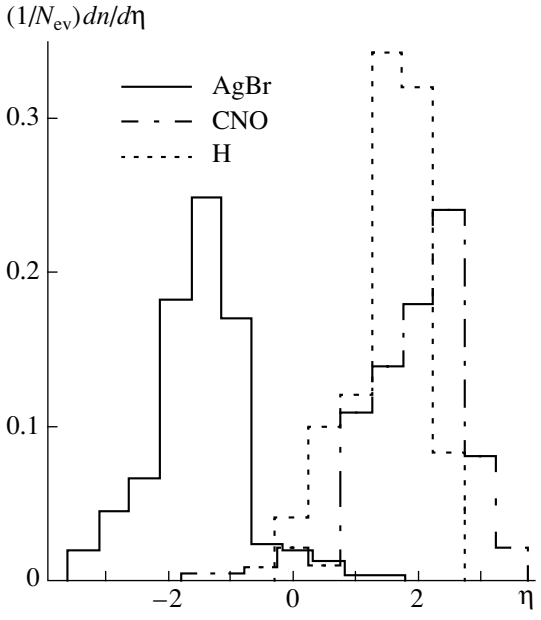

Fig. 7. Pseudorapidity spectra of shower particles in various n_h bins for ^{7}Li projectiles of momentum 3 GeV/c per nucleon.

$n_s \geqslant 15$. The pseudorapidity distributions of charged shower particles in the various n_s bins are plotted in Fig. 9. This figure clearly demonstrates that, with increasing n_s, the peaks of the distributions are shifted toward lower values of η and that the excess of particles tends to appear in the central rapidity region.

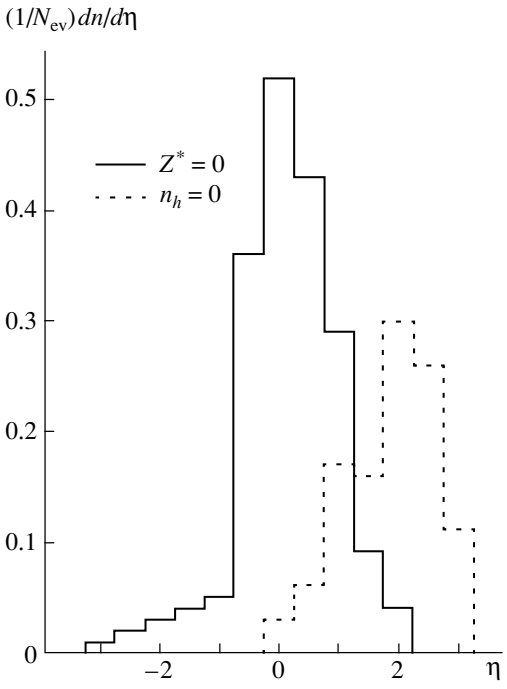

Fig. 8. Pseudorapidity distributions of shower particles from central events, $Z^* = 0$, and from projectile-fragmentation events, $n_h = 0$.

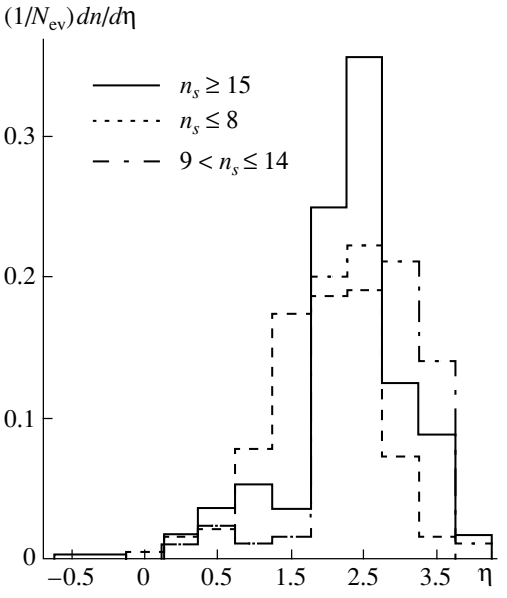

Fig. 9. Pseudorapidity distributions of charged shower particles in ^{7}Li interactions with emulsion nuclei for events with selected n_s values.

8. CONCLUSIONS

The present study of the interactions of ^{7}Li projectiles with emulsion at 3 GeV/c per projectile nucleon has led to the following conclusions:

(1) The mean multiplicities $\langle n_s \rangle$, $\langle n_g \rangle$, and $\langle n_b \rangle$ of secondary particles depend on the impact parameter and increase with increasing target mass number.

(2) The mean multiplicity $\langle n_s \rangle$ of shower particles for ^{7}Li projectiles is less than that for ^{6}Li projectiles, which implies a decrease in the number of participant nucleons, typically by two neutrons.

(3) By studying the function of $Z_{\max}$, the highest charge of a projectile fragment emitted in an interaction event, we have found that the structure of the ^{7}Li nucleus is basically $\alpha + t$ or $\alpha + d + n$.

(4) A smooth projectile-mass dependence of the F/B ratio has been observed for target fragments; at the same time, a strong dependence has been revealed in the case of relativistic charged secondaries.

(5) The collisions in question seem to become more central with increasing n_s, as well as with increasing projectile mass.

(6) The angular distributions of shower particles have lent support to the limiting-fragmentation hypothesis.

REFERENCES

1. S. El-Sharkawy, M. A. Jilany, N. N. Abd-Allah, *et al.,* Nuovo Cimento A **112**, 941 (1999).
2. M. A. Jilany, N. N. Abd-Allah, and A. Abd-ElDaim, Int. J. Mod. Phys. E **4**, 815 (1995).
3. M. El-Nadi *et al.,* J. Phys. G **24**, 2265 (1998).
4. S. El-Sharkawy, Phys. Scr. **50**, 97 (1994).
5. M. Tariq *et al.,* Nuovo Cimento A **107**, 2687 (1994).
6. M. L. Cherry *et al.,* Eur. Phys. J. C **5**, 641 (1998).
7. B. K. Singh and S. K. Tuli, Nucl. Phys. A **602**, 487 (1996).
8. M. El-Nadi *et al.,* Egypt. J. Phys. **24**, 101 (1993).
9. P. L. Jain *et al.,* Phys. Rev. C **44**, 844 (1991).
10. M. K. Hagab and J. Hufner, Phys. Lett. B **105B**, 103 (1981).
11. M. El-Nadi *et al.,* Egypt. J. Phys. **24**, 49 (1993).
12. W. E. Meyerhof, *Elements of Nuclear Physics* (McGraw-Hill, New York, 1989).
13. M. I. Adamovich *et al.,* Preprint No. E1-10-838, OIYaI (Joint Institute for Nuclear Research, Dubna, 1977).
14. M. M. Sherif *et al.,* Int. J. Mod. Phys. E **2**, 4 (1994).
15. V. Antonchik *et al.,* Yad. Fiz. **39**, 1228 (1984) [Sov. J. Nucl. Phys. **39**, 774 (1984)].
16. B. V. Ameeva *et al.,* Preprint No. P1-89-560, OIYaI (Joint Institute for Nuclear Research, Dubna, 1989).
17. V. E. Dudkin *et al.,* Nucl. Phys. A **568**, 906 (1994).
18. DGKLMTW Collab., JINR Commun., Dubna, No. PL-8313 (1974).
19. M. Bogdanski *et al.,* Helv. Phys. Acta **42**, 485 (1969).
20. A-ABDDKLMTUIB Collab., Z. Phys. A **302**, 133 (1981).
21. P. Singh and H. Khushnood, Int. J. Mod. Phys. E **7**, 659 (1998).
22. A. El-Naghy and N. N. Abd-Allah, Turk. J. Phys. **18**, 1106 (1994).

Physics of Atomic Nuclei, Vol. 64, No. 5, 2001, pp. 917–920. Translated from Yadernaya Fizika, Vol. 64, No. 5, 2001, pp. 986–989.

ELEMENTARY PARTICLES AND FIELDS
Theory

New Recoil-Effect-Induced Contributions to the Fine Shift of S Levels in the Muonium Atom

N. A. Boikova[1)], Yu. N. Tyukhtyaev[1)], and R. N. Faustov

Scientific Council for the Interdisciplinary Problem Cybernetics, Russian Academy of Sciences, ul. Vavilova 40, Moscow, 117967 Russia

Received January 26, 2000

Abstract—A new $\alpha^6\mu^3/(m_1m_2)\ln(m_1m_2)$ correction that arises in one-photon particle interaction in the muonium atom is found and calculated. © *2001 MAIK "Nauka/Interperiodica".*

Although relativistic two-body theory is of interest in and of itself, its application to calculating the structure of the energy levels in hydrogen-like atoms is also of paramount importance. Since such atoms are the most accessible to both theoretical and experimental investigations, they offer the possibility of testing the fundamentals of quantum theory. In addition, a comparison of theoretical and experimental spectroscopic data on hydrogen-like atoms can be used to refine the value of the fine-structure constant α, which is expressed in terms of the universal fundamental constants. Finally, the results of such investigations can play an important role in practical applications like metrology.

In a number of recent studies, logarithmic corrections to the fine shift of the S levels in hydrogen-like atoms were considered to the sixth order in the constant α. For the sake of convenience, we represent these corrections in the form

$$\Delta E_{nS}\left(\alpha^6\right) = \frac{\alpha^6\mu^3}{m_1m_2}\left(C_0\ln\beta^{-1} + C_1\ln\alpha^{-1} + C_2\beta\ln^2\beta\right), \quad \beta = \frac{m_1}{m_2}, \quad \mu = \frac{m_1m_2}{m_1+m_2}. \tag{1}$$

It was shown in [1, 2] that

$$C_1 = \begin{cases} 0 & \text{for } m_1 \neq m_2 \\ \dfrac{1}{32}\alpha^6 m\delta_{l0}n^{-3} & \text{for } m_1 = m_2 = m. \end{cases}$$

In [3], we considered the coefficient C_2; here, we are going to calculate C_0.

Our consideration is based on the quasipotential equation [4, 5]

$$(E - \varepsilon_{1p} - \varepsilon_{2p})\,\Psi_E(p,E) = (2\pi)^{-3}\int d^3q V_E(p,q,E)\,\Psi_E(q,E), \tag{2}$$

where $\varepsilon_{ip} = \sqrt{p^2+m_i^2}$ and V_E is the quasipotential given by

$$V_E = F_E^{-1} - \left(\hat{G}_E^+\right)^{-1}.$$

Here, we have

$$F_E^{-1} = (2\pi)^3\delta^3(p-q)\,(E - \varepsilon_{1p} - \varepsilon_{2p}),$$

$$[\ldots]^+ = u_1^*u_2^*[\ldots]\gamma_{10}\gamma_{20}u_1u_2,$$

u_i is the Dirac bispinor of the ith particle, and

$$\hat{G}(p,q,E) = (2\pi)^{-2}\int G(p_0,q_0,p,q,E)\,dp_0dq_0. \tag{3}$$

We now isolate the interaction with a Coulomb kernel in the original equation and denote by ΔE_n the correction to the energy level E_n of the nonrelativistic Schrödinger equation with a Coulomb potential:

$$\left(F_{E_n}^{-1} + \Delta E_n - K_c^+ - \tilde{V}_E\right)\Psi_E = 0, \tag{4}$$

$$\Delta E_n = E - E_n, \quad \tilde{V}_E = V_E - K_c^+,$$

$$K_c(p,q) = e_1e_2\gamma_{10}\gamma_{20}(p-q)^{-2}.$$

In the nonrelativistic equation, the energy eigenvalues for the Coulomb interaction and the corresponding eigenfunctions are determined by the expressions

$$E_n = m_1 + m_2 - \frac{\mu\alpha^2}{2n^2},$$

$$E_n = E_{1n} + E_{2n} = \eta_1E_n + \eta_2E_n,$$

$$\eta_1 = \frac{E_n^2 + m_1^2 - m_2^2}{2E_n^2}, \quad \eta_2 = \frac{E_n^2 + m_2^2 - m_1^2}{2E_n^2},$$

$$E_{1n} = m_1 - \frac{\mu^2\alpha^2}{2m_1n^2},$$

[1)] Saratov State University, Astrakhanskaya ul. 83, Saratov, 490071 Russia.

$$E_{2n} = m_2 - \frac{\mu^2\alpha^2}{2m_2 n^2}, m_1^2 - E_{1n}^2 \quad (5)$$
$$= m_2^2 - E_{2n}^2 = \frac{\mu^2\alpha^2}{n^2},$$

$$\Psi_{1S}(p) = \varphi_1(0)\frac{8\pi\omega}{\left(p^2+\omega^2\right)^2}, |\varphi_1(0)|^2 = \frac{\omega^3}{\pi}, \quad (6)$$
$$\omega = \mu\alpha,$$

$$\Psi_{2S}(p) = \varphi_2(0)\frac{16\pi\Omega}{\left(p^2+\Omega^2\right)^2}, |\varphi_2(0)|^2 = \frac{\Omega^3}{\pi}, \quad (7)$$
$$\Omega = \frac{1}{2}\omega.$$

Since

$$\left(p^2 + \frac{\omega^2}{n^2}\right) = (\varepsilon_{1p} - E_{1n})(\varepsilon_{1p} + E_{1n})$$
$$= (\varepsilon_{2p} - E_{2n})(\varepsilon_{2p} + E_{2n}),$$

we have

$$(\varepsilon_{1p} + \varepsilon_{2p} - E_n) = \frac{\left(p^2 + \omega^2/n^2\right)(\varepsilon_{1p} + \varepsilon_{2p} + E_n)}{(\varepsilon_{1p} + E_{1n})(\varepsilon_{2p} + E_{2n})}.$$

If we use the last relation in Eq. (4), we arrive at the simplest relativistic generalization of the Coulomb wave function:

$$\varphi_c' = \Omega_p \Psi_c, \quad \Omega_p = \frac{(\varepsilon_{1p} + m_1)(\varepsilon_{2p} + m_2)}{2\mu(\varepsilon_{1p} + \varepsilon_{2p} + m_1 + m_2)}. \quad (8)$$

According to perturbation theory, the exchange of a transverse photon between the muon and the electron generates a correction to the fine shift of S levels,

$$\Delta E_{nS} = \left\langle \varphi_{nS}' \right| (K_T)_{0F}^{+} \left| \varphi_{nS}' \right\rangle, \quad (9)$$

where

$$(K_T)_{0F}^{+} = F^{-1}(G_0 K_T G_0)^{+} F^{-1},$$
$$K_T = \frac{e_1 e_2}{k^2}\left(\delta_{ij} - \frac{k_i k_j}{k^2}\right)\gamma_1^i \gamma_2^j, \quad i,j = 1,2,3.$$

We use an integral representation of the Dirac delta function to perform the two-time operation in Eq. (3); as a result, we reduce integration with respect to the relative momenta p_0 and q_0 to contour integrals. In the ensuing calculations, it is convenient to employ the simplest recipes of the residue theory like

$$\int_{-\infty}^{\infty} \frac{dp_0 e^{ip_0 t}}{(p_0 + E - \varepsilon_p + i\varepsilon)(E - p_0 - \varepsilon_p + i\varepsilon)} \quad (10)$$
$$= \frac{\pi i}{E - \varepsilon_p} e^{-i(\varepsilon_p - E - i\varepsilon)|t|}.$$

The matrix structure of the expression for K_T is simplified owing to the symmetry properties of the integrand. As a result, the fine shift as given by (9) can be expressed in terms of integrals with respect to 3-momenta. Specifically, we have

$$\Delta E_{nS} \quad (11)$$
$$= \frac{4\alpha^6\mu^5}{(2\pi)^4}\int \frac{d^3p N_p \Omega_p}{\left(p^2+\omega^2\right)^2}\int \frac{d^3q N_q \Omega_q}{\left(q^2+\omega^2\right)^2 (p-q)^2}$$
$$\times\left\{-(p+q)^2\left(\frac{1}{M_{1p}} + \frac{1}{M_{1q}}\right)\left(\frac{1}{M_{2p}} + \frac{1}{M_{2q}}\right)\right.$$
$$+\frac{\left(p^2-q^2\right)^2}{(p-q)^2(\varepsilon_{1p}+\varepsilon_{1q})(\varepsilon_{2p}+\varepsilon_{2q})}$$
$$\times\left[\frac{\left(p^2+q^2\right)^2}{M_{1p}M_{1q}M_{2p}M_{2q}}\right.$$
$$\left.\left.+4 + 2\left(p^2+q^2\right)\left(\frac{1}{M_{1p}M_{1q}} + \frac{1}{M_{2p}M_{2q}}\right)\right]\right\},$$

where

$$N_p = \sqrt{\frac{M_{1p}M_{2p}}{\varepsilon_{1p}\varepsilon_{2p}}}, \quad M_{1p} = \varepsilon_{1p} + m_1,$$
$$M_{2p} = \varepsilon_{2p} + m_2.$$

The coefficients of the logarithmic terms, C_0 and $C_2\beta$, are a priori unknown. Therefore, it is natural to analyze first the contributions of order $\alpha^6\mu^3/(m_1 m_2) \times \ln^2\beta^{-1}$. Such corrections are associated with typical integrals referred to here as standard integrals:

$$I_{\rm st}^1 = \int_0^\infty \frac{dp}{p^2+\gamma^2}\int_0^\infty \frac{dq}{q^2+\gamma^2}\frac{\sqrt{p^2+\beta^2}\sqrt{q^2+\beta^2}}{\sqrt{p^2+1}+\sqrt{q^2+1}}, \quad (12)$$
$$\beta \ll 1;$$

$$I_{\rm st}^2 = \int_0^\infty \frac{dpp}{\sqrt{p^2+\beta^2}\left(p^2+\gamma^2\right)}\int_0^\infty \frac{dq}{\sqrt{q^2+1}}\ln\left|\frac{p-q}{p+q}\right|,$$
$$\gamma = \frac{\alpha\beta}{1+\beta}.$$

The integral $I_{\rm st}^1$ stems from terms proportional to $\left(p^2-q^2\right)/(p-q)^2$ and is free from positive powers of p and q in the numerator. The integral $I_{\rm st}^2$ arises in the terms of ΔE_{nS} that include the Coulomb factor $(p-q)^{-2}$. The calculation of C_2 yields

$$C_2 = 1/\pi^2,$$

so that the corresponding correction is

$$\Delta E_{1S} = \frac{\alpha^6\mu^3\beta}{m_1 m_2 \pi^2}\left(\frac{\pi^2}{2} + \sqrt{2} + \ln\beta^{-1}\right)\ln\beta^{-1}, \quad (13)$$

$$\Delta E_{2S} = \frac{\alpha^6\mu^3\beta}{8m_1 m_2 \pi^2}\left(\frac{\pi^2}{2} + \sqrt{2} + \ln\beta^{-1}\right)\ln\beta^{-1}.$$

Let us now investigate the different standard integral

$$I^3_{\rm st} = \int\limits_0^\infty \frac{dkN_k}{k^2+\alpha^2\mu^2} \int\limits_0^\infty \frac{dqN_q}{\varepsilon_{1q}\varepsilon_{2q}}, \tag{14}$$

where

$$N_k = N_{\beta k} N_{1k},$$
$$N_{\beta k} = \sqrt{\frac{\sqrt{k^2+\beta^2}+\beta}{\sqrt{k^2+\beta^2}}},$$
$$N_{1k} = \sqrt{\frac{\sqrt{k^2+1}+1}{\sqrt{k^2+1}}}.$$

A feature peculiar to (14) is that there are two independent integrals with respect to the variables k and q. We begin by considering the integral

$$\int\limits_0^\infty \frac{dq}{\varepsilon_{1q}\varepsilon_{2q}} N_{\beta q} N_{1q}. \tag{15}$$

Both radicals are clearly less than unity, while the integral $\int\limits_0^\infty \frac{dq}{\varepsilon_{1q}\varepsilon_{2q}}$, calculated in our previous study, includes the factor $\ln\beta^{-1}$ [3]. It only remains to estimate the integral

$$\int\limits_0^\infty \frac{dq}{\varepsilon_{1q}\varepsilon_{2q}} \sqrt{\frac{\varepsilon_{1q}+m_1}{2\varepsilon_{1q}}} \left(1 - \sqrt{\frac{\varepsilon_{2q}+m_2}{2\varepsilon_{2q}}}\right). \tag{16}$$

It can easily be shown that this integral does not contain the factors $\ln\beta^{-1}$.

Similarly, we can get rid of the radical N_{1k}. After that, it is possible to isolate quantities proportional to α^5 in the integral $\int\limits_0^\infty \frac{dk}{k^2+\alpha^2\mu^2} N_{\beta k}$ and to calculate exactly the coefficient of the logarithmic term,

$$I^3_{\rm st} = \frac{2\alpha^6\mu^3}{m_1 m_2} \left(\frac{1}{\sqrt{2}} \ln\left(1+\sqrt{2}\right) - 1\right) \ln\beta^{-1}. \tag{17}$$

This integral is a kind of reference: through a comparison with it, we can disclose expressions that contain the contributions of interest.

By way of example, we consider the following part of the correction ΔE_{nS}:

$$\Delta E' = \frac{\alpha^6\mu^5}{2\pi^4} \int \frac{d^3pN_p\Omega_p}{\left(p^2+\alpha^2\mu^2\right)^2} \times \int \frac{d^3qN_q\Omega_q}{\left(q^2+\alpha^2\mu^2\right)^2} \frac{\left(p^2-q^2\right)^2}{(p-q)^4} \frac{p^2+q^2}{M_{1p}M_{1q}}. \tag{18}$$

Using the symmetry of the integrand with respect to the substitution $p \leftrightarrow q$ and performing some simple reductions, we arrive at

$$\Delta E' = \frac{\alpha^6\mu^5}{4\pi^4} \int \frac{d^3pN_p}{\left(p^2+\alpha^2\mu^2\right)^2} \times \int \frac{d^3qN_q}{\left(q^2+\alpha^2\mu^2\right)^2} \frac{\left(p^2-q^2\right)^2}{(p-q)^4} \frac{q^2}{(\varepsilon_{1p}+\varepsilon_{1q})(\varepsilon_{2p}+\varepsilon_{2q})}. \tag{19}$$

Integration with respect to the angles is straightforward. Using the formula

$$\int d^2\theta_p \frac{\left(p^2-q^2\right)^2}{(p-q)^4} = 4\pi,$$

we obtain

$$\Delta E' = \frac{4\alpha^6\mu^3}{\pi^2} \times \int\limits_0^\infty \frac{dpN_p}{\left(p^2+\alpha^2\mu^2\right)^2} \int\limits_0^\infty \frac{dqN_q}{(\varepsilon_{1p}+\varepsilon_{1q})(\varepsilon_{2p}+\varepsilon_{2q})}. \tag{20}$$

The last integral can easily be recast into the standard form $I^3_{\rm st}$:

$$\Delta E' = \frac{2}{\pi^2} I^3_{\rm st} = \frac{4\alpha^6\mu^3}{\pi^2 m_1 m_2} \left(\frac{1}{\sqrt{2}} \ln\left(1+\sqrt{2}\right) - 1\right) \ln\beta^{-1}. \tag{21}$$

Let us now analyze the divergences in expression (11) for the fine shift. We represent the difference of the divergent integrals in the form

$$\Delta E_\infty = \frac{\alpha^6\mu^5}{2\pi^4} \int \frac{d^3p\Omega_pN_p}{\left(p^2+\alpha^2\mu^2\right)^2} \times \int \frac{d^3q\Omega_qN_q}{\left(q^2+\alpha^2\mu^2\right)^2} \left[\frac{\left(p^2-q^2\right)^2}{(p-q)^4} \times \frac{p^4}{M_{1p}M_{1q}M_{2q}M_{2p}(\varepsilon_{1p}+\varepsilon_{1q})(\varepsilon_{2p}+\varepsilon_{2q})} - \frac{1}{M_{2q}M_{1q}}\right]. \tag{22, 23}$$

Upon integration with respect to the angles and simple reductions, we arrive at

$$\Delta E_\infty = \frac{2\alpha^6\mu^3}{\pi^2} \int\limits_0^\infty \frac{dqN_q}{\left(q^2+\alpha^2\mu^2\right)M_{2q}} \times \left\{\int\limits_0^\infty \frac{dpN_pp^2}{M_{2p}(\varepsilon_{1p}+\varepsilon_{1q})(\varepsilon_{2p}+\varepsilon_{2q})} - \int\limits_0^\infty \frac{dpN_pM_{1p}}{\left(p^2+\alpha^2\mu^2\right)}\right\}. \tag{24}$$

Each term in the difference diverges logarithmically in the variable p. After some simple algebra, we find, however, that the divergences cancel:

$$\Delta E_\infty = \frac{2\alpha^6\mu^3}{\pi^2}\int\limits_0^\infty \frac{dqN_qM_{2q}^{-1}}{q^2+\alpha^2\mu^2}\int\limits_0^\infty dpN_p \qquad (25)$$
$$\times\left\{\frac{m_1+E_1}{p^2+\alpha^2\mu^2}+\frac{1}{\varepsilon_{1p}+\varepsilon_{1q}}\right.$$
$$\left.\times\left(\frac{\varepsilon_{1p}+E_1}{\varepsilon_{1p}+E_1}+\frac{M_{2q}}{\varepsilon_{2p}+\varepsilon_{2q}}\right)\right\}.$$

The first two terms do not involve the quantities $\ln\beta^{-1}$, while, apart from a numerical factor, the last term corresponds to the correction ΔE_{pq}:

$$\Delta E_\infty = \frac{1}{\pi^2}I_{\rm st}. \qquad (26)$$

Summing all contributions from the one-photon particle interaction in the muonium atom, we arrive at

$$\Delta E_{1S} = \frac{4\alpha^6\mu^3}{\pi^2 m_1 m_2}\left(\frac{1}{\sqrt{2}}\ln\left(1+\sqrt{2}\right)-1\right)\ln\beta^{-1}, \qquad (27)$$

$$\Delta E_{2S} = \frac{\alpha^6\mu^3}{2\pi^2 m_1 m_2}\left(\frac{1}{\sqrt{2}}\ln\left(1+\sqrt{2}\right)-1\right)\ln\beta^{-1}. \qquad (28)$$

In the hydrogen-like atom with a nuclear charge Ze, the shift of the S levels is obtained according to expression (9), where the eigenfunction Ψ_{nS} satisfies the equation

$$\left(p^2+Z^2\alpha^2\mu^2/n^2\right)^2\Psi_{nS}(p) \qquad (29)$$
$$=\frac{\mu\alpha Z}{\pi^2}\int\frac{d^3q}{(p-q)^2}\Psi_{nS}(q),$$

the value of this function at the origin being

$$|\Psi_{nS}(0)|^2 = \frac{(Z\alpha\mu)^3}{\pi n^3}. \qquad (30)$$

Therefore, we find, for arbitrary n and Z, that

$$\Delta E_{nS} = \frac{4(Z\alpha)^6\mu^3}{\pi^2 m_1 m_2 n^3}\left(\frac{1}{\sqrt{2}}\ln\left(1+\sqrt{2}\right)-1\right)\ln\beta^{-1}. \qquad (31)$$

We now present the numerical frequency values corresponding to the shifts of the $1S$ and $2S$ levels in the muonium atom (the subscripts 1 and 2 label quantities referring to the electron and the muon, respectively):

$$\delta\nu_{1S}^{e\mu} = -80\ \text{kHz}, \quad \delta\nu_{2S}^{e\mu} = -10\ \text{kHz}, \qquad (32)$$

$$\delta\nu^{e\mu}(1S-2S) = -70\ \text{kHz}.$$

In the conventional hydrogen atom and in the muonic hydrogen atom, the differences of the shifts of the $1S$ and $2S$ levels are

$$\delta\nu^{ep}(1S-2S) = -9\ \text{kHz}, \qquad (33)$$
$$\delta\nu^{\mu p}(1S-2S) = -128.1\ \text{kHz}.$$

The results that we obtained for the above contributions to the fine shift of the S levels in the hydrogen-like atom are on the same order of magnitude as the corresponding corrections (without logarithms) calculated in [6–8]:

$$\Delta E_{nS} = \frac{(Z\alpha)^6}{n^3}\frac{m_1^2}{m_2}\left(4\ln 2-\frac{7}{2}\right).$$

The precise measurements reported in [9] yielded

$$\nu^{e\mu}(1S-2S) = 2455528941.0\,(9.8)\ \text{MHz}. \qquad (34)$$

Thus, the corrections obtained here are still beyond the experimental accuracy.

ACKNOWLEDGMENTS

We are grateful to S.N. Bagaev, V.I. Savrin, and O.A. Khrustalev for interest in this study.

REFERENCES

1. R. N. Fell, Phys. Rev. Lett. **68**, 25 (1992).
2. R. N. Fell, I. B. Khriplovich, A. I. Milstein, and A. S. Yelkhovsky, Phys. Lett. A **181**, 172 (1993).
3. N. A. Boikova, Yu. N. Tyukhtyaev, and R. N. Faustov, Yad. Fiz. **61**, 866 (1998) [Phys. At. Nucl. **61**, 781 (1998)].
4. A. A. Logunov and A. N. Tavkhelidze, Nuovo Cimento **29**, 380 (1963).
5. V. V. Dvoeglazov, Yu. N. Tyukhtyaev, and R. N. Faustov, Fiz. Élem. Chastits At. Yadra **25**, 144 (1994) [Phys. Part. Nucl. **25**, 58 (1994)].
6. M. I. Eides and H. Grotch, Phys. Rev. A **55**, 3351 (1997).
7. A. S. Elkhovskiĭ, Zh. Éksp. Teor. Fiz. **113**, 865 (1998) [JETP **86**, 472 (1998)].
8. V. M. Shabaev, A. N. Artemyev, T. Beier, and G. Soff, J. Phys. B **31**, L337 (1998).
9. V. Meyer, S. N. Bagaev, *et al.,* hep-ex/9907013.

Translated by M. Kobrinsky

Physics of Atomic Nuclei, Vol. 64, No. 5, 2001, pp. 921–936. Translated from Yadernaya Fizika, Vol. 64, No. 5, 2001, pp. 990–1005.

ELEMENTARY PARTICLES AND FIELDS
Theory

Electron Excitation of Nucleon Resonances: Structure Functions and Transition Form Factors

V. I. Rus'kin* **and P. B. Kharchevnikov****

Kazakhstan Institute of Physics and Technology, Almaty, Republic of Kazakhstan

Received December 2, 1999; in final form, April 5, 2000

Abstract—The electron excitation of nucleon resonances is discussed both from the theoretical and from the experimental point of view. This discussion is based on a phenomenological approach that employs the conservation of the electromagnetic and vector-meson hadronic currents and the requirements of limiting chiral invariance. For the electron excitation of $J^\pi = 1/2^\pm, 3/2^\mp, 5/2^\pm, \ldots$ nucleon resonances, the structure functions are defined in terms of Sachs transition form factors. The resulting resonance structure functions for $l + N \to l + R$ processes are used in parametrizing smooth (background) structure functions for $l + N \to l + X$ inelastic scattering. © *2001 MAIK "Nauka/Interperiodica".*

1. INTRODUCTION

Electromagnetic transition form factors carry important information about spin effects that are associated with the collective interaction of quarks and gluons in the nucleon [1–3]. Data on the transition form factors for the $p \to \Delta^+(1232)$ transition were previously used in clarifying the role of diquark [4] and quark–gluon [5] configurations in the structure of the nucleon, in estimating the deformation of the quark wave functions for the nucleon and for the resonance because of hyperfine chromomagnetic interaction [6], and in testing the conservation of hadron helicity in exclusive reactions [7].

However, the validity of such estimates is determined by the reliability of the empirical values used for the transition form factors. There are a few sources of systematic errors in determining transition form factors on the basis of experimental data.

First of all, there is an ambiguity is separating the electron-excitation process from background processes. Because of dynamical resonance coupling to the background [1], this is a rather complicated task, especially in the case of exclusive reactions like single-pion electroproduction on a nucleon [8, 9].

We further note that transition form factors that belong to different types and which determine the same matrix element of the electromagnetic hadronic current appear in the structure functions and, hence, in the $l + N \to l + R$ differential cross section with different kinematical factors [10]. The explicit form of these factors is of importance not only in extracting empirical values of transition form factors from data on the differential cross section but also in simulating transition form factors.

Finally, various assumptions on the relationship between the longitudinal transition form factor and the transverse transition form factors are made, in just the same way as in the case of the elastic form factors for the nucleon [11], in extracting empirical values for transition form factors from data on the differential cross section.

In the present study, we express the structure functions for the electron excitation of $J = l + 1/2$ $(l = 0, 1, 2, \ldots)$ nucleon resonances in terms of the Sachs transition form factors of the type $G_i^{(l)}(Q^2)$, $i = 1, 2, 3$, where the subscript value of $i = 1$ corresponds to the longitudinal transition form factor, while the other two subscript values correspond to the transverse transition form factors. In just the same way as elastic Sachs form factors, they are free from kinematical singularities, obey some useful kinematical constraints, and appear in the $l + N \to l + R$ differential cross section without forming mixed terms of the type $G_i^{(l)} G_j^{(l)}$, $i \neq j$. In order to describe Sachs transition form factors, one can make use of the generalized vector-dominance model [12], which was successfully applied to elastic Sachs form factors.

The resulting resonance structure functions make it possible to express background structure functions in terms of simple parametric forms that reproduce the results obtained by measuring structure functions in the threshold [13] and in the deep-inelastic [14] region of the deep-inelastic-scattering process $l + N \to l + X$.

*e-mail: ruskin@satsun.sci.kz
**e-mail: pavel@satsun.sci.kz

1063-7788/01/6405-0921$21.00

Here, we use the Feynman metric and the system of units where $\hbar = c = 1$. We also adopt the following notation: q and q' are the 4-momenta of, respectively, the initial and the scattered lepton ($q^2 = q'^2 = m_l^2 \simeq 0$); p and p' are the 4-momenta of, respectively, the nucleon involved and the nucleon resonance ($p^2 = M^2$, $p'^2 = M_R^2$); k is the virtual-photon 4-momentum, $k_\mu = p_\mu - p'_\mu$, $k^2 = -Q^2 \le 0$; $\mathcal{P}_\mu \equiv p'_\mu + p_\mu$, $\mathcal{P}^2 = 2M_R^2 + 2M^2 - k^2$, $(k,\mathcal{P}) = M_R^2 - M^2$, $Q_\pm \equiv (M_R \pm M)^2 - k^2$; $(k,\mathcal{P})_\mu \equiv k^2\mathcal{P}_\mu - (k,\mathcal{P})k_\mu$, $k(\alpha_1,\alpha_l) \equiv k_{\alpha_1}k_{\alpha_2}\cdots k_{\alpha_l}$; $g_{\mu\nu}$ is the metric tensor, diag $g_{\mu\nu} = (1,-1,-1,-1)$; γ_μ is a Dirac matrix in the Pauli representation, $\gamma^5 = i\gamma^0\gamma^1\gamma^2\gamma^3$, $\sigma_{\mu\nu} = (\gamma_\mu\gamma_\nu - \gamma_\nu\gamma_\mu)/2$; $\varepsilon_{\mu\lambda_1\lambda_2\lambda_3}$ is the fully antisymmetric unit tensor ($\varepsilon_{0123} = 1$), $\varepsilon_\mu \equiv \varepsilon_{\mu\lambda_1\lambda_2\lambda_3}\gamma^{\lambda_1}\gamma^5\mathcal{P}^{\lambda_2}k^{\lambda_3}$, $\varepsilon_{\alpha\mu} \equiv \varepsilon_{\sigma\alpha\lambda_1\lambda_2}\varepsilon_{\sigma\mu\lambda_3\lambda_4} \times \mathcal{P}^{\lambda_1}k^{\lambda_2}\mathcal{P}^{\lambda_3}k^{\lambda_4}$; $u(p,s)$ is a bispinor that describes a free-nucleon state characterized by the polarization s; and $u_{\alpha_1,\alpha_2,\ldots,\alpha_l}(p',s')$ is the Rarita–Schwinger spin-tensor that describes the state of a stable nucleon resonance of spin $J = l + 1/2, l = 1,2,\ldots$, and polarization s'. This spin-tensor satisfies the Dirac equation

$$(\hat{p}' - M_R)u_{\alpha_1,\alpha_2,\ldots,\alpha_l}(p',s') = 0 \qquad (1)$$

and obeys the following additional constraints:

(i) $u_{\alpha_1,\alpha_2,\ldots,\alpha_l}(p',s')$ is symmetric under the interchange of any pair of tensorial indices.

(ii) $p'^{\alpha_i}u_{\ldots\alpha_i\ldots}(p',s') = 0$.

(iii) $\gamma^{\alpha_i}u_{\ldots\alpha_i\ldots}(p',s') = 0$ for any tensorial index α_i.

In addition, the following normalization condition must be satisfied:

$$\bar{u}_{\alpha_1,\alpha_2,\ldots,\alpha_l}(p',s')u^{\alpha_1,\alpha_2,\ldots,\alpha_l}(p',s') = 2M_R(-1)^l. \qquad (2)$$

2. DETERMINATION OF SACHS TRANSITION FORM FACTORS

In accordance with relativistic invariance and with parity conservation, the matrix element of the electromagnetic hadronic current for the $1/2^+ \to J^\pi$ transition can be expressed in terms of four invariant transition structure functions $f_i^{(l)}(k^2)$ ($i = 1,2,3,4$) as [15]

$$\langle R|J_\mu(0)|N\rangle = \bar{u}^{\alpha_1,\alpha_2,\ldots,\alpha_{l-1},\alpha}(p',s')\frac{k(\alpha_1,\alpha_{l-1})}{(M_R+M)^{l-1}} \qquad (3)$$

$$\times\left[\frac{f_1^{(l)}(k^2)}{M_R+M}k_\alpha\gamma_\mu - \frac{f_2^{(l)}(k^2)}{(M_R+M)^2}k_\alpha\sigma_{\mu\nu}k^\nu - \frac{f_3^{(l)}(k^2)}{(M_R+M)^2}k_\alpha k_\mu - f_4^{(l)}(k^2)g_{\mu\alpha}\right]\tilde{A}u(p,s),$$

where $\tilde{A} = 1$ for transitions characterized by a normal spin–parity ($J^\pi = 1/2^+,\ 3/2^-,\ 5/2^+,\ldots$) and $\tilde{A} = \gamma^5$ for transitions characterized by an anomalous spin-parity ($J^\pi = 1/2^-, 3/2^+, 5/2^-,\ldots$).

From current conservation, it follows that

$$f_3^{(l)}(k^2) = \frac{(M_R \mp M)(M_R+M)}{k^2}f_1^{(l)}(k^2) - \frac{(M_R+M)^2}{k^2}f_4^{(l)}(k^2), \qquad (4)$$

where the upper (lower) sign in the factor $(M_R \mp M)$ is taken for a transition characterized by a normal (anomalous) spin-parity.

According to (4), the number of independent gauge-invariant transition form factors reduces to three, and they can be defined as

$$F_1^{(l)}(k^2) = \frac{(M_R+M)^2}{k^2}f_1^{(l)}(k^2),$$
$$F_2^{(l)}(k^2) = f_2^{(l)}(k^2), \qquad (5)$$
$$F_3^{(l)}(k^2) = \frac{M_R+M}{M_R-M}\frac{(M_R+M)^2}{k^2}f_4^{(l)}(k^2).$$

In this case, the matrix element (3) can be recast into the form

$$\langle R|J_\mu(0)|N\rangle = \bar{u}^{\alpha_1,\alpha_2,\ldots,\alpha_{l-1},\alpha}(p',s')\frac{k(\alpha_1,\alpha_{l-1})}{(M_R+M)^{l-1}} \qquad (6)$$

$$\times\left[\frac{F_1^{(l)}(k^2)}{(M_R+M)^3}k_\alpha(k^2\gamma_\mu - (M_R \mp M)k_\mu) - \frac{F_2^{(l)}(k^2)}{(M_R+M)^2}k_\alpha\sigma_{\mu\nu}k^\nu - \frac{F_3^{(l)}(k^2)}{(M_R+M)^3}(M_R-M)(k^2g_{\alpha\mu} - k_\alpha k_\mu)\right]\tilde{A}u(p,s).$$

We note that the gauge-invariant transition form factors $F_i^{(l)}(k^2)$ are analogs of the Dirac and Pauli elastic form factors.

In order to go over from the gauge-invariant form factors, $F_i^{(l)}(k^2)$ to the Sachs transition form factors we can make use of the identities [16]

$$\bar{u}^{\alpha_1,\alpha_2,\ldots,\alpha_{l-1},\alpha}(p',s')\frac{k(\alpha_1,\alpha_{l-1})}{(M_R+M)^{l-1}} \times\Big[k_\alpha\left(k^2\gamma_\mu - (M_R \mp M)k_\mu\right)$$

$$-\frac{1}{Q_\pm}\left(k_\alpha(k,\mathcal{P})_\mu(M_R\pm M)-ik^2k_\alpha\varepsilon_\mu\right)\Big]\times\tilde{A}u(p,s)\equiv 0,$$

$$\bar{u}^{\alpha_1,\alpha_2,\ldots,\alpha_{l-1},\alpha}(p',s')\frac{k(\alpha_1,\alpha_{l-1})}{(M_R+M)^{l-1}}\times\Big[k_\alpha\sigma_{\mu\nu}k^\nu+\frac{1}{Q_\pm}\big(k_\alpha(k,\mathcal{P})_\mu-ik_\alpha\varepsilon_\mu(M_R\pm M)\big)\Big]\tilde{A}u(p,s)\equiv 0, \quad (7)$$

$$\bar{u}^{\alpha_1,\alpha_2,\ldots,\alpha_{l-1},\alpha}(p',s')\frac{k(\alpha_1,\alpha_{l-1})}{(M_R+M)^{l-1}}\times\Big[(M_R-M)(k^2g_{\alpha\mu}-k_\alpha k_\mu)-\frac{M_R-M}{Q_+Q_-}\left(k_\alpha(k,\mathcal{P})_\mu(k^2+(k,\mathcal{P}))+k^2\varepsilon_{\alpha\mu}\right)\Big]\times\tilde{A}u(p,s)\equiv 0,$$

which make it possible to reduce the matrix element (6) to the form

$$\langle R|J_\mu(0)|N\rangle=\bar{u}^{\alpha_1,\alpha_2,\ldots,\alpha_{l-1},\alpha}(p',s')\frac{k(\alpha_1,\alpha_{l-1})}{(M_R+M)^{l-1}}\times\left[\frac{G_1^{(l)}(k^2)}{(M_R+M)^2}\frac{k_\alpha(k,\mathcal{P})_\mu}{Q_\pm}-\frac{G_2^{(l)}(k^2)}{Q_+Q_-}\varepsilon_{\alpha\mu}-\frac{G_3^{(l)}(k^2)}{(M_R+M)Q_\pm}\left(ik_\alpha\varepsilon_\mu+\frac{1}{4M_R}\varepsilon_{\alpha\mu}\right)\right]\tilde{A}u(p,s), \quad (8)$$

where the Sachs transition form factors $G_i^{(l)}(k^2)$ are related to $F_i^{(l)}(k^2)$ by the equations

$$G_1^{(l)}(k^2)=\frac{M_R-M}{M_R+M}F_1^{(l)}(k^2)+F_2^{(l)}(k^2)-\frac{M_R-M}{M_R+M}\frac{k^2+(k,\mathcal{P})}{Q_\mp}F_3^{(l)}(k^2),$$

$$G_2^{(l)}(k^2)=\frac{M_R-M}{(M_R+M)^3}k^2F_3^{(l)}(k^2)-\frac{Q_\mp}{4M_R(M_R+M)}\times\left[\frac{k^2}{(M_R+M)^2}F_1^{(l)}(k^2)+\frac{M_R-M}{M_R\mp M}F_2^{(l)}(k^2)\right], \quad (9)$$

$$G_3^{(l)}(k^2)=\frac{k^2}{(M_R+M)^2}F_1^{(l)}(k^2)+\frac{M_R-M}{M_R\mp M}F_2^{(l)}(k^2).$$

As in Eqs. (4)–(8), the upper (lower) sign in the factors $(M_R\mp M)$ and $Q_\mp$ is taken for transitions characterized by a normal (anomalous) spin–parity.

The condition requiring that the gauge-invariant transition form factors not have kinematical singularities imposes kinematical constraints on the Sachs transition form factors at $k^2=0$, $k^2=(M_R+M)^2$, and $k^2=(M_R-M)^2$. According to (9), we easily obtain

$$G_2^{(l)}(k^2=0)=-\frac{(M_R\mp M)^2}{4M_R(M_R+M)}G_3^{(l)}(k^2=0), \quad (10)$$

$$G_2^{(l)}(Q_\mp=0)=0,$$

$$G_1^{(l)}(Q_\pm=0)=\frac{1}{2}\frac{M_R+M}{M_R\pm M}\times\left(G_3^{(l)}(Q_\pm=0)\pm\frac{M_R+M}{M}G_2^{(l)}(Q_\pm=0)\right).$$

In the case of $1/2^+\to 1/2^\pm$ transitions, the matrix element (3) does not contain a term involving $f_4^{(0)}(k^2)\equiv 0$. As a result, we have $F_3^{(0)}(k^2)\equiv 0$ and $G_2^{(0)}(k^2)\equiv 0$. Accordingly, the matrix element of the electromagnetic hadronic current for the $1/2^+\to 1/2^\pm$ transition can be represented in the form

$$\langle R|J_\mu(0)|N\rangle=\bar{u}(p',s')\left[\frac{G_1^{(0)}(k^2)}{M_R+M}\frac{(k,\mathcal{P})_\mu}{Q_\pm}-\frac{G_3^{(0)}(k^2)}{Q_\pm}i\varepsilon_\mu\right]\tilde{A}u(p,s). \quad (11)$$

The form factors $G_1^{(0)}(k^2)$ and $G_3^{(0)}(k^2)$ then obey the kinematical constraints

$$G_1^{(0)}(Q_\pm=0)=\frac{M_R+M}{M_R\pm M}G_3^{(0)}(Q_\pm=0). \quad (12)$$

3. STRUCTURE FUNCTIONS FOR THE ELECTRON EXCITATION OF NUCLEON RESONANCES

In the one-photon approximation, the invariant amplitude for the electron excitation of a resonance R is determined by the photon propagator and the matrix elements of the leptonic and the hadronic current:

$$\mathcal{A}^{(R)}=\frac{e^2}{k^2}\langle l'|j^\mu(0)|l\rangle\langle R|J_\mu(0)|N\rangle. \quad (13)$$

Accordingly, the quantity obtained by averaging the squared modulus of the amplitude over the initial spin states and summing the result over the final spin states can be expressed in terms of the leptonic and the hadronic tensor ($l^{\mu\nu}$ and $W_{\mu\nu}^{(R)}$, respectively) as

$$\overline{|\mathcal{A}^{(R)}|^2}=\left(\frac{e^2}{k^2}\right)^2l^{\mu\nu}W_{\mu\nu}^{(R)}. \quad (14)$$

The explicit form of the leptonic tensor is well known to be

$$l^{\mu\nu} = 2\left[q'^{\mu}q^{\nu} + q^{\mu}q'^{\nu} + \frac{k^2}{2}g^{\mu\nu}\right]. \qquad (15)$$

By using relativistic invariance, parity conservation, and electromagnetic-hadronic-current conservation, we can in general express the hadronic tensor

$$W_{\mu\nu}^{(R)} \equiv \frac{1}{2}\sum_{s',s}\langle R(p',s')|J_{\mu}(0)|N(p,s)\rangle \times\langle R(p',s')|J_{\nu}(0)|N(p,s)\rangle^{+} \qquad (16)$$

in terms of two invariant structure functions $W_{1,2}^{(R)}(k^2,(k,p))$ [17] and represent the squared modulus of the amplitude and, accordingly, the $l+N\to l+R$ differential cross section as

$$\overline{|\mathcal{A}^{(R)}|^2} = \left(\frac{e^2}{k^2}\right)^2 \times 8q_0q_0'M\cos^2\left(\frac{\theta}{2}\right) \times\left[2\tan^2\left(\frac{\theta}{2}\right)W_1^{(R)} + W_2^{(R)}\right], \qquad (17)$$

$$\frac{d^2\sigma^{(R)}}{dq_0'd\cos\theta} = \frac{\pi\alpha^2}{2q_0^2}\frac{\cos^2(\theta/2)}{\sin^4(\theta/2)} \times\left[2\tan^2\left(\frac{\theta}{2}\right)W_1^{(R)} + W_2^{(R)}\right], \qquad (18)$$

where q_0 and q_0' are the the energies of, respectively, the incident and the scattered lepton; θ is the lepton scattering angle in the laboratory frame; and $\alpha = e^2/4\pi \simeq 1/137$ is the fine-structure constant.

In order to determine the hadronic tensor (16) in terms of transition form factors, it is necessary to know the operator of summation over the polarizations of $J = l + 1/2$ ($l = 1,2,3,\dots$) particles,

$$\Lambda_l^{\alpha\beta}(p') \equiv \sum_{s'} u^{\beta_1,\beta_2,\dots,\beta_{l-1},\beta}(p',s') \times\bar{u}^{\alpha_1,\alpha_2,\dots,\alpha_{l-1},\alpha}(p',s')k(\alpha_1,\alpha_{l-1})k(\beta_1,\beta_{l-1}). \qquad (19)$$

The explicit form of this operator is [16]

$$\Lambda_l^{\alpha\beta}(p') = -\eta_l\left(\frac{Q_+Q_-}{M_R^2}\right)^{l-1}(\hat{p}' + M_R) \times\left[g^{\beta\alpha} - \frac{2}{3M_R^2}p'^{\beta}p'^{\alpha} - \frac{1}{3}\gamma^{\beta}\gamma_{\alpha} + \frac{1}{3M_R}(p'^{\beta}\gamma^{\alpha} - \gamma^{\beta}p'^{\alpha})\right], \qquad (20)$$

where

$$\eta_l \equiv \frac{(l!)^2}{(2l)!\cdot 2^{l-2}}. \qquad (21)$$

By using the matrix elements (8) and operator (20) in (16) and evaluating the traces of the γ matrices, we obtain [16]

$$W_{\mu\nu}^{(R)} = \eta_l\left(\frac{Q_+Q_-}{M_R^2(M_R+M)^2}\right)^l\left[-\left(G_1^{(l)}(k^2)\right)^2\times\frac{Q_{\mp}\mathcal{K}^2}{6(M_R+M)^2}\left(\frac{\mathcal{P}_{\mu}\mathcal{P}_{\nu}}{\mathcal{P}^2} + \frac{(k,\mathcal{P})^2}{\mathcal{P}^2\mathcal{K}^4}\mathcal{K}_{\mu}\mathcal{K}_{\nu} - \frac{(k,\mathcal{P})}{\mathcal{P}^2\mathcal{K}^2}(\mathcal{P}_{\mu}\mathcal{K}_{\nu} + \mathcal{K}_{\mu}\mathcal{P}_{\nu})\right) + \left(\frac{2}{3}\frac{M_R^2(M_R+M)^2}{Q_{\mp}}\left(G_2^{(l)}(k^2)\right)^2 + \frac{1}{8}Q_{\mp}\left(G_3^{(l)}(k^2)\right)^2\right)\left(-g_{\mu\nu} + \frac{\mathcal{P}_{\mu}\mathcal{P}_{\nu}}{\mathcal{P}^2} + \frac{\mathcal{K}_{\mu}\mathcal{K}_{\nu}}{\mathcal{K}^2}\right)\right], \qquad (22)$$

where we have introduced the notation $\mathcal{K}_{\mu} \equiv k_{\mu} - \mathcal{P}_{\mu}(k,\mathcal{P})/\mathcal{P}^2$ and where we have used the relations $(\mathcal{K},\mathcal{P}) = 0$ and $\mathcal{P}^2\mathcal{K}^2 = -Q_+Q_-$.

Taking into account, in (16), the matrix elements (11) and the operator of summation over the polarizations of spin-1/2 particles,

$$\sum_{s'} u(p',s')\bar{u}(p',s') = (\hat{p}' + M_R), \qquad (23)$$

we find for $1/2^+ \to 1/2^{\pm}$ transitions that

$$W_{\mu\nu}^{(R)} = -\left(G_1^{(0)}(k^2)\right)^2\frac{Q_{\mp}\mathcal{K}^2}{(M_R+M)^2} \times\left(\frac{\mathcal{P}_{\mu}\mathcal{P}_{\nu}}{\mathcal{P}^2} + \frac{(k,\mathcal{P})^2}{\mathcal{P}^2\mathcal{K}^4}\mathcal{K}_{\mu}\mathcal{K}_{\nu} - \frac{(k,\mathcal{P})}{\mathcal{P}^2\mathcal{K}^2}(\mathcal{P}_{\mu}\mathcal{K}_{\nu} + \mathcal{K}_{\mu}\mathcal{P}_{\nu})\right) + Q_{\mp}\left(G_3^{(0)}(k^2)\right)^2 \times\left(-g_{\mu\nu} + \frac{\mathcal{P}_{\mu}\mathcal{P}_{\nu}}{\mathcal{P}^2} + \frac{\mathcal{K}_{\mu}\mathcal{K}_{\nu}}{\mathcal{K}^2}\right). \qquad (24)$$

Expressions for the structure functions in terms of the Sachs form factors can easily be found [16] by contracting the hadronic and the leptonic tensor. By additionally taking into account nucleon-resonance instability with the aid of the Breit–Wigner representation for the production amplitude [this is equivalent to replacing $\delta(S_x - M_R^2)$ by the Breit–Wigner factor $\mathrm{BW}(S_x)$], we find, for the structure functions describing $l = 1,2,3,\dots$ transitions, that

$$2MW_1^{(l)}(S_x,Q^2)=\frac{\eta_l}{6}\left(1-\frac{M}{M_R}\right)^{2l}\left(1+\frac{Q^2}{M_R^2-M^2}\right)^{2l}\left[1+\frac{4M^2Q^2}{(M_R^2+Q^2-M^2)^2}\right]^{l}$$
$$\times\left((M_R\mp M)^2+Q^2\right)\left[\frac{3}{4}\left(G_3^{(l)}(Q^2)\right)^2+\frac{4M_R^2(M_R+M)^2}{\left((M_R\mp M)^2+Q^2\right)^2}\left(G_2^{(l)}(Q^2)\right)^2\right]\mathrm{BW}(S_x),$$
$$\nu W_2^{(l)}(S_x,Q^2)=\frac{\eta_l}{6}\,\frac{Q^2}{M_R^2+Q^2-M^2}\left(1-\frac{M}{M_R}\right)^{2l}\left(1+\frac{Q^2}{M_R^2-M^2}\right)^{2l} \tag{25}$$
$$\times\left[1+\frac{4M^2Q^2}{(M_R^2+Q^2-M^2)^2}\right]^{l-1}\left((M_R\mp M)^2+Q^2\right)\left[\frac{3}{4}\left(G_3^{(l)}(Q^2)\right)^2\right.$$
$$\left.+\frac{4M_R^2(M_R+M)^2}{\left((M_R\mp M)^2+Q^2\right)^2}\left(G_2^{(l)}(Q^2)\right)^2+\frac{Q^2}{(M_R+M)^2}\left(G_1^{(l)}(Q^2)\right)^2\right]\mathrm{BW}(S_x),$$

where $2M\nu=2(k,p)=M_R^2+Q^2-M^2$. For the structure functions describing the $1/2^+\to 1/2^\pm$ ($l=0$) transitions, we similarly obtain

$$2MW_1^{(0)}(S_x,Q^2)=\left((M_R\mp M)^2+Q^2\right)\times\left(G_3^{(0)}(Q^2)\right)^2\mathrm{BW}(S_x),$$
$$\nu W_2^{(0)}(S_x,Q^2)=\frac{Q^2}{M_R^2+Q^2-M^2} \tag{26}$$
$$\times\left((M_R\mp M)^2+Q^2\right)\left[\frac{Q^2}{(M_R+M)^2}\left(G_1^{(0)}(Q^2)\right)^2+\left(G_3^{(0)}(Q^2)\right)^2\right]\mathrm{BW}(S_x).$$

The Breit–Wigner factor

$$\mathrm{BW}(S_x)\equiv\frac{M_R\Gamma_R(S_x)}{\pi\left[\left(S_x-M_R^2\right)^2+M_R^2\Gamma_R^2(S_x)\right]}, \tag{27}$$

which appears in expressions (25) and (26), represents the distribution of the square of the invariant mass of products originating from the decay of a resonance with 4-momentum squared $p'^2=S_x$ and with the total hadronic-decay width $\Gamma_R(S_x)$ near the value $S_x=M_R^2$.

4. GENERALIZED VECTOR-DOMINANCE MODEL FOR TRANSITION FORM FACTORS

The conserved vector-meson hadronic currents that describe an $N\to R$ transition have the same structure as the electromagnetic hadronic current (8). In just the same way as in the case of elastic form factors [11, 12], this makes it possible to represent the isoscalar (s) and isovector (v) transition form factors as

$$G_i^{(l)s,v}(Q^2)=\left(G_i^{(l)s,v}(Q^2)\right)_{\mathrm{VDM}}+\left(G_i^{(l)s,v}(Q^2)\right)f^{(l)}(Q^2). \tag{28}$$

The first term in (28) takes into account *virtual photon → vector meson* transitions and can be written in the form

$$\left(G_i^{(l)s,v}(Q^2)\right)_{\mathrm{VDM}}=\sum_{k=1}^{n(s,v)}g_i^{(l)s,v}(k)\Big/\left(1+\frac{Q^2}{m_k^2}\right), \tag{29}$$
$$i=1,2,3,$$

which is conventional within the vector-dominance model (VDM). In expression (29), $n(s,v)$ is the number of the isoscalar (isovector) vector mesons that are taken into account in the model; $m_1^2<m_2^2<\ldots<m_{n(s,v)}^2$, $m_1=m_\omega$ in the case of isoscalar and $m_1=m_\rho$ in the case of isovector mesons; and $g_i^{(l)s,v}(V)\equiv g_{i,VNR}^{(l)}/g_V$ are the residues at the poles of vector mesons V at $k^2=m_V^2$, where $g_{i,VNR}^{(l)}$ is the VNR coupling constant and g_V is the vector-meson decay constant for the electron–positron channel.

The second term in (28) takes into account *virtual photon → vector meson → multiparticle intermediate states* transitions. Assuming, as in the case of elastic form factors [12], that the behavior of the transition form factors in the vicinities of vector-meson poles is determined exclusively by pole contributions and that the contribution of cuts does not distort the asymptotic behavior of the transition form factors that is predicted by limiting chiral invariance [17], we can represent the function $f^{(l)}(Q^2)$ in the form

$$f^{(l)}(Q^2)=\frac{-\alpha_l\left(Q^2/\Lambda_l^2\right)}{1+\left(Q^2/\Lambda_l^2\right)^2}, \tag{30}$$

where $0\le\alpha_l\le 1$.

The limiting chiral invariance of the matrix elements (8) and (11) of the hadronic currents imposes

rather stringent constraints on the asymptotic behavior (for $Q^2 \gg M_R^2$) of the longitudinal form factor and the transverse form factors:

$$G_2^{(l)s,v}(Q^2)/G_3^{(l)s,v}(Q^2) = -\frac{Q_\mp}{4M_R(M_R+M)},$$
$$G_1^{(l)s,v}(Q^2)/G_3^{(l)s,v}(Q^2) \simeq \mathrm{const}/Q^2. \quad (31)$$

Together with the kinematical constraints (10) and (12) and the condition

$$G_i^{(l)s,v}(0) = \left(G_i^{(l)s,v}(0)\right)_{\mathrm{VDM}} = \sum_{k=1}^{n(s,v)} g_i^{(l)s,v}(k), \quad (32)$$

the requirements (31) of limiting chiral invariance make it possible to represent the pole transition form factors (29) as

$$\left(G_1^{(l)s,v}(Q^2)\right)_{\mathrm{VDM}} = \frac{G_1^{(l)s,v}(0)}{\prod\limits_{k=1}^{n(s,v)}\left(1+\frac{Q^2}{m_k^2}\right)}, \quad (33)$$

$$\left(G_2^{(l)s,v}(Q^2)\right)_{\mathrm{VDM}} = -\frac{Q_\mp}{4M_R(M_R+M)}\left(G_3^{(l)s,v}(Q^2)\right)_{\mathrm{VDM}}, \quad (34)$$

$$\left(G_3^{(l)s,v}(Q^2)\right)_{\mathrm{VDM}} = \frac{G_3^{(l)s,v}(0)+\dfrac{Q^2}{m_1^2}K^{(l)s,v}}{\prod\limits_{k=1}^{n(s,v)}\left(1+\dfrac{Q^2}{m_k^2}\right)}, \quad (35)$$

where

$$K^{(l)s,v} \equiv G_3^{(l)s,v}(0) - g_3^{(l)s,v}(1)\prod_{j=2}^{n(v)}\left(1-\frac{m_1^2}{m_j^2}\right). \quad (36)$$

The residues $g_i^{(l)s,v}(V)$ are related by the equations

$$g_1^{(l)s,v}(j) = \frac{G_1^{(l)s,v}(0)}{\prod\limits_{k\neq j}^{n(s,v)}\left(1-\frac{m_j^2}{m_k^2}\right)}, j = 1,2,\ldots,n(s,v); \quad (37)$$

$$g_2^{(l)s,v}(1) = \frac{m_1^2-(M_R\mp M)^2}{4M_R(M_R+M)}g_3^{(l)s,v}(1),$$
$$g_2^{(l)s,v}(j) = \frac{m_j^2-(M_R\mp M)^2}{4M_R(M_R+M)} \quad (38)$$
$$\times\left[G_3^{(l)s,v}(0) - g_3^{(l)s,v}(1)\prod_{\substack{k\neq 1\\ k\neq j}}^{n(s,v)}\left(1-\frac{m_1^2}{m_k^2}\right)\right]$$
$$\times\left[\prod_{\substack{k\neq 1\\ k\neq j}}^{n(s,v)}\left(1-\frac{m_j^2}{m_k^2}\right)\right]^{-1};$$

$$g_3^{(l)s,v}(j) \quad (39)$$
$$= \left[G_3^{(l)s,v}(0) - g_3^{(l)s,v}(1)\prod_{\substack{k\neq 1\\ k\neq j}}^{n(s,v)}\left(1-\frac{m_1^2}{m_k^2}\right)\right]$$
$$\times\left[\prod_{\substack{k\neq 1\\ k\neq j}}^{n(s,v)}\left(1-\frac{m_j^2}{m_k^2}\right)\right]^{-1}, \quad j = 2,3,\ldots,n(s,v).$$

For $1/2^+ \to 1/2^\pm$ transitions, relations (34) and (38) do not hold, since we have $G_2^{(l)s,v}(Q^2) \equiv 0$. Relation (34) reduces the number of independent transition form factors to two. Their asymptotic behavior depends on the number $n(s,v)$ of vector mesons that are taken into account in the model. However, the residues (37)–(39) at the heavy-meson poles decrease fast in magnitude with increasing meson mass. As a consequence, $K^{(l)s,v} \gtrsim 0$, so that the transition form factors $G_i^{(l)s,v}(Q^2)$ do not have zeros for $Q^2 > 0$.

5. RESONANCES AND BACKGROUND IN THE INELASTIC LEPTON–NUCLEON SCATTERING $l + N \to l + X$

The resonance-scattering region, where structure functions behave irregularly in response to changes in S_x, is empirically specified as $(M+\mu)^2 \le S_x \le 4\ \mathrm{GeV}^2$, where μ is the pion mass. The resonance peaks of $\Delta(1232)$, $N(1520)$, and $N(1680)$, which are very distinct in this region for $Q^2 \le 1\ \mathrm{GeV}^2$, die out fast with increasing Q^2, which suggests a power-law reduction of the transition form factors with Q^2, this being peculiar to vector dominance. For $Q^2 > 6\ \mathrm{GeV}^2$, the behavior of the structure functions in the resonance region has a nearly smooth (background) character, which is similar to that in the Bjorken region ($S_x \gg M_R^2$, $Q^2 \gg M_R^2$). In view of this behavior of the structure functions in the resonance region, it is reasonable to represent them as

$$\nu W_2(S_x,Q^2) = \nu W_2^{(R)}(S_x,Q^2) + \nu W_2^{(B)}(S_x,Q^2),$$
$$2MW_1(S_x,Q^2) = 2MW_1^{(R)}(S_x,Q^2) \quad (40)$$
$$+ 2MW_1^{(B)}(S_x,Q^2).$$

The resonance structure functions

$$\nu W_2^{(R)}(S_x,Q^2) = \sum_l \nu W_2^{(l)}(S_x,Q^2), \quad (41)$$

$$2MW_1^{(R)}(S_x,Q^2)=\sum_l 2MW_1^{(l)}(S_x,Q^2)$$

are given by (25) and (26). For all processes involving the electron excitation of $J=l+1/2$ ($l=0,1,2,\ldots$) nucleon resonances, they exhibit a power-law decrease with increasing Q^2 and S_x and do not contribute to the structure functions (40) in the deep-inelastic region. With the exception of $l+N\to l+(R\to X)$, all processes, including the interference between the resonances and the background (this interference is disregarded here), must then be taken into account in the background structure functions $\nu W_2^{(B)}$ and $2MW_1^{(B)}$.

In considering the background structure functions $\nu W_2^{(B)}(S_x,Q^2)$ and $2MW_1^{(B)}(S_x,Q^2)$, we have made use of the well-known special features in the behavior of $\nu W_2(S_x,Q^2)$ and $2MW_1(S_x,Q^2)$ in the region specified by the inequalities $S_x\gg 4\ \mathrm{GeV}^2$ and $Q^2\gg 4\ \mathrm{GeV}^2$—specifically, we mean here scale invariance in the Bjorken limit ($S_x\to\infty,\ Q^2\to\infty,\ Q^2/S_x=$ const) and the Regge pole behavior in the Regge limit ($S_x\to\infty,\ Q^2/S_x\to 0$), as well as the assumption that there is a smooth transition between the Regge and the Bjorken region. The structure function $\nu W_2(S_x,Q^2)=\nu W_2^{(B)}(S_x,Q^2)$ satisfying these requirements can be represented as [18]

$$\nu W_2^{(B)}(S_x,Q^2)=\frac{Q^2}{S_x+Q^2-M^2}\Phi(S_x,Q^2)\times\left[1+\frac{4M^2Q^2}{(S_x+Q^2-M^2)^2}\right]^{-1}\times\sum_m b_m\left(\frac{S_x+Q^2-M^2}{c_0+Q^2}\right)^{\alpha_m(0)}. \quad (42)$$

In order to determine the structure function $2MW_1^{(B)}(S_x,Q^2)$, it is then convenient to use the relation

$$2MW_1^{(B)}(S_x,Q^2)=\left[1+\frac{4M^2Q^2}{(S_x+Q^2-M^2)^2}\right]\times\frac{S_x+Q^2-M^2}{Q^2}\frac{\nu W_2^{(B)}(S_x,Q^2)}{1+R(S_x,Q^2)}, \quad (43)$$

which is a corollary of the unitarity condition relating the structure functions W_1 and W_2 to the imaginary parts of the amplitudes for the forward [$t=(k-k')^2=0$] scattering of a longitudinally (l) and a transversely (t) polarized virtual photon by a nucleon. The ratio of the total cross sections for the absorption of a longitudinally and a transversely polarized photon by a nucleon,

$$R(S_x,Q^2)=\sigma^{(l)}_{\gamma N\to X}(S_x,Q^2)/\sigma^{(t)}_{\gamma N\to X}(S_x,Q^2), \quad (44)$$

obeys the obvious constraint

$$\lim_{Q^2\to 0}R(S_x,Q^2)=0 \quad (45)$$

and admits a rather simple parametrization—in particular, within perturbative QCD [19].

In expression (42), we have used the notation

$$b_m\equiv\frac{\beta_m(0)}{\beta_{\mathcal{P}}(0)}\left(\frac{c_0}{s_0}\right)^{\alpha_m(0)}, \quad (46)$$

where $\alpha_m(0)$ is the intercept, $\beta_m(Q^2)=\beta_m(0)\times\left(c_0/(c_0+Q^2)\right)^{\alpha_m(0)}$ is the residue at the mth Regge pole, and summation is performed over Regge poles with a positive signature and positive intercepts [$\alpha_{\mathcal{P}}(0)=1+\Delta,\quad \alpha_f(0)=\alpha_{a_2}(0)=0.5,\quad \alpha_\pi(0)=-0.025$, and $\alpha_\eta(0)=-0.2$].

The factor $\Phi(S_x,Q^2)$ controls the behavior of the background structure functions in the resonance [$S_x<4\ \mathrm{GeV}^2$] and in the threshold [$(S_x)_{\mathrm{th}}=(M+\mu)^2$] region of the variable S_x. In particular, it must take into account resonance-to-background coupling (Blum–Gilman duality), which is empirically manifested [20] in the same Q^2 dependence of the background and the resonance structure function in the vicinities of all resonance peaks, with the exception of $\Delta(1232)$, which lies in the threshold region. The function $\Phi(S_x,Q^2)$ must not violate, at least in a power-law way, scale invariance in the Bjorken limit or the Regge pole behavior in the Regge limit and must vanish at the elastic-scattering threshold—that is, at $S_x=(M+\mu)^2$.

All these requirements are satisfied for the function

$$\Phi(S_x,Q^2)=\left[1+\frac{4M^2Q^2}{(S_x+Q^2-M^2)^2}\right]\times\left(S_x-(M+\mu)^2\right)^{\kappa(Q^2)}\times\frac{(S_x+M^2)^{3-\kappa(Q^2)}}{(S_x+Q^2-M^2)^3}. \quad (47)$$

The first factor in (47) determines a transition to the static limit $\mathbf{k}^2/k_0^2\to 0$, which lies beyond the physical region of the scattering process $l+N\to l+X$. The second factor controls the threshold behavior of the structure function for $S_x\to(S_x)_{\mathrm{th}}$, while the third factor determines a transition from the Regge to the resonance region.

Finally, the background structure functions are given by

$$2MW_1^{(B)}(S_x,Q^2)=\left[1+\frac{4M^2Q^2}{(S_x+Q^2-M^2)^2}\right]\times\frac{\left(S_x-(M+\mu)^2\right)^{\kappa(Q^2)}}{1+R(S_x,Q^2)} \quad (48)$$

Table 1. Fitted values of the parameters in the resonance component of the structure functions

Resonance	$\mathcal{A}^p_{1/2}$ $\mathcal{A}^p_{3/2}$	$\mathcal{A}^n_{1/2}$ $\mathcal{A}^n_{3/2}$	$G^p_3(0)$	$G^n_3(0)$	$G^v_3(0)$	$G^s_3(0)$	$\frac{G^v_3(0)}{\alpha_v}$	$\frac{G^s_3(0)}{\alpha_s}$	$\frac{G^s_1(0)}{G^v_1(0)}$
$\Delta(1232)$	-141 ± 5	-141 ± 5	5.04	-5.04	5.04	–	15.686	–	–
	-258 ± 11	-258 ± 11	± 0.21	± 0.21	± 0.21		± 0.210		
$N(1520)$	-22 ± 10	-65 ± 13	10.05	-9.43	19.48	0.620	60.629	1.045	0.031
	167 ± 80	-144 ± 14	± 0.68	± 1.09	± 1.77	± 1.770	± 1.770	± 1.770	± 0.094
$N(1680)$	-17 ± 10	31 ± 13	33.61	-11.32	44.93	22.29	139.838	37.563	0.500
	-127 ± 12	-30 ± 14	± 3.54	± 5.01	± 8.55	± 8.55	± 8.550	± 8.550	± 0.033

$$\times \frac{(S_x+M^2)^{3-\kappa(Q^2)}}{(S_x+Q^2-M^2)^3} \sum_m b_m \left(\frac{S_x+Q^2-M^2}{c_0+Q^2}\right)^{\alpha_m(0)},$$

$$\nu W_2^{(B)}(S_x,Q^2) = \frac{Q^2}{S_x+Q^2-M^2} \times \left(S_x-(M+\mu)^2\right)^{\kappa(Q^2)} \times \frac{(S_x+M^2)^{3-\kappa(Q^2)}}{(S_x+Q^2-M^2)^3} \sum_m b_m \left(\frac{S_x+Q^2-M^2}{c_0+Q^2}\right)^{\alpha_m(0)},$$

with the exponent $\kappa(Q^2)$ of the threshold factor being parametrized as

$$\kappa(Q^2) = \kappa_0 - \frac{a_1(Q^2)^2}{(Q^2)^2+a_2Q^2+a_3}, \qquad (49)$$

where a_1 is the threshold-channel probability without allowing for final-state interaction at $Q^2=0$ ($a_1 \simeq \kappa_0 - 3/2$).

We note that all the parameters in (48) have a clear physical meaning, whereas expressions (48) themselves admit an obvious generalization to the case where there is a logarithmic violation of scale invariance in the Bjorken limit.

6. VALUES OF THE PARAMETERS IN THE BACKGROUND STRUCTURE FUNCTIONS

With the exception of the parameters a_2 and a_3, which determine the Q^2 dependence of the exponent $\kappa(Q^2)$ [see Eq. (49)], all the parameters in the background structure functions (48) can be estimated on the basis of data on the total cross section for hadron photoproduction on a proton [21],

$$\sigma^{\gamma p}_{\rm tot}(S_x) = \frac{4\pi^2\alpha}{S_x-M^2} \times 2MW_1^p(S_x,Q^2=0). \quad (50)$$

In calculating the resonance component of the cross section, we have taken into account only those three nucleon resonances, $\Delta(1232)$, $N(1520)$, and $N(1680)$, that makes a decisive contribution to the observed first, second, and third resonance peaks. For the Breit–Wigner factor (27), we have used the simplest representation taking no account of the kinematical S_x dependence of the total hadronic-decay width Γ_i. The resonance masses M_i and the resonance decay widths Γ_i were set to their tabular values [22].

The proton transition form factors at $Q^2=0$, $|G_3^{(i)p}(0)|$, were estimated on the basis of data [23] on the $\gamma p R_i$ helicity coupling constants $\mathcal{A}^{(i)}_\lambda$, which appear in the definition of the radiative-decay width of the $J=l+1/2$ resonance:

$$\Gamma^{(i)}_\gamma(S_x=M_i^2) = \frac{M_i^2-M^2}{4M_i^2}\frac{2M}{\pi M_i(2J+1)} \times \left(|\mathcal{A}^{(i)}_{1/2}|^2+|\mathcal{A}^{(i)}_{3/2}|^2\right). \qquad (51)$$

In turn, this width is related to $|G_3^{(i)}(0)|$ by the equation [16]

$$\Gamma^{(i)}_\gamma(S_x=M_i^2) = \frac{\alpha\eta_l}{6(l+1)}\frac{M_i^2-M^2}{2M_i} \times \frac{(M_i-M)^{2l}(M_i\mp M)^2}{M_i^{2l+1}} \left(G_3^{(i)}(0)\right)^2. \qquad (52)$$

The numerical values of the quantity $G_3^{(i)p}(0)$ and of the helicity coupling constants $\mathcal{A}^{(i)p}_{3/2}$ and $\mathcal{A}^{(i)p}_{1/2}$ (in 10^{-3} GeV$^{-1/2}$ units), which were used in calculating this quantity, are quoted in Table 1.

A fit of expression (50) to the entire body of data [21] collected by Blum and Caldwell (150 experimental points in the S_x interval from 1.233 to 343.6 GeV^2) yielded the following values for the parameters in the background structure functions (at $\chi^2/{\rm NDF}=1.06$):

$$\Delta = 0.058 \pm 0.003, \quad c_0 = 0.509 \pm 0.007\ \mathrm{GeV}^2,$$
$$b_{\mathcal{P}} = 0.350 \pm 0.082, \quad (b_f + b_{a_2}) = 0.511 \pm 0.095,$$
$$b_\pi = 0.360 \pm 0.052, \quad b_\eta = -0.339 \pm 0.156,$$
$$\kappa_0 = 2.328 \pm 0.014. \qquad (53)$$

The results of this fit are shown by the solid curve in Fig. 1. The dashed curve illustrates the behavior of the background component of the cross section (50).

An independent fit of only the background component of the cross section at the fixed value of $\kappa_0 = 2.328$ to Caldwell data (33 experimental points in the S_x interval from 32.1 to 343.6 GeV^2, where there is virtually no resonance contribution) yields parameter values close to those in (53) (at $\chi^2/\mathrm{NDF} = 1.1$):

$$\Delta = 0.077 \pm 0.013, \quad c_0 = 0.563 \pm 0.070\ \mathrm{GeV}^2,$$
$$b_{\mathcal{P}} = 0.350 \pm 0.062, \quad (b_f + b_{a_2}) = 0.521 \pm 0.045,$$
$$b_\pi = 0.360 \pm 0.082, \quad b_\eta = -0.339 \pm 0.278.$$

This demonstrates that the values in (53) are weakly sensitive to the values of the resonance parameters in Table 1.

The parameters b_f and b_{a_2} can be estimated on the basis of the EMC [24] and BCDMS [25] data by using the compilation of the ratios of the proton-to-neutron structure functions from [14], while the parameters a_1, a_2, and a_3, which appear in the definition (49) of the exponent $\kappa(Q^2)$, can be determined from data on the difference of the proton and neutron structure functions in the deep-inelastic region ($S_x > 20\ \mathrm{GeV}^2, Q^2 > 6\ \mathrm{GeV}^2$).

Considering that the signs of the residues for the isovector Regge trajectories of a_2 and π are reversed in going over from the proton to the neutron, we find for the background structure functions that

$$\frac{\nu W_2^n}{\nu W_2^p} = \frac{b_{\mathcal{P}} u^{1.058} + (b_f - b_{a_2}) u^{0.5} - b_\pi u^{-0.025} + b_\eta u^{-0.2}}{b_{\mathcal{P}} u^{1.058} + (b_f + b_{a_2}) u^{0.5} + b_\pi u^{-0.025} + b_\eta u^{-0.2}} \qquad (54)$$

and

$$\nu W_2^p - \nu W_2^n = 2\,\frac{Q^2}{S_x + Q^2 - M^2} \times \frac{(S_x - (M+\mu)^2)^{\kappa(Q^2)} (S_x + M^2)^{3-\kappa(Q^2)}}{(S_x + Q^2 - M^2)^3} \times (b_{a_2} u^{0.5} + b_\pi u^{-0.025}), \qquad (55)$$

where $u \equiv (S_x + Q^2 - M^2)/(c_0 + Q^2)$.

A fit of expression (54) to data from [24, 25] (71 experimental points) at the parameters set to the values in (53) yields (at $\chi^2/\mathrm{NDF} = 0.30$)

$$b_f = 0.500 \pm 0.054, \qquad b_{a_2} = 0.011 \pm 0.010. \qquad (56)$$

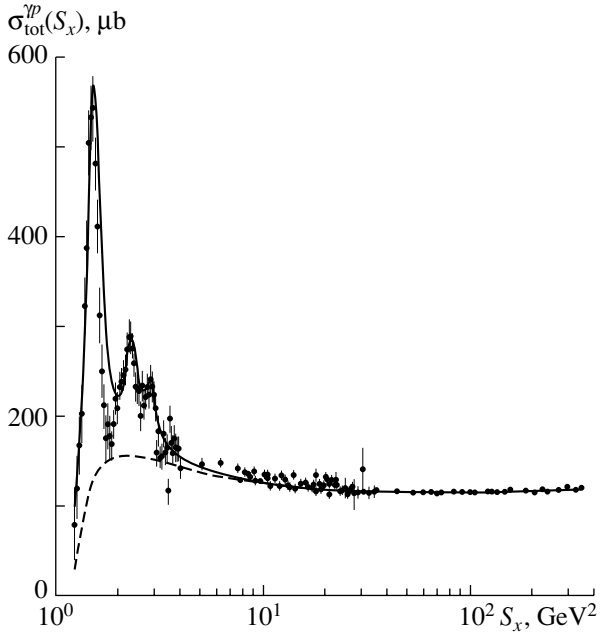

Fig. 1. Total cross section for hadron production on a proton: (experimental points) data of Blum and Caldwell according to the compilation from [21], (solid curve) fit in terms of expression (50), and (dashed curve) behavior of the background component of the cross section (50).

At fit of expression (55) to the same data at the parameters set to the values in (53) and (56) and at $a_1 = \kappa_0 - 3/2 = 0.828$ leads to (at $\chi^2/\mathrm{NDF} = 0/31$)

$$a_2 = -6.900 \pm 1.297\ \mathrm{GeV}^2, \qquad (57)$$
$$a_3 = 29.659 \pm 5.219\ \mathrm{GeV}^4.$$

The results of this fit for the values of $Q^2 = 11.5$ and 90.0 GeV^2 are shown by the solid and dashed curves in Figs. 2 and 3.

7. STRUCTURE FUNCTIONS IN THE THRESHOLD AND THE RESONANCE REGION

For $Q^2 > 6\ \mathrm{GeV}^2$, the contribution of $l + N \to l + (R \to X)$ resonance processes is negligibly small even in the resonance region $S_x \le 4\ \mathrm{GeV}^2$. This makes it possible to use the SLAC data from [13] on the behavior of the structure function $\nu W_2^p(S_x, Q^2)$ in the range $1.16 \le S_x \le 1.985\ \mathrm{GeV}^2$ for $Q^2 > 6\ \mathrm{GeV}^2$ in order to verify the reliability of the definition (48) of the background structure function $\nu W_2^{(B)p}(S_x, Q^2)$. For the parameters a_1, a_2, and a_3, a fit of expression (48) to the entire body of data from [13] (72 experimental points) at the parameters set to the values in

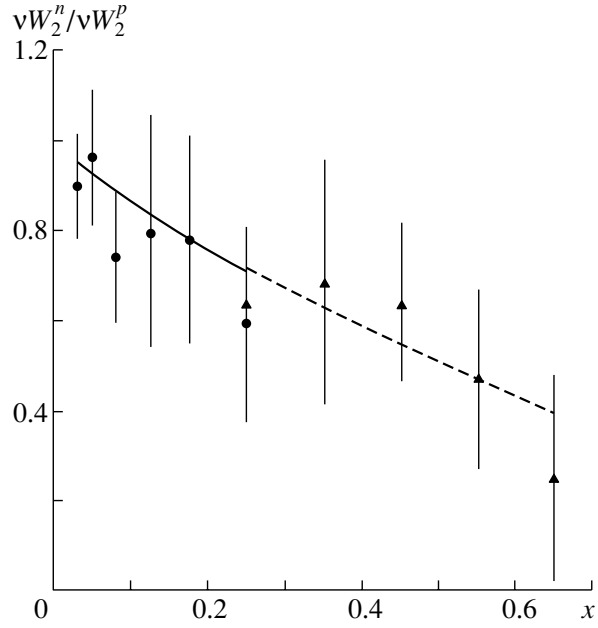

Fig. 2. Ratio of the neutron to the proton background structure function in the deep-inelastic-scattering region. The solid and the dashed curve represent the results of a fit in terms of expression (54) at $Q^2 = 11.5$ and 90.0 GeV^2, respectively. Points show experimental data from [24, 25] that are quoted according to the compilation from [14]: (closed circles) $Q^2 = 11.5$ GeV^2 and (closed triangles) $Q^2 = 90.0$ GeV^2.

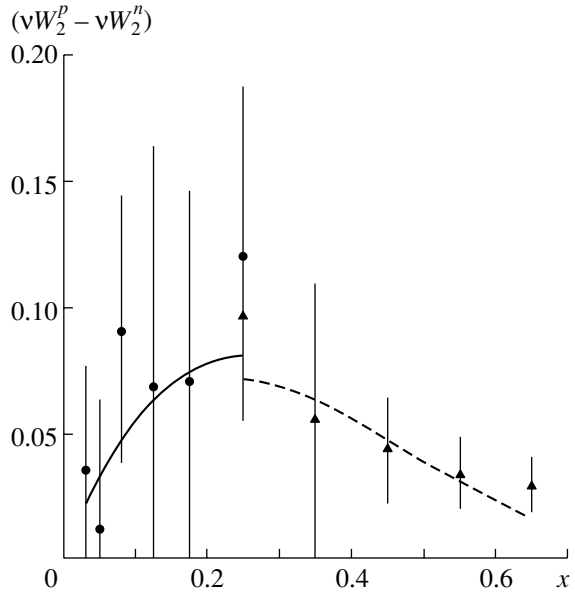

Fig. 3. Difference of the proton and the neutron background structure function in the deep-inelastic-scattering region. The notation is identical to that in Fig. 2.

(53) and (56) yields values close to those in (57) (at $\chi^2/\mathrm{NDF} = 0.62$):

$$a_1 = 0.828 \pm 0.014, \quad a_2 = -6.905 \pm 0.966 \text{ GeV}^2,$$
$$a_3 = 29.650 \pm 5.017 \text{ GeV}^4. \qquad (58)$$

A noticeable deviation (with $\chi_i^2 > 2$ per point) from experimental values is observed only at 5 of 72 experimental points. The results of this fit are shown by solid curves in Fig. 4.

Thus, the background structure functions given by (48) with the parameter values

$$\Delta = 0.058 \pm 0.003, \quad c_0 = 0.509 \pm 0.007 \text{ GeV}^2,$$
$$b_{\mathcal{P}} = 0.350 \pm 0.082, \quad b_f = 0.500 \pm 0.005,$$
$$b_{a_2} = 0.011 \pm 0.010, \quad b_\pi = 0.360 \pm 0.052,$$
$$b_\eta = -0.339 \pm 0.156, \quad \kappa_0 = 2.328 \pm 0.014,$$
$$a_1 = 0.828 \pm 0.014, \quad a_2 = -6.905 \pm 0.966 \text{ GeV}^2,$$
$$a_3 = 29.650 \pm 5.017 \text{ GeV}^4 \qquad (59)$$

faithfully reproduce available experimental data from [13].

8. TRANSITION FORM FACTORS IN THE GENERALIZED VECTOR-DOMINANCE MODEL

In order to assess the possibility of extracting transition form factors from data on inelastic lepton–nucleon scattering ($l + N \to l + X$) in the resonance region ($S_x \le 4$ GeV^2) at high values of Q^2 ($Q^2 > 3$ GeV^2), we make use of the expressions for the transition form factors within the generalized vector-dominance model.

The proton and neutron transition form factors for the resonances $\Delta(1232)(i = 1)$, $N(1520)(i = 2)$, and $N(1680)(i = 3)$ are related to the isoscalar (s) and isovector (v) transition form factors by the equations

$$G_{3,1}^{(1)p}(Q^2) = -G_{3,1}^{(1)n}(Q^2) = G_{3,1}^{(1)v}(Q^2), \quad i = 1,$$
$$G_{3,1}^{(i)p}(Q^2) = \frac{1}{2}(G_{3,1}^{(i)s}(Q^2) + G_{3,1}^{(i)v}(Q^2)), \qquad (60)$$
$$G_{3,1}^{(i)n}(Q^2) = \frac{1}{2}\left(G_{3,1}^{(i)s}(Q^2) - G_{3,1}^{(i)v}(Q^2)\right), \quad i = 2, 3.$$

Assuming that $G_3^{(i)s}(0) < G_3^{(i)v}(0)$, which is equivalent to the conditions $G_3^{(i)p}(0) > 0$ and $G_3^{(i)n}(0) < 0$, we can find the values $G_3^{(i)v}(0)$ and $G_3^{(i)s}(0)$ and the ratio $G_1^{(i)s}(0)/G_1^{(i)v}(0)$. From the condition requiring that the transition form factors (28) have no zeros,

$$g_3^{(i)v}(1) \le G_3^{(i)v}(0)/\alpha_v, \qquad g_3^{(i)s}(1) \le G_3^{(i)s}(0)/\alpha_s, \qquad (61)$$

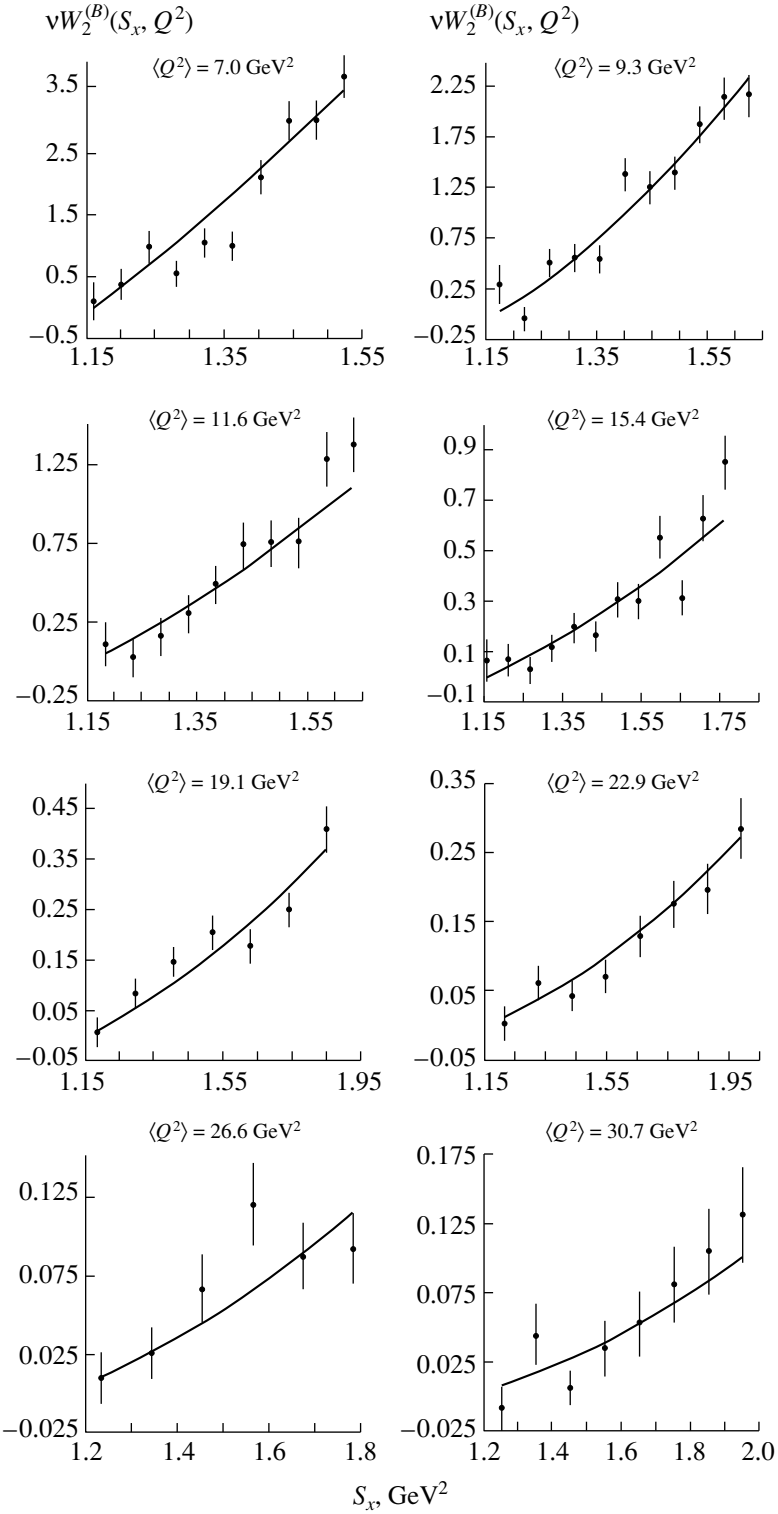

Fig. 4. Background structure functions in the resonance region. The solid curves represent the results obtained by fitting, to data from [13], expression (48), which features three free parameters (a_1, a_2, and a_3).

we can obtain the maximum possible values of the residues at ρ- and ω-meson poles of the transition form factors, $G_3^{(i)v}(0)/\alpha_v$ and $G_3^{(i)s}(0)/\alpha_s$. All these estimates are given in Table 1.

In order to estimate the free parameters $g_3^{(i)v}(1)$, $g_3^{(i)s}(1)$, α_i, and Λ_i^2, we have made use of data from [26] on the differential cross section for $e^- + p \to e^- + X$ inelastic scattering. It should

be noted, however, that, instead of tabular data on $\frac{1}{\Gamma_t}\frac{d^2\sigma}{dq_0' d\Omega'}$, the authors of [26] present a semiempirical parametrization of the data that extrapolates them to the region of low Q^2 values according to the dipole law. For this reason, the expression

$$\frac{1}{\Gamma_t}\frac{d^2\sigma}{dq_0' d\Omega'} = \frac{4\pi^2\alpha}{S_x - M^2}\left(1 + \frac{4M^2Q^2}{(S_x + Q^2 - M^2)^2}\right) \times \left(\frac{1 + \varepsilon R(S_x, Q^2)}{1 + R(S_x, Q^2)}\right)\frac{S_x + Q^2 - M^2}{Q^2}\,\nu W_2(S_x, Q^2) \quad (62)$$

was fitted only on the basis of data in the region specified by the inequalities $0.5 \le Q^2 \le 3.0\ \mathrm{GeV}^2$ and $1.2 \le S_x \le 4\ \mathrm{GeV}^2$, where the role of the longitudinal transition form factors is insignificant [9], so that only the transverse form factors $(G_3^{(i)p}(Q^2))^2$ were taken into account in the resonance component of the structure function νW_2. At the parameters set to the values in (59), expression (62) involves, in addition to the transition form factors that are to be determined from experimental data, an unknown function $R(S_x, Q^2) = \sigma_l(S_x, Q^2)/\sigma_t(S_x, Q^2)$. It should be noted, however, that, in the case of lepton scattering at angles $\theta < 10^\circ$ in the target rest frame, we have $\varepsilon \simeq 1$, so that $(1 + \varepsilon R)/(1 + R) \simeq 1$; as a result, the differential cross section is virtually independent of $R(S_x, Q^2)$. In the transverse transition form factors (35), we took into account the vector mesons $\rho(770), \rho_A(1100), \rho(1250)$, $\omega(783), \omega(1600)$, and $\phi(1600)$, whose squared masses in GeV^2 were set to the values

$$m_{1v}^2 = 0.593, \quad m_{2v}^2 = 1.210, \quad m_{3v}^2 = 1.603,$$
$$m_{1s}^2 = 0.615, \quad m_{2s}^2 = 2.756, \quad m_{3s}^2 = 2.780,$$

which provide the best description [15] of the elastic electromagnetic form factors for the pion and the nucleon. The resulting parameter values are

$$g_3^{(1)v}(1) = 15.686 \pm 0.012, \quad \alpha_1 = 0 \pm 0.001;$$
$$g_3^{(2)v}(1) = 60.144 \pm 0.116,$$
$$g_3^{(2)s}(1) = 1.045 \pm 0.239, \quad \alpha_2 = 0 \pm 0.012;$$
$$g_3^{(3)v}(1) = 139.838 \pm 1.036, \quad (63)$$
$$g_3^{(3)s}(1) = 37.563 \pm 0.063, \quad \alpha_3 = 0.138 \pm 0.012;$$
$$\Lambda_3^2 = 2.625 \pm 0.528\ \mathrm{GeV}^2.$$

The results of this fit are shown in Fig. 5. It can be seen that, for all three resonances considered here, the resonance-to-background ratio at the resonance point is greater than unity up to $Q^2 = 5\ \mathrm{GeV}^2$. Owing to this, a reliable measurement of the differential cross sections for $l + N \to l + X$ reactions at high values of Q^2 in the resonance region would make it possible to determine empirically the transition form factors for the resonances $\Delta(1232)$, $N(1520)$, and $N(1680)$ at values of Q^2 not accessible to a partial-wave analysis of single-pion electroproduction on a nucleon.

9. RESONANCE MULTIPOLE AMPLITUDES AND TRANSITION FORM FACTORS

The Coulomb (C) or the longitudinal (S), the magnetic (M), and the electric (E) resonance amplitudes for nucleon-resonance photoexcitation in $\gamma^* + N \to R_i \to \pi + N$ processes can be expressed in terms of the multipole transition form factors as [15]

$$(l+1)S_{(l+1)^-}^{(i)}(S_x, Q^2) = a_l L_i^{(-)}(Q^2)\left(K_i(Q^2)\right)^l G_S^{(i)}(Q^2)\mathcal{A}_{\mathrm{BW}}^{(i)}(S_x),$$
$$(l+1)M_{(l+1)^-}^{(i)}(S_x, Q^2) = b_l L_i^{(-)}(Q^2)\left(K_i(Q^2)\right)^l G_M^{(i)}(Q^2)\mathcal{A}_{\mathrm{BW}}^{(i)}(S_x), \quad (64)$$
$$(l+1)E_{(l+1)^-}^{(i)}(S_x, Q^2) = c_l L_i^{(-)}(Q^2)\left(K_i(Q^2)\right)^l G_E^{(i)}(Q^2)\mathcal{A}_{\mathrm{BW}}^{(i)}(S_x)$$

in the case of transitions characterized by a normal spin–parity ($1/2^+ \to 3/2^-, 5/2^+, 7/2^-, \ldots$) and as

$$(l+1)S_{l^+}^{(i)}(S_x, Q^2) = a_l L_i^{(+)}(Q^2)\left(K_i(Q^2)\right)^l G_{\tilde{S}}^{(i)}(Q^2)\mathcal{A}_{\mathrm{BW}}^{(i)}(S_x),$$
$$(l+1)E_{l^+}^{(i)}(S_x, Q^2) = b_l L_i^{(+)}(Q^2)\left(K_i(Q^2)\right)^l G_{\tilde{E}}^{(i)}(Q^2)\mathcal{A}_{\mathrm{BW}}^{(i)}(S_x), \quad (65)$$
$$(l+1)M_{l^+}^{(i)}(S_x, Q^2) = c_l L_i^{(+)}(Q^2)\left(K_i(Q^2)\right)^l G_{\tilde{M}}^{(i)}(Q^2)\mathcal{A}_{\mathrm{BW}}^{(i)}(S_x)$$

in the case of transitions characterized by an anomalous spin–parity ($1/2^+ \to 3/2^+, 5/2^-, 7/2^+, \ldots$).

Here, we have used the following notation: $l = J - 1/2$, J is the nucleon-resonance spin;

$$\eta_l = \frac{(l!)^2}{(2l)!\cdot 2^{l-2}}, \quad a_l = \left(\frac{\eta_l}{6(l+1)}\right)^{1/2},$$
$$b_l = \left(\frac{\eta_l}{96(l+2)}\right)^{1/2}, \quad c_l = \left(\frac{\eta_l}{96l}\right)^{1/2};$$
$$L_i^{(\mp)}(Q^2) = \left(\frac{\mathbf{a}((M_i \mp M)^2 + Q^2)}{|\mathbf{q}_i|}\right)^{1/2},$$
$$K_i(Q^2) = \left(1 - \frac{M}{M_i}\right)\left(1 + \frac{Q^2}{M_i^2 - M^2}\right)$$

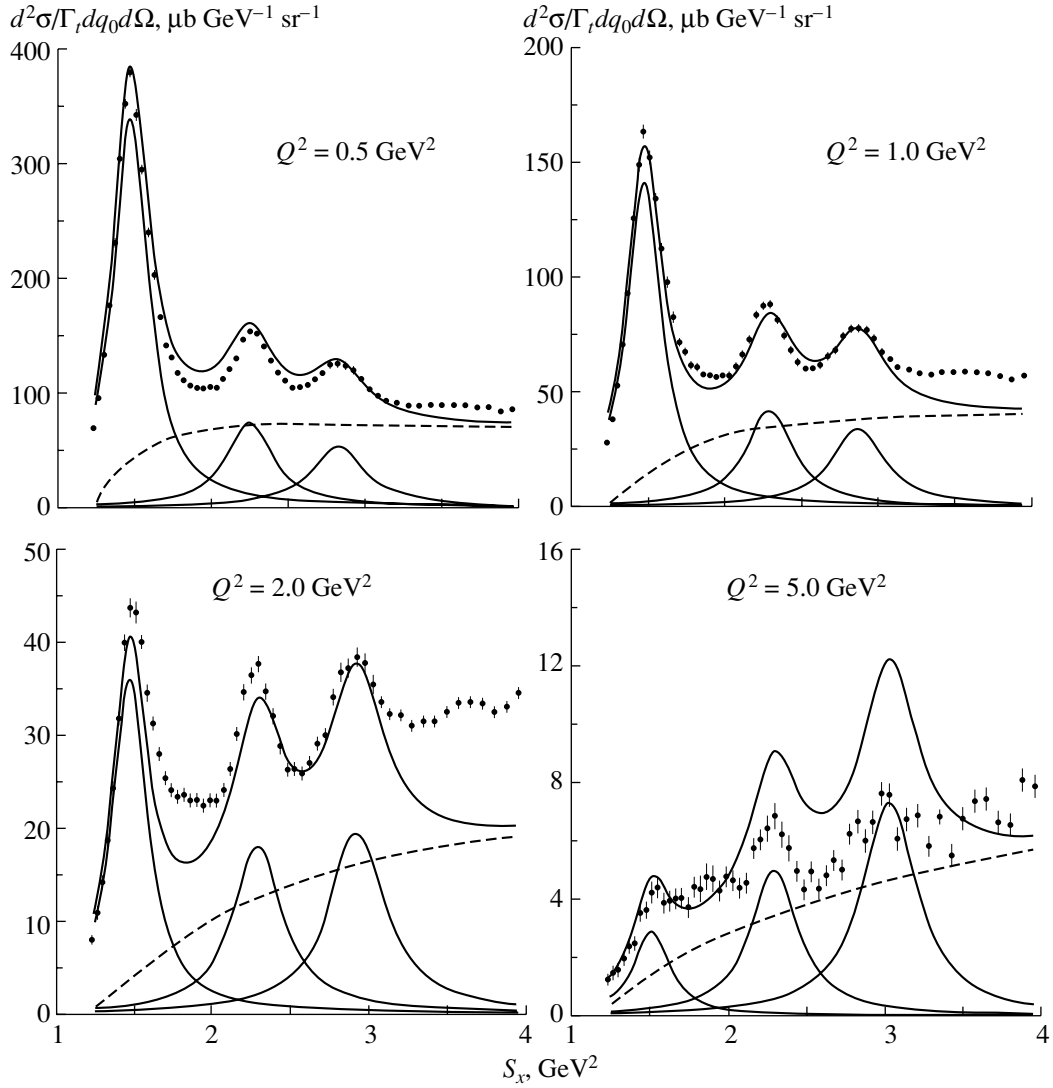

Fig. 5. Differential cross section for $e^- + p \to e^- + X$ scattering processes in the resonance region. The solid curves represent the results obtained by fitting, to data from [26], expression (62) featuring the transition form factors (28), which were obtained within the generalized vector-dominance model. The dashed curves illustrate the behavior of the background component of the cross section (62).

$$\times \left(1 + \frac{4M^2Q^2}{(M_i^2 + Q^2 - M^2)^2}\right)^{1/2},$$

$$\mathcal{A}^{(i)}_{\rm BW}(S_x) = \frac{\sqrt{\Gamma^{(i)}_{\pi N}}}{M_i^2 - S_x - iM_i\Gamma_i};$$

$|\mathbf{q}_i| = ((M_i^2 + M^2 - \mu^2)^2 - 4M_i^2M^2)^{1/2}/2M_i$ is the absolute value of the pion 3-momentum in the resonance rest frame; $\Gamma^{(i)}_{\pi N}$ is the ith-resonance width with respect to the decay into a pion and a nucleon; and $\alpha = 1/137$ is the fine-structure constant.

In the case of resonance decay through a specific charged channel a, we have $\Gamma^{(i)a}_{\pi N} = \kappa_i^a X_i \Gamma_i$, where $X_i = \Gamma^{(i)}_{\pi N}/\Gamma_i$, Γ_i is the total hadronic-decay width of the ith resonance, and κ_i^a is the channel charge factor.

The limiting-chiral-invariance requirements (31) significantly simplify the relationship between the multipole and the Sachs form factors; that is,

$$G^{(i)}_S(Q^2) = G^{(i)}_S(Q^2) = \frac{\sqrt{Q^2}}{M_i + M} G^{(i)}_{\rm C}(Q^2),$$

$$G^{(i)}_{\rm C}(Q^2) = G^{(i)}_1(Q^2),$$

$$G^{(i)}_M(Q^2) = \frac{4r_i}{\sqrt{1 + r_i^2}} G^{(i)}_3(Q^2), \qquad (66)$$

$$G^{(i)}_E(Q^2) = \frac{4}{\sqrt{1 + r_i^2}} G^{(i)}_3(Q^2),$$

Table 2. Ratios of the magnetic and the electric resonance amplitude

Transition	r_i	Amplitude ratio	
$p \to \Delta^+(1232)$	-0.0234 ± 0.0325	$E^{(1)}_{1^+}/M^{(1)}_{1^+}$	-0.0135 ± 0.0188
$n \to \Delta^0(1232)$	-0.0234 ± 0.0325		-0.0135 ± 0.0188
$p \to N^+(1520)$	0.768 ± 0.062	$M^{(2)}_{2^-}/E^{(2)}_{2^-}$	0.443 ± 0.031
$n \to N^0(1520)$	0.100 ± 0.104		0.058 ± 0.060
$p \to N^+(1680)$	0.929 ± 0.010	$M^{(3)}_{3^-}/E^{(3)}_{3^-}$	0.657 ± 0.001
$n \to N^0(1680)$	6.463 ± 15.717		4.570 ± 11.114

$$G^{(i)}_{\bar{E}}(Q^2) = \frac{4\bar{r}_i}{\sqrt{1+\bar{r}_i^2}} G^{(i)}_3(Q^2),$$
$$G^{(i)}_{\bar{M}}(Q^2) = \frac{4}{\sqrt{1+\bar{r}_i^2}} G^{(i)}_3(Q^2),$$

where

$$r_i = -\bar{r}_i = \left(\mathcal{A}^{(i)}_{3/2} - \sqrt{\frac{l+2}{l}}\mathcal{A}^{(i)}_{1/2}\right) \times \left(\sqrt{\frac{l+2}{l}}\mathcal{A}^{(i)}_{3/2} + \mathcal{A}^{(i)}_{1/2}\right)^{-1}. \quad (67)$$

In this case, the ratios of the magnetic and electric resonance amplitudes are constant:

$$M^{(i)}_{(l+1)^-}(S_x,Q^2)/E^{(i)}_{(l+1)^-}(S_x,Q^2) = \frac{b_l}{c_l}\frac{G^{(i)}_M(Q^2)}{G^{(i)}_E(Q^2)} = r_i\sqrt{\frac{l}{l+2}},$$
$$E^{(i)}_{l^+}(S_x,Q^2)/M^{(i)}_{l^+}(S_x,Q^2) = \frac{b_l}{c_l}\frac{G^{(i)}_{\bar{E}}(Q^2)}{G^{(i)}_{\bar{M}}(Q^2)} = r_i\sqrt{\frac{l}{l+2}}. \quad (68)$$

For the resonances $\Delta(1232)$, $N(1520)$, and $N(1680)$, which are of interest to us, we can estimate the ratios in (68) by using the values in Table 1 for the $\gamma N R_i$ helicity coupling constants $\mathcal{A}^{(i)}_\lambda$ for the proton and the neutron. The results of this estimation are given in Table 2.

The proton and neutron Sachs transition form factors calculated with the parameters given in (63) are displayed in Fig. 6. The rough estimates $G^{(1)v}_1(0) = -1.69$; $G^{(2)v}_1(0) = 10.86$, $G^{(2)s}_1(0) = 0.337$; and $G^{(3)v}_1(0) = 4.51$, $G^{(3)s}_1(0) = 2.26$ were obtained by using the empirical maximum values [9] (in $\mu b^{1/2}$)

$$S^{(1)p}_{1^+}(S_x = M_1^2, Q^2 = 0.434\ \mathrm{GeV}^2) = -0.218,$$
$$S^{(2)p}_{2^-}(S_x = M_2^2, Q^2 = 0.5\ \mathrm{GeV}^2) = 0.10,$$
$$S^{(3)p}_{3^-}(S_x = M_3^2, Q^2 = 1.0\ \mathrm{GeV}^2) = 0.01$$

for the amplitudes and the values of the ratios $G^{(i)s}_1(0)/G^{(i)v}_1(0)$ from Table 1.

It can be seen that the transition form factors as constructed within the generalized vector-dominance model with the parameter values from (63), which were determined on the basis of data on inelastic-scattering processes $e^- + p \to e^- + X$, comply rather well with the empirical values obtained in [9] for Sachs transition form factors from data of the partial-wave analysis [2] of $\gamma^* + p \to R^+_i \to (\pi + N)^+$ processes.

That the ratios of the electric and magnetic resonance amplitudes are constant, which follows from limiting chiral invariance, implies the invariability of the ratios of transverse resonance helicity amplitudes. The values presented in Table 2 for the ratios of the magnetic and electric resonance amplitudes correspond to the following values of the ratios $\mathcal{A}^{(i)p}_{3/2}(S_x,Q^2)/\mathcal{A}^{(i)p}_{1/2}(S_x,Q^2)$ of the resonance helicity amplitudes:

$$\mathcal{A}^{(1)p}_{3/2}/\mathcal{A}^{(1)p}_{1/2} = -\mathcal{A}^{(1)n}_{3/2}/\mathcal{A}^{(1)n}_{1/2} = 1.830 \pm 0.141;$$
$$\mathcal{A}^{(2)p}_{3/2}/\mathcal{A}^{(2)p}_{1/2} = -7.597 \pm 1.984,$$
$$\mathcal{A}^{(2)n}_{3/2}/\mathcal{A}^{(2)n}_{1/2} = 2.219 \pm 0.609; \quad (69)$$
$$\mathcal{A}^{(3)p}_{3/2}/\mathcal{A}^{(3)p}_{1/2} = -7.463 \pm 0.043,$$
$$\mathcal{A}^{(3)n}_{3/2}/\mathcal{A}^{(3)n}_{1/2} = -0.968 \pm 0.712.$$

These values differ significantly from the values

$$\mathcal{A}^{(i)p,n}_{3/2}(S_x,Q^2)/\mathcal{A}^{(i)p,n}_{1/2}(S_x,Q^2) \simeq 0, \quad (70)$$

which follow from the requirement of hadron-helicity conservation [27] for $Q^2 \gg M^2$. In accordance with (70), the resonance multipole amplitude must satisfy the relations

$$E^{(1)p,n}_{1^+}(S_x,Q^2) \simeq M^{(1)p,n}_{1^+}(S_x,Q^2), \quad (71)$$

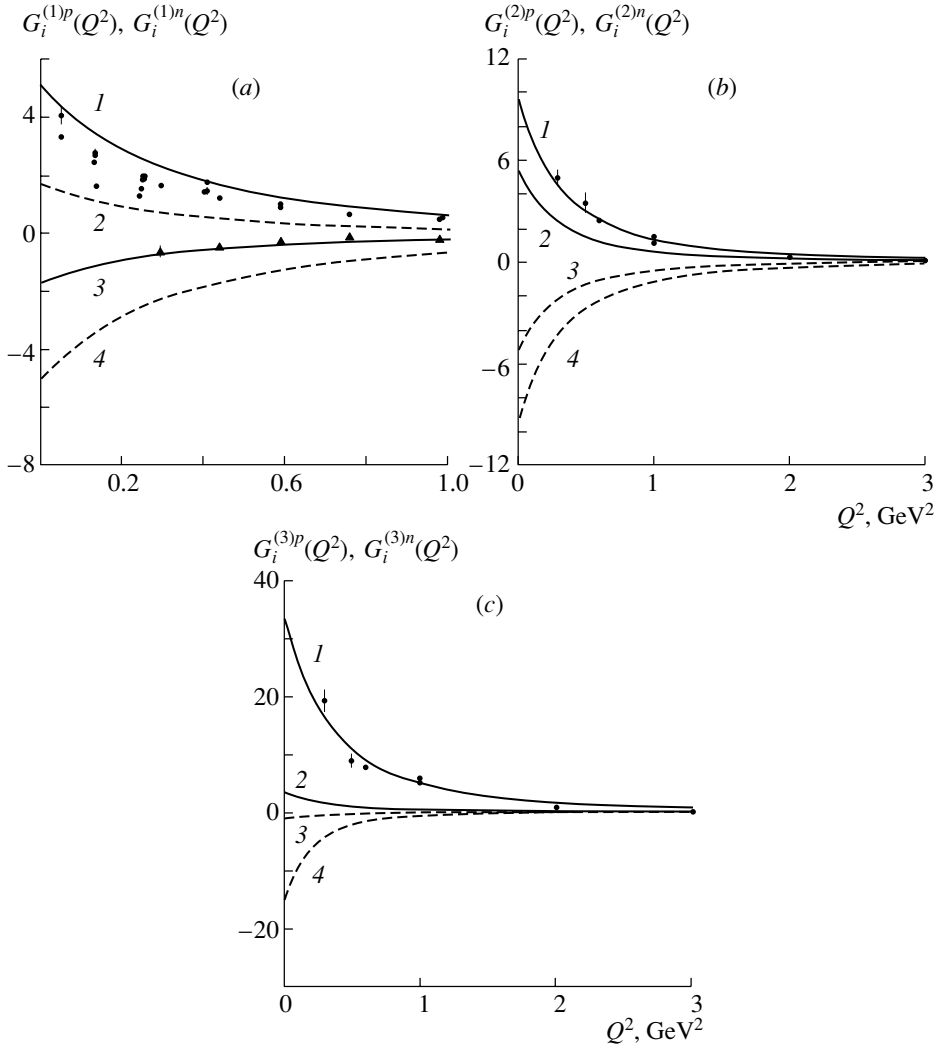

Fig. 6. Proton (solid curves) and neutron (dashed curves) Sachs transition form factors within the generalized vector-dominance model: (*a*) $N \to \Delta(1232)$, (*b*) $N \to N(1520)$, and (*c*) $N \to N(1680)$. Experimental points correspond to the results obtained in [9] by estimating the proton transition form factors on the basis of data from a partial-wave analysis of $\gamma^* + p \to R_i^+ \to (\pi + N)^+$ processes. Curves *1*, *2*, *3*, and *4* represent the results of the calculation of $G_3^{(1,2,3)p}$ (closed circles), $G_1^{(1)n}$ and $G_1^{(2,3)p}$, $G_1^{(1)p}$ (closed triangles) and $G_1^{(2,3)n}$, and $G_3^{(1,2,3)n}$, respectively.

$$E_{2^-}^{(2)p,n}(S_x, Q^2) \simeq -M_{2^-}^{(2)p,n}(S_x, Q^2),$$
$$E_{3^-}^{(3)p,n}(S_x, Q^2) \simeq -M_{3^-}^{(3)p,n}(S_x, Q^2),$$

while the transverse Sachs form factors must obey the equalities

$$G_2^{(1)}(Q^2) = \frac{(\sqrt{3} - 3r_1)}{(\sqrt{3} + r_1)} \frac{(M_1 + M)^2 + Q^2}{4M_1(M_1 + M)} G_3^{(1)}(Q^2),$$
$$G_2^{(2)}(Q^2) = \frac{\sqrt{3}}{r_2} \frac{(M_2 - M)^2 + Q^2}{4M_2(M_2 + M)} G_3^{(2)}(Q^2),$$
$$G_2^{(3)}(Q^2) = \frac{3\sqrt{2} + \sqrt{3} + (3 - \sqrt{6})r_3}{\sqrt{2} - \sqrt{3} + (\sqrt{6} + 1)r_3} \times \frac{(M_3 - M)^2 + Q^2}{4M_3(M_3 + M)} G_3^{(3)}(Q^2). \qquad (72)$$

Substituting the values of $r_i^{p,n}$ from Table 2 into (72), we obtain

$$G_2^{(1)\binom{p}{n}}(Q^2) = (1.055 \pm 0.077) \times \frac{(M_1 + M)^2 + Q^2}{4M_1(M_1 + M)} G_3^{(1)\binom{p}{n}}(Q^2),$$
$$G_2^{(2)\binom{p}{n}}(Q^2) = \begin{pmatrix} 2.255 \pm 0.182 \\ 17.321 \pm 18.010 \end{pmatrix} \times \frac{(M_2 - M)^2 + Q^2}{4M_2(M_2 + M)} G_3^{(2)\binom{p}{n}}(Q^2), \qquad (73)$$
$$G_2^{(3)\binom{p}{n}}(Q^2) = \begin{pmatrix} 2.247 \pm 0.025 \\ 0.434 \pm 0.676 \end{pmatrix}$$

$$\times\frac{(M_3-M)^2+Q^2}{4M_3(M_3+M)}G_3^{(3)\binom{p}{n}}(Q^2).$$

Data on the Q^2 dependence of the differential cross section for $e^-+p\to e^-+X$ processes in the region of the resonances $N(1520)$ and $N(1680)$ make it possible to discriminate between (31) and (73) quite readily, since the resonance structure functions depend on the squares of the transition form factors. This is impossible in the region of the resonance $\Delta(1232)$, in which case relations (31) and (73) differ only in sign.

10. CONCLUSION

The background structure functions given by (48) reproduce fairly well available experimental data, including data from [13], which were obtained in the threshold and in the resonance ($1.2\le S_x\le 4$ GeV^2) region at Q^2 values so high ($Q^2>6$ GeV^2) that the contribution of the resonance structure functions (25) is negligibly small.

The parameters that control the behavior of the background structure functions in the Regge region are weakly sensitive to the number of nucleon resonances that are taken into account and to the values of their masses and hadronic-decay widths. For this reason, only the parameters a_1, a_2, and a_3, which appear in the definition (49) of the exponent of the threshold factor $(S_x-(M+\mu)^2)^{\kappa(Q^2)}$ in (48), can affect the results obtained by extracting the transition form factors for the nucleon from data on the differential cross section for inelastic lepton–nucleon scattering.

In general, the resonance structure functions (25) are expressed in terms of the squares of three Sachs transition form factors. Because of the limiting chiral invariance of the electromagnetic current determining the *nucleon → nucleon resonance* transition, the transverse transition form factors are related by Eq. (31). That the ratios of the electric and magnetic resonance amplitudes (E/M) or the ratios $\mathcal{A}_{3/2}^{(i)}/\mathcal{A}_{1/2}^{(i)}$ of the transverse resonance helicity amplitudes for virtual hadron photoproduction on a nucleon are constant is an important corollary of Eq. (31).

The expressions obtained for the transition form factors on the basis of the generalized vector-dominance model allowing for the requirements of limiting chiral invariance reproduce fairly well data from [26] on the differential cross sections for $e^-+p\to e^-+X$ processes in the region specified by the inequalities $1.2\le S_x\le 4$ GeV^2 and $0\le Q^2\le 6$ GeV^2.

REFERENCES

1. R. P. Feynman, *Photon–Hadron Interactions* (Benjamin, Reading, 1972; Mir, Moscow, 1975).
2. F. Foster and G. Hughes, Rep. Prog. Phys. **46**, 1445 (1983).
3. P. Stoler, Phys. Rep. **226**, 103 (1993).
4. P. Kroll *et al.,* Z. Phys. A **342**, 429 (1992).
5. Z. Li and N. Burkert, Phys. Rev. D **46**, 70 (1992).
6. N. Isgur and G. Karl, Phys. Rev. D **18**, 4187 (1978).
7. G. A. Warren and C. E. Carlson, Phys. Rev. D **42**, 3020 (1990).
8. F. I. Akhiezer and M. P. Rekalo, *Electrodynamics of Hadrons* (Naukova Dumka, Kiev, 1977).
9. S. N. Koltochnik, V. I. Rus'kin, and P. B. Kharchevnikov, Izv. Akad. Nauk Resp. Kaz., Ser. Fiz.-Mat., No. 2, 50 (1995).
10. H. D. Scadron and H. F. Jones, Ann. Phys. (N.Y.) **81**, 1 (1973); R. C. E. Devenish and D. H. Lyth, Nucl. Phys. B **93**, 109 (1975).
11. S. N. Koltochnik, V. I. Rus'kin, and P. B. Kharchevnikov, Yad. Fiz. **55**, 1942 (1992) [Sov. J. Nucl. Phys. **55**, 1077 (1992)].
12. P. B. Kharchevnikov, S. N. Koltochnik, and V. I. Rus'kin, Z. Phys. A **344**, 305 (1992).
13. P. E. Bosted *et al.,* SLAC-PUB-6374 (1993).
14. R. G. Roberts and M. R. Whalley, J. Phys. G **17**, 1 (1991).
15. S. N. Koltochnik, V. I. Rus'kin, and P. B. Kharchevnikov, Izv. Akad. Nauk Resp. Kaz., Ser. Fiz.-Mat., No. 2, 31 (1995).
16. V. I. Rus'kin, Preprint No. 87-08, IFVÉ AN KazSSR (Alma-Ata, 1987).
17. B. L. Ioffe, V. A. Khose, and L. N. Lipatov, *Hard Processes* (Énergoatomizdat, Moscow, 1983; North-Holland, Amsterdam, 1984).
18. V. I. Rus'kin and O. S. Kosmachev, *Multiparticle Hadron Production* (Nauka, Alma-Ata, 1983), p. 91.
19. F. J. Ynduráin, *Quantum Chromodynamics* (Springer-Verlag, New York, 1983; Mir, Moscow, 1986).
20. C. E. Carlson and N. C. Mukhopadhyay, Phys. Rev. D **47**, R1737 (1993).
21. S. I. Alekhin *et al.,* CERN-HERA 87-01 (Geneva, 1987).
22. G. P. Yost *et al.,* Phys. Lett. B **204**, 38 (1988).
23. R. L. Crawford, Phys. Lett. B **204**, 378 (1988).
24. J. J. Aubert *et al.,* Nucl. Phys. B **293**, 740 (1987).
25. A. Benvenuti *et al.,* Phys. Lett. B **237**, 599 (1990).
26. F. W. Brasse *et al.,* Nucl. Phys. B **110**, 413 (1976).
27. S. J. Brodsky and G. P. Lepage, Phys. Rev. D **23**, 1152 (1981).

Translated by A. Isaakyan

Physics of Atomic Nuclei, Vol. 64, No. 5, 2001, pp. 937–940. Translated from Yadernaya Fizika, Vol. 64, No. 5, 2001, pp. 1006–1009.

ELEMENTARY PARTICLES AND FIELDS
Theory

Synchrotron Radiation from a Longitudinally Polarized Relativistic Spinning Particle in Pseudoclassical Theory

G. V. Grigoryan* **and R. P. Grigoryan****

Yerevan Physics Institute, ul. Brat'ev Alikhanian 2, AM-375036, Armenia

Received May 24, 2000

Abstract—The spin dependence of the intensity and polarization of synchrotron radiation from a longitudinally polarized particle moving at a constant speed along a circle in a uniform magnetic field is investigated within the pseudoclassical approach. © *2001 MAIK "Nauka/Interperiodica".*

It is well known that synchrotron radiation from a polarized particle involves a contribution proportional to the particle spin. The dependence of quantities characterizing synchrotron radiation on the polarized-electron spin was investigated by Sokolov and Ternov [1] within quantum field theory. The spin dependence of synchrotron radiation can be employed to measure the degree of transverse beam polarization in accelerators [2]. A method for determining the degree of longitudinal beam polarization on the basis of synchrotron radiation from the beam was proposed in [3]. All estimates in the quoted studies were obtained within QED.

Since the electron spin is a first-order quantity in the Planck constant $\hbar$, the spin contribution to the features of synchrotron radiation in this order is of classical nature. The semiclassical theory of synchrotron radiation was developed in [4, 5]. The general expressions for the spin dependence of the characteristics of synchrotron radiation were derived in [4]. These formulas can be used to calculate the spin contribution to the emission intensity in the case of longitudinally polarized particles.

At the same time, the electron spin can be described in terms of Grassmann variables at the classical level within the pseudoclassical theory of a relativistic spinning particle. The quantization of this theory leads to the Dirac theory of the electron. That a spin in an external field can be consistently described at the classical level in terms of Grassmann variables makes it possible to study spin effects in radiation processes on the basis of classical equations of motion.

In [6], Lienard–Wiechert potentials for a relativistic spinning particle with an anomalous magnetic momentum were derived within the pseudoclassical approach. With the aid of the general expressions for these potentials, some particular cases of the motion of such a particle were investigated to the leading order in the spin **S**. Among other things, the spin dependence of the intensity and polarization of synchrotron radiation from a transversely polarized particle was investigated for the case where the particle moves at a constant speed along a circle.

The expressions describing the spin dependence of the observables of radiation from a relativistic particle are derived much more straightforwardly within our approach than within QED.

Using the formulas obtained in [6], we study here the spin dependence of the intensity and polarization of synchrotron radiation from a longitudinally polarized particle having no anomalous magnetic moment and moving at a constant speed along a circle in a uniform external magnetic field.

The pseudoclassical theory of interactions of a relativistic spinning particle with an electromagnetic field provides an example of a constrained gauge theory. Fixing the gauge by imposing additional constraints, we find that the vector potential A^μ of the electromagnetic field satisfies the equation (for more details, see [6])

$$\Box A^\mu = j^\mu, \tag{1}$$

where

$$j^\mu(y) = g\int d\tau \dot{x}^\mu \delta(x(\tau) - y)$$
$$+\frac{\partial}{\partial y^\nu}\int d\tau \delta(x(\tau) - y)p_{\mu\nu}(\tau). \tag{2}$$

Here, y is the observation point, g is a charge, x_μ is the coordinate of the particle, an overdot denotes differentiation with respect to the parameter τ varying along the particle trajectory, and $p_{\mu\nu}$ is the tensor of

*e-mail: gagri@lx2.yerphy.am
**e-mail: rogri@lx2.yerphy.am

the dipole moment of the particle (its explicit form is given below).

In deriving Eq. (1), the gauge was fixed by imposing the conditions [6]

$$\partial_\mu A^\mu = 0, \quad \dot{x}^2 = 1, \quad q_\mu = -p_{\mu\nu}\dot{x}^\nu = 0. \qquad (3)$$

The second relation in (3) means that τ is the proper-time parameter, while the third relation ensures the vanishing of the electric dipole moment q_μ for a point-like particle (this must always be so).

The first term in (34) represents the contribution of the charge of a spinning particle to the current, while the second term is the contribution of its dipole moment to the current.

In the case of a particle without an anomalous magnetic moment—and we consider here precisely this case—the tensor $p_{\mu\nu}$ in the chosen gauge is given by [6]

$$p_{\mu\nu} = -\frac{g}{m^2}\varepsilon_{\mu\nu\lambda\sigma}W^\lambda \dot{x}^\sigma, \qquad (4)$$

where W_μ is the pseudoclassical analog of the Pauli–Lubanski vector. In the reference frame comoving with the particle, it can be expressed in terms of the particle-spin vector $\mathbf{S} = (S_i)$ as

$$\frac{W_\mu}{m} = \left(\gamma(\mathbf{v}\cdot\mathbf{S}),\ S_i + \gamma^2\frac{v_i(\mathbf{v}\cdot\mathbf{S})}{\gamma+1}\right), \qquad (5)$$

where $\mathbf{v} \equiv (v^i) = dx^i/dt$ is the particle 3-velocity and $dt/d\tau = \gamma = \left(\sqrt{1-\mathbf{v}^2}\right)^{-1}$ (in pseudoclassical theory, the tensor $p_{\mu\nu}$ and the vectors W_μ and S_i are quadratic in Grassmann variables; the explicit expressions for them are irrelevant here).

A solution to Eq. (1) with current (34) in terms of the retarded fields was obtained in [7]. Here, we present only that part of this solution which describes the radiation field. We have

$$F^{\mu\nu}_{\rm ret}(y) \qquad (6)$$
$$= \frac{1}{2\pi\rho}\left[g\left(k^{[\mu}\ddot{x}^{\nu]} - (\ddot{x}k)k^{[\mu}\dot{x}^{\nu]}\right) + P_1^{[\mu\nu]}\right]\Bigg|_{\tau=\tau_r},$$

where $\rho = \dot{x}^\nu R_\nu$, $k_\mu = R_\mu/\rho$, $R^\mu \equiv y^\mu - x^\mu(\tau)$, and $R^\mu R_\mu = 0$; all quantities in (6) are taken at the instant τ_r determined by the equation $\tau_r = \tau - R(\tau_r)$, where $P_1^{\mu\nu}$ is given by[1)]

$$P_1^{\mu\nu} = T^{\mu\alpha}k_\alpha k^\nu, \quad T^{\mu\nu} = \dddot{p}^{\mu\nu} - 3(\ddot{x}k)\dot{p}^{\mu\nu} \qquad (7)$$
$$+3(\ddot{x}k)^2 p^{\mu\nu} - (\dddot{x}k)p^{\mu\nu}.$$

[1)]The brackets $[\ldots]$ in (6) imply complete antisymmetrization: $A_{[\alpha\beta\gamma]} = 1/3!\,\{A_{\alpha\beta\gamma} + A_{\beta\gamma\alpha} + A_{\gamma\alpha\beta} - A_{\beta\alpha\gamma} - A_{\alpha\gamma\beta} - A_{\gamma\beta\alpha}\}$.

The first term in (6) describes the contribution of the charge of a spinning particle, while the second term represents the contribution of its dipole moment.

Let us consider the motion of a longitudinally polarized particle ($\mathbf{v}||\mathbf{S}$) in a uniform magnetic field $\mathbf{B}$. The angular velocity of rotation of the particle without an anomalous magnetic moment is equal to the angular velocity of spin precession. Thus, the particle helicity λ is conserved, and we obtain

$$v^k = \lambda\frac{v}{S}S^k, \quad \lambda = \pm 1, \qquad (8)$$
$$(\mathbf{v}\cdot\mathbf{a}) = (\mathbf{S}\cdot\mathbf{a}) = 0, \quad \dot{\gamma} = 0, \quad \dot{\boldsymbol{\omega}} = 0, \qquad (9)$$

where $\mathbf{a} = d\mathbf{v}/dt$.

Taking into account this relation and expression (5), we find that the components p_{0i} and p_{ij} of the dipole-moment tensor (4) and their derivatives can be represented as

$$p_{0i} = \dot{p}_{0i} = \ddot{p}_{0i} = 0,$$

$$p_{ij} = -\frac{g}{m}\varepsilon_{ijk}S_k, \qquad (10)$$
$$\dot{p}_{ij} = -\frac{g}{m}\varepsilon_{ijk}\dot{S}_k = -\gamma\frac{g}{m}\left(\omega_i S_j - \omega_j S_i\right),$$
$$\ddot{p}_{ij} = \gamma^2\frac{g}{m}\omega^2\varepsilon_{ijk}S_k. \qquad (11)$$

With the aid of (6), we obtain the contribution $E_i^{\rm dip}$ of the particle dipole moment to the radiation electric field in the form

$$E_i^{\rm dip} = \left(F_{i0}^{\rm rad}\right)^{\rm dip} = \frac{1}{4\pi\rho}\left(P_{1,i0} - P_{1,0i}\right)$$
$$= -\frac{1}{4\pi\rho}\left[T_{0l}k^l k_i - T_{i\lambda}k^\lambda k_0\right]\Big|_{\tau=\tau_r} \qquad (12)$$
$$= -\frac{1}{4\pi\rho}\left[\left(\delta_{ij}k_0^2 - k_i k_j\right)T_{0j} + T_{ij}k_j k_0\right]\Big|_{\tau=\tau_r},$$

where T_{0i} and T_{ij} are the components of the tensor $T_{\mu\nu}$. It can easily be seen that the components T_{0i} vanish identically by virtue of Eqs. (34).

Taking into account the relations

$$\dot{x}^\mu = \gamma(1,\mathbf{v}), \quad \rho = \gamma(R - (\mathbf{v}\cdot\mathbf{R}))$$
$$= \gamma R(1 - (\mathbf{v}\cdot\mathbf{n})), \quad \gamma = 1/\sqrt{1-\mathbf{v}^2},$$
$$\ddot{x}^\mu = \left(\gamma^4(\mathbf{v}\cdot\mathbf{a}), \gamma^2\mathbf{a} + \gamma^4\mathbf{v}(\mathbf{v}\cdot\mathbf{a})\right),$$
$$k^\alpha = \left(\frac{R}{\rho}, \frac{\mathbf{R}}{\rho}\right) = \frac{R}{\rho}n^\alpha, \qquad (13)$$
$$\dddot{x}^\mu = \left(\dot{a}^0,\ \gamma^3\mathbf{b} + 3\gamma^5(\mathbf{v}\cdot\mathbf{a})\mathbf{a} + \dot{a}^0\mathbf{v}\right),$$
$$\dot{a}^0 = \gamma^5\left[(\mathbf{v}\cdot\mathbf{b}) + \mathbf{a}^2\right] + 4\gamma^7(\mathbf{v}\cdot\mathbf{a})^2,$$

where $\mathbf{b} = d\mathbf{a}/dt$, we recast expression (12) into the form

$$E_i^{\rm dip} = -\frac{R^2}{4\pi\rho^3}T_{ij}n_j = \frac{1}{4\pi R(1-(\mathbf{n}\cdot\mathbf{v}))^3}\frac{g}{m\gamma} \times \left[\frac{3(\mathbf{a}\cdot\mathbf{n})}{1-(\mathbf{n}\cdot\mathbf{v})}\left(\omega_i(\mathbf{S}\cdot\mathbf{n}) - S_i(\boldsymbol{\omega}\cdot\mathbf{n})\right) + \varepsilon_{ijk}n_jS_k\left(\frac{3(\mathbf{a}\cdot\mathbf{n})^2}{(1-(\mathbf{n}\cdot\mathbf{v}))^2} - \frac{\omega^2}{1-(\mathbf{n}\cdot\mathbf{v})}\right)\right]\Bigg|_{\tau=\tau_r}. \quad (14)$$

For the strength $E_i^{\rm ch}$ of the electric field generated by a charged spinless particle, the substitution of expressions (13) into the first term in (6) yields the well-known expression

$$E_i^{\rm ch} = \frac{g}{4\pi R(1-(\mathbf{v}\cdot\mathbf{n}))^3} \times \left[(n_i - v_i)(\mathbf{a}\cdot\mathbf{n}) - a_i(1-(\mathbf{v}\cdot\mathbf{n}))\right]\Big|_{\tau=\tau_r}, \quad (15)$$

$$E_i^{\rm rad} = F_{i0}^{\rm rad} = E_i^{\rm ch} + E_i^{\rm dip}.$$

The intensity of synchrotron radiation is proportional to $(E_i^{\rm rad})^2 = \left(E_i^{\rm ch} + E_i^{\rm dip}\right)^2$. To the first order in the spin, the contribution of the dipole moment to the intensity of radiation is determined by the term $2E_i^{\rm ch}E_i^{\rm dip}$. Using expressions (14) and (15), we arrive at

$$2E_i^{\rm ch}E_i^{\rm dip} = 2\left(\frac{g}{4\pi R}\right)^2\frac{\lambda S v}{m\gamma(1-(\mathbf{v}\cdot\mathbf{n}))^6}\omega^2(\boldsymbol{\omega}\cdot\mathbf{n}) = -2\left(\frac{g}{4\pi R}\right)^2\frac{\lambda S v\omega^3}{m\gamma(1-v\cos\theta)^6}\sin\theta\sin\varphi, \quad (16)$$

where θ and φ are the angles that determine the direction of the vector $\mathbf{n}$ in the basis formed by the vectors $\mathbf{v}$, $\mathbf{a}$, and $\mathbf{B}$ (see Fig. 1).

With the aid of (16), we find that, to the first order in the particle spin, the contribution of the dipole moment to the synchrotron-radiation intensity takes the form

$$\frac{d\mathcal{I}^{\rm dip}}{dt_0 d\Omega} = -\left(\frac{g}{4\pi}\right)^2\frac{2\lambda}{(1-v\cos\theta)^5}\frac{\omega^3 vS\sin\theta\sin\varphi}{m\gamma}. \quad (17)$$

From this expression, we see that, to the first order in the spin, the total contribution of the dipole moment of a longitudinally polarized particle to the synchrotron-radiation intensity vanishes. Upon integrating Eq. (17) over the upper (up) hemisphere ($0 \le \varphi \le \pi,\ 0 \le \theta \le \pi$), we obtain

$$\frac{d\mathcal{I}_{\rm up}^{\rm dip}}{dt_0} = -\frac{g^2}{4\pi}\frac{4+v^2}{8m}\omega^3 v\lambda S\gamma^6. \quad (18)$$

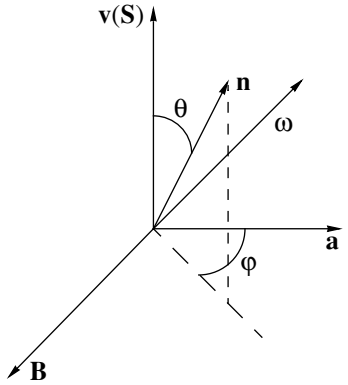

Fig. 1. Reference frame for angles in studying the angular characteristics of radiation.

Using expression (17) and considering that

$$\frac{d\mathcal{I}_{\rm up}^{\rm dip}}{dt_0} = -\frac{d\mathcal{I}_{\rm down}^{\rm dip}}{dt_0}, \quad (19)$$

$$\frac{d\mathcal{I}_{\rm up(down)}^{\rm tot}}{dt_0} = \frac{g^2}{4\pi}\frac{a^2}{3}\gamma^4 + \frac{d\mathcal{I}_{\rm up(down)}^{\rm dip}}{dt_0}, \quad (20)$$

we find that the asymmetry of synchrotron radiation into the upper and lower (down) hemispheres can be characterized as

$$\delta = \frac{\dfrac{d\mathcal{I}_{\rm up}^{\rm dip}}{dt_0} - \dfrac{d\mathcal{I}_{\rm down}^{\rm dip}}{dt_0}}{\dfrac{d\mathcal{I}_{\rm up}^{\rm tot}}{dt_0} + \dfrac{d\mathcal{I}_{\rm down}^{\rm tot}}{dt_0}} = -\frac{3(4+v^2)}{8mv}\omega\gamma^2\lambda S. \quad (21)$$

In the ultrarelativistic case, we have

$$\delta = -\frac{15}{8m}\omega\gamma^2\lambda S. \quad (22)$$

Rewriting this expression in terms of the Schwinger field $H_0 = m^2/g = 4.41\times10^9$ T and considering that $S = 1/2$ and $\omega m\gamma = gB$, we arrive at

$$\delta = -\frac{15}{16}\gamma\lambda\frac{B}{H_0}. \quad (23)$$

Our estimate $\delta = -0.38\times10^{-4}$, which was obtained at $E = 45$ GeV (the energy available at the LEP), the magnetic-field strength of $B = 2$ T, and $\lambda = 1$, agrees with the estimate derived in [3] on the basis of QED formulas [4].

We will now study the polarization properties of synchrotron radiation, following the ideas developed in [4]. For this purpose, we expand the electric-field strength $\mathbf{E}^{\rm rad}$ in the components in the orthonormal basis formed by the vectors $\mathbf{e} = \mathbf{a}/a$ and $[\mathbf{n}\times\mathbf{e}]$,

$$\mathbf{E}^{\rm rad} = E_1\mathbf{e} + E_2\left[\mathbf{n}\times\mathbf{e}\right]. \quad (24)$$

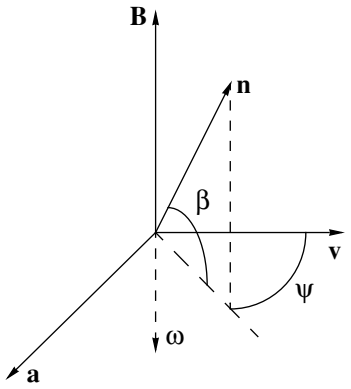

Fig. 2. Reference frame for angles in describing radiation from a fast particle.

This basis is advantageous in that it provides a convenient reference frame for the angles that can be used to describe emission from a fast particle (see Fig. 2). Indeed, the main contribution to the emission comes from the region of small angles β and ψ (about $1/\gamma$), since the angle between the vectors **n** and **v** is of order $1/\gamma$. As was indicated in [4], the vectors **E** and **n** are not orthogonal, but this mismatch is about $1/\gamma$. For this reason, expansion (24) can be used to calculate the leading contribution in the parameter $1/\gamma$. Using expressions (14) and (15) and expansion (24), we obtain the expressions for E_1 and E_2 in the form

$$E_1 = \frac{ga}{\pi R(\mu^2+\psi^2)^3} \tag{25}$$
$$\times\left((\psi^2-\mu^2)+\frac{4a\lambda S}{m\gamma}\frac{\beta(\mu^2-5\psi^2)}{(\mu^2+\psi^2)^2}\right)\Bigg|_{\tau=\tau_r},$$

$$E_2 = -\frac{2ga}{\pi R(\mu^2+\psi^2)^3} \tag{26}$$
$$\times\left(\beta\psi-\frac{4a\lambda S}{m\gamma}\frac{\psi(2\mu^2-\psi^2)}{(\mu^2+\psi^2)^2}\right)\Bigg|_{\tau=\tau_r},$$

where $\mu^2=\gamma^{-2}+\beta^2$.

ACKNOWLEDGMENTS

We are grateful to I. V. Tyutin and A. Airapetyan for stimulating discussions.

This work was supported in part by the International Association for the Promotion of Cooperation with Scientists from the Independent States of the Former Soviet Union (grant nos. INTAS-96-538 and INTAS-93-1038) and by the Russian Foundation for Basic Research under the agreement with the International Association for the Promotion of Cooperation with Scientists from the Independent States of the Former Soviet Union (grant no. INTAS–RFBR-95-0829).

REFERENCES

1. *Synchrotron Radiation,* Ed. by A. A. Sokolov and I. M. Ternov (Nauka, Moscow, 1966; Academie-Verlag, Berlin, 1968).
2. V. N. Korchuganov *et al.,* Preprint No. 77–83, IYaF (Budker Institute of Nuclear Physics, Novosibirsk, 1977); S. A. Belomestnykh, A. E. Bondar', *et al.,* Nucl. Instrum. Methods **227**, 173 (1984).
3. I. P. Karabekov and S. I. Karabekian, in *Proceedings of the Fifth European Particle Accelerator Conference, EPAC-96,* Vol. 2, p. 1743; A. V. Airapetian, R. O. Avakian, I. P. Karabekov, *et al.,* in *Proceedings of the SPIN-96 Conference High-Energy Electron Polarimeter Based on High-Energy Spin Physics, Amsterdam,* Vol. 1, p. 762.
4. V. N. Baier, V. M. Katkov, and V. S. Fadin, *Radiation from Relativistic Electrons* (Atomizdat, Moscow, 1973); V. N. Baier, V. M. Katkov and V. M. Strakhovenko, *Electromagnetic Processes at High Energies in Oriented Single Crystals* (World Sci., Singapore, 1998).
5. I. M. Ternov and V. A. Bordovitsyn, Vestn. Mosk. Univ., Ser. 3: Fiz., Astron., No. 24, 69 (1983); No. 28, 21 (1983).
6. S. A. Arakelyan, G. V. Grigoryan, and R. P. Grigoryan, Yad. Fiz. **63**, 2211 (2000) [Phys. At. Nucl. **63**, 2115 (2000)]; hep-th/9902159.
7. J. R. Ellis, J. Math. Phys. **7**, 1185 (1965).

Translated by R. Rogalyov

Physics of Atomic Nuclei, Vol. 64, No. 5, 2001, pp. 941–945. From Yadernaya Fizika, Vol. 64, No. 5, 2001, pp. 1010–1014.

ELEMENTARY PARTICLES AND FIELDS
Theory

Top-Quark Mass in the Minimal Top-Condensation Model with Extra Dimensions*

A. B. Kobakhidze**

Department of Physics, University of Helsinki, P.O. Box 9 (Siltavuorenpenger 20C), FIN-00014 Helsinki, Finland, and E. Andronikashvili Institute of Physics, Georgian Academy of Sciences, ul. Tamarashvili 6, GE-380077 Tbilisi, Republic of Georgia

Received March 9, 2000

Abstract—The minimal model of dynamical electroweak-symmetry breaking through top condensation in the presence of compact large extra dimensions is studied. It is shown that, owing to the power-law evolution of gauge and Yukawa couplings, the original predictions of Bardeen, Hill, and Lindner for the top-quark mass are significantly lowered and that, even for a small cutoff scale Λ of a few TeV, one can obtain experimentally allowed values. © *2001 MAIK "Nauka/Interperiodica".*

Despite the success of the Standard Model (SM) in describing experimental data with impressive accuracy, the physics mechanism behind electroweak-symmetry breaking (EWSB) and a somewhat related explanation of the masses and mass hierarchies of elementary particles remain an outstanding problem. Top condensation is an interesting mechanism for dynamical EWSB (for an overview, see [1] and references therein). The beauty and strength of this mechanism lie in the fact that, usually, the set of underlying assumptions is rather limited and that the mechanism can explain simultaneously the dynamical generation of the heavy-top-quark mass and EWSB (entirely or at least partly). A detailed investigation of the minimal scenario, where EWSB follows from top-quark condensation alone, was performed by Bardeen, Hill, and Lindner (BHL) [2]. Eliminating the SM Higgs sector in favor of the local attractive interaction

$$\mathcal{L}_{\rm NJL}^{\text{4- dim}} = G(\overline{Q}_L t_R)(\overline{t}_R Q_L) \qquad (1)$$

[here, $Q_L^T = (t_L, b_L)$ is the third-generation left-handed quark doublet and t_R is the corresponding right-handed singlet, color and weak-isospin indices being suppressed], which is of the Nambu–Jona-Lasinio type, they obtained, in the fermion-bubble approximation for sufficiently attractive G ($G > \frac{8\pi^2}{3}\frac{1}{\Lambda^2}$), a nontrivial solution to the gap equation. This solution relates the top-quark mass $m_{\rm top}$ to the ultraviolet-cutoff parameter Λ and the four-fermion coupling G,

$$m_{\rm top}^2 = \frac{\Lambda^2 - (8\pi^2/3)G^{-1}}{\ln(\Lambda^2/m_{\rm top}^2)}, \qquad (2)$$

and to the W-boson mass,

$$m_W^2 = \frac{3g_2^2}{32\pi^2} m_{\rm top}^2 \left(\ln(\Lambda^2/m_{\rm top}^2) + \frac{1}{2}\right). \qquad (3)$$

For a large cutoff parameter, $\Lambda \simeq 10^{15}$ GeV, the bubble approximation predicts a value of $m_{\rm top} \simeq 163$ GeV for the top-quark mass, while, for a smaller cutoff parameter value of $\Lambda \simeq 10$ TeV, $m_{\rm top} \simeq 1$ TeV. This requires G to be fine-tuned in order to cancel the quadratic cutoff-parameter dependence in (2).

An improvement for the top-quark mass can be achieved by considering a low-energy effective field theory that is just the full SM, which treats the composite Higgs field as an elementary degree of freedom. The only difference is the compositness condition that the Higgs field becomes static at high energies of about Λ—that is, $Z_{\rm H}(\Lambda) = 0$—thus recovering from the SM Lagrangian, together with equation of motion, the structure of the basic Nambu–Jona-Lasinio Lagrangian (1). This compositness condition means that the top-quark mass is governed by an infrared fixed-point solution to the renormalization-group equations [3]. Unfortunately, the full analysis on the basis of renormalization-group equations yields unacceptable predictions for the top-quark mass, $m_{\rm top} \simeq 220$–430 GeV for $\Lambda \simeq 10^{19}$–10^4 GeV [2]. Thus, the minimal BHL model and its various modifications (two Higgs and supersymmetric versions), while being phenomenologically viable in many aspects [4], have a common drawback:

*This article was submitted by the author in English.

**e-mail: archil.kobakhidze@helsinki.fi

they predict too high a value for the top-quark mass to fit experimental data. Therefore, one is led to consider more complex symmetry-breaking scenarios involving more condensates and more parameters [1, 4].

In this study, I consider the minimal BHL model, assuming the existence of extra dimensions with relatively large compactification radii that tend to produce lower values for the top-quark mass, in agreement with experimental data, even for a lower cutoff scale Λ. In this way, the fine tuning required for large Λ is avoided. Extra spacetime dimensions naturally appear in string theory; therefore, such an idea is highly motivated from the fundamental point of view. In recent years, the possibility of large extra dimensions has received considerable attention; in particular, their role was explored for gauge-coupling unification [5, 6], for neutrino-mass generation [7], for supersymmetry breaking [8], and for providing an alternative solution to the gauge-hierarchy problem [9]. The cosmological implications [10], various phenomenological issues [11], and possible collider signatures [12] of extra dimensions having large radii were also investigated.

In order to implement compact extra dimensions in practice, one introduces towers of Kaluza–Klein (KK) excitations associated with gauge and matter fields. The exact details of the spectrum of KK states are, to some extent, model-dependent. Here, I closely follow the models described in [5], where the extra dimensions are compactified on the S/Z_2 orbifold (a circle subjected to further identification $y_\alpha \to -y_\alpha$, $\alpha = 1, ..., \delta$; δ denotes the number of compact dimensions). In this case, KK excitations can be decomposed into even $[\Phi_+(x,y)]$ and odd $[\Phi_-(x,y)]$ fields,

$$\Phi_+(x,y) = \sum_{n_1=0}^{\infty} ... \sum_{n_\delta=0}^{\infty} \Phi^{(n_\alpha)}(x)\cos(n_\alpha y_\alpha/R),$$

$$\Phi_-(x,y) = \sum_{n_1=1}^{\infty} ... \sum_{n_\delta=1}^{\infty} \Phi^{(n_\alpha)}(x)\sin(n_\alpha y_\alpha/R), \quad (4)$$

where R is the radius of compact dimensions (for the sake of simplicity, I assume that all extra dimensions have the same radius). Since the appropriate transformation of the fields under Z_2 parity is determined by interactions, half of the original KK states can be projected out according to the Z_2 parity of the fields. If only the odd tower is left, the zero mode is missing.

Nonsupersymmetric theories can be more straightforwardly embedded into higher dimensions than supersymmetric ones, because KK states must not any longer form $N = 2$ multiplets, in contrast to what is usually assumed in the supersymmetric case. Thus, as a minimal scenario, I assume that gauge bosons (even Z_2) have KK excitations, while chiral SM fermions (even Z_2), living at the orbifold fixed points, do not. At each KK level, this requires introducing additional scalar fields (odd Z_2) that transform according to the adjoint representations of each SM gauge symmetry group in order to make corresponding gauge bosons massive [5]. Within this framework, I assume that, in four dimensions, an infinite number of four-fermion interactions

$$\mathcal{L}_{\rm NJL}^{(4+\delta)\text{- dim}} = \sum_{n_1=0}^{\infty} ... \sum_{n_\delta=0}^{\infty} G^{n_\alpha}(\overline{Q}_L t_R)(\overline{t}_R Q_L) \quad (5)$$

with $G^{n_\alpha} = (M_0^2 + n_\alpha^2/R^2)^{-1}$ effectively appear in addition to the ordinary Nambu–Jona-Lasinio interaction. The set of four-fermion interactions in (5) can be viewed as the result of integration over some heavy (M_0^2) state and its KK excitations $(M_0^2 + n_\alpha^2/R^2)$ [13]. Introducing auxiliary fields $H^{n_\alpha} = G^{n_\alpha}(\overline{t}_R Q_L)$, one can rewrite Lagrangian (5) in the equivalent form

$$\mathcal{L}_{\rm NJL}^{(4+\delta)\text{- dim}} = \sum_{n_1=0}^{\infty} ... \sum_{n_\delta=0}^{\infty} \left[-(M_0^2 + n_\alpha^2/R^2)|H^{n_\alpha}|^2 + (\overline{Q}_L t_R)H^{n_\alpha} + \text{h.c.}\right]. \quad (6)$$

The static fields H^{n_α} acquire gauge-invariant kinetic and self-interacting terms after taking into account radiative corrections. Below the cutoff scale Λ, one therefore obtains the SM Lagrangian describing the interactions of gauge and Higgs bosons and their KK excitations with each other and with chiral fermions living at the orbifold fixed points:

$$\mathcal{L}_{\rm NJL}^{(4+\delta)\text{-dim}} = \mathcal{L}_{\rm kin}^{\rm gauge} + \mathcal{L}_{\rm kin}^{\rm fermion} + \sum_{n_1=0}^{\infty} ... \sum_{n_\delta=0}^{\infty} [Z_{\rm H}\,|D_\mu H^{n_\alpha}|^2 - M_{H^{n_\alpha}}^2\,|H^{n_\alpha}|^2 - \frac{1}{2}\lambda(H^{n_\alpha +} H^{n_\alpha})^2 + \left((\overline{Q}_L t_R)H^{n_\alpha} + \text{h.c.}\right)]. \quad (7)$$

Here, $\mathcal{L}_{\rm kin}^{\rm gauge}$ and $\mathcal{L}_{\rm kin}^{\rm fermion}$ are the gauge and fermionic kinetic terms, respectively, and $D_\mu = \partial_\mu - \sum_{n_1=0}^{\infty} ... \sum_{n_\delta=0}^{\infty} \left(ig_2\tau^a A_{\mu a}^{n_\alpha} + ig_1 B_\mu^{n_\alpha}\right)$. In perfect analogy with [2], one must demand $Z_{\rm H} \to 0$; equivalently, rescaling the Higgs field and its KK excitations $H^{n_\alpha} = h^{n_\alpha}/\sqrt{Z_{\rm H}}$ in order to normalize canonically the kinetic terms in (6) leads, for the top–Yukawa coupling, to

$$g_t = \frac{1}{Z_{\rm H}} \to \infty \quad (8)$$

as energy approaches Λ.

Let us now examine how the BHL predictions for the top-quark mass change in the presence of extra dimensions. First, we note that, since the fermions, and particularly top quark, have no KK excitations in our minimal approach, it is obvious

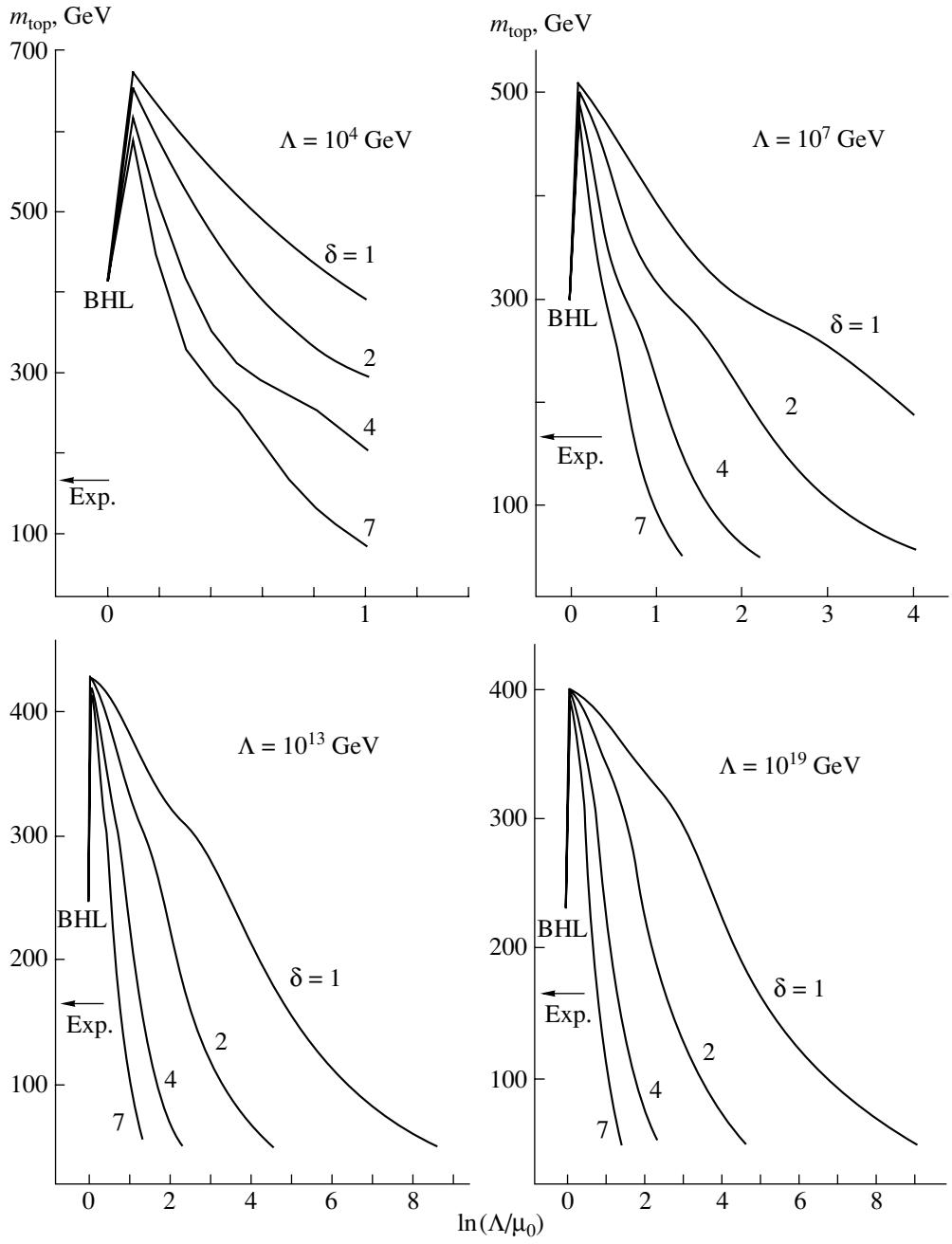

Fig. 1. Top-quark mass as a function of Λ/μ_0 at $\Lambda = 10^4$, 10^7, 10^{13}, and 10^{19} GeV for $\delta = 1$, 2, 4, and 7. The intersection of the curves at $\Lambda = \mu_0$ corresponds to the BHL predictions, while the left-going arrow indicates the central experimental value for the top-quark mass.

that, in the fermion-bubble approximation, the results for the top-quark mass are identical to those in the BHL model [see (2) with $G \equiv G^{n_\delta=0}$]. However, the improvement on the basis of renormalization-group equations is expected to be drastically different because the contributions of KK states to β and γ functions lead to the power-law running of the gauge and Yukawa couplings (for a proper treatment of renormalization-group equations in extra dimensions, see [5]), which is accompanied by the corresponding changes in the fixed-point solutions to renormalization-group equations (see [13] for fixed-point solutions in supersymmetric theories with large extra dimensions).

One-loop diagrams contributing to the anomalous dimensions of the top quark consist of top–Higgs and top–gauge internal states. Since the top quark has no KK excitations in our minimal approach, the

diagrams contribute as the equivalent SM diagrams each time one traverses the Higgs or the gauge KK threshold. This is because the KK number is not conserved in the vortices since translational invariance is broken in extra dimensions. The Higgs–gauge loops contributing to the anomalous dimension of the Higgs field also make the same contribution as equivalent SM diagrams since, now, the KK number must be conserved at vortices. The only contribution of KK modes to gauge-coupling β functions comes from diagrams involving gauge loops and loops of Z_2-odd adjoint scalars. Thus, we conclude that, above the energy $\mu_0 \approx 1/R$, the renormalization-group equations for the top–Yukawa coupling $Y_t \equiv g_t^2/(4\pi)$ and the gauge couplings α_i $(i = 1, 2, 3)$ are

$$\frac{dY_t}{d\ln\mu} = \frac{3}{2\pi}Y_t^2 + \frac{Y_t}{4\pi}\left[\frac{3}{2}Y_t - c_i\alpha_i\right]\frac{d\mathcal{J}}{d\ln\mu}, \qquad (9)$$

$$\frac{d\alpha_i}{d\ln\mu} = \frac{b_i - b_i'}{2\pi}\alpha_i^2 + \frac{b_i'}{2\pi}\alpha_i^2\frac{d\mathcal{J}}{d\ln\mu},$$

where

$$b_i = \left(\frac{41}{10}, -\frac{19}{6}, -7\right),$$
$$b_i' = \left(\frac{1}{10}, -\frac{41}{6}, -\frac{21}{2}\right), \qquad (10)$$
$$c_i = \left(\frac{17}{12}, \frac{9}{4}, 8\right).$$

In (9), $\mathcal{J}$ is an integral of the elliptic Jacobi theta function [5],

$$\mathcal{J}(\mu/\mu_0, \delta) = \int\limits_{r/(\mu/\mu_0)^2}^{r} \frac{dx}{x}\left[\vartheta_3(0, e^{-x})\right]^\delta,$$
$$\vartheta_3(u, q) = \sum_{n=-\infty}^{+\infty} q^{n^2}e^{i2nu}, \qquad (11)$$

where $r = [\Gamma(1 + \delta/2)]^{\delta/2}$ (Γ is the Euler gamma function). Below the compactification scale μ_0, the top–Yukawa and gauge couplings run according to the usual four-dimensional SM renormalization-group equations, which is easily recovered from (9) by setting $\delta = 0$ or, alternatively, $\mu/\mu_0 = 1$ $[d\mathcal{J}(\mu/\mu_0, 0)/d\ln\mu = d\mathcal{J}(1, \delta)/d\ln\mu = 2]$.

The figure shows the top-quark mass $m_{\rm top} = g_t v$, $v \simeq 174$ GeV, as a function of Λ/μ_0. These results were obtained by numerically solving the full set of Eqs. (9) with compositeness condition (8) at $\Lambda = 10^4$, 10^7, 10^{13}, and 10^{19} GeV for $\delta = 1$, 2, 4, and 7. The values $m_{\rm top}(0)$ $(\Lambda = \mu_0)$ in the figure are clearly the BHL predictions $m_{\rm top}(0) = m_{\rm top}^{\rm BHL}$. When the radius of the extra dimensions is close to Λ ($\Lambda/\mu_0 \lesssim 2.5$–$10^4$ for $\delta = 7$–1), $m_{\rm top}$ increases further since the gauge contributions to the evolution of the top–Yukawa coupling Y_t are more significant than in the case of the four-dimensional SM. This is a direct consequence of our minimal approach, where the chiral fermions are assumed to live at the orbifold fixed points; therefore, they do not feel the extra dimensions. For larger Λ/μ_0, however, $m_{\rm top}$ decreases fast, and one can obtain values of the top-quark mass in the experimentally allowed range even for $\Lambda = 10^4$ GeV and $\delta \geq 5$ (demanding $\mu_0 \geq 1$ TeV). This happens because of the power-law $(1/\delta(\Lambda/\mu_0)^\delta)$ running of Y_t [in contrast to the logarithmic running $(\ln(\Lambda/\mu_0))$ in the SM] [5, 13], which leads to extremely small values of Y_t when Λ/μ_0 or δ (or both) increases even for a small cutoff scale Λ of about a few TeV. Thus, the problem of quadratic divergences can be potentially solved within our framework.

To conclude, I have studied the minimal BHL model for dynamical EWSB, assuming the existence of compact extra dimensions with relatively large radii. It has been shown that, owing to the power-law evolution of the gauge and Yukawa couplings, the original BHL predictions for the top-quark mass are significantly lowered, with the result that, even for a small cutoff scale Λ of a few TeV, one can obtain experimentally allowed values of $m_{\rm top}$, provided that the number of extra dimensions with $R \approx 1$ TeV^{-1} is not less than five. For future colliders, this offers the exciting possibility of probing not only the composite nature of the Higgs boson but also the structure of spacetime.

ACKNOWLEDGMENTS

I am grateful to Z. Berezhiani, G. Dvali, J. Chkareuli, I. Gogoladze, and Z. Tavartkiladze for stimulating discussions on various aspects of higher dimensional theories.

This work was supported by the Academy of Finland under the project no. 163394, by INTAS under the grant no. 96-155, by the Georgian Academy of Sciences under the grant no. 2-10, and the Georgian Young Scientists Presidential Award.

REFERENCES

1. G. Cvetič, hep-ph/9702381.
2. W. Bardeen, C. Hill, and M. Lindner, Phys. Rev. D **41**, 1647 (1990).
3. B. Pendleton and G. Ross, Phys. Lett. B **98B**, 291 (1981); C. Hill, Phys. Rev. D **24**, 691 (1981).
4. M. Lindner and E. Schnapka, in *Heavy Flavours II,* Ed. by A. J. Buras and M. Lindner (World Sci., Singapore, 2001); hep-ph/9712489.
5. K. R. Dienes, E. Dudas, and T. Gherghetta, Phys. Lett. B **436**, 55 (1998); Nucl. Phys. B **537**, 47 (1999).

6. D. Ghilencea and G. G. Ross, Phys. Lett. B **442**, 165 (1998); C. Bachas, hep-ph/9807415; P. H. Frampton and A. Rasin, hep-ph/9903479.
7. N. Arkani-Hamed, S. Dimopoulos, G. Dvali, and J. March-Russell, hep-ph/9811448; K. R. Dienes, E. Dudas, and T. Gherghetta, hep-ph/9811428.
8. E. A. Mirabelli and M. Peskin, Phys. Rev. D **58**, 065002 (1998).
9. N. Arkani-Hamed, S. Dimopoulos, and G. Dvali, Phys. Lett. B **429**, 506 (1998); H. Hatanaki, T. Inami, and C. S. Lim, Mod. Phys. Lett. A **13**, 2601 (1998); I. Antoniadis and C. Bachas, hep-th/9812093.
10. K. Benakli and S. Davidson, hep-ph/9810280; K. R. Dienes, E. Dudas, T. Gherghetta, and A. Riotto, hep-ph/9809406; G. Dvali and S.-H. H. Tye, hep-ph/9812483.
11. N. Arkani-Hamed, S. Dimopoulos, and G. Dvali, hep-ph/9807344; K. Benakli, hep-ph/9809582; Z. Berezhiani and G. Dvali, hep-ph/9811378.
12. I. Antoniadis, K. Benakli, and M. Quiros, Phys. Lett. B **331**, 313 (1994); G. F. Giudice, R. Ratazzi, and J. D. Wells, Nucl. Phys. B **544**, 3 (1999); E. A. Mirabelli, M. Perelstein, and M. Peskin, hep-ph/9811337; T. Han, J. D. Lykken, and R.-J. Zhang, hep-ph/9811350; J. L. Hewett, hep-ph/9811356.
13. B. A. Dobrescu, hep-ph/9812349.
14. M. Lanzagorta and G. G. Ross, Phys. Lett. B **349**, 319 (1995); S. A. Abel and S. F. King, hep-ph/9809467.

Physics of Atomic Nuclei, Vol. 64, No. 5, 2001, pp. 946–951. Translated from Yadernaya Fizika, Vol. 64, No. 5, 2001, pp. 1015–1021.

ELEMENTARY PARTICLES AND FIELDS
Theory

Instantons in Non-Cartesian Coordinates

A. A. Abrikosov, Jr.

Institute of Theoretical and Experimental Physics, Bol'shaya Cheremushkinskaya ul. 25, Moscow, 117259 Russia

Received December 22, 1999; in final form, May 11, 2000

Abstract—The multi-instanton solutions of 't Hooft and of Jackiw, Nohl, and Rebbi are generalized to the case of curvilinear coordinates. The resulting formulas are considerably simplified if the transformation of coordinates is supplemented with a gauge transformation. As a result, the gauge field develops a term that has the same form as in Cartesian coordinates and which describes pseudoparticles and a compensating addition of a geometric origin (it is determined by the coordinate frame used). The singularities of the compensating field are irrelevant to physical quantities, but they can affect gauge-dependent quantities.

1. INTRODUCTION

The years that have passed since the discovery of instantons [1] have not given a decisive answer to the question of their role in QCD [2, 3]. As long as the nature of confinement remains a puzzle, speculations on instantons at large distances cannot be complete. Additional information about this region can be deduced by studying instanton effects in phenomenological models like the bag model [4]. Such an analysis makes it possible to assess the degree to which confinement affects pseudoparticles, and vice versa.

Conventional models of hadrons appear to be more natural in curvilinear coordinates. By way of example, $(3+1)$-dimensional cylindrical coordinates—that is, spherical coordinates supplemented with time—seem to suggest themselves for a bag. At the same time, a $(2+2)$-dimensional system of cylindrical coordinates [$(2+1)$-dimensional system of spatial cylindrical coordinates plus time] should be preferred for strings. Nonetheless, instantons are traditionally considered in Cartesian coordinates, which represent an ideal option in a free vacuum. The present study is aimed at attracting the attention of theorists to this problem and at developing a conventient technique. We will express the multi-instanton solutions of 't Hooft and of Jackiw, Nohl, and Rebbi [5] in terms of curvilinear coordinates and simplify the resulting formulas by means of a gauge transformation. The result is universal and is independent of the method of derivation. It can be hoped that the geometric ideas developed here will prove to be useful for other non-Abelian topological solutions as well, including the most general multi-instanton solution obtained in [6].

The ensuing exposition is organized as follows. In Section 2, we recall the foundations of the theory being considered. We discuss curvilinear coordinates in Subsection 2.1 and consider multi-instanton solutions in Subsection 2.2. In Section 3, the general multi-instanton configuration is expressed in terms of curvilinear coordinates. We show how the resulting expressions can be simplified by making a gauge transformation along with the coordinate transformation. The appearance of an additional connection in the group space is the price paid here for beauty. We will refer to this connection as a compensating connection. In Section 4, we will exemplify our general analysis by considering the most symmetric $O(4)$ spherical coordinates. In Section 5, we discuss singularities that arise upon the application of the compensating gauge transformation. The basic results are summarized in Section 6.

2. BASIC INFORMATION

2.1. Curvilinear Coordinates

Let us consider a flat four-dimensional Euclidean spacetime, whose points can be specified by either Cartesian coordinates x^μ or curvilinear coordinates q^α. The system of coordinates q is defined by the metric tensor $g_{\alpha\beta}(q)$,

$$ds^2 = dx_\mu^2 = g_{\alpha\beta}(q)\, dq^\alpha\, dq^\beta. \qquad (1)$$

In curvilinear coordinates, one has to use the covariant derivatives D_α instead of the conventional partial derivatives $\partial/\partial x^\mu$. For example, the derivative of the covariant vector A_β is given by

$$D_\alpha A_\beta = \partial_\alpha A_\beta - \Gamma^\gamma_{\alpha\beta} A_\gamma. \qquad (2)$$

The function $\Gamma^\alpha_{\beta\gamma}$ is referred to as a Christoffel symbol of the second kind or a Levi-Civita connection. It can

easily be calculated if we know the metric tensor and the matrix $g^{\beta\gamma}$ reciprocal to it ($g_{\alpha\beta}\, g^{\beta\gamma} = \delta^\gamma_\alpha$):

$$\Gamma^\alpha_{\beta\gamma} = \frac{1}{2} g^{\alpha\delta} \left(\frac{\partial g_{\delta\beta}}{\partial q^\gamma} + \frac{\partial g_{\delta\gamma}}{\partial q^\beta} - \frac{\partial g_{\beta\gamma}}{\partial q^\delta} \right). \quad (3)$$

Instead of the metric $g_{\alpha\beta}$, it is often convenient to use a vierbein—that is, the set of four vectors e^a_α, $a = 1, \ldots, 4$, such that

$$g_{\alpha\beta}(q) = \delta_{ab}\, e^a_\alpha(q)\, e^b_\beta(q). \quad (4)$$

Tensor quantities can have both conventional coordinate (Greek) and vierbein (Latin) indices. A transition between them is performed via multiplication by e^a_α:

$$A^a = e^a_\alpha\, A^\alpha. \quad (5)$$

The covariant derivatives of tensors carrying Latin indices are calculated with the aid of the spin connection $R^a_{\alpha\, b}(q)$,

$$D_\alpha A^a = \partial_\alpha A^a + R^a_{\alpha\, b}\, A^b. \quad (6)$$

The spin connection $R^a_{\alpha\, b}$ can be expressed in terms of the Levi-Civita connection $\Gamma^\beta_{\alpha\delta}$ as

$$R^a_{\alpha\, b} = e^a_\beta\, \partial_\alpha e^\beta_b + e^a_\beta\, \Gamma^\beta_{\alpha\gamma}\, e^\gamma_b = e^a_\beta\, (D_\alpha e^\beta)_b. \quad (7)$$

It can easily be shown that, if covariant derivatives are defined in this way, the metric $g_{\alpha\beta}$ and the vierbein e^a_α are covariantly constant.

In general, the vierbein is defined within orthogonal transformations $e^\alpha_a \to j^\alpha_a = O^\alpha_\beta e^\beta_a$ preserving the metric, $g_{\alpha\beta} = O^\gamma_\alpha\, g_{\gamma\delta}\, O^\delta_\beta$. Under such transformations, relation (4) is invariant, whence it follows that the sets of vectors e^α_a and j^α_a are equivalent. A specific choice of vierbein is determined by the formulation of the problem.

If the system of curvilinear coordinates is orthogonal and if the off-diagonal elements of the metric are equal to zero, $g_{\alpha\beta}(q) = G_\alpha(q)\, \delta_{\alpha\beta}$, it is convenient to render the vierbein consistent with the coordinate system by choosing it in the form

$$e^\alpha_a = \sqrt{G_\alpha(q)}\, \delta^\alpha_a. \quad (8)$$

This simplifies the relevant calculations significantly because, in the case of this option, only four of 16 elements of the matrix e^α_a are nonzero. We will refer to such a vierbein as a natural vierbein. In terms of Cartesian coordinates, the natural vierbein has the form $c^\mu_a = \delta^\mu_a$.

2.2. Instantons

Let us consider pure $SU(2)$ Yang–Mills gauge theory. Here, we will make use of the matrix notation. The vector potential of the gauge field is $\hat{A}_\mu = \frac{1}{2}\tau^a A^a_\mu$, where τ^a are the Pauli matrices. The covariant derivative in terms of Cartesian coordinates is $D_\mu = \partial_\mu - i\,\hat{A}_\mu$, and the action functional for this theory has the form

$$S = \int \frac{\operatorname{tr} \hat{F}^2_{\mu\nu}}{2g^2}\, d^4x = \int \frac{\operatorname{tr} \hat{F}_{\alpha\beta}\, \hat{F}^{\alpha\beta}}{2g^2}\, \sqrt{g}\, d^4q, \quad (9)$$

where $g = \det ||g_{\alpha\beta}||$. The gauge-field strength $\hat{F}_{\alpha\beta}$ is specified by a universal formula (that is a formula that is independent of the choice of coordinates):

$$\hat{F}_{\alpha\beta}(\hat{A}) = \partial_\alpha \hat{A}_\beta - \partial_\beta \hat{A}_\alpha - i \left[\hat{A}_\alpha,\, \hat{A}_\beta \right]. \quad (10)$$

It is well known that the action functional (9) is invariant under gauge transformations; that is,

$$\hat{A}_\mu \to \hat{A}^\Omega_\mu = \Omega^\dagger\, \hat{A}_\mu(x)\, \Omega + i\, \Omega^\dagger\, \partial_\mu \Omega\,, \quad (11)$$

where Ω is a unitary 2×2 matrix; that is, $\Omega^\dagger = \Omega^{-1}$.

The classical field equations have self-dual ($F_{\mu\nu} = \tilde{F}_{\mu\nu} = \frac{1}{2}\epsilon_{\mu\nu\lambda\sigma}\, F^{\lambda\sigma}$) solutions referred to as instantons. The most universal self-dual configuration found explicitly[1)] is due to Jackiw, Nohl, and Rebbi. It generalizes the multi-instanton solution of 't Hooft ('t Hooft ansatz) [5] and involves four parameters more in relation to the latter. The two solutions can be represented in the general form

$$\hat{A}_\mu(x) = -\frac{\hat{\eta}^-_{\mu\nu}}{2} \partial_\nu \ln \Pi(x), \quad (12)$$

where $\hat{\eta}_{\mu\nu}$ is the matrix version of the 't Hooft η symbol [7],

$$\hat{\eta}^\pm_{\mu\nu} = -\hat{\eta}^\pm_{\nu\mu} = \begin{cases} \tau^a\, \epsilon^{a\mu\nu} \text{ for } & \mu, \nu = 1, 2, 3 \\ \pm\tau^a\, \delta^{\mu a} \text{ for } & \nu = 4. \end{cases} \quad (13)$$

The 't Hooft ('tH) solution differs from the Jackiw–Nohl–Rebbi (JNR) solution in the form of the scalar function $\Pi(x)$. For the topological charge N, the two versions of this function are given by

$$\Pi_{\text{'tH}}(x) = 1 + \sum_{n=1}^{N} \frac{\rho_n^2}{(x - y_n)^2},$$

$$\Pi_{\text{JNR}}(x) = \sum_{n=1}^{N+1} \frac{\rho_n^2}{(x - y_n)^2}. \quad (14)$$

[1)] The general solution from [6] is known only implicitly.

The parameters in $\Pi_{\rm 'tH}$ can readily be interpreted as the radii (ρ_n) and the coordinates (y_n) of pseudoparticles; however, the structure of $\Pi_{\rm JNR}$ is not so transparent.

The popular regular and singular gauges for an instanton of radius ρ occurring at the point y can also be represented in the form (12), provided that the function $\Pi(x)$ is chosen appropriately (in the case of the regular gauge, however, it is necessary to make the substitution $\hat\eta^-_{\mu\nu} \to \hat\eta^+_{\mu\nu}$):

$$\Pi_{\rm reg}(x) = \frac{\rho^2}{(x-y)^2+\rho^2}, \qquad (15)$$

$$\Pi_{\rm sing}(x) = 1 + \frac{\rho^2}{(x-y)^2}.$$

In the following, we will generalize the solution in (12) to the case of curvilinear coordinates. We will nowhere rely on the explicit expressions for $\Pi(x)$, and the results to be obtained will be valid in all cases considered here.

3. INSTANTONS IN CURVILINEAR COORDINATES

3.1. Problem and Its Solution

Problem. It is straightforward to express the covariant vector $\hat A_\mu$ (12) in terms of curvilinear coordinates q. After that, however, the constant tensor $\hat\eta_{\mu\nu}$ appears to be a nontrivial function of coordinates:

$$\hat\eta_{\mu\nu} \to \hat\eta_{\alpha\beta}(q) = \hat\eta_{\mu\nu}\frac{\partial x^\mu}{\partial q^\alpha}\frac{\partial x^\nu}{\partial q^\beta} = \hat\xi_{ab}\, c^a_\alpha\, c^b_\beta. \qquad (16)$$

Here, $c^a_\alpha = \delta^a_\mu \frac{\partial x^\mu}{\partial q^\alpha}$ are the components of the natural Cartesian vierbein in terms of the new coordinates and $\hat\xi_{ab}$ is a constant matrix tensor and is given by

$$\hat\xi_{ab} = \delta^\mu_a\, \delta^\nu_b\, \hat\eta_{\mu\nu}. \qquad (17)$$

In Cartesian coordinates, $\hat\xi_{ab}$ coincides with $\hat\eta_{\mu\nu}$, taking its place in curvilinear coordinates.

From the point of view of the coordinates q, c^a_α is an important particular case of vierbein for zero spin connection $R^a_{\alpha\, b}$. It is desirable to know whether it is possible to generalize Eq. (16) and to replace c^a_α in it by an arbitrary vierbein e^a_α without complicating $\hat\xi_{ab}$.

Solution. A positive answer to this question is associated with the special features of the η symbols, which project coordinate space onto the gauge group (more precisely, they project self-dual rank-2 antisymmetric tensors into the group algebra). It is well known that the substitution $c^a_\alpha \to e^a_\alpha$ for the vierbein reduces to the rotation $c^a_\alpha = O^a_b(q)\, e^\beta_a$, under which the ξ symbols change and become dependent on the coordinates: $\hat\xi_{ab} \to \hat\xi'_{ab}(q) = O^c_a(q)\, O^d_b(q)\, \hat\xi_{cd}$. However, four-dimensional rotations can be compensated by relevant gauge transformations owing to the properties of the projection of the $O(4)$ space group onto the $SU(2)$ gauge group.

In the coordinates q, we choose a vierbein $e^a_\alpha(q)$. We assume that there exists a unitary matrix $\Omega(q)$ such that

$$\Omega^\dagger(q)\, \hat\eta_{\alpha\beta}(q)\, \Omega(q) = e^a_\alpha(q)\, e^b_\beta(q)\, \hat\xi_{ab}. \qquad (18)$$

It can be seen that the gauge transformation associated with the matrix Ω factorizes the coordinate dependence of the tensor $\hat\eta$ and transfers it to $e^a_\alpha(q)$. As a matter of fact, the role of Ω is to render the color orientation of gauge fields consistent with the new vierbein.

It is obvious that relation (18) forms a set of equations for the elements of the matrix Ω. By virtue of the above considerations, the only condition for the sought solution to exist is the requirement that the orientation of the new vierbein $e^a_\alpha(q)$ be coincident with the orientation of the original system of coordinates x. Otherwise, the right- and the left-hand side of Eq. (18) have different duality properties. For an arbitrary vierbein, this condition has the form $\det||c^\alpha_a|| \times \det||e^a_\alpha(q)|| > 0$.

Upon a gauge rotation, the instanton field involves two terms,

$$\hat A^\Omega_\alpha(q) = -\frac{1}{2} e^a_\alpha\, \hat\xi_{ab}\, e^{b\,\beta}\, \partial_\beta \ln\Pi(q) + i\,\Omega^\dagger\, \partial_\alpha\Omega. \quad (19)$$

The first term has a nearly standard form and is independent of the matrix Ω, whereas the second carries information about the system of coordinates q. It has a geometric origin. We will refer to it as a compensating gauge connection, since it compensates for the coordinate dependence of the tensor $\hat\eta_{ab} = e^\alpha_a\, e^\beta_b\, \hat\eta_{\alpha\beta}$, transforming it from a covariantly constant tensor into a merely constant tensor $\hat\xi_{ab}$.

So far, we have not actually required the duality of the $\hat\eta$ symbol. However, the matrices Ω and the compensating connections for $\hat\eta^+$ and $\hat\eta^-$ are different. In general, the quantities $\hat A^{\rm comp\,\pm}_\alpha$ represent the self-dual and the anti-self-dual projection of the spin connection onto the gauge group:

$$\hat A^{\rm comp\,\pm}_\alpha = i\,\Omega^\dagger_\pm\, \partial_\alpha\Omega_\pm = -\frac{1}{4}\, R^{ab}_\alpha\, \hat\xi^\pm_{ab}. \qquad (20)$$

It is noteworthy that the last formula does not involve the gauge-transformation matrix Ω. In order to write explicitly multi-instanton solutions in non-Cartesian coordinates, it is sufficient to know the vierbein and the spin connection. This simplifies the calculations considerably, since Eq. (18) is very involved. By explicitly calculating the instanton field [Eqs. (19) and (20)], we have also proven de facto the

existence of such a solution and the meaningfulness of this approach.

It should be emphasized that the proposed procedure can be applied to any vierbein. From the practical point of view, however, it is convenient to use a four-component natural vierbein in orthogonal coordinates.

3.2. Triviality of the Compensating Field

That the vector potential $\hat{A}^{\mathrm{comp}}$ is trivial—that is, it is the pure gauge (20)—is quite natural. It would have been strange if a mere coordinate transformation, $x^\mu \to q^\alpha$, had had physical implications. It is interesting, however, that triviality of the compensating field proves to be peculiar to a flat space. The point is that the strength $\hat{F}_{\alpha\beta}(\hat{A}^{\mathrm{comp}})$ of the gauge field corresponding to the vector potential (20) is related to the Riemann curvature $R^{\gamma\delta}_{\alpha\beta}$ of space by the equation

$$\hat{F}_{\alpha\beta}(\hat{A}^{\mathrm{comp}\,\pm}) = -\frac{1}{4}R^{\gamma\delta}_{\alpha\beta}\hat{\xi}^{\pm}_{\gamma\delta}. \qquad (21)$$

Thus, we see that, if $R^{\gamma\delta}_{\alpha\beta} = 0$, $\hat{F}_{\alpha\beta}(\hat{A}^{\mathrm{comp}}) = 0$ as well; hence, $\hat{A}^{\mathrm{comp}}$ is a pure gauge. In a curved space, however, the gauge connection specified by Eq. (20) is no longer trivial, so that it can have physical implications, including gravitational instantons.

3.3. Duality and Topological Charge

It is well known that instanton and multi-instanton solutions satisfy classical field equations. Since the vector potential (19) was obtained from solution (12) by means of a gauge transformation, it is also a classical solution. As to duality equations, they have a somewhat different form in curvilinear coordinates. If we make use of quantities carrying coordinate indices, then

$$\hat{F}_{\alpha\beta} = \frac{\sqrt{g}}{2}\,\epsilon_{\alpha\beta\gamma\delta}\,\hat{F}^{\gamma\delta} = \frac{1}{2}\,E_{\alpha\beta\gamma\delta}\,\hat{F}^{\gamma\delta}. \qquad (22a)$$

In the duality equations, the antisymmetric ϵ symbol must therefore be replaced by its non-Cartesian generalization $E_{\alpha\beta\gamma\delta} = \sqrt{g}\,\epsilon_{\alpha\beta\gamma\delta}$. Upon a transition from Greek (coordinate) to Latin (vierbein) indices, however, the equation takes the original form

$$\hat{F}_{ab} = \frac{1}{2}\,\epsilon_{abcd}\,\hat{F}^{cd}. \qquad (22b)$$

The topological charge of the solution is given by the integral

$$q = \frac{1}{32\pi^2}\int \epsilon_{\alpha\beta\gamma\delta}\,\mathrm{tr}\,\hat{F}^{\alpha\beta}\,\hat{F}^{\gamma\delta}\,d^4q, \qquad (23a)$$

which can also be written in the vierbein notation

$$q = \frac{1}{32\pi^2}\int \epsilon_{abcd}\,\mathrm{tr}\,\hat{F}^{ab}\,\hat{F}^{cd}\,\sqrt{g}\,d^4q. \qquad (23b)$$

The general expression for the instanton-field strength $\hat{F}_{\alpha\beta}$ in arbitrary coordinates is rather cumbersome. Fortunately, it is simplified for one instanton. In Cartesian coordinates, the instanton vector potential in the regular gauge is ($r^2 = x_\mu^2$)

$$\hat{A}^I_\mu = \frac{\hat{\eta}^+_{\mu\nu}}{2}\partial_\nu \ln\left(r^2+\rho^2\right). \qquad (24)$$

The combined coordinate and Ω_+ gauge transformations reduce it to

$$\hat{A}^I_\alpha = \frac{1}{2}e^a_\alpha\,\hat{\xi}^+_{ab}\,e^{b\,\beta}\,\partial_\beta \ln(r^2+\rho^2) + \hat{A}^{\mathrm{comp}\,+}. \qquad (25)$$

With the aid of the definition in (10), we obtain

$$\hat{F}_{ab}(\hat{A}^I) = -\frac{2\,\hat{\xi}^+_{ab}}{(r^2+\rho^2)^2}; \qquad (26)$$

that is, the field obviously proves to be self-dual.

The same expression can be obtained by performing a change of coordinates and an Ω_+ rotation of the instanton-field strength calculated in Cartesian coordinates, $\hat{F}_{\mu\nu} = -2\hat{\eta}_{\mu\nu}/(x^2+\rho^2)^2$, and by making use of relation (18). Equations (25) and (26) generalize the regular gauge to the case of arbitrary curvilinear coordinates.

3.4. Homogeneous Gauge Transformations

It is well known that the multi-instanton solutions (12) admit homogeneous gauge transformations,

$$\hat{\eta} \to U^\dagger\,\hat{\eta}\,U, \qquad (27)$$

where U is a unitary matrix, $U^\dagger = U^{-1}$. They are equivalent to a left multiplication of Ω by U, $\Omega \to U\,\Omega$ ($\Omega^\dagger \to \Omega^\dagger\,U^\dagger$); from the point of view of the q system, they reduce to rotations of the Cartesian coordinate system x.

From Eq. (20), it can easily be seen that these transformations do not affect the form of $\hat{A}^{\mathrm{comp}}$. This means that the compensating connection is universal and is independent of the embedding of the original (Cartesian) instanton in the gauge group. The solution specified by Eqs. (19) and (20) is unambiguously determined by the tensor $\hat{\xi}_{ab}$. Arbitrariness in choosing $\hat{\xi}_{ab}$ reduces to the homogeneous gauge transformations

$$\hat{\xi} \to V^\dagger\,\hat{\xi}\,V \qquad (28)$$

with a unitary matrix V, $V^\dagger = V^{-1}$. These transformations are equivalent to a right multiplication of

Ω by V, $\Omega \to \Omega V$ ($\Omega^\dagger \to V^\dagger \Omega^\dagger$), and rotate solution (19) as a discrete unit.

We can see that the result is independent of either the specific form of $\hat{\eta}$ or the intermediate matrix Ω; that is, it could be obtained by directly solving the field equations in curvilinear coordinates.

4. EXAMPLE

By way of example, we consider an instanton situated at the center of the $O(4)$ spherical-coordinate system. In these coordinates, a point is specified by three angles and the modulus of the radius vector: $q^\alpha = (\chi, \phi, \theta, r)$. The polar axis is aligned with the x^1 axis of the original system of Cartesian coordinates:

$$x^1 = r\cos\chi, \tag{29a}$$

$$x^2 = r\sin\chi\sin\theta\cos\phi, \tag{29b}$$

$$x^3 = r\sin\chi\sin\theta\sin\phi, \tag{29c}$$

$$x^4 = r\sin\chi\cos\theta. \tag{29d}$$

For this choice, the system of spherical coordinates is oriented in the same way as the original system of Cartesian coordinates.

The metric tensor and the natural vierbein are diagonal matrices:

$$g_{\alpha\beta} = \mathrm{diag}\,(r^2,\, r^2\sin^2\chi\sin^2\theta,\, r^2\sin^2\chi,\, 1), \tag{30a}$$

$$e^a_\alpha = \mathrm{diag}\,(r,\, r\sin\chi\sin\theta,\, r\sin\chi,\, 1). \tag{30b}$$

We must now consistently implement the above procedure, starting from the instanton vector potential in the regular gauge [Eq. (24)]. In addition to the instanton component proper, it is necessary to calculate the compensating connection. In order to do this, we must first find the Christoffel symbol $\Gamma^\alpha_{\beta\gamma}$, then determine the spin connection R^{ab}_α, and finally compute $\hat{A}^{\mathrm{comp}+}$. By definition, the $\hat{\xi}^+_{ab}$ symbol coincides with $\hat{\eta}^+_{ab}$ as given by Eqs. (13) and (17). Omitting intermediate transformations, we immediately present the eventual result:

$$\hat{A}^I_\chi = \frac{\tau_x}{2}\left(\frac{r^2-\rho^2}{r^2+\rho^2}\right), \tag{31a}$$

$$\hat{A}^I_\phi = -\frac{\tau_x}{2}\cos\theta + \frac{\tau_y}{2}\sin\chi\sin\theta\left(\frac{r^2-\rho^2}{r^2+\rho^2}\right) + \frac{\tau_z}{2}\cos\chi\sin\theta, \tag{31b}$$

$$\hat{A}^I_\theta = -\frac{\tau_y}{2}\cos\chi + \frac{\tau_z}{2}\sin\chi\left(\frac{r^2-\rho^2}{r^2+\rho^2}\right), \tag{31c}$$

$$\hat{A}^I_r = 0. \tag{31d}$$

The corresponding strength of the Yang–Mills field is given by Eq. (26).

The same procedure can be applied to a singular gauge. Recall that we perform a change of coordinates and a gauge transformation, these transformations for the regular and the singular gauge being different. By way of example, we indicate that the instanton field in a regular gauge involves the tensor $\hat{\eta}^+_{\alpha\beta}$ and that it is transformed with the aid of the matrix Ω_+; at the same time, the singular gauge dependent on $\hat{\eta}^-_{\alpha\beta}$ must be rotated by means of the matrix Ω_-. Naturally, the resulting compensating connections are also different.

It turns out that, if an instanton occurs at the origin of coordinates, the two different procedures applied to different original vector potentials lead to the same result given by (31). Moreover, the matrices Ω_+ and Ω_- are related by the equation

$$\Omega_+|_{O(4)} = \Omega^\dagger_-|_{O(4)} = \Omega^{-1}_-|_{O(4)}$$

or

$$\Omega_-|_{O(4)} = \Omega^\dagger_+|_{O(4)} = \Omega^{-1}_+|_{O(4)}. \tag{32}$$

This means that the matrix Ω^2_+ transforms the regular gauge into the singular gauge, while the matrix Ω^2_- implements the inverse transformation. The solution given by (31) is in between.

It would be of interest to clarify the reason behind this coincidence. It can be shown that, for an arbitrary choice of vierbein, the regular and the singular gauge are different, $O(4)$ spherical coordinates representing an exception. It is important in this connection that the quantities $\hat{\eta}^\pm_{\mu\nu}$ are given by expressions (13) and that the fourth coordinate coincides with the radius. A violation of these conditions would lead to distinctions in the results; however, this leaves the possibility of reparametrizing the sphere S^3, $(\mathbf{q}, q^4) \to (\mathbf{q}', q^4)$, and of changing the vierbein without affecting $e^4_\alpha = \delta^4_\alpha$.

5. SINGULARITIES

The above vector potential (31) is singular, since neither $\hat{A}^I_\theta$ nor $\hat{A}^I_\phi$ vanishes at $\chi = 0, \pi$ and $\theta = 0, \pi$—that is, near the x_1x_4 Cartesian coordinate plane. These singularities arise upon applying a gauge transformation, so that they must not change observables. However, they can affect gauge-variant quantities. We will explain this point by considering the example of the Chern–Simons number.

It is well known that the topological charge (23) can be represented as the surface integral $q = \oint K^\alpha\, dS_\alpha$ [2, 3], where

$$K^\alpha = \frac{\epsilon^{\alpha\beta\gamma\delta}}{16\pi^2}\,\mathrm{tr}\left(\hat{A}_\beta\hat{F}_{\gamma\delta} + \frac{2i}{3}\hat{A}_\beta\hat{A}_\gamma\hat{A}_\delta\right). \tag{33}$$

Although the charge q is gauge-invariant, K^α depends on the choice of gauge. This circumstance is often used when an instanton is interpreted as a tunnel transition. Let us consider an instanton in the gauge $\hat{A}_4 = 0$. In this case, the total topological charge is decomposed into the sum of integrals over the hyperplanes $x_4 = \pm\infty$; that is, $q = N_{\rm CS}(\infty) - N_{\rm CS}(-\infty)$. The quantity

$$N_{\rm CS}(t) = \int_{x_4=t} K^4\, dS_4 \qquad (34)$$

is referred to as a Chern–Simons number. An instanton represents a $\Delta N_{\rm CS} = 1$ transition between three-dimensional vacua (that is, between the hyperplanes $x_4 = \pm\infty$).

At first glance, formulas (31) strongly resemble the situation described above. First of all, we again have $\hat{A}_4 = 0$ as in (31d). It is tempting to consider the radius as time and assign a sphere of radius r the Chern–Simons number $N_{\rm CS}(r)$. By analogy, the topological charge would seem to be determined as the difference $\Delta N_{\rm CS} = N_{\rm CS}(r)|_0^\infty$. However, the calculations do not confirm this; in fact, we obtain $\Delta N_{\rm CS} = 1/2$. The second half of the topological charge q comes from the singularities at $\theta = 0, \pi$. It should be recalled that the topological charge is concentrated at the origin, $q = N_{\rm CS}^{\rm sing}(0) = 1$, in the singular gauge and at infinity, $q = N_{\rm CS}^{\rm reg}(\infty) = 1$, in the regular gauge. Thus, the Ω gauge transformation changes the distribution of $N_{\rm CS}$.

It can be seen that, in our approach, gauge-variant quantities depend on the coordinate system. In particular, they can be concentrated at the singularities of the Ω transformation. It is the opinion of the present author that this may conceal additional possibilities for simplifying relevant calculations by appropriately choosing curvilinear coordinates.

6. CONCLUSION

It has been demonstrated how one can generalize explicit (multi)instanton solutions to the case of curvilinear coordinates and make them consistent with the vierbein in that representation. A gauge transformation reduces the coordinate-dependent, albeit covariantly constant, $\hat{\eta}_{ab}$ symbol to the constant $\hat{\xi}_{ab}$. The vector potential appears to be the sum of the instanton component and the compensating gauge connection (19).

The compensating gauge connection can be calculated in three steps:

(i) First, it is necessary to calculate the Christoffel symbol $\Gamma^\alpha_{\beta\gamma}$ (3).

(ii) By taking the covariant derivative of the vierbein (7), one can then find the spin connection R^{ab}_α.

(iii) The compensating vector potential (20) can be obtained by contracting the spin connection with the corresponding $\hat{\xi}_{ab}$ symbol.

The proposed solution is advantageous in that it is quite clear and in that it is constructed directly from geometric objects (vierbein, spin connection, projection operator $\hat{\xi}_{ab}$). The matrix Ω, which is not always readily calculable, is not involved explicitly—it serves for explanatory purposes exclusively. If the system of curvilinear coordinates is orthogonal, a gauge consistent with it can be obtained by using a natural vierbein. It would be of great interest to find out new possibilities associated with this. For a detailed exposition of the matters discussed here and for further examples, the interested reader is referred to [8].

ACKNOWLEDGMENTS

I am grateful to A.A. Roslyĭ for discussions and to S. Narison for the possibility of reporting the results of this study at the QCD-99 Conference. I am also indebted to R. Jackiw for telling me the history of the discovery of multi-instanton solutions.

This work was supported by the Russian Foundation for Basic Research (project nos. 97-02-16131 and 00-02-17808).

REFERENCES

1. A. A. Belavin, A. M. Polyakov, A. S. Schwartz, and Yu. S. Tyupkin, Phys. Lett. B **59B**, 85 (1975).
2. *Instantons in Gauge Theories,* Ed. by M. A. Shifman (World Sci., Singapore, 1994).
3. T. Schäfer and E. V. Shuryak, Rev. Mod. Phys. **70**, 323 (1998).
4. A. Chodos, R. L. Jaffe, C. B. Thorn, and V. F. Weisskopf, Phys. Rev. D **9**, 3471 (1974).
5. R. Jackiw, C. Nohl, and C. Rebbi, Phys. Rev. D **15**, 1642 (1977).
6. M. F. Atiah, N. J. Hitchin, V. G. Drinfeld, and Yu. I. Manin, Phys. Lett. B **65B**, 185 (1978).
7. G.'t Hooft, Phys. Rev. D **14**, 3432 (1976).
8. A. A. Abrikosov, Jr., hep-th/9906008.

Translated by A. Isaakyan

Physics of Atomic Nuclei, Vol. 64, No. 5, 2001, pp. 952–955. Translated from Yadernaya Fizika, Vol. 64, No. 5, 2001, pp. 1022–1025.

XXX International Conference on the Physics of Interaction of Fast Charged Particles with Matter

Parametric X-ray Radiation from 500-MeV Electrons in a Tungsten Single Crystal with a Surface Mosaicity Less Than 1.5′

Yu. N. Adischev*, I. E. Vnukov, V. N. Zabaev, B. N. Kalinin, A. A. Kiryakov, Yu. P. Kunashenko, Yu. L. Pivovarov, A. P. Potylitsyn, and S. R. Uglov

Institute for Nuclear Physics, Tomsk Polytechnic University, pr. Lenina 30, Tomsk, 634034 Russia

Received November 4, 2000

Abstract—The yield of parametric x-ray radiation from a tungsten single crystal irradiated with a $E = 500$ MeV electron beam from the Tomsk Sirius synchrotron was studied experimentally in Bragg geometry. The tungsten sample was 1.7 mm thick and had a surface mosaicity less than 1.5′; it was oriented in such a way that the (111) face was at the Bragg angle of $\theta_B = 45°$ with respect to the electron-beam direction. The x-ray photons were detected at the angle of $2\theta_B = 90°$ with respect to the electron beam. The angular distributions of parametric x rays are compared with those calculated with allowance for actual experimental conditions. © *2001 MAIK "Nauka/Interperiodica".*

Crystals having a perfect crystallographic lattice—for example, silicon—are being successfully used now as deflectors (on the basis of channeling in bent crystals) for extracting charged particles (including heavy ions) from accelerators.

The efficiency of extraction for crystals with a large atomic number like tungsten significantly exceeds that which is attained for crystals with a small atomic number. However, modern technologies for growing thick tungsten crystals necessary for producing deflectors do not guarantee the perfectness and homogeneity of the crystal structure along particle trajectories.

The objective of this study is to investigate, by using a 500-MeV electron beam from the Tomsk synchrotron, the structure of a tungsten single crystal on the basis of spectral angular characteristics of parametric x rays and radiation accompanying channeling and to develop methods for orienting crystals in heavy-ion beams.

Tungsten single crystals are planned to be used for extracting light and heavy nuclei from the JINR nuclotron (Dubna) [1]. The crystal under study represents a block of dimensions $1.7 \times 10 \times 15$ mm grown by the method of zone melting with subsequent grinding and etching. A large face of the crystal deviated from the (111) plane by not more than 30′. The crystal was preliminarily investigated with an x-ray diffractometer. "Rocking curves" measured for various surface points showed that the surface mosaicity was less than 80″.

*e-mail: adischev@interact.phtd.tpu.edu.ru

The experimental procedure was similar to that described in [2]. Electrons accelerated in the vacuum chamber of the synchrotron were directed onto an internal tungsten target for 15 ms, the pulse-repetition frequency being 5 Hz. The spectral and angular distributions of parametric x rays were measured by an x-ray spectrometer based on a silicon PIN diode that had the input window of diameter 5 mm and which was arranged in Bragg geometry at the angle of $2\theta_B = 90°$ with respect to the electron-beam axis at a distance of 97 cm from the target. For the 13.95- and 17.8-keV lines of the ^{241}Am L series, the energy resolution of the spectrometer was 1.5 keV, and the detection efficiency was approximately 60%.

The energy equivalent of the lower threshold of the spectrometer amounted to 5 keV, and the maximum energy of photon detection was 50 keV. The number of accelerated electrons was monitored by an inductive current sensor with an error of 5% and by a synchrotron-radiation sensor with an error of 20%. The number of electrons that had traversed the target was determined by measuring the total energy of bremsstrahlung by a Wilson quantameter with an error of 10%.

Throughout the measurements, the current of accelerated electrons was maintained at a level such that the counting rate in the spectrometer was less than 2×10^2 photons per spill. Even at this counting rate, the energy resolution of the PIN spectrometer was markedly impaired.

The tungsten single crystal was oriented with respect to the electron beam by using a goniometer with angular steps of $\Delta\theta_{\text{vert}} = 2 \times 10^{-5}$ rad and

1063-7788/01/6405-0952$21.00

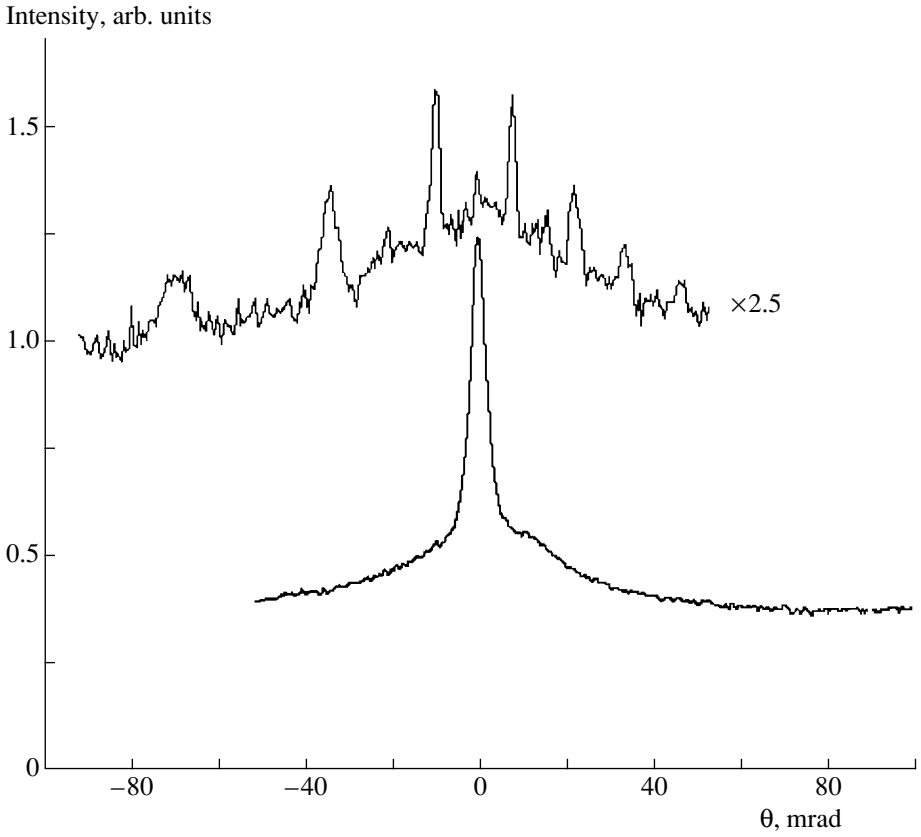

Fig. 1. Orientation dependences of the γ-radiation yield during the channeling of 500-MeV electrons in a tungsten single crystal.

$\Delta\theta_{\text{horizon}} = 7 \times 10^{-6}$ rad for the rotation about the vertical and the horizontal axis, respectively.

In order to achieve a precise orientation of the crystal, we used the effect of γ radiation from electrons during channeling. The radiation was recorded by a NaI detector that was arranged at an angle of 7° with respect to the beam and which detected Compton photons from the target. As the crystal was rotated about the vertical axis, we measured the orientation dependence of the yield of photons with an energy exceeding the threshold of 511 keV.

Figure 1 shows the orientation dependences of the yield of γ radiation from the rotating crystal for $\alpha =$ (upper curve) 16 mrad and (lower curve) 0, where α is the angle between the electron momentum and the $\langle 111 \rangle$ axis; in the latter case, the electron momentum is parallel to the axis. By using these dependences, the crystal was oriented in such a way that the $\langle 111 \rangle$ axis was aligned with the electron beam to within 0.1 mrad. Thereafter, the crystal was rotated through an angle of 45° with respect to the electron beam in order to implement Bragg geometry.

Figure 2 displays the spectrum of parametric x rays that was obtained in Bragg geometry from the (222) and (444) planes of the tungsten single crystal. In this spectrum, we can see a characteristic peak that occurs at the photon energy of $\omega = 9.6$ keV and which corresponds to the (222) second-order diffraction according to the Bragg formula

$$\omega = \frac{\pi\hbar cn}{dsin\theta_B}, \quad n = 1, 2, 3, ..., \qquad (1)$$

where d is the interplane spacing.

The second peak at $\omega = 19.2$ keV, which corresponds to the next order of (444) diffraction, is less pronounced, which is due to the dynamical deterioration of the PIN spectrometer resolution in this energy region.

The FWHM of the first peak is 3 keV, which is associated with the superposition of closely lying principal spectral lines of the L series in the characteristic x-ray radiation from tungsten (8.4, 8.33, 9.67, 9.96 and 11.29 keV).

The yield of photons of characteristic x rays was measured for a tungsten-crystal disorientation up to $\theta = 40°$ with respect to the electron-beam axis, the Bragg condition (1) being violated in this case. A contribution from these photons to the first spectral peak amounts to 30%.

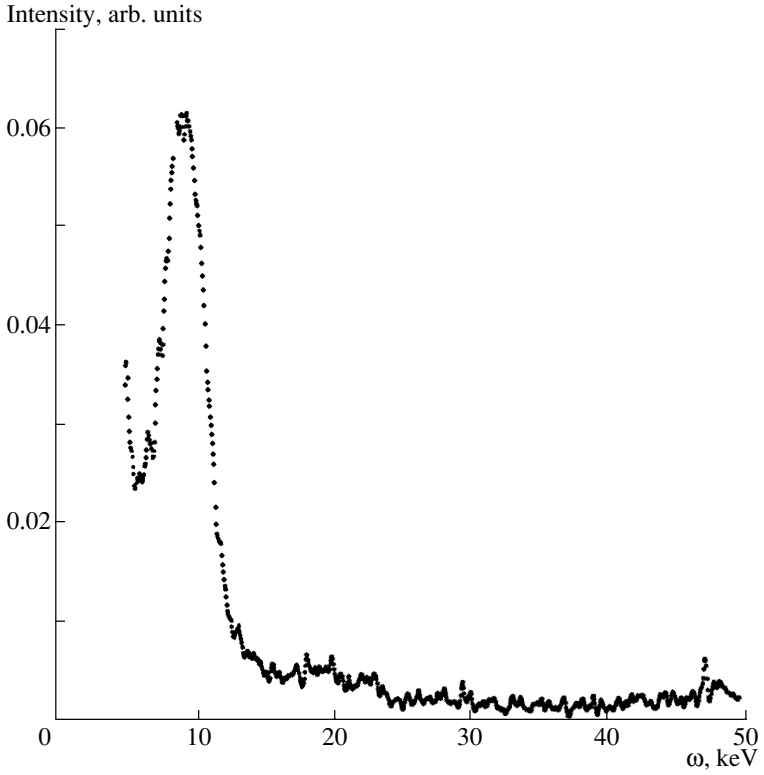

Fig. 2. Spectrum of parametric x rays generated by 500-meV electrons traversing a tungsten single crystal.

The angular distribution of photons of parametric x-ray radiation was measured in the horizontal plane by rotating the crystal about the vertical axis θ, the PIN spectrometer being immobile.

For the (222) reflex at $\omega = 9.6$ keV, the orientation dependence of the yield of photons belonging to parametric x-ray radiation is plotted in Fig. 3 according to measurements at a fixed position of the spectrometer at an angle of $2\theta_B = 90°$, which corresponds to $\theta = 0$ in the figure. The FWHM of the orientation dependence amounts to 4 mrad.

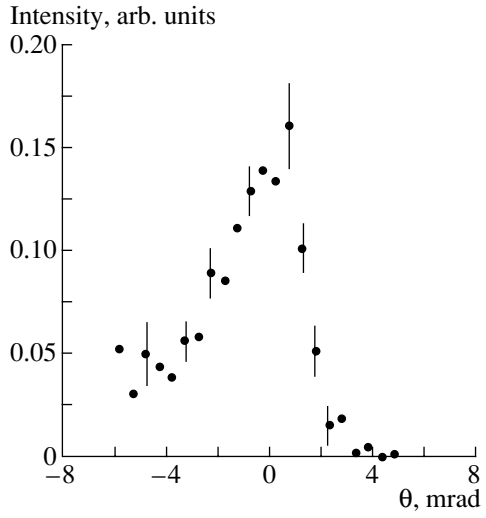

Fig. 3. Orientation dependence of the yield of photons of parametric x-ray radiation generated by 500-MeV electrons traversing a tungsten single crystal.

Figure 4 displays the orientation dependences of parametric x-ray radiation that were obtained from a Monte Carlo simulation performed with allowance for the initial angular divergence of the beam of electrons scattered in the crystal, electron energy losses, the mosaic structure of the crystal, the absorption of the photons of this radiation in the crystal, and the spectrometer aperture. The simulation was based on kinematical theory [3]. The FWHM of the theoretical orientation dependence is $\Delta\theta \simeq 5$ mrad, which is in excess of the width of the experimental dependence.

In the photon-energy range $\omega = 9.6$–19.2 keV, the contribution from bremsstrahlung diffraction is negligible; for this reason, the narrowing of the curve must be explained in terms of a different mechanism.

In the majority of previous experiments performed with light-atom crystals (diamond, silicon), good agreement with the kinematical theory of parametric x-ray radiation was observed [2]. The discrepancy found here is possibly associated with the contribution from the diffraction of real photons of transition x rays to the total photon yield [4]. A simulation of

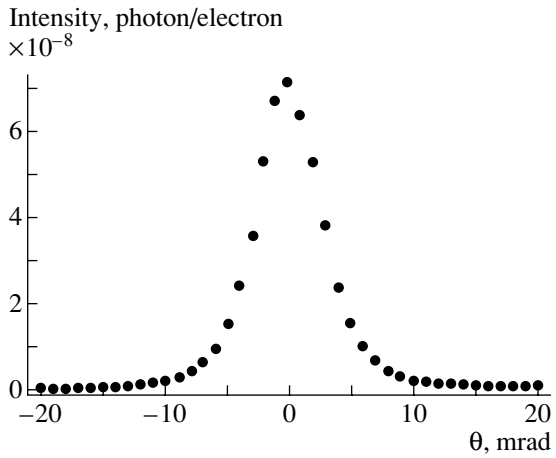

Fig. 4. Result of a Monte Carlo simulation of the orientation dependence of the yield of parametric x rays.

the contribution from diffracted transition x rays for a silicon single crystal was performed in [5], where the angular cone of diffracted transition x rays was shown to be significantly narrower than that of parametric x rays.

The effects of parametric x rays and diffracted transition x rays have not yet been investigated experimentally for heavy-atom crystals, where the plasmon energy ω_p is much higher than that in diamond and silicon.

It seems necessary to develop, on the basis of the dynamical theory of parametric x rays, methods for simulating the properties of radiation in heavy-atom crystals.

The results obtained here confirm that the effect of parametric x rays generated in a tungsten single crystal can be used in extracting heavy particles from an accelerator for orienting a crystal and controlling its bend.

ACKNOWLEDGMENTS

We are grateful to V.V. Boiko for placing a tungsten crystal at our disposal.

REFERENCES

1. A. S. Artem'ev, V. V. Boiko, A. D. Kovalenko, and A. M. Taratin, Soobshch. Ob'edin. Inst. Yad. Issled., Dubna, No. R1-99-12v (1999).
2. Yu. N. Adishchev, R. D. Babadzhanov, S. A. Vorob'ev, *et al.,* Zh. Éksp. Teor. Fiz. **93**, 1942 (1987) [Sov. Phys. JETP **66**, 1107 (1987)].
3. N. Nitta, Phys. Rev. B **45**, 7621 (1992).
4. M. Yu. Andreyashkin, V. N. Zabaev, V. V. Kaplin, *et al.,* Pis'ma Zh. Éksp. Teor. Fiz. **65**, 594 (1997) [JETP Lett. **65**, 625 (1997)].
5. K. H. Brenzinger, C. Herberg, B. Limburg, *et al.,* Z. Phys. A (in press).

Translated by V. Bukhanov

Physics of Atomic Nuclei, Vol. 64, No. 5, 2001, pp. 956–960. Translated from Yadernaya Fizika, Vol. 64, No. 5, 2001, pp. 1026–1030.

XXX International Conference on the Physics of Interaction of Fast Charged Particles with Matter

Orientation Effects Accompanying the Propagation of Ultrarelativistic Electrons through Crystals

S. V. Blazhevich*, G. L. Bochek[1)], W. I. Kulibaba[1)], N. I. Maslov[1)], and B. I. Shramenko[1)]

Belgorod State University, Studencheskaya ul. 12, Belgorod, 308007 Russia

Received November 4, 2000

Abstract—The results obtained by experimentally investigating the dynamics of the propagation of 1.2-GeV electrons through a thin silicon single crystal are discussed. The orientation dependences of electron scattering into a small solid angle, which are measured at various scattering angles, under conditions where the effects of crystallographic axes and planes manifest themselves are interpreted. It is shown that there are such electron-scattering directions for which the orientation "independence" of the scattering intensity with respect to a specific crystallographic plane is observed and that there also exists a crystal-axis orientation for which the region of a uniform angular distribution of the intensity is observed.

1. INTRODUCTION

Experimental investigation of the dynamics of the propagation of electrons with an energy of about 1 GeV is of interest in connection with the possibility of using the instructive classical approach for its description. At the same time, relativistic effects in the propagation and scattering of fast particles and in radiation from them are pronounced at such energies.

In this study, we present the results obtained from an experimental investigation of orientation effects in the scattering of ultrarelativistic electrons in a silicon single crystal. The experiments were performed at the 2000-MeV linear electron accelerator of the Kharkov Institute for Physics and Technology.

A typical experimental procedure was used in electron-scattering experiments. A crystalline target was placed in a chamber equipped with a goniometer that made it possible to orient the target with respect to the axis of incident electron beam to within 5×10^{-5} rad. The particles that had traversed the target were detected by a small germanium detector (0.5×0.5 mm) positioned at a distance of 15 m from the target; this corresponded to measuring the flux of particles scattered into a solid angle of about 1×10^{-9} sr. The angular distribution of scattered particles was measured by scanning the scattered beam in the transverse plane by displacing the detector. In this study, we measured the angular distributions of particle-flux density versus the orientation of a given crystallographic axis or a given plane with respect to the axis of the incident-particle beam; we also explored orientation dependences.

2. ELECTRON PROPAGATION AT SMALL ANGLES TO A CRYSTALLOGRAPHIC AXIS

The propagation of ultrarelativistic electrons was experimentally investigated by using a 1200-MeV electron beam incident at small angles with respect to a crystallographic axis on a silicon single crystal 10 μm thick cut along the (111) plane. The incident beam was collimated to a diameter of 0.3 mm and had an angular divergence of 10^{-5} rad. At the detector position fixed on the axis of the incident-particle beam, we measured the dependence of forward electron scattering (at zero angle θ) on the orientation of the $\langle 111 \rangle$ crystal axis. Fixing the detector in a position displaced in the transverse plane, we measured the corresponding orientation dependences of scattering. The dependence of forward electrons scattering on the angle ψ of orientation of the $\langle 111 \rangle$ crystal axis is depicted in Fig. 1 (solid curve), which shows a narrow region of orientation angles near the incident-beam axis. Here, the transmission intensity is normalized to that corresponding to the transmission through a disoriented crystal. It can be seen that a strong scattering effect is observed in the region of small orientation angles, where we have $I_\psi \ll 1$ for the transmission intensity. Coherent effects in the interaction of fast charged particles with an ordered atomic medium are pronounced in thin crystals. In the orientation dependence of transmission, the present experiment revealed here a new feature, a local transmission-intensity minimum at small orientation angles, which

[1)]Kharkov Institute for Physics and Technology, ul. Akademicheskaya 1, Kharkov, 310108 Ukraine.
*e-mail: blazh@belgorod.bpqu.su

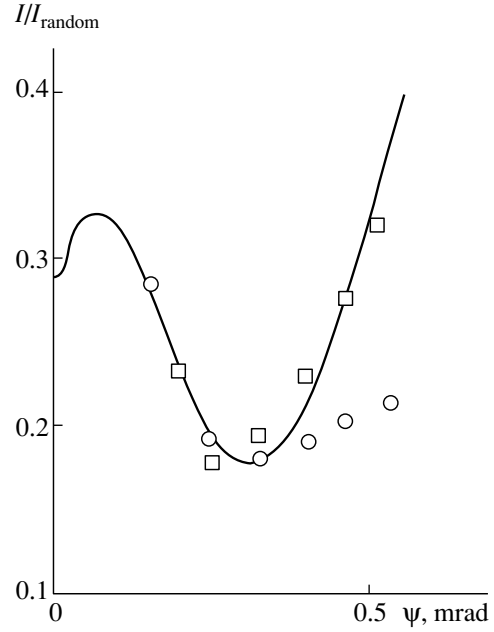

Fig. 1. Orientation dependence of the forward-transmission intensity for 1200-MeV electrons incident on a Si crystal 10 μm thick at small angles to the ⟨111⟩ axis.

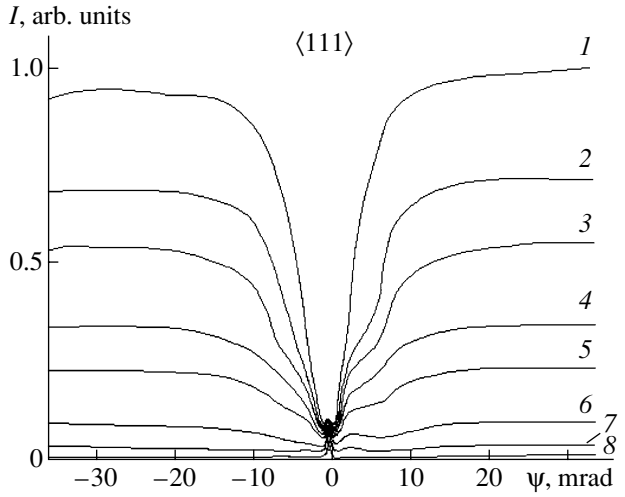

Fig. 2. Orientation dependence of scattering and transmission for 500-MeV electrons incident on a Si crystal 10 μm thick at scattering angles θ of (*1*) 0, (*2*) 0.08, (*3*) 0.12, (*4*) 0.16, (*5*) 0.18, (*6*) 0.23, (*7*) 0.27, and (*8*) 0.3 mrad. The root-mean-square angle of incoherent scattering is $\theta_s = 0.15$ mrad. Data presented in this figure and in Figs. 3, 5, and 6 are normalized to the transmission intensity for a disoriented crystal (see main body of the text).

resembles the well-known effect of blocking. This feature was not previously predicted, so that it calls for an adequate theoretical description. Another feature in the measured orientation dependence manifests itself in a comparison with the results of a calculation based on a theoretical model that takes into account the multiple azimuthal scattering of relativistic electrons by atomic chains in a crystal [1]. It turned out that the calculation (Fig. 1, open circles) yields a much more gently sloping orientation dependence than that measured experimentally. A qualitative explanation for this discrepancy is provided by a model that takes into account the scatter of particles in the polar angle [2] and which leads to an additional reduction of the transmission intensity at small orientation angles. In Fig. 1, open squares represent this dependence with allowance for the scatter in the polar angle.

Figures 2 and 3 display experimental results obtained by measuring the transmission (curve *1*) and the scattering of electrons at various angles in the plane whose normal is aligned with the axis of crystal rotation. Figure 2 shows the results of measurements performed with a 500-MeV electron beam under the same conditions as those described above. The results from [3], which were obtained with a 760-MeV electron beam incident on a crystal 80 μm thick under the conditions of a much poorer angular resolution (the detection solid angle was 1.2×10^{-8} sr) are shown in Fig. 3 for the sake of comparison.

Special attention should be given to the relationship between the intensity of transmission through a disoriented crystal and the intensity of transmission through an analogous crystal oriented in such a way that one of its crystallographic axes is aligned with the incident electron beam. At a local peak, a typical transmission curve for an oriented crystal at a low angular resolution has an intensity that is commensurate with that of transmission through a disoriented crystal. As to the measurements carried out with a high angular resolution, they give much larger ratios of these values. This circumstance agrees well with the concept that the electrons undergo multiple azimuthal scattering on atomic chains in a crystal. From Figs. 2 and 3, it can be seen that there exists a crystal-axis orientation such that almost all orientation curves intersect; that is, there is a scattering-angle region where the angular distribution of the intensity is uniform.

3. PROPAGATION OF ELECTRONS AT SMALL ANGLES TO A CRYSTALLOGRAPHIC PLANE

Experimental investigation of the influence of atomic planes in a crystal on the propagation of relativistic charged particles is aimed at clarifying some orientation effects that differ geometrically from

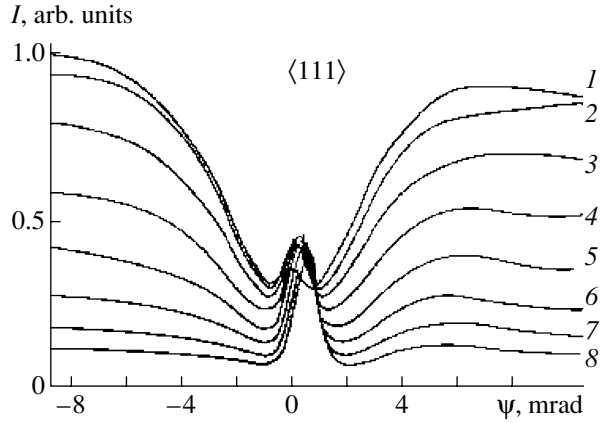

Fig. 3. Orientation dependence of scattering and transmission for 760-MeV electrons incident on a Si crystal 80 μm thick at scattering angles θ of (*1*) 0, (*2*) 0.17×10^{-3}, (*3*) 0.34×10^{-3}, (*4*) 0.51×10^{-3}, (*5*) 0.65×10^{-3}, (*6*) 0.80×10^{-3}, (*7*) 0.89×10^{-3}, and (*8*) 1.03×10^{-3} mrad.

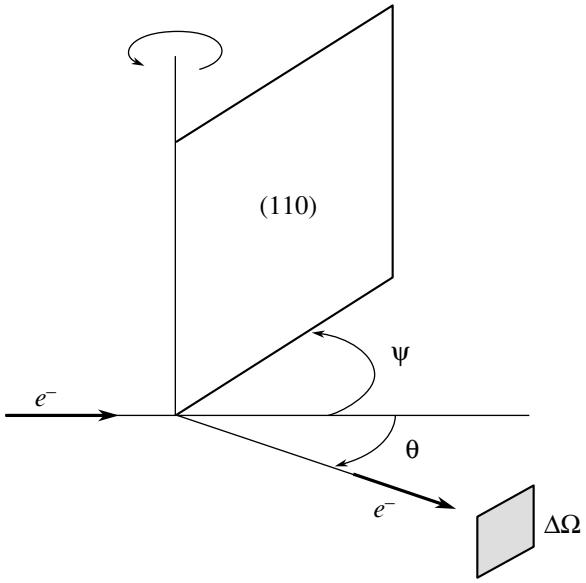

Fig. 4. Geometry of the experiment studying the orientation dependence of transmission ($\theta = 0$) and scattering at specific angles θ for 1200-MeV electrons incident at small angles ψ to a crystallographic plane.

those considered for the case of axes, but which are of no less interest both for fundamental physics and for the possible applications.

In this article, we present the results obtained by measuring the orientation dependence of the transmission and scattering of 1200-MeV electrons by the (110) atomic planes in a silicon crystal 10 μm thick. The crystal was oriented in such a way that the target-rotation axis in the goniometer lay in a plane parallel to the (110) planes and that the orientation angles ψ and the observation angles θ (see Fig. 4) lay in the same plane orthogonal to the (110) atomic planes. The measurements were performed in the same geometry and with the same detector as those described above. The results are displayed in Fig. 5. As can be seen from this figure, the intensity of electron transmission into a small forward solid angle is minimal when the (110) plane of the crystal is oriented along the incident-beam axis; that is, electrons incident on the crystal along atomic planes are scattered more strongly than those in a disoriented crystal. In other words, the electrons are scattered more intensely under the conditions of planar channeling than in the case of a disoriented crystal. It can also be seen that the electrons are scattered symmetrically with respect to the plane. Furthermore, Fig. 5 shows that the intensity of scattering at angles $\theta > \theta_s$ (where θ_s is the multiple-scattering angle in a disoriented crystal) in the region of small orientation angles ψ proves to be greater than that in the case of a stronger disorientation. The position of the intensity peak does not correspond to the orientation of crystalline planes along the incident-beam axis—the orientation dependence becomes asymmetric with respect to the orientation angle of $\psi = 0$. The above effect was also observed by Ermak *et al.* [4], who studied the angular distributions of electrons scattered at various orientations of the crystalline plane; they called this effect a quasirefraction. In the theoretical study of Fomin [5], this phenomenon was explained by the concerted effect of the incoherent multiple scattering of electrons and their planar channeling.

From Fig. 5, it can also be seen that there is an angle $\theta^* \approx \theta_s$ at which the scattering intensity is virtually independent of orientation; this can be used in measurements of orientation dependences for monitoring the beam current.

4. OBSERVATION OF ORIENTATION DEPENDENCE OF THE FORWARD PROPAGATION OF RELATIVISTIC ELECTRONS INCIDENT ON A CRYSTAL AT SMALL ANGLES TO AN AXIS IN THE CASE OF PLANAR CHANNELING

In transmission experiments, it is possible in principle to observe, on a single curve of orientation dependence, the effect of orientation of both crystal planes and axes. Conceivably, this is not a new possibility, but we deem that it is of interest as a demonstration of a crystalline-structure manifestation in the angular structure of a particle flux that has traversed a crystal.

The relevant results of our measurements are illustrated in Fig. 6, which shows the intensity of

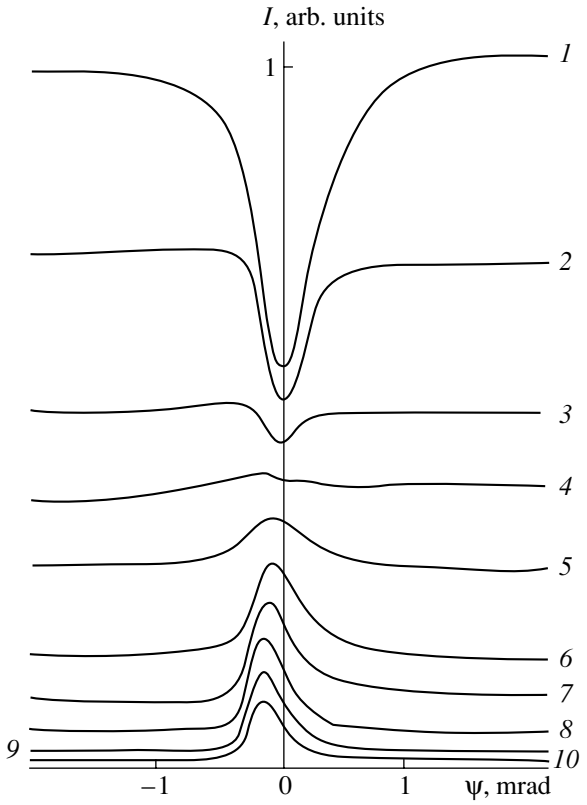

Fig. 5. Transmission and scattering of 1200-MeV electrons into the solid angle $\Delta\Omega = 10^{-9}$ sr that are incident on a Si crystal 10 μm thick versus the angle ψ of orientation of the (110) plane at the observation angles θ of (*1*) 0, (*2*) 0.047, (*3*) 0.067, (*4*) 0.084, (*5*) 0.103, (*6*) 0.13, (*7*) 0.148, (*8*) 0.186, (*9*) 0.231, and (*10*) 0.273 mrad.

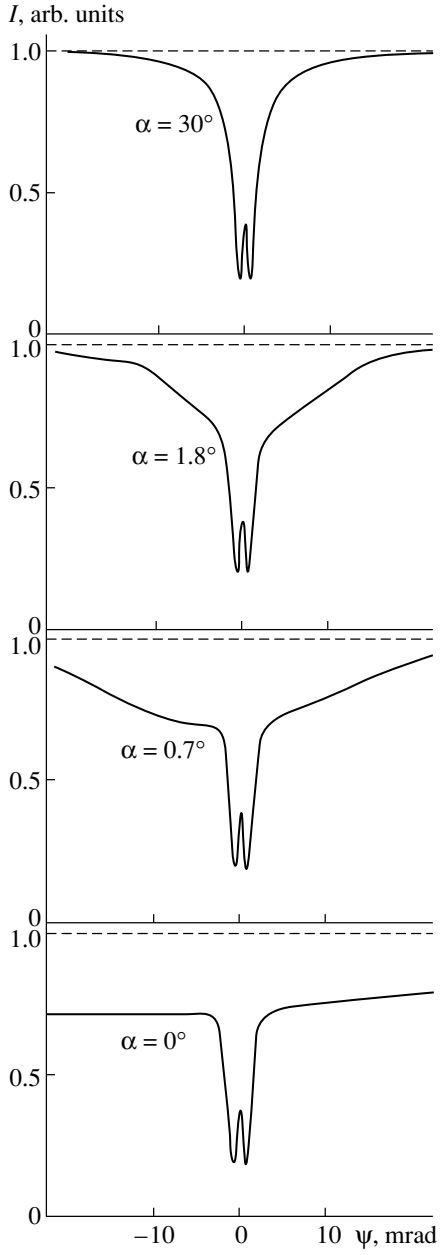

Fig. 6. Manifestation of the (110) crystallographic plane in the orientation dependence of the transmission of 500-MeV electrons into the solid angle $\Delta\Omega = 10^{-8}$ sr that are incident on a Si crystal at small angles to the $\langle 111 \rangle$ axis.

relativistic-electron transmission as a function of the angle ψ of the crystal rotation about a certain axis (orthogonal to the incident-beam axis) for various values of the angle α that specifies the orientation of the normal to one of the planes whose intersection forms the $\langle 111 \rangle$ crystallographic axis with respect to the crystal-rotation axis.

The lower curve in Fig. 6 corresponds to the atomic-plane orientation orthogonal to the crystal-rotation axis in the goniometer ($\alpha = 0°$). In this case, rotation of the crystal rotates the atomic plane without changing the orientation of its normal and the crystal appears to be oriented in such a way that, for all values of ψ, the incident beam lies in the atomic plane. In this case, a disoriented crystal therefore turns out to be in fact oriented, but this orientation is determined by a plane rather than by a crystallographic axis; naturally, the transmission intensity is then lower than that for a "truly" disoriented crystal (see Fig. 6, the upper curve). At small α (second and third curves in Fig. 6), the effect of changing the atomic-plane orientation is observed in the orientation dependence of the transmission intensity, but this effect is much weaker than that of the change in the crystallographic-axis orientation, manifesting itself as a broader minimum on the curve.

5. CONCLUSION

The results obtained from our experimental investigation of the transmission and scattering of rela-

tivistic electrons reflect some of the most characteristic orientation phenomena, including new effects like the blocking of particle transmission at very small angles to a crystallographic axis and the asymmetry of scattering by atomic planes. Our results can be of use for studying both the dynamics of particle transmission through an oriented crystal and processes associated with propagation dynamics like photon emission, the production of electron–positron pairs, and nuclear reactions in a crystal.

ACKNOWLEDGMENTS

This work was supported in part by the Russian Foundation for Basic Research, project no. 00-02-17523, and by the Ministry of Education and Science of Ukraine (Program of Studies on Atomic Science and Technology of the Kharkov Institute for Physics and Technology for 1996–2000, topic no. 03/32).

REFERENCES

1. V. I. Truten', S. P. Fomin, and N. F. Shul'ga, Preprint No. 32-11, KhFTI (Institute for Physics and Technology, Kharkov, 1982).
2. S. V. Blazhevich, G. L. Bochek, V. I. Kulibaba, *et al.,* in *Proceedings of the XXI All-Union Conference on the Physics of Charged-Particle Interaction with Crystals* (Mosk. Gos. Univ., Moscow, 1992), p. 9.
3. D. I. Adeĭshvili, A. P. Antipenko, S. V. Blazhevich, *et al.,* Zh. Éksp. Teor. Fiz. **92**, 1574 (1987) [Sov. Phys. JETP **65**, 882 (1987)].
4. V. P. Ermak, S. V. Kas'yan, K. S. Kokhnyuk, *et al.,* Vopr. At. Nauki Tekh., Ser.: Yad.-Fiz. Issled. (Teor. Éksp.), No. 3, 18 (1990).
5. S. P. Fomin, in *Proceedings of the XX All-Union Conference on the Physics of Charged-Particle Interaction with Crystals* (Mosk. Gos. Univ., Moscow, 1990), p. 34.

Translated by V. Bukhanov

Physics of Atomic Nuclei, Vol. 64, No. 5, 2001, pp. 961–962. Translated from Yadernaya Fizika, Vol. 64, No. 5, 2001, pp. 1031–1033.

XXX International Conference on the Physics of Interaction of Fast Charged Particles with Matter

Estimate of the Polarization Fields of a Relativistic Atom in a Solid

V. A. Aleksandrov, A. S. Sabirov, and G. M. Filippov

Chuvash State University, Moskovskii pr. 15, Cheboksary, 428015 Russia

Received November 4, 2000

Abstract—The magnetic and electric polarization fields of a relativistic hydrogen atom in a solid are analyzed. At atomic distances, these fields differ only slightly from the corresponding fields of an ionized atom. © *2001 MAIK "Nauka/Interperiodica".*

1. INTRODUCTION

When atomic particles move through a solid, there arise polarization fields, which play an important role. In particular, some features of the divergence of the fragments of molecular ions in the case of Coulomb explosion can be interpreted by taking into account the polarization of a medium. The effect of these fields is well understood in the nonrelativistic case. However, the formulas of nonrelativistic theory are inapplicable at high particle velocities, in particular, because polarization fields cannot be described by the scalar potential alone in this case. Polarization fields induced by a relativistic pointlike charge in a metal were calculated in [1], where both electric and magnetic fields were found to increase with the Lorentz factor. It is interesting to find out how these fields act on particles of a cluster moving at a speed close to the speed of light. This problem arises in studying the aforementioned Coulomb explosion of relativistic molecular ions in a solid film. In this study, the magnetic and the electric component of the polarization field of a relativistic atom moving in a solid are calculated within the formalism of dielectric functions.

2. POLARIZATION FIELDS OF A MOVING ATOM

The electric field of an atom in its rest frame is a potential field; that is, $\mathbf{E}' = -\mathrm{grad}\,\Phi'(\mathbf{x}')$, where

$$\Phi'(\mathbf{x}') = \frac{\gamma^2}{2\pi^2}\int d^3\mathbf{q}\,\frac{\rho(\mathbf{k})}{k^2}\times\left(\frac{1}{\varepsilon_l(\mathbf{k},\omega)}-1 + \frac{v^2q_\perp^2}{c^2q^2}\frac{\varepsilon_t(\mathbf{k},\omega)-1}{\varepsilon_t(\mathbf{k},\omega)-k^2c^2/\omega^2}\right)\Bigg|_{\omega=k_zv} e^{i\mathbf{q}\cdot\mathbf{x}'}, \quad (1)$$

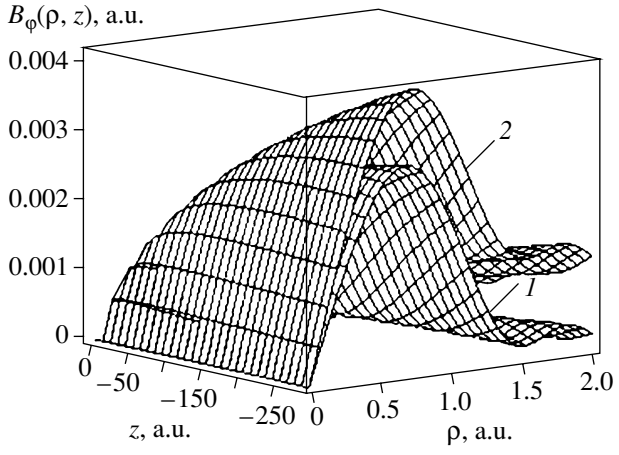

Fig. 1. Pattern of the magnetic field $B_\varphi(\rho, z)$ of (*1*) a relativistic hydrogen atom and (*2*) a proton that move through carbon. The origin of coordinates is at the center of the atom, and $\gamma = 10$.

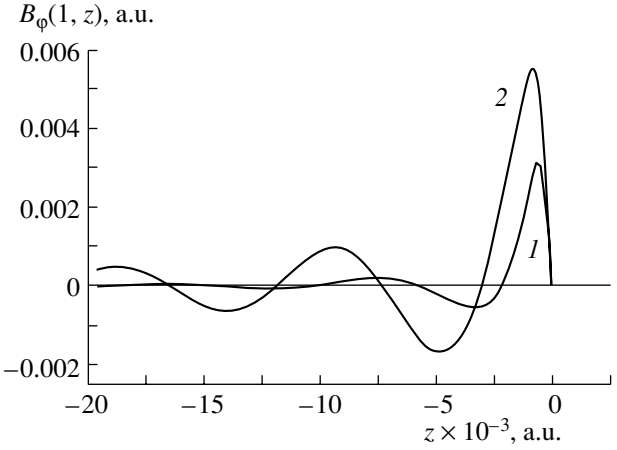

Fig. 2. Magnetic field $B_\varphi(1, z)$ of (*1*) a relativistic hydrogen atom and (*2*) a proton that move through carbon. The origin of coordinates is at the center of the atom, and $\gamma = 10$.

1063-7788/01/6405-0961$21.00

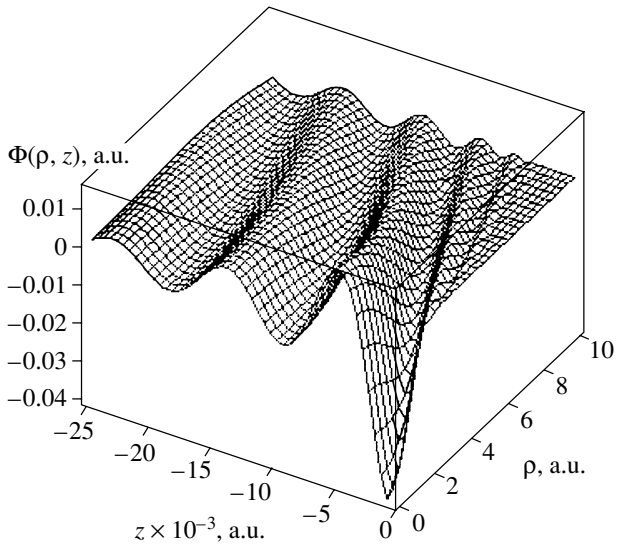

Fig. 3. Pattern of the electric-field potential $\Phi(\rho, z)$ in the rest frame in the wake region ($\gamma = 10$).

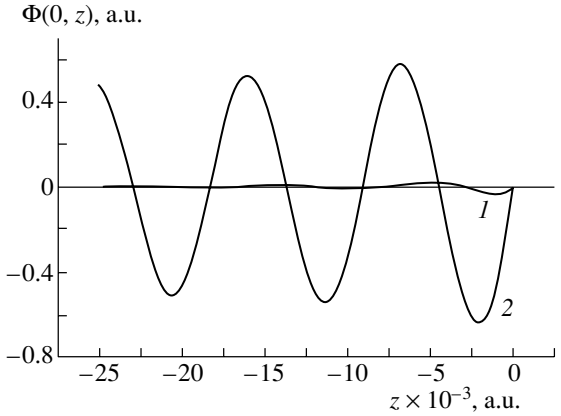

Fig. 4. Electric-field potential $\Phi(0, z)$ for (*1*) a relativistic hydrogen atom and (*2*) a proton that move through carbon ($\gamma = 10$).

$\mathbf{k} = (\mathbf{k}_\perp, k_z)$, and $\mathbf{q} = (\mathbf{q}_\perp, \gamma q_z)$. The magnetic component of the polarization field is given by

$$\mathbf{B}'_\perp(\mathbf{x}') = \frac{-i\gamma^2}{2\pi^2 c}\int d^3\mathbf{q}\,\frac{\rho(\mathbf{k})}{k^2}[\mathbf{q}\times\mathbf{v}]\left(\frac{1}{\varepsilon_l(\mathbf{k},\omega)} - 1 + \frac{(\varepsilon_t(\mathbf{k},\omega)-1)}{(\varepsilon_t(\mathbf{k},\omega) - k^2c^2/\omega^2)}\right)\Bigg|_{\omega=k_z v} e^{i\mathbf{q}\cdot\mathbf{x}'}. \quad (2)$$

The polarization fields of an atom are calculated with the aid of the following model expressions for the transverse and longitudinal dielectric functions:

$$\varepsilon_t(\mathbf{k},\omega) = 1 - \omega_0^2/\omega^2,$$

$$\varepsilon_l(\mathbf{k},\omega) = 1 - \frac{\omega_0^2}{\omega^2 + \omega_0^2 - \omega_k^2 + i\delta\omega},$$

$$\omega_k = \omega_0 + k^2/2.$$

If the charge distribution $\rho(\mathbf{q})$ in an atom is axisymmetric with respect to the z axis, expressions (1) and (2) can be reduced to double integrals.

Expressions (1) and (2) do not involve charge self-interaction—the polarization fields correspond to the reaction of the particles of a medium to external particles moving in this medium. Because of the mutual shielding of charges, fields (1) and (2) are weaker than those of an individual moving charge; however, this is so only far off the atom. At small distances corresponding to large q, shielding has only a slight effect on the polarization fields, which can considerably affect the state of atomic electrons. The magnitude and the configuration of these fields are of interest for experimenters studying the propagation of relativistic atomic particles through solid films.

When a ground-state hydrogen atom moves along a straight line, the magnetic field in the cylindrical coordinates (ρ, φ, z) has only a φ component. Figure 1 presents the pattern of the magnetic field $B_\varphi(\rho, z)$ for a moving atom and for a proton in the coordinate frame whose origin is at the center of the particle being considered. Figure 2 shows the magnetic field of an atom and of a proton in the wake region. The maximal values of the magnetic field behind a particle are proportional to the Lorentz factor γ and can be large. The distance from the center of the atom to the nearest peak is proportional to the particle energy and is quite large.

Figure 3 shows the potential pattern of the atomic electric field in the rest frame. For the wake region, Fig. 4 presents the electric-field potential on the symmetry axis for an atom and that for a proton that moves at the same velocity. At the peaks, the polarization-field potential in the wake region can take large values, which are proportional to the energy of the atom. The distance from the center of the atom to the nearest peak is large and increases with the Lorentz factor.

To summarize, we note that, owing to weak shielding, the field of an ultrarelativistic particle disturbs a large volume of a solid and induces, at a small change in the charge density, large polarization fields, which increase with energy. The magnetic field is less affected by the mutual shielding of the particles in the atom involved than the electric field. Because the polarization fields of a relativistic particle cover extensive regions, these fields are expected to depend strongly on the thickness of the film traversed by the particle.

REFERENCES

1. V. A. Aleksandrov, A. S. Sabirov, and G. M. Filippov, in *Proceedings of the XXVIII International Conference on the Physics of Charged-Particle Interaction with Crystals* (Mosk. Gos. Univ., Moscow, 1998), p. 52.

Translated by R. Tyapaev

Physics of Atomic Nuclei, Vol. 64, No. 5, 2001, pp. 963–965. Translated from Yadernaya Fizika, Vol. 64, No. 5, 2001, pp. 1034–1036.

XXX International Conference on the Physics of Interaction of Fast Charged Particles with Matter

Asymmetry of Parametric X-ray Radiation from Polarized Electrons (Quantum Approach)

A. V. Mazunin, A. P. Potylitsyn, V. A. Serdyutsky*, and M. N. Strikhanov[1)]

Institute for Nuclear Physics, Tomsk Polytechnic University, pr. Lenina 30, Tomsk, 634034 Russia

Received November 4, 2000

Abstract—The asymmetry of parametric x rays emitted by polarized electrons is considered on the basis of quantum theory. The asymmetry value is calculated for emission both in the Bragg direction and in directions different from the Bragg direction by an angle of order γ^{-1}. The asymmetry is computed for the longitudinal and for the transverse polarization of the electrons. © *2001 MAIK "Nauka/Interperiodica".*

Measurement of quantities that characterize the polarization of relativistic particles is of great interest in connection with planned experiments with polarized electron, positron, and proton beams.

Parametric x rays in crystals were predicted in [1] and experimentally discovered in [2] 15 years ago. This radiation, together with Cherenkov radiation and transition radiation, belongs to the class of so-called polarization radiations. Many features of parametric x rays can be adequately described within classical electrodynamics [3]. However, the quantum approach developed in [4] makes it possible to compute quantum corrections and understand this process at the microscopic level.

In contrast to coherent bremsstrahlung and emission that accompanies channeling, which are due to a periodic modulation of the trajectories by the crystal potential, parametric x rays are caused by the scattering of virtual photons by electrons located at regular intervals in a crystal.

On the basis of the quantum approach, we calculate here the asymmetry of parametric x rays, which is defined as

$$A = \left(\frac{d\sigma_\uparrow}{d\Omega} - \frac{d\sigma_\downarrow}{d\Omega}\right) / \left(\frac{d\sigma_\uparrow}{d\Omega} + \frac{d\sigma_\downarrow}{d\Omega}\right), \qquad (1)$$

where $d\sigma_{\uparrow,\downarrow}/d\Omega$ stands for the cross sections calculated in the neighborhood of the Bragg direction for oppositely polarized electrons. As was shown in [4], the matrix element for this process has the form

$$Y(\mathbf{k}, a) = P(\mathbf{k}, a)\, U^+_{\mathbf{p}'s'} \mathbf{e}_{\mathbf{h}a} \cdot \boldsymbol{\alpha} U_{\mathbf{p}s} + Q(\mathbf{k}, a)\, U^+_{\mathbf{p}'s'} U_{\mathbf{p}s}, \quad (2)$$

where $U_{\mathbf{p}s}$ is the four-component spinor describing an electron of momentum $\mathbf{p}$ and spin s, $\mathbf{k}$ is the momentum of a photon of parametric x rays, e_{ha} $(a = 1, 2)$ are the unit polarization vectors of a photon of momentum $\mathbf{k_h} = \mathbf{k} + \mathbf{h}$, and $\mathbf{h}$ is a vector of the reciprocal lattice of the crystal. The functions $P(\mathbf{k}, a)$ and $Q(\mathbf{k}, a)$ are defined in [4]. Upon going over to the two-component spinors and the system of units in which $\hbar = m = c = 1$, where m is the electron mass, the matrix element (2) takes the form

$$Y(\mathbf{k}, a) = \nu^+_{s'} \{P(\mathbf{k}, a)(A_p + i\boldsymbol{\sigma} \cdot \mathbf{B}_p) + Q(\mathbf{k}, a)(A_q + i\boldsymbol{\sigma} \cdot \mathbf{B}_q)\} \nu_s, \qquad (3)$$

where ν_s and $\nu_{s'}$ are the two-component spinors. We also use here the notation

$$A_p = \frac{\mathbf{e}_{\mathbf{h}a} \cdot \mathbf{p}}{\gamma + 1} + \frac{\mathbf{e}_{\mathbf{h}a} \cdot \mathbf{p}'}{\gamma' + 1},$$
$$A_q = 1 + \frac{\mathbf{p} \cdot \mathbf{p}'}{(\gamma + 1)(\gamma' + 1)}, \qquad (4)$$
$$\mathbf{B}_p = \left[\mathbf{e}_{\mathbf{h}a}, \left(\frac{\mathbf{p}}{\gamma - 1} - \frac{\mathbf{p}'}{\gamma' + 1}\right)\right],$$
$$\mathbf{B}_q = \frac{\left[\mathbf{p}', \mathbf{p}\right]}{(\gamma' + 1)(\gamma + 1)},$$

where $\mathbf{p}$ and γ are the momentum and the energy of the initial-state electron, while $\mathbf{p}'$ and γ' are the momentum and energy of the final-state electron. The polarization $\boldsymbol{\xi}$ of the initial-state electron is described in terms of the density matrix

$$\rho = \frac{1}{2}(1 + \boldsymbol{\xi} \cdot \boldsymbol{\sigma}). \qquad (5)$$

Squaring expression (3) and performing summation

[1)]Moscow State Engineering Physics Institute (Technical University), Kashirskoe sh. 31, Moscow, 115409 Russia.

*e-mail: serd@interact.phtd.tpu.edu.ru

over the polarizations of the final-state electron, we arrive at

$$|Y|^2 = \frac{1}{2}\left(\mathrm{tr}_1 + \mathrm{tr}_2\right), \tag{6}$$

$$\mathrm{tr}_1 = |P|^2\left(|A_p|^2 + |\mathbf{B}_p|^2\right) + |Q|^2\left(|A_q|^2 + |\mathbf{B}_q|^2\right) + 2\mathrm{Re}\left(PQ^*\right)\left(A_pA_q + \mathbf{B}_p\cdot\mathbf{B}_q\right), \tag{7}$$

$$\mathrm{tr}_2 = 2\mathrm{Im}\left(PQ^*\right)\{A_p\left(\boldsymbol{\xi}\cdot\mathbf{B}_q\right) - A_q\left(\boldsymbol{\xi}\cdot\mathbf{B}_p\right) + \boldsymbol{\xi}\left[\mathbf{B}_p,\mathbf{B}_q\right]\} = 2\mathrm{Im}\left(PQ^*\right)K(\boldsymbol{\xi}). \tag{8}$$

The conservation laws imply that

$$\mathbf{p}' = \mathbf{p} - \mathbf{k} - \mathbf{h} = \mathbf{p} - \mathbf{k}_\mathbf{h}, \quad \gamma' = \gamma - \omega. \tag{9}$$

Retaining only the leading terms in the expansion in powers of γ^{-1}, we reduce (4) to the form

$$A_p = 2(\mathbf{e}_{\mathbf{h}a}\cdot\boldsymbol{\beta}), \quad A_q = 2, \tag{10}$$

$$\mathbf{B}_p = \frac{1}{\gamma}[\mathbf{e}_{\mathbf{h}a}\times\mathbf{b}], \quad \mathbf{B}_q = \frac{1}{\gamma}[\boldsymbol{\beta}\times\mathbf{k}_\mathbf{h}],$$

where $\mathbf{b} = (\mathbf{k}_h - \boldsymbol{\beta}\omega)(1 - 1/\gamma) + \boldsymbol{\beta}\omega/\gamma$, $\boldsymbol{\beta}$ is the velocity of the initial particle, and ω is the energy of a photon of parametric x rays. The factor $K(\boldsymbol{\xi})$ depends on the particle momenta and the photon polarization vectors. Specifically, we have

$$K(\boldsymbol{\xi}) = \sum_{i=1}^{4} K_i(\boldsymbol{\xi}), \tag{11}$$

where

$$K_1(\boldsymbol{\xi}) = -\frac{2}{\gamma}\left(\mathbf{e}_{\mathbf{h}a}\cdot\boldsymbol{\beta}\right)\boldsymbol{\xi}\cdot[\mathbf{k}_\mathbf{h}\times\boldsymbol{\beta}], \tag{12}$$

$$K_2(\boldsymbol{\xi}) = -\frac{2}{\gamma}\boldsymbol{\xi}\left[\mathbf{e}_{\mathbf{h}a}\times\mathbf{b}\right] = -\frac{2}{\gamma}\mathbf{e}_{\mathbf{h}a}\cdot[\mathbf{b}\times\boldsymbol{\xi}],$$

$$K_3(\boldsymbol{\xi}) = \frac{1}{\gamma^2}\mathbf{e}_{\mathbf{h}a}\cdot[\boldsymbol{\beta}\times\mathbf{k}_\mathbf{h}]\left(\boldsymbol{\xi}\cdot\mathbf{k}_\mathbf{h}\right),$$

$$K_4(\boldsymbol{\xi}) = -\frac{\omega}{\gamma^2}\left(1 - \frac{2}{\gamma}\right)\mathbf{e}_{\mathbf{h}a}\cdot[\boldsymbol{\beta}\times\mathbf{k}_\mathbf{h}]\left(\boldsymbol{\xi}\cdot\boldsymbol{\beta}\right).$$

Using the above formulas, we obtain

$$A = \frac{2\mathrm{Im}\left(PQ^*\right)\left[K(\boldsymbol{\xi}) - K(-\boldsymbol{\xi})\right]}{\mathrm{tr}_1}, \tag{13}$$

where summation over photon polarizations is implied. The virtual-photon polarization vectors $\mathbf{e}_{\mathbf{h}a}$ are expressed in terms of the polarization vectors $\mathbf{e}_{\mathbf{k}a}$ of the on-mass-shell photon, and summation is performed according to the formula

$$\sum_a e_{ia}e_{ja} = \delta_{ij} - n_in_j, \tag{14}$$

where $n_i = k_i/|\mathbf{k}|$.

The asymmetry given by (13) depends on the dielectric permittivity $\epsilon = 1 + \chi_0' + i\chi_0''$, where χ_0' and χ_0'' are, respectively, the real and the imaginary part of the dielectric susceptibility. If the dielectric permittivity is real, $\epsilon = 1 + \chi_0'$, then the factor $\mathrm{Im}\left(PQ^*\right)$ in (13) vanishes. However, this factor does not vanish in the region where $\chi_0'' \neq 0$ (for example, near the K edge of absorption):

$$\mathrm{Im}\left(PQ^*\right) = -P_0Q_0\chi_0''/2. \tag{15}$$

The quantities P_0 and Q_0 in (15) are nothing but the functions P and Q evaluated at $\epsilon = 1 + \chi_0'$.

For scattering in the forward direction, only the second term contributes to the asymmetry; in the region of anomalous absorption in a crystal ($\omega \sim 10$ keV$/mc^2$, $\chi_0'' \sim 10^{-3}$), we therefore find for 5-MeV electrons ($\gamma \sim 10^1$) that

$$A \sim \chi_0''\omega/\gamma \sim 10^{-5}\text{–}10^{-6}.$$

For photons emitted in directions close to the Bragg direction (characterized by the unit vector $\mathbf{n}_\mathrm{B} = \mathbf{p}/p - \mathbf{h}/|\mathbf{k}|$), the expression for the asymmetry takes the form

$$A = \omega\chi_0''\cot\left(2\theta_B\right). \tag{16}$$

At $\omega = 10$ keV$/mc^2$, $\chi_0'' = 10^{-3}$, and $\theta_\mathrm{B} = 5^\circ$, we obtain $A \sim 10^{-4}$. This estimate complies with the results from [5], which were obtained by calculating quantum corrections to transition radiation. We have also calculated the asymmetry for photons emitted in the directions deviating from the Bragg direction by angles not exceeding that of order γ^{-1}.

The contributions of the spin-dependent terms $K_i(\boldsymbol{\xi})$ to the asymmetry A are given by

$$\sum_a\left(\mathbf{e}_{\mathbf{k}a}\cdot\mathbf{e}_{\mathbf{h}a}\right)\left(\mathbf{e}_{\mathbf{k}a}\cdot\mathbf{h}\right)K_1(\boldsymbol{\xi}) = \left(2\beta^2\omega^2/\gamma\right) \times\left(\mathbf{n}\cdot\hat{k}_\mathbf{h}\right)\left[\left(\mathbf{n}\cdot\hat{k}_\mathbf{h}\right)\left(\mathbf{n}_0\cdot\hat{k}_\mathbf{h}\right) - \left(\mathbf{n}_0\cdot\mathbf{n}\right)\right] \times\left(\xi_y\hat{k}_{\mathbf{h}x} - \xi_x\hat{k}_{\mathbf{h}y}\right), \tag{17}$$

where $\boldsymbol{\xi} = (\xi_x, \xi_y, \xi_z)$ and only the transverse polarization contributes;

$$\sum_a\left(\mathbf{e}_{\mathbf{k}a}\cdot\mathbf{e}_{\mathbf{h}a}\right)\left(\mathbf{e}_{\mathbf{k}a}\cdot\mathbf{h}\right)K_2(\boldsymbol{\xi}) = \left(2\omega^2/\gamma\right)\left(\mathbf{n}\cdot\hat{k}_\mathbf{h}\right)\{\xi_y\left[\beta\left(1 - 2/\gamma\right)\left(\mathbf{n}\cdot\hat{k}_\mathbf{h}\right)\left(\hat{k}_{\mathbf{h}x} - n_x\right) + \left(n_x\hat{k}_{\mathbf{h}z} - n_z\hat{k}_{\mathbf{h}x}\right)\right] - \xi_x\left[x\leftrightarrow y\right]\}, \tag{18}$$

where $\boldsymbol{\xi} = (\xi_x, \xi_y, 0)$ and only the transverse polarization contributes;

$$\sum_a (\mathbf{e}_{\mathbf{k}a} \cdot \mathbf{e}_{\mathbf{h}a}) (\mathbf{e}_{\mathbf{k}a} \cdot \mathbf{h}) K_2(\boldsymbol{\xi}) \qquad (19)$$

$$= -\left(2\omega^2/\gamma\right)\left(\mathbf{n} \cdot \hat{k}_{\mathbf{h}}\right)\left(n_y \hat{k}_{\mathbf{h}x} - n_x \hat{k}_{\mathbf{h}y}\right)\xi_{\parallel},$$

where $\boldsymbol{\xi} = (0, 0, \xi_z) = (0, 0, \xi_{\parallel})$ and the contribution of the longitudinal polarization is zero because the projections of the unit polarization vectors of the real photon, n_y, and of the virtual photon, $\hat{k}_{\mathbf{h}y}$, onto the diffraction plane (x–z) vanish;

$$\sum_a (\mathbf{e}_{\mathbf{k}a} \cdot \mathbf{e}_{\mathbf{h}a}) (\mathbf{e}_{\mathbf{k}a} \cdot \mathbf{h}) K_3(\boldsymbol{\xi}) = \left(\omega^3\beta/\gamma\right) \qquad (20)$$

$$\times \left(n_x \hat{k}_{\mathbf{h}z} - n_y \hat{k}_{\mathbf{h}x}\right)\left(\xi_x \hat{k}_{\mathbf{h}x} + \xi_y \hat{k}_{\mathbf{h}y} + \xi_z \hat{k}_{\mathbf{h}z}\right),$$

where both the transverse and the longitudinal polarizations contribute; and

$$\sum_a (\mathbf{e}_{\mathbf{k}a} \cdot \mathbf{e}_{\mathbf{h}a}) (\mathbf{e}_{\mathbf{k}a} \cdot \mathbf{h}) K_4(\boldsymbol{\xi}) \qquad (21)$$

$$= \frac{\omega^3\beta^2}{\gamma^2}\left(\mathbf{n} \cdot \hat{k}_{\mathbf{h}}\right)(1 - 2/\gamma)\left(n_y \hat{k}_{\mathbf{h}x} - n_x \hat{k}_{\mathbf{h}z}\right)\xi_{\parallel},$$

where only the longitudinal polarization contributes.

It is obvious that the third and the fourth term [expressions (20) and (21)] can be neglected since their contribution to the asymmetry is of order $\chi_0'' \omega^2/\gamma^2 \sim 10^{-10}$, whereas the contribution of the first and the second term [expressions (17)–(19)] is on the order of 10^{-5}–10^{-6} ($\chi_0'' = 10^{-3}$, $\omega = 2.5$ keV/mc^2, $\theta_{\mathrm{B}} = \pi/8$).

Let us now discuss the results that we obtained. It is worth noting that the asymmetry for scattering strictly in the Bragg direction is rather great in relation to the asymmetry for directions deviating from the Bragg direction by an angle within γ^{-1}. This is because only the contribution of $P(\mathbf{k}, a)$ to the expression for tr_1 (which appears in asymmetry and which determines the cross section for unpolarized electrons),

$$\mathrm{tr}_1 = \sum_a \left|P(\mathbf{k}, a)(\mathbf{e}_{\mathbf{h}a} \cdot \boldsymbol{\beta}) + Q(\mathbf{k}, a)\right|^2 \qquad (22)$$

$$= \sum_a \left|\frac{(\mathbf{e}_{\mathbf{k}a} \cdot \mathbf{e}_{\mathbf{h}a})(\mathbf{e}_{\mathbf{h}a} \cdot \boldsymbol{\beta})}{\omega^2(\mathbf{k}) - \omega^2(\mathbf{k}_{\mathbf{h}})} + \frac{\mathbf{e}_{\mathbf{k}a} \cdot \mathbf{h}}{\omega^2(\mathbf{k}_{\mathbf{h}})\,\omega(\mathbf{k})}\right|^2,$$

is traditionally taken into account [4]. However, it is necessary to include $Q(\mathbf{k}, a)$ for the Bragg direction, in which case $(\mathbf{e}_{\mathbf{h}a} \cdot \boldsymbol{\beta}) = 0$ and $|P(\mathbf{k}, a)|^2 = 0$. We then obtain formula (16) and the corresponding estimate of the asymmetry. If there appears a deviation from the Bragg direction, the asymmetry in (13) is determined by the fast growing function $P(\mathbf{k}, a)$ in (22), with the result that, for angles of order $(\mathbf{n} \cdot \mathbf{n}_{\mathrm{B}}) \sim \gamma^{-1}$, the effect is two orders of magnitude smaller than that considered above.

REFERENCES

1. I. D. Feranchuk and A. V. Ivashin, J. Phys. (Paris) **46**, 1981 (1985).
2. S. A. Vorob'ev, B. N. Kalinin, S. Pak, and A. P. Potylitsyn, Pis'ma Zh. Éksp. Teor. Fiz. **41**, 3 (1985) [JETP Lett. **41**, 1 (1985)].
3. A. V. Shchagin, V. I. Pristupa, and N. A. Khizhnyak, Phys. Lett. A **148**, 485 (1990).
4. H. Nitta, Phys. Rev. B **45**, 7621 (1992).
5. V. N. Baier and V. M. Katkov, Phys. Lett. A **252**, 263 (1999).

Translated by R. Rogalyov

Physics of Atomic Nuclei, Vol. 64, No. 5, 2001, pp. 966–970. Translated from Yadernaya Fizika, Vol. 64, No. 5, 2001, pp. 1037–1041.

XXX International Conference on the Physics of Interaction of Fast Charged Particles with Matter

Polarization Bremsstrahlung from Relativistic Electrons Moving in a Small-Grained Medium

N. N. Nasonov*, V. A. Nasonova, and I. G. Popov

Laboratory for Radiation Physics, Belgorod State University, Studencheskaya ul. 12, Belgorod, 308007 Russia

Received November 4, 2000

Abstract—Polarization bremsstrahlung from relativistic electrons moving in a medium consisting of very small crystals oriented at random is studied theoretically. The results of this analysis predict a sharp dependence of the spectral and angular features of the radiation on the crystal dimensions and on the angle of observation. The possibility of developing, on the basis of the phenomena considered in the present study, a new method for studying lowly ordered media is highlighted. © *2001 MAIK "Nauka/Interperiodica"*.

1. INTRODUCTION

If a fast charged particle moves in a medium, the scattering of the Coulomb field of such a particle on the atomic electrons of the medium generates polarization bremsstrahlung [1]. An important feature peculiar to polarization bremsstrahlung is that the effective impact parameter for a collision of a fast particle with an atom is large, commensurate with atomic dimensions [2]. Because of this circumstance, the features of polarization bremsstrahlung from a fast particle moving in a condensed medium are greatly affected by interatomic correlations in the medium [2]. For example, the spectral and angular distributions of the intensity of polarization bremsstrahlung from relativistic electrons moving in an amorphous medium and in a polycrystalline sample are markedly different [3], in contrast to what is observed for the distribution of the intensity of conventional bremsstrahlung.

In the present study, we consider the spectral and angular distribution of the intensity of polarization bremsstrahlung from relativistic electrons moving in a condensed medium characterized by the presence of short-range order in the arrangement of the medium atoms and by the absence of long-range order. The theory of polarization bremsstrahlung in such media has not yet been developed. At the same time, experimentalists have accumulated a vast body of relevant data requiring explanation. The authors of [4] measured the spectrum of collimated radiation from electrons traversing a film from diamond-like carbon. According to x-ray investigations, the film material does not have a crystal structure. Nonetheless, the theory of polarization bremsstrahlung in an amorphous medium failed to describe the measured spectra. The results obtained in [4] could not be explained by the theory of polarization bremsstrahlung in polycrystalline samples either. In order to fill this gap, we consider here polarization bremsstahlung from relativistic electrons moving in a condensed medium consisting of small crystals oriented at random.

The spectral and angular distribution obtained for polarization bremsstrahlung on the basis of the model that we adopt for a small-grained medium depends sharply on the crystal dimensions and agrees with unexpected experimental results [4].

2. GENERAL RELATIONS

Let us consider the structure of the electromagnetic field excited by a relativistic charged particle moving in a condensed medium. In order to find the Fourier transform of the electric field, $\mathbf{E}_{\omega\mathbf{k}} = (2\pi)^{-4}\int dtd^3r\mathbf{E}(\mathbf{r},t)\exp(-i\mathbf{k}\cdot\mathbf{r}+i\omega t)$, we will make use of the conventional Maxwell equations

$$(k^2-\omega^2)\mathbf{E}_{\omega\mathbf{k}}-\mathbf{k}(\mathbf{k}\cdot\mathbf{E}_{\omega\mathbf{k}}) = 4\pi i\omega\mathbf{j}_{\omega\mathbf{k}} + \frac{i\omega e}{2\pi^2}\mathbf{v}\delta(\omega-\mathbf{k}\cdot\mathbf{v}), \quad (1)$$

where $\mathbf{j}_{\omega\mathbf{k}}$ is the Fourier transform of the density of the induced current of medium electrons and $\mathbf{v}$ is the velocity of our fast particle (we use the system of units where $h = c = 1$).

In the x-ray frequency range, which is considered here,

$$I \ll \omega \ll m, \quad (2)$$

where I is the mean ionization potential of an atom and m is the electron mass. In this case, the atomic electrons involved in the scattering of the pseudophoton field of the incident particle by an atom can be treated as nearly free particles, while the Compton shift of the scattered-pseudophoton frequency

*e-mail: nnn@bsu.edu.ru

is small. Within the traditional approach in x-ray-scattering theory, the density of the induced medium-electron current must then be defined as [5, 6]

$$\mathbf{j} = -\frac{e^2}{m}\mathbf{A}(\mathbf{r},t)\hat{n}\,,\ \hat{n} = \sum_j \delta(\mathbf{r}-\mathbf{r}_j), \qquad (3)$$

where $\mathbf{A}$ is the vector potential of the electromagnetic field and $\mathbf{r}_j$ is the radius vector of the jth medium electron; summation in (3) is performed over all medium electrons. It is important that the coordinates of atomic electrons remain nearly constant throughout the time of a collision between a relativistic incident particle and a medium atom.

From (1) and (3), we obtain the equation

$$(k^2-\omega^2)\mathbf{E}_{\omega\mathbf{k}} - \mathbf{k}(\mathbf{k}\mathbf{E}_{\omega\mathbf{k}}) \qquad (4)$$
$$+\int d^3k' G(\mathbf{k}'-\mathbf{k})\mathbf{E}_{\omega\mathbf{k}'} = \frac{i\omega e}{2\pi^2}\mathbf{v}\delta(\omega-\mathbf{k}\cdot\mathbf{v}),$$

$$G(\mathbf{k}'-\mathbf{k}) = \frac{e^2}{2\pi^2 m}\sum_j e^{i(\mathbf{k}'-\mathbf{k})\cdot\mathbf{r}_j},$$

which makes it possible to take into account, in the simplest way, both the collective and the individual contribution of medium electrons to the elastic scattering of the pseudophoton field of a fast particle moving in a medium.

In the function $G(\mathbf{k}'-\mathbf{k})$, we further isolate the mean component by taking the average over all $\mathbf{r}_j$; that is,

$$G(\mathbf{k}'-\mathbf{k}) \equiv \langle G(\mathbf{k}'-\mathbf{k})\rangle + \tilde{G}(\mathbf{k}'-\mathbf{k}), \qquad (5)$$
$$\langle G(\mathbf{k}'-\mathbf{k})\rangle = \omega_0^2\delta(\mathbf{k}'-\mathbf{k})\,,\ \omega_0^2 = \frac{4\pi e n_0}{m},$$

where n_0 is the mean density of medium electrons. By using this representation, we rewrite Eq. (4) in the form

$$(k^2-k_0^2)\mathbf{E}_{\omega\mathbf{k}'} + \int d^3k'\tilde{G}(\mathbf{k}'-\mathbf{k}) \qquad (6)$$
$$\times\left(\mathbf{E}_{\omega\mathbf{k}'} - \mathbf{k}\frac{\mathbf{k}\cdot\mathbf{E}_{\omega\mathbf{k}'}}{k_0^2}\right)$$
$$= \frac{i\omega e}{2\pi^2}\left(\mathbf{v}-\mathbf{k}\frac{\mathbf{k}\cdot\mathbf{v}}{k_0^2}\right)\delta(\omega-\mathbf{k}\cdot\mathbf{v}),$$

where $k_0^2 = \omega^2\varepsilon(\omega) = \omega^2(1-\omega_0^2/\omega^2)$, $\varepsilon(\omega)$ being the conventional mean dielectric permittivity of the medium.

Assuming that the scattering in question is weak, we will solve Eq. (6) within perturbation theory. The Fourier transform of the scattered field (field of polarization bremsstrahlung) is then given by

$$\mathbf{E}^{PB}_{\omega\mathbf{k}} = -\frac{i\omega e}{2\pi^2}\frac{1}{k^2-k_0^2}\int\frac{d^3k'}{k'^2-k_0^2}\tilde{G}(\mathbf{k}'-\mathbf{k})$$

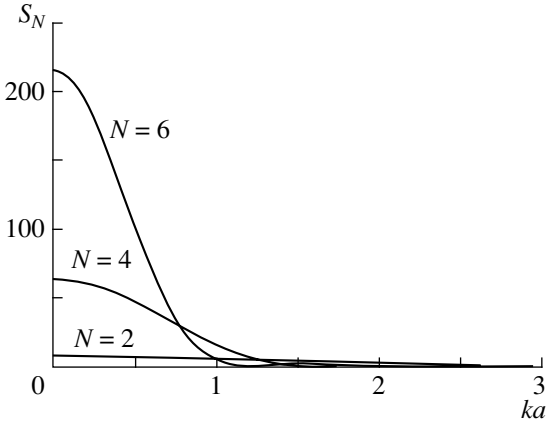

Fig. 1. Crystalline-grain structure factor as a function of momentum transfer.

$$\times\left(\mathbf{v}-\mathbf{k}'\frac{\mathbf{k}'\cdot\mathbf{v}}{k_0^2} - \frac{\mathbf{k}}{k_0^2}\left(\mathbf{k}\cdot\mathbf{v} - \frac{\mathbf{k}\cdot\mathbf{k}'}{k_0^2}\mathbf{k}'\cdot\mathbf{v}\right)\right)$$
$$\times\delta(\omega-\mathbf{k}'\cdot\mathbf{v}). \qquad (7)$$

In order to determine the spectral and angular distribution of the intensity of polarization bremsstrahlung, it is necessary to calculate the Fourier integral

$$\mathbf{E}^{PB}_{\omega} = \int d^3k\, e^{i\mathbf{k}\cdot\mathbf{n}r}\mathbf{E}^{PB}_{\omega\mathbf{k}}, \qquad (8)$$

where $\mathbf{n}$ is a unit vector in the radiation direction.

Evaluating the integral in (8) in the far asymptotic region by the stationary-phase method, we obtain

$$\omega\frac{dN^{PB}}{d\omega d\Omega} = e^2\int\frac{d^3k}{k^2+2k_0\mathbf{n}\cdot\mathbf{k}}\frac{d^3k'}{k'^2+2k_0\mathbf{n}\cdot\mathbf{k}'}$$
$$\times\langle\tilde{G}(\mathbf{k})\tilde{G}^*(\mathbf{k}')\rangle\mathbf{a}_{\mathbf{k}}\cdot\mathbf{a}_{\mathbf{k}'}\delta\left(\omega(1-\sqrt{\varepsilon}\mathbf{n}\cdot\mathbf{v})-\mathbf{k}\cdot\mathbf{v}\right)$$
$$\times\delta\left(\omega(1-\sqrt{\varepsilon}\mathbf{n}\cdot\mathbf{v})-\mathbf{k}'\cdot\mathbf{v}\right), \qquad (9)$$
$$\mathbf{a}_{\mathbf{k}} = \mathbf{v}\frac{\mathbf{k}\cdot\mathbf{v}}{1-\sqrt{\varepsilon}\mathbf{n}\cdot\mathbf{v}} - \mathbf{k}\frac{1}{\varepsilon}$$
$$-\mathbf{n}\left(\mathbf{n}\cdot\mathbf{v}\frac{\mathbf{k}\cdot\mathbf{v}}{1-\sqrt{\varepsilon}\mathbf{n}\cdot\mathbf{v}} - \mathbf{n}\cdot\mathbf{k}\frac{1}{\varepsilon}\right),$$

where angular brackets denote averaging over the coordinates of all medium electrons.

3. SPECTRAL AND ANGULAR DISTRIBUTION OF RADIATION

In order to describe the properties of the radiation under study, we will make use of the general expression (9). First of all, it is necessary to calculate the correlation function $\langle\tilde{G}(\mathbf{k})\tilde{G}^*(\mathbf{k}')\rangle$. We assume that the medium consists of crystals containing N_c atoms that are regularly arranged and which have Z electrons. The density n_c of crystalline grains, the mean density n_a of atoms, and the mean density

n_0 of medium electrons are related by the obvious equations $n_0 = Zn_a = ZN_c n_c$. In the case being considered, the coordinates of a fixed medium electron are given by

$$\mathbf{R}_{jlp} = \mathbf{r}_j + \mathbf{r}_{jl} + \mathbf{u}_{jl} + \mathbf{r}_{jlp}, \tag{10}$$

where $\mathbf{r}_j$ is the radius vector of the jth crystalline grain, $\mathbf{r}_{jl}$ is the radius vector of the equilibrium position of the lth atom in the jth crystalline grain, $\mathbf{u}_{jl}$ is the thermal displacement of this atom, and $\mathbf{r}_{jlp}$ is the coordinate of the pth electron in the atom. In performing the above averaging, we rely on the statistical model of the atom with exponential screening. The result of the averaging has the form

$$\langle \tilde{G}(\mathbf{k})\tilde{G}^*(\mathbf{k}')\rangle = \frac{2e^4 n_c}{\pi m^2}\left[N_c Z\left(1 - \frac{1}{(1+k^2R^2)^2}\right) + N_c Z^2 \frac{1-e^{-k^2u^2}}{(1+k^2R^2)^2}\right. \tag{11}$$
$$\left. + \overline{\left|\sum_{l=1}^{N_c} e^{i\mathbf{k}\cdot\mathbf{r}_{jl}}\right|^2} Z^2 \frac{e^{-k^2u^2}}{(1+k^2R^2)^2}\left(1 - \frac{4\pi n_c}{k}\int_0^\infty d\,r\, r\,\sin(kr)(1-W(r))\right)\right]\delta(\mathbf{k}-\mathbf{k}'),$$

where R is the radius of screening in the Thomas–Fermi model of the atom, u is the root-mean-square amplitude of thermal vibrations of crystalline atoms, the overbar denotes averaging over all possible orientations of a crystalline grain, and $W(r)$ is the probability of finding two crystalline grains at a distance r from each other. This probability is $W(r) \to 1$ for $r \to \infty$ and $W(r) = 0$ for r values less than the crystalline-grain dimensions.

The first term in (11), which is proportional to Z, corresponds to the noncoherent contribution of the medium electrons to the radiation yield. The second represents the electron contribution that is coherent with respect to an individual atom, but which is noncoherent with respect to a crystalline grain. The above formula predicts a suppression of the independent contribution to the polarization-bremsstrahlung yield from the atoms of the partially ordered medium being considered, an effect of great importance indeed. Let us somewhat expand on this point. According to (11), the term being discussed is very small in the momentum-transfer region $k < 1/u$. This effect is fully analogous to the well-known effect of suppression of the noncoherent component of bremsstrahlung from relativistic particles in a crystal [7]. However, the effective momentum transfer in the bremsstrahlung process satisfies the condition $k_{\text{eff}} \approx 1/m \gg 1/u$; therefore, the suppression effect is quite small. In contrast to this, the region $k < 1/u$, where polarization bremsstrahlung is suppressed, overlaps completely the momentum-transfer region $k < 1/R$ (the strong inequality $R \gg u$ is almost always satisfied), which is of importance for the formation of the polarization-bremsstrahlung yield that is coherent with respect to the electrons of an individual atom.

Thus, we can see that, if polarization radiation is generated by a relativistic particle moving through a small-grained medium, the radiation yield is formed owing primarily to the medium-electron contribution that is coherent with respect to an individual crystalline grain. This contribution is described by the last term in expression (11). According to (11), the correlation in the relative arrangement of the crystalline grains leads to a suppression of coherent radiation at low momentum transfers ($k \ll 1/L$, L being the characteristic crystalline-grain dimension), but this effect is manifested at very low frequencies ω that do not satisfy the condition in (2), which is adopted here.

We note that, in the limiting case $u \to \infty$ (which corresponds to an amorphous medium), the second term in (11), which corresponds to a coherent radiation from a fast particle interacting with an individual medium atom, becomes dominant.

The crystalline-grain structure factor in (11) can be represented in the form [5]

$$S(k) = \overline{\left|\sum_{l=1}^{N_c} e^{i\mathbf{k}\cdot\mathbf{r}_{jl}}\right|^2} = \sum_{l,l'=1}^{N_c} \frac{\sin k|\mathbf{r}_{jl} - \mathbf{r}_{jl'}|}{k|\mathbf{r}_{jl} - \mathbf{r}_{jl'}|}. \tag{12}$$

A further simplification is possible only if we choose a specific arrangement of the atoms in a crystalline grain.

Let us consider the simplest model of a crystalline grain having a cubic lattice with N atoms along a face (in this case, $N_c = N^3$ and $L = Na$, a being a lattice constant). From (12), it then follows that

$$S(k) = N^3 S_N(ka) \tag{13}$$
$$= N^3\left[1 + \frac{6}{N^2}\sum_{j=1}^{N}(N-j)f(j) + \frac{12}{N^2}\sum_{j=1}^{N}(N-j)\right.$$
$$\left.\times \sum_{l=1}^{N}(N-l)f(\sqrt{j^2+l^2}) + \frac{8}{N^3}\sum_{j=1}^{N}(N-j)\right.$$

$$\times\sum_{l=1}^{N}(N-l)\sum_{p=1}^{N}(N-p)f(\sqrt{j^2+l^2+p^2})\Bigg],$$

$$f(\sqrt{j^2+l^2+p^2})=\frac{\sin ka\sqrt{j^2+l^2+p^2}}{ka\sqrt{j^2+l^2+p^2}}.$$

The dependence $S_N(ka)$ computed by formula (13) for various values of N is displayed in Fig. 1. The curves in the figure demonstrate a sharp shrinkage of the spectrum of momentum transfers in polarization-bremsstrahlung formation with increasing crystalline-grain size. This result is quite natural, since a crystalline grain appears, in this case, as a large atom whose dimensions specify the coherence region in the radiation.

Substituting (11) and (13) into the general expression (9), we represent the spectral and angular distribution of the polarization-bremsstrahlung intensity in the form

$$\omega\frac{dN^{PB}}{dt\,d\omega d\Omega}\approx\frac{Z^2e^6n_a}{\pi^2m^2}\int\frac{d^3k}{(k^2+2\omega\sqrt{\varepsilon}\mathbf{n}\cdot\mathbf{k})^2}S_N(ka)\frac{e^{-k^2u^2}}{(1+k^2R^2)^2}$$

$$\times\left[(\mathbf{v}^2-(\mathbf{n}\cdot\mathbf{v})^2)\omega^2+(k^2-(\mathbf{n}\cdot\mathbf{k})^2)\frac{1}{\varepsilon^2}-2\frac{\omega}{\varepsilon}(\mathbf{k}\cdot\mathbf{v}-(\mathbf{n}\cdot\mathbf{v})(\mathbf{n}\cdot\mathbf{k}))\right]\delta\left[\omega(1-\sqrt{\varepsilon}\mathbf{n}\cdot\mathbf{v})-\mathbf{k}\cdot\mathbf{v}\right]. \quad (14)$$

It should be borne in mind that, at small observation angles θ ($\mathbf{n}\cdot\mathbf{v}=v\cos\theta$) satisfying the condition $\theta^2\le\rho^2=\gamma^{-2}+\omega_0^2/\omega^2$ [$\gamma=(1-v^2)^{-1/2}$], the bremsstrahlung from a fast electron is dominant. Of greatest interest is therefore the distribution in (14) at large observation angles $\theta^2\gg\rho^2$, where expression (14) assumes the form

$$\omega\frac{dN^{PB}}{dt\,d\omega d\Omega}=\frac{2Z^2e^6n_a}{\pi m^2}F_N(\omega a,\theta,\rho),$$

$$F_N=\int\limits_{1-\cos\theta}^{\infty}dx\,x\,S_N(\omega\,a\,x)\frac{e^{-\omega^2u^2x^2}}{(1+\omega^2R^2x^2)^2}$$

$$\times\Bigg[2\frac{1+\cos^2\theta}{\sqrt{(x^2-2(1-\cos\theta))^2+4\rho^2\sin^2\theta}}-1$$

$$+\frac{x^2-2(1-\cos\theta)}{\sqrt{(x^2-2(1-\cos\theta))^2+4\rho^2\sin^2\theta}}$$

$$-\frac{8\rho^2\sin^2\theta\cos^2\theta}{((x^2-2(1-\cos\theta))^2+4\rho^2\sin^2\theta)^{3/2}}\Bigg], \quad (15)$$

which is convenient for numerically analyzing the properties of polarization bremsstrahlung.

4. DISCUSSION

Proceeding to analyze the result that we obtained, we note that, at $N=1$, expression (15) actually describes polarization bremsstrahlung in an amorphous medium because, in the x region that makes a dominant contribution to the integral in (15), the Debye–Waller factor is $e^{-\omega^2u^2x^2}\approx1$. Therefore, expression (15) makes it possible to trace the transformation suffered by the properties of polarization bremsstrahlung as the degree of ordering in the medium structure becomes greater.

The curves in Fig. 2 represent the dependences $F_N(\omega a)$ that were calculated by formula (15) at fixed values of the parameters ρ and θ for various values of N.

According to our results, the spectra of polarization bremsstrahlung from a relativistic particle moving in an amorphous and a small-grained medium differ markedly. The frequency (ω) region where the response of crystalline-grain electrons to the electromagnetic perturbation generated by a fast particle is coherent shrinks with increasing number of atoms in a crystal grain. Therefore, the spectrum of polarization bremsstrahlung is suppressed in the region of high frequencies, but it grows in the region of low frequences. It should be noted that photoabsorption has a rather strong effect on the measured spectrum of polarization bremsstrahlung from a fast particle moving in a condensed medium. Since photoabsorption is especially pronounced for soft x rays, the effect described in the present study can be observed in an actual experiment as a uniform suppression of polarization bremsstrahlung over the entire spectrum. It is precisely this effect of the total suppression of polarization bremsstrahlung from relativistic electrons moving through a film of diamond-like carbon that was observed in the experiment reported in [4].

From the curves in Fig. 3, we can see that the yield of polarization bremsstrahlung decreases with

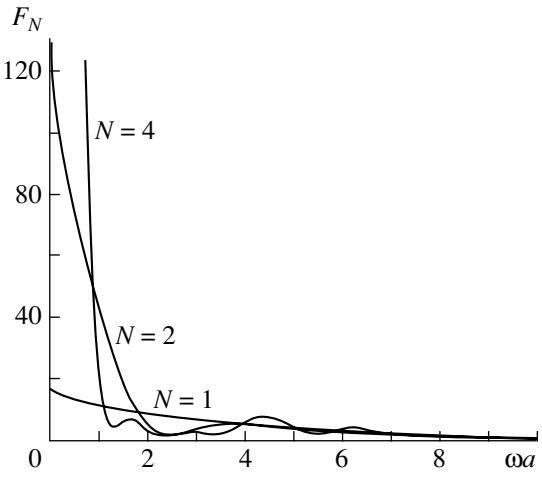

Fig. 2. Normalized spectrum of collimated radiation. The curves were computed for the parameter values of $R/a = 0.1$, $u/R = 0.2$, $\rho \approx \gamma^{-1} = 0.01$, and $\theta = \pi/2$.

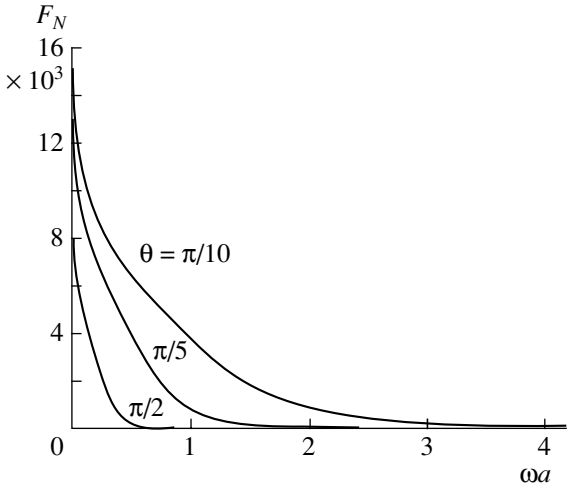

Fig. 3. Normalized spectrum of radiation for various values of the observation angle. The curves were computed for the parameter values of $N = 8$, $R/a = 0.1$, $u/R = 0.2$, and $\rho \approx \gamma^{-1} = 0.01$.

increasing observation angle θ. This is explained by an increase in the momentum transfer in the process, whereby the degree of coherence is reduced.

To conclude, we note that the observed sharp grain-size dependence of the properties of the spectrum of polarization bremsstrahlung from relativistic particles moving through a small-grained medium can be used to develop an efficient method for studying the structure of partly ordered media.

ACKNOWLEDGMENTS

This work was supported by Russian Foundation for Basic Research (project no. 99-02-18183) and by the Ministry for Higher Education of the Russian Federation (grant no. 97-07.2-151).

REFERENCES

1. M. Ya. Amus'ya, V. M. Buĭmistrov, B. A. Zon, *et al., Polarization Bremsstrahlung from Particles and Atoms* (Nauka, Moscow, 1987).
2. N. N. Nasonov, Nucl. Instrum. Methods Phys. Res. B **145**, 19 (1998).
3. S. V. Blazhevich, A. S. Chepurnov, V. K. Grishin, *et al.,* Phys. Lett. A **254**, 230 (1999).
4. S. V. Blazhevich, A. S. Chepurnov, V. K. Grishin, *et al.,* Phys. Lett. A **211**, 309 (1996).
5. R. W. James, *The Optical Principles of the Diffraction of X-rays* (Bell, London, 1950; Inostrannaya Literatura, Moscow, 1950).
6. Z. G. Pinsker, *Dynamical Scattering of X Rays in Perfect Crystals* (Nauka, Moscow, 1974).
7. M. L. Ter-Mikaelian, *High-Energy Electromagnetic Processes in Condensed Media* (Akad. Nauk Arm. SSR, Yerevan, 1969; Wiley, New York, 1972).

Translated by A. Isaakyan

Physics of Atomic Nuclei, Vol. 64, No. 5, 2001, pp. 971–976. Translated from Yadernaya Fizika, Vol. 64, No. 5, 2001, pp. 1042–1047.

XXX International Conference on the Physics of Interaction of Fast Charged Particles with Matter

Effect of Anomalous Photoabsorption on Parametric X-ray Radiation from Relativistic Electrons

C. K. Gary[1], V. V. Kaplin[2], N. N. Nasonov[*], M. A. Piestrup[1], and S. R. Uglov[2]

Belgorod State University, Studencheskaya ul. 12, Belgorod, 306007 Russia

Received November 4, 2000

Abstract—Parametric x-ray radiation from relativistic electrons moving in a crystal is theoretically investigated in Bragg geometry. It is shown that the effect of anomalous photoabsorption can manifest itself within this geometry of the scattering of the pseudophoton field of a fast particle. In this case, the angular distribution of the radiation changes significantly, while the total radiation yield can increase by a factor of 3. © *2001 MAIK "Nauka/Interperiodica".*

1. INTRODUCTION

The effect of anomalously low absorption (Borrmann effect [1]) can occur in the coherent scattering of x rays in a crystal. Theoretical investigations of a similar phenomenon—parametric x-ray radiation, which consists in the coherent scattering of the pseudophoton field of a fast particle moving in a crystal—revealed that there is no Borrmann effect in parametric x-ray radiation [2, 3]. It should be noted that the results presented in [2, 3] were obtained for parametric x-ray radiation in Laue geometry without taking into account the contribution to the formation of the radiation yield from transition radiation emitted by a fast particle at the entrance surface of a crystal. A more detailed analysis showed that anomalous photoabsorption can yet occur in parametric x-ray radiation owing to the Bragg diffraction of the aforementioned transition radiation from a fast electron at the entrance surface of the crystal [4].

Of considerably greater interest is nonetheless the possible manifestation of the Borrmann effect in the scattering of the pseudophoton field of a fast particle, since the yield of this process is proportional to the target thickness, in contrast to the yield of the diffracted transition radiation.

The objective of this study is to analyze in detail parametric x-ray radiation generated by relativistic electrons in a semi-infinite absorbing crystal. In contrast to what was done in [2, 3], we consider here Bragg geometry. Our basic result is the prediction of the Borrmann effect in parametric x-ray radiation under the conditions of the present analysis.

[1]Adelphi Technology, Palo Alto, USA.

[2]Nuclear Physics Institute, Tomsk Polytechnic University, pr. Lenina 2a, Tomsk 50, 634050 Russia.

[*]e-mail: nnn@bsu.edu.ru

2. GENERAL RELATIONS

Let us investigate the structure of the electromagnetic field excited by a relativistic electron moving from a vacuum and entering a crystal that is characterized by the periodically varying dielectric permittivity $\varepsilon(\omega, \mathbf{r}) = 1 + \chi_0(\omega) + \sum_{\mathbf{g}}' \chi_{\mathbf{g}}(\omega) e^{i\mathbf{g}\cdot\mathbf{r}}$, where $\mathbf{g}$ is a set of reciprocal-lattice vectors of the crystal. We assume that the crystal thickness exceeds the photoabsorption length; this makes it possible to consider the crystal as a semi-infinite one.

In order to find the Fourier transform of the excited electric field, $\mathbf{E}_{\omega\mathbf{k}} = (2\pi)^{-4} \int dt d^3r \times \exp(-i\mathbf{k}\cdot\mathbf{r} + i\omega t)\mathbf{E}(\mathbf{r}, t)$, we will make use of the conventional Maxwell equations

$$\left(k^2 - \omega^2\right)\mathbf{E}_{\omega\mathbf{k}} - \mathbf{k}(\mathbf{k}\cdot\mathbf{E}_{\omega\mathbf{k}}) - \omega^2\chi^0\mathbf{E}_{\omega\mathbf{k}} \qquad (1)$$

$$-\omega^2 \sum_g{}' \chi_{-\mathbf{g}}\mathbf{E}_{\omega\mathbf{k}+\mathbf{g}} = \frac{i\omega e}{2\pi^2}\mathbf{v}\delta(\omega - \mathbf{k}\cdot\mathbf{v}),$$

where $\mathbf{v}$ is the velocity of the radiating electron.

Since the susceptibilities satisfy the condition χ_0, $\chi_{\mathbf{g}} \ll 1$ in the x-ray region, Eq. (1) can be solved within the well-known two-wave approximation of the dynamical theory of diffraction [5]. By considering that the components $\mathbf{E}_{\omega\mathbf{k}}$ and $\mathbf{E}_{\omega\mathbf{k}+\mathbf{g}}$ are virtually transverse in the x-ray range of frequencies for relativistic particles [6], we can straightforwardly reduce Eq. (1) to the simple set of equations

$$\left(k^2 - \omega^2 - \omega^2\chi_0\right)E_{\lambda 0} - \omega^2\chi_{-\mathbf{g}}\alpha_\lambda E_{\lambda\mathbf{g}} \qquad (2)$$

$$= \frac{i\omega e}{2\pi^2}\mathbf{e}_{\lambda 0}\cdot\mathbf{v}\delta(\omega - \mathbf{k}\cdot\mathbf{v}),$$

$$\left((\mathbf{k}+\mathbf{g})^2 - \omega^2 - \omega^2\chi_0\right)E_{\lambda\mathbf{g}} = \omega^2\chi_{\mathbf{g}}\alpha_\lambda E_{\lambda 0},$$

1063-7788/01/6405-0971$21.00

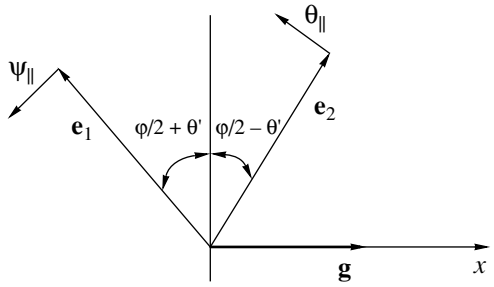

Fig. 1. Geometry of scattering.

where the as-yet-undefined quantities are given by

$$\mathbf{E}_{\omega\mathbf{k}} = \sum_{\lambda=1}^{2} \mathbf{e}_{\lambda 0} E_{\lambda 0}, \quad \mathbf{E}_{\omega\mathbf{k}+\mathbf{g}} = \sum_{\lambda=1}^{2} \mathbf{e}_{\lambda\mathbf{g}} E_{\lambda\mathbf{g}},$$
$$\mathbf{e}_{10} = \mathbf{e}_{1\mathbf{g}} = \frac{[\mathbf{k}_\parallel \times \mathbf{e}_x]}{k_\parallel}, \quad \mathbf{e}_{20} = \frac{[\mathbf{k} \times \mathbf{e}_{10}]}{k},$$
$$\mathbf{e}_{2\mathbf{g}} = \frac{[\mathbf{k}+\mathbf{g} \times \mathbf{e}_{10}]}{|\mathbf{k}+\mathbf{g}|}, \tag{3}$$
$$\alpha_1 = 1, \quad \alpha_2 = \mathbf{k}\cdot(\mathbf{k}+\mathbf{g})/k\,|\mathbf{k}+\mathbf{g}|,$$
$$\mathbf{k} = \mathbf{k}_\parallel + \mathbf{e}_x k_x, \quad \mathbf{e}_x \cdot \mathbf{k}_\parallel = 0.$$

Equations (2) describe the field in the target. The corresponding equations for this field in a vacuum (beyond the target),

$$\left(k^2 - \omega^2\right) E^v_{\lambda 0} = \frac{i\omega e}{2\pi^2} \mathbf{e}_{\lambda 0} \cdot \mathbf{v} \delta\left(\omega - \mathbf{k}\cdot\mathbf{v}\right), \tag{4}$$
$$\left(k_\mathbf{g}^2 - \omega^2\right) E^v_{\lambda g} = 0,$$

follow from (2) in the limit $\chi_0 = \chi_\mathbf{g} = 0$. Here, we have $\mathbf{k}_\mathbf{g} = \mathbf{k} + \mathbf{g}$. Below, we assume that the reflecting crystallographic plane is parallel to the crystal surface. The reciprocal-lattice vector $\mathbf{g}$ is then parallel to the normal $\mathbf{e}_x$ to the crystal surface (see Fig. 1).

The radiation field $E^v_{\lambda\mathbf{g}}$ is determined as a solution to the corresponding equation in (4). The result is

$$E^v_{\lambda\mathbf{g}} = a_{\lambda\mathbf{k}_\parallel} \delta\left(k_{\mathbf{g}x} - p\right), \quad p = \sqrt{\omega^2 - k_\parallel^2}. \tag{5}$$

In order to determine an unknown coefficient $a_{\lambda\mathbf{k}_\parallel}$, it is necessary to find solutions to the remaining equations in (2) and (4) and to employ conventional boundary conditions for the electromagnetic field at the target surface. Considering that, in the x-ray frequency range, the photon wave vector in a vacuum differs insignificantly from that in a crystal, we introduce the variable ξ through the relation

$$k_{\mathbf{g}x} = p + \xi, \quad \xi \ll g. \tag{6}$$

By using relation (6), we can represent solutions to Eqs. (2) and (4) in the form

$$E_{\lambda\mathbf{g}} = b_{\lambda\mathbf{k}_\parallel} \delta\left(\xi - \xi_*\right) \tag{7}$$
$$- \frac{i\omega e}{2\pi^2} \frac{\omega^2 \chi_\mathbf{g} \alpha_\lambda}{4p^2\,|v_x|} \frac{\mathbf{e}_{\lambda 0}\cdot\mathbf{v}}{(\xi-\xi_1)(\xi-\xi_2)} \delta\left(\xi - \xi_0\right),$$
$$E_{\lambda 0} = \frac{2p}{\omega^2 \chi_\mathbf{g} \alpha_\lambda} \left(\xi - \frac{\omega^2}{2p}\chi_0\right) E_{\lambda\mathbf{g}},$$
$$E^v_{\lambda 0} = \frac{i\omega e}{2\pi^2} \frac{1}{2p\,|v_x|} \frac{\mathbf{e}_{\lambda 0}\cdot\mathbf{v}}{\Delta - \xi} \delta\left(\xi - \xi_0\right),$$

where

$$\xi_{1,2} = \frac{1}{2}\left(\Delta \pm \sqrt{\left(\Delta - \frac{\omega^2}{p}\chi_0\right)^2 - \beta_\lambda^2}\right), \tag{8}$$
$$\xi_0 = \frac{1}{v_x}\left(\omega - \mathbf{k}_\parallel\cdot\mathbf{v}_\parallel + p v_x\right) + \Delta,$$
$$\beta_\lambda^2 = \frac{\omega^4}{p^2} \chi_\mathbf{g} \chi_{-\mathbf{g}} \alpha_\lambda^2, \quad \Delta = g\left(\frac{g}{2p} - 1\right) \ll g.$$

In the case of the Bragg geometry of scattering (and we consider precisely this case), the quantity ξ_* is determined by the relations

$$\xi_* = \begin{cases} \xi_2 \text{ for } \left(\Delta - \dfrac{\omega^2}{p}\chi_0\right)^2 < \beta_\lambda^2 \\ \xi_1 \text{ for } \left(\Delta - \dfrac{\omega^2}{p}\chi_0\right)^2 > \beta_\lambda^2, \Delta - \dfrac{\omega^2}{p}\chi_0 > 0 \\ \xi_2 \text{ for } \left(\Delta - \dfrac{\omega^2}{p}\chi_0\right)^2 > \beta_\lambda^2, \ \Delta - \dfrac{\omega^2}{p}\chi_0 < 0. \end{cases} \tag{9}$$

By using Eqs. (5) and (7) and the boundary conditions

$$\int d\xi \left(E_{\lambda 0} - E^v_{\lambda 0}\right) = \int d\xi \left(E_{\lambda\mathbf{g}} - E^v_{\lambda\mathbf{g}}\right) = 0, \tag{10}$$

we find that the coefficient $a_{\lambda\mathbf{k}_\parallel}$ is given by the expression

$$a_{\lambda\mathbf{k}_\parallel} = \frac{i\omega e}{2\pi^2} \frac{\omega^2 \chi_\mathbf{g} \alpha_\lambda}{4p^2\,|v_x|} \frac{\mathbf{e}_{\lambda 0}\cdot\mathbf{v}}{\xi_* - \frac{\omega^2}{2p}\chi_0} \tag{11}$$
$$\times \left(\frac{\xi_0 - \xi_*}{(\xi_0 - \xi_1)(\xi_0 - \xi_2)} - \frac{1}{\xi_0 - \Delta}\right),$$

which completely describes the properties of the radiation field.

3. CONTRIBUTION OF PARAMETRIC X RAYS: EFFECT OF ANOMALOUS PHOTOABSORPTION

In order to find the spectral and angular distribution of the radiation in question, we make use of the general expression (11). In order to determine the radiation amplitude A_λ, we apply the stationary-phase method to compute the Fourier integral

$$E_\lambda^{\text{rad}} = \int d^3 k_\mathbf{g} e^{i\mathbf{k}_\mathbf{g}\cdot\mathbf{n}r} E^v_{\lambda\mathbf{g}} \to A_\lambda \frac{e^{i\omega r}}{r}, \tag{12}$$
$$A_\lambda = -2\pi i \omega n_x a_{\lambda\omega\mathbf{n}_\parallel},$$

where $\mathbf{n} = \mathbf{n}_\parallel + \mathbf{e}_x n_x$ is a unit vector in the direction of radiation, $\mathbf{e}_x \cdot \mathbf{n}_\parallel = 0$.

For the purposes of the ensuing analysis, it is convenient to define the angular variables $\boldsymbol{\theta}$ and $\boldsymbol{\psi}$ through the relations (see Fig. 1)

$$\mathbf{v} = e_1\left(1 - \frac{1}{2}\gamma^{-2} - \frac{1}{2}\psi^2\right) + \boldsymbol{\psi}, \quad \mathbf{e}_1 \cdot \boldsymbol{\psi} = 0,$$
$$\mathbf{n} = \mathbf{e}_2\left(1 - \frac{1}{2}\theta^2\right) + \boldsymbol{\theta}, \qquad (13)$$
$$\mathbf{e}_2 \cdot \boldsymbol{\theta} = 0, \quad \mathbf{e}_1 \cdot \mathbf{e}_2 = \cos\varphi$$

and the dielectric susceptibilities χ_0 and $\chi_\mathbf{g}$ as

$$\chi_0 = -\frac{\omega_0^2}{\omega^2} + i\chi_0'', \qquad (14)$$
$$\chi_\mathbf{g} = \chi_{-\mathbf{g}} = -\frac{\omega_\mathbf{g}^2}{\omega^2} + i\chi_\mathbf{g}'',$$

where ω_0 is the plasmon frequency and $\omega_\mathbf{g}^2 = \omega_0^2 e^{-g^2u^2}(F(\mathbf{g})/Z)$, u, $F(\mathbf{g})$, and Z being, respectively, the root-mean-square amplitude of thermal vibrations of the atoms, the atomic form factor, and the number of electrons in an atom; we consider here a reflection for which the lattice structure factor is equal to unity.

From Eqs. (11)–(14), it follows that the spectral and angular distribution of the radiation being studied can be represented as

$$\omega\frac{dN_\lambda}{d\omega d^2\theta} = \frac{e^2}{\pi^2}\frac{\Omega_\lambda^2}{|\tau_\lambda \pm f_\lambda - i\delta_\lambda|^2}\left|A_\lambda^{\mathrm{PXR}} + A_\lambda^{\mathrm{DTR}}\right|^2,$$
$$A_\lambda^{\mathrm{PXR}} = \frac{\omega_\mathbf{g}^2}{\omega^2}|\alpha_\lambda|\frac{\tau_\lambda \pm f_\lambda}{\left(\gamma^{-2} + \frac{\omega_0^2}{\omega^2} + \Omega^2\right)\left(\gamma^{-2} + \frac{\omega_0^2}{\omega^2} + \Omega^2 - \frac{\omega_\mathbf{g}^2}{\omega^2}|\alpha_\lambda|(\tau_\lambda \pm f_\lambda)\right)}, \qquad (15)$$
$$A_\lambda^{\mathrm{DTR}} = \frac{1}{\gamma^{-2} + \frac{\omega_0^2}{\omega^2} + \Omega^2} - \frac{1}{\gamma^{-2} + \Omega^2},$$

where

$$\tau_\lambda = \frac{g^2}{2\omega_\mathbf{g}^2|\alpha_\lambda|}\left(\frac{g}{2\omega n_x} - 1 + 2\frac{\omega_0^2}{g^2}\right),$$
$$f_\lambda = \sqrt{\tau_\lambda^2 - 1 - 2i\delta_\lambda(\tau_\lambda - \kappa_\lambda)},$$
$$\delta_\lambda = \frac{\omega^2}{2\omega_\mathbf{g}^2|\alpha_\lambda|}\chi_0'', \quad \kappa_\lambda = \frac{\chi_\mathbf{g}''}{\chi_0''}|\alpha_\lambda|, \qquad (16)$$
$$\Omega_1 = \theta_\perp - \psi_\perp, \quad \Omega_2 = 2\theta' + \theta_\parallel + \psi_\parallel,$$
$$\Omega^2 = \Omega_1^2 + \Omega_2^2, \quad \alpha_1 = 1, \quad \alpha_2 = \cos\varphi.$$

In Eq. (15), the quantities A_λ^{PXR} and A_λ^{DTR} represent the contributions of, respectively, parametric x rays and diffracted transition radiation (DTR) [7]. The plus (minus) sign corresponds to the case of $\xi_* = \xi_1$ ($\xi_* = \xi_2$) [see Eq. (9)].

Let us first consider the contribution of parametric x rays to the total radiation yield. According to (15), this contribution is given by

$$\omega\frac{dN_\lambda^{\mathrm{PXR}}}{d\omega d^2\theta} = \frac{e^2}{\pi^2}\frac{\omega_\mathbf{g}^4}{\omega^4}\frac{\Omega_\lambda^2\alpha_\lambda^2}{\left(\gamma^{-2} + \frac{\omega_0^2}{\omega^2} + \Omega^2\right)} \qquad (17)$$
$$\times\left|\gamma^{-2} + \frac{\omega_0^2}{\omega^2} + \Omega^2 - \frac{\omega_\mathbf{g}^2}{\omega^2}|\alpha_\lambda|(\tau_\lambda \pm f_\lambda)\right|^{-2}.$$

It can easily be seen that the dependence of the distribution in (17) on the emitted-photon energy ω is associated primarily with the fast variable $\tau_\lambda(\omega)$ from (16), which shows that, at fixed values of the orientation angle θ' and of the observation angle $\theta_\parallel$, the spectrum of parametric x rays is concentrated in the vicinity of the frequency $\omega_\mathrm{B}' = \omega_\mathrm{B}\left(1 + \left(\theta' + \theta_\parallel\right)\cot(\varphi/2)\right)$, where $\omega_\mathrm{B} = g/2 \times \sin(\varphi/2)$ is the Bragg frequency, the relative frequency of the spectrum being very small: $\Delta\omega/\omega \sim 2\omega_\mathbf{g}^2/g^2 \sim 10^{-4}$.

For the ensuing analysis, it is convenient to separate the real and the imaginary part of the function f_λ:

$$f_\lambda = \begin{cases} f_\lambda' - i\,\mathrm{sgn}(\tau_\lambda - \kappa_\lambda) f_\lambda'', & \text{for } \tau_\lambda^2 > 1 \\ -\mathrm{sgn}(\tau_\lambda - \kappa_\lambda) f_\lambda' + i f_\lambda'' & \text{for } \tau_\lambda^2 < 1, \end{cases}$$
$$f_\lambda' = \frac{1}{\sqrt{2}}\sqrt{\sqrt{\left(\tau_\lambda^2 - 1\right)^2 + 4\delta_\lambda^2(\tau_\lambda - \kappa_\lambda)^2} + \tau_\lambda^2 - 1},$$
$$f_\lambda'' = \frac{1}{\sqrt{2}}\sqrt{\sqrt{\left(\tau_\lambda^2 - 1\right)^2 + 4\delta_\lambda^2(\tau_\lambda - \kappa_\lambda)^2} - \tau_\lambda^2 + 1}. \qquad (18)$$

We note that, because of the smallness of the absorption factor ($\delta_\lambda \ll 1$), the function f_λ'' is small in the region of normal dispersion ($\tau_\lambda^2 > 1$) and that

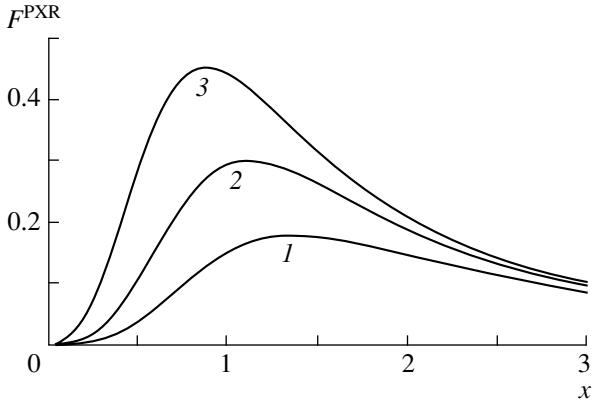

Fig. 2. Normalized angular distribution of parametric x rays with allowance for anomalous photoabsorption at $q_\lambda = 0.8$ and $x = \gamma_*\Omega$ for $\kappa_\lambda = (1)\,0, (2)\,0.7$, and $(3)\,0.95$.

the function $f_\lambda^{'}$ is small in the region of anomalous dispersion ($\tau_\lambda^2 < 1$). With allowance for Eqs. (9) and (18), expression (17) can be recast into the simple form

$$\omega\frac{dN_\lambda^{PXR}}{d\omega d^2\theta} = \frac{e^2}{\pi^2}\frac{\Omega_\lambda^2}{\left(\gamma^{-2}+\gamma_*^{-2}+\Omega^2\right)^2}R_\lambda^{PXR}(\tau_\lambda),$$

$$R_\lambda^{PXR} = \left[\left(p_\lambda - \tau_\lambda - \mathrm{sgn}(\tau_\lambda - \kappa_\lambda)\,f_\lambda^{'}\right)^2 + \left(f_\lambda^{''}\right)^2\right]^{-1}, \quad (19)$$

where

$$\gamma_* = \omega_B/\omega_0, \quad p_\lambda = \frac{\gamma^{-2}+\gamma_*^{-2}+\Omega^2}{\omega_{\mathbf{g}}^2\,|\alpha_\lambda|/\omega_B^2}. \quad (20)$$

The above result demonstrates the physical essence of parametric x-ray radiation as the coherent Bragg scattering of the screened Coulomb field of a fast electron by a set of atomic crystal planes. Indeed, the factor appearing in front of the function R_λ^{PXR} in (19) describes the spectral and angular distribution of the Coulomb field of a particle in a medium whose mean dielectric permittivity is $\varepsilon(\omega) = 1 - \omega_0^2/\omega^2$ (in the vicinity of the Bragg frequency, $\omega \approx \omega_B$), while the quantity R_λ^{PXR} can be treated as the coefficient of reflection of this field by a crystal.

It can easily be shown that the denominator of the function $R_\lambda^{PXR}(\tau_\lambda(\omega))$ has a resonance character in the region of frequencies ω that correspond to the condition $\tau_\lambda(\omega) > 1$; that is, parametric x rays are formed in the region of normal dispersion. The position and the height of the peak of parametric x-ray radiation are determined by the single generalized parameter p_λ (20), which is greatly dependent on the radiating-particle energy, the photon-observation angle, and the orientation angle. Since the spectral width of the peak of parametric x-ray radiation is $\Delta\omega \sim 1$ eV at a fixed value of the parameter p_λ, the approximation

$$R_\lambda^{PXR} \to \frac{\pi}{f_\lambda^{''}}\delta\left(p_\lambda - \tau_\lambda - f_\lambda^{'}\right) \quad (21)$$

is sufficient for describing experiments that employ conventional x-ray detectors with an energy resolution of about 100 eV.

Considering that the absorption factor δ_λ is small, we find from (19) and (21) that

$$\omega\frac{dN_\lambda^{PXR}}{d\omega d^2\theta} = \frac{e^2\omega_{\mathbf{g}}^4}{\pi g^2}\frac{1}{\omega\chi_0^{''}}\frac{\left(1-1/p_\lambda^2\right)^2}{\left(1-1/p_\lambda^2\right)^2 + 2\left(1-\kappa_\lambda\right)/p_\lambda} \times \frac{\Omega_\lambda^2 - \alpha_\lambda^2}{\left(\gamma^{-2}+\gamma_*^{-2}+\Omega^2\right)^2}\delta(\omega - \omega_B). \quad (22)$$

This expression differs from the traditional formula in the kinematical theory of parametric x rays [8, 9] only by a factor that involves the parameters p_λ and κ_λ.

It can easily be seen that only in the region of sufficiently high radiating-particle energies can dynamical-scattering effects manifest themselves. To demonstrate this, we note that, in the region of low energies,

$$\gamma \ll \gamma_*, \quad (23)$$

it follows from (20) that $p_\lambda \gg 1$, irrespective of the observation-angle value. Expression (22) then coincides with that in kinematical theory.

In the energy region where the condition opposite to (23) is satisfied, the parameter p_λ is on the order of unity for observation angles in the region $\Omega_\lambda \leqslant \gamma_*^{-1}$, where the bulk of the radiation is concentrated. In this case, the distribution in (22) is extremely sensitive to variations in the parameter κ_λ. In order to demonstrate this, we consider, for $\gamma \gg \gamma_*$, the angular distribution of parametric x rays that follows from (22). We have

$$\omega\frac{dN_\lambda^{PXR}}{dxx} = \frac{e^2\omega_{\mathbf{g}}^4\alpha_\lambda^2\sin^2(\varphi/2)}{g^4\chi_0^{''}}F^{PXR}(x,\kappa_\lambda,q_\lambda), \quad (24)$$

$$F^{PXR} = \frac{x^2}{\left(1-q_\lambda+x^2\right)^2 + 2q_\lambda\left(1-\kappa_\lambda\right)\left(1+x^2\right)} \times \left(1 - \frac{q_\lambda^2}{\left(1+x^2\right)^2}\right)^2,$$

where $x = \gamma_*\Omega$ and $q_\lambda = e^{-g^2u^2/2}\left(F(\mathbf{g})/Z\right)|\alpha_\lambda|$. The function F^{PXR} calculated for a strong reflection ($q_\lambda \approx 1$) is illustrated by the curves in Fig. 2, which

are plotted for various values of the parameter κ_λ. We can see that the polarization-bremsstrahlung yield grows significantly as κ_λ tends to unity, and this is the main result of the present study.

The effect being discussed is similar to the anomalous photoabsorption of x rays in a crystal [1]. The latter is manifested in the Bragg diffraction of x rays under the condition $\kappa_\lambda \approx 1$. In the diffraction of the pseudophoton field of a fast particle—it is precisely the case considered here—the effective absorption factor f_λ'' also decreases for $\kappa_\lambda \to 1$. It is important to note that, according to formula (18), which determines the dependence $f_\lambda''(\tau_\lambda)$ (for example, we have $f_\lambda'' \simeq \delta_\lambda\sqrt{(\tau_\lambda-1)/(\tau_\lambda+1)}$ in the limiting case of $\kappa_\lambda = 1$), the above suppression of photoabsorption is realized only near the region of anomalous dispersion, $\tau_\lambda(\omega) \approx 1$. In accordance with (21), the position of the maximum in the spectral distribution of parametric x-ray radiation is determined by the parameter p_λ [the corresponding value is $\tau_\lambda = \tau_\lambda^* \approx (p_\lambda^2+1)/2p_\lambda$]. At low radiating-particle energies that satisfy the condition in (23), the parameter p_λ is large. In this case, $f_\lambda'' \simeq \delta_\lambda$; that is, the effect of anomalous photoabsorption does not manifest itself in kinematical parametric x-ray radiation. At high energies, $\gamma \gg \gamma_*$, we have $p_\lambda \approx (1+x^2)\, q_\lambda \sim 1$ for strong reflections ($q_\lambda \approx 1$) in the region $x \leqslant 1$, which is of particular interest [see formula (24)]. In this case, the effect of anomalously low photoabsorption, $f_\lambda''(\tau_\lambda^*) \ll \delta_\lambda$, can show up if the coefficient κ_λ is sufficiently close to unity.

4. CONTRIBUTION OF DIFFRACTED TRANSITION RADIATION: INTERFERENCE OF DIFFRACTED TRANSITION RADIATION AND PARAMETRIC X-RAY RADIATION

Returning to the general formula (15), we consider the contribution of diffracted transition radiation, whose spectral and angular distribution can be represented in the form

$$\omega\frac{dN_\lambda^{\mathrm{DTR}}}{d\omega d^2\theta} = \frac{e^2}{\pi^2}\Omega_\lambda^2 \tag{25}$$
$$\times\left(\frac{1}{\gamma^{-2}+\Omega^2} - \frac{1}{\gamma^{-2}+\gamma_*^{-2}+\Omega^2}\right)^2 \times R_\lambda^{\mathrm{DTR}}(\tau_\lambda),$$
$$R_\lambda^{\mathrm{DTR}} = \left[\left(\tau_\lambda + \mathrm{sgn}(\tau_\lambda-\kappa_\lambda)\, f_\lambda'\right)^2 + \left(\delta_\lambda + f_\lambda''\right)^2\right]^{-1},$$

which is similar to that in (19). As follows from formula (25), diffracted transition radiation is generated when transition radiation from a relativistic electron that traverses the entrance surface of the crystal target undergoes Bragg reflection from the crystal [7].

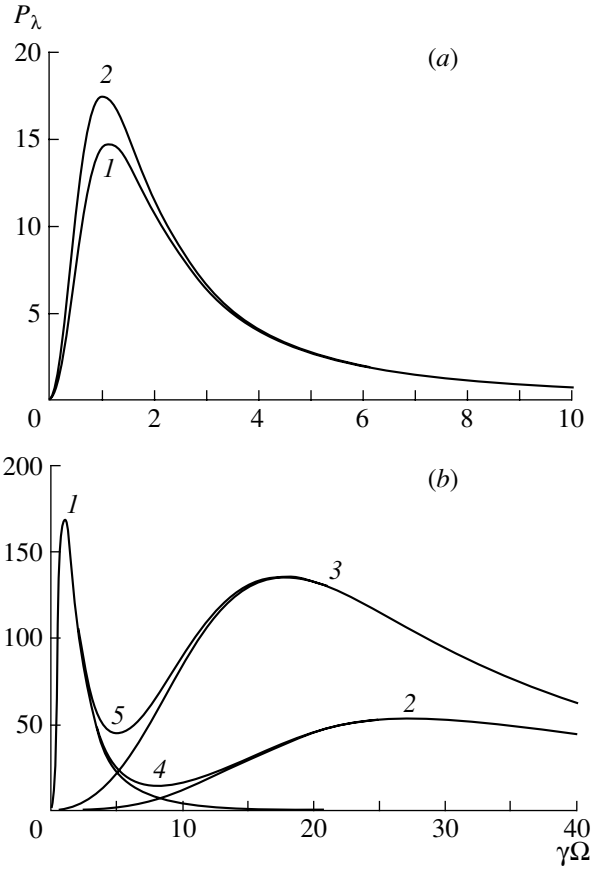

Fig. 3. Normalized angular distributions of parametric x-ray radiation, diffracted transition radiation, and total radiation with and without allowance for anomalous photoabsorption (presented in the figure are the quantities P_λ^{DTR}, P_λ^{PXR}, and $P_\lambda = P_\lambda^{\mathrm{DTR}} + P_\lambda^{\mathrm{PXR}}$ defined by the relations $dN_\lambda^{\mathrm{DTR}}/d^2\theta = A_\lambda P_\lambda^{\mathrm{DTR}}$ and $dN_\lambda^{\mathrm{PXR}}/d^2\theta = A_\lambda P_\lambda^{\mathrm{PXR}}$, where $A_\lambda = e^2 q_\lambda/4\pi\sin(\varphi/2)^2$: (*a*) curves *1* and *2* representing the contribution of parametric x rays at $\kappa_\lambda = 0$ and 0.95, respectively, correspond to $q_\lambda = 0.8$, $\gamma_*\chi_0'' = 1/300$, and $\gamma/\gamma_* = 0.5$ (there is virtually no contribution from diffracted transition radiation); (*b*) curves *1*, *2*, *3*, *4*, and *5* representing the contributions of, respectively, diffracted transition radiation, parametric x rays at $\kappa_\lambda = 0$, parametric x rays at $\kappa_\lambda = 0.95$, total radiation at $\kappa_\lambda = 0$, and total radiation at $\kappa_\lambda = 0.95$ correspond to $\gamma/\gamma_* = 20$, all other parameters being identical to those in Fig. 3*a*.

It can easily be shown that the coefficient of reflection R_λ^{DTR} attains a maximum value of about unity in the anomalous-dispersion region $\tau_\lambda^2(\omega) < 1$.

Absorption reduces the yield of diffracted transition radiation; however, it does not play a crucial role, as it does in parametric x-ray radiation from a relativistic particle moving in a semi-infinite medium. The formula for the angular distribution of diffracted

transition radiation—it follows from (25) without taking into account absorption—has the form

$$\frac{dN_\lambda^{\mathrm{DTR}}}{d^2\theta} = \frac{16e^2\omega_{\mathbf{g}}^2|\alpha_\lambda|}{3\pi^2 g^2}\Omega_\lambda^2 \times \left(\frac{1}{\gamma^{-2}+\Omega^2} - \frac{1}{\gamma^{-2}+\gamma_*^{-2}+\Omega^2}\right)^2. \quad (26)$$

This formula and the corresponding formula following from (22) for the angular distribution of parametric x rays make it possible to compare the contributions of the radiation mechanisms under investigation. First of all, we note that our analysis of the interference term in the general formula (15) has revealed that the interference between parametric x-ray radiation and diffracted transition radiation is insignificant.

The expression that follows from (22) and which describes the angular distribution of parametric x rays has the form

$$\frac{dN_\lambda^{\mathrm{PXR}}}{d^2\theta} = \frac{e^2\omega_{\mathbf{g}}^2|\alpha_\lambda|}{\pi g^2}\frac{q_\lambda}{\gamma_*^2\chi_0''}\frac{\Omega_\lambda^2}{\left(\gamma^{-2}+\gamma_*^{-2}+\Omega^2\right)^2} \times \frac{\left(1-1/p_\lambda^2\right)^2}{\left(1-1/p_\lambda\right)^2 + 2\left(1-\kappa_\lambda\right)/p_\lambda}, \quad (27)$$

where $p_\lambda = \left(\gamma^{-2}+\gamma_*^{-2}+\Omega^2\right)/q_\lambda\gamma_*^{-2}$.

In order to compare the dependences in (26) and (27), it is convenient to choose the quantity $\gamma\Omega$ for an angular variable. In this case, the ratio γ/γ_* becomes the main parameter in both distributions. The distributions calculated on the basis of (26) and (27) are displayed in Fig. 3, along with the computed distribution of the total radiation. The curves presented in this figure demonstrate that parametric x-ray radiation is dominant at low radiating-particle energies $\gamma < \gamma_*$ such that the effect of anomalous photoabsorption is not manifested here. At the same time, we can see that, at energies so high that $\gamma \gg \gamma_*$, the contribution of diffracted transition radiation dominates the observation-angle region $\Omega \leqslant \gamma_*^{-1}$, while the peak of parametric x-ray radiation is formed near the observation-angle value of $\Omega \approx \gamma_*^{-1}$. From these curves, we also see that the yield of parametric x-ray radiation increases considerably under the conditions where the effect of anomalous photoabsorption manifests itself and that the peak in the angular distribution of parametric x-ray radiation is shifted to the region of small observation angles.

ACKNOWLEDGMENTS

This work was supported in part by the Russian Foundation for Basic Research (project no. 00-02-16388) and by the program Russian Universities—Basic Research (grant no. 991702).

REFERENCES

1. G. Borrmann, Z. Phys. **42**, 1157 (1941).
2. V. A. Bazylev and N. K. Zhevago, *Radiation from Fast Particles in Matter and in External Fields* (Nauka, Moscow, 1987).
3. A. Caticha, Phys. Rev. B **45**, 9541 (1992).
4. N. Nasonov, Phys. Lett. A **260**, 391 (1999).
5. Z. G. Pinsker, *Dynamical Scattering of X Rays in Perfect Crystals* (Nauka, Moscow, 1974).
6. A. M. Afanas'ev and M. A. Aginyan, Zh. Éksp. Teor. Fiz. **74**, 570 (1978) [Sov. Phys. JETP **47**, 300 (1978)].
7. A. Caticha, Phys. Rev. A **40**, 4322 (1989).
8. M. L. Ter-Mikaelian, *High-Energy Electromagnetic Processes in Condensed Media* (Akad. Nauk Arm. SSR, Yerevan, 1969; Wiley, New York, 1972).
9. I. D. Feranchuk and A. V. Ivashin, J. Phys. (Paris) **46**, 1981 (1985).

Translated by A. Isaakyan

Physics of Atomic Nuclei, Vol. 64, No. 5, 2001, pp. 977–982. Translated from Yadernaya Fizika, Vol. 64, No. 5, 2001, pp. 1048–1053.

XXX International Conference on the Physics of Interaction of Fast Charged Particles with Matter

Transformation of Operator Equations Describing the Interaction of Relativistic Particles with an Electric Field

A. J. Silenko*

Institute of Nuclear Problems, Belarussian State University, Minsk, Belarus

Received November 4, 2000

Abstract—A method is developed for solving relativistic wave equations for the Hamiltonian in the Foldy–Wouthuysen representation. These equations are recast into a quadratic form, whereby we get rid of square roots of operators. Applications of the method are exemplified by considering the interaction of a particle with a field characterized by a harmonic potential. © *2001 MAIK "Nauka/Interperiodica".*

1. INTRODUCTION

The Foldy–Wouthuysen representation is very convenient for studying the interaction of relativistic particles with an external field—in particular, in a situation where a charged particle moves through a crystal [1]. This representation is advantageous above all in that the operators of physical observables (like coordinate, momentum, spin, and angular momentum) are given by expressions that fully correspond to analogous operators in nonrelativistic quantum mechanics. This circumstance substantially simplifies a derivation of the equations of motion for a particle and a spin. However, solving relativistic wave equations in the Foldy–Wouthuysen representation is significantly complicated by the fact that the expression for the Hamiltonian $\mathcal{H}$ involves square roots of operators. For example, the equation involving the Hamiltonian for a free spin-1/2 particle has the form[1)]

$$\mathcal{H}\Psi = \rho_3\sqrt{\mathbf{p}^2+m^2}\Psi, \quad \rho_3 = \begin{pmatrix} 1 & 0 \\ 0 & -1 \end{pmatrix}, \qquad (1)$$

where Ψ is the wave function (bispinor) in the Foldy–Wouthuysen representation, $\mathbf{p} = -i\nabla$ is the momentum operator, and ρ_3 is a Pauli matrix. Here, 0, ± 1 represent the relevant 2×2 matrices acting on spinor components.

Naturally, the square root of operators is also present in expressions describing the interaction of particles in an external field. In order to obtain a quantum-mechanical solution to the problem, it is necessary to recast an equation of the type in (1) to a quadratic form not involving a square root of operators. It is important to solve this problem, in particular, for studying the interaction of relativistic charged particles with crystals. For example, it was the quadratic form of a relativistic wave equation in the Foldy–Wouthuysen representation that was used in [2] in a quantum-mechanical treatment of the rotation of the spin of a channeling particle.

A method that makes it possible to go over to a quadratic form of a relativistic wave equation is proposed in the present study. This method also permits solving the inverse problem—that of going over from a quadratic form of a relativistic wave equation to an equation for the Hamiltonian. The latter is of importance for spinless particles.

2. OPERATOR SQUARING

Let us consider the simplest case for the problem in question, that of the equation for the Hamiltonian describing a spin-1/2 particle in an external field. We have

$$i\frac{\partial}{\partial t}\Psi = \mathcal{H}\Psi, \quad \mathcal{H}\Psi = \left[\rho_3\sqrt{\mathbf{p}^2+m^2} + V(\mathbf{r})\right]\Psi, \qquad (2)$$

where $V(\mathbf{r})$ is the operator that represents the energy of particle interaction with the field. We assume that the external field is time-independent ($\partial V/\partial t = 0$), in which case the total particle energy E is constant and is one of the eigenvalues of the Hamiltonian:

$$\mathcal{H}\Psi = E\Psi.$$

For $V(\mathbf{r}) = V_0 = \text{const}$, a reduction of Eq. (2) to a quadratic form is performed by means of operator squaring, which is possible owing to the commutativity of the operators $\sqrt{\mathbf{p}^2+m^2}$ and V_0. Let us

*e-mail: silenko@inp.minsk.by

[1)]Use is made here of the relativistic system of units where $\hbar = c = 1$.

rearrange all operator terms to the left-hand side of the equation:

$$\left[i\frac{\partial}{\partial t} - V_0 - \rho_3\sqrt{\mathbf{p}^2+m^2}\right]\Psi = 0.$$

Multiplying the resulting equation from the left by the operator

$$i\frac{\partial}{\partial t} - V_0 + \rho_3\sqrt{\mathbf{p}^2+m^2},$$

we obtain the required quadratic equation in the form

$$\left[(i\frac{\partial}{\partial t} - V_0)^2 - \mathbf{p}^2 - m^2\right]\Psi = 0. \qquad (3)$$

For stationary states, the operator $i(\partial/\partial t)$ can be replaced by the energy E, whereupon Eq. (3) assumes the form

$$\left[\mathbf{p}^2 + m^2 - (E - V_0)^2\right]\Psi = 0. \qquad (4)$$

However, this simple method does not work when the interaction energy V depends on $\mathbf{r}$. In this case, a multiplication of the equation

$$\left[i\frac{\partial}{\partial t} - V(\mathbf{r}) - \rho_3\sqrt{\mathbf{p}^2+m^2}\right]\Psi = 0 \qquad (5)$$

from the left by the operator

$$i\frac{\partial}{\partial t} - V(\mathbf{r}) + \rho_3\sqrt{\mathbf{p}^2+m^2}$$

yields

$$\left\{\left[i\frac{\partial}{\partial t} - V(\mathbf{r})\right]^2 - \mathbf{p}^2 - m^2 \right. \qquad (6)$$
$$\left. - \left[\rho_3\sqrt{\mathbf{p}^2+m^2}, V(\mathbf{r})\right]\right\}\Psi = 0,$$

where $[\ldots,\ldots]$ stands for a commutator. Different methods for reducing Eq. (2) to a quadratic form by squaring, such as a multiplication of Eq. (5) from the left by the operator

$$i\frac{\partial}{\partial t} - V(\mathbf{r}) - \rho_3\sqrt{\mathbf{p}^2+m^2},$$

also lead to Eq. (6). For stationary states, it can be represented as

$$\left\{\mathbf{p}^2 + m^2 + 2EV(\mathbf{r}) - [V(\mathbf{r})]^2 \right. \qquad (7)$$
$$\left. + \left[\rho_3\sqrt{\mathbf{p}^2+m^2}, V(\mathbf{r})\right]\right\}\Psi = E^2\Psi.$$

It can easily be seen that Eqs. (6) and (7) are non-Hermitian, since they involve the anti-Hermitian operator $\left[\rho_3\sqrt{\mathbf{p}^2+m^2}, V(\mathbf{r})\right]$. In accordance with the general properties of operator equations, the eigenfunctions Ψ_i of such equations do not form an orthogonal set of functions, while the eigenvalues E_i^2 of the braced operator on the left-hand side of Eq. (7) are complex. It follows that only when the above anti-Hermitian operator can be disregarded is it possible to go over to a quadratic form of a relativistic wave equation by means of squaring. Obviously, this operator is not always negligible. A method that enables one to go over to a quadratic form and which is free from the above flaw is described in the next section.

3. RELATION BETWEEN THE QUADRATIC AND THE LINEAR FORM OF RELATIVISTIC WAVE EQUATIONS

In order to implement a correct transition to a quadratic form of relativistic wave equations, we will establish a relation between relevant quadratic and linear equations. For this, we will make use of the method for linearizing quadratic equations that was developed for spinless particles (see [3]). The external field will be assumed to be time-independent.

Let us consider a general relativistic wave equation in the quadratic form

$$\left[(\mathcal{E} - V)^2 - (\mathbf{p} - \mathbf{a})^2 - m^2\right]\psi = 0, \quad \mathcal{E} = i\frac{\partial}{\partial t}, \quad (8)$$

where the operators V and $\mathbf{a}$, which characterize the interaction of a particle with an external field, can have an arbitrary form and involve the operators of the coordinate $\mathbf{r}$, of the momentum $\mathbf{p}$, and of the spin $\mathbf{s}$. For a spinless and a spin-1/2 particle, the wave function ψ is one-component and two-component, respectively. At $s = 0$, Eq. (8) coincides with the Klein–Gordon equation.

In order to linearize Eq. (8), we introduce the functions ϕ and χ defined by the conditions

$$\psi = \phi + \chi, \quad (\mathcal{E} - V)\psi = m(\phi - \chi).$$

Equation (8) is equivalent to the following linear equation for the wave function $\Psi = \begin{pmatrix}\phi\\ \chi\end{pmatrix}$ [3]:

$$\mathcal{E}\Psi = \mathcal{H}\Psi = \left[V + \rho_3\left(\frac{\boldsymbol{\pi}^2}{2m} + m\right) + i\rho_2\frac{\boldsymbol{\pi}^2}{2m}\right]\Psi.$$

Here, $\boldsymbol{\pi} = \mathbf{p} - \mathbf{a}$ and ρ_i are the Pauli matrices,

$$\rho_1 = \begin{pmatrix}0 & 1\\ 1 & 0\end{pmatrix}, \ \rho_2 = \begin{pmatrix}0 & -i\\ i & 0\end{pmatrix}, \ \rho_3 = \begin{pmatrix}1 & 0\\ 0 & -1\end{pmatrix}.$$

The Hamiltonian $\mathcal{H}$ can be represented as

$$\mathcal{H} = V + \rho_3\mathcal{M} + \mathcal{O}, \quad \mathcal{M} = \frac{\boldsymbol{\pi}^2}{2m} + m, \quad \mathcal{O} = i\rho_2\frac{\boldsymbol{\pi}^2}{2m}. \qquad (9)$$

The Hamiltonian is pseudo-Hermitian [3, 4], since its even (diagonal) terms V and $\rho_3\mathcal{M}$ are Hermitian and the odd (off-diagonal) term $\mathcal{O}$ is anti-Hermitian.

The wave function is normalized by the condition [3–5]

$$\int \Psi^\dagger \rho_3 \Psi dV = \int (\phi^\dagger \phi - \chi^\dagger \chi) dV = 1.$$

In this case, an operator that transforms the Hamiltonian and the wave functions to any other representation must possess the property [3–5]

$$U^{-1} = \rho_3 U^\dagger \rho_3.$$

As a result, it turns out that the transformation of the Hamiltonian $\mathcal{H}$ to the diagonal form has much in common with the Foldy–Wouthuysen transformation (see [4]). It can be shown that, at $V = 0$, it follows from the anticommutativity of the operators $\rho_3\mathcal{M}$ and $\mathcal{O}$ ($\rho_3\mathcal{M}\mathcal{O} = -\mathcal{O}\rho_3\mathcal{M}$) that the operator $\mathcal{H}$ is reduced to a diagonal form with the aid of the operator that is given by

$$U = \frac{\epsilon + \mathcal{M} + \rho_3\mathcal{O}}{\sqrt{2\epsilon(\epsilon + \mathcal{M})}}, \quad U^{-1} = \frac{\epsilon + \mathcal{M} - \rho_3\mathcal{O}}{\sqrt{2\epsilon(\epsilon + \mathcal{M})}}, \quad (10)$$

where $\epsilon = \sqrt{\mathcal{M}^2 + \mathcal{O}^2} = \sqrt{m^2 + \boldsymbol{\pi}^2}$, and which is similar to the operator of the Foldy–Wouthuysen transformation for free particles (see [1, 6]).

At $V = 0$, the transformed Hamiltonian is given by

$$\mathcal{H} = U\mathcal{H}U^{-1} = \rho_3\epsilon.$$

In general ($V \neq 0$), a reduction of the Hamiltonian in (9) to a diagonal form is performed in two steps. Assuming that the interaction energy V is small in relation to the total energy of a relativistic particle ($|V| \ll \epsilon$), we can first make a transformation with the operator U given by (10). As a result, the expression for the Hamiltonian assumes the form[2)]

$$\mathcal{H}' = \rho_3\epsilon + \mathcal{E}' + \mathcal{O}', \quad \rho_3\mathcal{E}' = \mathcal{E}'\rho_3, \quad \rho_3\mathcal{O}' = -\mathcal{O}'\rho_3.$$

Since the condition $|\mathcal{O}'| \ll \epsilon$ is now satisfied, we can perform, at the second step, a transformation that is similar to the Foldy–Wouthuysen transformation for nonrelativistic particles (see [1, 7]). If we take into account only the largest corrections, the resulting expression for the Hamiltonian takes the form

$$\mathcal{H}'' = \rho_3\epsilon + \mathcal{E}' + \frac{1}{4}\rho_3\left(\mathcal{O}'^2\frac{1}{\epsilon} + \frac{1}{\epsilon}\mathcal{O}'^2\right). \quad (11)$$

In the case where the Hamiltonian $\mathcal{H}$ is given by (9), we retain only terms of orders V^2 and $\partial^2 V/\partial x_i \partial x_j$, disregarding terms proportional to $(\nabla V)^2$ and the derivatives of V of orders higher than two. In this approximation, the transformed Hamiltonian has the form

$$\mathcal{H}'' = \rho_3\epsilon + V - \frac{1}{16}\left\{\frac{1}{\epsilon^4}, (\boldsymbol{\pi}\cdot\nabla)(\boldsymbol{\pi}\cdot\nabla)V\right\}, \quad (12)$$

where $\{\dots,\dots\}$ stands for an anticommutator. For spinless particles in an electromagnetic field, we have $V = e\Phi$ and $\boldsymbol{\pi} = \mathbf{p} - e\mathbf{A}$, where e is the particle charge and Φ and $\mathbf{A}$ are, respectively, the scalar and the vector potential of an external field. We emphasize that, for a diagonalized Hamiltonian, we can use only the upper wave function ϕ. For nonrelativistic particles, Eq. (12) reduces to the conventional Schrödinger equation

$$\mathcal{H}''\phi = \left[m + \frac{(\mathbf{p} - e\mathbf{A})^2}{2m} + e\Phi\right]\phi. \quad (13)$$

4. QUADRATIC FORM OF RELATIVISTIC WAVE EQUATIONS FOR SPIN-1/2 PARTICLES

The results obtained in the preceding section will now be used to find the quadratic form of relativistic wave equations for spin-1/2 particles interacting with an electrostatic field. Solving this problem is of paramount importance for studying the interaction of relativistic particles with crystals.

In accordance with the results presented in [8–10], the Hamiltonian operator taken in the Foldy–Wouthuysen representation and determined to terms of orders $(e\Phi)^2$ and $e\partial^2\Phi/\partial x_i\partial x_j$ inclusive has the form[3)]

$$\mathcal{H}'' = \rho_3\epsilon + e\Phi + \frac{1}{4}\left\{\left(\frac{e}{2(\epsilon+m)} + \mu'\right)\frac{1}{\epsilon}, [(\boldsymbol{\sigma}\cdot[\mathbf{p}\times\mathbf{E}]) - (\boldsymbol{\sigma}\cdot[\mathbf{E}\times\mathbf{p}]) + \Delta\Phi]\right\} - \frac{e}{16}\left\{\frac{2\epsilon^2 + 2\epsilon m + m^2}{\epsilon^4(\epsilon+m)^2}, (\mathbf{p}\cdot\nabla)(\mathbf{p}\cdot\nabla)\Phi\right\}, \quad (14)$$

$$\epsilon = \sqrt{m^2 + \mathbf{p}^2},$$

where μ' is the anomalous magnetic moment. The wave functions ϕ and χ are spinors in the case being considered, while $\boldsymbol{\sigma}$ is the Pauli matrix acting on the components of each of these functions. In the present case, the interaction energy in Eq. (12) assumes the form

$$V = e\Phi + \frac{1}{4}\left\{\left(\frac{e}{2(\epsilon+m)} + \mu'\right)\frac{1}{\epsilon}, [(\boldsymbol{\sigma}\cdot[\mathbf{p}\times\mathbf{E}]) - (\boldsymbol{\sigma}\cdot[\mathbf{E}\times\mathbf{p}]) + \Delta\Phi]\right\} - \frac{e}{16}\left\{\frac{1}{\epsilon^2(\epsilon+m)^2}, (\mathbf{p}\cdot\nabla)(\mathbf{p}\cdot\nabla)\Phi\right\}, \quad \mathbf{a} = 0. \quad (15)$$

[2)]The odd term $\mathcal{O}'$ is still anti-Hermitian.

[3)]The vector potential of an electrostatic field is equal to zero.

From Eqs. (8), (12), and (15), it follows that the quadratic equation has the form

$$\left[\left(\mathcal{E}-e\Phi-\frac{1}{4}\left\{\left(\frac{e}{2(\epsilon+m)}+\mu'\right)\frac{1}{\epsilon},[(\boldsymbol{\sigma}\cdot[\mathbf{p}\times\mathbf{E}])\right.\right.\right.$$
$$\left.-(\boldsymbol{\sigma}\cdot[\mathbf{E}\times\mathbf{p}])+\Delta\Phi]\right\} \qquad (16)$$
$$\left.+\frac{e}{16}\left\{\frac{1}{\epsilon^2(\epsilon+m)^2},(\mathbf{p}\cdot\nabla)(\mathbf{p}\cdot\nabla)\Phi\right\}\right)^2-\mathbf{p}^2-m^2\Bigg]$$
$$\psi=0.$$

In solving Eq. (16), the operator ϵ can be replaced by the total particle energy E in small terms (which involve anticommutators) [2]. Since the operator $\mathcal{E}$ is also replaced by E for stationary states of the particle being considered, Eq. (16) reduces, with the above accuracy, to the form

$$\left\{E^2-2eE\Phi+e^2\Phi^2-[\frac{e}{2(E+m)}+\mu'] \qquad (17)\right.$$
$$\times[(\boldsymbol{\sigma}\cdot[\mathbf{p}\times\mathbf{E}])-(\boldsymbol{\sigma}\cdot[\mathbf{E}\times\mathbf{p}])+\Delta\Phi]$$
$$\left.+\frac{e}{4E(E+m)^2}(\mathbf{p}\cdot\nabla)(\mathbf{p}\cdot\nabla)\Phi-\mathbf{p}^2-m^2\right\}\psi=0.$$

Equation (17) is a quadratic equation for the energy-operator eigenvalues, which does not involve a square root of operators. Equations (16) and (17) differ from the equation derived in [2] by the presence of a term that is proportional to $(\mathbf{p}\cdot\nabla)(\mathbf{p}\cdot\nabla)\Phi$. However, this term does not contribute to the motion of the spin of a charged particle in crystals.

5. PARTICLES IN THE FIELD OF A HARMONIC POTENTIAL

In order to illustrate a transition from a first-order relativistic wave equation to a second-order equation, we consider here a particle in the field of a harmonic potential $\Phi=ax^2/2$. Such a potential can approximate the field of crystal planes in the case where a particle moves through a straight crystal. We choose the x axis to be orthogonal to the set of crystal planes and the y axis to be parallel to the direction of particle translational motion.

Going over from the first-order Eq. (14) to the second-order Eq. (17) and discarding small terms, we find for spin-1/2 particles that

$$T\psi=\left[\frac{p_x^2}{2E}+\frac{eax^2}{2}+\frac{\lambda}{E}\left(\frac{\mu_0 m}{E+m}+\mu'\right)\right. \qquad (18)$$
$$\left.\times\sqrt{E^2-m^2}\,ax\right]\psi,$$

$$T=\frac{E^2-m^2-p_y^2}{2E},$$

where $\mu_0=e/2m$ is the Dirac magnetic moment and $\lambda=\pm1$ is an eigenvalue of the operator σ_z ($\sigma_z\psi=\lambda\psi$). Equation (18) is in accord with that derived in [2]. Since

$$T=\frac{(E+\sqrt{m^2+p_y^2})(E-\sqrt{m^2+p_y^2})}{2E}$$
$$\approx E-\sqrt{m^2+p_y^2},\quad p_y^2\gg p_x^2,$$

the operator on the right-hand side of Eq. (18) characterizes the transverse energy of the particles, while the quantity T determines the eigenvalues of this operator. Equation (18) can be recast into the form [2]

$$\left(-\frac{1}{2E}\frac{d^2}{dX^2}+\frac{eaX^2}{2}\right)\kappa(X)=\left(T-\frac{eax_0^2}{2}\right)\kappa(X),$$
$$X=x+x_0,\quad \kappa(X)=\psi(X-x_0), \qquad (19)$$
$$x_0=\frac{\lambda}{eE}\left(\frac{\mu_0 m}{E+m}+\mu'\right)\sqrt{E^2-m^2}.$$

Disregarding $eax_0^2/2$ against T [4] and considering that the transverse energy of the particles is much less than the energy of their translational motion, we represent the energy spectrum in the form

$$E_n=(m^2+p_y^2)^{1/2}+\frac{(ea)^{1/2}}{(m^2+p_y^2)^{1/4}}\left(n+\frac{1}{2}\right), \qquad (20)$$
$$n=0,1,2,\ldots.$$

For spinless particles moving in the field of a harmonic potential, the second-order Klein–Gordon equation has the form

$$\left[\left(\mathcal{E}-\frac{eax^2}{2}\right)-\mathbf{p}^2-m^2\right]\psi=0. \qquad (21)$$

In this case, the energy spectrum is also given by expression (20).

In an arbitrary electrostatic field, the Hamiltonian has the form (12), where $V=e\Phi$ and $\mathbf{a}=0$. This form is convenient for deriving the operator equation of motion of the particles. Since

$$\frac{d\mathbf{p}}{dt}=i[\mathcal{H}'',\mathbf{p}],$$

this equation has the form

$$\frac{d\mathbf{p}}{dt}=e\mathbf{E}-\frac{e}{16}\left\{\frac{1}{\epsilon^4},(\mathbf{p}\cdot\nabla)(\mathbf{p}\cdot\nabla)\mathbf{E}\right\}. \qquad (22)$$

The second term on the right-hand side of (22) is a quantum correction to the relevant classical equation. A similar derivation of the operator equation of motion for spin-1/2 particles leads to a spin-dependent result:

[4] This quantity characterizes the shift of the energy levels that is due to the magnetic moment of the particles.

$$\frac{d\mathbf{p}}{dt} = e\mathbf{E} - \frac{1}{4}\left\{\left(\frac{e}{2(\epsilon+m)} + \mu'\right)\frac{1}{\epsilon}, [\nabla(\boldsymbol{\sigma}\cdot[\mathbf{p}\times\mathbf{E}]) - \nabla(\boldsymbol{\sigma}\cdot[\mathbf{E}\times\mathbf{p}]) - \Delta\mathbf{E}]\right\}$$
$$-\frac{e}{16}\left\{\frac{2\epsilon^2+2\epsilon m+m^2}{\epsilon^4(\epsilon+m)^2}, (\mathbf{p}\cdot\nabla)(\mathbf{p}\cdot\nabla)\mathbf{E}\right\}.$$

6. DISCUSSION OF THE RESULTS

It is well known that, in the Foldy–Wouthuysen representation, relativistic wave equations involve a square root of operators. From the results obtained in the present study, it follows that the problem of going over to the quadratic form of relativistic wave equations cannot be rigorously solved by merely squaring the operators involved. This problem cannot be solved by means of the operator squaring of the Dirac equation either. A multiplication of this equation

$$(\gamma^\mu\pi_\mu + m)\Psi = 0,$$

where Ψ is a bispinor, from the left by the operator $\gamma^\mu\pi_\mu - m$ is known to lead to the equation [11]

$$\left[(\mathcal{E}-e\Phi)^2 - \boldsymbol{\pi}^2 - m^2 + e(\boldsymbol{\Sigma}\cdot\mathbf{H}) - ie(\boldsymbol{\alpha}\cdot\mathbf{E})\right]\psi = 0, \qquad (23)$$

where $\boldsymbol{\alpha} = \gamma^0\boldsymbol{\gamma}$ and $\boldsymbol{\Sigma} = i[\boldsymbol{\gamma}\times\boldsymbol{\gamma}]/2$. Since the matrix $\boldsymbol{\alpha}$ is off-diagonal, Eq. (23) is also off-diagonal.

In order to find a quadratic form of relativistic wave equations, we invoke here a solution to the inverse problem—that of going over from the quadratic to the linear form of relevant equations, which determines the Hamiltonian in the Foldy–Wouthuysen representation. For spin-1/2 particles, use is made of the method developed previously for linearizing the relativistic wave equation describing spinless particles (Klein–Gordon equation). Linearization, implemented with the aid of the Pauli matrices, leads to an equation where the Hamiltonian is pseudo-Hermitian and off-diagonal. It is necessary to reduce it to a diagonal form. Previously, this problem was solved either for particular cases [4] or in the nonrelativistic approximation [12], but, here, a reduction of the Hamiltonian to a diagonal form that characterizes the Foldy–Wouthuysen representation has been performed for relativistic particles in external fields. As a result, it turns out that, in addition to a simple extraction of the square root,

$$a^2 = b^2 + c^2 \;\;\rightarrow\;\; a = \pm\sqrt{b^2+c^2},$$

the resulting Hamiltonian develops a term that is proportional to a double commutator:

$$\left[\boldsymbol{\pi}^2, [\boldsymbol{\pi}^2, \Phi]\right] = -4(\boldsymbol{\pi}\cdot\nabla)(\boldsymbol{\pi}\cdot\nabla)\Phi.$$

In the majority of cases, this term is small, as it is in the above example of a particle moving in the field of a harmonic potential. It is important, however, that the method in question makes it possible to avoid the emergence of anti-Hermitian or off-diagonal terms, which are relatively large, as one can see from Eqs. (6), (7), and (23).

A transition from a quadratic to a linear form of relativistic wave equations makes it possible to establish a one-to-one correspondence between these forms. Owing to this, the inverse transition—from the linear to the quadratic form of these equations—can be implemented in a comparatively simple way, whereby we obtain a solution to the problem that we addressed here, that of reducing the equation for the Hamiltonian in the Foldy– Wouthuysen representation to a conveniently soluble form. In many cases, the resulting second-order equation can be solved quite straightforwardly, as we have seen from the example considered above. The proposed method can be applied to spinless particles as well. In that case, it permits constructing the Hamiltonian and deriving an operator equation of motion for relativistic particles in an external field.

7. CONCLUSION

A convenient method has been developed for solving relativistic wave equations for spin-1/2 particles interacting with an external field. The presence of the square root of operators is an obstacle to directly solving the equation for the Hamiltonian in the Foldy–Wouthuysen representation for relativistic particles. It has been shown that the square root can be removed by recasting the equation being considered into a quadratic form. The example of particle motion in the field of a harmonic potential has demonstrated the efficiency of the proposed method.

REFERENCES

1. L. L. Foldy and S. A. Wouthuysen, Phys. Rev. **78**, 29 (1950).
2. A. Ya. Silenko, Zh. Éksp. Teor. Fiz. **107**, 1240 (1995) [JETP **80**, 690 (1995)].
3. A. S. Davydov, *Quantum Mechanics* (Fizmatgiz, Moscow, 1963; Pergamon, Oxford, 1976).
4. K. M. Case, Phys. Rev. **95**, 1323 (1954).
5. H. Feshbash and F. Villars, Rev. Mod. Phys. **30**, 24 (1958).

6. D. M. Fradkin and R. H. Good, Rev. Mod. Phys. **33**, 343 (1961).
7. J. D. Bjorken and S. D. Drell, *Relativistic Quantum Mechanics* (McGraw-Hill, New York, 1964; Nauka, Moscow, 1978).
8. E. I. Blount, Phys. Rev. **128**, 2454 (1962).
9. A. I. L'vov, Preprint No. 344 FIAN (Lebedev Institute of Physics, USSR Academy of Sciences, Moscow, 1987).
10. A. Ya. Silenko, Teor. Mat. Fiz. **105**, 46 (1995).
11. V. B. Berestetskii, E. M. Lifshitz, and L. P. Pitaevskii, *Quantum Electrodynamics* (Nauka, Moscow, 1989; Pergamon, Oxford, 1982).
12. J. A. Young and S. A. Bludman, Phys. Rev. **131**, 2326 (1963).

Translated by A. Isaakyan

Physics of Atomic Nuclei, Vol. 64, No. 5, 2001, pp. 983–989. Translated from Yadernaya Fizika, Vol. 64, No. 5, 2001, pp. 1054–1060.

XXX International Conference on the Physics of Interaction of Fast Charged Particles with Matter

Motion of the Spin of Particles and Nuclei of Arbitrary Spin in the Electric Field of Crystals

A. J. Silenko*

Institute of Nuclear Problems, Belarussian State University, Minsk, Belarus

Received November 4, 2000

Abstract—The possibility of verifying the conclusions of quantum theory on the motion of the spin of particles and nuclei of arbitrary spin in an electric field is analyzed. The theory predicts that the planar channeling of particles and nuclei with higher spins (one or more) through straight crystals is accompanied by the rotation of their spin. For some nuclei, the spin-rotation angle per unit length is about 10^{-1} rad/cm . For ultrarelativistic nuclei undergoing planar channeling through bent crystals, the spin-rotation angle per unit length is on the order of 1 rad/cm, which makes it possible to verify the validity of the Bargmann–Michel–Telegdi equation for particles and nuclei of higher spins. © *2001 MAIK "Nauka/Interperiodica".*

1. INTRODUCTION

Investigation of the motion of the spin of charged particles in crystals is of importance both for measuring the magnetic moments of short-lived particles [1–3] and for testing the conclusions drawn from QED [4, 5]. In order to describe the motion of a spin, use is made of the Bargmann–Michel–Telegdi equation [6]. This equation was derived semiclassically in [7]; for spin-1/2 particles, it was obtained on the basis of QED methods [8, 9]. We emphasize that, for spin-1/2 particles, a rigorous quantum-mechanical analysis does not confirm the presence of second-order terms in spin in the equation describing the motion of a spin [4, 5, 9], but such terms usually arise in semiclassical equations [10–16].

Until recently, rigorous quantum-mechanical methods for describing the motion of a spin were applied only to spin-1/2 particles. Spin-1 particles were considered in [14], but the method used there is not satisfactory, since it leads to incorrect results for spin-1/2 particles (see [17]). For particles with an arbitrary spin, the equations of motion of a particle and a spin were obtained on the basis of quantum-mechanical methods in [18, 19]. In a uniform field, the equation of motion of a spin coincides with the Bargmann–Michel–Telegdi equation.[1)] It was confirmed in [18] that, for spin-1/2 particles, the relevant equations involve no second-order terms in spin, which are proportional to the derivatives of the field strengths. At the same time, the Lagrangian for $s \geq 1$ particles (s is the particle spin) includes such terms, and it was found in [18, 19] that these terms depend not only on the electric quadrupole but also on the magnetic dipole moment of a particle.

However, the results obtained in [18, 19] call for an experimental corroboration for the following reasons. For $s = 1$ particles in a magnetic field, the authors of [21–24] derived quadratic equations that are consistent neither with the results from [18, 19] nor with the Bargmann–Michel–Telegdi equation. Moreover, it is well known that, for spin-1 particles, the normal magnetic moment (magnetic moment of a pointlike particle) is $\mu_{\rm norm} = e/(2m)$ and corresponds to the g factor of $g_{\rm norm} = 1$. For particles with an arbitrary spin, we have $\mu_{\rm norm} = e/(2m)$ and $g_{\rm norm} = 1/s$ [25–29]. At the same time, it follows from the Bargmann–Michel–Telegdi equation that the magnetic moment μ must be broken down into the terms $\mu_0 = es/m$ and $\mu' = \mu - \mu_0 = (g-2)es/(2m)$.

In this study, we will consider methods for experimentally testing the results obtained in [18, 19] by measuring the rotation of the spin of nuclei that undergo planar channeling in straight and bent crystals.

We use here the relativistic system of units in which $\hbar = c = 1$.

2. EQUATION OF MOTION OF A SPIN WITH ALLOWANCE FOR SECOND-ORDER TERMS IN SPIN

The equation of motion of a spin can be derived with the aid of the Lagrangian for particles with an

* e-mail: silenko@inp.minsk.by

1) For particles with an arbitrary spin, a quantum-mechanical equation of motion of a spin that is coincident with the Bargmann–Michel–Telegdi equation was previously derived in [20] from a general consideration.

arbitrary spin. This Lagrangian obtained in [18, 19] has the form

$$\mathcal{L} = \mathcal{L}_1 + \mathcal{L}_2,$$

$$\mathcal{L}_1 = \frac{e}{2m}\left\{\left(g-2+\frac{2}{\gamma}\right)(\mathbf{s}\cdot\mathbf{B}) - (g-2)\frac{\gamma}{\gamma+1}(\mathbf{s}\cdot\mathbf{v})(\mathbf{v}\cdot\mathbf{B}) + \left(g-2+\frac{2}{\gamma+1}\right)(\mathbf{s}\cdot[\mathbf{E}\times\mathbf{v}])\right\}, \quad (1)$$

$$\mathcal{L}_2 = \frac{Q}{2s(2s-1)} \times \left[(\mathbf{s}\cdot\nabla) - \frac{\gamma}{\gamma+1}(\mathbf{s}\cdot\mathbf{v})(\mathbf{v}\cdot\nabla)\right] \times \left[(\mathbf{s}\cdot\mathbf{E}) - \frac{\gamma}{\gamma+1}(\mathbf{s}\cdot\mathbf{v})(\mathbf{v}\cdot\mathbf{E}) + (\mathbf{s}\cdot[\mathbf{v}\times\mathbf{B}])\right] + \frac{e}{2m^2}\frac{\gamma}{\gamma+1}(\mathbf{s}\cdot[\mathbf{v}\times\nabla]) \times \left[\left(g-1+\frac{1}{\gamma}\right)(\mathbf{s}\cdot\mathbf{B}) - (g-1)\frac{\gamma}{\gamma+1}(\mathbf{s}\cdot\mathbf{v})(\mathbf{v}\cdot\mathbf{B}) + \left(g-\frac{\gamma}{\gamma+1}\right)(\mathbf{s}\cdot[\mathbf{E}\times\mathbf{v}])\right],$$

where $g = 2\mu m/(es)$; e, m, and μ are, respectively, the charge, the mass, and the total magnetic moment of a particle; $\mathbf{v}$ is its velocity; γ is the Lorentz factor; Q is the quadrupole moment; $\mathbf{s}$ is the spin operator; and $\mathbf{E}$ and $\mathbf{B}$ are the electric-field strength and the magnetic-field induction, respectively. In the Lagrangian given by (1), $\mathcal{L}_1$ and $\mathcal{L}_2$ contain terms that are, respectively, linear and quadratic in spin. The Hermitian form of expression (1) can be obtained by means of the substitution $\mathcal{L} \to (\mathcal{L} + \mathcal{L}^\dagger)/2$. The equation of motion of a spin is obtained with the aid of the formula [18]

$$\frac{d\mathbf{s}}{dt} = -i[\mathcal{L}, \mathbf{s}], \quad (2)$$

where $[\ldots,\ldots]$ is a commutator. For Lagrangian (1), it has the form

$$\frac{d\mathbf{s}}{dt} = \left(\frac{d\mathbf{s}}{dt}\right)_{\mathrm{BMT}} + \left(\frac{d\mathbf{s}}{dt}\right)_q, \quad (3)$$

$$\left(\frac{d\mathbf{s}}{dt}\right)_{\mathrm{BMT}} = \frac{e}{2m}\left\{\left(g-2+\frac{2}{\gamma}\right)[\mathbf{s}\times\mathbf{B}] - (g-2)\frac{\gamma}{\gamma+1}[\mathbf{s}\times\mathbf{v}](\mathbf{v}\cdot\mathbf{B}) + \left(g-2+\frac{2}{\gamma+1}\right)[\mathbf{s}\times[\mathbf{E}\times\mathbf{v}]]\right\}, \quad (4)$$

$$\left(\frac{d\mathbf{s}}{dt}\right)_q = \frac{Q}{4s(2s-1)}\left(\left\{\left([\mathbf{s}\times\nabla] - \frac{\gamma}{\gamma+1}[\mathbf{s}\times\mathbf{v}](\mathbf{v}\cdot\nabla)\right), \left((\mathbf{s}\cdot\mathbf{E}) - \frac{\gamma}{\gamma+1}(\mathbf{s}\cdot\mathbf{v})(\mathbf{v}\cdot\mathbf{E}) + (\mathbf{s}\cdot[\mathbf{v}\times\mathbf{B}])\right)\right\} + \left\{\left((\mathbf{s}\cdot\nabla) - \frac{\gamma}{\gamma+1}(\mathbf{s}\cdot\mathbf{v})(\mathbf{v}\cdot\nabla)\right), \left([\mathbf{s}\times\mathbf{E}] - \frac{\gamma}{\gamma+1}[\mathbf{s}\times\mathbf{v}](\mathbf{v}\cdot\mathbf{E}) + [\mathbf{s}\times[\mathbf{v}\times\mathbf{B}]]\right)\right\}\right) + \frac{e}{4m^2}\frac{\gamma}{\gamma+1}\left(\left\{[\mathbf{s}\times[\mathbf{v}\times\nabla]], \left[\left(g-1+\frac{1}{\gamma}\right)(\mathbf{s}\cdot\mathbf{B}) - (g-1)\frac{\gamma}{\gamma+1}(\mathbf{s}\cdot\mathbf{v})(\mathbf{v}\cdot\mathbf{B}) + \left(g-\frac{\gamma}{\gamma+1}\right)(\mathbf{s}\cdot[\mathbf{E}\times\mathbf{v}])\right]\right\} + \left\{\left(\mathbf{s}\cdot[\mathbf{v}\times\nabla]\right), \left[\left(g-1+\frac{1}{\gamma}\right)[\mathbf{s}\times\mathbf{B}] - (g-1)\frac{\gamma}{\gamma+1}[\mathbf{s}\times\mathbf{v}](\mathbf{v}\cdot\mathbf{B}) + \left(g-\frac{\gamma}{\gamma+1}\right)[\mathbf{s}\times[\mathbf{E}\times\mathbf{v}]]\right]\right\}\right), \quad (5)$$

where $\{\ldots,\ldots\}$ is an anticommutator. The quantities $(d\mathbf{s}/dt)_{\mathrm{BMT}}$ and $(d\mathbf{s}/dt)_q$ characterize the motion of a spin described by the terms in Lagrangian (1) that are, respectively, linear [Bargmann–Michel–Telegdi (BMT) equation (4)] and quadratic [equation (5)] in spin. We note that Eq. (5) is not consistent with the semiclassical Good equation [10], where the second-order terms in spin at $Q = 0$ are given by

$$\left(\frac{d\mathbf{s}}{dt}\right)_{\mathrm{G}} = \frac{eg}{2m^2}\frac{\gamma}{\gamma+1}\Big[\mathbf{s}\times[\mathbf{v}\times\nabla]\Big] \times \left\{(\mathbf{s}\cdot\mathbf{B}) - \frac{\gamma}{\gamma+1}(\mathbf{s}\cdot\mathbf{v})(\mathbf{v}\cdot\mathbf{B}) + \Big(\mathbf{s}\cdot[\mathbf{E}\times\mathbf{v}]\Big)\right\}. \quad (6)$$

Here, we have used the notation adopted in this study.

Even for $g \gg 1$, Eq. (5) differs from (6) by the presence of the second term.

For spin-1/2 particles, the relations

$$\{s_i, s_j\} = \delta_{ij}/2$$

remove the operator $\mathbf{s}$ from the Lagrangian $\mathcal{L}_2$ and from Eq. (5). This is the reason why, for such particles, the equations of motion of a spin do not involve second-order terms in spin (this circumstance has already been noted above).

It should be emphasized that not only is Eq. (4) equivalent to the semiclassical Bargmann–Michel–Telegdi equation, but it is also consistent with the classical equation derived in [4, 5]. The latter follows from the fact that the magnetic moment of a macroscopic body is equal to the total magnetic moment of electrons. Since macroscopic bodies have a large mass, the quantity μ_0, which involves the mass of the body in the denominator, is small in relation to μ; therefore, we have $\mu \approx \mu'$. In this case, the equation of motion of a spin corresponds to the equation for the anomalous magnetic moment, and this was found in [4, 5].

Equation (5) includes two terms, which describe the motion of a spin due to, respectively, the electric quadrupole and the magnetic dipole moment of particles. The equation of motion induced by the quadrupole moment was derived in [30], and it coincides with the first term on the right-hand side of Eq. (5).

As was shown in the Introduction, however, there exists the problem of rendering Eqs. (3)–(5) consistent with the results obtained in the theory of spin-1 particles and with the values of the intrinsic magnetic moment μ_0. This problem is investigated in the next section.

3. SPIN-1 PARTICLES IN THE ELECTROMAGNETIC FIELD

The authors of [21–23] investigated the interaction of spin-1 particles with a magnetic field. They considered three versions of the theory of spin-1 particles and found that they lead to consistent results (later on, these results were corroborated in [24]). These authors also derived second-order equations for the eigenvalues of the Hamiltonian. In the weak-field approximation,[2)] one obtains a linear equation that is consistent neither with the Lagrangian in (1) nor with the Bargmann–Michel–Telegdi equation.

In view of this contradiction, we have calculated the Hamiltonian for relativistic spin-1 particles in an electromagnetic field. We have used the weak-field approximation and disregarded terms involving the derivatives of the electric- and the magnetic-field strength ($\mathbf{E}$ and $\mathbf{H}$, respectively). The calculation, performed within Proca theory (see [31]), employed, as a starting point, the generalized Sakata–Taketani equation for particles with an anomalous magnetic moment. The Hamiltonian specified by this equation was reduced to a form diagonal in two spinors by using the Foldy–Wouthuysen transformation [32]. In this representation, the resulting expression for the Hamiltonian has the form

$$\mathcal{H} = \beta\epsilon + e\Phi + \frac{e}{4m}\left[-\left\{\left(g-2+\frac{2m}{\epsilon}\right), (\mathbf{\Pi}\cdot\mathbf{H})\right\}\right.$$
$$+\left\{\frac{g-2}{2\epsilon(\epsilon+m)}, (\mathbf{\Pi}\cdot\boldsymbol{\pi})(\boldsymbol{\pi}\cdot\mathbf{H}) + (\boldsymbol{\pi}\cdot\mathbf{H})(\mathbf{\Pi}\cdot\boldsymbol{\pi})\right\}$$
$$-\left\{\left(\frac{g-2}{2}+\frac{m}{\epsilon+m}\right)\frac{1}{\epsilon}, (\mathbf{\Sigma}\cdot[\mathbf{E}\times\boldsymbol{\pi}])\right. \qquad (7)$$
$$\left.\left.-(\mathbf{\Sigma}\cdot[\boldsymbol{\pi}\times\mathbf{E}])\right\}\right], \quad \epsilon = \sqrt{\boldsymbol{\pi}^2+m^2},$$

where $\boldsymbol{\pi} = \mathbf{p} - e\mathbf{A}$; $\mathbf{p} = -i\nabla$ is the momentum operator; Φ and $\mathbf{A}$ are, respectively, the scalar and the vector potential of the external field; and

$$\mathbf{\Pi} = \begin{pmatrix} \mathbf{s} & 0 \\ 0 & -\mathbf{s} \end{pmatrix}, \quad \beta = \begin{pmatrix} 1 & 0 \\ 0 & -1 \end{pmatrix}, \quad \mathbf{\Sigma} = \begin{pmatrix} \mathbf{s} & 0 \\ 0 & \mathbf{s} \end{pmatrix}.$$

Here, $\mathbf{s}$ is the spin matrix for spin-1 particles and 0, ± 1 denote the corresponding 3×3 matrices. The operator $\mathcal{H}$ acts on the six-component wave function (bispinor) $\Psi = \begin{pmatrix} \phi \\ \chi \end{pmatrix}$. The g factor $g = g_{\text{norm}} = 1$ corresponds to the particle with a normal magnetic moment (Proca particle).

For the particular case of nonrelativistic particles in a magnetic field, formula (7) complies with the Hamiltonian derived by Case [33], who also used the Foldy–Wouthuysen transformation. This formula is also consistent with the Hamiltonian obtained in [34] for relativistic particles in a magnetic field that are characterized by the g factor of $g = 2$.

In just the same way as in the theory of spin-1/2 particles [9], the polarization operator for spin-1 particles in the Foldy–Wouthuysen representation is equal to the matrix $\mathbf{\Pi}$.[3)] From the formula

$$\frac{d\mathbf{\Pi}}{dt} = i[\mathcal{H}, \mathbf{\Pi}],$$

[2)] Within this approximation, the energy of particle–field interaction is assumed to be low in relation to the total particle energy, including the rest energy.

[3)] The use of the matrix $\mathbf{\Sigma}$ for the polarization operator also leads, upon a transition to the semiclassical approximation, to formula (9) (see below) for the angular velocity of spin rotation.

we find, with the aid of expression (7), that the equation of motion of a spin can be represented as

$$\frac{d\mathbf{\Pi}}{dt} = \frac{e}{4m}\left[\left\{\left(g-2+\frac{2m}{\epsilon}\right),[\mathbf{\Sigma}\times\mathbf{H}]\right\}\right. \quad (8)$$
$$-\left\{\frac{g-2}{2\epsilon(\epsilon+m)},[\mathbf{\Sigma}\times\boldsymbol{\pi}](\boldsymbol{\pi}\cdot\mathbf{H})+(\boldsymbol{\pi}\cdot\mathbf{H})[\mathbf{\Sigma}\times\boldsymbol{\pi}]\right\}$$
$$-\left\{\left(\frac{g-2}{2}+\frac{m}{\epsilon+m}\right)\frac{1}{\epsilon},[\mathbf{\Pi}\times[\mathbf{E}\times\boldsymbol{\pi}]]\right.$$
$$\left.\left.-[\mathbf{\Pi}\times[\boldsymbol{\pi}\times\mathbf{E}]]\right\}\right].$$

Since we can recast Eq. (8) into the form

$$\frac{d\mathbf{\Pi}}{dt} = \frac{1}{2}\left([\mathbf{\Omega}\times\mathbf{\Pi}]-[\mathbf{\Pi}\times\mathbf{\Omega}]\right),$$

a transition to a description within the semiclassical approximation consists in averaging the operator of the angular velocity of spin rotation,

$$\mathbf{\Omega} = \frac{e}{4m}\left[-\beta\left\{\left(g-2+\frac{2m}{\epsilon}\right),\mathbf{H}\right\}\right.$$
$$+\beta\left\{\frac{g-2}{2\epsilon(\epsilon+m)},\boldsymbol{\pi}(\boldsymbol{\pi}\cdot\mathbf{H})+(\boldsymbol{\pi}\cdot\mathbf{H})\boldsymbol{\pi}\right\} \quad (9)$$
$$\left.-\left\{\left(\frac{g-2}{2}+\frac{m}{\epsilon+m}\right)\frac{1}{\epsilon},[\mathbf{E}\times\boldsymbol{\pi}]-[\boldsymbol{\pi}\times\mathbf{E}]\right\}\right],$$

over the wave functions of stationary states. For free particles, the lower spinor is equal to zero in the Foldy–Wouthuysen representation. For particles in an external field, the ratio of the lower and the upper spinor is at maximum on the same order of magnitude as $W_{\rm int}/E$, where $W_{\rm int}$ is the energy of the particle–field interaction and E is the total particle energy. Thus, we have $(\chi^\dagger\chi)/(\phi^\dagger\phi)\sim(W_{\rm int}/E)^2$. For this reason, the contribution of the lower spinor is negligibly small; in the semiclassical approximation, the angular velocity of spin rotation ($\boldsymbol{\omega}$) is therefore given by

$$\boldsymbol{\omega} = \frac{e}{2m}\left\{-\left(g-2+\frac{2}{\gamma}\right)\mathbf{H}\right.$$
$$+(g-2)\frac{\gamma}{\gamma+1}\mathbf{v}(\mathbf{v}\cdot\mathbf{H})$$
$$\left.-\left(g-2+\frac{2}{\gamma+1}\right)[\mathbf{E}\times\mathbf{v}]\right\},$$

where $\gamma=\epsilon/m$ and $\mathbf{v}=\boldsymbol{\pi}/\epsilon$. This formula is fully consistent with that presented in [18] and with the Bargmann–Michel–Telegdi equation.

Thus, a rigorous calculation has revealed that, upon the Foldy–Wouthuysen transformation, the Hamiltonian determined on the basis of Proca theory (with allowance for an anomalous magnetic moment) is inconsistent with the results presented in [21–24], but it is fully consistent with the data from [18, 19] and with the Bargmann–Michel–Telegdi equation [6].

By analyzing the reasons behind the inconsistency of the results obtained in [21–24] and in the present study, we emphasize that the use of a second-order wave equation requires extreme caution. A transition from a linear to a quadratic form of wave equations cannot be performed by merely eliminating some components of the wave function, since this would lead to the emergence of non-Hermitian terms in the resulting equation. This would result in complex-valued particle energies and in the nonorthogonality of the wave functions. We note that the second-order wave equation used in [21] includes a term that is proportional to $\pi_\mu\pi^\nu$ and which is non-Hermitian;[4] that is,

$$(\pi_\mu\pi^\nu)^\dagger = \pi^\nu\pi_\mu = \pi_\mu\pi^\nu + [\pi^\nu,\pi_\mu]$$
$$= \pi_\mu\pi^\nu - ieg^{\nu\rho}F_{\rho\mu} \neq \pi_\mu\pi^\nu,$$

where $g^{\nu\rho}=\mathrm{diag}\{1,-1,-1,-1\}$ is the metric tensor and $F_{\rho\mu}$ is the electromagnetic-field-strength tensor. In this connection, the presence of imaginary values in the energy spectrum of a particle in a magnetic field (this fact was indicated in [23]) is quite natural.

A second possible reason for the above inconsistency is that the representation used in [21–24] to derive the equations being discussed can be different from the Foldy–Wouthuysen representation.

Thus, it follows from the theory of spin-1 particles that the quantum-mechanical equation of motion of a spin of such particles is consistent with the Bargmann–Michel–Telegdi equation.

4. MOTION OF PARTICLE AND NUCLEAR SPINS IN PLANAR CHANNELING THROUGH STRAIGHT AND BENT CRYSTALS

Successful experiments devoted to measuring the rotation of the spin of short-lived spin-1/2 charged particles [2, 3] create preconditions for experimentally testing the results obtained in [18, 19] and for applying these results in practice.

We assume that the crystal is bent in such a way that the plane of the bend is orthogonal to crystallographic planes and denote the bend radius by R. We choose the x axis to be orthogonal to the set of planes in the direction of the bend and the y axis to be orthogonal to the x axis in the plane of the bend. Channeled particles or nuclei execute translational motion along the y axis and vibrational motion along the x axis. Since particles (nuclei) move at small

[4] A correct transition to a second-order wave equation is described in [31].

angles with respect to crystallographic planes, the kinetic energy of their translational motion considerably exceeds the vibrational energy. The potential of the planes does not exceed values on the order of 100 eV; therefore, the vibrational motion of channeled particles (nuclei) is nonrelativistic, occurring at speeds much less than the speed of light. It follows that, in Eqs. (4) and (5), we can disregard terms proportional to $(\mathbf{v}\cdot\nabla)$ and $(\mathbf{v}\cdot\mathbf{E})$ and additionally set $\mathbf{B}=0$. For the problem being considered, these equations then take the form

$$\left(\frac{d\mathbf{s}}{dt}\right)_{\mathrm{BMT}} = \frac{e}{2m} \times\left\{\left(g-2+\frac{2}{\gamma+1}\right)\Big[\mathbf{s}\times[\mathbf{E}\times\mathbf{v}]\Big]\right\}, \tag{10}$$

$$\left(\frac{d\mathbf{s}}{dt}\right)_{q} = \frac{Q}{4s(2s-1)} \times\left(\Big\{[\mathbf{s}\times\nabla],(\mathbf{s}\cdot\mathbf{E})\Big\}+\Big\{(\mathbf{s}\cdot\nabla),[\mathbf{s}\times\mathbf{E}]\Big\}\right) +\frac{e}{4m^2}\frac{\gamma}{\gamma+1}\left(g-\frac{\gamma}{\gamma+1}\right) \times\left(\Big\{\Big(\mathbf{s}\cdot[\mathbf{v}\times\nabla]\Big),\Big[\mathbf{s}\times[\mathbf{E}\times\mathbf{v}]\Big]\Big\} +\Big\{\Big[\mathbf{s}\times[\mathbf{v}\times\nabla]\Big],\Big(\mathbf{s}\cdot[\mathbf{E}\times\mathbf{v}]\Big)\Big\}\right). \tag{11}$$

Equations (10) and (11) are valid both for particles and for nuclei.[5)] There is no fundamental difference between them in describing the motion of a spin, since nuclei, in just the same way as almost all particle species, are composite objects. Since both particles and nuclei are bound by strong interaction, the effect of their internal structure on the interaction with an electromagnetic field can be disregarded in many cases.

The equation of motion of a spin is broken down into two parts that are described by Eqs. (10) and (11). When particles and nuclei are channeled in straight crystals, the term that is linear in spin [see Eq. (10)] does not contribute to the motion of a spin. In the case of channeling in bent crystals, however, it is one to two orders of magnitude greater than the terms of second order in spin, which are given by Eq. (11). At the same time, the presence of quadratic terms leads to the important effect of spin oscillations [35].

[5)]The nuclear-spin operator is traditionally denoted by $\mathbf{I}$. To avoid confusion, however, we reserve the former notation $\mathbf{s}$ for this operator in the formulas that are given below.

Let us first consider the motion of a spin in straight crystals. The second term in Eq. (11) is negligibly small even for light nuclei. By way of example, we indicate that, for relativistic deuterons, the result that this term yields for the spin-rotation angle per unit of the traveled distance is about 10^{-6} rad/cm at $|\partial E_x/\partial x|\sim 10^{22}$ V/m^2. Such small values of the spin-rotation angle cannot be observed experimentally. We can therefore disregard the second term in Eq. (11) and represent it as

$$\left(\frac{d\mathbf{s}}{dt}\right)_{q} = \frac{Q}{2s(2s-1)}\Big\{[\mathbf{s}\times\mathbf{e}_x],s_x\Big\}\frac{\partial E_x}{\partial x}. \tag{12}$$

It can easily be seen that $ds_x/dt=0$, whence it follows that, in straight crystals, the spin rotates about the x axis. Equation (12) is not trivial because it describes the rotation of the spin of not only nonrelativistic but also relativistic particles. By analogy with Eq. (9), we can introduce here the operator $\mathbf{\Omega}$ of the angular velocity of spin precession as

$$\mathbf{\Omega} = -\frac{Q}{2s(s-1)}\{\mathbf{e}_x,s_x\}\frac{\partial E_x}{\partial x}.$$

Since the angular velocity $\Omega=|\mathbf{\Omega}|$ of spin precession is independent of the particle energy, the spin-rotation angle φ per unit length is in inverse proportion to the velocity,

$$\frac{\Delta\varphi}{\Delta l}=\frac{\Omega}{v}=\frac{Q}{s(2s-1)}\frac{1}{v}\left|s_x\frac{\partial E_x}{\partial x}\right|.$$

The spin-rotation angle is minimal at $v\approx c$, in which case it assumes a value of $(\Delta\varphi/\Delta l)_{\min}\sim|Q(\partial E_x/\partial x)|$. Since the quadrupole moment of the deuteron is small, the spin-rotation angle is small for deuterons: $(\Delta\varphi/\Delta l)_{\min}\sim 10^{-4}$ rad/cm. For nuclei having a large quadrupole moment, however, this quantity is accessible to experimental observations.

From (12), it follows that the direction of spin rotation is invariant under the reversal of the sign of the spin projection; at the same time, the angular-velocity vector is reversed in this case.

Let us now discuss channeling through a bent crystal. The presence of the term linear in spin then leads to a spin rotation through large angles about the z axis. From Eq. (10), it follows that, for this geometry, the spin-rotation angle per unit length is given by

$$\frac{\Delta\varphi}{\Delta l}=\frac{e}{2m}\left(g-2+\frac{2}{\gamma+1}\right)|\bar{E}_x|,$$

where $|\bar{E}_x|$ is the absolute value of the electric-field strength (it depends on the bend of the crystal). It is well known that the spin-rotation angle is then given by the Lyuboshitz formula [36], which is valid both in

Spin-rotation angle for nuclei traversing bent crystals

Nucleus	Spin	Mass, amu	μ/μ_N	Energy, GeV	Radius of the crystal bend, m	g	γ	$\Delta\varphi/\Delta l$, rad/cm
^{2}H	1	2.014102	+0.8574			+1.714	213	−0.10
^{6}Li	1	6.015122	+0.8220			+4.91	71.4	0.35
^{7}Li	3/2	7.016004	+3.2564	400	3	+15.11	61.2	1.34
^{9}Be	3/2	9.012182	−1.1775			−7.02	47.6	−0.71

classical and in quantum theory [37] and which has the form

$$\varphi = \left(\frac{\gamma-1}{\gamma} + \frac{g-2}{2}\frac{\gamma^2-1}{\gamma}\right)\theta, \quad \theta = \frac{l}{R}, \qquad (13)$$

where θ is the mean momentum-rotation angle, l is the traveled distance, and R is the radius of the crystal bend. For ultrarelativistic ($\gamma \gg 1$) particles, this expression reduces to the formula

$$\varphi = \frac{(g-2)\gamma}{2}\theta,$$

which was previously obtained by Baryshevskiĭ [1]. The spin-rotation angle the per unit length is given by

$$\frac{\Delta\varphi}{\Delta l} = \left(\frac{\gamma-1}{\gamma} + \frac{g-2}{2}\frac{\gamma^2-1}{\gamma}\right)\frac{1}{R}. \qquad (14)$$

From (13), it follows that, since $\theta \ll 1$, large spin-rotation angles can be obtained only under the condition $\gamma \gg 1$; that is, the nuclei involved must be ultrarelativistic. Since the g factor increases with increasing mass of the nuclei, a rotation through a given angle can be attained at a smaller value of the Lorentz factor γ for heavier nuclei.

In the case of channeling that occurs in bent crystals, spin motion due to the second-order terms in spin leads to simultaneous rotations about the x and the z axis. In this case, the spin oscillates [35], so that the spin projection onto the z axis is not conserved.

5. DISCUSSION OF THE RESULTS AND CONCLUSIONS

At present, the validity of the Bargmann–Michel–Telegdi equation [6] has been proven experimentally only for spin-1/2 particles. Previously, a quantum-mechanical derivation of this equation was given in [8, 9] precisely for such particles. The authors of [18, 19] presented a quantum-mechanical derivation of the Bargmann–Michel–Telegdi equation for particles of arbitrary spin and determined terms in the Lagrangian that are of second order in the spin. These important results call for an experimental verification, since there were some problems in rendering the results from [18, 19] consistent with the existing theory of spin-1 particles. This is reason why, in the present study, the quantum-mechanical equation of motion of the spin of spin-1 particles having an anomalous magnetic moment has been derived on the basis of Proca theory. Our calculation has revealed that this equation corresponds to the Bargmann–Michel–Telegdi equation. This means that, in distinction to what was stated previously in [21–24], we have validated here the Bargmann–Michel–Telegdi equation and the results from [18, 19] for spin-1 particles.

The results obtained in [18, 19] can be verified in experiments of two types. First, investigation of nuclear-spin rotation in the case of planar channeling in straight crystals makes it possible to test the theoretical description that those studies provide for second-order effects in spin. For nuclei having a large quadrupole moment (on the order of 10^{-24} cm^2), the spin-rotation angle per unit length is about 10^{-2}–10^{-1} rad/cm in this case. By way of example, we indicate that, for ^{25}Na ($I = 5/2, Q = 2.3 \times 10^{-25}$ cm^2), ^{25}Mg ($I = 5/2,\ Q = 2.2 \times 10^{-25}$ cm^2), and ^{153}Eu ($I = 5/2,\ Q = 2.9 \times 10^{-24}$ cm^2), the values of the spin-rotation angle per unit length in a tungsten crystal are 6×10^{-3}, 6×10^{-3}, and 8×10^{-2} rad/cm, respectively.

Second, one can test the conclusion from [18] that the Bargmann–Michel–Telegdi equation is valid (in the linear approximation in spin) for particles of arbitrary spin. Such a test can be implemented in a planar channeling of ultrarelavistic particles through bent crystals. The experimental setting for this case has much in common with that used in [2, 3]. Of particular importance for such experiments is the energy of nuclei; it can be taken to be close to that which was chosen in [2, 3] for experiments with Σ^+ hyperons (375 GeV).

In just the same way as in [2, 3], initial beams can be polarized via scattering on a polarized nuclear target. The resulting polarization of a nuclear beam that has traversed a crystal can be determined by observing the elastic scattering of the beam on a nuclear target (see [38]).

In the channeling of nuclei through bent crystals, the spin-rotation angle per unit length is usually quite large (about 1 rad/cm). For some extremely light nuclei, the results of the calculation of the spin-rotation angle are quoted in the table.

The relations obtained in the present study can be used to determine the magnetic dipole and electric quadrupole moments of short-lived nuclei by measuring the spin-rotation angle in planar channeling through bent and straight crystals, respectively. A short lifetime seriously complicates a determination of nuclear moments by conventional methods, but it does not seem to be an obstacle to finding them from a measurement of the spin-rotation angle in channeling. Investigation of beta-radioactive nuclei is especially promising owing to a high asymmetry of beta decay. By taking advantage of this, one can determine the polarization state of the initial nucleus by recording decay products, a daughter nucleus and an electron (positron). In general, such an experiment can be performed according to a procedure similar to that in experiments pursuing the magnetic moments of short-lived particles, both already performed [2, 3, 39] and planned [40].

ACKNOWLEDGMENTS

I am grateful to Yu.L. Pivovarov for enlightening comments and for a discussion on the results presented in this article.

REFERENCES

1. V. G. Baryshevskiĭ, Pis'ma Zh. Tekh. Fiz. **5**, 182 (1979) [Sov. Tech. Phys. Lett. **5**, 73 (1979)].
2. D. Chen, I. F. Albuquerque, V. V. Baublis, *et al.,* Phys. Rev. Lett. **69**, 3286 (1992).
3. A. V. Khanzadeev, V. M. Samsonov, R. A. Carrigan, and D. Chen, Nucl. Instrum. Methods Phys. Res. B **119**, 266 (1996).
4. A. Ya. Silenko, Poverkhnost, No. 8, 61 (1997).
5. A. Ya. Silenko, Poverkhnost, No. 5, 97 (1998).
6. V. Bargmann, L. Michel, and V. L. Telegdi, Phys. Rev. Lett. **2**, 435 (1959).
7. V. B. Berestetskiĭ, E. M. Lifshitz, and L. P. Pitaevskiĭ, *Quantum Electrodynamics* (Nauka, Moscow, 1989; Pergamon, Oxford, 1982).
8. D. M. Fradkin and R. H. Good, Rev. Mod. Phys. **33**, 343 (1961).
9. A. Ya. Silenko, Teor. Mat. Fiz. **112**, 161 (1997).
10. R. H. Good, Phys. Rev. **125**, 2112 (1962).
11. P. Nyborg, Nuovo Cimento **31**, 1209 (1964); **32**, 1131 (1964).
12. A. I. Solomon, Nuovo Cimento **26**, 1320 (1962).
13. E. Plante, Nuovo Cimento Suppl. **4**, 246 (1966); **4**, 291 (1966); **5**, 944 (1967).
14. K. Rafanelli, Nuovo Cimento A **67**, 48 (1970).
15. V. G. Bagrov and V. A. Bordovitsyn, Izv. Vyssh. Uchebn. Zaved., Fiz., No. 2, 67 (1980).
16. I. M. Ternov and V. A. Bordovitsyn, Usp. Fiz. Nauk **132**, 345 (1980) [Sov. Phys. Usp. **23**, 679 (1980)].
17. S. L. Cherkas, Izv. Nats. Akad. Nauk Belarusi, Ser. Fiz.-Mat. Nauk, No. 3, 79 (1999).
18. A. A. Pomeranskiĭ and I. B. Khriplovich, Zh. Éksp. Teor. Fiz. **113**, 1537 (1998) [JETP **86**, 839 (1998)].
19. A. A. Pomeransky and R. A. Sen'kov, Phys. Lett. B **468**, 251 (1999).
20. D. Zwanziger, Phys. Rev. B **139**, 1318 (1965).
21. W. Tsai and A. Yildiz, Phys. Rev. D **4**, 3643 (1971).
22. T. Goldman and W. Tsai, Phys. Rev. D **4**, 3648 (1971).
23. W. Tsai, Phys. Rev. D **4**, 3652 (1971).
24. J.-F. Roux, Lett. Nuovo Cimento **40**, 63 (1984).
25. F. J. Belinfante, Phys. Rev. **92**, 997 (1953).
26. K. M. Case, Bull. Am. Phys. Soc. (Detroit—Ann Arbor Meeting, Mar. 1954).
27. C. R. Hagen and W. J. Hurley, Phys. Rev. Lett. **24**, 1381 (1970); **25**, 197 (1970); W. J. Hurley, Phys. Rev. D **3**, 2339 (1971).
28. R. Cecchini, Nuovo Cimento A **43**, 181 (1978).
29. R. Cecchini and M. Tarlini, Nuovo Cimento A **47**, 1 (1978).
30. A. Ya. Silenko, in *Proceedings of the XXIX International Conference on the Physics of Charged-Particle Interaction with Crystals* (Mosk. Gos. Univ., Moscow, 1999), p. 29.
31. J. A. Young and S. A. Bludman, Phys. Rev. **131**, 2326 (1963).
32. L. L. Foldy and S. A. Wouthuysen, Phys. Rev. **78**, 29 (1950).
33. K. M. Case, Phys. Rev. **95**, 1323 (1954).
34. D. L. Weaver, Phys. Rev. D **14**, 2824 (1976).
35. V. G. Baryshevsky and A. G. Shechtman, Nucl. Instrum. Methods Phys. Res. B **83**, 250 (1993).
36. V. L. Lyuboshits, Yad. Fiz. **31**, 986 (1980) [Sov. J. Nucl. Phys. **31**, 509 (1980)].
37. A. Ya. Silenko, Zh. Éksp. Teor. Fiz. **107**, 1240 (1995) [JETP **80**, 690 (1995)].
38. S. De Benedetti, *Nuclear Interactions* (Wiley, New York, 1964; Atomizdat, Moscow, 1968).
39. V. V. Baublis, I. V. Ivanov, I. G. Ivochkin, *et al.,* Nucl. Instrum. Methods Phys. Res. B **90**,150 (1994).
40. V. M. Samsonov, Nucl. Instrum. Methods Phys. Res. B **119**, 271 (1996).

Translated by A. Isaakyan

Physics of Atomic Nuclei, Vol. 64, No. 5, 2001, pp. 990–993. Translated from Yadernaya Fizika, Vol. 64, No. 5, 2001, pp. 1061–1065.

XXX International Conference on the Physics of Interaction of Fast Charged Particles with Matter

Propagation of Fast Charged Particles along a Nanotube

N. F. Shul'ga*, A. A. Greenenko, V. I. Truten, and S. P. Fomin

Kharkov Institute for Physics and Technology, ul. Akademicheskaya 1, Kharkov, 310108 Ukraine

Received November 4, 2000

Abstract—The results obtained by investigating the motion of fast charged particles in a nanotube along its axis are presented. It is shown that dynamical chaos may arise when a positively charged particle moves along the axis of a nanotube. © *2001 MAIK "Nauka/Interperiodica".*

1. INTRODUCTION

A nanotube is a hollow cylinder whose surface is formed by regularly spaced carbon atoms. The diameter of a nanotube may range up to several tens of angstrom. Modern technologies make it possible to prepare a nanotube of length a few hundred micrometers [1, 2]. In recent years, much attention has been given to effects associated with the propagation of a beam of charged particles along nanotubes, because such structures offer new possibilities for controlling beam parameters and for generating electromagnetic radiation [3–6]. In [3–5], the motion of fast particles in a nanotube along its axis was described in the continuous-surface-potential approximation, where the potential of the atoms forming the nanotube is averaged over its surface. In such a field, a particle can execute a finite motion along the nanotube axis. The continuous surface potential of a nanotube is axisymmetric; hence, any finite motion of a particle in such a field is regular and quasiperiodic. However, it is not always correct to describe particle motion in a nanotube within this approximation. In just the same way as in the case of particle channeling in a crystal [7, 8], the potential of a nanotube can sometimes be represented as the sum of the continuous potentials of individual atomic chains on the nanotube surface that are parallel to the nanotube axis. The continuous potential of the set of atomic chains of a nanotube then differs substantially from an axisymmetric potential. In the present study, we focus on some features of such a potential of a nanotube and on some special properties of a finite motion of positively charged particles in such a field. In particular, we present typical trajectories and the Poincaré sections for a finite motion of a positively charged particle in a nanotube. It is shown that, in the continuous potential of the atomic chains in a nanotube, a particle can execute not only a regular but also a chaotic motion.

*e-mail: shulga@kipt.kharkov.ua

2. DESCRIPTION OF THE MODEL

In many respects, the problem of the motion of a fast charged particle in the field of a nanotube along its axis is similar to the problem of the motion of a particle in an oriented crystal along some of its crystallographic axes (see [7, 8] and references therein). Therefore, the motion of a particle in the field of a nanotube can be described in terms of the theory of particle channeling in a crystal. We now proceed to consider the motion of a fast charged particle in the field of a nanotube along its axis, relying on this analogy. The continuous potential of a nanotube can be determined by averaging the total potential of atoms forming the nanotube over its axis (z axis):

$$U(\boldsymbol{\rho}) = \frac{1}{L}\sum_n \int u(\mathbf{r} - \mathbf{r}_n)\, dz. \qquad (1)$$

Here, $\boldsymbol{\rho}$ stands for coordinates in the plane orthogonal to the nanotube axis, $u(\mathbf{r} - \mathbf{r}_n)$ is the potential of the nanotube atom occurring at the point $\mathbf{r}_n$, and L is the nanotube length. The atoms in a nanotube are located at the vertices of hexagons that are arranged periodically over the nanotube surface. In such an arrangement, the hexagons can be differently oriented with respect to the nanotube axis, the continuous potential of the nanotube being dependent on their orientation.

Typical configurations of the continuous nanotube potential that correspond to the (10, 0) and (10,1) orientations of the hexagons on the nanotube surface are shown in Figs. 1 and 2, respectively. As in the case of a crystal, the continuous nanotube potential in the cases being considered is the sum of the continuous potentials of isolated atomic chains. However, the atomic chains in a nanotube are arranged periodically over the nanotube surface, in contrast to the arrangement of atoms in a crystal. As a result, the total potential of the atomic chains develops a deep and wide well for a positively charged particle inside the nanotube. It follows that, as in the case

1063-7788/01/6405-0990$21.00

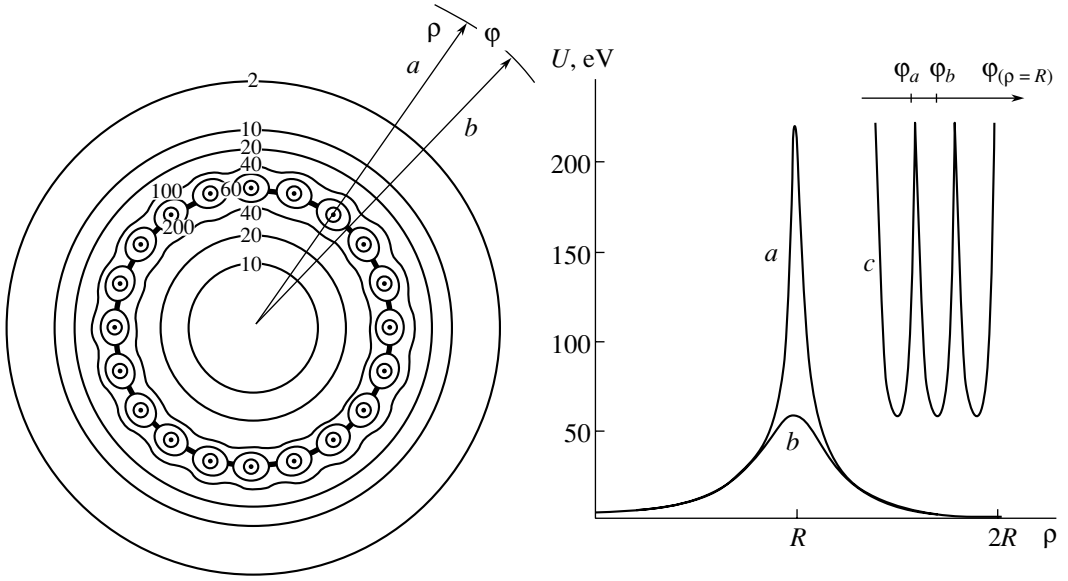

Fig. 1. Equipotential surfaces of the continuous potential of a (10, 0) nanotube. The right panel displays the potential plotted versus (*a*, *b*) the radial distance from the nanotube axis and (*c*) the azimuthal angle φ at the radial distance R equal to the nanotube radius. The numbers on the lines indicate the potential energy of the interaction of a proton with the nanotube (in eV).

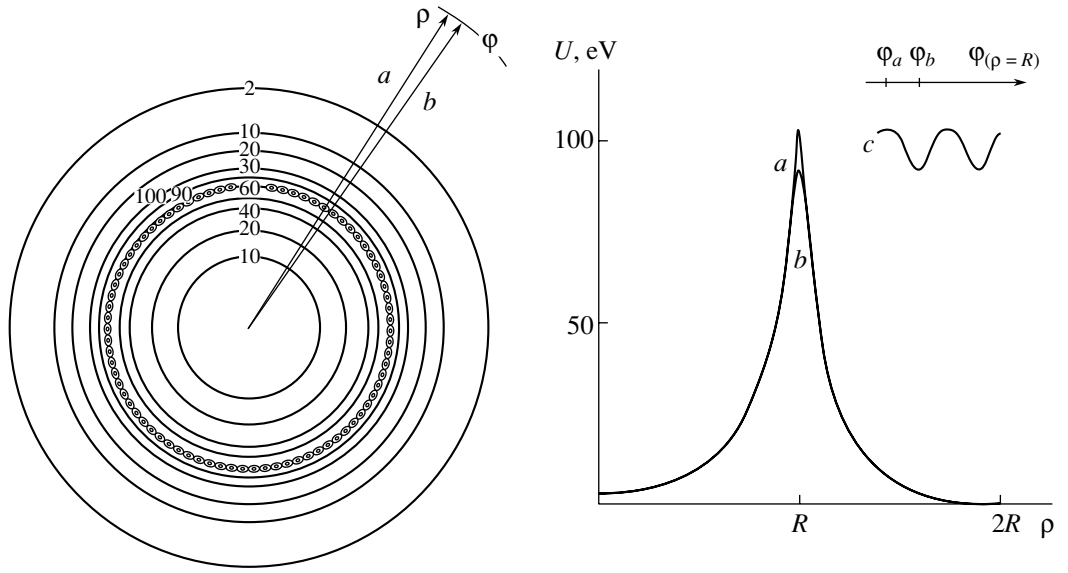

Fig. 2. As in Fig. 1, but for a (10,1) nanotube.

of channeling in a crystal, a particle can execute here a finite motion along the axis of a nanotube. For negatively charged particles, the potential well is very close to the nanotube surface, so that such particles can execute a finite motion only near the nanotube surface.

A finite motion of a particle in the continuous field of a nanotube was investigated in [3–5] by using the nanotube potential averaged over the azimuthal angle φ:

$$U(\boldsymbol{\rho}) = \frac{1}{2\pi}\int_0^{2\pi} d\varphi U(\boldsymbol{\rho}). \qquad (2)$$

This approximation is justified if the particles cannot approach closely the nanotube surface or if the continuous potential of the nanotube depends only slightly on the azimuthal angle φ [this condition is satisfied for a (10,1) nanotube].

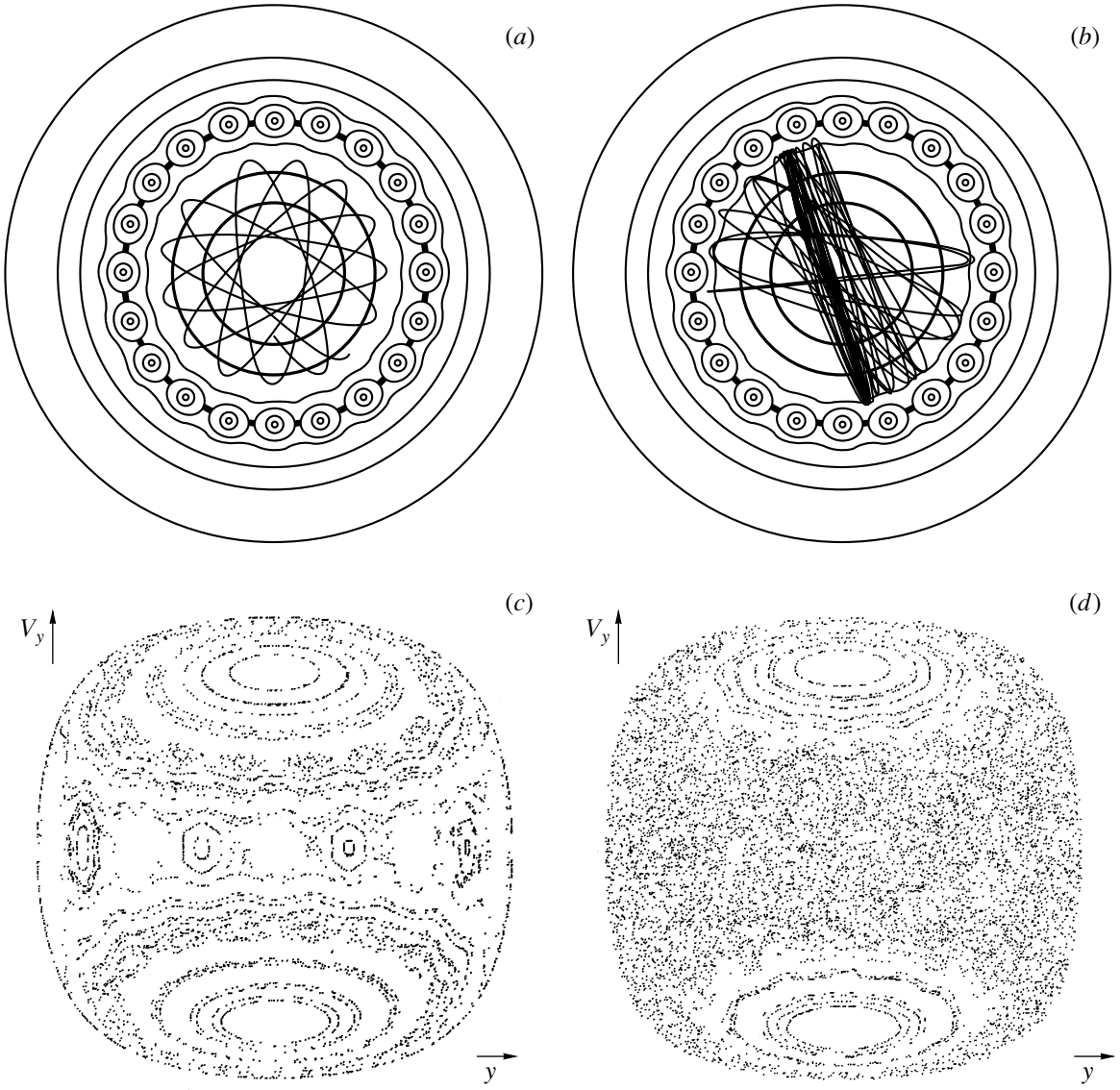

Fig. 3. (*a*, *b*) Typical trajectories and (*c*, *d*) Poincaré sections for the finite motion of fast protons in the field of a (10,0) nanotube at the transverse-motion energies of (*a*, *b*) 30 eV and (*c*, *d*) 50 eV.

From the equipotential surfaces in Fig. 1, it can be noticed that the shape of the potential in the immediate vicinity of the nanotube surface may deviate considerably from an axisymmetric shape. This deviation is readily illustrated in Figs. 1 and 2, where the potential is plotted versus (*a*, *b*) the radial distance from the nanotube axis and (*c*) the azimuthal angle at the radial distance R equal to the nanotube radius.

Thus, the equipotential surfaces demonstrate that the motion of particles that closely approach the nanotube surface may differ substantially from motion in the axisymmetric field (2). In what follows, we briefly discuss some features of particle motion in the field of a nanotube that are associated with the violation of axial symmetry in the nanotube potential.

3. RESULTS AND DISCUSSION

The longitudinal component $p_\parallel$ of the momentum of a fast particle moving along the axis of the nanotube (z axis) in its continuous field (1) is conserved. In just the same way as in the case of particle channeling in a crystal, the motion of a particle in the continuous field of a nanotube is described by the two-dimensional equation of motion in the plane orthogonal to the nanotube axis; that is,

$$\ddot{\boldsymbol{\rho}} = -\frac{1}{\varepsilon_\parallel}\frac{\partial}{\partial \boldsymbol{\rho}} U(\boldsymbol{\rho}), \qquad (3)$$

where $\varepsilon_\parallel = \sqrt{p_\parallel^2 + m^2}$ and $U(\boldsymbol{\rho})$ is given by Eq. (1). For high-energy particles, $\varepsilon_\parallel$ is close to the total particle energy ε, $\varepsilon_\parallel \approx \varepsilon$.

For Eq. (3), the first integral of the motion represents the energy of the transverse motion of a particle,

$$\varepsilon_\perp(\boldsymbol{\rho}_0) = \frac{\varepsilon\dot{\boldsymbol{\rho}}^2}{2} + U(\boldsymbol{\rho}). \quad (4)$$

It is determined by the point at which the particle enters the nanotube endface and by its angle of incidence ψ,

$$\varepsilon_\perp(\boldsymbol{\rho}_0) = \varepsilon_\perp + U(\boldsymbol{\rho}_0), \quad (5)$$

where $\varepsilon_\perp = \varepsilon\psi^2/2$. Depending on the values of ψ and $\boldsymbol{\rho}_0$, a particle in the nanotube can execute either finite or infinite motion. In what follows, we will consider the features of the finite motion of positively charged particles in the field of a nanotube. A positively charged particle executes a finite motion in a nanotube if $\boldsymbol{\rho}_0 < R$ (R is the nanotube radius) and if the energy of the transverse motion, $\varepsilon_\perp(\boldsymbol{\rho}_0)$, is small in relation to the depth of the nanotube potential well, $U_{\max}$.

If the continuous potential of the nanotube is close to the axisymmetric potential (2), the angular momentum of transverse motion becomes conserved, in addition to the energy of transverse motion. In this case, the two variables in the equation of motion (3) are separated, and the motion of a particle in a nanotube is regular and quasiperiodic.

If the axial symmetry of the nanotube potential is severely violated, as in the case shown in Fig. 1, then the motion of a particle in the field of the nanotube may be very intricate—it may be either regular or chaotic. This is illustrated in Fig. 3, which shows (*a*, *b*) typical trajectories of a particle in the continuous field of a nanotube at various energies of transverse motion and (*c*, *d*) the corresponding Poincaré sections. A method for obtaining Poincaré sections is outlined in [8, 9].

Our results indicate that, at small values of the energy of transverse motion (when the particle being considered cannot approach the surface of a nanotube; see Fig. 3*a*), the motion of the particle is regular (quasiperiodic) for almost all initial conditions. This is because, in this case, the particle moves in the domain where the continuous nanotube potential is approximately axisymmetric.

If the energy of transverse motion is close to the maximum depth of the potential well, the motion of a particle in the field of a nanotube is chaotic for significant part of initial conditions (see Fig. 3*b*). Thus, a positively charged fast particle moving along the axis of a nanotube may chaotically oscillate in its continuous field—that is, there arises dynamical chaos.

In studying radiation associated with the propagation of particles along a nanotube and in determining the time over which a particle resides in a nanotube, it is important to take into account the above type of dynamical chaos. The point is that, when a particle executes a regular motion in a potential well, radiation from this particle occurs at regular intervals, so that interference effects are significant. This gives rise to sharp peaks at definite frequencies in the radiation spectrum. However, chaotic motion destroys interference effects, and the radiation spectrum appears to be a slowly varying function of frequency.

ACKNOWLEDGMENTS

This work was supported in part by the International Association for the Promotion of Cooperation with Scientists from the Independent States of the Former Soviet Union (grant no. INTAS-97-30392).

REFERENCES

1. A. V. Eletskiĭ, Usp. Fiz. Nauk **167**, 945 (1997) [Phys. Usp. **40**, 899 (1997)].
2. J. W. Mintmire, B. I. Dunlap, and C. I. White, Phys. Rev. Lett. **68**, 631 (1992).
3. V. V. Klimov and V. S. Letokhov, Phys. Lett. A **222**, 424 (1996).
4. L. A. Gevorgian, K. A. Ispirian, and R. K. Ispirian, Nucl. Instrum. Methods Phys. Res. B **145**, 155 (1998).
5. G. V. Dedkov, Nucl. Instrum. Methods Phys. Res. B **143**, 584 (1998).
6. X. Artru, in *Book of Abstracts of the IV International Symposium Radiation from Relativistic Electrons in Periodic Structures, Lake Baikal, Russia, 1999,* p. 27.
7. D. S. Gemmell, Rev. Mod. Phys. **46**, 129 (1974).
8. A. I. Akhiezer and N. F. Shul'ga, *High-Energies Electrodynamics in Media* (Nauka, Moscow, 1993).
9. A. J. Lichtenberg and M. A. Lieberman, *Regular and Stochastic Motion* (Springer-Verlag, New York, 1982; Mir, Moscow, 1984).

Translated by R. Rogalyov

Physics of Atomic Nuclei, Vol. 64, No. 5, 2001, pp. 994–998. Translated from Yadernaya Fizika, Vol. 64, No. 5, 2001, pp. 1066–1070.

XXX International Conference on the Physics of Interaction of Fast Charged Particles with Matter

Transition Radiation from a Relativistic Electron Obliquely Incident on a Thin Metal Plate of Finite Transverse Dimensions

S. N. Dobrovolsky* **and N. F. Shul'ga****

Kharkov Institute for Physics and Technology, Akademicheskaya ul. 1, Kharkov, 310108 Ukraine

Received November 4, 2000

Abstract—The problem of transition radiation generated by the oblique motion of a relativistic electron through a thin metal plate of finite transverse dimensions is considered. The expressions for the spectral and angular densities of radiation emitted forward and backward are obtained. It is shown that, in the millimeter and the submillimeter range, the spectra of both forward and backward radiation for targets of finite transverse dimensions can differ substantially from the corresponding spectra for an infinite plate.

1. INTRODUCTION

In [1, 2], we considered infrared transition radiation generated by a relativistic electron traversing a thin plate of finite transverse dimensions at a right angle. We showed that both the longitudinal and the transverse dimension of a target can significantly affect the radiation intensity. This is because the longitudinal and the transverse dimension of the region where the radiation is formed are both macroscopic. If the transverse dimension of the formation region, $\lambda\gamma$ (λ is the radiation wavelength, and γ is the electron Lorentz factor), is commensurate with the transverse dimension of the target or exceeds it, the intensity of the transition radiation is much lower than that in the case of an infinite plate. The effect might be significant under the conditions of experiments reported in [3, 4]. The transition radiation from a relativistic electron obliquely incident on a target is of special interest. The reason is that, in this case, the bulk of transition radiation into the backward hemisphere (backward radiation) is not emitted along the particle trajectory. This facilitates the detection of the radiation. For the oblique motion of a relativistic electron through an infinite thin metal plate, transition radiation was theoretically analyzed in [5, 6]. The present study aims at analyzing the effect of finite transverse dimensions of the target on transition radiation generated by a relativistic electron obliquely incident to a thin metal target. Here, this is done for the simplest situation where the electron trajectory passes through the center of a thin metal disk.

*e-mail: dobrovolsky@kipt.kharkov.ua
**e-mail: shulga@kipt.kharkov.ua

2. DESCRIPTION OF THE METHOD USED

We consider radiation generated by a relativistic electron whose trajectory passes through the center of a thin metal disk of radius a at an angle ϕ to the z axis directed normally to the target surface (Fig. 1). Without loss of generality, we assume that the electron moves in the zx plane. The target is considered to be thin if its thickness a_z is much less than the radiation wavelength λ. However, we also assume that $a_z \gg \Delta$, where Δ is the depth of field penetration into the target. In this case, that part of the proper field of the electron which missed the screen diffracts on it, whereas that part of the field which hits the screen is completely reflected from it into the backward hemisphere. Within the target, the field of the medium response completely screens the Coulomb field of the electron. As soon as the electron leaves the target, there arises the field associated with the transition radiation in addition to the diffraction field. The former completely screens the proper field of the electron near the target surface.

In order to calculate the spectral and angular radiation density in the problem being considered, it is necessary above all to take into account the boundary conditions at the target surface for the field surrounding the electron. We represent the radiation electric fields in the forward $[\mathbf{E}^{(+)}(\mathbf{r},t)]$ and in the backward $[\mathbf{E}^{(-)}(\mathbf{r},t)]$ hemisphere as the sum of the emitted-radiation field and the proper field of the electron; that is,

$$\mathbf{E}^{(\pm)}(\mathbf{r},t) = \mathbf{E}^{(e)}(\mathbf{r},t) + \mathbf{E}'^{(\pm)}(\mathbf{r},t), \qquad (1)$$

where $\mathbf{E}^{(e)}(\mathbf{r},t)$ is the proper field of the electron, while $\mathbf{E}'^{(+)}(\mathbf{r},t)$ and $\mathbf{E}'^{(-)}(\mathbf{r},t)$ are the radiation fields in the forward and the backward hemisphere, respectively. The field $\mathbf{E}'^{(+)}(\mathbf{r},t)$ is the sum

1063-7788/01/6405-0994$21.00

of the diffraction-radiation field $\mathbf{E}^{(d)}(\mathbf{r},t)$ and the transition-radiation field $\mathbf{E}^{(\mathrm{tr})}(\mathbf{r},t)$ [1, 2]:

$$\mathbf{E}'^{(+)}(\mathbf{r},t)=\mathbf{E}^{(d)}(\mathbf{r},t)+\mathbf{E}^{(\mathrm{tr})}(\mathbf{r},t). \qquad (2)$$

By using the boundary conditions for the tangential and the normal component of the electric field and for the electric displacement vectors at the target surface (see [5, 6]), we find that the radiation field $\mathbf{E}'^{(\pm)}(\mathbf{r},t)$ in the target plane ($z=0$) can be represented as

$$\mathbf{E}'^{(\pm)}_{\parallel}(\mathbf{r},t)=-\Theta(a-\rho)\,\mathbf{E}^{e}_{\parallel}(\mathbf{r},t),$$
$$\mathbf{E}'^{(\pm)}_{\perp}(\mathbf{r},t)=\Theta(a-\rho)\,\mathbf{E}^{e}_{\perp}(\mathbf{r},t), \qquad (3)$$

where $\mathbf{E}'^{(\pm)}_{||}(\mathbf{r},t)$ and $\mathbf{E}'^{(\pm)}_{\perp}(\mathbf{r},t)$ ($\mathbf{r}=\boldsymbol{\rho}+z\mathbf{e}_z$, $\mathbf{e}_z$ being a unit vector along the z axis) are the radiation-field components parallel and orthogonal to the target surface, respectively, and $\Theta(x)$ is the Heaviside step function [$\Theta(x)=1$ for $x\geqslant 0$, and $\Theta(x)=0$ for $x<0$].

The radiation field $\mathbf{E}'(\mathbf{r},t)$ can be represented as a superposition of plane electromagnetic waves of frequency ω and wave vector $\mathbf{k}$; that is,

$$\mathbf{E}'(\mathbf{r},t) \qquad (4)$$
$$=\frac{1}{(2\pi)^4}\int d\mathbf{k}d\omega e^{i(k\cdot r-\omega t)}\mathbf{E}_{\mathbf{k},\omega}\delta\left(\frac{\omega^2}{c^2}-\mathbf{k}^2\right),$$

where $\delta\left(\omega^2/c^2-\mathbf{k}^2\right)$ is a Dirac delta function, c is the speed of light, and $\mathbf{E}_{\mathbf{k},\omega}$ stands for expansion coefficients determined by condition (2). Using (2) and (4), we obtain the Fourier components $\mathbf{E}'_{\boldsymbol{\chi},\omega}(z)$ of the radiation fields with respect to time and transverse coordinates in the form

$$\mathbf{E}'^{(\pm)}_{\parallel\boldsymbol{\chi},\omega}(z) \qquad (5)$$
$$=-e^{\pm iz\sqrt{k^2-\chi^2}}\int\limits_{S_2}d^2\rho'\mathbf{E}^{(e)}_{\parallel\omega}\left(\boldsymbol{\rho}',z=0\right)e^{-i\boldsymbol{\chi}\cdot\boldsymbol{\rho}'},$$
$$\mathbf{E}'^{(\pm)}_{\perp\boldsymbol{\chi},\omega}(z)$$
$$=e^{\pm iz\sqrt{k^2-\chi^2}}\int\limits_{S_2}d^2\rho'\mathbf{E}^{(e)}_{\perp\omega}\left(\boldsymbol{\rho}',z=0\right)e^{-i\boldsymbol{\chi}\cdot\boldsymbol{\rho}'},$$

where $\mathbf{E}^{(e)}_{\omega}(\boldsymbol{\rho},z)$ is the time Fourier component of the proper field of the electron, while $\boldsymbol{\chi}$ is the transverse component of the wave vector $\mathbf{k}$ ($\mathbf{k}=\boldsymbol{\chi}+k_z\mathbf{e}_z$). Integration in the $z=0$ plane is performed over the area S_2 occupied by the screen.

In order to find the Fourier components of the radiation field $\mathbf{E}'^{(\pm)}_{\boldsymbol{\chi},\omega}(z)$, it is therefore necessary to know, in the $z=0$ plane, the Fourier component of the Coulomb field of a relativistic electron moving at a velocity $\mathbf{v}$ forming an angle ϕ with the z axis. For this purpose, we use the Fourier expansion of the proper field of the electron in a vacuum [5–7]. We have

$$\mathbf{E}^{(e)}_{\omega}(\mathbf{r}) \qquad (6)$$
$$=\frac{ie\omega}{\pi v_z c}\int d^3k e^{i\mathbf{k}\cdot\mathbf{r}}\frac{\left(\beta\dfrac{\mathbf{v}}{v}-\dfrac{c\mathbf{k}}{\omega\varepsilon}\right)}{\left(k^2-\dfrac{\omega^2}{c^2}\varepsilon\right)}\delta\left(\frac{\omega}{v_z}-\frac{\mathbf{k}\cdot\mathbf{v}}{v_z}\right),$$

where $\beta=v/c$.

To terms of order γ^{-1}, the proper field of a relativistic electron can be considered to be transverse with respect to its velocity (see [5, 6]). To terms of order γ^{-2}, the field of the electron that moves in a vacuum in the zx plane at a velocity $\mathbf{v}$ at an angle ϕ to the z axis can be represented in the form

$$\mathbf{E}^{(e)}_{\omega}(\boldsymbol{\rho},z)\approx\frac{e\omega}{v_z^2\gamma}2K_1\left(\frac{\omega\rho}{v\gamma}\sqrt{1+\sin^2\phi\frac{z^2-x^2}{\rho^2}-\sin 2\phi\frac{zx}{\rho^2}}\right) \qquad (7)$$
$$\times\frac{\boldsymbol{\rho}-\sin\phi\left(\mathbf{e}_x\left[z\cos\phi+x\sin\phi\right]+\mathbf{e}_z\left[x\cos\phi-z\sin\phi\right]\right)}{\rho\sqrt{1+\sin^2\phi\frac{z^2-x^2}{\rho^2}-\sin 2\phi\frac{zx}{\rho^2}}}\exp\left[i\frac{\omega}{v_z}\left(z\cos\phi+x\sin\phi\right)\right],$$

where K_1 is a Macdonald function of the first order [8] and $\boldsymbol{\rho}=x\mathbf{e}_x+y\mathbf{e}_y$, $\mathbf{e}_x$, and $\mathbf{e}_y$ being unit vectors along the x and y axes, respectively.

Substituting (7) into (5) and considering that the integration surface is the surface of a disk of radius a, we represent the Fourier components of the forward- and the backward-radiation field as

$$\mathbf{E}'^{(\pm)}_{\boldsymbol{\chi},\omega}(z)=\frac{2e\omega}{v_z^2\gamma}\int\limits_{-\pi}^{\pi}\int\limits_{0}^{a}\rho d\rho d\alpha K(\rho,\phi,\alpha) \qquad (8)$$
$$\times\left[\pm\cos\alpha\cos\phi\left(\mathbf{e}_x\cos\phi+\mathbf{e}_z\sin\phi\right)+\mathbf{e}_y\sin\alpha\right]$$
$$\times\exp\left[-i\left(\boldsymbol{\chi}\cdot\boldsymbol{\rho}\pm z\sqrt{k^2-\chi^2}-\frac{\omega\rho}{v_z}\cos\alpha\sin\phi\right)\right],$$

where

$$K(\rho,\phi,\alpha)=\frac{K_1\left(\dfrac{\omega\rho}{v_z\gamma}\sqrt{1-\sin^2\phi\cos^2\alpha}\right)}{\sqrt{1-\sin^2\phi\cos^2\alpha}},$$
$$\chi=\omega c^{-1}\sin\vartheta,$$

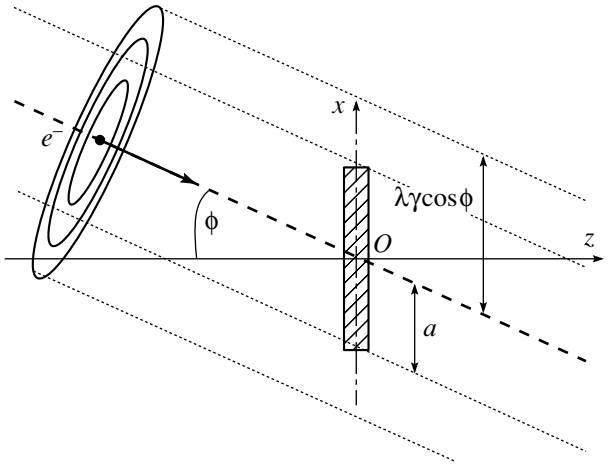

Fig. 1. Oblique incidence of a relativistic electron on a thin metal disk.

and the angle ϑ determines the direction of radiation.

3. RESULTS AND DISCUSSION

For the spectral and angular densities of the electromagnetic-energy flux in the forward (plus sign) and the backward (minus sign) hemisphere through the detector surface xy at a distance $z = z_0$ from the target, we have [5, 6]

$$\frac{d^3S_z^{(\pm)}}{d\omega\, d\Omega} = \frac{1}{(2\pi)^4 c}\omega^2 \left|\left[\mathbf{E}'^{(\pm)}_{\boldsymbol{\chi},\omega}(z_0) \times \mathbf{H}'^{(\pm)}_{-\boldsymbol{\chi},-\omega}(z_0)\right]\cdot \mathbf{e}_z\right|, \tag{9}$$

where $\mathbf{H}'_{\boldsymbol{\chi},\omega}(z)$ is the vector of the radiation magnetic field. For forward radiation, expression (9) is meaningful only at large distances z_0 from the target, where the radiation field can be separated from the proper field of the particle involved. At smaller distances, it is necessary to take into account the interference between these fields (see [1]). For backward radiation, expression (9) is valid at arbitrary distances from the target.

Expressing $\mathbf{H}'_{\boldsymbol{\chi},\omega}(z)$ in terms of $\mathbf{E}'_{\boldsymbol{\chi},\omega}(z)$ (see [7]) and using (8), we find for $\cos\phi \gg \gamma^{-1}$ that the spectral and angular density of the electromagnetic-energy flux of forward and backward radiation that traverses the $z = z_0$ plane is given by

$$\frac{d^3S_z^{(\pm)}}{d\omega\, d\Omega} = \frac{e^2}{\pi^2 c}\,\beta^2\cos^2\phi\,\frac{|(\sin\vartheta - \beta\sin\phi\cos\varphi)^2 + \beta^2\sin^2\phi\cos^2\vartheta\sin^2\varphi|A^2 + \sin^2\vartheta\cos^2\vartheta\sin^2\varphi(B^2 - A^2)}{\left[(1-\beta\sin\phi\sin\vartheta\cos\varphi)^2 - \beta^2\cos^2\vartheta\cos^2\varphi\right]^2}. \tag{10}$$

Here, the angle ϑ for forward and backward radiation is reckoned from, respectively, the positive and the negative direction of the z axis; φ is the azimuthal angle of radiation; and

$$A = \frac{\int\limits_{-\pi}^{\pi} d\alpha \int\limits_0^u tdtK(t,\phi,\alpha)\cos\alpha\exp\left[-it\gamma\cos\alpha(\sin\vartheta\cos\varphi - \beta\sin\phi) - it\gamma\beta\sin\alpha\sin\vartheta\sin\varphi\right]}{\int\limits_{-\pi}^{\pi} d\alpha \int\limits_0^\infty tdtK(t,\phi,\alpha)\cos\alpha\exp\left[-it\gamma\cos\alpha(\sin\vartheta\cos\varphi - \beta\sin\phi) - it\gamma\beta\sin\alpha\sin\vartheta\sin\varphi\right]},$$
$$B = \frac{\int\limits_{-\pi}^{\pi} d\alpha \int\limits_0^u tdtK(t,\phi,\alpha)\sin\alpha\exp\left[-it\gamma\cos\alpha(\sin\vartheta\cos\varphi - \beta\sin\phi) - it\gamma\beta\sin\alpha\sin\vartheta\sin\varphi\right]}{\int\limits_{-\pi}^{\pi} d\alpha \int\limits_0^\infty tdtK(t,\phi,\alpha)\sin\alpha\exp\left[-it\gamma\cos\alpha(\sin\vartheta\cos\varphi - \beta\sin\phi) - it\gamma\beta\sin\alpha\sin\vartheta\sin\varphi\right]}, \tag{11}$$

where

$$u = \frac{\omega a}{v_z\gamma},$$
$$K(t,\phi,\alpha) = \frac{K_1\left(t\sqrt{1-\sin^2\phi\cos^2\alpha}\right)}{\sqrt{1-\sin^2\phi\cos^2\alpha}}.$$

The functions $A(u,\vartheta,\varphi,\gamma,\phi)$ and $B(u,\vartheta,\varphi,\gamma,\phi)$ determine the effect of the transverse dimensions of the target on the radiation generated by a relativistic electron whose trajectory passes through the center of a thin ideally conducting disk at an angle ϕ to the axis of the disk. The expressions obtained for the spectral and angular density of the radiation are valid for arbitrary angles of electron incidence on the target, with the exception of those that correspond to sliding incidence, in which case the condition $\cos\phi \gg$

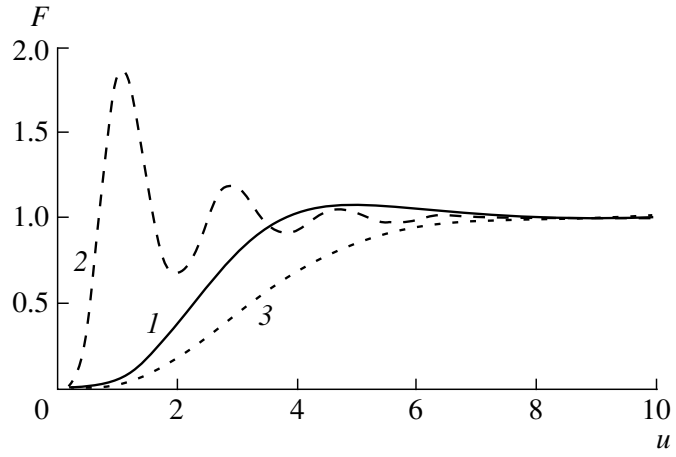

Fig. 2. Function $F = |A(u, \vartheta, \varphi, \gamma, \phi)|^2$ versus the parameter $u = \omega a/v_z\gamma$ at $\phi = \pi/4$, $\gamma = 200$, $\varphi = 0$, and various values of the angle ϑ: $\vartheta = (1)\ \phi + \gamma^{-1}$, $(2)\ \vartheta = \phi + 5\gamma^{-1}$, and $(3)\ \vartheta = \phi + 0.5\gamma^{-1}$.

γ^{-1} is violated. According to (10), the functions $A(u, \vartheta, \varphi, \gamma, \phi)$ and $B(u, \vartheta, \varphi, \gamma, \phi)$ are close to unity for $u \gg 1$. In this case, the spectral and angular density of radiation is identical to that for the case of electron motion through a plate that is infinite in the transverse direction:

$$\frac{d^3S_z^{(\pm)}}{d\omega\, d\Omega} = \frac{e^2}{\pi^2 c}\,\beta^2\cos^2\phi\frac{(\sin\vartheta - \beta\sin\phi\cos\varphi)^2 + \beta^2\sin^2\phi\cos^2\vartheta\sin^2\varphi}{\left[(1-\beta\sin\phi\sin\vartheta\cos\varphi)^2 - \beta^2\cos^2\vartheta\cos^2\varphi\right]^2}. \quad (12)$$

This expression coincides with the corresponding expression obtained in [5, 6].

For $u \ll 1$, the functions $A(x, \vartheta, \varphi, \gamma, \phi)$ and $B(x, \vartheta, \varphi, \gamma, \phi)$ are much smaller than unity. In this region, the spectral and angular density of the radiation is much smaller than that for $u \gg 1$.

It is very difficult to analyze the effect that the transverse size of the disk exerts on the radiation intensity at arbitrary angles of the radiation and arbitrary values of the parameter u. For this reason, we restrict our consideration of the process to the simplest case of $\varphi = 0$. Here, the spectral and angular density of the radiation is determined solely by the function $A(u, \vartheta, \varphi, \gamma, \phi)$ [according to (11), $B(x, \vartheta, \varphi, \gamma, \phi) = 0$ at $\varphi = 0$]. Figure 2 displays the results of numerical calculations for the function $F = |A(u, \vartheta, \varphi, \gamma, \phi)|^2$ at $\phi = \pi/4$, $\gamma = 200$, and various values of the angle ϑ. These results show that, in just the same way as in the case of normal incidence, both forward and backward transition radiation are reduced in relation to the case of an infinite plate in the region $u \leqslant 1$ (that is, when the effective transverse size of the radiation-formation region, $\lambda\gamma\cos\phi$, exceeds the characteristic transverse size of the target, a; see Fig. 1). For backward radiation, this is explained by the fact that a smaller (in relation to the case of an infinite plate) part of the electron field incident on the plate is reflected into the backward hemisphere. For forward radiation, the reduction is due to the diffraction radiation, which significantly contributes to the total energy flux of the emitted radiation for $\lambda\gamma\cos\phi \geqslant a$.

The angular dependence of the spectral and angular distribution (10) of the radiation in the region $u \geqslant 1$ peaks at angles of order $\phi \pm \gamma^{-1}$. The reduction of the radiation intensity does not exhaust changes in the region $u \leqslant 1$—in addition, the main angular maxima are shifted toward larger deviations from the angle of electron incidence, and new oscillating peaks appear.

For electron energies of about 100 MeV, the effective transverse size of the radiation-formation region is macroscopic in the millimeter range of the radiation wavelength. It is comparable with the transverse size of the targets used in the experiments reported in [3, 4]. In such cases, data analysis must rely on expressions (10), which take into account the possible effect of the transverse target dimension on the characteristics of the spectral and angular density of the radiation. Our results show that, in the millimeter and submillimeter ranges, calculations allowing for the transverse dimensions of the target yield a radiation

intensity that can be less than that for an infinite plate by one order of magnitude or more.

REFERENCES

1. N. F. Shul'ga and S. N. Dobrovol'skiĭ, Zh. Éksp. Teor. Fiz. **117**, 668 (2000) [JETP **90**, 579 (2000)].
2. N. F. Shul'ga and S. N. Dobrovol'skiĭ, Poverkhnost, No. 5, 110 (1999).
3. Y. Shibata, K. Ishi, T. Takahashi, *et al.,* Phys. Rev. E **49**, 785 (1994).
4. U. Happek, A. J. Sievers, and E. B. Blum, Phys. Rev. Lett. **67**, 2962 (1991).
5. M. L. Ter-Mikaelian, *High Energy Electromagnetic Processes in Condensed Media* (Akad. Nauk Arm. SSR, Yerevan, 1969; Wiley, New York, 1972).
6. G. M. Garibyan and Yan Shi, *Transition X Rays* (Akad. Nauk Arm. SSR, Yerevan, 1983).
7. L. D. Landau and E. M. Lifshitz, *The Classical Theory of Fields* (Nauka, Moscow, 1988; Pergamon, Oxford, 1975).
8. H. B. Dwight, *Tables of Integrals and Other Mathematical Data* (Macmillan, London, 1961; Nauka, Moscow, 1983).

Translated by M. Kobrinsky

Physics of Atomic Nuclei, Vol. 64, No. 5, 2001, pp. 999–1000. Translated from Yadernaya Fizika, Vol. 64, No. 5, 2001, pp. 1071–1072.

NEWS ITEMS

Georgiĭ Borisovich Khristiansen
May 31, 1927–August 4, 2000

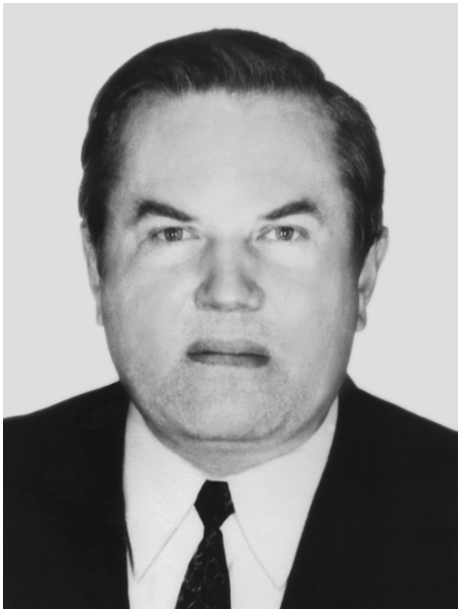

Russian science has suffered a heavy blow. Academician Georiĭ Borisovich Khristiansen, professor at Moscow State University and an eminent scientist in the realms of cosmic-ray and high-energy physics, died on August 4, 2000. He was 73 years old.

G.B. Khristiansen was born in Moscow on May 31, 1927. In 1950, he graduated from the Faculty of Physics at Moscow State University (MSU). Even in his undergraduate years, when he began studying, under the supervision of D.V. Skobel'tsyn and G.T. Zatsepin, ultrahigh-energy cosmic rays at the high-mountain Pamir station of the Lebedev Institute of Physics (USSR Academy of Sciences, Moscow), Khristiansen had cherished keen interest in these realms of physics, which had remained the main subject of his investigations.

Having finished his postgraduate studies (supervised by Skobel'tsyn) at the Nuclear Physics Department of the Faculty of Physics (MSU) in 1953 and received his candidate's degree, Khristiansen, together with S.N. Vernov, was involved in planning and, later on, in creating, at MSU, a new array that was capable of recording extensive atmospheric showers (EAS) generated by cosmic rays of energies 10^{15}–10^{17} eV and which was unique at that time. The Department of Ultrahigh-Energy Particles, which was organized at the Institute of Nuclear Physics (MSU) on the basis of this array, called EAS MSU, was headed by Khristiansen for nearly 40 years.

The discovery of a knee in the energy spectrum of primary cosmic radiation at an energy of about 3×10^{15} eV was the most outstanding result obtained by Khristiansen. In 1970, this result was registered by the Committee for Inventions and Discoveries at the Council of Ministers of the USSR as a scientific discovery. At present, the existence of the knee has been confirmed by the studies of a few tens of laboratories worldwide. However, the problem of this knee and of the interpretation of its nature remains topical in cosmic-ray physics, and arrays aimed at studying it further are still being constructed.

In the early 1970s, a group of researchers headed by Khristiansen performed a detailed comparison of the measured characteristics of EASs with theoretical predictions. This comparison revealed that it would be absolutely incorrect to extrapolate the Feynman scaling model, which was popular in the early 1970s, from the energies of the ISR collider to the energy range 10^{14}–10^{15} eV. This conclusion had been drawn six years before the emergence of its experimental corroboration in experiments at the SPS collider.

The research style of Khristiansen was characterized by a constant quest for new, nonconventional methods that would make it possible to study various facets of cosmic-ray physics. At the very beginning of the operation of the EAS MSU array, he initiated and supervised the fabrication of large-area scintillation counters, which were unknown in the Soviet Union at that time and which were used in detecting atmospheric showers. At the EAS MSU array, Khristiansen investigated the radiation of radio waves that is generated by an extensive atmospheric shower traversing the atmosphere. In the early 1970s, Khristiansen proposed a promising new method that was later dubbed the method of Cherenkov light pulse shape and which made it possible to reconstruct an individual cascade curve of a shower in the atmosphere and to determine simultaneously its energy. This method immediately aroused keen interest. It was used by almost all laboratories worldwide studying EASs to explore their Cherenkov radiation.

Khristiansen played a great part in creating new arrays at various institutes of the Soviet Union and Russia. He supervised the construction of the EAS array at the Samarkand University and was one of

1063-7788/01/6405-0999$21.00

the founding fathers of the giant shower array in Yakutsk. In the late 1980s, Khristiansen headed the work on designing and creating the new EAS-1000 array for studying cosmic rays of extremely high energies (10^{19}–10^{21} eV).

Khristiansen began teaching physics very early. At the Department of Nuclear Physics (Faculty of Physics, MSU), he delivered a number of original lecture courses for students who specialized in cosmic-ray physics. He gave much attention to tutoring students, postgraduates, and young physicists not only from the Faculty of Physics at MSU but also from other physics institutions of both Russia and foreign countries. He created a robust scientific school in the physics of ultrahigh-energy cosmic rays. His disciples successfully work in various fields of physics. For many years, he had been the Chairman of the Dissertation Council of the Higher Certification Commission at MSU.

Khristiansen was elected to corresponding membership and to membership in the Russian Academy of Sciences in 1990 and 1997, respectively. He was awarded a Lenin Prize, a State Prize of the Ukrainian SSR, and a Lomonosov Prize of MSU for his scientific achievements; he was also decorated with the Badge of Honour.

Of great importance was the activity of Khristiansen as a Deputy Chairman of the Scientific Council at the Russian Academy of Sciences for the interdisciplinary problem "Cosmic-Ray Physics," where he was in charge of scientific organization and coordination of studies in cosmic-ray physics in Russia and of regular international conferences on cosmic rays. He was also a member of the Cosmic-Ray Commission of the Union of Pure and Applied Physics at UNESCO.

The memory of Georgiĭ Borisovich Khristiansen will always live in the hearts of his friends and disciples.

G.T. Zatsepin, N.N. Kalmykov, G.F. Krymskiĭ,
G.V. Kulikov, V.A. Matveev, M.I. Panasyuk,
V.A. Rubakov, V.A. Sadovnichiĭ,
A.N. Skrinskiĭ, Yu.A. Fomin